SAPIENZA
UNIVERSITÀ DI ROMA

Department of Drug Chemistry and Technologies

NOVEL *BONA-FIDE* NOXs INHIBITORS AND DUAL EZH2/HDACs EPIGENETIC MODULATORS: INNOVATIVE STRATEGIES TO FIGHT CANCEROUS AND NON-CANCEROUS DISEASES

Beatrice Noce

Ph.D. PROGRAM IN PHARMACEUTICAL SCIENCES

XXXVII cycle

Tutor and Supervisor
Prof. Antonello Mai

Coordinator
Prof. Franco Mazzei

A.Y. 2023/2024

Oh me! Oh life! of the questions of these recurring,
Of the endless trains of the faithless, of cities fill'd with the foolish,
Of myself forever reproaching myself, (for who more foolish than I, and who more faithless?)
Of eyes that vainly crave the light, of the objects mean, of the struggle ever renew'd,
Of the poor results of all, of the plodding and sordid crowds I see around me,
Of the empty and useless years of the rest, with the rest me intertwined,
The question, O me! so sad, recurring—What good amid these, O me, O life?

Answer.

That you are here—that life exists and identity,
That the powerful play goes on, and you may contribute a verse.

Walt Whitman - O me! O Life!

Director of PhD program

Prof. Franco Mazzei

Department of Drug Chemistry and Technologies

Sapienza University of Rome

Scientific Tutor and Main Supervisor

Prof. Antonello Mai

Full Professor in Medicinal Chemistry

Istituto Pasteur - Fondazione Cenci Bolognetti

Department of Drug Chemistry and Technologies

Sapienza University of Rome

Foreign Supervisor

Prof. Francesco Bertoni

Professor at Università della Svizzera Italiana (USI)

Head of the Lymphoma Genomics group

Institute of Oncology Research

Bellinzona, Switzerland

Foreign Tutor

Dr. Afua Adjeiwaa Mensah

Senior Investigator at the Lymphoma Genomics group

Institute of Oncology Research

Bellinzona, Switzerland

LIST OF PUBBLICATIONS

- Cassandri M, Porrazzo A, Pomella S, **Noce B**, Zwergel C, Aiello FA, Vulcano F, Milazzo L, Camero S, Pajalunga D, Spada M, Manzi V, Gravina GL, Codenotti S, Piccione M, Tomaciello M, Signore M, Barillari G, Marchese C, Fanzani A, De Angelis B, Quintarelli C, Vakoc CR, Chen EY, Megiorni F, Locatelli F, Valente S, Mai A, Rota R, Marampon F. HDAC3 genetic and pharmacologic inhibition radiosensitizes fusion positive rhabdomyosarcoma by promoting DNA double-strand breaks. **Cell Death Discov.** 2024 Aug 6;10(1):351. doi: 10.1038/s41420-024-02115-y.
- Fiorentino F, Fabbrizi E, Raucci A, **Noce B**, Fioravanti F, Valente S, Paolini C, De Maria R, Steinkühler C, Gallinari P, Rotili D, Mai A, Uracil- and PyridineContaining HDAC Inhibitors Displayed Cytotoxicity in Colorectal and Glioblastoma Cancer Stem Cells. **ChemMedChem**. 2024 Jul 2; 19(13):e202300655. doi: 10.1002/cmdc.202300655. Epub 2024 Apr 29.
- Reis J, Gorgulla C, Massari M, Marchese S, Valente S, **Noce B**, Basile L, Törner R, Cox III H, Viennet T, Hee Yang M, Ronan M, Rees M, Roth J, Capasso L, Nebbioso A, Altucci L, Mai A, Arthanari H, Mattevi A. Targeting ROS production through isoform-selective inhibition of NADPH oxidase. **Nature Chemical Biology**. 2023 Dec;19(12):1540-1550. doi: 10.1038/s41589-023-01457-5. Epub 2023 Oct 26.
- Zwergel C, Aventaggiato M, Garbo S, Di Bello E, Fassari B, **Noce B**, Castiello C, Beatrice Noce - 3 Lambona C, Barreca F, Rotili D, Fioravanti R, Schmalz T, Weyand M, Niedermeier A, Tripodi M, Colotti G, Steegborn C, Battistelli C, Tafani M, Valente S, Mai A. Novel 1,4-Dihydropyridines as Specific Binders and Activators of SIRT3 Impair Cell Viability and Clonogenicity and Downregulate Hypoxia-Induced Targets in Cancer Cells. **Journal of Medicinal Chemistry**. 2023 Jul 27;66(14):9622-9641. doi: 10.1021/acs.jmedchem.3c00337. Epub 2023 Jul 13.
- **Noce B**, Di Bello E, Fioravanti R, Mai A. LSD1 inhibitors for cancer treatment: Focus on multi-target agents and compounds in clinical trials. **Frontiers in Pharmacology**. 2023 Feb 2;14:1120911. doi: 10.3389/fphar.2023.1120911. eCollection 2023.
- Di Bello E, Sian V, Bontempi G, Zwergel C, Fioravanti R, **Noce B**, Castiello C, Tomassi S, Corinti D, Passeri D, Pellicciari R, Mercurio C, Varasi M, Altucci L, Tripodi M, Strippoli R, Nebbioso A, Valente S, Mai A. Novel pyridine-containing histone deacetylase inhibitors strongly arrest proliferation, induce apoptosis and modulate miRNAs in cancer cells. **European Journal**

of Medicinal Chemistry. 2023 Feb 5;247:115022. doi: 10.1016/j.ejmech.2022.115022. Epub 2022 Dec 15.

- **Front Cover**: Chemically Diverse S. mansoni HDAC8 Inhibitors Reduce Viability in Worm Larval and Adult Stages (ChemMedChem 3/2023). Cover design by **Dr Beatrice Noce** and Dr Elisabetta Di Bello. More information can be found in the Research Article by Beatrice Noce, Antonello Mai et al.
- **Noce B**, Di Bello E, Zwergel C, Fioravanti R, Valente S, Rotili D, Masotti A, Salik Zeya Ansari M, Trisciuoglio D, Chakrabarti A, Romier C, Robaa D, Sippl W, Jung M, Häberli C, Keiser J, Mai A. Chemically Diverse S. mansoni HDAC8 Inhibitors Reduce Viability in Worm Larval and Adult Stages. **ChemMedChem**. 2023 Feb 1;18(3):e202200510. doi: 10.1002/cmdc.202200510. Epub 2022 Nov 8.
- Di Bello E, **Noce B**, Fioravanti R, Zwergel C, Valente S, Rotili D, Fianco G, Trisciuoglio D, Mourão MM, Sales P Jr, Lamotte S, Prina E, Späth GF, Häberli C, Keiser J, Mai A. Effects of Structurally Different HDAC Inhibitors against Trypanosoma cruzi, Leishmania, and Schistosoma mansoni. **ACS Infectious Disease**. 2022 Jul 8;8(7):1356-1366. doi: 10.1021/acsinfecdis.2c00232. Epub 2022 Jun 22.
- Fioravanti R, Rodriguez V, Caroli J, Chianese U, Benedetti R, Di Bello E, **Noce B**, Zwergel C, Corinti D, Viña D, Altucci L, Mattevi A, Valente S, Mai A. Heterocycle-containing tranylcypromine derivatives endowed with high anti-LSD1 activity. **Journal of Enzyme Inhibition and Medicinal Chemistry**. 2022 Dec;37(1):973- 985. doi: 10.1080/14756366.2022.2052869.
- Di Bello E, **Noce B**, Fioravanti R, Mai A. Current HDAC Inhibitors in Clinical Trials. **Chimia**. 2022 April, 76, 448, doi: 10.2533/chimia.2022.448.

Submitted (under-review):

- **Noce B,** Marchese S, Massari M, Reis J, Lambona C, Raucci A, Cestelôa M, Mormino A, Garofalo S, Limatola C, Basile L, Gottinger A, Binda C, Mattevi A, Mai A, and Valente S. The Design of *bona-fide* Benzyltriazolopyrimidine-based NADPH Oxidase Inhibitors Lead to the Discovery of the *First-in-Class* Potent Dual Covalent NOX2/MAO-B Inhibitor

ABBREVIATIONS LIST

7-AAD: 7-Aminoactinomycin D; AEBP2:Adipocyte Enhancer-Binding Protein 2; BET: bromodomain and extra terminal; bFGF: basic-fibroblast growth factor; BINAP: 2,2'-Bis(diphenylphosphino)-1,1'-binaphthyl; BRDs: bromodomains; BSA: bovine serum albumin; BV2: microglial cell line; CETSA: cellular thermal shift assay; $CDCl_3$: deuterated chloroform; CoA: coenzyme A; CU: connecting unit; DCE: 1,2-dichloroethane; DCM: dichlorometane; DFM: FBS-supplemented medium; DH: dehydrogenase DMAP: 4-dimethylaminopyridine; DMF: N,N-dimethylformamide; DMSO: dimethylsulfoxide; DNMT1: DNA methyl transferase 1; DOHH2: lymphoma cell line; DOT1L: DOT1 Like Histone Lysine Methyltransferase; DUOX: Dual Oxidase; EDB: EED-binding domain; EDG: electron donating group; EDTA: ethylenediaminetetraacetic acid; EED: Embryonic Ectoderm Development; EGF: epidermal growth factor; EGFR: epidermal growth factor receptor; EHMT1: Euchromatic Histone Lysine Methyltransferase 1, also known as G9a-like protein; EM: electron microscopy; EMT: epithelial-mesenchymal transition; ER: endoplasmic reticulum; EtOH: ethanol; EWG: electron withdrawing group; EZH1: Enhancer of Zeste Homologue 1; EZH2: Enhancer of Zeste Homologue 2; EZH2i: EZH2 inhibitor; FAD: flavin adenine dinucleotide; FBS: fetal bovine serum; c-Myc: transcription factors; GAPDH: glyceraldehyde-3-P dehydrogenase; H3K27: histone 3 lysine 27; HATs: histone acetyltransferases; HATU: Hexafluorophosphate Azabenzotriazole Tetramethyl Uronium; HDACs: histone deacetylases; HEK293: non-cancer human hembrionic kidney cell line; HIF1α: hypoxia-inducible factor-1α; HKDMs: histone lysine demethylases; HKMTs: histone lysine methyltransferases; IC_{50}: half maximal inhibitory concentration; INF-γ: interferon gamma; KDMs: lysine demethylases; Ki: inhibition constant; KMTs: lysine methyltransferases; KRAS: Ki-ras2 Kirsten rat sarcoma viral oncogene homolog; LC-MS: liquid chromatography-mass spectrometry; LC-MS: liquid chromatography/mass spectrometry; LPS: lipopolysaccharides; LS174T: colorectal carcinoma cell line; LS180: colorectal carcinoma cell line; LS513: colorectal carcinoma cell line; LSD1: Lysine Specific Demethylase 1; MAPK: mitogen-activated protein kinase; MCLA: 2-Methyl-6-(4-methoxyphenyl)-3,7-dihydroimidazo[1,2-a]pyrazin-3-one, hydrochlorid; MCSS and SANT2: EZH2 domain; MS: mass spectrometry; MTT: 3-(4,5-dimethylthiazol-2-yl)-2,5-diphenyltetrazolium bromide; NADPH: Nicotinamide adenine dinucleotide phosphate; ncRNA: non-coding RNA; NOX: NADPH oxidase; PARP: poly(ADP-ribose)polymerase; PMA: phorbol 12-myristate 13-acetate; PBS: phosphate buffer saline; PcG: polycomb group; PCLs: Polycomb-like proteins; PhoRC: Phorepressive complex; PLB-985: acute myeloid leukemia cell line; PPI: protein-protein interaction; PRC: polycomb repressive complex; PR-DUB:

Polycomb Repressive Deubiquitinase; PRMT1: Protein Arginine Methyltransferase 1; PRMTs: arginine methyltransferases; PTM: post-translational modifications; PTSA: *para*-toluenesulfonic acid; PyBOP: benzotriazol-1-yloxytripyrrolidinophosphonium hexafluorophosphate; RbAp46/48: Retinoblastoma Associated protein 47 or 48; RPMI: cell culture medium; RT-PCR: real time polymerase chain reaction; SAH: S-adenosyl homocysteine; SAM: S-adenosyl-L-methionine; SAR: structure activity relationship; SDS-PAGE: sodium dodecyl sulfate polyacrylamide gel electrophoresis; SET: Su(var)3-9, Enhancer-of-zeste and Trithorax (methyltransferases catalytic domain; siRNA: small interference RNA; $SOCl_2$: Thionyl chloride; SU-DHL-4: lymphoma cell line; SUZ12: Suppressor of Zeste 12; t-BuOK: Potassium tert-butoxide; TEA: triethylamine; THF: tetrahydrofuran; TLC: thin-layer chromatography; Tris-HCl: 2-Amino-2-(hydroxymethyl)propane-1,3-diol hydrochloride; Tween-20: detergent; U937: histiocytic lymphoma cell line; Vefs: SUZ12 domain; ZBG: zinc-binding group.

Standard Abbreviations and Acronyms: 2b Guidelines Abbreviations and Acronyms (acs.org)

INDEX

ABSTRACT

In the present thesis, I describe the core projects undertaken during my PhD period, with the support and collaboration of my research team and under the guidance of my Scientific Supervisor, Professor Antonello Mai.

Firstly, I dealt with the design and synthesis of novel NADPH oxidases (NOXs) inhibitors, pursued through two parallel project lines. The first line of investigation focused on the development of *bona-fide* triazolopyrimidine-based NOXs inhibitors, while the second aimed in the obtaining of quinoline-based NOXs inhibitors. Secondly, in addition to NOX inhibitors, I turned my focus to the design and synthesis of novel multi-targeting agents capable of simultaneously inhibiting two crucial epigenetic targets: the Enhancer of Zeste Homolog 2 (EZH2) and the Histone Deacetylases (HDACs). This dual-target approach is pivotal, given the complex role these proteins play in cancer progression and epigenetic regulation. The successful outcomes of this research were significantly enhanced by collaborations with various research groups and my enriching visiting PhD experience at the Institute of Oncology Research in Bellinzona, Switzerland. These collaborations allowed me to obtain important biochemical and biological data, enabling a comprehensive evaluation of the inhibitory activities of the newly synthesized compounds. Furthermore, these compounds were assessed for their anticancer potential against both solid and hematological tumors, as well as for their neuroprotective properties. Through this multifaceted approach, my work not only advances our understanding of NOX inhibition and epigenetic modulation but also contributes to the broader quest for effective therapeutic agents in cancer treatment, and beyond.

Development of VAS2870 analogues as triazolopyrimidine-based NOXs inhibitors

NADPH oxidases (NOXs) are the only known human enzymes solely in charge of ROS production. In addition to their roles in innate immunity and response to stressful conditions, NOXs are part of the redox signaling pathways that sustain cell proliferation, oncoprotein (e.g. RAS) driven cell transformation, and neuroinflammation. Recently, our group identified VAS2870 as a covalent inhibitor of mainly NOX1 and NOX5, by alkylating the conserved Cys668 in the active site, blocking productive substrate binding. To enhance potency and selectivity towards NOXs, we conducted a series of chemical modifications, leading to the discovery of compound **9a** that preferentially inhibited NOX2 with an IC_{50} of 0.155 μM, and only

upon its pre-activation. Tested against NOX2-overexpressing PLB-985 cells, compound **9a** proved to be the most effective, with IC_{50} of 0.135 μM. Surprisingly, we considered that **9a** bears the pargyline (*N*-benzyl-*N*-methylprop-2-yn-1-amine) moiety, a well-known irreversible and selective monoamine oxidase B (MAO-B) inhibitor. When evaluated towards *human* MAO-A and MAO-B, **9a** proved to be a selective MAO-B inhibitor ($SI_{MAO-B/MAO-A}$ = 465), that could be considered the *first-in-class* dual NOX2/MAO-B irreversible inhibitor, with a balanced potency against both targets. Finally, given the involvement of NOX2 and MAO-B in neuroinflammatory pathways, we further investigated the effects of **9a** in the BV2 microglia neuroinflammation cell model. It reduced ROS production and downregulated mRNA transcripts of pro-inflammatory genes, demonstrating more potent effects than either single-target or their combined effects.

Development of M41 analogues as quinoline-based NOXs inhibitors

In cancers, dysregulation of NOX enzymes affects ROS production, leading to redox unbalance and tumor progression. NOXs present a therapeutic target, yet current drugs often lack selectivity: there is a need for isoenzyme-selective inhibitors. Our project focused on the molecular simplification of M41, a lead-compound discovered through two ultra-large *in silico* screens of 350 million compounds, which stood out for its promising K_i values towards NOX isoforms. Given the adaptable binding mode of M41, we investigated the contributions of the various chemical groups, obtaining a first series of simplified derivatives. Particularly, the quinoline derivatives **10t** and **10s** exhibited single-digit micromolar IC_{50} values and isoform selectivity for NOX2 and NOX5, respectively. Building on these results, a second series of derivatives (based on the two just mentioned lead-compounds) was developed, with the bisquinoline compound **15a** identified as the best candidate for targeting NOX2. The study also assessed 15a's potential in *KRAS*-mutant colorectal cancer, where NOX2 is upregulated. Compound **15a** enhanced the effectiveness of the $KRAS^{G12D}$ inhibitor MRTX1133 in these cancer cells. The findings underscore the importance of structural features for NOX selectivity and potency and suggest potential therapeutic benefits in KRAS-driven cancers.

Development of novel dual EZH2/HDAC inhibitors

Since the histone-modifying enzymes EZH2 and HDACs synergistically control several epigenetic-dependent carcinogenic pathways, we synthesized novel dual EZH2/HDAC inhibitors. This was achieved by merging the structure of Tazemetostat, the only FDA-approved EZH2 inhibitor, with pharmacophore moieties from various established HDAC inhibitors. In biochemical assay, most of our hybrid compounds exhibited nanomolar inhibition of EZH2, with some achieving even picomolar potency, while displaying sub-micromolar to nanomolar inhibition of HDACs. When tested across diffuse large B cell lymphomas (DLBCL) cell lines, a histological subtype that comprises a defined genetic subset of EZH2 mutated tumors, these hybrid inhibitors showed significant antiproliferative effects, with low micromolar concentrations sufficient to inhibit cell proliferation. In both DOHH2 cell line (wild-type EZH2) and WSU-DLCL2 cell line (mutated EZH2), the dual inhibitors modulated specific histone marks, confirming their targets engagement. Additionally, these compounds induced G1 phase cell cycle arrest, leading to a cytostatic effect and an accumulation of cells in sub-G1, indicating a cytotoxic impact. Finally, we further evaluated the two most promising dual compounds, **18a** and **19a**, based on the just-mentioned assays, by analyzing their effects on the transcriptomes of DOHH2 and WSU-DLCL2 cell lines. These dual inhibitors significantly downregulated transcriptional targets of the oncogene MYC, as well as genes involved in mTORC1 signaling, DNA repair, G2-M cell cycle checkpoint, and oxidative phosphorylation. Overall, the transcriptome analyses revealed that **18a** and **19a** were at least as effective, if not more so, than single-target agents in modulating the expression of genes associated with lymphomagenesis.

PART I.

DESIGN, SYNTHESIS, AND BIOLOGICAL EVALUATION OF NOVEL TRIAZOLOPYRIMIDINE- AND QUINOLINE-BASED *BONA-FIDE* NADPH OXIDASES INHIBITORS FOR CANCEROUS AND NON-CANCEROUS DISEASES

1. Introduction

1.1. The dual role of reactive oxygen species (ROS)

Reactive Oxygen Species (ROS) are a class of oxygen-derived small molecules, including oxygen radicals [superoxide ($O_2^{\bullet -}$), hydroxyl ($^{\bullet}OH$), peroxyl (RO_2)] and non-radicals [hydrogen peroxide (H_2O_2), hypochlorous acid (HOCl), and ozone (O_3)], which can quickly convert into radicals. [1] Due to their chemical instability, ROS are highly reactive and therefore prone to interact with and adversely affect the biochemical function of a large number of macromolecules, like nucleic acids, proteins, lipids, and carbohydrates. [2] Under normal physiological conditions, ROS generated during metabolic processes are swiftly neutralized or converted by natural endogenous antioxidants, which help maintain ROS levels within a controlled range. However, when ROS production exceeds normal levels, the body's antioxidants may be insufficient to neutralize them, leading to irreversible damage to cells and tissues. This imbalance between oxidants and antioxidants is known as oxidative stress. [3] Oxidative stress could be considered the principal cause of various diseases, such as neurodegenerative diseases, inflammation, cellular aging, and tumor forms. This vision was radically changed with the discovery of a positive role of ROS in the so-called 'Redox Biology' event. In this phenomenon, low levels of ROS are required to activate signaling pathways to trigger biological processes. [4] The cell production of ROS can be roughly divided into two categories:

- ROS can be released as waste products of fundamental biological processes (an example is the mitochondrial oxidative metabolism) [5] or also as by-products of biological processes that intentionally produce them in the cellular response to xenobiotics, cytokines, and invading bacteria, as part of a signal transduction pathway or as part of a cellular defense mechanism. [6] [7]
- ROS can be released by the NADPH oxidases (NOXs), the first example of an enzymatic system that produces ROS not as a by-product but as a primary function. This family of membrane enzymes requires nicotinamide adenine dinucleotide phosphate (NADPH) in the reduced form for their activity. [8]

With the discovery of NOX enzymes came to light another beneficial role of ROS: their involvement in innate immunity and host defense. Clinical research on Chronic Granulomatous Disease (CGD) has greatly contributed to the understanding of ROS in innate immunity. The condition was first identified in 1957 by Berendes *et al.*, who described a rare syndrome in young boys characterized by recurrent pyogenic infections and granulomatous reactions. [9] A decade later, Quie

et al. demonstrated that phagocytes from CGD patients exhibited diminished bactericidal capacity; [10] in the same year Baehner and Nathan, independently, discovered the absence of the respiratory burst in these phagocytes. [11] This laid the groundwork for subsequent discoveries, including Klebanoff's identification in 1975 of ROS as key players in the destruction of pathogens and the discovery by Segal *et al.* in 1978 of a protein in the membranes of neutrophils, at that time known as 'cytochrome b558'. [12] [13] This protein was later identified as a component of the NADPH oxidase complex, named NOX2, as delineated by Cross *et al.* in 1984. [14] These findings collectively led to the recognition of CGD as a disorder stemming from the defective activation of NOX enzymes, particularly NOX2, highlighting the enzyme's critical function in the oxidative burst essential for effective immune responses. To summarize, ROS levels in living organisms must be strictly regulated by homeostasis: in living organisms, they can be both beneficial and detrimental. When present in either excessive or insufficient concentrations, dysregulated ROS production is well-known to be harmful to health, highlighting the necessity for precise regulation. This dual nature of ROS has led to the concept of ROS as a 'double-edged sword,' a notion that requires deeper examination to fully understand its implications. In this context, the investigation of NOXs, the only enzymes known to produce ROS as a primary product rather than a by-product, is crucial for unraveling the precise regulatory mechanisms needed to maintain the delicate balance between physiological and pathological states. [2]

2. The NADPH oxidase family

The identification of NOX2 was quickly followed by the discovery of the first NOX2-related enzyme by two research groups, independently. Initially, it was called mitogenic oxidase 1 (mox-1), [15] or NADPH oxidase homolog 1 (NOH-1), [16] but this enzyme is now designated as NOX1. Shortly after the discovery of NOX1, additional isoforms, NOX3, NOX4, and NOX5, were cloned. [17] [18] [19] [20]. Simultaneously, two larger enzymes within the NOX family were identified, DUOX1 and DUOX2, which were originally named thyroid oxidases. [21] [22] The description of NOX isoforms is focused, in the present thesis, on mammalian NOX homologs and subunits.

Often described as '*professional ROS producers*', NOXs are unique enzymes only dedicated to the generation of ROS by transferring electrons across biological

membranes ultimately reducing molecular oxygen as the last electron acceptor. [23] In mammals there are seven different isoforms (NOX1-5 and DUOX1/2), each differing in their products, subunit composition, and regulatory mechanisms (**Figure 1**). [24] NOX1, NOX2, NOX3, and NOX5 generate superoxide, which is subsequently converted to hydrogen peroxide (H_2O_2) through non-enzymatic processes, while NOX4 and DUOX1-2 produce hydrogen peroxide directly.

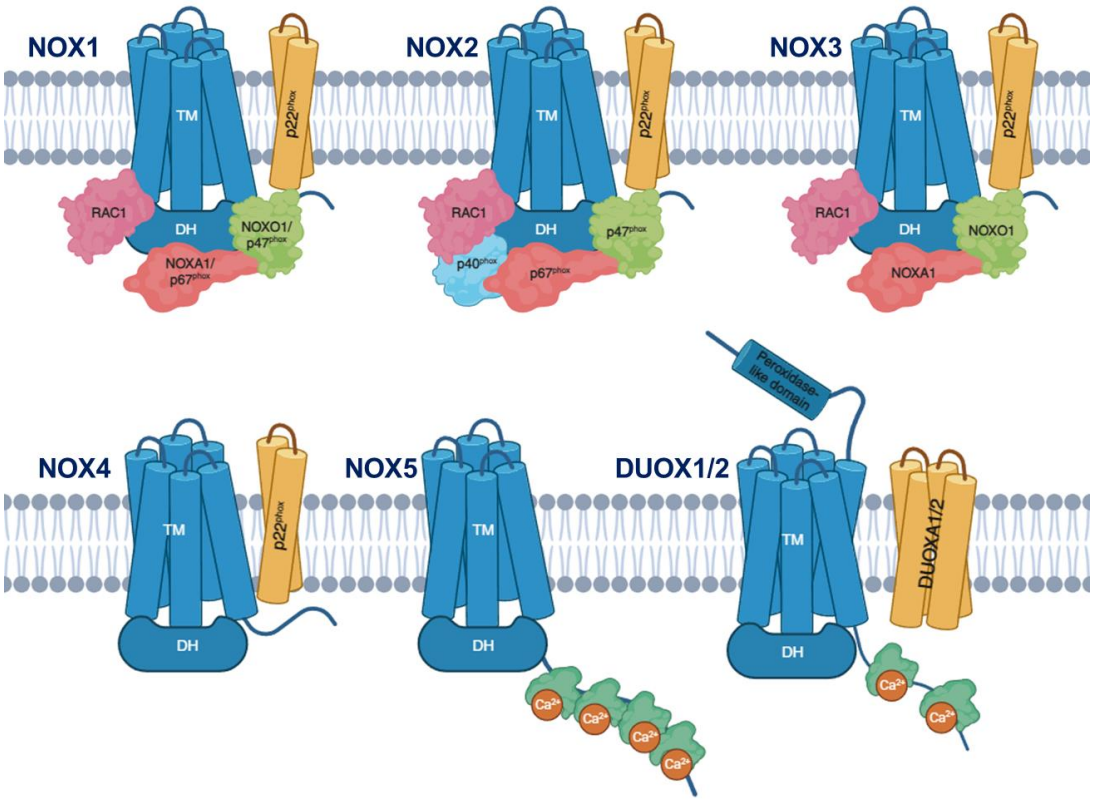

Figure 1. *Cartoon representation of the seven members of the mammalian NOX family (NOX1-5 and DUOX1/2). The cytosolic and membrane subunits required for each NOX enzyme are shown. [Figure created with BioRender.com.]* [25]

Structurally, NOX enzymes share a similar catalytic core composed of two domains. The C-terminal dehydrogenase domain (DH), the most conserved domain among the seven isoforms, houses the binding sites for nicotinamide adenine dinucleotide phosphate (NADPH) and for the flavin adenine dinucleotide (FAD). The N-terminal transmembrane domain (TM) contains six helices (except for DUOX1/2 that have seven) arranged in a pyramidal formation, with four conserved histidines, localized in helix 3 and 5, coordinating two non-covalent heme groups that create an electron

transfer chain across the membrane. [26] [27] [28] In DUOX proteins, due to an additional N-terminal transmembrane domain, the histidines are instead found in the fourth and sixth transmembrane domains. [1] This structure operates as a cohesive unit that facilitates the transfer of electrons across cellular membranes. The process begins with the reduction of the non-covalently bound FAD cofactor by NADPH, converting it into $FADH_2$. Following this, electrons are transferred one at a time through the two hemes, ultimately reaching the final acceptor, an oxygen molecule located in the extracellular space (**Figure 2**). [27] [28]

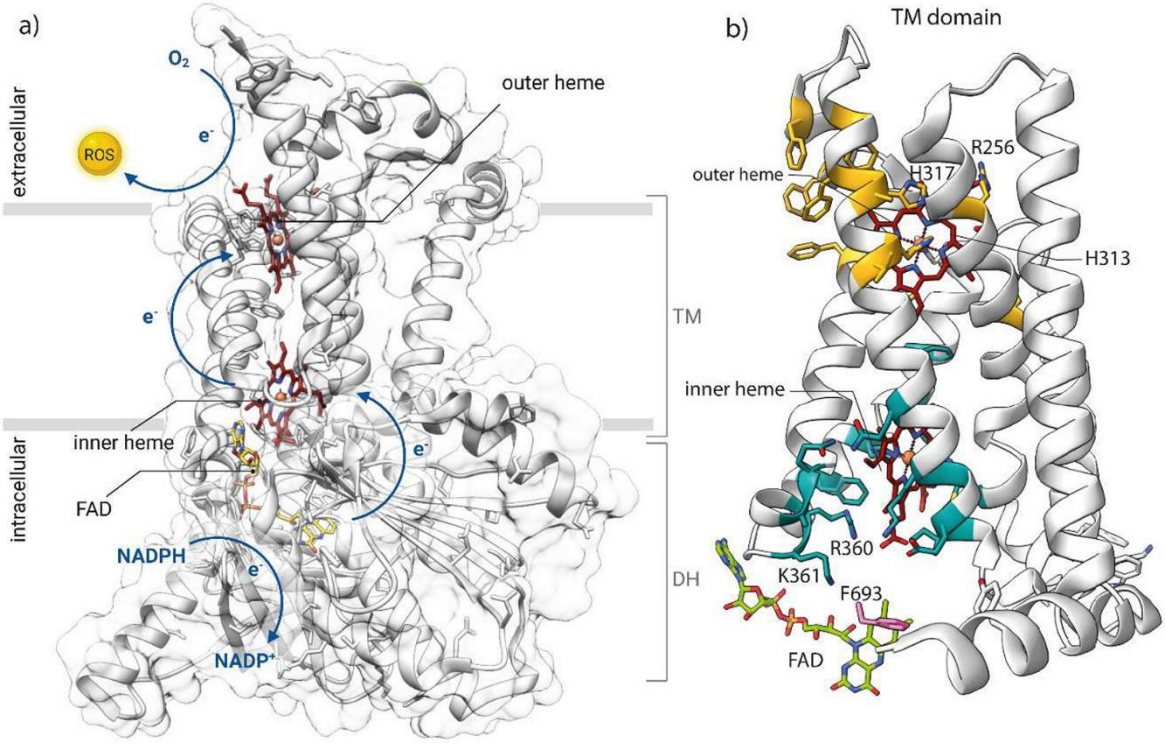

Figure 2. *Example of architecture of the catalytic core and mechanism of electron transfer. The structures of the dehydrogenase (DH) domain (PDB 5O0X) and the transmembrane (TM) domain (PDB 5O0T) of Cylindrospermum stagnale NOX5 have been reported.* ***a)*** *The heme groups are shown in dark red, while the FAD cofactor is depicted in yellow. The blue arrows show the electron flow, which starts from the FAD cofactor reduction by NADPH; electrons are so transferred to the inner heme, followed by electron hopping to outer heme, and culminating in the reduction of* O_2. ***b)*** *In the focused view of the TM domain, key amino acid residues are highlighted. The top section illustrates the oxygen-binding and reacting site, represented as a small cavity exposed to the external environment. This cavity is lined by the propionate 7 of the outer heme and the side chains of conserved residues R256, H317, and H313, depicted in golden rod color. The bottom section of the TM domain shows its*

interaction surface with the DH domain, emphasizing the highly conserved R360 in the D loop, depicted in dark cyan, located near propionate 6 of the inner heme. Near the interdomain interface, a conserved residue from the DH domain's C-terminus, F693, is shown in hot pink. This residue acts as a toggle-switch, controlling access to the NADPH substrate, thereby initiating catalysis. Additionally, a positively charged residue, K361 (also in dark cyan), is located close by. In this case, the FAD cofactor is depicted in chartreuse. [25]

Other structural features, such as EF hands, an extra NH_2-terminal transmembrane domain, and/or a peroxidase homology domain, are specific to certain family members and will be discussed more deeply in the following specific section. Despite these common features, each isoform presents peculiar items, differing from each other in their tissue distribution, activation mechanism, and specific activities. [29] [25] Particularly, NOX1, NOX2, and NOX3 require the presence of $p22^{phox}$ and the recruitment of cytosolic subunits for their activity. [29] [30] [31] In contrast, NOX4 also relies on $p22^{phox}$ but does not need additional cytosolic subunits. [19] NOX5, DUOX1, and DUOX2 differ in this: they do not form complexes with $p22^{phox}$; instead, they have EF-hand domains that enable calcium-dependent activation. [27] Among these, DUOX1 and DUOX2 are the most sequence-divergent members of the NOX family and associate with distinct auxiliary subunits, DUOXA1 or DUOXA2, which are essential for their proper function. [32] [33] In the context of their different tissue distribution, **Table 1** provides a detailed overview of the subcellular localization of NOX enzymes, highlighting how their location varies depending on the type of tissue and cell involved.

Table 1. *Tissue distribution and subcellular localization of NOX enzymes.* [34]

NOX isoform	Cellular distribution	Subcellular localization
NOX1	Colon epithelium, vascular smooth muscle cells, endothelial cells, uterus, placenta	Intracellular membranes close to ER, endosomes, caveolae
NOX2	Neutrophils, macrophages, endothelial cells, vascular smooth muscle cells, skeletal muscle cells, cardiomyocytes	Cell membrane, phagosomes, perinuclear
NOX3	Inner ear (vestibular system, cochlea), brain, lungs	Plasma membrane
NOX4	Kidney, vascular smooth muscle cells, fibroblasts, osteoclasts, neurons, endothelial cells	Focal adhesions, ER, nucleus, mitochondria
NOX5	Vascular smooth muscle cells, endothelial cells, bone marrow, lymph nodes, spleen, reproductive tissues, stomach, pancreas, fetal tissues	Plasma membrane, ER
DUOX1/2	Thyroid, airway epithelia, prostate, digestive system (DUOX2)	Apical membrane

NOX enzymes are present in nearly all cells and tissues, but their levels vary depending on the specific NOX isoform and the type of cell. NOX1 is most highly expressed in the colon's epithelial cells but is also found in vascular smooth muscle cells, endothelial cells, the uterus, and the placenta. It can be activated by factors like platelet-derived growth factor (PDGF), prostaglandin F2α, and angiotensin II.

[35] NOX1-generated ROS help maintain gut microbiota balance and are linked to inflammatory bowel disease and colon cancer, where they may promote cancer cell growth and survival. [1] [36] [37] NOX2 is mainly found in neutrophils and plays a key role in immune responses. In phagocytes, NOX2 expression increases in response to interferon-γ. Similarly, its expression is elevated in myofibroblasts following carotid artery injury and in cardiomyocytes after an acute myocardial infarction. Additionally, NOX2 gene expression is upregulated by angiotensin II in various tissues, including adipose tissue, the aorta, the heart, smooth muscle cells of resistance arteries, and pancreatic islets. [38] [39] [40] NOX3 is primarily located in the inner ear, where it is involved in hearing and balance. It is also present in the brain and lungs, but its role in these areas is not yet clear. [29] [41] NOX4 is heavily expressed in the kidneys, bone-resorbing osteoclasts, fibroblasts, and endothelial cells. The hydrogen peroxide (H_2O_2) it produces is important for cell growth, movement, and death. NOX4 overexpression has been associated with cancer spread and cardiovascular diseases, like atherosclerosis and high blood pressure. [42] NOX5 is found in tissues like the testis, spleen, lymph nodes, and various parts of the reproductive and cardiovascular systems. Its role in many of these tissues isn't fully understood, but it may be important in the early stages of immune cell development. [43] NOX5 overactivity has been linked to the development and progression of cancers, such as those of the prostate, pancreas, breast, esophageal, and melanoma. [44] DUOX1 and DUOX2 are primarily expressed in the thyroid gland, where they are crucial for producing thyroid hormones. [22] DUOX1 is also found in airway tissues and the prostate, while DUOX2 is present in the salivary glands and throughout the gastrointestinal tract. Mutations in the DUOX2 gene can lead to severe congenital hypothyroidism due to impaired thyroid hormone production. [45] Overall, NOX enzymes play significant roles in various tissues, influencing processes, like immune function, cancer progression, and cardiovascular health. The variety of roles that NOX enzymes play in different cells has made them increasingly important in research, attracting significant attention over the past few decades.

3. The NADPH oxidase 2 (NOX2): NOX prototype

NOX2, the first identified isoform of the NOX family, is the most studied and characterized. It serves as the prototype for understanding the entire NOX enzyme family. The detailed biochemical study of NOX2 has been crucial in unraveling the functional roles of the whole family. [46] Initially, NOX2 was primarily associated with its role in innate immunity. Human NOX2 is, in fact, mostly expressed in professional phagocytes, such as neutrophils and macrophages, which are essential for antimicrobial host defense. The critical role of NOX2 in immune function is highlighted by chronic granulomatous disease (CGD), an inherited immunodeficiency syndrome, where the failure of NOX2 to function properly leads to an inability to produce this respiratory burst, resulting in severe and recurrent infections. [13] [47] In addition to its central role in innate immunity, it was later discovered that NOX2 also participates in other physiological processes, including signal transduction, angiogenesis, and cell death. [48] [49] [50] However, its function in immune defense remains a key model for the NOX family's broader roles. NOX2 is a multi-component system that includes the transmembrane flavocytochrome b558, composed of NOX2 and $p22^{phox}$, along with cytosolic proteins $p47^{phox}$, $p67^{phox}$, and $p40^{phox}$, and small GTP-binding proteins Rac1 or Rac2 (**Figure 3**). These components work together to ensure that NOX2 is activated only under appropriate conditions, allowing for controlled production of ROS. [51]

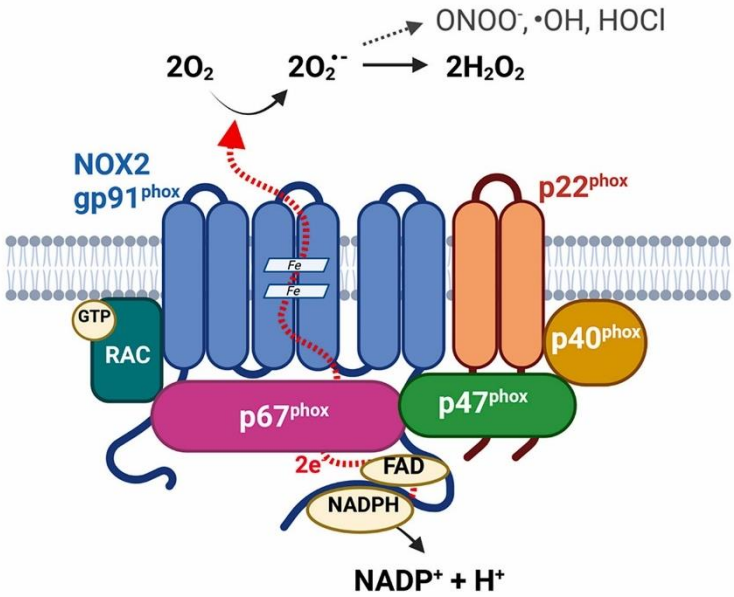

Figure 3. *The activated NOX2 complex consists of several key components: the integral membrane proteins NOX2/gp91^{phox} and p22^{phox}, along with the associated cytosolic*

components p40^{phox}, p47^{phox}, p67^{phox}, and the GTP-bound small GTPase Rac1 or Rac2. Within this complex, NOX2 catalyzes the transfer of two electrons from cytosolic NADPH to oxygen (O_2) outside the cytoplasm, producing superoxide anion radicals ($O^{2\bullet-}$). These superoxide radicals can either dismutate into hydrogen peroxide (H_2O_2) or further react to generate other ROS, contributing to the oxidative burst, that is crucial for immune defense. [52]

3.1. The components of NOX2

3.1.1. The flavocytochrome b558

The flavocytochrome b558 complex is formed by NOX2 and p22^{phox} in a 1:1 ratio, forming a heterodimeric structure.

NOX2, the larger subunit, is a protein made up of 570 amino acids. It is encoded by the CYBB gene, which is located on the X chromosome at locus Xp21.1 and consists of 13 exons spanning a total of 30 kilobases. The six transmembrane helices of the TM domain are connected by five inter-helix loops designated from A to E, from the N-terminal extremity to the C-terminal end. The A, C, and E loops face the membrane's extracellular side, or the phagosome's internal space. The B and D loops face the cytosol and likely participate in controls on NOX2 electron transfer. [39] NOX2 is heavily N-linked glycosylated within Asparagine residues on extracellular C- and E- loops identified by site-directed mutagenesis studies (Asn131, Asn148, and Asn239) (**Figure 4**). [53] The transmembrane domain of NOX2 contains two pairs of highly conserved bis-histidyl heme-binding motifs. These pairs are located on the third and fifth helices of the protein. In helix 3, the histidine residues are spaced 14 amino acids apart (His101 and His115), while in helix 5, they are 13 residues apart (His209 and His222). The imidazole rings of these histidine residues serve as the axial and distal ligands for the iron atoms within two B-type hemes, positioning the hemes perpendicular to the plane of the membrane. This orientation is crucial for the proper function of NOX2 in electron transfer and ROS generation. [54]

p22^{phox} is the smaller subunit of the heterodimeric flavocytochrome b558 complex and is encoded by the CYBA gene located on chromosome 16 at locus 16q24. It is a 194-amino-acid, non-glycosylated protein with hydrophobic regions that likely span the membrane at least two, and possibly four, times. The C-terminal region of p22^{phox} (amino acids 133-194) is cytoplasmic and contains a proline-rich domain (PRR), which is crucial for the binding of p47^{phox} to flavocytochrome b558. [55] p22^{phox}

plays a key role by providing high-affinity binding sites for cytosolic NADPH oxidase subunits, as supported by numerous studies on $p22^{phox}$–$p47^{phox}$ interactions. Beyond this, $p22^{phox}$ is also essential for the proper processing and maturation of NOX2. [56] A study by Zhu *et al.* in 2006 used deletion mutagenesis of human $p22^{phox}$ to identify regions crucial for flavocytochrome b558 assembly, enzymatic activity, NOX2 maturation, and cell surface expression. The research found that, in addition to the C-terminal regions, the N-terminal region also contains important signals affecting the assembly of flavocytochrome b558 (**Figure 4**). [57]

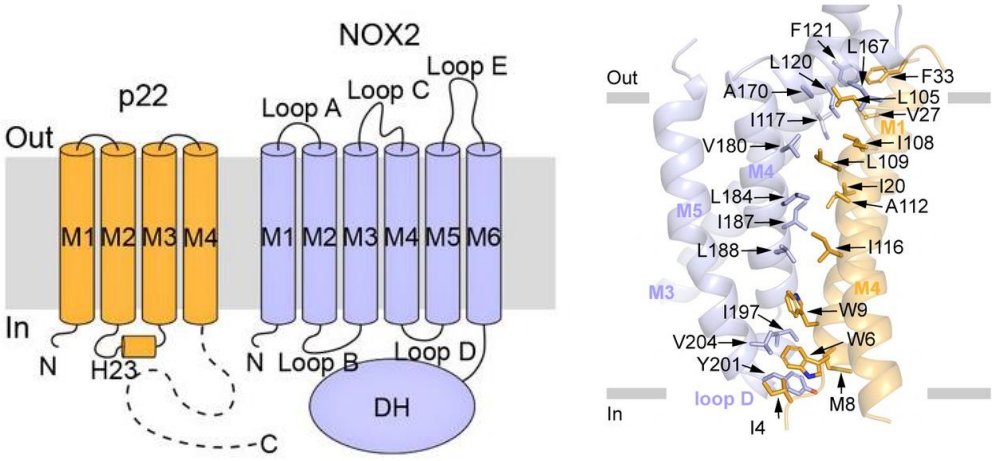

Figure 4. *On the left is reported the topology of p22 and NOX2 subunits. Transmembrane helices are shown as cylinders and unmodeled disordered regions are shown as dashed lines. The cartoon representation on the right shows the interface between NOX2 and p22. Residues participating in the interaction between NOX2 and p22 are shown as sticks. In both, the phospholipid bilayer is shown as gray layers.* [58]

3.1.2. The cytosolic components of NOX2

As we already said, the phagocytic NADPH oxidase is a multicomponent complex involving the transmembrane heterodimer comprising NOX2 and $p22^{phox}$, and the three cytosolic protein factors $p40^{phox}$, $p47^{phox}$, $p67^{phox}$, together with the small GTP-binding protein (Rac1 or Rac2). $p47^{phox}$ is a 390-amino acid protein with a molecular mass of 44.7 kDa, which comprises an N-terminal PX domain that interacts with lipids; a bis-SH3 domain that binds $p22^{phox}$; an autoinhibitory region (AIR); and a C-terminal proline-rich region (PRR). [26] [1] The activator protein $p67^{phox}$ features several

key structural domains crucial for its function. It's a 526-amino-acid protein with a molecular mass of 59,8 kDa. At its N-terminal end, it contains four successive tetratricopeptide repeat (TPR) motifs, which form the Rac-binding region. This region is responsible for interacting with the small GTPase Rac, a critical step in the activation of the NOX complex. [59] Additionally, p67^{phox} has a highly conserved activation domain (AD) that plays a central role in initiating the electron transfer process within the oxidase complex. Following the AD, p67^{phox} includes a first SH3 domain, a "Phox and Bem 1" (PB1) domain, and a C-terminal SH3 domain, which is involved in interacting with the p47^{phox} subunit. [60] [61] p40^{phox}, a 339-amino-acid protein with a molecular mass of 39,0 kDa, starts with an N-terminal PX domain that binds to phosphoinositides within the membrane. This is followed by an SH3 domain and a PB1 domain, which facilitate interactions with other subunits. These domains collectively contribute to the proper assembly and regulation of NOX2. What is known is that p40phox is not essential for NOX2 activation. [62]

This cytosolic trimer displays an elongated shape as represented in **Figure 5**.

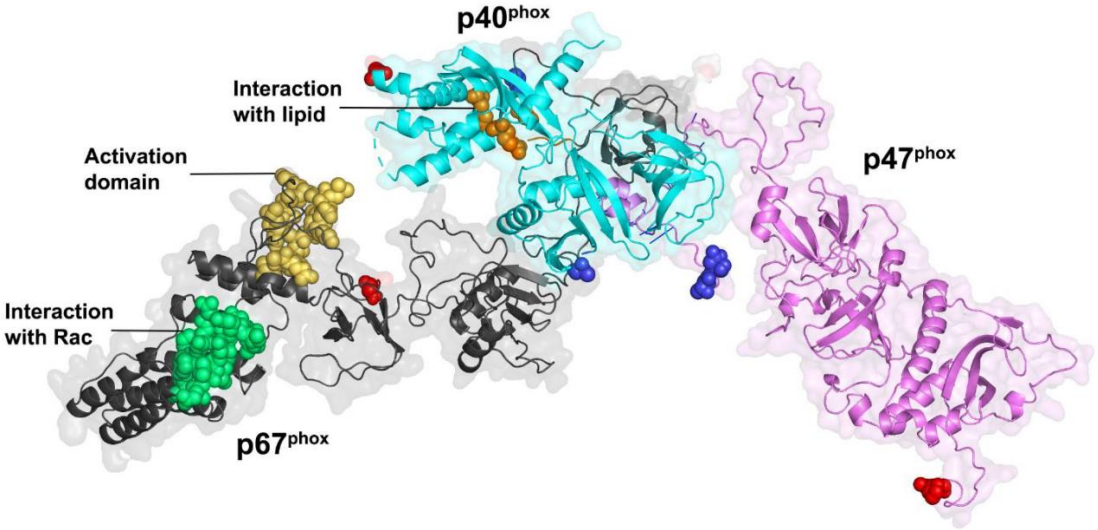

Figure 5. *Representation of the trimeric cytosolic components of NOX2 with an emphasis on the interaction sites critical for the assembly and function of the complex. p40^{phox} is depicted with cyan ribbons, with its lipid-interacting PX domains highlighted by orange spheres. p47^{phox} is represented by light purple ribbons. p67^{phox} is shown with gray ribbons, where the N-terminal extremities are indicated in red, and the C-terminal ends are in blue. In p67^{phox} the β hairpin involved in Rac interaction, which includes residues 115–130, is marked by green spheres, while the activation domain, spanning residues 199–210, is highlighted by yellow spheres.* [29]

Upon cellular activation, the phox components undergo phosphorylation, triggering conformational changes that expose previously hidden interaction sites. These changes enable the phox components to translocate to the plasma membrane, where they assemble with the cytochrome b558 heterodimer. This assembly is crucial for the formation of the active NADPH oxidase complex, which then initiates the production of ROS as part of the cell's defense mechanism. Rac belongs to the Rho family of small GTPases, which plays a crucial role in regulating various signaling pathways. Its structure includes a core with an N-terminal guanosine-binding site, a geranylgeranyl tail, and a C-terminal polybasic region that aids in membrane anchoring following prenylation. Rac's activity is controlled by the type of guanine nucleotide it binds to. When bound to GDP (guanosine 5′-diphosphate), Rac remains inactive, whereas GTP (guanosine 5′- triphosphate) triggers the active state, thereby allowing propagation of a signaling response after the interaction with downstream effectors. [63] The switch between active and inactive states is finely regulated by guanine-nucleotide-exchange factors (GEFs), which facilitate the release of GDP and the binding of GTP, and by GTPase-activating proteins (GAPs), which enhance the intrinsic GTPase activity of Rac, thus downregulating its activity. [64] A mutation, where glutamine is replaced by leucine at position 61 (Q61L), results in a Rac protein that is constitutively active and always in the GTP-bound state, bypassing normal regulatory mechanisms. [65] In mammals, Rac exists in three isoforms, Rac1, Rac2, and Rac3. [1] In monocytes and macrophages, all are expressed, but Rac2 predominates in human neutrophils (**Figure 6**). [26]

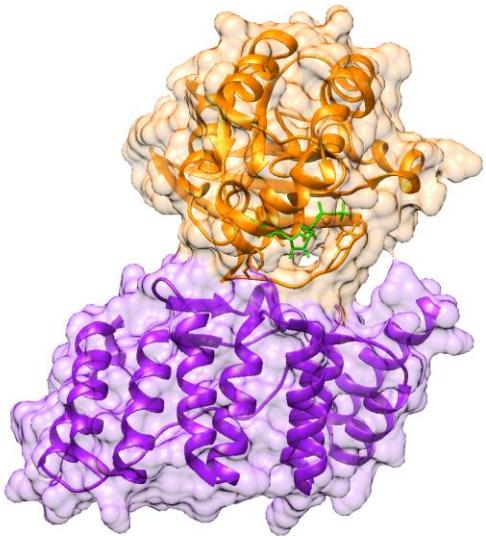

Figure 6. *Atomic structure of Rac in complex with p67^{phox} (PDB 1E96). Rac is represented in orange ribbon, p67^{phox} is represented in purple ribbon, and the GTP molecule is depicted in stick (green) within Rac.*

3.1.3. The activation mechanism of NOX2

Noreng *et al.* in 2022 through cryo-electron microscopy (cryo-EM) provided detailed images of how NOX2 and p22^{phox} come together to form their heterodimeric membrane complex, giving insights into the configuration of the NADPH oxidase in its inactive state. Additionally, structural analyses of the p67^{phox}–Rac1 complex and other cytosolic factor interactions enhanced the understanding of how these components come together and interact with the NOX2–p22^{phox} core. [31] Although these advancements, the precise mechanism by which cytosolic factors come together to activate the NOX2–p22^{phox} complex at the membrane was unclear. Recently, Liu and co-workers resolved the structure of human NOX2 in the activated state (**Figure 7**). [66]

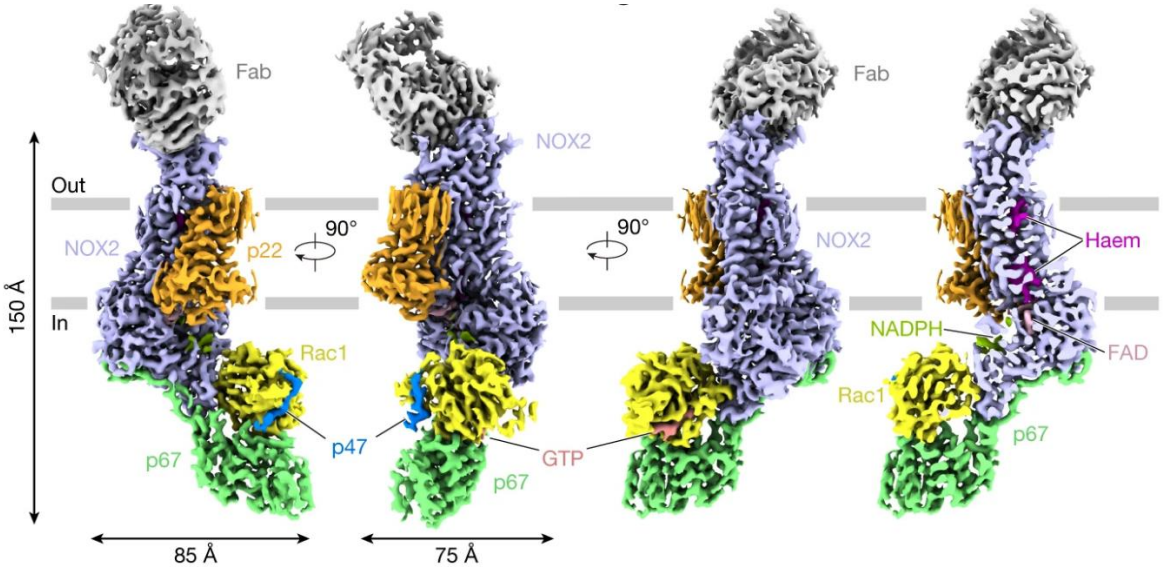

Figure 7. *Different views of the cryo-EM map of the activated NOX2 complex. GTP is coloured in salmon, Heme, FAD, and NADPH are depicted in magenta, pink, and pea green, respectively. The phospholipid bilayer is shown as grey layers.* [66]

They demonstrate the structural rearrangements of the NOX2 dehydrogenase domain to facilitate the transfer of electrons. In particular, the study highlights the distinct roles of p47^{phox}, p67^{phox}, and Rac1 in NOX2 activation: p67^{phox} and Rac1 directly bind to NOX2, where they clamp onto the DH domain and induce its contraction, crucial for activating NOX2, while p47^{phox} organizes the assembly of cytosolic factors, without direct interaction with NOX2, suggesting that p47^{phox} functions mainly as a scaffolding organizer rather than an activator. The contraction

of the DH domain induced by p67–Rac1 binding reduces the distance between the nucleotide-binding domain (NBD) and the flavin-binding domain (FBD), akin to the NOX5 structure from *Cylindrospermum stagnale*, [27] but larger than that in DUOX1 under high-calcium conditions. [33] This implies that DUOX1 has a less efficient electron transfer mechanism compared to NOX2 (**Figure 8**). [66]

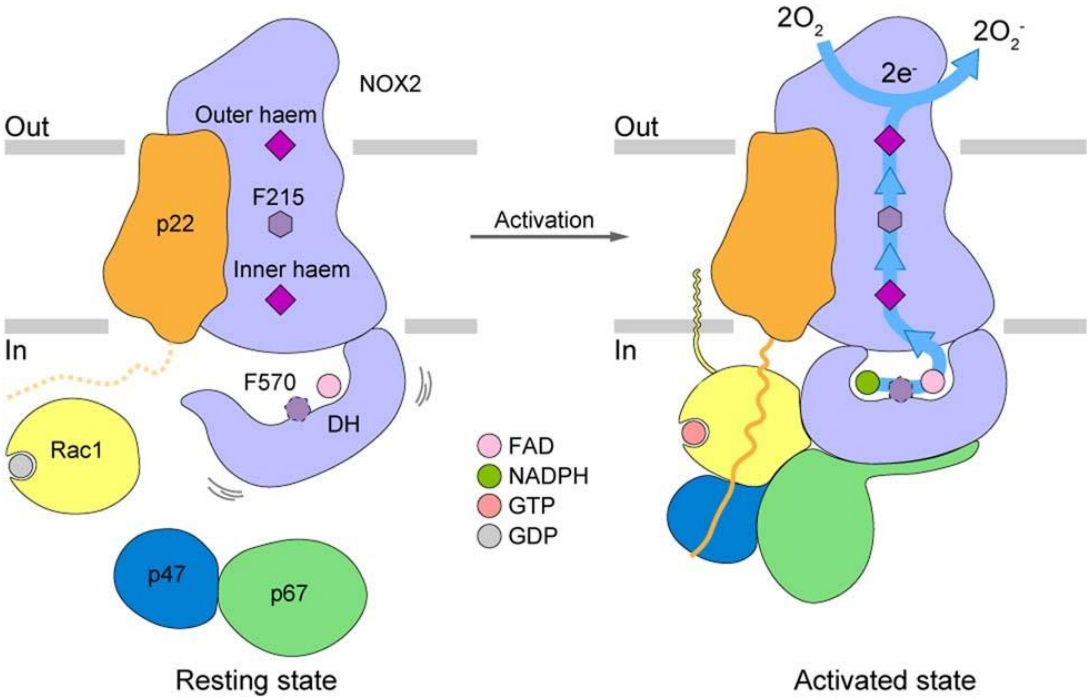

Figure 8. *Model for NOX2 activation. In the activated state, the binding of cytosolic factors promotes the docking of the DH domain onto the bottom of the TM domain and the contraction of the DH domain, stabilizing the binding of NADPH and bringing NADPH close to FAD.* [66]

4. NOX1

NOX1 shares almost 60% sequence identity with NOX2. [17] The human and mouse NOX1 gene is located on the X chromosome, with a molecular mass of 55-60 kDa. [67] This suggests that NOX1 is most likely not N-glycosylated, despite the presence of two NXT/S consensus glycosylation in the extracellular domains. [68] NOX1 is mainly expressed in the colon but also prostate, uterus, placenta, osteoclasts, and vascular cells, as well as in several cell lines, such as the colon tumor cell lines Caco-2, DLD-1, and HT-29. [69] [15] [70] [71] Like NOX2, NOX1 pairs with the $p22^{phox}$ subunit and is

activated by RAC1 along with the cytosolic proteins NOXO1 and NOXA1 (which stand for NOX Organizer 1 and NOX Activator 1, respectively) (**Figure 9**). [72] These proteins are analogous to the $p47^{phox}$ and $p67^{phox}$ subunits found in NOX2.

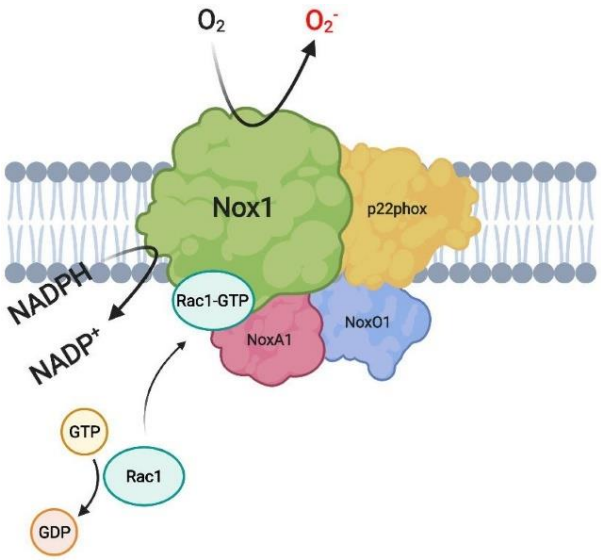

Figure 9. *Proposed structure of the NOX1 complex consisting of NOX1, $p22^{phox}$, GTP-bound Rac1, NOXA1, and NOXO1.*

Despite NOXA1 sharing only about 28% amino acid similarity with $p67^{phox}$, it has a comparable domain structure. [73] Both have NH_2-terminal tetricopeptide repeat (TPR) domains that interact with Rac. Both have activation domains (AD), which functional role is thus far only documented for the $p67^{phox}$-NOX2 interaction. Both $p67^{phox}$ and NOXA1 have COOH-terminal SH3 binding domains, which interact with $p47^{phox}$ and NOXO1, respectively. This structural similarity allows NOXA1 to bind effectively with both NOXO1 and RAC, playing a crucial role in NOX1 activation. Also $p47^{phox}$ and NOXO1 are homologous and share a similar structure (around 25%), including a conserved phox domain (PX), that binds to phospholipids in the membrane, although they differ in phospholipid specificity. They also both interact through tandem Src homology 3 (SH3) domains with the proline-rich region (PRR) of $p22^{phox}$. Unlike $p47^{phox}$, NOXO1 lacks the autoinhibitory region (AIR), which suggests that NOX1 can be activated by NOXO1 in combination with NOXA1 even without a stimulus. The activation of NOX1 appears to be less dependent on stringent regulation compared to NOX2. [74] (**Figure 10**). Upon stimulation, serine phosphorylation alters the conformation of the autoinhibitory

region of p47^{phox}, enabling its translocation to the membrane, where it regulates subunit interactions. [75]

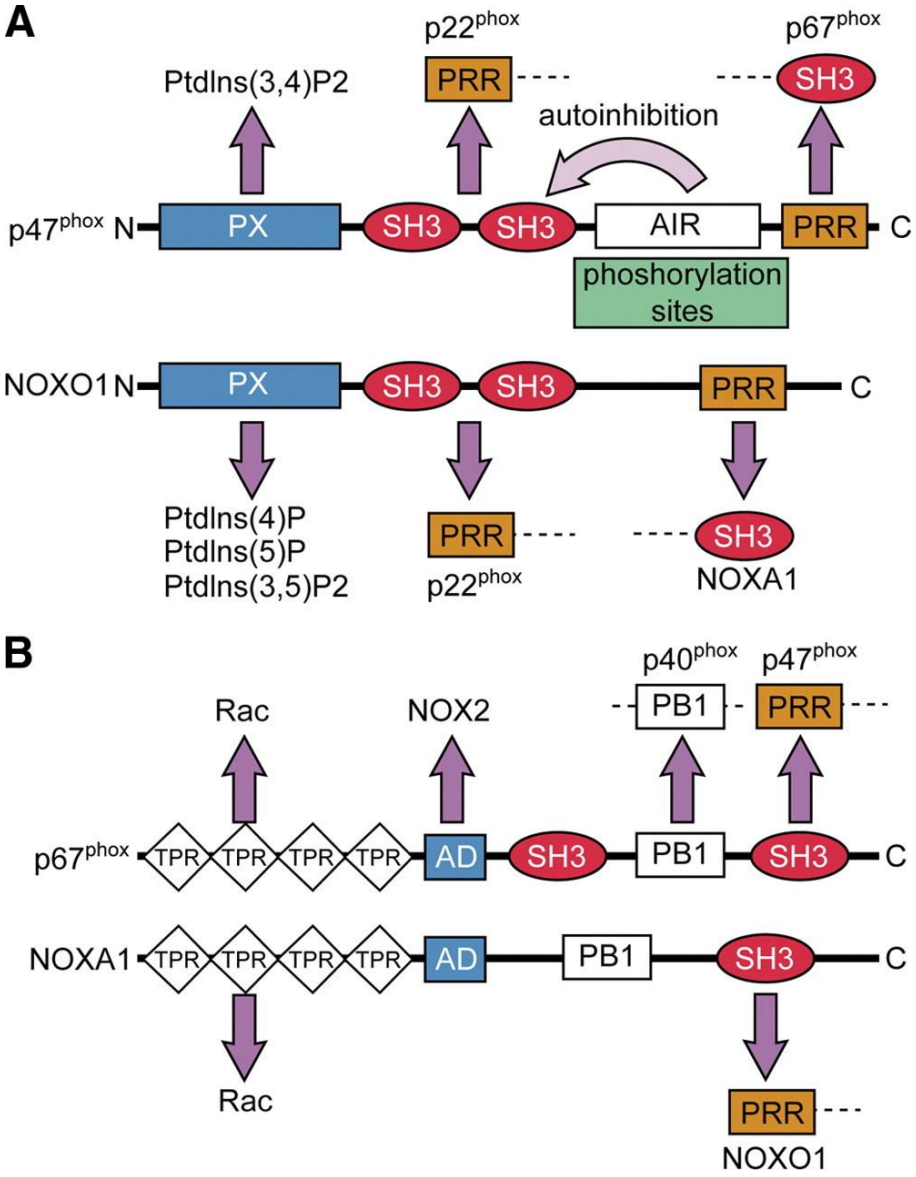

Figure 10. ***A)*** *The two organizer homologs, p47^{phox} and NOXO1, share a similar set of motifs.* ***B)*** *Also the similarity between the two activator homologs, p67phox and NOXA1, is reported.* [1]

5. NADPH oxidase 3: the NOX of the inner ear

NOX3, whose function was described for the first time in 2004, shares around 56% amino acid identity with NOX2. Its gene is located on chromosome 6. [76] NOX3, also known as the NADPH oxidase of the inner ear, is obviously typically expressed in the inner ear. In fact, ROS produced by NOX3 located in the cochlea are related to hearing loss, [77] while the ones produced by the isoform 3 of NOXs in the vestibule cause loss of gravitational perception. [78] Low levels of NOX3 have also been identified in the brain and lungs. [41] [29] For what concerns the NOX3 activation mechanism, the role of the cytosolic subunits and activation patterns isn't always so clear. NOX3 is a $p22^{phox}$-dependent enzyme, that is required for its activation. However, *in vivo* the situation is different and remains unclear because no vestibular dysfunction has been reported for $p22^{phox}$-deficient CGD patients. [79] NOXO1 is crucial for NOX3 activation, both in vitro and in vivo. Inactivation of NOXO1 in mice produces a phenotype similar to NOX3 deficiency, suggesting that NOXO1 is essential for NOX3 function. [80] The role of NOXA1 in NOX3 activation is unclear, with studies showing contradictory results. Further in vivo research is needed to determine its necessity. Regarding $p47^{phox}$ and $p67^{phox}$, their physiological relevance is doubtful, especially for $p47^{phox}$, as well as for the NOX3's dependence on Rac. For all these reasons, some biochemical results would rather argue in favor of a constitutive activation of NOX3. However, further studies are necessary. [81]

6. NADPH oxidase 4: the renox

The primary sequence of NOX4 catalytic domain comprises 578 amino acids with a molecule mass of 28 kDa, while the full NOX4 protein is 66.5 kDa. [42] Compared with NOX1 and NOX3, NOX4 is distantly related to $gp91^{phox}$/NOX2, exhibiting only 39% identity in amino acid sequence. [74] The gene for human NOX4 is located on chromosome 11. Also known as 'Renox', it is largely expressed in the kidney. NOX4 is also expressed in osteoclasts, [82] [83] endothelial cells, [84] [85] smooth muscle cells, [86] [87] hematopoietic stem cells, [88] fibroblasts, [89] [90] keratinocytes, [91] melanoma cells, [92] and neurons. [93] NOX4 generates ROS through its interaction with the $p22^{phox}$ subunit. Unlike other isoforms, NOX4 does not require the recruitment of cytosolic subunits or Rac for its activation, making it a constitutively active enzyme. [94] Although constitutively active, its expression is presumably regulated by the cellular

localization of NOX4, activation factors such as disulfide isomerase (PDI), or factor Poldip2 (**Figure 11**). [95] [96]

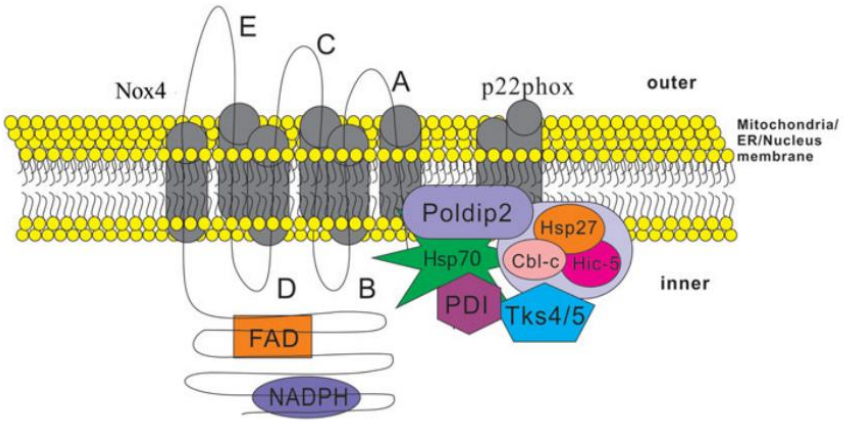

Figure 11. *Schematic illustration of structure and regulatory proteins of NOX4.* [42]

NOX4 expression increases in response to oxidative stress and is upregulated by several stimuli, including Transforming Growth Factor (TGF)-β1, [89] Tumor Necrosis Factor (TNF)-α, [97] and angiotensin II. [98] Additionally, NOX4-mediated ROS production can be triggered by hypoxia, lipopolysaccharide (LPS), insulin, and angiotensin. Additionally, NOX4 produces H_2O_2 as a unique (or major) ROS product. [99]

7. NADPH oxidase 5: the atypical one

NOX5, which shares 27% identity with NOX2, was the last of the seven isoforms to be identified. It was independently discovered by two research groups in 2001. Cheng *et al.* identified it as a cDNA that encodes a protein consisting of 565 amino acids, while Banfi *et al.* reported it as a cDNA predicting a protein of over 700 amino acids. [17] [20] The human NOX5 gene is located on chromosome 15. It is described as a protein of 85 kDa, this suggests that it is a non-glycosylated protein. [100] NOX5 is a monomeric protein that shares with the rest of the NOX family the catalytic core. It contains, in addition, a CalModulin Binding Domain (CaMBD) and EF-hand domain and does not require activating or organizing subunits. [101] However, given the presence of this regulatory domain, the activation of NOX5 is mediated by an increase in cytoplasmic concentration of Ca^{2+}. [20] Specifically, NOX5 regulation occurs through a direct interaction between the N-terminal EF-hand regulatory domain and the C-terminal catalytic region of the DH domain (CDHD). The

interaction site is composed of two main segments: segment 637-660, known as REFBD (Regulatory EF-hand Binding Domain), and segment 489-505, a phosphorylatable region called PhosR. The latter consists of 17 amino acid residues that interact with NOX5-EF in a calcium-dependent manner, and phosphorylation of this region increases the enzyme's sensitivity to calcium ions. The REFBD segment consists of 24 amino acids that interact with the EF regulatory domain in a calcium-dependent manner and play an autoinhibitory role (**Figure 12**). [102]

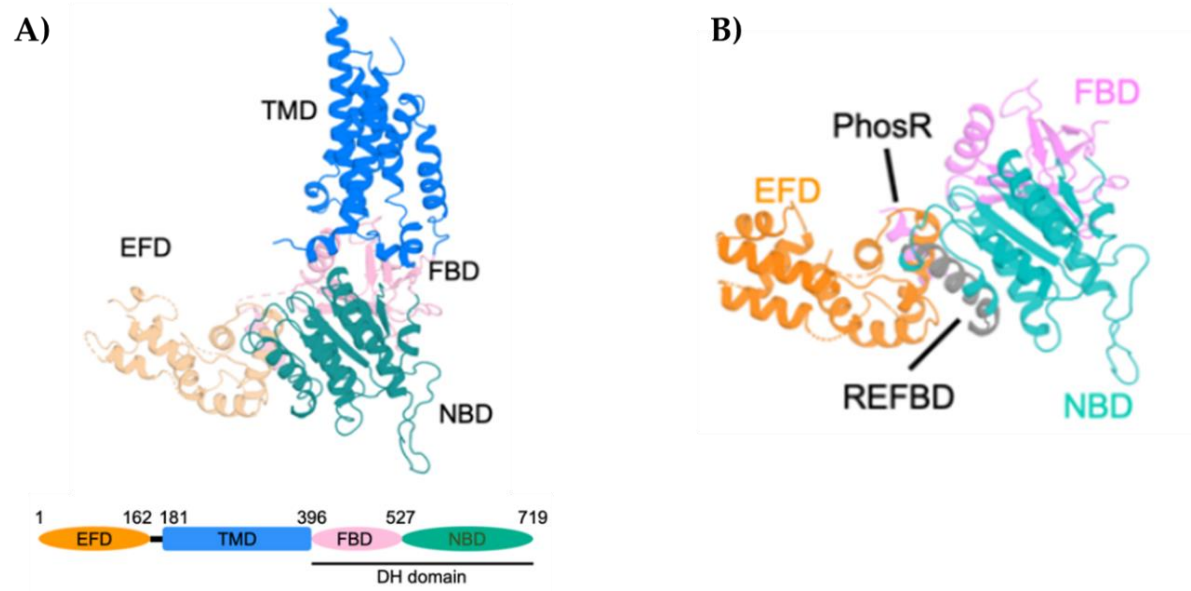

Figure 12. A) *Domain architecture and structure of human NOX5.* **B)** *Structural details of the cytosolic DH domain of human NOX5.* (*EFD: EF-hand domain; TMD: transmembrane domain; FBD: FAD-binding domain; NBD: NADPH-binding domain; DHD: dehydrogenase domain).* [103]

Other proteins, such as calmodulin, heat shock protein 90 (Hsp90), caveolin-1, and tyrosine kinase c-Abl modulate the activity of NOX5 but are not strictly necessary for its functionality. [104] [105] [106] NOX5 is expressed in several human tissues, including lymphoid testicles, testes, endothelial cells, and smooth muscle. [17] [101] [69] Recent data imply NOX5 in cell transformation and cancer. [107] However, our dependence on rodents as models of human disease and the absence of NOX5 in the genomes of rodents both hindered our understanding of the functional meaning of NOX5 in humans. [43] The evolutionary process by which rodents have lost this enzyme is unknown, but data suggest that the NOX5 functions are replaced by other members

of the NADPH family oxidase. It is important to consider that the presence of NOX5 is not limited only to vertebrates: NOX5-like proteins are also found in plants, fungi, protists, and cyanobacteria. The first crystallographic structural model of the catalytic core of NOX5 was obtained using *Cylindrospermum stagnale* as a model system (*cs*NOX5). It is a cyanobacterium whose NOX5 shares 40% sequence identity with *h*NOX5. [27] This wide distribution of NOX5 homologs in the different realms has, therefore, suggested that NOX5 is the oldest member of the NOX family. [108]

7.1. The mechanism of activation of NOX5

The activation of NOX5 differs from that of other NOXs, like NOX1, NOX2, NOX3, and NOX4, as it does not rely on regulatory subunits. Similar to DUOX1 and DUOX2, NOX5 activation is regulated by an increase in calcium ion concentration due to the presence of a calcium-binding regulatory domain that contains four EF-hand domains. [101]

At the molecular level, the activation mechanism involves the interaction of the EF-hand domain with the catalytic DH domain, leading to the enzyme's activation. [107] Although the affinity between REFBD and DH is relatively low (with a K_d of about 1 μM), the intramolecular interaction between these two domains, as they are on the same polypeptide chain, is energetically favored, stabilizing the two regions and potentially increasing the affinity for NOX5-EF. [109] [110] It is also important to note the presence of a calmodulin-binding site near the EF regulatory domain. Both binding sites regulate NOX5 in a calcium-dependent manner but with significant structural differences. [111] The aromatic residues essential for interaction with calmodulin in the CaMBD are absent in REFBD. Additionally, REFBD is more hydrophobic and has an equal number of positive and negative charges, while CaMBD is positively charged. These two regulatory mechanisms, through CaMBD and REFBD, are still compatible as they interact with the catalytic DH domain in separate regions. CaMBD is located just after the third NADPH-binding subregion, while REFBD is positioned immediately before it. [104] This arrangement indicates that both domains are close to the "molecular switch," allowing regulatory signals to be transmitted to the conserved aromatic residue in the C-terminal region, which controls NADPH's access to its binding site. [104] It is hypothesized that calmodulin does not function as an independent activator, but rather through a synergistic mechanism involving the activation of NOX5's REFBD. [101] It is crucial to emphasize that calmodulin does not

activate the enzyme when calcium levels are saturated; however, when calcium levels are low and insufficient to fully activate the EF domain, the presence of calmodulin helps increase NOX5 activity. [27]

In 2024, Cui *et al.* determined cryo-EM structures of human dimeric NOX5 from pre- to post-reaction states, underlying this Ca^{2+}-dependent NOX5 activation (**Figure 13**). [103]

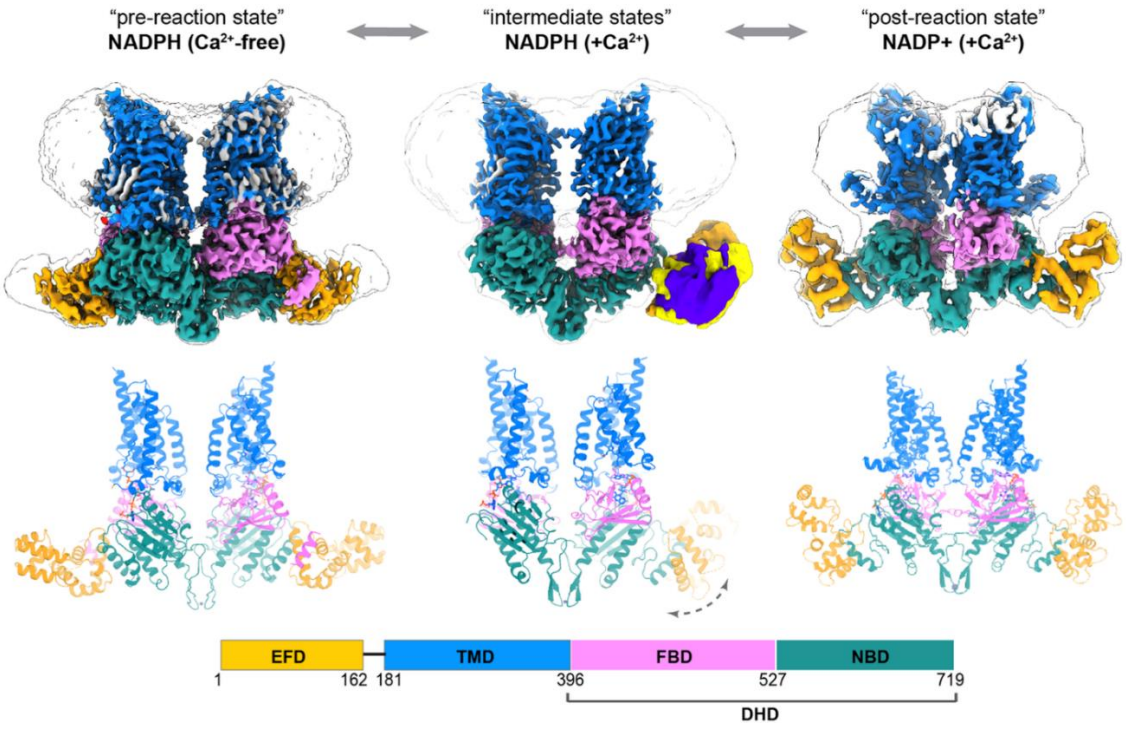

Figure 13. *Structures of NOX5 in the pre-reaction (EGTA + NADPH), intermediate (Ca^{2+} + NADPH), and post-reaction (Ca^{2+} + $NADP^+$) states. These conformations represent the EF-hand domains movements during the NOX5 activation process.* [103]

When Ca^{2+} binds, it prompts the EFD to show the REFBD motif, causing a minor disruption in the NBD. Simultaneously, the EFD moves upward (shortening the distance by more than 12 Å between EFD and TMD), loosening the preTM1 helix that lies above the NADPH binding site. These changes work together to relax the NADPH-binding pocket, allowing the nicotinamide group of NADPH to become more flexible. This increased flexibility initiates the electron transfer between

NADPH and FAD, ultimately resulting in the production of superoxide (**Figure 14**). [103]

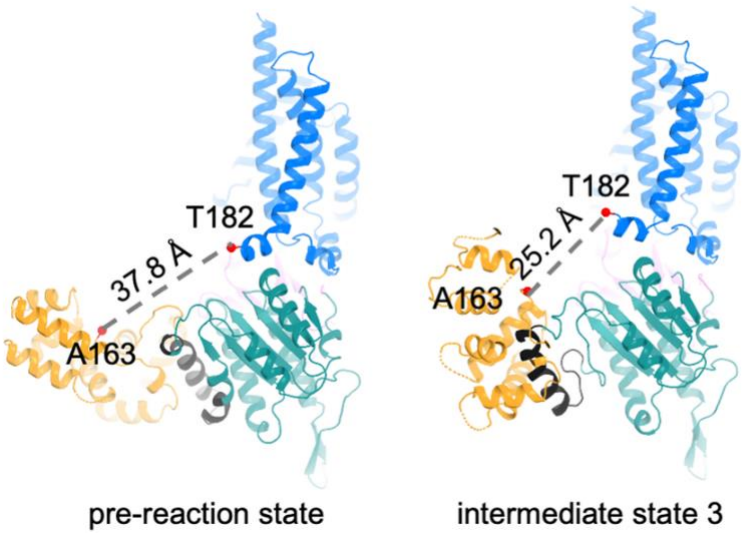

Figure 14. *Conformational changes between pre-reaction and intermediate states of NOX5 (EFD, REFBD, NBD, FBD, and TMD are depicted in orange, black, green, light pink, and light blue, respectively).* [103]

Furthermore, they identified an unexpected putative cysteine-based Zn^{2+}-binding site, mutations of which disrupt the enzymatic activity of NOX5. Specifically, they identified a Zn^{2+} between the two CXXC motifs at the dimer interface. The mutation of C568S or C571S at the zinc finger could destabilize the NOX5 dimer, leading to diminished enzymatic activity of NOX5. Moreover, when TPEN, a zinc chelator, was introduced, it led to a dose-dependent decrease in NOX5 activity. These results indicate that the CXXC motif at the dimer interface forms a zinc finger, which plays a key role in maintaining NOX5 protein stability and its kinase activity (**Figure 15**). To summarize, the Zn^{2+}-binding region provides an extra surface for potential binding protein partners. [103]

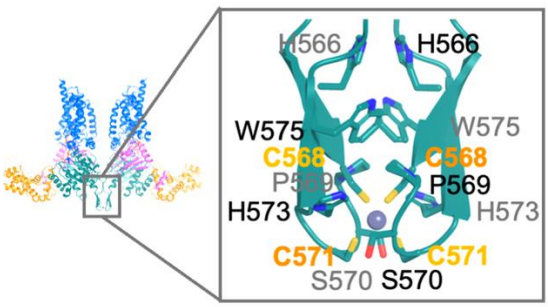

Figure 15. *Structural details of the zinc-binding site at the dimer interface of human NOX5.* [103]

8. Dual oxidase 1 and 2: the thyroid oxidases

Dual oxidases 1 and 2 (DUOX1 and DUOX2) were the first identified thyroid NADPH oxidases, which are fundamental for thyroid hormone production. [112] The discovery of all the isoforms observed so far has always preceded the understanding of their functions. However, for the two thyroid NADPH oxidases, DUOX1 and DUOX2, the case was different. For a long time, it was known that thyroid epithelial cells produced H_2O_2 on the plasma membrane in a calcium and NADPH-dependent manner. [113] Therefore, researchers were trying to identify NADPH oxidases involved in this function. It took fifteen years to achieve this goal. [114] The genes for both isoforms, DUOX1 and DUOX2, are located on chromosome 15. [115] DUOX enzymes are glycosylated. Structurally, in addition to a homologous domain with NOX-1/2/3/4 and an EF-hand structural domain, DUOX1 and DUOX2 proteins have a seventh transmembrane domain in the amino-terminal region. [116] Additionally, they possess peroxidase homology domain (PHD). It is unclear whether the DUOX PHD functions as a peroxidase. One study suggests that it has peroxidase activity when expressed as a recombinant protein. However, from a structural perspective, this is surprising. [117] In fact, DUOX peroxidase homologous domains lack many amino acid residues identified as essential for peroxidase function. Nevertheless, the peroxidase homologous region of DUOX2 appears to be functionally important, as hypothyroidism has been reported in patients with mutations in the extracellular domain.

In the thyroid, a deficiency in thyroid peroxidase leads to severe hypothyroidism due to the lack of peroxidase-dependent hormone synthesis. [118] [32] Indeed, H_2O_2 is the limiting factor in the oxidation of iodide in thyroid hormone synthesis. Iodine enters the thyroid as iodide through an active transport process mediated by the Na^+/I^- symporter. Iodide is oxidized to a higher oxidation state before acting as an agent capable of iodinating thyroglobulin, the precursor of thyroid hormones. [21] Both the iodination of thyroglobulin and the oxidative coupling of the resulting iodotyrosines into iodothyronines occur in the follicular space, in close contact with the apical pole of the thyrocytes. [119] Three different systems are co-localized within the apical plasma membrane and cooperate in the hormone-generating reaction: an iodide transporter, thyroid peroxidase, and an H_2O_2-generating system. [120] There has been a heated debate about whether thyroid oxidases generate hydrogen peroxide directly or if hydrogen peroxide is generated via a superoxide intermediate. It has been observed that the immature and partially glycosylated form of DUOX2 generates superoxide anion, while the mature form generates

hydrogen peroxide. It is hypothesized that post-translational modifications favor the intramolecular dismutation of superoxide into hydrogen peroxide. Overall, it is likely that the primary product of DUOX enzymes is superoxide and that a rapid dismutation into hydrogen peroxide often precludes the detection of a superoxide intermediate. [121]

Both DUOX1 and DUOX2 are highly expressed in the thyroid. DUOX1 has also been described in airway epithelium and the prostate, while DUOX2 has been found in the ducts of the salivary gland, the rectal mucosa, throughout the gastrointestinal tract (including the duodenum, colon, and cecum), in the airway epithelium, and the prostate. [122] [123] [80] [124] DUOX1 and DUOX2 have mixed regulation: in addition to possessing an EF regulatory domain, they also require oligomerization with their auxiliary protein called dual oxidase activator (DUOXA). Similar to the homologous genes in humans that encode for DUOX1 and DUOX2, also DUOXA protein is encoded by DUOXA1 and DUOXA2 (**Figure 16**). [118] [125] In 2021, Wu *et al.* present the cryo-EM structures of *human* DUOX1–DUOXA1 complex in both high-calcium and low-calcium states, providing insights into the structure and mechanism of calcium activation for DUOX. [126]

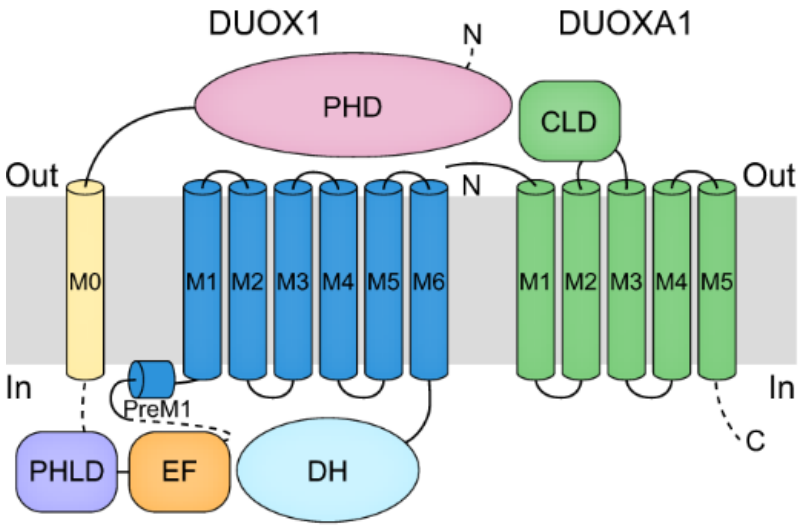

Figure 16. *Topology of an example of DUOX enzymes: hDUOX1 and hDUOXA1 subunits (PHD represents the peroxidase homology domain, PHLD represents the pleckstrin homology-like domain, and CLD the claudin-like domain).* [126]

The N-terminal PHD domain of *human* dual oxidase 1 (*h*DUOX1) has sequence similarity to other peroxidases. Typically, functional peroxidases rely on a histidine-coordinated heme cofactor for catalysis. However, in the PHD domain of *h*DUOX1, crucial residues necessary for heme binding, such as the histidine that ligates the heme, are absent. This absence is supported by the fact that no heme density was observed in the structure of the *h*DUOX1 PHD, indicating that this domain is likely not catalytically active as a peroxidase. Instead, the PHD domain might serve a non-enzymatic role in *h*DUOX1.

There are shown two putative cation densities in PHD (cation binding site 1 and 2, CBS1 and CBS2). Mutations on both CBS1 and CBS2 fail into the DUOXA1 assembling with DUOX1 probably because these mutations could affect the folding of the PHD domain, which suggests that CBS1 and CBS2 play important roles in stabilizing the protein structure of DUOX1, potentially contributing to the overall protein stability required for proper assembly with DUOXA1. [126]

8.1. Conformational change of a thyroid oxidase upon calcium activation

In the comparison of the DUOX1 structures in low-calcium and high-calcium states, the structural changes in the extracellular and transmembrane layers are minimal. However, significant conformational changes occur in the cytosolic layer. In the absence of calcium, the EF module transitions from an extended to a contracted shape. Specifically, EF2 moves away from the DH domain. Additionally, the PHLD undergoes an outward rotation of 17.2° relative to the TMD and DH domains. These conformational changes disrupt several inter-domain interactions observed in the high-calcium state.

As a result, the docking of the DH domain onto the TMD weakens, increasing the mobility of the DH domain. The increased mobility of the DH domain likely reduces the efficiency of electron transfer, thereby diminishing DUOX's catalytic activity (**Figure 17**). [126]

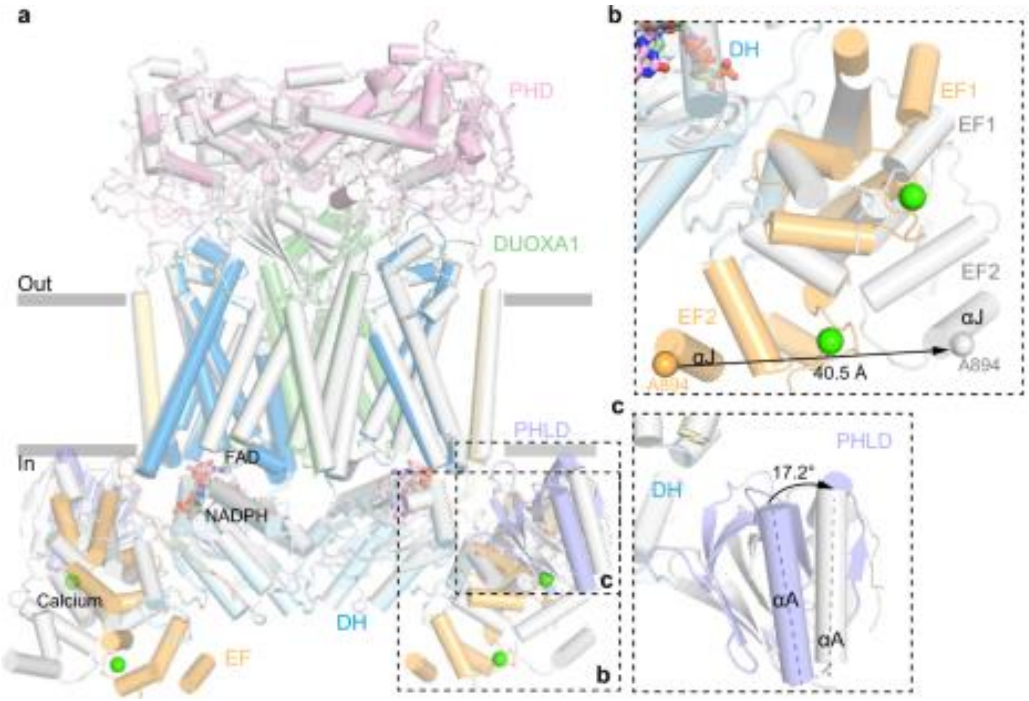

Figure 17. ***a)*** *Structural comparison of hDUOX–hDUOXA1 complex between the high-calcium state (colored) and the low-calcium state (gray).* ***b,c)*** *Close-up view of the conformational changes of EF-hand and PHLD modules.* [126]

In the study by Sun in 2020, DH domain flexibility depends on the dimer status of *mouse* DUOX1-DUOXA1 complex since it is resolvable in the dimer but not dimer-of-dimer. [32] On the other hand, both active and inactive *h*DUOX1-DUOXA1 cryo-EM structures by Wu and co-workers are characterized as dimer-of-dimers and the electron density maps allow for modeling of all intracellular domains. Despite these differences, both studies indicate that the cytosolic DH domains of DUOX1 are dynamically flexible and can be rigidified through dimerization or binding of calcium. In general, a closer examination of the structural differences between the high and low calcium *h*DUOX1-DUOXA1 complexes reveals the direct impacts of calcium-dependent EF-hand conformation on DH domain stabilization. [28]

9. NOXs and diseases

ROS play critical roles in numerous cellular signaling pathways, so the NOX family is implicated in various pathological conditions. Below is a summary of the main pathophysiological consequences of NOX-mediated ROS generation, focusing on cardiovascular and neurodegenerative diseases, the immune system, and cancer (**Figure 18**). [49] [25]

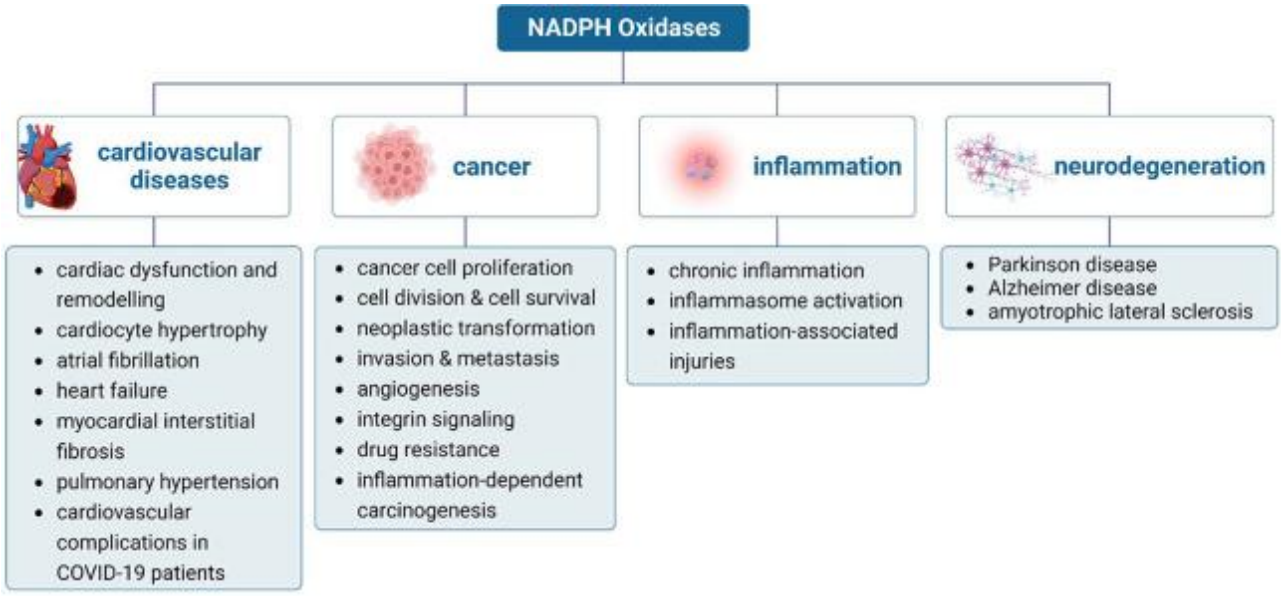

Figure 18: *Overview of the main pathophysiological consequences of NOX-mediated ROS generation.* [25]

9.1. NOXs and cardiovascular diseases

NOX enzymes play a critical role in cardiovascular diseases through oxidative stress, disrupting cellular signaling and damaging essential molecules. This leads to issues like endothelial dysfunction and impaired vascular tone. NOX activation, particularly by angiotensin II (Ang II), contributes to conditions, such as hypertension, diabetes, and atherosclerosis by promoting inflammation and vascular damage. [127] [128] In animal models, knockouts of NOX1, NOX2, and NOX4 show protection against these conditions. [129] NOX-derived ROS also lead to dysfunction in other systems, including endothelial nitric oxide synthase (eNOS), causing hypertension and conditions like abdominal aortic aneurysm (AAA). [130] [131] NOX enzymes are involved in cardiac hypertrophy, arrhythmias, and ischemia-reperfusion (IR) injury, with ROS levels determining whether the effects are

protective or harmful. In atherosclerosis, NOX enzymes oxidize LDL, contributing to plaque formation, though NOX4 may have a protective role due to its anti-inflammatory effects. [132] NOX overactivation has also been observed in COVID-19-related cardiovascular complications, suggesting a role in thrombotic events. [133] [134] Overall, NOX enzymes are critical in cardiovascular disease progression and represent potential therapeutic targets for managing oxidative stress-related conditions.

9.2. NOXs and cancer

Intracellular production of ROS has been experimentally linked to cancer development. [135] ROS can cause DNA damage by modifying bases and sugars, creating DNA-protein cross-links, and inducing strand breaks. Due to the low redox potential of guanine (G), its oxidation to 8-oxo-dG is one of the most common forms of damage. [136] This alteration resembles thymine (T), leading to frequent G-to-T transversions, common mutations in lung, breast, ovarian, gastric, and colorectal cancers. [137] Additionally, ROS can disrupt signaling pathways that regulate cancer growth and progression. ROS have been shown to directly inhibit protein tyrosine phosphatases (PTPs) by oxidizing the sulfur atom in the catalytic site cysteine, forming a "sulfenamide modification" with the nitrogen of the adjacent amide backbone. [138] This inactivation of PTPs is critical for activating receptor protein tyrosine kinases, which promote cancer cell differentiation, proliferation, and survival. Thus, ROS-induced PTP inhibition plays a significant role in the progression and maintenance of malignant cells. [139] As a result, there has been growing interest in understanding the specific roles played by different NOX isoforms in tumor development and progression. Studying these isoforms is crucial for uncovering their precise functions in cancer and exploring potential therapeutic targets for treatment. [25]

9.3. NOXs and inflammation

Extensive research over the past decades on immune defense mechanisms, particularly during phagocytosis, has significantly enhanced our understanding of the NOX enzyme family. [140] [141] These studies have revealed how NOX enzymes, beyond just NOX2, contribute to immune responses by generating ROS, playing vital roles in pathogen elimination, inflammation regulation, and tissue protection.

[142] This growing knowledge has provided valuable insights into the entire NOX family's diverse physiological functions and clinical relevance in immune defense and disease processes. [143] Decades of research on phagocytosis have expanded the understanding of the NOX family, particularly in conditions like chronic granulomatous disease (CGD), where mutations in NOX2, the primary ROS source in polymorphonuclear leukocytes (PMNs), lead to increased infection susceptibility. In bacterial infections, compounds like interleukin-8 regulate PMN migration and NADPH-oxidase activation. NOX2-generated ROS help destroy pathogens and disable bacterial virulence factors. [144] For example, in *Staphylococcus aureus*, HOCl oxidizes quorum-sensing peptides, neutralizing virulence. Though NOX2 is central to innate immunity, other NOX enzymes contribute. [145] For example, DUOX1/2, found in airway mucous membranes, produces H_2O_2, which lactoperoxidase is used to generate microbiocidal compounds. Studies in *Drosophila* highlight DUOX1/2's importance in gut immunity, as silencing *Duox* increases susceptibility to infections. [123] NOX1 also supports mucosal immunity in the colon, while NOX4 interacts with toll-like receptor 4 (TLR4) to activate immune-related transcription factors like NF-κB. [146]

9.4. NOXs and neurodegenerative disorders

The human nervous system, consuming about 20% of the body's oxygen, produces high levels of ROS, which can lead to oxidative stress. This stress plays a crucial role in neuroinflammation and neurodegenerative diseases like Parkinson's disease (PD), Alzheimer's disease (AD), and amyotrophic lateral sclerosis (ALS). [147] [148] NOX enzymes, particularly NOX1, NOX2, and NOX4, contribute significantly to ROS production in the brain and are heavily implicated in these conditions. [149] In Parkinson's disease, NOX enzymes contribute to neuron degeneration and α-synuclein aggregation. [150] NOX2 is linked to oxidative stress in microglia and neurons, while NOX4 and NOX1 are involved in mitochondrial dysfunction and α-synuclein misfolding, respectively. [151] These processes worsen oxidative damage and contribute to neurodegeneration. In Alzheimer's disease, NOX2 and NOX4 are involved in ROS-mediated damage caused by amyloid-β (Aβ) plaques, contributing to vascular dysfunction, blood-brain barrier breakdown, and tau protein accumulation. [152] [153] NOX-derived ROS are also linked to mitochondrial dysfunction and cell death processes such as ferroptosis in AD patients. [154] Similarly, in ALS, NOX2-derived ROS contributes to motor neuron degeneration, with studies

showing that removing NOX1 or NOX2 slows disease progression and improves survival. [155] NOX activity disrupts key pathways such as IGF1 signaling, exacerbating motor neuron damage. [156] Collectively, NOX enzymes are central to the oxidative stress mechanisms driving these neurodegenerative diseases, highlighting them as potential therapeutic targets.

9.5. NOX1 pathological implications: cardiovascular and neurodegenerative diseases

NOX1 has emerged as a critical player in both cardiovascular and neurodegenerative pathologies, with its contributions being closely tied to its cellular localization and functional properties. First identified in 1999, NOX1 is predominantly situated in the plasma membrane of vascular smooth muscle cells and endosomes, implicating its role in vascular health and disease. [157] This enzyme is upregulated in response to several stimuli, including vasoactive agonists, growth factors, pro-inflammatory cytokines, and advanced glycation end products. [158] Its activation initiates a cascade of events that significantly disrupt normal cardiovascular function. In cardiovascular diseases, NOX1 has been shown to decrease nitric oxide (NO) availability, which is vital for maintaining vascular tone and endothelial function. [159] The enzyme's activation triggers the epidermal growth factor receptor (EGFR), further promoting cellular proliferation and vascular remodeling, processes central to atherosclerosis and hypertension. [160] Experimental models with NOX1 overexpression have provided compelling evidence linking this enzyme to pathological vascular changes. These include heightened superoxide production, endothelial dysfunction, and aortic hypertrophy, which are hallmarks of cardiovascular diseases. Moreover, NOX1 is integral to angiotensin II-induced hypertension and the formation of atherosclerotic plaques. [161] In these conditions, NOX1 expression is often coupled with the upregulation of its activator protein NOXA1, underscoring a complex regulatory network that accelerates disease progression. Conversely, the inhibition or downregulation of NOX1 in genetic models attenuates these pathological changes, highlighting its potential as a therapeutic target for cardiovascular disease intervention. [162] Beyond its established role in cardiovascular pathology, NOX1 is also implicated in the pathogenesis of neurodegenerative diseases, where its contribution to oxidative stress and inflammation is particularly detrimental. NOX1 is expressed in various cell types within the central nervous system (CNS), including neurons, astrocytes, microglia,

and endothelial cells that form the blood-brain barrier (BBB). [163] Its enzymatic activity leads to the production of ROS, which not only exacerbate oxidative damage but also trigger neuroinflammatory responses. In the context of Alzheimer's disease (AD), NOX1 activity has been associated with the accumulation of β-amyloid (Aβ) proteins, the principal components of amyloid plaques. Aβ accumulation, a hallmark of AD, contributes to cerebral amyloid angiopathy (CAA), a condition marked by Aβ deposition in the walls of cerebral blood vessels. [164] This leads to a reduction in Aβ clearance, resulting in white matter hyperintensities, microhemorrhages, and cognitive decline. The vascular deposition of Aβ also causes vascular fragility, disrupts tight junction proteins, and increases the permeability of the BBB, thereby facilitating further neuroinflammation and oxidative stress. Once activated, microglia surrounding Aβ-laden blood vessels release superoxide and nitric oxide, further propagating neuronal damage. [165] This oxidative assault compromises neuronal survival, eventually leading to cell death. Additionally, chronic activation of NOX1 in the CNS accelerates the breakdown of the BBB, facilitating the infiltration of peripheral immune cells and contributing to neurodegenerative progression. The sustained oxidative environment generated by NOX1 activation creates a vicious cycle of inflammation, BBB disruption, and neuronal degeneration. [166] This cascade of events is believed to be central not only to Alzheimer's disease but also to other neurodegenerative disorders where oxidative stress and vascular dysfunction are prominent, such as Parkinson's disease and amyotrophic lateral sclerosis (ALS). [167] [168] [155] In summary, NOX1's role extends beyond simple ROS production; it acts as a central regulator of both cardiovascular and neurodegenerative processes. Its capacity to modulate oxidative stress, vascular integrity, and inflammatory responses places it at the heart of pathophysiological mechanisms that drive disease progression in a range of conditions. The growing body of evidence surrounding NOX1 underscores its potential as a therapeutic target, with inhibitors of NOX1 showing promise in preclinical studies aimed at mitigating oxidative damage and restoring normal cellular function. However, further research is needed to unravel the intricate signaling networks governed by NOX1, paving the way for novel therapeutic interventions that could curb its detrimental effects across various organ systems.

9.6. The large number of pathological implications of NOX2

Overproduction of ROS may initiate a hyper-inflammatory response that not only exacerbates tissue damage, but also contributes to long-term pathological changes. This mechanism links NOX-derived ROS to a wide range of diseases where chronic inflammation, fibrosis, and oxidative damage are central features. A particularly significant enzyme in this context is NOX2, whose ROS production has been implicated in various disease processes. In fact, given the high expression of the NOX2 isoform in various organs, it becomes apparent that its involvement spans a wide range of pathological conditions. [169] Thus, the widespread expression of NOX2 in various organs makes it a central player in a broad spectrum of pathological processes, where the fine balance between protective ROS generation and harmful oxidative stress is often tipped, leading to disease. This highlights the potential of NOX2 as a therapeutic target in treating a wide range of ROS-driven conditions. [49]

9.6.1. NOX2 and neuroinflammatory diseases

Neuroinflammation

Ravelli *et al*., in 2019, investigated the involvement of NOX2 in promoting neuroinflammation during the development of experimental autoimmune encephalomyelitis (EAE), a widely used animal model that mimics multiple sclerosis (MS). [170] The inflammatory response in MS is a key driver of tissue damage and disease progression. A central feature of this inflammation is the overproduction of ROS, which contributes to the destruction of myelin and neuronal injury. Through their research, the authors demonstrated that NOX2 significantly contributes to neuroinflammation by elevating ROS production. This oxidative stress exacerbates the immune response, leading to more pronounced neuronal damage and worsening the disease's clinical symptoms. The study underscores the potential of targeting NOX2 as a therapeutic strategy for reducing neuroinflammation and limiting the progression of MS. [170]

In 2024, Choi and colleagues examined how inhibiting NOX2 can improve resistance to viral-induced neuroinflammation by promoting the M1 polarization of macrophages. NOX2 inhibition affects the immune response, particularly during viral infections that target the nervous system. Viral neuroinflammation often involves the recruitment of immune cells, including macrophages, which can adopt either a pro-inflammatory (M1) or anti-inflammatory (M2) phenotype. M1

macrophages are typically associated with effective antiviral responses, whereas M2 macrophages tend to support tissue repair and suppress inflammation. [171] The researchers found that inhibiting NOX2 promoted the M1 polarization of macrophages, enhancing their ability to mount a robust immune response against viral infections. This shift in macrophage polarization occurred primarily in extraneural tissues (tissues outside the nervous system), suggesting that the immune response in peripheral tissues could play a significant role in controlling neuroinflammation. By promoting M1 macrophage activity, NOX2 inhibition reduced viral spread and subsequent inflammation within the nervous system, ultimately leading to improved resistance to viral neuroinflammation. [171]

Traumatic Brain Injury

Traumatic brain injury (TBI) continues to be a leading cause of death globally, with numbers rising despite advancements in immediate care for head trauma. [172] [173] Research using animal models, specifically rodents with cortical impact injuries, highlights the role of NOX2-generated ROS in promoting neuroinflammation and neuronal death. In one experiment, TBI was induced in both NOX2-deficient (knockout) and wild-type mice. In wild-type mice, NOX2 levels increased primarily in the microglial cells of the injured hemisphere, whereas knockout mice showed significantly smaller contusion areas, fewer TUNEL-positive cells (which indicate cell death), and reduced levels of harmful metabolites like O_2^- and $ONOO^-$. [167] Other studies also demonstrated a sharp rise in NOX activity in the cortex and hippocampus regions shortly after the impact, while the use of NOX2 inhibitors such as apocynin or NOX2ds-tat led to a significant reduction in $O_2^{\bullet-}$ levels, oxidative stress markers, disruption of the blood-brain barrier, microglial activation, and neuronal death. [174] [175] [176]

Alzheimer's Disease

One hallmark of AD is the accumulation of beta-amyloid (Aβ) proteins in the brain, particularly the Aβ(1–40) and Aβ(1–42) peptides, which are generated from amyloid precursor protein (APP). [177] These peptides accumulate in the extracellular space, forming fibrils in AD patients. [178] Aβ fibrils have been shown to activate NOX2 in microglial cells and other immune cells, leading to ROS production and the release of inflammatory cytokines, exacerbating tissue damage. [179] Postmortem analysis of

human AD brains revealed elevated NOX2 activity in the cortex compared to healthy controls and increased levels of $p47^{phox}$ and $p67^{phox}$ in membrane fractions. [180] Furthermore, NOX2 may also impair cerebral blood flow in AD patients. [181] In transgenic mice that overexpress Aβ, the introduction of nitric oxide (NO) led to reduced blood flow, but this impairment was absent in NOX2-deficient mice, indicating NOX2's involvement in vascular dysfunction triggered by Aβ. [182] While the amyloid plaque load between NOX2-expressing and NOX2-deficient mice was similar, the NOX2-deficient mice showed less behavioral decline, supporting the role of NOX2 as a key contributor to AD and highlighting it as a target for novel therapies. [183]

Parkinson's Disease

Parkinson's disease (PD) is the second most common neurodegenerative disorder, characterized by motor symptoms such as tremors, rigidity, and slowed movements, alongside cognitive and mood-related impairments. Pathologically, PD is marked by the loss of dopaminergic neurons in the substantia nigra and the accumulation of misfolded alpha-synuclein proteins, known as Lewy bodies. [184] Despite extensive research, the precise cause of PD remains unclear, though both genetic and environmental factors are thought to play a role. Oxidative stress is widely regarded as a key driver in PD progression, with studies showing that environmental toxins like MPTP can trigger microglial activation and induce oxidative damage. [185] NOX2, in particular, plays a crucial role by producing ROS, which directly harms neurons while also promoting inflammatory responses that further aggravate neurodegeneration. In an MPTP-induced PD mouse model, increased NOX2 expression was observed alongside elevated ROS levels in the substantia nigra. [186] However, NOX2-deficient mice displayed less oxidative damage and neurodegeneration compared to their wild-type counterparts. [187] These findings were corroborated by human studies that revealed elevated NOX2 protein levels in the brains of PD patients. This evidence supports the potential for NOX2-targeted drugs in slowing PD progression. [151]

Amyotrophic Lateral Sclerosis

Amyotrophic Lateral Sclerosis (ALS), also known as Lou Gehrig's disease, is a rare but devastating neurodegenerative disorder that leads to the progressive loss of

motor neurons, resulting in muscle paralysis and, eventually, death. [188] While only a small fraction of ALS cases is linked to genetic mutations, such as in the SOD1 gene, oxidative stress is believed to be a major factor in disease progression. [189] Animal models of ALS, such as the SOD1G93A transgenic mouse, have been instrumental in uncovering the role of NOX enzymes in ALS. [156] In both human ALS patients and SOD1G93A mice, elevated NOX2 expression and increased oxidative stress markers were detected in the spinal cord. [155] When NOX2 was genetically deleted in these mice, neurodegeneration was delayed, and survival rates significantly improved. Some studies suggest that NOX1 may also contribute to ALS, though NOX2 appears to play the dominant role.Taken together, these findings highlight the significant role of NOX enzymes, particularly NOX2, in a wide range of neurodegenerative disorders (**Figure 19**), making them attractive targets for therapeutic interventions aimed at reducing oxidative stress and its associated damage.

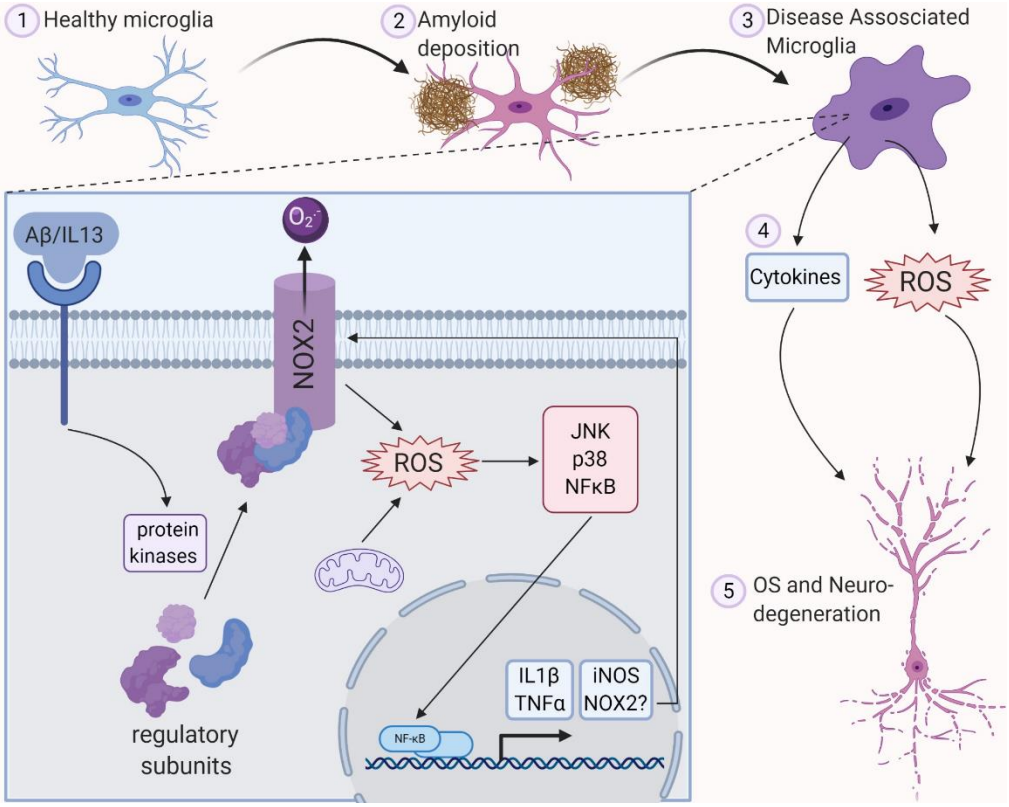

Figure 19: *Neuroinflammation and oxidative stress (OS) are key contributors to the development and progression of neurodegenerative diseases. The accumulation of damaged proteins and injured neurons triggers the activation of disease-associated microglia (DAM) through damage-associated molecular patterns (DAMPs). Once activated, DAM promotes*

chronic inflammation and produce reactive oxygen species (ROS), further exacerbating neuronal damage. In microglia, NOX2 is the primary source of ROS, and its activation in DAM is closely associated with DAMP signaling, inflammation, and the deposition of amyloid plaques, particularly in brain blood vessels. Furthermore, ROS generated from NOX2 and mitochondria can act as signaling molecules that amplify immune responses. This suggests that intracellular ROS signaling may be a key driver of the excessive inflammation and oxidative stress observed in neurodegenerative diseases. [190]

9.6.2. NOX2 and vascular diseases

Excessive ROS production, particularly from NOX2, plays a detrimental role in the pathogenesis of numerous cardiovascular diseases (CVDs).

Hypertension

Hypertension is closely linked to oxidative stress, with NOX2 being a primary source of ROS in vascular tissues. [191] Elevated NOX2 expression and activity are consistently observed in experimental models of hypertension, often driven by angiotensin II (Ang-II), a potent vasoconstrictor that activates NOX2 in vascular endothelial and smooth muscle cells. [192] The superoxide produced by NOX2 scavenges nitric oxide (NO), a crucial vasodilator, reducing NO bioavailability, endothelial dysfunction, and impaired vasodilation. [193] In studies using NOX2-deficient (NOX2−/−) mice, significant reductions in blood pressure (BP) were noted, especially under Ang-II infusion or chronic hypertension models. This suggests that NOX2-derived ROS contribute to the hypertensive state by dysregulating the balance between vasoconstrictor and vasodilator forces. [194] NOX2 inhibitors such as VAS2870 and the specific peptide inhibitor NOX2ds-tat improve endothelial function by reducing ROS production, restoring NO levels, and normalizing BP. [195] [196] [197] However, some studies indicate that in long-term or chronic hypertension models, NOX2 inhibition alone may not fully reverse the hypertensive phenotype, suggesting that other ROS sources or compensatory mechanisms may be involved. [198]

Atherosclerosis

NOX2-derived ROS play a critical role in the pathogenesis of atherosclerosis by promoting oxidative modifications of low-density lipoproteins (LDL) and endothelial dysfunction, two key drivers of plaque formation. [199] In both human atherosclerotic plaques and animal models, NOX2 expression is elevated, particularly in macrophages and endothelial cells, which contribute to the local oxidative environment. [200] Superoxide from NOX2 oxidizes LDL into oxidized LDL (oxLDL), which is then taken up by macrophages to form foam cells, the building blocks of atherosclerotic plaques. [201] Additionally, NOX2-mediated ROS drive the proliferation and migration of vascular smooth muscle cells (VSMCs) from the media into the intima, contributing to neointimal hyperplasia and further plaque development. [202] In NOX2-deficient models, reductions in plaque size, lipid peroxidation, and VSMC migration have been observed. Moreover, the inhibition of NOX2 reduces oxidative stress in the vasculature, improves NO bioavailability, and limits endothelial dysfunction, highlighting NOX2 as a key regulator of the oxidative mechanisms that accelerate atherosclerosis. [203]

NOX2 as a Mediator of Hyperglycemia-Induced Damage in Diabetes

In diabetes, particularly type 2 diabetes, hyperglycemia and elevated free fatty acids induce oxidative stress, which plays a significant role in vascular complications. [204] NOX2 is highly activated in response to hyperglycemia, contributing to both insulin resistance and vascular damage. [205] The chronic activation of NOX2 in endothelial cells, pancreatic β-cells, and adipocytes leads to excessive ROS production, impairing insulin signaling pathways and promoting inflammation. In NOX2−/− diabetic models, glucose tolerance and insulin sensitivity improve, underscoring NOX2's role in metabolic dysfunction. [206] Additionally, vascular complications such as endothelial dysfunction and the accelerated development of atherosclerosis in diabetes are attenuated in the absence of NOX2. [207] These findings suggest that NOX2 not only mediates the oxidative stress associated with glucose toxicity but also drives the vascular complications of diabetes. [208]

Platelet Activation and Thrombosis

Upon platelet activation, NOX2 is rapidly upregulated and produces ROS, which serve as second messengers to enhance platelet aggregation and thrombus formation. [209] NOX2-derived ROS activate key signaling pathways, including protein kinase C (PKC) and Src kinases, which promote platelet granule release and integrin activation, essential steps in thrombus formation. [210] In studies with NOX2−/− mice and NOX2-deficient patients, platelet aggregation is markedly impaired, and thrombus formation is significantly reduced. [211] [212] This identifies NOX2 as a key contributor to thrombotic disorders, where excessive platelet activation leads to the formation of blood clots, potentially causing myocardial infarction or stroke. [213] To summarize, NOX2-derived ROS are implicated in the progression of numerous cardiovascular pathologies, from hypertension and atherosclerosis to diabetes and cerebrovascular diseases. The overproduction of ROS by NOX2 disrupts the redox balance, leading to endothelial dysfunction, inflammation, fibrosis, and thrombosis (**Figure 20**). [191]

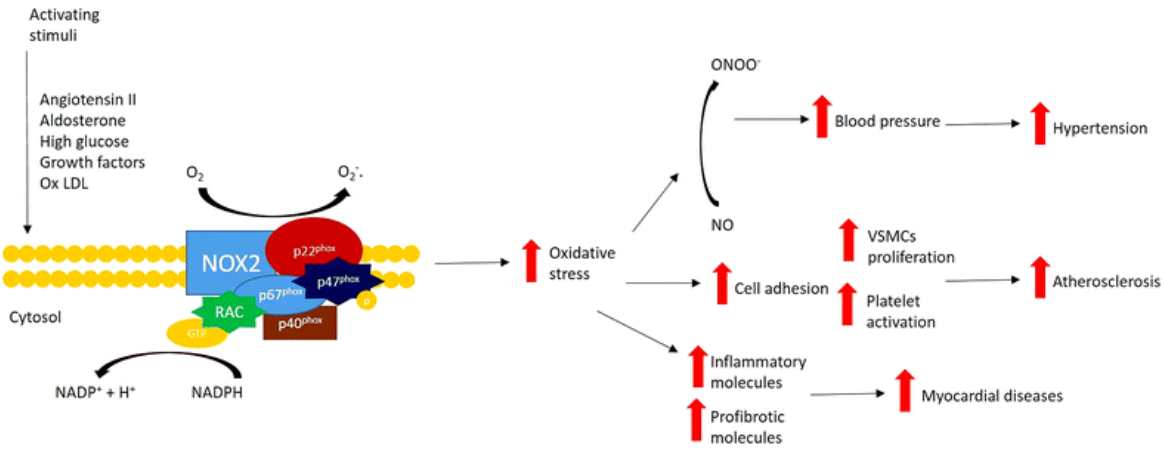

Figure 20: *Schematic illustration of NOX2 involvement in cardiovascular diseases. NOX2 promotes several effects on vascular homeostasis. The activation of NOX2 increases the development of hypertension, atherosclerosis, and myocardial diseases.* [191]

9.6.3. NOX2 and COVID-19

The COVID-19 disease, caused by the SARS-CoV-2 coronavirus, rapidly spread worldwide due to its high transmissibility and virulence. While some patients exhibit mild symptoms, others develop severe complications like acute respiratory distress syndrome (ARDS), initially affecting the lungs and potentially extending to the central nervous system (CNS). [214] This can manifest through neurological symptoms such as headaches, fatigue, motor issues, and even seizures. Additionally, the hypoxic states induced by severe cases of COVID-19 can lead to thromboembolic events. The infection is initiated when the viral Spike protein binds to the angiotensin-converting enzyme 2 (ACE2) receptor in human cells. This interaction not only facilitates viral entry but also leads to an increase in angiotensin II levels, which activates the NOX2 enzyme, triggering the release of ROS and pro-inflammatory molecules like tumor necrosis factor-α (TNF-α) and interleukins (IL-1β, IL-2, and IL-6). [215] This inflammatory response is further intensified by the activation of nuclear factor κ B (NF-κB), which upregulates pro-inflammatory genes and promotes neuroinflammation. [216] Both the viral infection and resulting hypoxia activate microglia in the brain, which in turn stimulates NOX2, contributing to oxidative stress. [217] The downregulation of ACE2 expression due to the viral Spike protein binding exacerbates the situation by increasing angiotensin II levels, fueling further NOX2 activation and oxidative stress. This interaction between angiotensin II and NOX2 in COVID-19 patients is thought to be linked to cardiovascular complications, including myocardial infarctions. [218] The ROS production initiated by NOX2 during COVID-19 infection appears to activate the NLRP3 inflammasome in infected cells, while also inhibiting antioxidant responses such as the nuclear factor erythroid 2–related factor 2 (NRF2) pathway. This leads to glutathione depletion and reduced expression of superoxide dismutase 3 (SOD3) in type II alveolar cells, worsening the disease. [219] A study by *Violi et al.* investigated the role of NOX2 in 182 COVID-19 patients requiring mechanical ventilation or suffering from thrombosis, revealing that NOX2 activation was 40% higher compared to controls. [134] The researchers also found that Toll-like receptor 7 (TLR-7), upregulated by viral RNA, contributed to NOX2 activation, assisting the virus in spreading and amplifying the immune response. NOX2 is also implicated in COVID-19-related thrombosis, as its overproduction of hydrogen peroxide and isoprostane, along with nitric oxide (NO) inactivation, leads to platelet aggregation. This was confirmed by measuring sNOX2-dp, a marker of NOX2 activation. Levels of sNOX2-dp were significantly higher in COVID-19 patients, particularly those in

intensive care, compared to those with milder cases, indicating a clear link between NOX2 activation and the severity of the disease (**Figure 21**). [220]

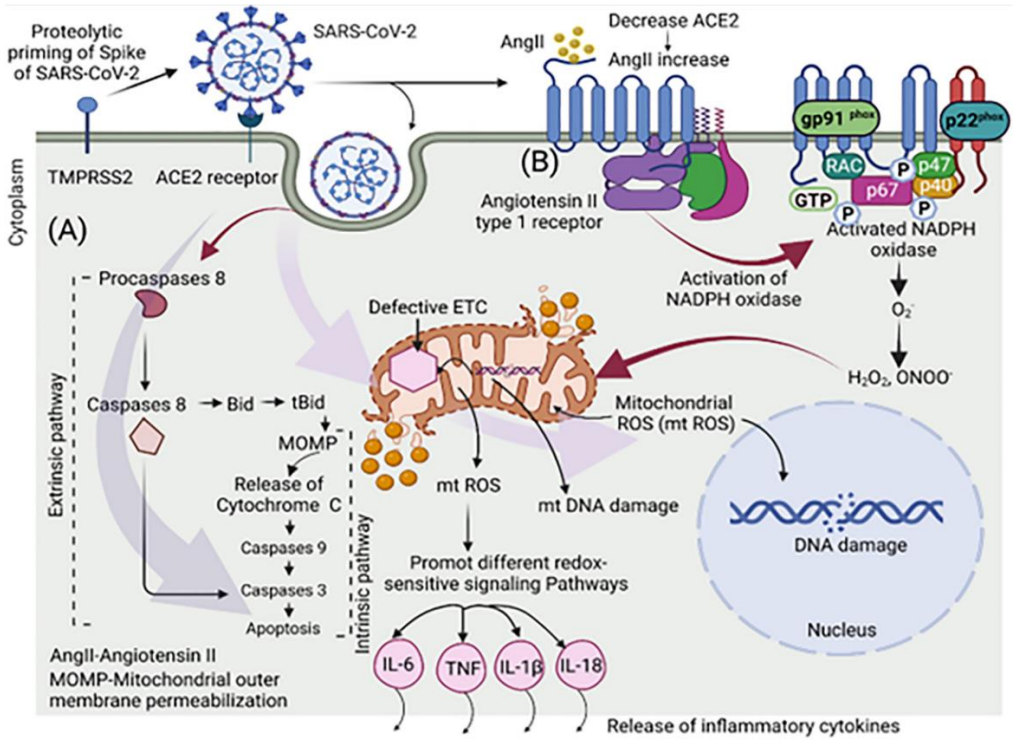

Figure 21: *Schematic illustration of redox imbalance in the endothelial cell upon infection with SARS-CoV-2. Upon infection with SARS-CoV-2, a redox imbalance occurs in endothelial cells through the AngII/AT1R/Nox axis pathway. The virus initially interacts with the ACE2 receptor on the surface of these cells, facilitating its entry via endocytosis. This interaction with viral glycoproteins leads to a downregulation of ACE2 expression, which in turn elevates the levels of angiotensin II (Ang II) due to reduced ACE2 activity. The increased Ang II then binds to the type 1 angiotensin receptor (AT1R), activating a cascade of signaling events within the cell. The AngII-AT1R interaction leads to the activation of NOXs. The production of ROS by NOX initiates oxidative stress, which begins to affect various cellular components. In particular, the ROS damage the electron transport chain (ETC) in mitochondria, leading to dysfunction in mitochondrial processes. This damage extends to mitochondrial DNA (mtDNA), impairing the formation of ETC complexes necessary for proper energy production. Furthermore, ROS also damage nuclear DNA, contributing to the overall cellular stress response. The mitochondrial ROS generated because of this process further amplify redox signaling pathways. These pathways promote the release of inflammatory cytokines, exacerbating the inflammatory state within the cell. As this feedback loop continues, the oxidative stress and inflammation resulting from SARS-CoV-2 infection contribute to endothelial dysfunction, which can have systemic effects, including vascular damage and complications throughout the body.* [221]

9.6.4. NOX2 and cancer

The development of knockout mice with NOX2 deficiency has played a crucial role in studying the role of NOX2-derived ROS in cancer. Studies on mice with a deficiency in the NOX2 subunit, such as Ncf1, have demonstrated reduced growth or incidence of tumors like melanomas and Lewis lung carcinoma, though other tumor types like prostate carcinoma or sarcoma seem unaffected. [222] [223] Further studies indicate that NOX2 is involved in metastasis. Mice deficient in the NOX2 subunit Cybb exhibit reduced lung metastasis after the introduction of melanoma cells and a lower incidence of spontaneous metastases. [224] [225] [226] The inhibition of NOX2 using histamine dihydrochloride (HDC), a NOX2 transduction inhibitor, also reduces lung melanoma metastases, but only in wild-type mice, not in NOX2-deficient ones. This suggests that NOX2-derived ROS contribute to metastasis by impairing natural killer (NK) cell function and that inhibiting NOX2 restores the ability of IFN-γ^+ NK cells to clear tumor cells. [224] Supporting studies confirm that hematogenous metastasis significantly decreases in mice lacking key NOX2 subunits like Cyba, Cybb, and Ncf1, with an increase in antitumor lymphocytes in tumor tissues of NOX2-deficient mice. [226] Although the precise mechanism remains unclear, evidence suggests that NOX2-derived ROS, particularly O_2^- and H_2O_2, are more involved in immunosuppression than other ROS, like those derived from myeloperoxidase (MPO). [227] Studies also suggest that HDC's efficacy depends on the presence of NOX2-expressing $Gr1^+$ myeloid cells, and it does not impact metastasis if NK cells are depleted. [228] HDC treatment increases tumor-infiltrating $CD8^+$ T cells and enhances the effectiveness of immune checkpoint inhibitors like anti-PD-1 and anti-PD-L1, suggesting that it promotes T cell-mediated tumor clearance. [228] In monocytic leukemic cells, especially in acute myeloid leukemia (AML), NOX2 plays a role in survival and expansion. Studies show that NOX2-derived ROS stimulate the transfer of mitochondria from stromal cells to AML cells, aiding in their survival. [229] Moreover, NOX2-derived ROS have been implicated in genomic instability and malignant expansion, particularly in models of Kras-induced myeloid leukemia. $Kras^+$ NOX2-deficient myeloid cells expand slower than NOX2-sufficient ones. [230] [231]

9.7. Effects of NOX3 in the inner ear and acute lung injury

NOX3, while historically less studied compared to other NADPH oxidase family members, has emerged as a crucial player in various physiological and pathological contexts. Its primary role was initially identified in the inner ear, where it significantly contributes to the formation of otoconia, small calcium carbonate crystals embedded in the statoconic gelatinous membrane. This membrane, present in the vestibular, utricular, and saccular systems, is essential for detecting linear acceleration and gravity, which are critical for maintaining balance and equilibrium. [80] In animal studies, specifically in mice with NOX3 mutations, the absence of NOX3 impairs the formation of the statoconic membrane, leading to a distinct "head tilt" phenotype indicative of disturbed equilibrium. Similarly, mutations affecting NOXO1, the protein that activates NOX3, result in a comparable "head-slant" phenotype, highlighting the intertwined roles of NOX3 and NOXO1 in otoconia formation and vestibular function. Although the cochlear implications of NOX3 are less clear, its involvement in hearing loss has been suggested through correlations with age-related hearing damage and ototoxic effects of drugs like cisplatin. [76] NOX3 is the most consistently expressed NADPH oxidase enzyme in the ear and is activated by cisplatin in vitro, linking it to oxidative stress-related hearing loss. [232] Recently, NOX3 has also been implicated in acute lung injury (ALI), an area where its role was not previously anticipated. Studies have shown unexpected NOX3 expression in the lungs of mice deficient in Toll-like receptor 4 (TLR4). This finding links NOX3 to the exacerbation of ALI, a severe condition associated with high mortality and limited treatment options. ALI is characterized by oxidative stress from both internal and external sources, including environmental pollutants and oxygen therapy. NOX3-derived reactive oxygen species (ROS) in the lungs contribute to this oxidative stress. Interestingly, TLR4 appears to exert a protective effect against ALI by inhibiting NOX3 induction through the TLR4-Trif-Stat3 signaling pathway. [203] In TLR4-deficient mice, the absence of TLR4 leads to increased NOX3 activity and greater lung damage. [233] Conversely, TLR4-NOX3 double-knockout mice exhibit less lung damage and lower mortality compared to those lacking only TLR4. The TLR4-Hsp70-Trif-NOX3 signaling pathway, involving the heat shock protein Hsp70, plays a crucial role in suppressing NOX3 activity and reducing ROS production, thus offering a potential therapeutic target for ALI. Overall, while NOX3's role in otoconia formation and balance is well-established, its involvement in hearing loss and lung injury opens new avenues for research and potential therapeutic interventions. The discovery of the TLR4-Hsp70-NOX3

pathway highlights NOX3's broader implications in oxidative stress-related diseases and offers promising targets for managing conditions like ALI. [234]

9.8. Pathological implications of NOX4

The NOX4 isoform was originally identified in the renal cortex and therefore initially called "Renox." Progressive kidney disease, such as diabetic nephropathy, continues to increase in the population annually. [235] Chronic kidney disease is characterized by glomerulosclerosis and tubulo-interstitial scarring, which often lead to renal failure. A significant aggravating factor in these pathologies is hyperglycemia, as demonstrated in diabetic nephropathy. Several mechanisms, including oxidative stress caused by NOX4, contribute to the onset of harmful effects on tissues affected by hyperglycemia. This was further supported by in vitro studies on high glucose-cultured kidney cells and in vivo studies on experimental models of diabetes, which demonstrated an overexpression of NOX4 in the kidneys and a consequent increase in ROS levels. [236] NOX4 is an important source of ROS and is also overexpressed in cases of heart failure, but its real implication in cardiovascular pathologies is controversial. *Zhang et al.* in 2010 found that NOX4 knockout mice showed more pronounced heart failure after abdominal aortic banding, while studies by *Kuroda et al.* in the same year showed protection from heart failure following chest aortic banding in NOX4 knockout mice. [237] [238] These observations suggest that NOX4 may influence chronic heart failure through mediating angiogenesis, a role also proven in hindlimb ischemia. However, deregulated activation of NOX4 in severe heart failure can result in toxic levels of ROS. [239] The involvement of NOX4 in stroke pathophysiology is linked to tissue damage from stroke as well as ischemia and reperfusion, events that deregulate NOXs and lead to elevated ROS levels. Animal models of focal cerebral ischemia have confirmed high levels of NOX2 and NOX4 mRNA and activity in the peri-infarct region of the cortex 2 to 48 hours after reperfusion. This was further supported by reduced superoxide and oxidative stress, smaller infarct volumes, and improved neurological function in these models following the administration of NOX inhibitors. [240] Additionally, ROS may stimulate osteoclasts, and reduced antioxidant defense can increase bone resorption, linking NOX4 to bone diseases. Bone is a dynamic organ that undergoes constant remodeling. While bone formation is mediated by osteoblasts, bone resorption is mediated by osteoclasts. [241] The substantial formation of hydrogen peroxide by NOX4 has been associated with

osteoclastogenesis. To demonstrate NOX4's impact on bone homeostasis, *Goettsch et al.* in 2015 showed that NOX4 knockout mice exhibited no activation in femoral lysate, resulting in wider and thicker bones compared to controls. Furthermore, these mutant mice had a bone mineral density (BMD) greater than 30% in the femur, suggesting that NOX4 promotes osteoclast differentiation, thereby worsening conditions like osteoporosis. [242] Finally, NOX4 is implicated in the malignant progression of pancreatic adenocarcinoma. ROS regulate the epithelial-to-mesenchymal transition (EMT) induced by transforming growth factor (TGF-β) in pancreatic cancer cells. [243] NOX4 plays a critical role in the exacerbation of pancreatic cancer, influencing EMT and contributing to the malignancy and lethality of pancreatic carcinoma. [244]

9.9. NOX5 overexpression in vascular diseases and cancer

9.9.1. NOX5 and vascular diseases

In humans, the NOX5 isoform is the main source of ROS at the vascular level. It is stimulated by vasoactive agents such as angiotensin II and endothelin-1, growth factors like platelet-derived growth factor (PDGF) and epidermal growth factor (EGF), as well as pro-inflammatory mediators. The increase in ROS production by NOX5 in endothelial cells is responsible for cell proliferation and the formation of capillary-like structures, which are key processes in atherosclerosis and angiogenesis. [245] In atherosclerosis, oxidative and inflammatory processes have been observed to lead to the overexpression of the NOX5 isoform in vascular cells and macrophages. NOX5 has therefore also been termed the "contractile isoform" because of the crosstalk between calcium signaling and redox signaling, affecting the molecular contraction mechanism in vascular smooth muscle cells. [246] NOX5 plays a critical role in the regulation of intermediate conductance calcium-activated K^+ channels (KCNN4), which are important for the contraction of coronary artery smooth muscle cells and play a fundamental role in the progression of atherosclerosis. [247] The high activation of NOX5 in endothelial cells leads to cell proliferation and the formation of capillary-like structures, which are important for both atherosclerosis and the angiogenic process. These processes are mediated by JNK kinases (c-Jun N-terminal kinases) and stromal cell-derived factor 1. On the other hand, activation of the protective renin-angiotensin system prevents actin cytoskeleton reorganization and inhibits thrombin-induced vascular inflammation by reducing the expression and activity of NOX5. [245] Moreover, NOX5 is crucial in

stroke pathophysiology, as overexpression in mice has been associated with increased blood pressure and a higher stroke risk. [245] However, the relationship between vascular NOX5 and blood pressure appears to be age-dependent. In a study on mice aged 16 to 20 weeks, expressing NOX5 specifically in vascular smooth muscle cells, no increase in blood pressure was observed, whereas in older mice (aged 30 to 35 weeks), blood pressure was significantly elevated. [246] [248] Through ROS production, NOX5 can also affect the function of the renal filtration barrier and regulate blood pressure. The ROS produced by NOX5 also induce inflammation, leading to the expression of cytokines and upregulation of Toll-like receptors, thus fueling ROS generation and contributing to oxidative stress and renal damage, especially in diabetic patients. [249]

9.9.2. NOX5 and cancer

The overexpression of NOX5 and the uncontrolled proliferation of redox-dependent cells have been extensively documented in various cancer types, including gastric cancer, malignant melanoma, breast cancer, prostate cancer, and esophageal cancer. [250] [251] Increased NOX activity and deregulated ROS production can lead to tissue damage, DNA damage, and unchecked cell proliferation, evident even in premalignant conditions such as Barrett's esophagitis. [252] NOX5 appears to play a particularly significant role in the development of esophageal adenocarcinoma, which is often associated with chronic gastroesophageal reflux. This has been linked to the presence of a truncated form of NOX5, lacking the EF-hand domain (NOX5-ε), induced by gastric acid, an important risk factor for this type of cancer. Gastric acid stimulation in the esophagus induces the transcription factor CREB (cAMP response element-binding protein), which promotes NOX5 overexpression. [253] [254] This highlights the association between NOX5 and chronic gastroesophageal reflux. Notably, the NOX5-ε variant is involved in calcium-dependent damage to the DNA region encoding the tumor suppressor gene p16, resulting in lower levels of this protein and contributing to cancer development. Chronic acid exposure is therefore correlated with the progression of Barrett's esophagus (BE) into adenocarcinoma of the esophagus (EA). [255] In EA, the CDKN2A gene, which encodes p16 and p14arf proteins, is the second most commonly mutated gene after the tumor suppressor protein p53. NOX5 overexpression promotes the hypermethylation of CDKN2A, driving the progression of BE and EA. [252] Key pathways implicated in NOX5-ROS-dependent processes include signaling molecules (MAP kinase, PI3K, PKC, and

p27Kip1), transcription factors (APE1/Ref-1, HIF-1α, AP-1, Nrf2, NF-κB, p53, FOXO, STAT5A, and β-catenin), and adapter proteins (Ruk/CIN 85), all of which contribute to the onset and exacerbation of various cancers. [256] The ability of cancer cells to spread to adjacent or distant tissues largely depends on oxygen and nutrients delivered via the vascular system. [257] Angiogenesis is crucial for the development of solid tumors, enabling the direct supply of nutrients to cancer cell clusters. The HIF-1α/VEGF/MMP signaling cascade, activated by hypoxia and ROS, regulates the formation of new blood vessels, promoting tumor growth. NOX5, along with NOX1, NOX2, and NOX4, isoforms present in endothelial cells, participates in every step of angiogenesis, playing a critical role in cancer-induced blood vessel formation. [258] [259] In a recent study by *Ashizawa et al.*, immunohistochemistry revealed a strong correlation between NOX5 expression and stage II or III colorectal cancer, with elevated NOX5 expression found in 60.5% of the analyzed tissues. [260] This implicated NOX5 in worsening disease, as patients with NOX5-positive tumors had significantly lower survival rates than those with NOX5-negative tumors. Additionally, NOX5 expression has been demonstrated in malignant melanoma and prostate cancer, particularly in tumor cells such as LNCaP, DU145, and PC3, which are derived from androgen-dependent prostate adenocarcinoma. [100]

9.10. Role of the DUOX1 and DUOX2 in thyroid tumorigenesis and pathologies

Thyroid hormone production is a multi-step process heavily dependent on redox reactions involving hydrogen peroxide (H_2O_2) as a key oxidative agent. This process occurs within the thyroid follicles, which are the main functional units of the thyroid gland where hormone synthesis, storage, and release happen. The follicles are lined by a single layer of polarized epithelial cells called thyrocytes. These thyrocytes form the walls of the follicle by surrounding a central lumen, which is filled with a protein-rich substance called colloid. [261] Thyroglobulin (TG) forms the main component of this colloid, acting as the precursor for thyroid hormones. Thyroid hormone synthesis involves the oxidative iodination of specific tyrosine residues on TG, known as iodide organification. The enzyme responsible for this step is thyroid peroxidase (TPO), which relies on a sufficient supply of H_2O_2 to function properly. The essential role of H_2O_2 was first documented in 1975 when researchers discovered reduced H_2O_2 production in human thyroid nodules with impaired

iodide organification. [262] Later research in porcine thyroid follicles revealed that DUOX1 and 2 were responsible for this production. [263] Specifically, DUOX2 is the main source of H_2O_2 in thyroid follicles, which is crucial for normal thyroid hormone production (**Figure 22**). [113] [264] However, excessive H_2O_2 levels, typically caused by heightened mitogenic signaling or oncogene activation, have been linked to the development of thyroid cancer. Elevated ROS levels under pathological conditions contribute to carcinogenesis, demonstrating the fine balance necessary for proper thyroid function. [265] [266] [267] In thyroid cancer, elevated DUOX1 mRNA levels have been detected in papillary thyroid carcinomas (PTCs) and follicular adenomas in patients with a history of childhood radiation exposure. [268] Overexpression of DUOX1 in radiation-induced thyroid tumors suggests that DUOX1 contributes to chronic oxidative stress, promoting genomic instability and tumor development. [269] H_2O_2 has been shown to induce RET/PTC1 rearrangements, frequently found in radiation-related PTCs. [270] Additionally, in vitro studies of primary human thyrocytes demonstrated that knockdown of DUOX1 with siRNA reduced radiation-induced DNA damage. [271] Additionally, insufficient DUOX2-derived H_2O_2 has been linked to thyroid dyshormonogenesis, both in vitro and in murine models with genetic knockout or spontaneous mutations in the *duox2* or *duoxa* genes. [272] Recent research also showed that mutations in a single *duox* gene in zebrafish resulted in hypothyroidism-related symptoms, such as growth retardation, goiter, and infertility. These symptoms were reversible with T4 hormone treatment. [273] However, in humans, the connection between congenital hypothyroidism (CH) and DUOX2 functionality is more complex. The first human case suggesting that defective thyroid NOX-dependent H_2O_2 production could cause hypothyroidism and goiter was reported in 2001 in two siblings. [274] A year later, inactivating mutations in DUOX2 were found in hypothyroid patients with defective iodine organification. [272] Since then, numerous studies have identified both transient CH in patients with single allele mutations and permanent CH in individuals with homozygous mutations in the *duox2* or *duoxa2* genes. [275] Both mono- and biallelic DUOX2 mutations have been found in cases of transient and permanent CH. Collectively, these findings underline the importance of DUOX2-derived H_2O_2 for proper thyroid function. [276] H_2O_2 has also been implicated in triggering the onset of autoimmune thyroid diseases. The most common of these conditions, Graves' disease and Hashimoto's thyroiditis, are associated with an imbalance in immune responses, with elevated levels of helper T-cells type 2 (TH-2) in Graves' disease and type 1 (TH-1) in Hashimoto's thyroiditis. These overactive

immune responses are thought to be linked to the dysregulation of DUOX1 and DUOX2, resulting in increased oxidative stress. The excessive H_2O_2 production exacerbates oxidative damage within the thyroid gland, potentially contributing to the autoimmune attack on thyroid tissues that characterizes these diseases. [277] [112]

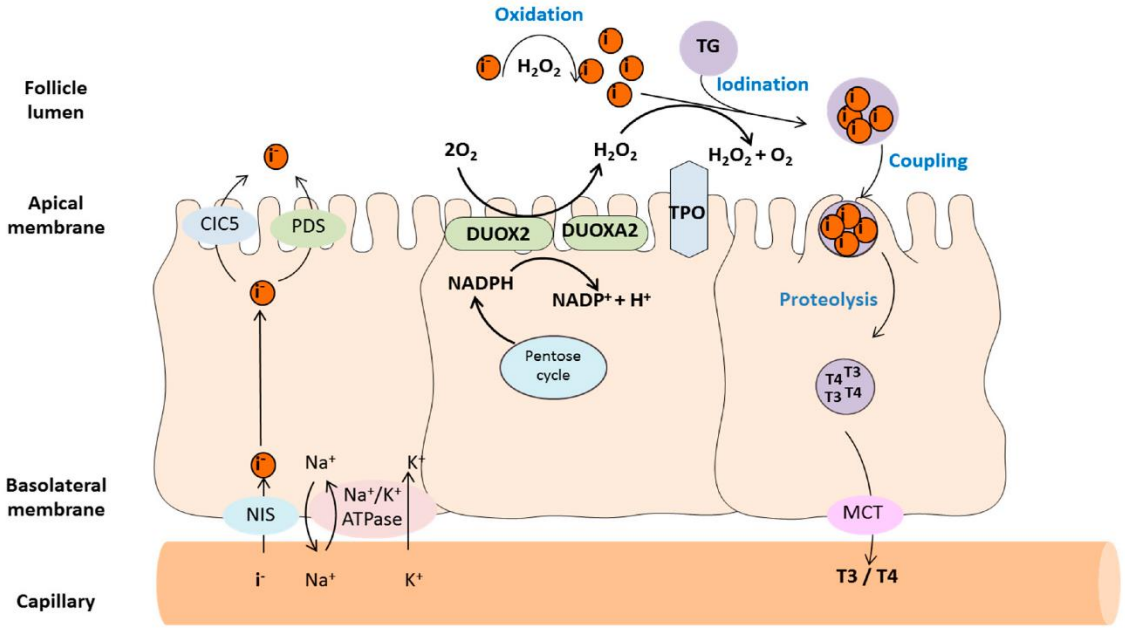

Figure 22: *Thyroid hormones (T4 and T3) are synthesized within the thyroid-specific protein thyroglobulin (TG), through a multistep process, and they remain bound to it until the protein is degraded and T4/T3 are released into the circulation. T4/T3 are then released into the capillary system by monocarboxylate transporters (MCT). Iodine is transported into the thyrocytes by the sodium/iodide symporter (NIS) located in their basolateral plasma membrane. The Na+/K+-ATPase maintains the Na+ gradient providing the energy for this transport. Iodine is then moved from the cytosol into the follicle lumen. The concentrated iodide is then rapidly oxidized by thyroid peroxidase (TPO) using H_2O_2 supplied by DUOX2.* [262]

10. NOXs inhibitors

Recently, the World Health Organization has shaped the new acronym '**naxib**' to define the class of NADPH oxidase inhibitors, [278] considering this one as a new therapeutic class, in connection with the introduction in clinical trials of the first-in-class NOXs inhibitor, Setanaxib (known before as GKT137831). [279] In general, several NOXs inhibitors have been developed, which can be differentiated into two main classes: antioxidants and true NOX binders. The first class exhibits scavenging properties by directly inhibiting ROS. The second class consists of molecules that specifically target NOX enzymes. However, the inhibitors known until now are not selective for the different isoforms and, also, have interference, suffering from off-targets effects, so it was impossible to discern between the non-specific effects exerted by these compounds and their specific binding to NOXs (if any).

The first small molecule used as a NOX inhibitor is **Diphenylene iodonium** (**DPI**), a pan-inhibitor of NOXs (IC_{50} of 0.24, 0.10, 0.09, and 0.02 μM for NOX1, NOX2, NOX4, and NOX5, respectively) acting as an uncompetitive inhibitor of flavoproteins. For this reason, this compound is able to inhibit other enzymes such as NOS, [280] xanthine oxidase, [281] cytochrome P450. [282] Over the years other small molecules have been reported as NOX inhibitors.

Apocynin, a methoxy-substituted catechol also known as acetovanillone, [25] is an intracellular inhibitor of NADPH oxidases by blocking the association of $p47^{phox}$ and $p67^{phox}$ with $gp91^{phox}$. [283] It seems to act as a prodrug that is initially oxidized into its supposed active form, diapocynin, its dimeric form. [284]

Another NOX inhibitor, **S17834**, a benzo(b)pyran-4-one, can suppress the stimulation of tumor necrosis factor-α (TNF-α), as well as reduce mRNA and protein expression in endothelial cells, while also inhibiting leukocyte adherence. Cohen and colleagues demonstrated that its effects are at least partially mediated by NOX inhibition. Notably, it decreased NOX activity in endothelial cell membrane fractions in a concentration-dependent manner, without influencing superoxide production by xanthine oxidase in a cell-free system. These findings suggest a direct interaction between S17834 and the NOX complex, though its selectivity for specific NOX isoforms has not been reported. [285]

Celastrol, a bioactive compound extracted from the medicinal plant *Tripterygium wilfordii*, showed inhibition on NOX1 and NOX2 (IC_{50} of 0.410 μM and 0.590 μM, respectively) if compared with its effect on NOX4 and NOX5 (IC_{50} of 2.7 μM and

3.13 μM, respectively). [286] This selective inhibition reflects the subunit-dependent nature of the first two isoforms of NOXs as well as the mechanism of action of the same Celastrol. In fact, Celastrol specifically binds to $p47^{phox}$, disrupting the binding with $p22^{phox}$. [287]

Ebselen, a seleno-indoline-like compound, was reported as a NOX2 inhibitor (IC_{50} of 0.3 μM, EC_{50} of 0.5 μM), establishing a covalent interaction with a cysteine residue of $p47^{phox}$, making it unable of interacting with $p22^{phox}$. [288] However, Apocynin and Ebselen suffer from off-target activities. [289]

In 2010, a high-throughput screen (HTS) followed by a structure-activity relationship (SAR) investigation led to the identification of compound **GKT136901**. This compound, a pyrazolopyridinedione, was claimed to selectively inhibit NOX1 and NOX4 isoforms, with K_i of 160 nM and 165 nM, respectively, compared to NOX2 (K_i of 1530 nM). [290]

Further refinement resulted in the compound **Setanaxib** (or **GKT137831**), which demonstrated a similar selectivity profile (K_i of 140 nM and 110 nM for NOX1 and NOX4, respectively). [290] However, it exhibited 15-fold lower potency on NOX2 (K_i of 1750 nM) and 3-fold lower potency on NOX5 (K_i of 410 nM). Both compounds exhibited favorable pharmacokinetic properties and proved effective in various animal models. [291] Setanaxib entered clinical trials to assess its effectiveness in oral administration for type 2 diabetes patients, targeting maximal inhibition of the renin-angiotensin-aldosterone system and residual albuminuria, while, currently, it is undergoing evaluation in clinical trials for patients with primary biliary cholangitis (PBC) and liver stiffness, as well as patients with idiopathic pulmonary fibrosis. [279]

A 2018 study identified in the natural compound **NOS31**, secreted by *Streptomyces* sp., a NOX inhibitor with a notable activity profile for NOX1, with an IC_{50} of 2 μM for NOX1, with at least 14-fold weaker activity against other NOX isoforms. Additionally, it exhibited antiproliferative effects in cell lines that overexpress NOX1, including colon and stomach cancer cells. NOS31 could serve as a valuable tool for research into NOX1 inhibition, although further studies are required to fully understand its mechanism of action and selectivity profile. [292]

Furthermore, Hong *et al.* identified **Naloxone**, a drug already approved by the FDA for opioid overdose treatment, also functions as a NOX2 inhibitor. [293] This finding emerged during research focused on developing anti-inflammatory therapies for

Parkinson's disease. The compound's ability to inhibit ROS production was identified as a key factor in its anti-inflammatory and neuroprotective actions. Naloxone binds to the catalytic subunit of microglial NOX2, with IC_{50} values of 1.96 μM for the (−) enantiomer and 2.52 μM for the (+) enantiomer. This interaction blocks the translocation of cytosolic subunits to the plasma membrane, thereby preventing NOX2 activation. Naloxone possesses ROS scavenging capabilities and does not interfere with xanthine oxidase activity. [293]

Through a screening of a library of 40000 compounds in T-REx-293 cells that overexpress NOX4, some NOX4 selective inhibitors were identified. Firstly, **GLX351322** shows IC_{50} of 5 μM on NOX4 in T-REx-293 cells compared to IC_{50} of 40 μM on NOX2 in hPBMC cells. Unfortunately, it doesn't seem selective on NOX4, given its capability to inhibit, also, NOX1 and NOX5. [294]

A new compound, **GLX481304** effectively inhibited both NOX2 and NOX4 with low IC_{50} values (IC_{50} of 1.25 μM on both NOX2 and 4 isoforms), while having minimal impact on NOX1, displaying beneficial role in isolated cardiomyocytes after a global ischemia period. [295]

The same research group undertook a SAR campaign on identified hits with selectivity for NOX4 over NOX2, developing **GLX481372**, that is active in the submicromolar range against both NOX4 and NOX5 isoforms (IC_{50} of 0.68 and 0.57 μM, respectively) and about 10-fold less active against NOX1, NOX2, and NOX3 (IC_{50} of 7, 16, and 3.2 μM, respectively). [296]

Finally, **GLX7013114**, and **GLX7013159**, whose structures have not yet been disclosed, have shown good and promising selectivity on NOX4 (IC_{50} of 0.3 μM on NOX4, with no reported activity against NOX1, NOX2, NOX3, and NOX5, for compound VII, and IC_{50} of 0.3 μM on NOX4, 1.5 μM on NOX2, and no inhibition on NOX1 and NOX5 for compound VIII). [297] [298]

In 2015, GlaxoSmithKline and the University of Geneva identified a NOX2 inhibitor, the 7-azaindole **GSK2795039**, through high-throughput screening. [299] This compound showed high selectivity for NOX2 (pIC_{50} value is 5.5 to 6.5, depending on assay performed) and effectively reduced ROS production in neurodegenerative disease models. However, it had poor bioavailability and high clearance.

Subsequent optimization led to **NCATS-SM7270**, which retained the core structure of GSK2795039 but was modified to improve potency and pharmacokinetic properties. [300] NCATS-SM7270 demonstrated better efficacy against NOX2 (IC_{50} of

2.1 μM) and improved drug-like properties, and it successfully reduced cortical cell death in a traumatic brain injury model. However, it was less effective in primary mouse neutrophils compared to GSK2795039 and had no additional benefits in NOX2 knockout mice. [301] Nevertheless, employing an extensive platform of biochemical and biophysical assays, it was proven that most compounds discovered as NOX-specific inhibitors exhibited substantial ROS scavenging and/or assay-interfering effects. [281]

Only recently, Zang *et al.* identified two potent indirect NOX2 inhibitors: **compound 50** and **compound 51**, two promising quinoline-containing hits, able to directly bind the SH3 domain within the $p47^{phox}$ subunit and hamper its interaction with NOX2. [302] [303]

In the field of peptide-based inhibitors, Pagano's research team developed a peptide-based NOX inhibitor known as **NOXA2ds-tat**. [195] This 18-amino acid peptide was designed by combining two sequences: an 18-amino acid peptide derived from the NOX2 intracellular B-loop (NOXA2ds), which binds strongly to the $p47^{phox}$ subunit of NOX2, and a 9-amino acid segment from the HIV-TAT sequence (tat) that allows the peptide to penetrate cells. The resulting compound, NOXA2ds-tat, effectively inhibits NOX2 with an IC_{50} of 0.74 μM by blocking the interaction between NOX2 and $p47^{phox}$, thereby preventing the assembly and activation of the NOX2 complex. Despite the high homology in B-loop sequences across NOX isoforms, NOXA2ds-tat was found to be selective for NOX2, with no inhibitory effects on NOX1 or NOX4. [304] Given the low oral bioavailability of the peptide, it has been administered parenterally in mouse models and human resistance artery smooth muscle cells. [305]

In 2013, the same research group developed another peptide, known as **NOXA1ds**. This peptide is based on a short sequence from the NOX1 activating subunit, NOXA1. [306] NOXA1ds effectively disrupts the association between NOX1 and NOXA1, leading to strong inhibition of NOX1 activity with IC_{50} values of 19 nM in cell lysates and 100 nM in whole HT29 cells. NOXA1ds was found to be selective for NOX1 over NOX2, NOX4, and NOX5, and it did not affect xanthine oxidase. This specificity made NOXA1ds useful for investigating the role of NOX1 in various forms of hypertension, including pulmonary arterial hypertension. [307]

In 2020, Reis *et al.* demonstrated that VAS compounds (**VAS2870** and **VAS3947**) were validated to be true inhibitors by forming a covalent adduct with the residue Cys668, a conserved cysteine localized within the DH domain of all NOX isoforms.

[281] The mechanism of action of VAS2870 and VAS3947 was unveiled to consist of the alkylation of the thiol group of cysteine by benzyl-triazolopyrimidine moiety, while 2-mercaptobenzoxazole and oxazole, respectively, act as outgoing groups, leaving a molecule of 210 Da covalently bound to the dehydrogenase domain of NOX, as shown by mass spectra experiments. [281] To further confirm the mechanism of action of VAS compounds, Reis *et al.* have performed site-specific mutagenesis to replace Cys668 with a serine and, in this case, no adduct was formed. Specifically, VAS2870 was more potent than its oxazole analogue, VAS3947 (IC_{50} **VAS2870** *h*NOX1 = 72.6 μM ± 3.7, *h*NOX2 = 1.1 ± 0.1 μM, *h*NOX4 = 12.3 ± 2.1 μM, *h*NOX5 = 1.8 ± 0.1 μM; IC_{50} **VAS3947** *h*NOX1 = 86.8 ± 2.0 μM, *h*NOX2 = 5.6 ± 1.6 μM, *h*NOX4 = 15.0 ± 4.5 μM, *h*NOX5 = 39.2 ± 3.5 μM). [281]

In 2023, always Reis and collaborators have discovered another NOX-specific inhibitor, **M41** (**Compound 54**), obtained from ultra-large *in silico* screening of a total of 350 million compounds. This lead compound has been validated by *in vitro* and *in cellulo* enzymatic assays with promising biochemical activity, especially against *human* NOX2 and NOX4 isoforms (IC_{50} *h*NOX2 = 5.1 ± 1.2 μM, IC_{50} *h*NOX4 = 5.7 ± 0.7 μM). [308] Given the adaptable binding mode of M41 to the DH domain-NOX5/FAD/$NADP^+$ complex studied via the high-resolution crystal structure, the possibility of simplifying the chemical structure of M41 was investigated, obtaining the **compound 10t**, able to preferentially inhibit NOX2 (IC_{50} *h*NOX1 = 71.2 μM, IC_{50} *h*NOX2 = 7.7 μM, IC_{50} *h*NOX4 = 81.2 μM, IC_{50} *h*NOX5 = 28 μM). Also, in cells expressing high levels of NOXs, compound 10t proved stronger inhibition of NOX2 (EC_{50} = 5.7 μM) over the other isoforms, and NOX2 engagement through CETSA experiments. [308] Moreover, compound M41 and compound 10t reduced the viability of the monocytic U937 cancer cell line, in agreement with the role of NOX2 in myeloid cells. [308]

The development of compound 10t, which originated from the molecular simplification of M41, is a key focus of my PhD project. For this reason, it will be examined in greater detail in the 'Experimental Section' of my thesis. However, since it has already been published as a promising NOX2 inhibitor, I have also decided to include a brief overview of it also in the 'NOX Inhibitors' section.

A representation of the chemical structures of all the mentioned NOX inhibitors is reported in **Figure 23**.

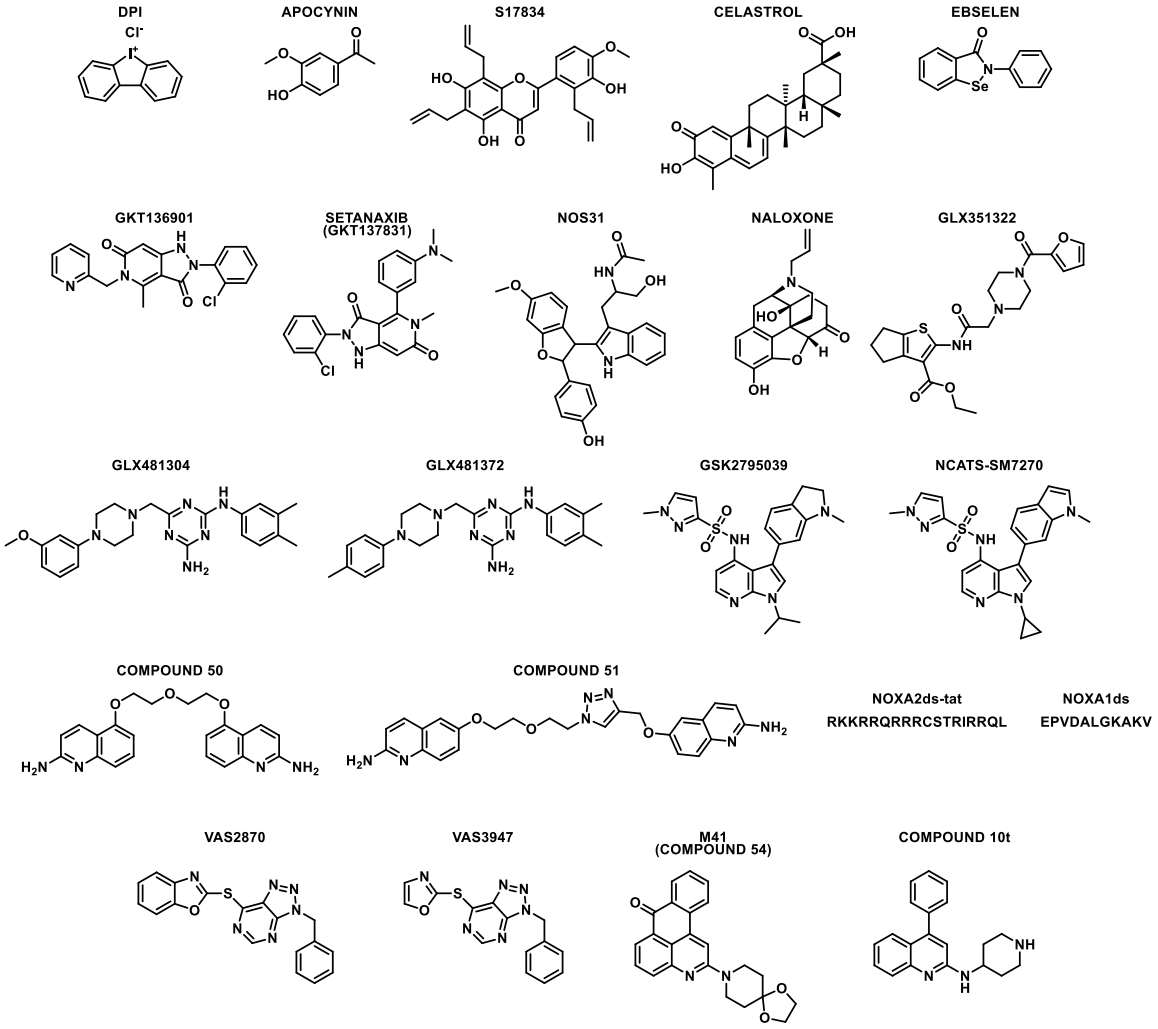

Figure 23: *Chemical structures of the mentioned NOX inhibitors.*

1. DEVELOPMENT OF TRIAZOLOPYRIMIDINE – CONTAINING NOXs INHIBITORS

1.1. Research project

In 2020, Prof. Andrea Mattevi's group of Pavia University, together with our research team, tested a total of 24 known NOX inhibitors using a standardized protocol to compare their anti-NOX activities. All the tested compounds showed assay-interfering activities, with the only exception of VAS2870 and VAS3947. VAS compounds exhibit high inhibitory potency against the dehydrogenase domain of NOX5 of *Cylindrospermum stagnale* (*cs*NOX5 bears a very significant 40% sequence identity to *human* NOX5). [281] [27] In particular, VAS2870 displays an IC_{50} of 0.257 ± 0.106 μM while VAS3947 of 6.09 ± 1.41 μM against DH *cs*NOX5. The research team hypothesized the formation of an adduct between the VAS derivatives and the enzyme. ESI-MS (**Figure 1.1**) undoubtedly confirmed the hypothesis, observing a 210 Da increase in the inhibitor-treated protein molecular weight. This was consistent with the alkylation of a cysteine's thiol by the benzyl-triazolopyrimidine moiety (210 Da) of VAS2870 and VAS3947, while the benzoxazoyl group and the oxazolyl one, respectively, acted as leaving groups. [281]

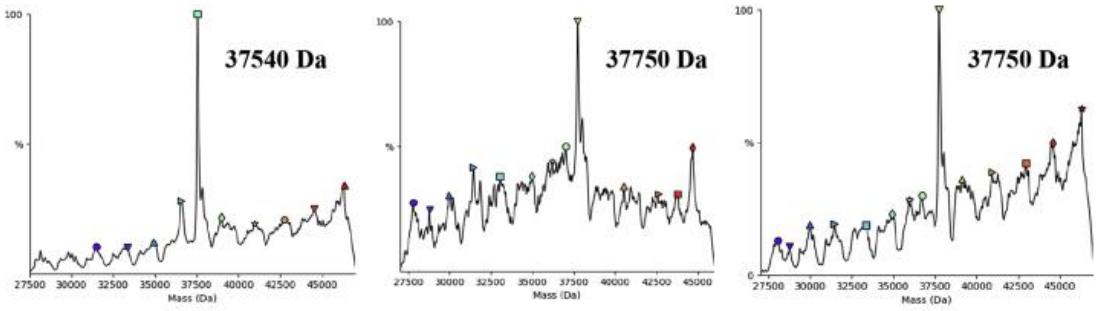

Figure 1.1: *ESI-MS spectra from DH csNOX5 without inhibitor (left), after incubation with VAS2870 (middle), and after incubation with VAS3947 (right).* [281]

The researchers identified in Cys668, a conserved cysteine present in the active site of the enzyme, the aminoacidic residue involved in the covalent binding. To confirm this, mutagenesis to replace Cys668 with Serine was performed. No increase in the mutated protein molecular weight was observed upon incubation with the inhibitors, demonstrating that no adduct is formed in the absence of Cys688 (**Figure**

1.2). VAS derivatives don't inhibit the mutated DH domain, confirming the mechanism of action of the compounds. [281]

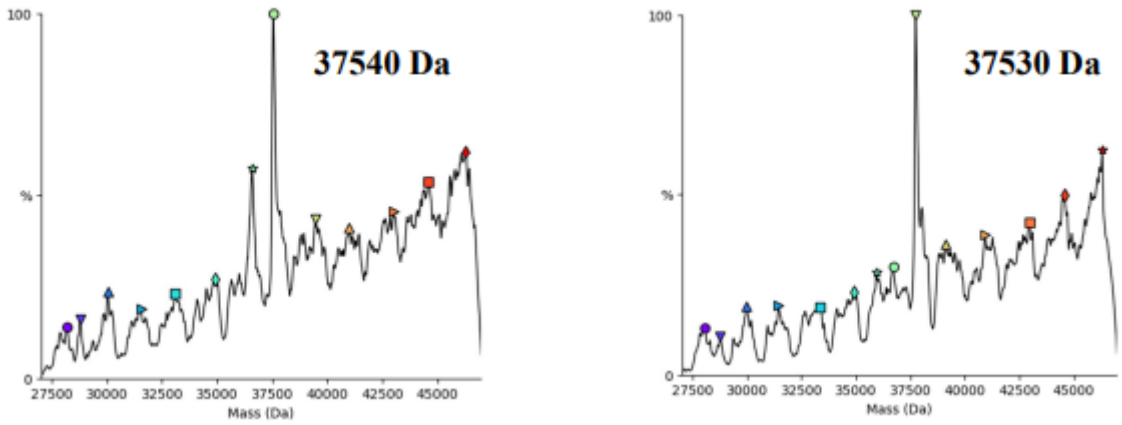

Figure 1.2: *ESI-MS spectra for mutant Cys668Ser DH csNOX5 without VAS2870 (left) and after incubation with VAS2870 (right).* [281]

The mode of inhibition observed with VAS2870 and VAS3947 impacts the initial step of the NOX catalytic cycle, specifically preventing NADPH binding and FAD reduction. By blocking the enzyme at the very beginning of the reaction, these inhibitors effectively halt the NOX catalytic process. This discovery highlights the potential for developing highly potent and selective NOX inhibitors, offering promising new directions for future research.

Starting from the chemical structure of VAS2870, more potent than its analogue VAS3947, we designed and, consequently, synthesized novel triazolopyrimidine-containing NOXs inhibitors. The goal was to identify tolerated and favorable structural modifications on this scaffold, aiming to enhance its potency and, particularly, the selectivity against the different NOX isoforms (**Figure 1.3**).

For this aim, we have planned different strategies:

(i) Removal of the leaving group to unveil any possible reversible non-covalent binding of benzyl-triazolopyrimidine derivatives to the NOX enzyme(s);

(ii) Replacement of the 2-thiobenzoxazole leaving group with other leaving groups, such as reported to be the chloro or the mesylate group;

(iii) Substitutions of the leaving group with the trapping ones, through the introduction of different acrylamide moieties, that are now established as pharmacologically powerful cysteine modifiers. [309] Through synthetically feasible routes, the acrylamide warheads have been connected to the C7 position of the triazolopyrimidine scaffold by means of cycloalkylamine or aromatic-ring linkers;

(iv) Introduction, at the *para* position of the benzyl group, of a propargylamine or propargylamide, moieties known to react with the isoalloxazine group of FAD cofactor since the crystal structure of *cs*DH-NOX5 revealed that the flavin is in close proximity to Cys668. In this way, a gap was opened to obtain dual Cys668/FAD covalent binders;

(v) Introduction, at the *para* position of benzyl group, of novel different cyclic (and non) tertiary amines aimed to obtain NOX2 selective inhibitors.

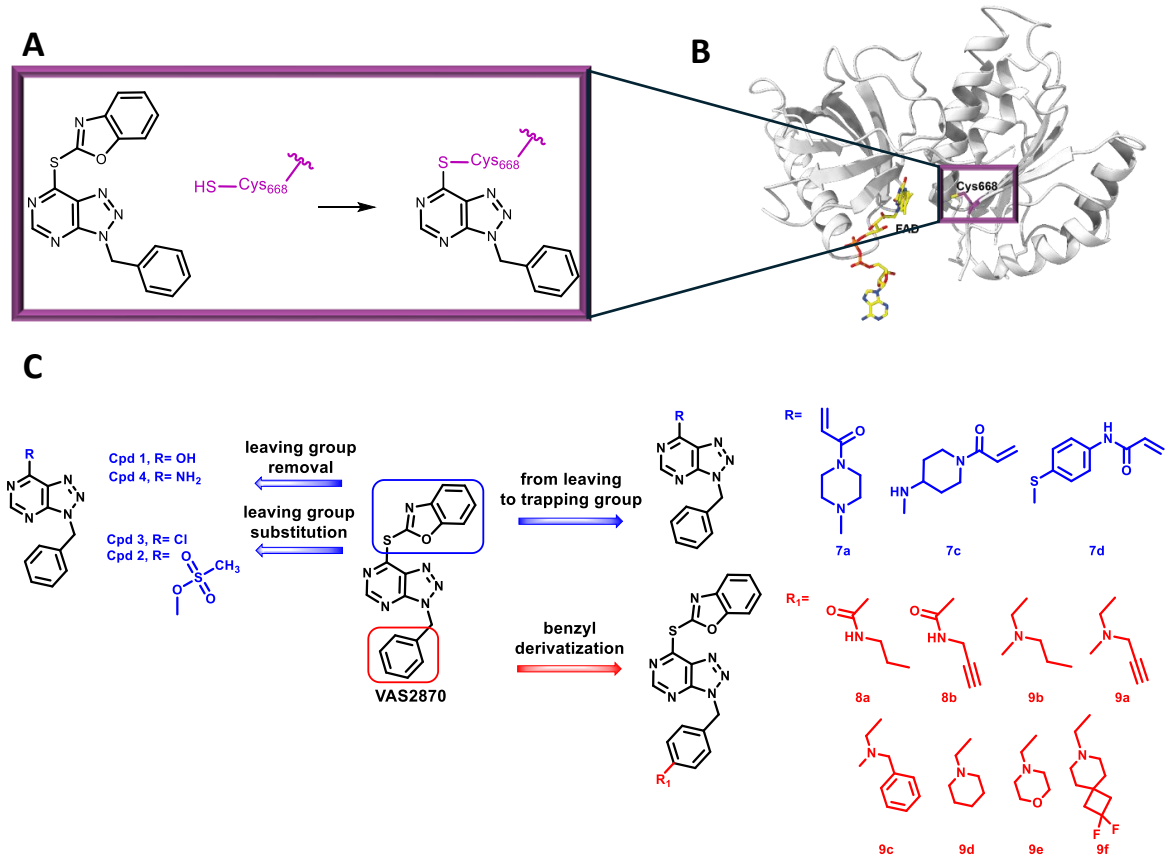

Figure 1.3. *Outline of this work. (**A**) Structure of the VAS2870-cysteine adduct. (**B**) Three-dimensional structure of the Cylindrospermum stagnale NOX5 dehydrogenase domain highlighting the targeted Cys668 and its proximity to the flavin. (**C**) Rational design of triazolopyrimidine-containing NOXs inhibitors.*

1.2. Results and discussion

1.2.1. Chemistry

For the synthesis of compounds **2-6** and **7a-d**, the commercially available 3-benzyl-3H-[1,2,3]triazolo[4,5-d]pyrimidin-7-ol **1** was treated with methanesulfonyl chloride, in a basic medium by triethylamine (TEA) in dry dichloromethane (DCM), to obtain the mesylate derivative **2**. Differently, the hydroxy derivative **1** was treated with thionyl chloride ($SOCl_2$), in dry chloroform ($CHCl_3$) and dry *N*,*N*-dymethylformamide (DMF), thus obtaining the chloro derivative **3**. The latter was treated with ammonia (NH_3) solution 7 N in methanol, in 1-butanol to provide the amino derivative **4**. The compound **3** also underwent two different nucleophilic displacement reactions with the *tert*-butyl piperazine-1-carboxylate and the *tert*-butyl 4-aminopiperidine-1-carboxylate, in a basic medium by TEA, in dry ethanol (EtOH) to give compounds **5** and **20,** respectively. The same compound **5** and **20** were treated with 4 N hydrogen chloride (HCl) in 1,4-dioxane and in dry tetrahydrofuran (THF) to afford the desired hydrochloride derivatives 3-benzyl-7-(piperazin-1-yl)-3H-[1,2,3]triazolo[4,5-d]pyrimidine **6** and 3-benzyl-N-(piperidin-4-yl)-3H-[1,2,3]triazolo[4,5-d]pyrimidin-7-amine **20,** that were isolated as colourless powders. Compounds **6** and **21** were treated with acryloyl chloride, in a basic medium by TEA and in dry DCM, providing the final compounds **7a** and **7c**. The reaction of compound **6** with acetyl chloride, in the same conditions as before, led to the compound **7b**. In addition, the chloro derivative **3** was treated with 4-aminothiophenol in a basic medium by TEA in dry EtOH to obtain the derivative 22, which was subjected to a reaction with acryloyl chloride, in a basic medium by TEA, in dry DCM, to afford the final compound **7d** (**Scheme 1.1**).

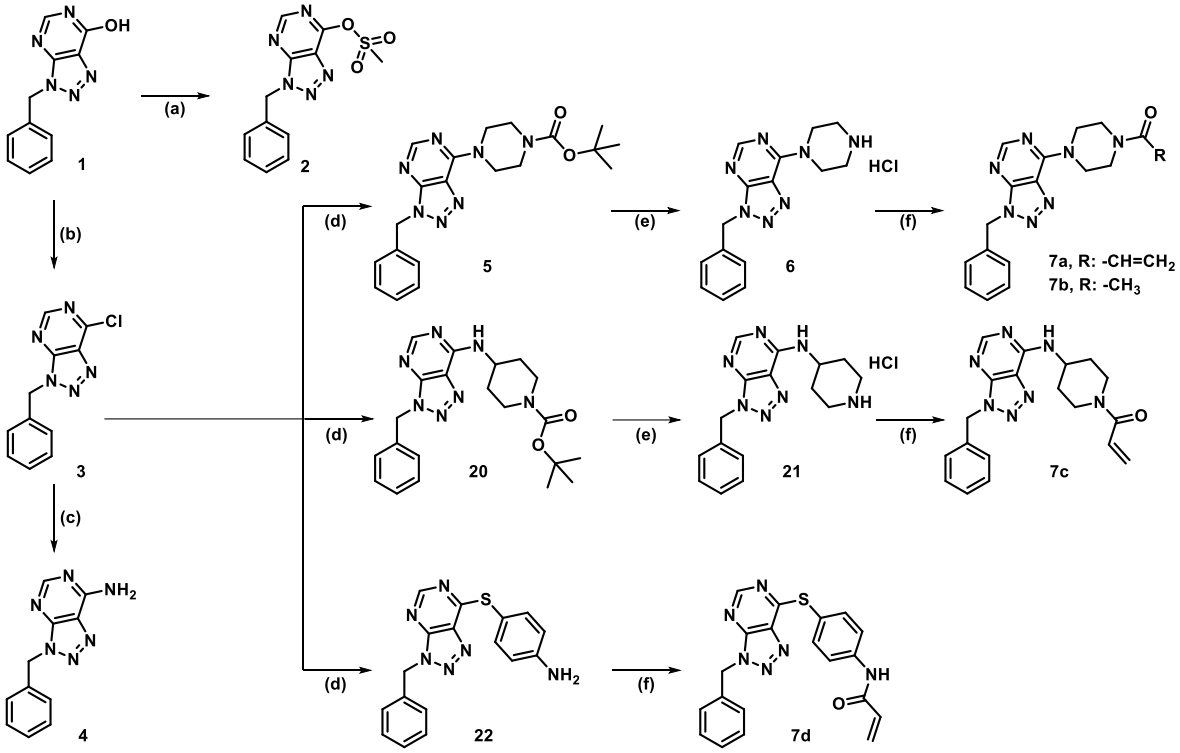

Scheme 1.1. Synthesis of compounds 2-6 and 7a-d. **Reagents and conditions. a)** Methanesulfonyl chloride, TEA, dry DCM, 0 °C to RT, 10 min; **b)** $SOCl_2$, dry $CHCl_3$, dry DMF, 80 °C, 3h; **c)** NH_3 in MeOH, 1-Butanol, 80 °C, 2h; **d)** tert-butyl piperazine-1-carboxylate or tert-butyl 4-aminopiperidine-1-carboxylate or 4-aminobenzenethiol, TEA, dry EtOH, 0 °C to RT, 1h; **e)** 4N HCl in 1,4-dioxane, dry THF, 0 °C to RT, 3h; **f)** acryloyl chloride or acetyl chloride, TEA, dry DCM, 0 °C to RT, 10 min.

For the synthesis of compounds **8a-b** the commercially available 1-(4-(bromomethyl)phenyl)ethan-1-one was treated with ethane-1,2-diol and *p*-toluenesulfonic acid (PTSA), in dry benzene, obtaining the compound **23**, that was then reacted with sodium azide, in dry DMF, overnight. The obtained 2-(4-(azidomethyl)phenyl)-2-methyl-1,3-dioxolane derivative **24** was reacted with sodium ethoxide and 2-cyanoacetamide, in dry EtOH providing the 5-amino-1-(4-(2-methyl-1,3-dioxolan-2-yl)benzyl)-1H-1,2,3-triazole-4-carboxamide **25**, that was treated with sodium ethoxide and ethyl formate in dry EtOH, thus affording the 3-(4-(2-methyl-1,3-dioxolan-2-yl)benzyl)-3H-[1,2,3]triazolo[4,5-d]pyrimidin-7-ol derivative **26**. This last compound underwent an acidic hydrolysis with 2N HCl in EtOH to give the corresponding ketone **27,** that was subjected to a bromination, in glacial acetic acid, followed by a basic treatment with 2N sodium hydroxide

(NaOH) and then by an acidic one with 2N HCl thus giving the 4-((7-hydroxy-3H-[1,2,3]triazolo[4,5-d]pyrimidin-3-yl)methyl)benzoic acid **28**. The reaction of this acid with benzotriazol-1-yloxytripyrrolidinophosphonium hexafluorophosphate (PyBOP), TEA, followed by 1-propylamine and propargylamine in dry DMF yielded the respective amides **29a** and **29b**. After cloruration reaction of these derivatives with $SOCl_2$ in dry $CHCl_3$ and dry DMF, the chloro derivatives **30a** and **30b** were treated with benzo[d]oxazole-2-thiol in a basic medium by TEA in dry EtOH, to obtain the corresponding compounds **8a** and **8b (Scheme 1.2)**.

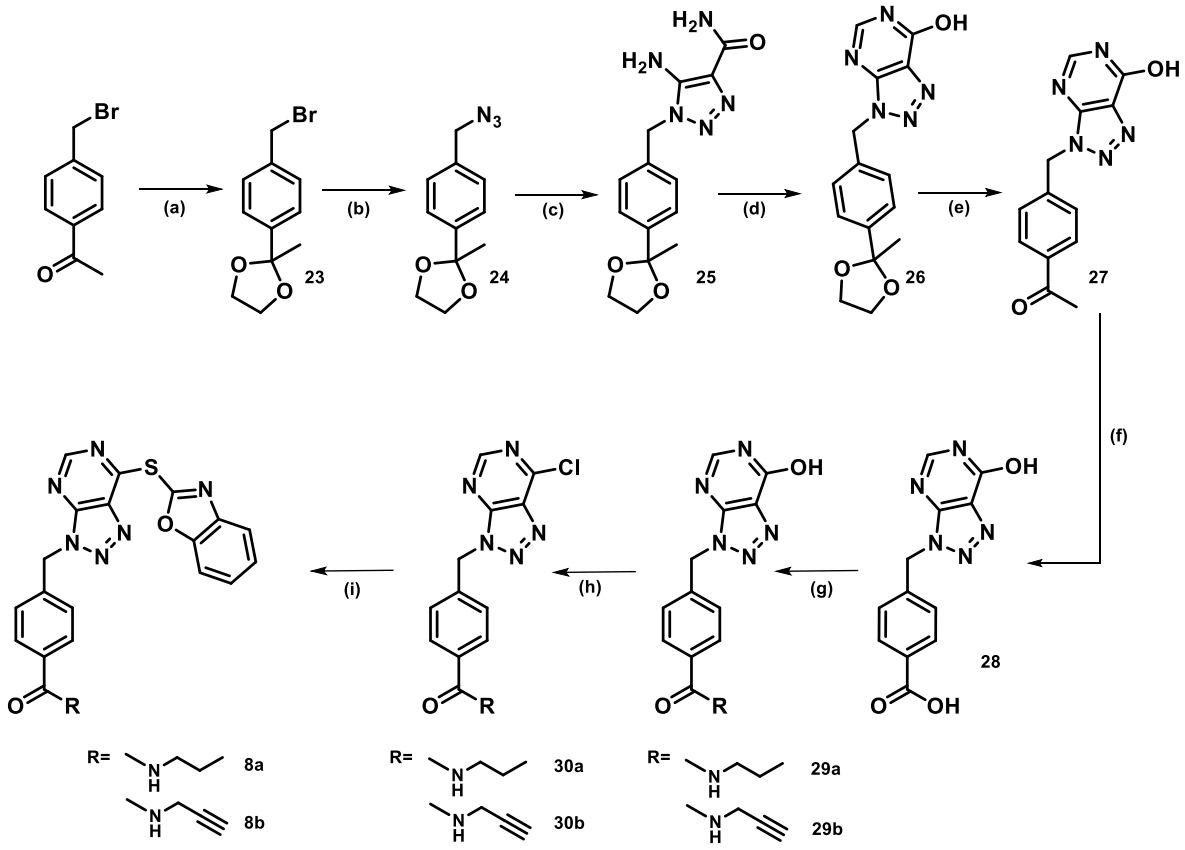

Scheme 1.2. Synthesis of compounds 8a-b. Reagents and conditions. a) Ethylene glycol, PTSA, dry benzene, 145 °C, overnight; **b)** Sodium azide, dry DMF, N_2, overnight; **c)** Cyanoacetamide, EtONa, dry EtOH, 80 °C, 3h; **d)** Ethyl formate, EtONa, dry EtOH, 80 °C, 2h 30; **e)** 2N HCl, EtOH, RT, 2h; **f)** ***i)*** Br_2, glacial acetic acid, 50 °C, 4h; ***ii)*** 2N NaOH, 0 °C, 1h; ***iii)*** 2N HCl, 0 °C; **g)** 1-propanamine or propargylamine, PyBOP, TEA, dry DMF, N_2, RT, overnight; **h)** $SOCl_2$, dry $CHCl_3$, dry DMF, 40 °C, 48h; **i)** 2-mercaptobenzoxazole, TEA, dry EtOH, 0°C, 30 min.

For the synthesis of compounds **9a-f**, the commercially available 4-(bromomethyl)benzaldehyde was treated with triethyl orthoformate, Dowex 50W X8 (HCR-W), in dry EtOH obtaining the 1-(bromomethyl)-4-(diethoxymethyl)benzene **31** that was reacted with sodium azide, in dry DMF. The obtained 1-(azidomethyl)-4-(diethoxymethyl)benzene derivative **32** was treated with sodium ethoxide and 2-cyanoacetamide, in dry EtOH providing the 5-amino-1-(4-(diethoxymethyl)benzyl)-1H-1,2,3-triazole-4-carboxamide **33**. The latter was treated with sodium ethoxide and ethyl formate in dry EtOH to afford the 3-(4-(diethoxymethyl)benzyl)-3H-[1,2,3]triazolo[4,5-d]pyrimidin-7-ol derivative **34,** that was subjected to acidic hydrolysis to remove the acetal group with 2N HCl in EtOH. The obtained aldehyde **35** underwent a reductive amination with sodium triacetoxyborohydride, in dry DMF, using the appropriate amine, thus obtaining the hydroxy derivatives **36a-f**. These derivatives were subjected to a cloruration reaction with $SOCl_2$, in dry $CHCl_3$ and dry DMF, thus giving the chloro derivatives **37a-f**. The nucleophilic displacement reactions with benzo[d]oxazole-2-thiol, in a basic medium by TEA, in dry EtOH, yielded the amine derivatives **9a-f (Scheme 1.3)**.

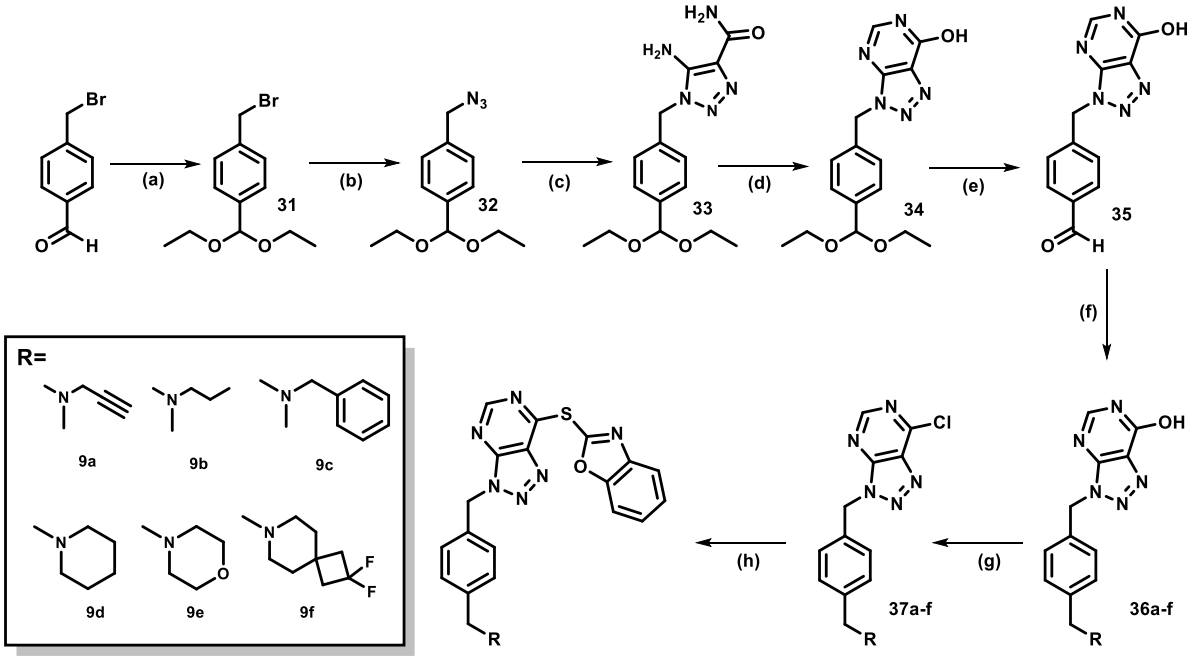

Scheme 1.3. Synthesis of compounds 9a-f. **Reagents and conditions. a)** Triethyl orthoformate, Dowex 50W X8, dry EtOH, RT, 3h; **b)** Sodium azide, dry DMF, N_2, RT, overnight; **c)** Cyanoacetamide, EtONa, dry EtOH, 80 °C, 3h; **d)** Ethyl formate, EtONa, dry EtOH, 80 °C, 2h30; **e)** 2N HCl, EtOH, 0°C to RT, 2h30; **f)**

$(CH_3COO)_3BHNa$, dry DMF, N_2, RT, 2h; **g)** $SOCl_2$, dry DMF, dry $CHCl_3$, 50 °C, overnight; **h)** 2-mercaptobenzoxazole, TEA, dry EtOH, 0 °C, 10 min.

1.2.2. Biochemical activity of compounds 1-9a

The first series of VAS2870 derivatives obtained was tested at 10 μM (except for the chloro derivative **3**, that was tested at 100 μM concentration) against the dehydrogenase domain (DH) of NOX5 from *Cylindrospermum stagnale* by Professor Andrea Mattevi's team of Pavia University (**Table 1.1**).

Table 1.1. *Biochemical Inhibition data of compounds **1**-**9a** against DH domain of csNOX5.*

CPD	MOLECULAR STRUCTURE	% INHIBITION *cs*NOX5 DH DOMAIN[a]
VAS2870	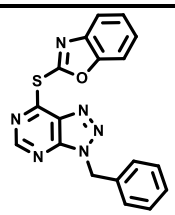	92.5 ± 2.5
1	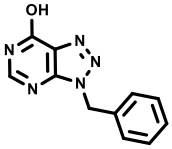	0
2	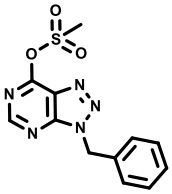	15.1 ± 2.5
3	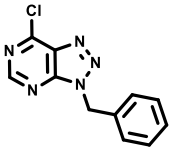	23.4 ± 4.8[b]
4	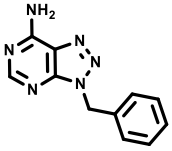	28.0 ± 9.2

5	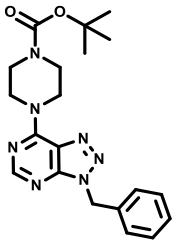	16.9 ± 8.2
6	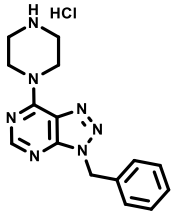	7.0 ± 3.2
7a	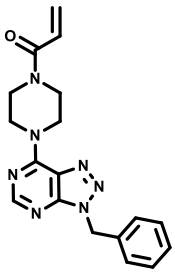	12.0 ± 3.0
7b	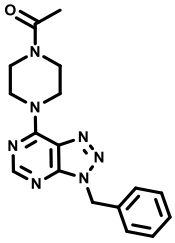	40.5 ± 14.8
7c	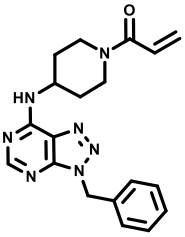	41.2 ± 9.7
7d	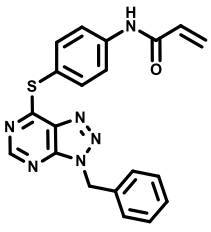	28.1 ± 2.8
8a	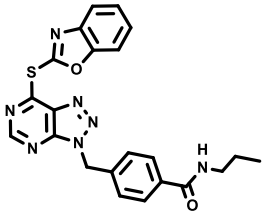	95.6 ± 0.1

8b	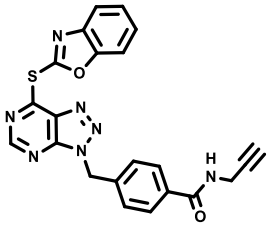	94.6 ± 1.0
9a	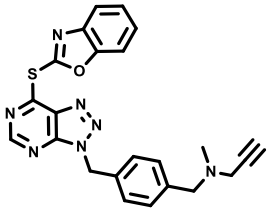	67.3 ± 4.6

[a]tested at 10 μM, [b] tested at 100 μM

Data collected in **Table 1.1** clearly show that the removal of the 2-thiobenzoxazole leaving group with the hydroxy derivative **1** completely abolished the inhibition activity of the DH domain of *cs*NOX5. Differently, with the corresponding amino isostere derivative **4,** the activity was partially maintained since it displayed 28% of inhibition at 10 μM, hence proving that without the leaving group the VAS structure could be able to bind to *cs*NOX5. Moving towards the substitution of the 2-thiobenzoxazole leaving group with the mesylate and chloro ones (compound **2** and compound **3**, respectively) a significant drop in inhibition activity was observed. For this reason, we decided to build up a trapping group instead of a leaving one by connecting an acrylamide to the triazolopyrimidine nucleus through a piperazine ring, a 4-aminopiperidine, and a 4-mercaptoaniline, thus obtaining compounds **7a**, **7c** and **7d**, respectively. Moreover, we also prepared the acetylpiperazine derivative **7b** as a non-trapping compound (negative control). Other than compounds **7a-d,** we also tested the piperazine intermediate derivatives **5** and **6**. A noteworthy inhibition activity was provided by the compounds **7b** and **7c** (40.5 and 41.2 %, respectively). Although the piperidine acrylamide **7c** displayed the highest inhibition percentage (41.2%), being less potent than **VAS2870** (92.5 %), this approach did not provide a Cys668 covalent binding as proved by mass spectrometry experiments (data not shown). Moreover, the absence of the acrylamide on the **7b** structure provided very similar potency to **7c**. Therefore, as this study did not allow us to improve the **VAS2870** potency, we decided to maintain the 2-thiobenzoxazole leaving group on C4 of the triazolopyrimidine nucleus and work on the *N*-benzyl moiety. Thus, aimed to investigate the possibility of obtaining a double Cys668/FAD covalent binder, we prepared the *p*-propargylamide derivative **8b** and its saturated compound **8a** as a negative control (for FAD covalent binding), and the *p*-propargylamine derivative **9a**. The assay

against the DH domain of *cs*NOX5 highlighted that all three new compounds bearing the 2-thiobenzoxazole group displayed similar potency to **VAS2870** in this assay, hence the presence of such leaving group was required. The results obtained from the new compounds towards the membrane *h*NOX1, -2, -4, and -5 (**Table 1.2**) highlighted that compound **8b** showed an IC_{50} of 17.3 μM against NOX2 while displaying an IC_{50} of 57.9 μM towards NOX4 and over 100 μM towards NOX1 and -5, thus proving the possibility of achieving selectivity among the NOX isoforms. Moreover, the best result was obtained with **9a** with the propargylamine group. For the first time we have achieved selectivity and potency in respect to the benchmark **VAS2870**, with IC_{50} value against NOX2 in the high nanomolar range, 2-fold more potent than the reference **VAS2870**, and displaying some degree of selectivity over the other NOX isoforms, especially when compared with NOX1 and NOX4, and to a lesser extent over NOX5 (SI NOX2/NOX1 = 39; SI NOX2/NOX4 = 74; SI NOX2/NOX5 = 9). Indeed, the reference compound **VAS2870** was equally potent against NOX2 and NOX5 (IC_{50} of 1.15 and 1.8 μM, respectively) even displaying some degree of selectivity mainly over NOX1.

Moreover, since the saturated analogue **8a** provided more potency than the corresponding alkine analog **8b** towards all the NOX isoforms, we speculated that the propargyl group failed to get covalent binding with FAD of the DH domain. This hypothesis was confirmed by mass spectrometry experiments, conducted by Professor Andrea Mattevi's team of Pavia University, highlighting the compound **9a** covalently bound to Cys668-DH-NOX5 (**Figure 1.4**), even in the absence of FAD, that is not retained by the protein after sample preparation.

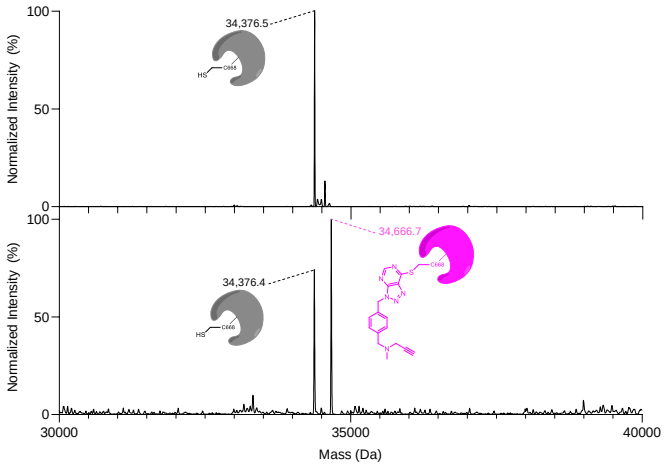

Figure 1.4. ***ESI-qTOF-HRMS of DH NOX5 after reaction with compound 9a.*** *Normalized deconvoluted mass spectra of the DMSO control and the inhibited protein are*

shown in the upper and lower panel, respectively. The mass difference between the inhibited and apoprotein peaks is 290.3 (theoretical 290.34 Da), corresponding to the expected adduct (with a mass error of -4.04 ppm), thus validating the covalent binding mode.

Next, given that compound **9a,** bearing a tertiary amine at the benzyl moiety, was the most potent NOX2 inhibitor, we designed and synthesized other 5 different amine analogues (**9b-f**) Tested against NOX1, -2, -4, and -5 isoforms only the cyclic amines piperidine (**9d**) and morfoline (**9e**) were tolerated, maintaining single digit micromolar inhibition potency and selectivity for NOX2 and NOX4, although less potent than 9a against NOX2 (**Table 1.2**).

Table 1.2. *Biochemical inhibition data against membrane full-length human NOXs.*

CPD	MOLECULAR STRUCTURE	IC_{50}, μM			
		***h*NOX1 (Amplex Red)**	***h*NOX2 (MCLA)**	***h*NOX4 (Amplex Red)**	***h*NOX5 (Amplex Red)**
VAS2870	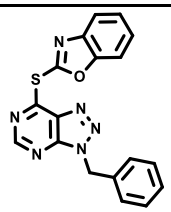	72.6 ± 3.7	1.15 ± 0.1	12.3 ± 2.1	1.8 ± 0.1
8a	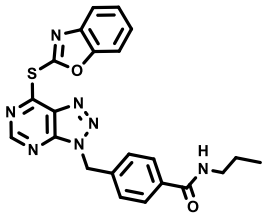	32.9 ± 2.9	3.77 ± 0.09	21.8 ± 1.1	6.5 ± 0.6
8b	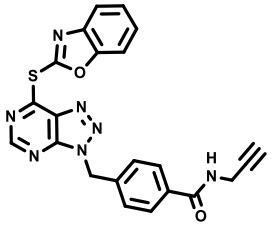	> 100	17.3 ± 2.6	57.9 ± 7.0	> 100

9a	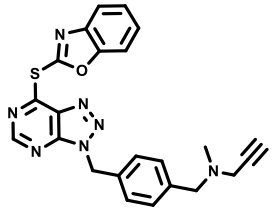	22.0 ± 6.7	0.567 ± 0.2	42.0 ± 16.0	5.2 ± 0.1
9b	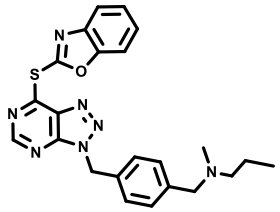	> 100	> 100	> 100	> 100
9c	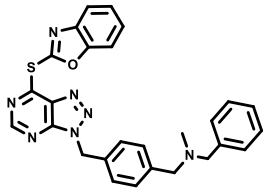	>100	12.9 ± 2.2	>100	14.3 ± 5.9
9d	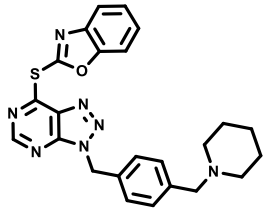	>100	8.1 ± 0.2	>100	4.72 ± 3.7
9e	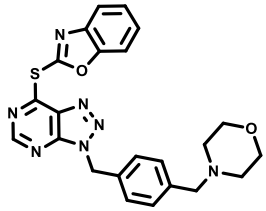	>100	1.9 ± 0.2	>100	2.06 ± 0.96
9f	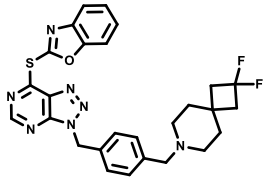	>100	13.8 ± 2.8	>100	46.6 ± 9.1

Furthermore, the results achieved *in vitro* on *human* NOX2 were also corroborated by Professor Andrea Mattevi's biochemical assay towards purified NOX2 and by *in cellulo* enzymatic assays on intact NOX2-overexpressing PLB-985 cells (**Table 1.3**). Even in these assays compound **9a** was the most potent, indeed it displayed IC_{50} values of 0.155 ± 0.2μM against the purified NOX2, thus being over 22-fold more potent than **VAS2870**, and of 0.135 μM against NOX2 in cells, over 2-fold better than **VAS2870** (IC_{50} of 0.304 μM). Compounds **8a** and **8b** showed lower potency than **VAS2870**, but still retaining a good inhibition with IC_{50} values in the single-digit micromolar (**8a**) and dual-digit micromolar (**8b**) range.

Table 1.3. *Biochemical inhibition data against purified hNOX2 and in NOX2-overexpressing PLB-985 cells.*

CPD	MOLECULAR STRUCTURE	IC_{50}, μM	
		Purified *h*NOX2 (NADPH depletion)	**NOX2-overexpressing PLB-985 cells (cytochrome c reduction)**
VAS2870		3.5 ± 0.2	0.304 ± 2.1
8a	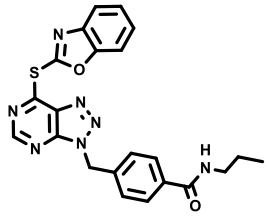	3.3 ± 0.06	2.81 ± 0.88
8b	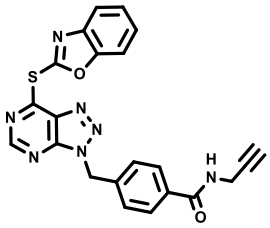	20.1 ± 0.5	17.6 ± 3.4
9a	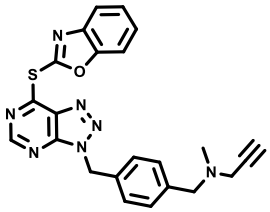	0.155 ± 0.03	0.135 ± 0.02

1.2.3. VAS2870 and 9a bind to NOX2 only upon protein activation

Even more interestingly, in collaboration with Professor Andrea Mattevi's team, we demonstrated the binding mode of compound **9a** and of **VAS2870** as a control, within the active site of NOX2, which occurs only upon protein activation, both *in vitro* and *in cellulo*.

The structure revealed that there are structural rearrangements of the NOX2 dehydrogenase domain to facilitate the transfer of electrons. [66] Here, we have experimentally elucidated the alterations of accessibility of the NOX2 active site upon its activation. Indeed, it has been already observed that the structural

comparisons between *human* NOX2 in its resting and activated states reveal significant rearrangements within the dehydrogenase domain. [66] Here, we have demonstrated that the active site becomes accessible to inhibitors, which covalently bind to the conserved cysteine residue Cys668 within the active site, [281] only in the presence of the cytosolic partners that enzymatically activate NOX2. This has been proven with compounds **9a** and **VAS2870** in both *in vitro* and cellular contexts (**Figure 1.5**).

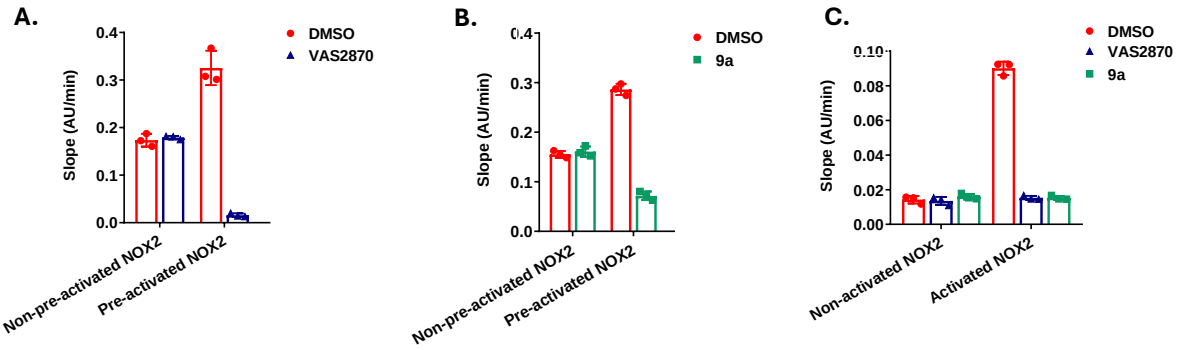

Figure 1.5. ***NOX2 active site is accessible to the ligand only upon protein pre-activation.*** ***(A)*** *In vitro cytochrome c reduction assay on NOX2-overexpressing isolated membranes after 30 minutes incubation with VAS2870 in the absence (left) or presence (right) of the cytosolic partners.* ***(B)*** *In vitro cytochrome c reduction assay on NOX2-overexpressing isolated membranes after 30 minutes incubation with* ***9a*** *in the absence (left) or presence (right) of the cytosolic partners.* ***(C)*** *In cellulo cytochrome c reduction assay on NOX2-overexpressing cells after 1 hour incubation with* ***VAS2870*** *or* ***9a*** *in the absence (left) or presence (right) of phorbol-myristate (PMA).*

In more detail, we co-incubated the isolated NOX2-overexpressing cell membranes with the ligands in the presence or absence of the cytosolic partners and removed the excess ligand and soluble activators by centrifugation. After the addition of fresh cytosolic activators, we measured the enzymatic activity *in vitro.* Results show that NOX2 is inhibited by **VAS2870** (**Figure 1.5A**) and by **9a** (**Figure 1.5B**) only when the membranes have been previously incubated with the cytosolic activators. Similarly, by investigating the *in cellulo* enzymatic activity of NOX2 physiologically over-expressed in PLB-985 cells, we found out that it is inhibited only when cells have been previously stimulated by phorbol-myristate (PMA) (**Figure 1.5C**).

1.2.4. Compound 9a: the *first-in-class* dual NOX2/MAO-B irreversible inhibitor

Afterwards, although compound **9a** did not covalently bind to the DH-NOX5 FAD cofactor, we considered that **9a** contains the pargyline (*N*-benzyl-*N*-methylprop-2-yn-1-amine) moiety, a well-known irreversible and selective monoamine oxidase B (MAO-B) inhibitor. [310] Thus, we decided to explore a possible binding of **9a** to the FAD in the active site of MAOs enzymes. Intriguingly enough, when tested towards human MAO-A and MAO-B, **9a** displayed an IC_{50} against MAO-A of 59.0 μM, differently it provided an IC_{50} against MAO-B of 0.127 μM, thus proving to be a selective MAO-B inhibitor ($SI_{MAO-B/MAO-A}$ = 465).

1.2.5. Crystal structure of compound 9a in complex with MAO-B

Crystallographic studies were carried out by our collaborators of Pavia University to elucidate the binding mode of **9a** to *human* MAO-B. The co-crystal structure was solved at 1.4 Å resolution. The exceptional resolution of the electron density map allowed us to unambiguously map the position of the inhibitor and confirm the N_5 covalent adduct formation (**Figure 1.6A**). Due to the poorer electron density map of the inhibitor in chain A the benzoxazole moiety was modeled only in chain B, and we refer to it for the description of the binding mode. The N-methyl-propargylamine moiety forms a delocalized double bond adduct with the N_5 of the Flavin and lies in between the "aromatic sandwich" (Tyr398-Tyr435 pair). The *para* substitution of the central aromatic ring perfectly fits the narrowed MAO-B's active site. Superposition with the structure in complex with rasagiline, a clinically used propargylamine-based *h*MAO-B inhibitor, showed no differences in the conformation of the active site's residues (**Figure 1.6B**), except for some differences at the entrance cavity, as previously observed. [310] In both cases, the gating Ile199 is in an open conformation, as typically observed in MAO-B structures in complex with bulky elongated inhibitors. [311] Moreover, the terminal benzoxazole moiety is wedged into the entrance cavity that adapts its conformation. Through this binding mode the ring displaces His115, Trp119 (that assumes a double conformation), and Phe103, residues that belong to the entrance loop giving access to the active site's cavity (**Figure 1.6C**).

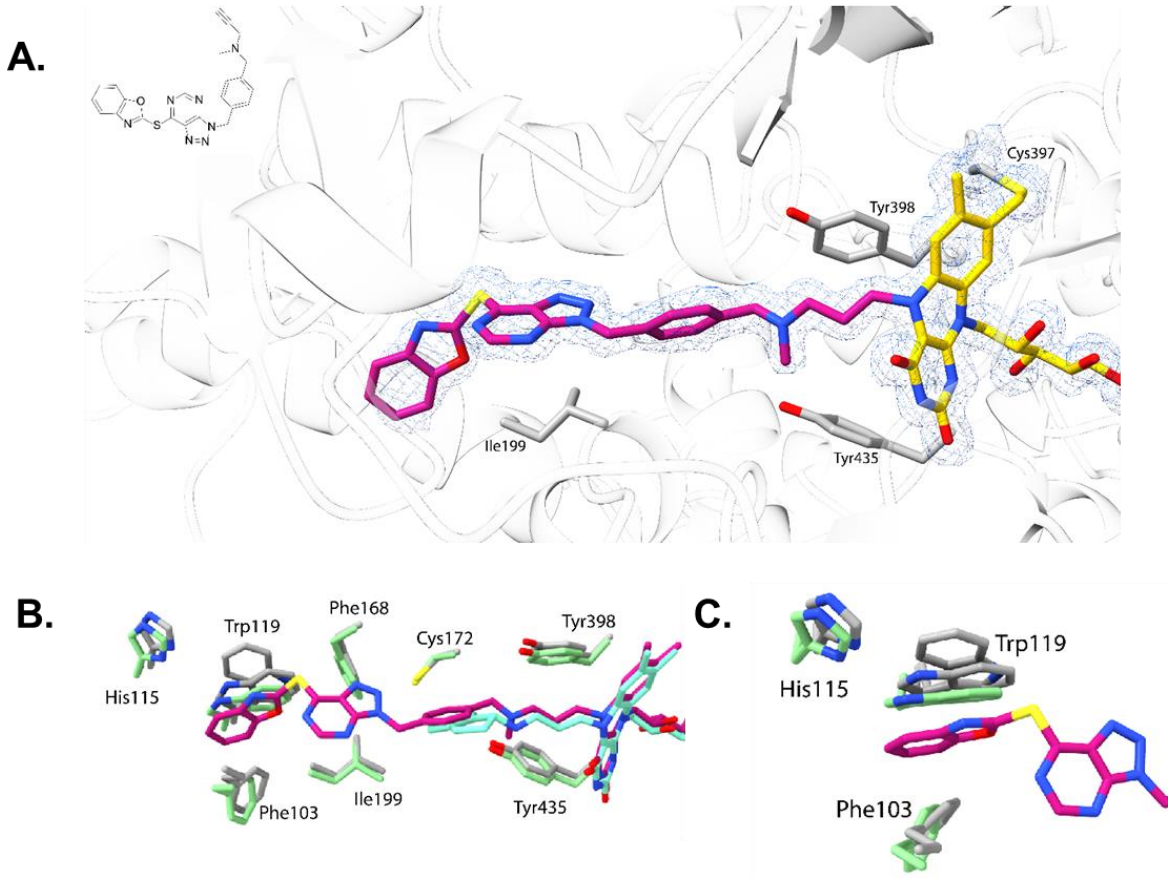

Figure 1.6. ***Crystal structure of human MAO-B in complex with inhibitor 9a at 1.4 Å resolution.*** *(**A**) Close-up view of the active site of chain B. Active site residues are shown in gray, FAD in dark yellow, and the inhibitor 9a with magenta carbon atoms; oxygen is shown in red, nitrogen in blue, and sulphur in light yellow. The protein overall fold is shown as light grey transparent ribbon. The refined 2Fo-Fc electron density for 9a and FAD (contoured at 1.5 σ) is shown as a blue mesh. (**B**) Superposition with PDB 1S2Q (hMAO-B in complex with rasagiline). FAD-**9a** adduct is shown in magenta, FAD-rasagiline adduct is shown in cyan, and hMAOB-**9a** active site's residues are shown in grey, in comparison with the conformation adopted in the co-crystal structure with rasagiline shown in light green. (**C**) Zoom-in of the terminal benzoxazole ring of **9a** and of the surrounding amino acids.*

Hence, the attempt to optimize both potency and selectivity of **VAS2870** towards NOXs allowed us to disclose the *first-in-class* dual NOX2/MAO-B irreversible inhibitor (**Figure 1.7**), even able to display balanced IC_{50} values against the two single targets.

This dual hybrid could represent an interesting chemical tool for studying the role of NOX2 [170] [312] and MAO-B in inflammatory [313] [314] and/or neurodegenerative diseases. [151] [315]

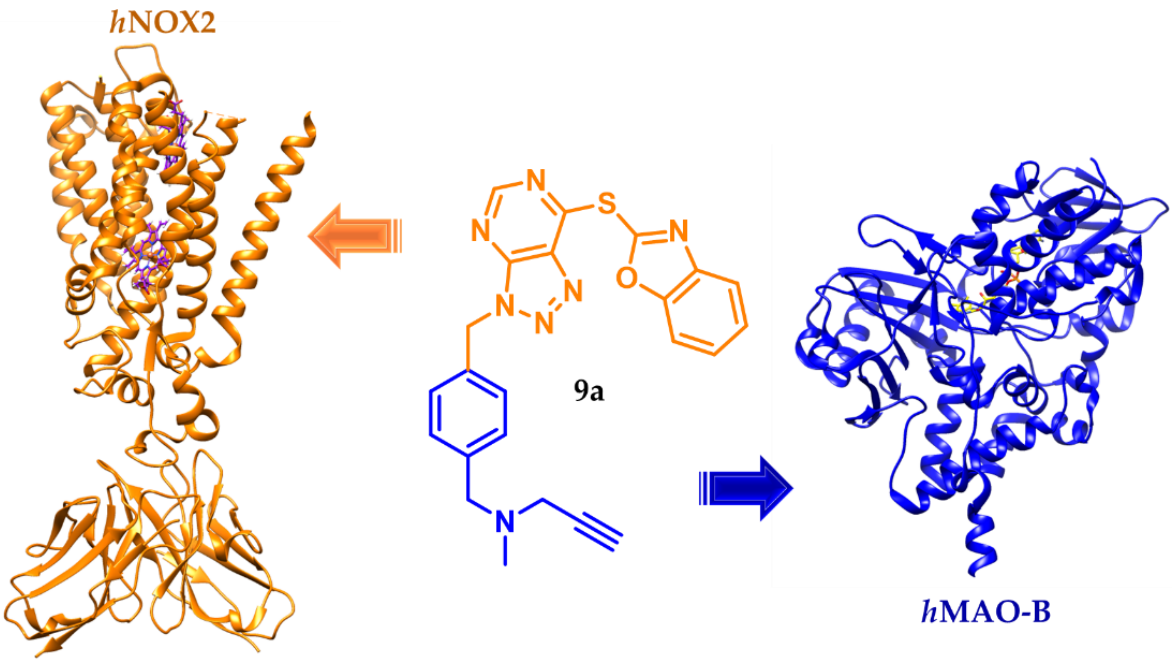

Figure 1.7. *Cartoon representation of dual inhibition of 9a towards NOX2 and MAO-B.*

1.2.6. Dual NOX2 and MAO-B inhibition effects in microglia BV2 cell line

It has been proven that NOX2 regulates cytokine induction in inflammation processes. In a study, evidence corroborated the hypothesis that NOX2 plays an important role in neuroinflammation. Indeed, NOX2 deletion resulted in clinical improvement of multiple sclerosis (MS) by preventing astrocyte activation, by impairing mRNA expression of proinflammatory cytokines IL1β, IL-6, and MCP-1 in both striatum and motor cortex. [170]

In a very recent study, the NOX2-specific deletion effectively attenuated retinal oxidative stress, immune dysregulation, the internal blood-retinal barrier (iBRB) injury, neurovascular unit (NVU) dysfunction. In the same work, first, it has been proven that NOX2-dependent ROS-driven pro-inflammatory signaling activated the ERK1/2 signaling pathway and mediated the shift of microglia activation to a

pro-inflammatory M1 phenotype, by triggering a neuroinflammatory flare. [316] Moreover, in a variety of inflammatory models it has been reported that also monoamine oxidase (MAO) inhibition provided a reduction of the cytokine expression. For instance, in an epithelial cell culture model LPS-induced IL-6 and IL-1β cytokine expression was downregulated by MAO-B inhibition and through the impairment of cAMP-PKA/EPAC signaling. [317]

Since pro-inflammatory microglia play a detrimental role in the progression of several neurodegenerative diseases, [318] [319] in collaboration with Professor Cristina Limatola's team of Sapienza University, we thought to evaluate the ability of our *first-in-class* dual NOX2/MAO-B inhibitor to impair both ROS production and inflammatory cytokine gene expression in a BV2 murine microglial cell model.

First, the ROS production in BV2 cells was investigated (**Figure 1.8A**) and the results show that upon LPS/IFNg stimulation the compounds 9a and VAS2870 at 10 μM were able to decrease the ROS levels, with the dual inhibitor **9a** reducing the ROS percentage to half, even better than **VAS2870**.

Then, cell viability was assessed to evaluate the cytotoxic effect of 10 μM **VAS2870**, MC4762 (**9a**), MAO-B inhibitor **rasagiline**, and the **VAS2870/rasagiline** combination, and all of them provided negligible effects in BV2 cells (**Figure1.8B**).

Next, after LPS/IFN-γ-driven pro-inflammatory stimuli and 48 h compounds treatment, the effect on the inducible nitric oxide synthase (iNOS), interleukin-1beta (IL-1B), and interleukin-6 (IL-6) mRNA expression was observed (**Figure1.8C, D,** and **E**, respectively).

The results show that **9a** nicely reduced the mRNA level of all three cytokines iNOS (over 10-fold), IL-1B (over 4-fold), and IL-6 (over 4-fold), even being more potent than the single target inhibitors and their pharmacological combination. Altogether our data demonstrated that compound **9a** is able to shape microglial pro-inflammatory phenotype, with a greater effect than VAS2870 and rasagiline and their combination, reducing the impact of LPS/IFNg stimulation *in vitro*.

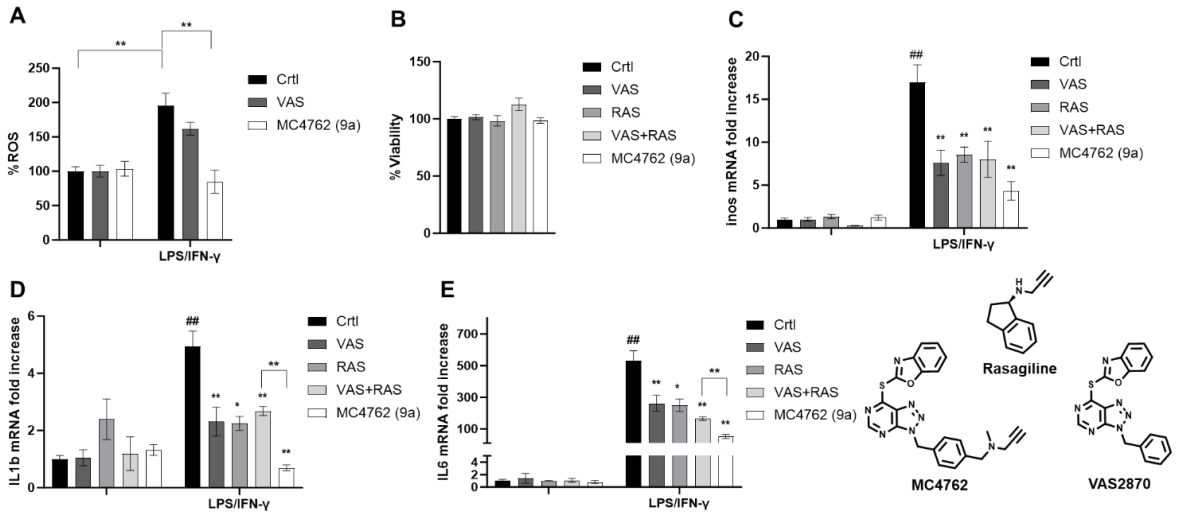

Figure 1.8. ***qRT-PCR analysis for the indicated transcripts in BV2 cells treated with the compounds at the concentration of 10 μM for 48 h.*** *CTR (control) represents the cells treated with the vehicle (DMSO). The values are expressed as fold of expression versus the control (arbitrary value = 1) and shown as mean ± SD. Statistically significant differences are reported (*, p<0.05; **, p<0.01) for three independent experiments.*

1.3. Conclusions

As NOXs have the specific role of generating ROS, and in correlation with their tissue/organ expression, their overexpression or misregulation can lead to important pathological conditions, such as cancers, neuroinflammations and neurodegenerations. To date, several reported inhibitors are not specific binders but only antioxidant/radical scavengers, thus just interfering with the redox reactions catalysed by NOXs. Recently some indirect inhibitors, as compounds 10 and 33, based on a bis-2-aminoquinoline scaffold, have been described as binders of the $p47^{phox}$ NOX2 cytosolic partner/activator, then leading to NOX2 activation impairment. Differently, the NOX1/4 selective inhibitor setanaxib, based on a pyrazolo[4,3-c]pyridine-3,6-dione backbone, entered clinical arena for type 2 diabetes, primary biliary cholangitis and liver stiffness, as well as for idiopathic pulmonary fibrosis. In the last years our research group start a medicinal chemistry campaign to discover *bona-fide* NOXs (selective) inhibitors. Recently, we discovered that the benzyl-triazolopyrimidine VAS2870 and its analogue VAS3947 were able to covalently bind to the cysteine 668 in the *cs*NOX5 active site, acting through its 2-thiobenzoxazole as a leaving group, as confirmed by mass spectra experiments. Thus, prompted by this finding and aimed to optimize both inhibition potency and

isoform selectivity, we performed chemical modifications at the pyrimidine-C4 position of VAS2870 to replace the leaving group or to change the leaving in trapping group, and at the benzyl moiety but keeping fixed the 2-thiobenzoxazole. The attempt to replace the leaving group revealed unsuccessful, differently among the benzyl derivatives, that one bearing the *N*-methylpropargylamine (**9a**) was the first and unique compound endowed with submicromolar inhibiting activity against the cell membrane preparation of NOX2 showing an IC_{50} of 0.567 μM, being 2-fold more potent than the reference VAS2870, and displaying from 9- to over 70-fold selectivity for NOX2 over the other NOX isoforms, as well. In addition, compound **9a** proved inhibition even towards the purified NOX2 and NOX2 overexpressing cells, other than target engagement by CETSA experiments. More importantly, **9a**, as well as VAS2870, demonstrated ability to bind and inhibit the NOX2 active site only upon its activation by cytosolic partners. Moreover, we designed the propargyl group at the VAS2870 benzyl moiety (**8b**, **9a**) to attempt the double cysteine 668/FAD cofactor covalent binder, but FAD was not trapped as highlighted by mass spectrometry experiments. Nonetheless, the observation that the (*N*-benzyl-*N*-methylprop-2-yn-1-amine) moiety of **9a** structurally corresponded to pargyline, a well-known MAO-B selective inhibitor, pushed us to screen **9a** against the human MAO-A and MAO-B and, surprisingly, it displayed high potency (IC_{50}: 0.127 μM) and selectivity (465-fold) for MAO-B over MAO-A. Therefore, with compound **9a** we found out the *first-in-class* dual covalent NOX2/MAO-B selective inhibitor, having a balanced potency against both targets, as well. The MAO-B/**9a** co-crystal structure was solved at very high resolution, highlighting a FAD covalent binding similar to the drug rasagiline, and with the terminal 2-thiobenzoxazole engaging important interactions within the entrance cavity. Moreover, based on literature evidence that both NOX2 and MAO-B are involved in neuroinflammation pathways, we tested compound **9a**, in comparison with the single target inhibitors VAS2870 (NOX2) and rasagiline (MAO-B), and their pharmacological combination, in a BV2 microglia cell model. The dual **9a** was able to decrease ROS production and, without affect cell viability, to downregulate the mRNA transcripts of proinflammatory genes, such as iNOS, IL-1β, and IL-6, highlighting stronger effects than both single target inhibitor and their combination.

Based on these results, the dual NOX2/MAO-B inhibitor **9a** could be considered as a new tool for further in-cell investigations including NOX2- and MAO-B-dependent neuroinflammation and/or neurodegeneration models.

1.4. Experimental section

1.4.1. Chemistry

Melting points were determined on a Buchi 530 melting point apparatus and are uncorrected. ^{1}H NMR and ^{13}C NMR spectra were recorded at 400 MHz on a Bruker AC 400 spectrometer; chemical shifts are reported in δ (ppm) units relative to the internal reference tetramethyl silane (Me_4Si). All compounds were routinely checked by TLC, ^{1}H NMR, and ^{13}C NMR spectra. TLC was performed on aluminum-backed silica gel plates (Merck DC, Alufolien Kieselgel 60 F254) with spots visualized by UV light. All solvents were reagent grade and, when necessary, were purified and dried by standard methods. The concentration of solutions after reactions and extractions involved using a rotary evaporator operating at a reduced pressure of ca. 20 Torr. Organic solutions were dried over anhydrous sodium sulfate. Elemental analysis has been used to determine the purity of the described compounds, which is >95 %. Analytical results are within ± 0.40 % of the theoretical values (Table S1 in Supporting Information). All chemicals were purchased from Sigma Aldrich, Milan (Italy), Alfa Aesar, Karlsruhe (Germany), Fluorochem, Manchester (UK), or BLD-Pharma, Kaiserslautern (Germany) and were of the highest purity.

General procedure for the synthesis of azido derivatives 24 and 32

Example: Synthesis of 2-(4-(azidomethyl)phenyl)-2-methyl-1,3-dioxolane (24): To a solution of 2-(4-(bromomethyl)phenyl)-2-methyl-1,3-dioxolane (2.181 g, 0.00848 mol) in dry DMF, sodium azide (1.103 g, 0.1696 mol) was added under nitrogen flow. After stirring at RT for 14h, water was added, and the resulting reaction mixture was extracted with diethyl ether (3x20 mL). The organic extracts were collected, washed with brine, dried with sodium sulfate, and concentrated under reduced pressure. The remaining residue was purified by column chromatography (SiO_2, eluting with ethyl acetate/n-hexane 1:20) to provide the pure compound **24**.

M.p. liquid; yield: 74.8 %; ^{1}H NMR ($CDCl_3$, 400 MHz, δ; ppm) δ 1.68 (s, 3H, -C*H*$_3$), 3.80 (t, 2H, J = 2 Hz, chetalic protons), 4.07 (t, 2H, J = 2 Hz, chetalic protons), 4.37 (s, 2H, -C*H*$_2$-), 7.32 (d, 2H, J = 8 Hz, aromatic protons), 7.53 (d, 2H, J = 8 Hz, aromatic protons).

General procedure for the synthesis of the amino carboxamide derivatives 25 and 33

Example: Synthesis of 5-amino-1-(4-(diethoxymethyl)benzyl)-1H-1,2,3-triazole-4-carboxamide (33): To a solution of sodium ethoxide, obtained solubilizing sodium (298.37 mg, 0.01297 mol) in dry EtOH was added the previously synthesized intermediate, 1-(azidomethyl)-4-(diethoxymethyl)benzene (**32**) (1.11 g, 0.00648 mol). After stirring at 80 °C for 1 hour and 30 minutes, EtOH was evaporated, and the reaction was quenched with ammonium chloride saturated solution. The pure white precipitate **33** was filtered off.

M.p. 240-242 °C, recrystallization solvent: acetonitrile/methanol; yield: 73.5 %; ^{1}H NMR (DMSO, 400 MHz, δ; ppm) δ 1.23 (t, 6H, J = 4 Hz, -O-CH$_2$-C*H*$_3$), 3.65 (m, 4H, -O-C*H*$_2$-CH$_3$), 5.47 (s, 2H, -C*H*$_2$-), 5.49 (s, 1H, -C*H*-), 7.27 (d, 2H, J = 6 Hz, aromatic protons), 7.38 (d, 2H, J = 6 Hz, aromatic protons), 7.92 (s, 2H, -CON*H*$_2$), 8.59 (s, 2H, -N*H*$_2$).

General procedure for the synthesis of the triazolo-pyrimidinol derivatives 26 and 34

Example: Synthesis of 3-(4-(2-methyl-1,3-dioxolan-2-yl)benzyl)-3H-[1,2,3]triazolo[4,5-d]pyrimidin-7-ol (26): To a solution of sodium ethoxide, obtained solubilizing sodium (515.24 mg, 0.0224 mol) in dry EtOH was added ethyl formate (1.44 mL, 0.01792 mol) and the previously synthesized 5-amino-1-(4-(2-methyl-1,3-dioxolan-2-yl)benzyl)-1H-1,2,3-triazole-4-carboxamide (**25**) (1.359 g, 0.00448 mol). After stirring at 80 °C for 3 hours, EtOH was evaporated, and the reaction was quenched with ammonium chloride saturated solution. The pure white precipitate **26** was filtered off.

M.p. >250 °C, recrystallization solvent: methanol; yield: 98.8 %; ^{1}H NMR (DMSO, 400 MHz, δ; ppm) δ 1.15 (s, 3H, -C*H*$_3$), 3.66 (t, 2H, J = 2 Hz, chetalic protons), 3.96 (t, 2H, J = 2 Hz, chetalic protons), 5.75 (s, 2H, -C*H*$_2$-), 7.32 (d, 2H, J = 8.4 Hz, aromatic protons), 7.40 (d, 2H, J = 8.4 Hz, aromatic protons), 7.88 (s, 1H, -OH), 8.27 (s, 1H, pyrimidine proton).

Synthesis of mesylate derivative 2: To a solution of commercially available 3-benzyl-3H-[1,2,3]triazolo[4,5-d]pyrimidin-7-ol (40 mg, 0.00017 mol) in dry DCM, TEA (0.037 mL, 0.00026 mol) and, at 0 °C, methanesulfonyl chloride (0.02 mL, 0.00025 mol) were added. The reaction was stirred at RT for 10 minutes. DCM was evaporated and the resulting reaction mixture was purified by column chromatography (SiO_2, eluting with ethyl acetate/n-hexane 1:1.5) to provide the pure compound **2**.

M.p. 170-171 °C, recrystallization solvent: toluene/acetonitrile; yield: 33.5 %; ^1H NMR ($CDCl_3$, 400 MHz, δ; ppm) δ 3.69 (s, 3H, -CH_3), 5.73 (s, 2H, -CH_2-), 7.36 (t, 3H, J = 2 Hz, aromatic protons), 7.44 (d, 2H, J = 2 Hz, aromatic protons), 8.70 (s, 1H, pyrimidine protons).

General procedure for the synthesis of the chloro derivatives 3, 30a, 30b, and 37a-f

Example: Synthesis of 3-benzyl-7-chloro-3H-[1,2,3]triazolo[4,5-d]pyrimidine, 3: To a solution of commercially available 3-benzyl-3H-[1,2,3]triazolo[4,5-d]pyrimidin-7-ol (50 mg, 0.00022 mol) in dry $CHCl_3$, dry N,N-DMF (0.05 mL, 0,000264 mol) was added and, at 0 °C, $SOCl_2$ (0.2 mL, 0,000242 mol). The reaction was stirred at 80 °C for 3 hours. After this time, the reaction was quenched with sodium bicarbonate and extracted with $CHCl_3$ (3x20 mL). The organic extracts were collected, washed with brine, dried with sodium sulfate, and concentrated under reduced pressure. The resulting reaction mixture was purified by column chromatography (SiO_2, eluting with ethyl acetate/n-hexane 1:1) to provide the pure compound **3**.

M.p. 88-91 °C, recrystallization solvent: cyclohexane/toluene; yield: 98.8 %; ^1H NMR ($CDCl_3$, 400 MHz, δ; ppm) δ 5.82 (s, 2H, -CH_2-), 7.30 (t, 3H, J = 2 Hz, aromatic protons), 7.40 (d, 2H, J = 2 Hz, aromatic protons), 8.86 (s, 1H, pyrimidine protons).

Synthesis of 3-benzyl-3H-[1,2,3]triazolo[4,5-d]pirimidin-7-amina, 4: To a solution of 3-benzyl-7-chloro-3H-[1,2,3]triazolo[4,5-d]pyrimidine (**3**) (117 mg, 0.00047 mol) in 1-butanol, a solution of methanolic ammonia 7N (0.68 mL, 0.00476 mol) was added. The reaction was stirred at 110 °C for 2 hours. The reaction was quenched with distilled water and the pure white precipitate 4 was filtered off.

M.p. 255-256 °C, recrystallization solvent: methanol; yield: 57.7 %; ^{1}H NMR (DMSO, 400 MHz, δ; ppm) δ 5.76 (s, 2H, -CH_2-), 7.33-7.34 (m, 5H, aromatic protons), 8.25 (s, 1H, -NH_2), 8.31 (s, 1H, pyrimidine protons), 8.45 (s, 1H, -NH_2).

General procedure for the synthesis of the 5, 20, and 22 derivatives

Example: Synthesis of 4-((3-benzyl-3H-[1,2,3]triazolo[4,5-d]pyrimidin-7-yl)tio)aniline (22): To a solution of 3-benzyl-7-chloro-3H-[1,2,3]triazolo[4,5-d]pyrimidine (**3**) (23.5 mg, 0.00009 mol) in dry EtOH, TEA was added (0.0133 mL, 0.00009 mol) and, at 0 °C, 4-aminothiophenol (11.97 mg, 0.00009 mol). The reaction was stirred at RT for 1 hour. After this time, the reaction was quenched with brine. The white precipitate 19 was filtered off.

M.p. 178-180 °C, recrystallization solvent: acetonitrile; yield: 99.8 %; ^{1}H NMR (DMSO, 400 MHz, δ; ppm) δ 5.72 (s, 2H, -NH_2), 5.96 (s, 2H, -CH_2-), 6.72 (d, 2H, J = 8.4 Hz, aromatic protons), 7.31 (d, 2H, J = 8.8 Hz, aromatic protons), 7.38-7.40 (m, 5H, aromatic protons), 8.85 (s, 1H, pyrimidine protons).

5, Tert-butyl 4-(3-benzyl-3H-[1,2,3]triazolo[4,5-d]pyrimidin-7-yl)piperazine-1-carboxylate: M.p. 133-136 °C, recrystallization solvent: toluene; yield: 66.7%; ^{1}H NMR (DMSO, 400 MHz, δ, ppm): 1.44 (s, 9H, -C-(CH_3)$_3$), 3.54 (d, 4H, J = 19.2, piperazine protons), 4.01 (s, 2H, piperazine protons), 4.56 (s, 2H, piperazine protons), 5.80 (s, 2H, -CH_2-), 7.28-7.37 (m, 5H, aromatic protons), 8.42 (s, 1H, pyrimidine proton).

General procedure for the synthesis of the acrylamide derivatives 7a, 7c, and 7d

Example: Synthesis of N-(4-((3-benzyl-3H-[1,2,3]triazolo[4,5-d]pyrimidin-7-yl)tio)fenil)acrylamide, 7d: To a solution of 4-((3-benzyl-3H-[1,2,3]triazolo[4,5-d]pyrimidin-7-yl)tio)aniline (**22**) (10 mg, 0.00003 mol) in dry DCM, TEA (0.005 mL, 0.000036 mol) and, at 0 °C, acryloyl chloride (0.00267 mL, 0.0000328 mol) were added. The reaction was stirred at RT for 10 minutes and, after this time, the reaction was quenched with distilled water and extracted with DCM (3x20 mL). The organic extracts were collected, washed with brine, dried with sodium sulfate, and concentrated under reduced pressure to obtain **7d**.

M.p. 190-193 °C, recrystallization solvent: acetonitrile; yield: 86.1 %; ^{1}H NMR (DMSO, 400 MHz, δ; ppm) δ 5.79 (dd, 1H, -CH=C*H*$_2$), 5.99 (s, 2H, -CH$_2$-), 6.31 (dd, 1H, -CH=C*H*$_2$), 6.5 (q, 1H, -C*H*=CH$_2$), 7.33-7.36 (m, 5H, aromatic protons), 7.65 (d, 2H, J = 8.8, aromatic protons), 7.83 (d, 2H, J = 8.4 Hz, aromatic protons), 8.83 (s, 1H, pyrimidine protons), 10.36 (s, 1H, -NH).

***7a, 1-(4-(3-benzyl-3H-[1,2,3]triazolo[4,5-d]pyrimidin-7-yl)piperazin-1-yl)prop-2-en-1-one*:** M.p. 140-143 °C, recrystallization solvent: toluene; yield: 33.3 %; ^{1}H NMR (DMSO, 400 MHz, δ; ppm) δ 3.80 (m, 4H, piperazine protons), 4.05 (s, 2H, piperazine protons), 4.60 (s, 2H, piperazine protons), 5.77 (dd, 1H, -CH=C*H*$_2$), 5.81 (s, 2H, -CH$_2$-), 6.18 (dd, 1H, -CH=C*H*$_2$), 6.88 (q, 1H, -C*H*=CH$_2$), 7.29-7.38 (m, 5H, aromatic protons), 8.45 (s, 1H, pyrimidine protons).

7c, 1-(4-((3-benzyl-3H-[1,2,3]triazolo[4,5-d]pyrimidin-7-yl)amino)piperidin-1-yl)prop-2-en-1-one: M.p. 72-73 °C, recrystallization solvent: cyclohexane/toluene; yield: 49.5 %; ^{1}H NMR (DMSO, 400 MHz, δ; ppm) δ1.55-1.58 (m, 2H, piperidine protons), 1.93-1.99 (m, 2H, piperidine protons), 2.78-2.84 (m, 1H, piperidine protons), 3.30-3.33 (m, 1H, piperidine protons), 3.36 (s, 2H, piperidine protons), 4.11-4.14 (d, 1H, J = 12.8, piperidine protons), 5.67-5.69 (dd, 1H, -CH=C*H*$_2$), 5.68 (s, 2H, -CH$_2$-), 6.12-6.14 (dd, 1H, -CH=C*H*$_2$), 6.80-6.86 (q, 1H, -C*H*=CH$_2$-), 7.29-7.44 (m, 5H, aromatic protons), 8.42 (s, 1H, pyrimidine proton), 8.97 (d, 1H, -NH).

General procedure for the synthesis of the 6 and 21 derivatives

Example: Synthesis of 3-benzyl-N-(piperidin-4-yl)-3H-[1,2,3]triazolo[4,5-d]pyrimidin-7-amino hydrochloride (21): To a solution of tert-butyl 4-((3-benzyl-3H-[1,2,3]triazolo[4,5-d]pyrimidin-7-yl)amino)piperidine-1-carboxylate (**20**) (43 mg, 0.000011 mol) in dry THF, 4N HCl in 1,4-dioxane was added (0.13 mL, 0.0011 mol) at 0 °C. The reaction was stirred at RT for 3 hours and, after this time, the reaction was quenched with diethyl ether. The pure white **21** precipitate was filtered off.

M.p. >250 °C, recrystallization solvent: methanol; yield: 77.9 %; ^{1}H NMR (DMSO, 400 MHz, δ; ppm) δ 1.84-1.92 (m, 2H, piperidine protons), 2.07 (d, 2H, J = 12 Hz, piperidine protons), 3.01-3.09 (q, 2H, piperidine protons), 3.35 (d, 2H, J = 12 Hz, piperidine protons), 4.46-4.48 (m, 1H, piperidine protons), 5.79 (s, 2H, J = 6.8 Hz, -CH_2-), 7.22-7.38 (m, 5H, aromatic protons), 8.43 (s, 1H, pyrimidine proton), 8.67 (d, 1H, J = 6.8 Hz, -NH-), 8.93-9.06 (m, 1H, *H*Cl), 9.19 (d, 1H, J = 7.2, -NH).

6, 3-benzyl-7-(piperazin-1-yl)-3H-[1,2,3]triazolo[4,5-d]pyrimidine hydrochloride: M.p. 151-152 °C, recrystallization solvent: toluene; yield: 75.5 %; ^{1}H NMR (DMSO, 400 MHz, δ; ppm) δ 3.31 (s, 4H, piperazine protons), 4.26 (s, 2H, piperazine protons), 4.78 (s, 2H, piperazine protons), 5.83 (s, 2H, -CH_2-), 7.29-7.48 (m, 5H, aromatic protons), 8.50 (s, 1H, pyrimidine proton), 9.47 (s, 2H, N*H*·*H*Cl).

Synthesis of 1-(4-(3-benzyl-3H-[1,2,3]triazolo[4,5-d]pyrimidin-7-yl)piperazin-1-yl)etan-1-one (7b): to a solution of 3-benzyl-7-(piperazin-1-yl)-3H-[1,2,3]triazolo[4,5-d]pyrimidine hydrochloride (**6**) (27 mg, 0.000081 mol) in dry DCM, TEA (0.03 mL, 0.00019 mol) was added and, at 0 °C, acetyl chloride (0.01 mL, 0.00011 mol). The reaction was stirred at RT for 30 minutes. After this time, the reaction was quenched with distilled water and extracted with DCM (3x20 mL). The organic extracts were collected, washed with brine, dried with sodium sulfate, and concentrated under reduced pressure. The obtained solid **7b** was triturated with diethyl ether and, after 30 minutes, filtered off.

M.p. 148-150 °C, recrystallization solvent: toluene; yield: 85.6 %; ^{1}H NMR (DMSO, 400 MHz, δ; ppm) δ 2.08 (s, 3H, -CH_3), 3.66 (d, 4H, J = 18.4 Hz, piperazine protons), 4.03 (d, 2H, J = 24.4 Hz, piperazine protons), 4.61 (d, 2H, J = 24.4 Hz, piperazine

protons), 5.81 (s, 2H, -CH_2-), 7.33-7.34 (m, 5H, aromatic protons), 8.44 (s, 1H, pyrimidine proton).

Synthesis of 2-(4-(bromomethyl)phenyl)-2-methyl-1,3-dioxolane (23): to a solution of the commercially available 1-(4-(bromomethyl)phenyl)ethanone (1.50 g, 0.7039 mol) in dry benzene, *p*-toluenesulfonic acid (20.6 mg, 0.0001197 mol) and ethylene glycol were added (0,79 mL, 0,01408 mol), using Dean-Stark apparatus. The reaction was stirred at 120 °C overnight. After this time, the reaction was quenched with sodium bicarbonate and extracted with ethyl acetate (3x20 mL). The organic extracts were collected, washed with brine, dried with sodium sulfate, and concentrated under reduced pressure, obtaining **23** as a pure white solid.

M.p. 148-150 °C, recrystallization solvent: toluene; yield: 96.7 %; ^{1}H NMR (DMSO, 400 MHz, δ; ppm) δ 1.66 (s, 3H, -CH_3), 3.80 (t, 2H, J = 2.4 Hz, chetalic protons), 4.06 (t, 2H, J = 2.4 Hz, chetalic protons), 4.52 (s, 2H, -CH_2-), 7.39 (d, 2H, J = 8.4 Hz, aromatic protons), 7.48 (d, 2H, J = 8.4 Hz, aromatic protons).

General procedure for the synthesis of the 27 and 35 derivatives

Example: Synthesis of 1-(4-((7-hydroxy-3H-[1,2,3]triazole[4,5-d]pyrimidin-3-yl)methyl)phenyl)ethan-1-one (27): To a solution of 3-(4-(2-methyl-1,3-dioxolan-2-yl)benzyl)-3H-[1,2,3]triazole[4,5-d]pyrimidin-7-olo (**26**) (1.54 g, 4.9087 mol) in EtOH, 2N HCl (36.8 mL, 73.6315 mol), at 0 °C, was added. The reaction was stirred at RT for 2 hours. After this time, EtOH was evaporated and distilled water was added. The pure white solid was filtered off to obtain **27**.

M.p. 249-250 °C, recrystallization solvent: methanol; yield: 72.2 %; ^{1}H NMR (DMSO, 400 MHz, δ; ppm) δ 2.56 (s, 3H, -$COCH_3$-), 5.86 (s, 2H, -CH_2-), 7.44 (d, 2H, J = 8.4 Hz, aromatic protons), 7.94 (d, 2H, J = 8.4 Hz, aromatic protons), 8.27 (s, 1H, pyrimidine proton), 12.68 (s, 1H, -OH-).

Synthesis of 4-((7-hydroxy-3H-[1,2,3]triazole[4,5-d]pyrimidin-3-yl)methyl)benzoic acid (28): to a solution of 1-(4-((7-hydroxy-3H-[1,2,3]triazole[4,5-d]pyrimidin-3-yl)methyl)phenyl)ethan-1-one (**27**) (200 mg, 0.00075969 mol) in glacial acetic acid, bromine (0.23 mL, 0.004558 mol) was added. The reaction was stirred at 50 °C for 4 hours. After this time, acetic acid was evaporated, and the reaction was quenched with 2 N NaOH (3.04 mL, 0.0060755 mol) dropwise, at 0 °C, until basic pH. The reaction was stirred at RT for 1 hour. Afterward, 2 N HCl was added dropwise, at 0 °C, until acidic pH. The formed precipitate was filtered off and dried to afford the pure white compound **28**.

M.p. >250°C, recrystallization solvent: methanol; yield: 45.0 %; ^{1}H NMR (DMSO, 400 MHz, δ; ppm) δ 5.86 (s, 2H, -CH_2-), 7.41 (d, 2H, J = 8 Hz, aromatic protons), 7.92 (d, 2H, J =8 Hz, aromatic protons), 8.27 (s, 1H, pyrimidine proton), 12.75 (s, 1H, -COOH-), 12.99 (s, 1H, -OH-).

General procedure for the synthesis of the 29a and 29b derivatives

Example: Synthesis of (4-((7-hydroxy-3H-[1,2,3]triazole[4,5-d]pyrimidin-3-yl)methyl)-N-(prop-2-in-1-yl)benzamide (29b): To a solution of 4-((7-hydroxy-3H-[1,2,3]triazole[4,5-d]pyrimidin-3-yl)methyl)benzoic acid (**28**) (110 mg, 0.0004056 mol) in dry DMF, TEA (0.283 mL, 0.002028 mol) and benzotriazol-1-yloxytripyrrolidinophosphonium hexafluorophosphate (PyBOP) (253.25 mg, 0.0004866 mol) were added, under nitrogen atmosphere. The reaction was stirred at RT for 45 minutes to afford the activation of the acid. Afterward, at 0 °C, propargylamine (0.111 mL, 0.00162 mol) was added and then the reaction was stirred at RT overnight. The reaction was quenched with brine. Afterward, 2N HCl was added dropwise, at 0 °C, until acidic pH and extracted with ethyl acetate (3x20 mL). The organic extracts were collected, washed with brine, dried with sodium sulfate, and concentrated under reduced pressure. The resulting reaction mixture was purified by column chromatography (SiO_2, eluting with chloroform/methanol 12:1) to provide the pure compound **29b**.

M.p. 220-223 °C, recrystallization solvent: acetonitrile/methanol; yield: 40.0 %; ^{1}H NMR (DMSO, 400 MHz, δ; ppm) δ 3.12 (t, 1H, J = 2.4 Hz, propargylic protons), 4.04 (q, 2H, -C*H*$_2$-C≡CH-), 5.83 (s, 2H, -CH_2-), 7.41 (d, 2H, J = 5.6 Hz, aromatic protons), 7.83 (d, 2H, J = 5.6 Hz, aromatic protons), 8.27 (s, 1H, pyrimidinic proton), 8.93 (t, 1H, J = 5.6 Hz, -CONH-), 12.64-12.75 (s, 1H, -OH-).

General procedure for the synthesis of the final compounds 8a, 8b, and 9a-f

Example: Synthesis of 4-((7-benzo[d]oxazol-2-yl-tio)-3H-[1,2,3]triazole[4,5-d]pyrimidin-3-yl)methyl)-N-(prop-2-in-1-yl)benzamide, 8b: To a solution of 4-((7-chloro-3H-[1,2,3]triazole[4,5-d]pyrimidin-3-yl)methyl)-N-(prop-2-in-1-yl)benzamide (**30b**) (52 mg, 0.000159146 mol) in dry EtOH, TEA (0.02 mL, 0.000159146 mol) and, at 0 °C, 2-mercaptobenxozaole (24 mg, 0.000159146 mol) were added. The reaction was stirred at RT for 30 minutes. The reaction was quenched with distilled water and extracted with DCM (3x20 mL). The organic extracts were collected, washed with brine, dried with sodium sulfate, and concentrated under reduced pressure. The resulting reaction mixture was purified by column chromatography (SiO_2, eluting with ethyl acetate/chloroform 1:6) to provide the pure compound **8b**.

M.p. 136-139 °C, recrystallization solvent: toluene; yield: 30.0 %; ^{1}H NMR ($CDCl_3$, 400 MHz, δ; ppm) δ 2.21 (s, 1H, propargylic protons), 4.17 (q, 2H, -C*H*$_2$-C≡CH), 5.80 (s, 2H, -CH_2-), 7.35-7.79 (m, 8H, aromatic protons), 8.74 (s, 1H, -NH-), 8.87 (S, 1H, -CONH-).

***8a, 4-((7-benzo[d]oxazol-2-yl-tio)-3H-[1,2,3]triazole[4,5-d]pyrimidin-3-yl)methyl)-N-(propyl)benzamide*:** M.p. 162-165 °C, recrystallization solvent: toluene/acetonitrile; yield: 32.2 %; ^{1}H NMR ($CDCl_3$, 400 MHz, δ; ppm) δ 0.90 (t, 3H, J=8 Hz, -NH-CH_2-CH_2-C*H*$_3$), 1.52-1.58 (m, 2H, NH-CH_2-C*H*$_2$-CH_3), 3.31-3.36 (q, 2H, -NH-C*H*$_2$-CH_2-CH_3), 5.80 (s, 2H, -CH_2-), 5.96 (s, 1H, -N*H*-CH_2-CH_2-CH_3), 7.35-7.39 (m, 4H, aromatic protons), 7.53 (dd, 1H, aromatic protons), 7.66 (d, 2H, J = 8.4 Hz, aromatic protons), 7.78 (dd, 1H, aromatic protons), 8.74 (s, 1H, pyrimidinic proton).

***9a, N-(4-((7-(benzo[d]oxazol-2-ylthio)-3H-[1,2,3]triazolo[4,5-d]pyrimidin-3-yl)methyl)benzyl)-N-methylprop-2-yn-1-amine*:** M.p. 102-105 °C, recrystallization solvent: cyclohexane/toluene; yield: 32.0 %; ^{1}H NMR ($CDCl_3$, 400 MHz, δ; ppm) δ 2.29 (s, 1H, -CH_2-C≡C*H*), 2.34 (s, 3H, -N-C*H*$_3$), 3.30 (s, 2H, -C*H*$_2$-C≡CH), 3.58 (s, 2H, -C*H*$_2$-N-CH_3), 5.84 (s, 2H, -N-C*H*$_2$-), 7.35 (d, 2H, aromatic protons, J=8 Hz), 7.42 (d, 2H, aromatic protons, J=8 Hz), 7.46-7.51 (m, 2H, aromatic protons), 7.62 (d, 1H, aromatic protons, J=7.2 Hz), 7.87 (d, 1H, aromatic protons, J=8 Hz), 8.84 (s, 1H, pyrimidinic protons).

9b, N-(4-((7-(benzo[d]oxazol-2-ylthio)-3H-[1,2,3]triazolo[4,5-d]pyrimidin-3-yl)methyl)benzyl)-N-methylpropan-1-amine: M.p. 154-155 °C, recrystallization solvent: toluene/acetonitrile; yield: 18.5 %; ^{1}H NMR ($CDCl_3$, 400 MHz, δ; ppm) δ 1.68-1.76 (m, 2H, -CH_2-C*H*$_2$-CH_3), 3.31 (s, 3H, -CH_3), 3.76 (t, 3H, J = 7.6 Hz, -CH_2-C*H*$_3$), 4.21(t, 2H, J = 7.6 Hz, -C*H*$_2$-CH_2-CH_3), 4.44 (s, 2H, -C*H*$_2$), 5.66 (s, 2H, -C*H*$_2$-), 7.34 (m, 6H, aromatic protons), 7.53 (dd, 2H, aromatic protons), 8.35 (s, 1H, pyrimidine proton).

9c, N-(4-((7-(benzo[d]oxazol-2-ylthio)-3H-[1,2,3]triazolo[4,5-d]pyrimidin-3-yl)methyl)benzyl)-N-methyl-1-phenylmethanamine: M.p. liquid, yield: 14.8 %; ^{1}H NMR ($CDCl_3$, 400 MHz, δ; ppm) δ 1.98 (s, 2H, -*CH*$_2$), 3.44 (s, 2H, -*CH*$_2$), 3.46 (s, 3H, -*CH*$_3$), 5.78 (s, 2H, -*CH*$_2$), 7.33 (m, 8H, aromatic protons), 7.52 (t, 3H, J = 6 Hz, aromatic protons), 7.78 (m, 2H, aromatic protons), 8.73 (s, 1H, pyrimidine proton).

9d, 2-((3-(4-(piperidin-1-ylmethyl)benzyl)-3H-[1,2,3]triazolo[4,5-d]pyrimidin-7-yl)thio)benzo[d]oxazole: M.p. 130-133 °C, recrystallization solvent: toluene; yield: 23.5 %; ^{1}H NMR ($CDCl_3$, 400 MHz, δ; ppm) δ 1.20 (s, 2H, -CH_2-), 1.36-1.47 (m, 2H, piperidine protons), 1.65-1.75 (m, 4H, piperidine protons), 2.49-2.55 (m, 2H, piperidine protons), 3.59-3.67 (m, 2H, piperidine protons), 5.75 (s, 2H, -C*H*$_2$-), 7.35-7.42 (m, 6H, aromatic protons), 7.53 (d, 1H, J = 8.8 Hz, aromatic protons), 7.78 (d, 1H, J = 8.8 Hz, aromatic protons), 8.75 (s, 1H, pyrimidine protons).

9e, 2-((3-(4-(morpholinomethyl)benzyl)-3H-[1,2,3]triazolo[4,5-d]pyrimidin-7-yl)thio)benzo[d]oxazole: M.p. 89-90 °C, recrystallization solvent: cyclohexane/toluene; yield: 89.9 %; ^{1}H NMR ($CDCl_3$, 400 MHz, δ; ppm) δ 2.32 (s, 4H, morpholine protons), 3.38 (s, 2H, -C*H*$_2$-) 3.61 (s, 4H, morpholine protons), 5.74 (s, 2H, -C*H*$_2$-), 7.23 (d, 2H, J = 7.6 Hz, aromatic protons), 7.36 (d, 2H, J = 7.6 Hz, aromatic protons), 7.34-7.39 (m, 2H, aromatic protons), 7.42 (dd, 1H, aromatic protons), 7.78 (dd, 1H, aromatic protons), 8.74 (s, 1H, pyrimidine protons).

9f, 2-((3-(4-((2,2-difluoro-7-azaspiro[3.5]nonan-7-yl)methyl)benzyl)-3H-[1,2,3]triazolo[4,5-d]pyrimidin-7-yl)thio)benzo[d]oxazole: M.p. liquid, yield: 11.0 %; ^{1}H NMR ($CDCl_3$, 400 MHz, δ; ppm) δ 1.23 (s, 4H, cyclobutane protons), 2.23-2.31 (m, 8H, piperidine protons), 5.23 (s, 2H, -CH_2-), 5.75 (s, 2H, -CH_2-), 7.35-7.42 (m, 6H, aromatic protons), 7.52 (dd, 1H, aromatic protons), 7.79 (dd, 1H, aromatic proton), 8.74 (s, 1H, pyrimidine proton).

Synthesis of 1-(bromomethyl)-4-(diethoxymethyl)benzene (31): to a solution of the commercially available 4-(bromomethyl)benzaldehyde (160 mg, 0.000804 mol) in dry EtOH, triethyl orthoformate (1.4 mL, 0.00819 mol) and Dowex 50W X8 (152.4 mg) were added. The reaction was stirred at RT for 3 hours. After this time, half amount of EtOH was evaporated and 2N sodium carbonate (152.4 mg) was added and stirred at RT for 20 minutes. Afterward, the solution was filtered to remove sodium carbonate and Dowex 50W X8, obtaining 209.7 mg of **28** as a yellow oil.

M.p. liquid; yield: 95.5 %; ^{1}H NMR (DMSO, 400 MHz, δ; ppm) 1.11-1.17 (m, 6H, -CH-(O-CH_2- CH_3)$_2$), 3.42-3.57 (m, 4H, -CH-(O-CH_2-CH_3)$_2$), 5.42 (s, 2H, -CH_2-), 5.45 (s, 1H, -C*H*-(O-CH_2-CH_3)$_2$), 6.38 (s, 2H, -NH_2), 7.21 (d, 2H, J = 8 Hz, aromatic protons), 7.38 (d, 2H, J = 8 Hz, aromatic protons), 6.38 (s, 2H, -NH_2).

General procedure for the synthesis of 36a-f derivatives

Example: Synthesis of 3-(4-((methyl(prop-2-yn-1-yl)amino)methyl)benzyl)-3H-[1,2,3]triazolo[4,5-d]pyrimidin-7-ol (36a): to a solution of 4-((7-hydroxy-3H-[1,2,3]triazole[4,5-d]pyrimid-3-yl)methyl)benzaldehyde (**35**) (20 mg, 0.000078 mol) in dry DCM, N-methyl-propargylamine (0.007 mL, 0.000078 mol) and sodium triacetoxyborohydride (21.6 mg, 0.00018 mol) were added, under nitrogen atmosphere. The reaction was stirred at RT for 4 hours. Afterward, the reaction was quenched with distilled water and extracted with DCM (3x20 mL). The organic extracts were collected, washed with brine, dried with sodium sulfate, and concentrated under reduced pressure. The resulting reaction mixture was purified by column chromatography (SiO_2, eluting with ethyl chloroform/methanol 15:1) to provide the pure white compound **36a**.

M.p. 185-186 °C; recrystallization solvent = acetonitrile; yield=66.2 %; ^{1}H NMR (DMSO, 400 MHz, δ; ppm) 2.23 (s, 3H, -N-CH_3), 3.24 (s, 1H, -C≡C*H*), 3.30 (s, 2H, -

CH_2-C≡CH), 3.53 (s, 2H, -CH_2-N-CH_3), (s, 2H, -CH_2-C≡CH), 5.80 (s, 2H, -N-CH_2-benzyl), 7.32-7.37 (m, 4H, aromatic protons), 8.33 (s, 1H, pyrimidinic proton), 12.76 (s, 1H, -OH).

Table 1.4. Elemental Analysis of compounds 2-9f.

CPD	MW	Elemental Analysis									
		Calculated, %					Found, %				
		C	N	O	H	Other	C	N	O	H	Other
2	305.31	47.21	22.94	15.72	3.63	10.50 (S)	47.31	22.90	15.74	3.65	10.52 (S)
3	245.67	53.78	28.51		3.28	14.43 (Cl)	53.86	28.47		3.29	14.41 (Cl)
4	226.24	58.40	37.15		4.46		58.48	37.11		4.47	
5	395.47	60.74	24.79	8.09	6.37		60.84	24.74	8.05	6.38	
6	331.81	54.30	29.55		5.47	10.68 (Cl)	54.38	29.51		5.48	10.66 (Cl)
7a	349.40	61.88	28.06	4.58	5.48		61.96	28.02	4.64	5.49	
7b	337.39	60.52	29.06	4.74	5.68		60.60	29.02	4.70	5.69	
7c	363.43	62.79	26.98	4.40	5.82		62.87	26.94	4.35	5.83	
7d	388.45	61.84	21.64	4.12	4.15	8.25 (S)	61.91	21.60	4.16	4.16	8.27 (S)
8a	445.50	59.31	22.01	7.18	4.30	7.20 (S)	59.38	21.97	7.21	4.31	7.17 (S)
8b	441.47	59.86	22.21	7.25	3.42	7.26 (S)	59.96	22.16	7.21	3.43	7.24 (S)
9a	441.51	62.57	22.21	3.62	4.34	7.26 (S)	62.64	22.17	3.59	4.35	7.23 (S)
9b	445.55	62.00	22.01	3.59	5.20	7.20 (S)	62.07	21.97	3.57	5.21	7.24 (S)
9c	493.59	65.70	19.86	3.24	4.70	6.50 (S)	65.78	19.82	3.21	4.71	6.47 (S)
9d	457.56	63.00	21.43	3.50	5.07	7.01 (S)	63.08	21.39	3.52	5.08	7.04 (S)
9e	459.53	60.12	21.34	6.96	4.61	6.98 (S)	60.20	21.30	6.99	4.62	6.95 (S)
9f	533.60	60.78	18.37	3.00	4.72	6.01 (S) 7.12 (F)	60.86	18.33	2.97	4.73	6.02 (S) 7.11 (F)

1.4.2. Materials and methods

1.4.2.1. Reagents

Roswell Park Memorial Institute (RPMI) 1640 medium with l-glutamine and sodium bicarbonate, penicillin, streptomycin, Lithium Dodecyl sulfate (LiDS), $MgCl_2$, flavin adenine dinucleotide disodium salt hydrate (FAD-Na_2), β-nicotinamide adenine dinucleotide 2′-phosphate reduced tetrasodium salt (NADPH), β-Nicotinamide adenine dinucleotide, reduced disodium salt hydrate (NADH), 1-methoxy phenazine methosulfate, Nitroblue tetrazolium, Sodium Azide, Phosphate-Buffered Saline (PBS), Sodium Di-Hydrogen Phosphate ($NaH_2PO_4 \cdot H_2O$), Isopropyl β-d-1-thiogalactopyranoside, Sodium chloride, Glycerol. Hepes, Leupeptin, Pepstatin, Phenylmethylsulfonyl fluoride. SigmaFastTM Protease Inhibitor Cocktail Tablets EDTA-Free, Hemin from Porcine, cytochrome c from equine heart, superoxide dismutase (SOD), Amplex Red, Sodium dithionite and horseradish peroxidase, Triton X-100 were purchased from Sigma-Aldrich. Potassium Phosphate Dibasic (K_2HPO_4) was purchased from Carlo Erba Reagents. Hydrochloric acid was purchased from Fluka. Magnesium Sulfate ($MgSO_4$) and Acetonitrile were purchased from Merck. Fetal bovine serum was purchased from Invitrogen. 6-(4-methoxyphenyl)-2-methyl-imidazo [1,2-a]pyrazin-3(7H)-one (MCLA) was purchased from MedChemExpress. Non-fluorescent coumarin boronic acid (CBA) was synthesized in-house. All Culture media, DMEM (Cat## 31966047), fetal bovine serum (FBS), penicillin G, and streptomycin, were from GIBCO Invitrogen (Carlsbad, CA). [281]

1.4.2.2. NOX expression and preparations

(Group of Prof. Andrea Mattevi, Department of Biology and Biotechnology Lazzaro Spallanzani, University of Pavia)

Bacterial NOX5 - The overexpression in *E. coli* and the preparation of cell membranes for the FLAG-$(His)_8$-SUMO N-terminally tagged *Cylindrospermum stagnale* NOX5 was performed as reported in Ceccon, 2017. [54] The C668S mutant of the dehydrogenase was prepared following the protocols reported in Magnani, 2017. [27]

Human NOX2 membrane preparation - PLB-985 cells were cultured in suspension at 1 × 10^6 cells/mL in RPMI at 37 °C with 5% CO_2. The medium was supplemented with 10% fetal bovine serum, 100 units/mL of penicillin and 100 μg/ml of streptomycin. Cells were centrifuged at 1000×g for 10 min, then resuspended in PBS and centrifuged again at 1000×g for 5 min and frozen at −80 °C. PLB-985 frozen pellets were resuspended at a concentration of 2 × 10^8 cells/ml in sonication buffer containing 10 mM Hepes (pH 7.4), 10 mM NaCl, 100 mM KCl, 12 mM EGTA, 3.5 mM $MgCl_2$, 1 mM phenylmethylsulfonyl fluoride and supplemented with 2 μM leupeptin, 2 μM pepstatin, and protease inhibitors, just before sonication. The lysate was centrifuged at 2000 rpm for 5 min at 4 °C, and the supernatant was collected. The cell pellet was resuspended in sonication buffer and sonicated again on ice two times. The cell lysate was centrifuged at 2000 rpm for 5 min at 4 °C, and the supernatant was collected. Both supernatants were ultra-centrifuged (200,000×g for 30 min) at 4 °C (Optima MAX-XP Ultracentrifuge, Beckman Coulter). Protein concentration was assessed by Biuret Assay. [281]

Human NOX4 membrane preparation - The cDNAs encoding for the human NOX4 (isoform 1) and the human p22phox were originally obtained from Genescript. NOX4 was subcloned into a pEG BacMam vector (a kind gift from Eric Gouaux (Oregon Health and Science University, Portland)). The construct contained a Kozak sequence, followed by a $(His)_6$ tag, an eGFP moiety, and a TEV cleavage site at the N-terminus. p22phox was subcloned into the pDsRed-monomer-N1 vector with a DsRed moiety at the C-terminus. HEK293-EBNA1-6E cells were obtained from Yves Durocher (NRC-BRI, Montreal, Canada). Cells were grown in suspension using FreeStyle medium (Invitrogen). The day before transfection, cells were seeded at a density of 5 × 10^5 cells/ml. Transient NOX4-p22 co-transfection of HEK293 EBNA-1 was performed using polyethylenimine (linear MW 25000, Polyscience Europe Gmbh) in a ratio 1:3 (0.6 μg NOX4 vector: 0.4 μg p22 vector: 3 μg polyethylenimine, per ml of culture). After 24 h, co-transfected cells were harvested by centrifugation (1200×g, 5 min, 4 °C). Cell pellet was flash-frozen in liquid nitrogen and stored at −80 °C. Cell viability was evaluated by Trypan Blue exclusion assay (Trypan Blue solution w/v, Sigma). The cell pellet was thawed on ice and resuspended in sonication buffer (20% (v/v) glycerol, 120 mM NaCl, 1 mM EGTA in PBS pH 7.4) supplemented with protease inhibitors (SigmaFastTM Protease Inhibitor Cocktail Tablets, EDTA-Free, Sigma-Aldrich) at 4 °C. Cells were sonicated on ice. The cell lysate was then centrifuged at 500×g for 5 min at 4 °C, and the

supernatant was transferred to a fresh tube. The cell pellet was resuspended again in sonication buffer and the sample was sonicated again on ice. Cell lysate was then centrifuged at 500×g for 5 min at 4 °C, and the supernatant was collected. Both supernatants were pooled. The supernatant was ultra-centrifuged (160,000×g for 45 min) at 4 °C (Optima MAX-XP Ultracentrifuge, Beckman Coulter). Finally, the pellet was resuspended and diluted in sonication buffer to a final protein concentration of at least 30–40 mg/ml measured by the Biuret assay, aliquoted and stored in the −80 °C freezer. Protein quality was evaluated by measuring the fluorescence of the eGFP moiety and the DsRed moiety using fluorescence intensity-based detection on SDS-PAGE gel (BioRad; ChemiDoc MP imager; Alexa Fluor 488 for eGFP detection, Alexa Fluor 546 for DsRed detection). [281]

1.4.2.3. Evaluation of NOX activity and NOX inhibitors in cell-free assays

(Group of Prof. Andrea Mattevi, Department of Biology and Biotechnology Lazzaro Spallanzani, University of Pavia)

Cytochrome c reduction assay on NOX2 membranes – This assay relies on the reduction of cytochrome c by the NOX-generated superoxide that can be monitored spectrophotometrically (absorbance at 550 nm). 156 μg of NOX2-p22 containing membranes were added to a reaction mixture containing 65 mM sodium phosphate buffer pH 7.0 with 1 mM EGTA, 1 mM $MgCl_2$, 2 mM NaN_3, 10 μM FAD, 100 μM LiDS, 160 nM recombinant cytosolic proteins p67phox, p47phox, Rac1 Q61L, and 200 μM cytochrome c. Ligands were added to the reaction mixture at a concentration of 100 μM and incubated for 10 min at 25 °C. The reaction was initiated by the addition of 200 μM NADPH. Measurements were performed using a ClarioStar plate reader and Cary 100 UV–Vis spectrophotometer. [281]

MCLA assay on NOX2 - MCLA is a chemiluminescent (654 nm) reagent that is highly sensitive to superoxide. 20 μg of NOX2-p22 containing membranes were added to a reaction mixture containing 65 mM sodium phosphate buffer pH 7.0 with 1 mM EGTA, 1 mM $MgCl_2$, 0.5 μM FAD, 100 μM LiDS, 160 nM recombinant cytosolic proteins p67phox, p47phox, Rac1 Q61L, and 1 μM MCLA. Ligands were added to the reaction mixture at a concentration of 100 μM and incubated for 10 min at 25 °C. The reaction was initiated by the addition of 200 μM NADPH.

Measurements were performed using a GloMax plate reader. The activity of NOX2 was evaluated also in the absence of the cytosolic proteins and $CaCl_2$, respectively. SOD was used as an additional negative control. [281]

Amplex red/peroxidase assay on NOX4 membranes – In this assay, hydrogen peroxide production is detected through the H_2O_2-dependent generation of the Resorufin by horseradish peroxidase. NOX4-containing membranes (100 μg) were added to a reaction mixture of PBS with 12.5 μM Amplex Red, 0.02 U/ml horseradish peroxidase and 40 μM FAD. The tested compounds (100 μM) were added to the mixture and incubated for 10 min at 4 °C. The reaction was started by adding 40 μM NADPH, a concentration chosen to minimize interference effects. Measurements were performed using a ClarioStar plate reader (excitation 572 nm/emission 583 nm). Catalase as well as membranes transfected with an empty vector were used as negative control to estimate the background signal. [281]

1.4.2.4. Statistical analysis

All graphs were prepared using GraphPad Prism™ and all data are expressed as mean ± standard deviation. Sigmoidal curve-fitting of concentration-response curve, IC_{50}-values and statistical tests were all performed with GraphPad Prism™. Concentration-response curves are presented as % of the control, with the control being the untreated condition.

1.4.2.5. Microglial cell line

(Dr. Stefano Garofalo, Group of Prof. Cristina Limatola, Department of Physiology and Pharmacology, Sapienza University of Rome)

BV2 murine microglial cells were cultured in DMEM supplemented with 10% heat-inactivated FBS, 100 IU/mL penicillin G, 100 mg/mL streptomycin, and 2.5 mg/mL amphotericin B and grown at 37 °C in a 5% CO_2 and humidified atmosphere. Cells were pre-incubated with 10 μM VAS2870, MC4762, and MAO B inhibitors Rasagiline. After 30 minutes, LPS 100 ng/mL + IFN-γ 20 ng/mL were added in the medium for additional 48 hours.

1.4.2.6. ROS production assay

(Dr. Stefano Garofalo, Group of Prof. Cristina Limatola, Department of Physiology and Pharmacology, Sapienza University of Rome)

After treatment, BV2 cells were incubated with CellROX™ Deep Red reagent (Cat## C10422) at 5 μM and incubated for 30 min at 37 °C as indicated by the manufacturer protocol. ROS levels were measured via spectrofluorometry, taking as 100% the median fluorescent intensity of cells treated with vehicle.

1.4.2.7. Viability assay

(Dr. Stefano Garofalo, Group of Prof. Cristina Limatola, Department of Physiology and Pharmacology, Sapienza University of Rome)

Cell viability was determined by MTT assay. Briefly, MTT (dissolved in PBS with a final density of 0.5 mg/ml) was added to the medium culture. After 2 h incubation, the MTT solution was extracted, mixed with DMSO, and shaken for 10 min. Finally, the absorption of the samples was read by regulating the 570-nanometer filter as the main wavelength and the 630-nanometer filter as the referenced wavelength. Blank was subtracted from all samples to obtain pure cellular absorption. Results are expressed as percentage of cell survival, taking as 100% the cells treated with vehicle.

1.4.2.8. RNA extraction, reverse transcription, and Real-Time PCR

(Dr. Stefano Garofalo, Group of Prof. Cristina Limatola, Department of Physiology and Pharmacology, Sapienza University of Rome)

BV2 cells were lysed in Trizol reagent for isolation of RNA. Reverse transcription reaction was performed in a thermocycler (MJ Mini Personal Thermal Cycler; Biorad) using IScript TM Reverse Transcription Supermix (Biorad) according to the manufacturer's protocol, under the following conditions: incubation at 25 ˚C for 5 min, reverse transcription at 42 ˚C for 30 min, inactivation at 85 ˚C for 5 min. Real-time PCR (rtPCR) was carried out in a I-Cycler IQ Multicolor rtPCR Detection System (Biorad) using SsoFast EvaGreen Supermix (Biorad) according to the manufacturer's instructions. The PCR protocol consisted of 40 cycles of denaturation at 95 ˚ C for 30 s and annealing/extension at 60 ˚ C for 30 s. For quantification analysis, the comparative Threshold Cycle (Ct) method was used.

The Ct values from each gene were normalized to the Ct value of GAPDH in the same RNA samples. Relative quantification was performed using the $2^{-\Delta\Delta Ct}$ method (Schmittgen & Livak, 2008) and expressed as fold change in arbitrary values. Primers used are:

inos fw: ACATCGACCCGTCCACAGTAT rev: CAGAGGGGTAGGCTTGTCTC

il1b fw: GCAACTGTTCCTGAACTCAACT rev: ATCTTTTGGGGTCCGTCAACT

il6 fw: GATGGATGCTACCAAACTGGA rev: TCTGAAGGACTCTGGCTTTG

2. DEVELOPMENT OF QUINOLINE – CONTAINING NOXs INHIBITORS: FIRST SERIES

2.1. Research Project

The project was initiated by two ultra-large *in silico* screens of 350 million compounds using the open-source platform VirtualFlow performed by our collaborator of Pavia University, team of Professor Andrea Mattevi. [308] [320] The first screen used the crystallographically determined conformation of the *cs*NOX5 DH with the FAD present at the active site, while the second screen targeted the protein without the FAD in the catalytic center. Of the 350 million compounds assessed, 340 million were sourced from the VirtualFlow version of the REAL Database (year 2018) provided by Enamine, [320] while the remaining 10 million compounds were from the ZINC15 library (year 2018). [321] The selection of hits was primarily based on the docking score. In total, 304 candidates were identified. Then, it was decided to retain compounds that showed 50% inhibition at a fixed concentration of 10 μM. This initial step led to 51 compounds. Subsequently, based on the following criteria: (**1**) thermal stabilization of more than 2 °C, (**2**) inhibition of the *cs*NOX5 DH with *K*i values in the low-micromolar range, and (**3**) no or minor ROS-scavenging or assay-interfering properties, eight candidates were finally selected for further investigation (**Figure 2.1a-c**). [308]

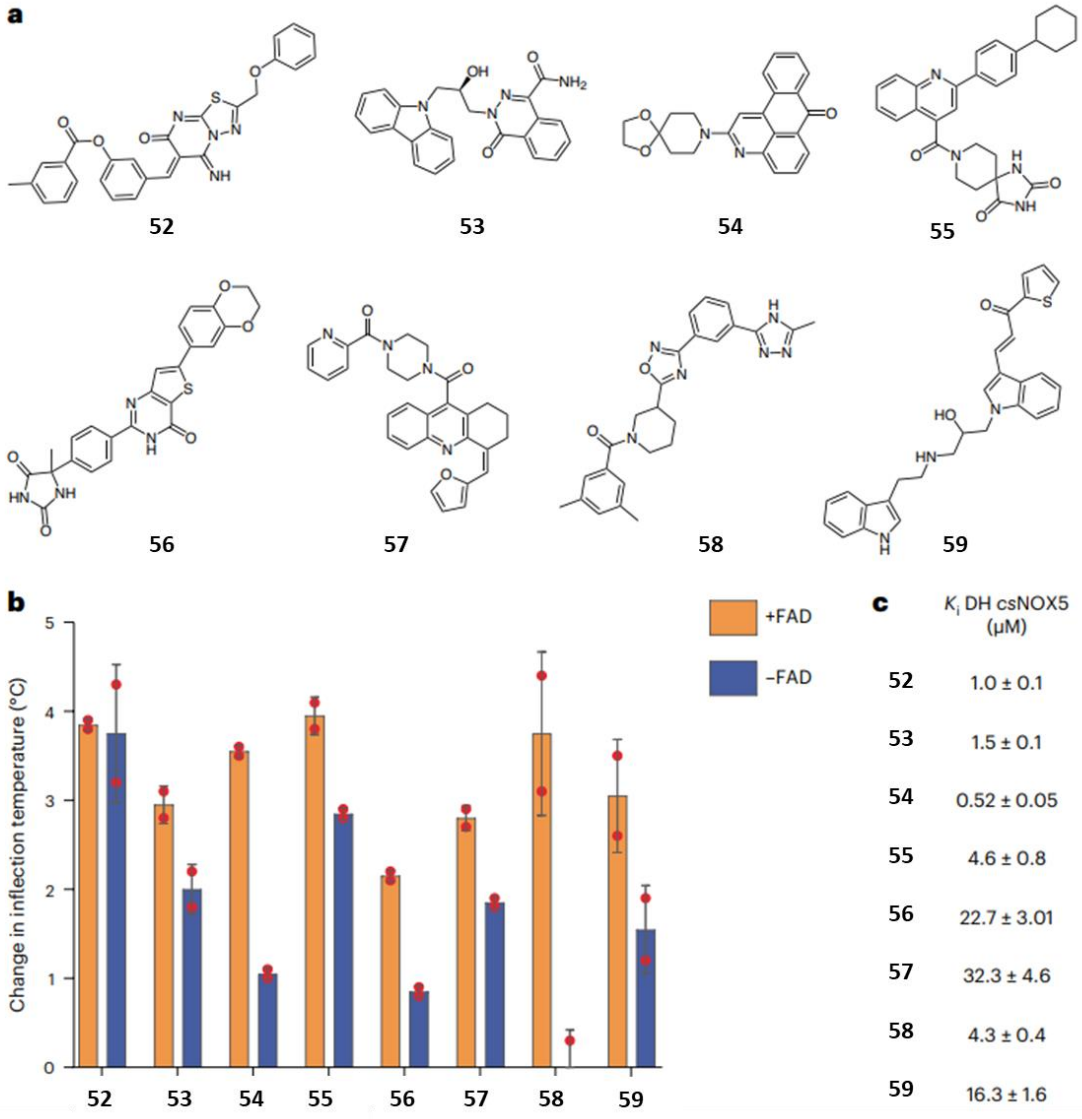

Figure 2.1. ***The eight candidates from screen 1. a.*** *Chemical structures of the selected inhibitors.* ***b.*** *Thermal shift assays on the csNOX5 DH in the absence (blue) and presence (orange) of FAD (mean ± s.d., n = 2 independent experiments, individually plotted as dots).* ***c.*** *Ki values ± s.d. against the csNOX5 DH are reported.* [308]

The eight just mentioned compounds were evaluated on *human* NOX1, NOX2, NOX4, and NOX5 using the membranes extracted from the enzyme-expressing cells. Five hits, compounds 52, 54, 56, 57, and 59, exhibited good inhibition against one or more NOX isoenzymes with single- or low double-digit micromolar IC_{50} values. Given these promising results, the eight selected inhibitors were tested on the purified DH of NOX4, as well as the purified and activated NOX1 and NOX2. Between all, **compound 54** (known also as **M41** as previously mentioned) stood out

for its *Ki* values in the double-digit micromolar range against purified NOX1 and, even more impressive, for its single-digit micromolar *Ki* against the purified NOX2 and DH of NOX4, consistent with the IC_{50} measured on the membrane-embedded NOXs (**Table 2.1**). [308]

Table 2.1. *Inhibition activities using membrane preparations and purified enzymes.* [308]

	NOX membrane preparations				Purified NOXs		
	IC_{50} NOX1 (μM)	IC_{50} NOX2 (μM)	IC_{50} NOX4 (μM)	IC_{50} NOX5 (μM)	K_i NOX1 (μM)	K_i NOX2 (μM)	K_i DH NOX4 (μM)
52	17.9 ± 3.1	40.2 ± 9.6	11.6 ± 2.6	0.36 ± 0.03	26.5 ± 3.9	39.2 ± 5.1	2.7 ± 0.1
53	>100	>100	>100	22.6 ± 4.7	>100	>100	1.9 ± 0.1
54	24.9 ± 2.6	5.1 ± 1.2	5.7 ± 0.7	>100	36.7 ± 7.0	7.7 ± 1.1	8.2 ± 0.5
55	91.8 ± 6.1	>100	89.3 ± 1.5	>100	>100	>100	1.2 ± 0.5
56	27.5 ± 5.2	15.6 ± 1.9	49.1 ± 7.6	>100	30.0 ± 2.6	12.0 ± 1.6	1.7 ± 0.5
57	27.6 ± 4.1	>100	44.7 ± 14.3	76.0 ± 3.0	>80	>100	5.4 ± 1.9
58	94.2 ± 5.0	>100	>100	>100	>100	>100	7.7 ± 0.7
59	39.1 ± 4.8	16.8 ± 3.5	75.7 ± 28.7	7.0 ± 0.2	>100	13.8 ± 1.7	7.4 ± 0.5

The results achieved through biochemical experiments were complemented by *in cellulo* enzymatic activities and target-engagement experiments, performing these experiments on HEK293 cells overexpressing NOX4 or NOX5 (Amplex Red or peroxidase protocol) and PLB-985 cells producing high levels of endogenous NOX2 (cytochrome c reduction). The NOX1 activities were too low to be measured probably because of insufficient levels of the cytosolic activators. **Compound 54** (**M41**) was effective against NOX2 (EC_{50} of 2.1 ± 0.9 μM) and NOX4 (EC_{50} = 1.5 ± 0.4 μM), consistent with the *in vitro* results. Additionally, CETSA experiments verify that the inhibitor directly binds to a NOX target within the cell, demonstrating that M41 is an effective NOX inhibitor. [308]

Furthermore, to investigate the effect of NOX inhibition on cancer cell lines, the PRISM technology was used, allowing the study of more than 900 DNA-barcoded cancer cell lines that belong to 45 different lineages. PRISM identified several leukemia and lymphoma cell lines sensitive to M41 (Compound 54), in particular the acute myeloid leukemia (AML) cell lines OCIAML5, U937, and MOLM13, the acute lymphocytic leukemia (T cell subtype) cells MOLT16, TALL1, and 697, and the non-Hodgkin lymphoma line NUDHL1 (**Figure 2.2a-c**). [308]

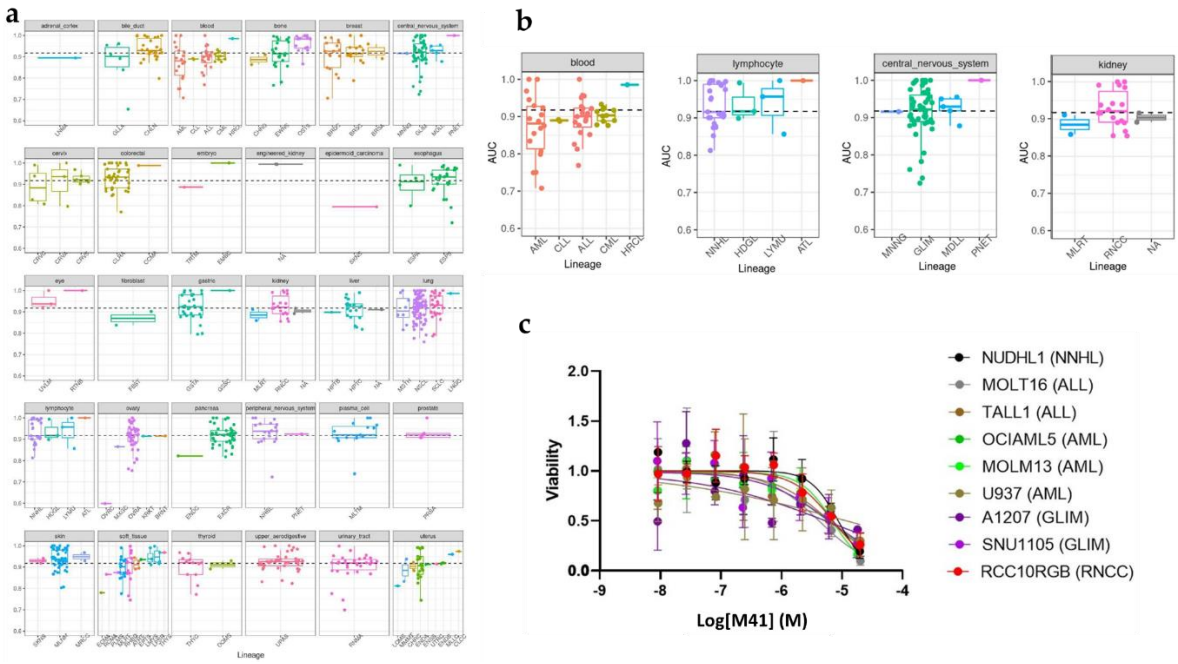

Figure 2.2. ***a.*** *Areas under the curve (AUC) from the PRISM screening on compound M41 with classification per lineages. The individual boxplots are sub-lineages.* ***b.*** *PRISM identified several cell lines in the blood, lymphocyte, central nervous system, and kidney sublineages responsive to M41.* ***c.*** *Dose-response to M41 by the PRISM-identified cell lines.* [308]

Considering the role of NOX2 in myeloid cells, [322] in collaboration with Professor Andrea Mattevi's team, we selected the monocytic U937 cell line, confirming that the cells are sensitive to M41 with IC_{50} value around 12 μM, in agreement with the PRISM analysis. Viability was assessed by ATP quantification and, in a second experiment, phorbol 12-myristate13-acetate was used to differentiate the monocytic U937 cells into macrophages [323] [324] where NOX2 acts as the primary source of ROS in the immune reaction against microbial infections. [325] We observed that

differentiation does not greatly alter the sensitivity to compound M41 (**Figure 2.3**). [308] Overall, the findings suggest that inhibiting NOX enzymes could be a promising strategy to disrupt redox signaling pathways that promote cancer cell growth, while also exploiting the cancer cells' vulnerability to ROS imbalance. In the context of AML, these effects align with current research emphasizing the importance of NOX2 in maintaining the self-renewal capacity of leukemia cells. [326] [322] [327] [230] [328]

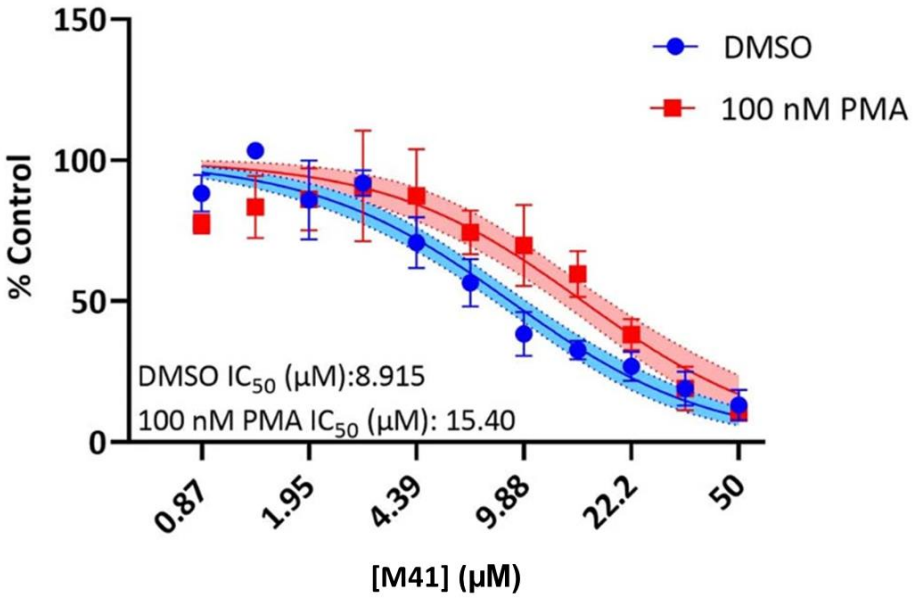

Figure 2.3. *Cell viability study (ATP quantification) on the U937 cells incubated for 72 hours with M41 with and without phorbol 12-myristate13-acetate (PMA).* [308]

Finally, knowing that ROS promote cancer growth, particularly in *Ras*-driven tumors, we decided to verify whether NOX inhibition could enhance the effect of the $KRAS^{G12D}$ inhibitor MRTX1133 in colorectal cancer cells. The experiments were conducted by Professor Haribabu Arthanari's team, at Harvard Medical School. Results showed that combining compound M41 with MRTX1133 improves its efficacy, indicating a potential therapeutic approach for *KRAS* mutant cancers. [308]

The promising results obtained for the lead compound M41, as well as the aim to achieve isoform-specific NOX inhibitors through appropriate modifications of a pan-NOX scaffold such as M41, led us to explore the binding mode of compound M41. [308]

Particularly, the obtaining of positive values in terms of Thermal Shift (1.1 ± 0.1 °C in the absence of FAD and 3.6 ± 0.1 °C with FAD present) of the most potent inhibitor, compound M41, and also the observation that the kinetics of M41 were consistent with a noncompetitive inhibition mechanism (**Figure 2.4**), has allowed the acquirement of the co-crystal structure of M41 with the DH domain of *cs*NOX5 in presence of $NADP^+$ (**Figure 2.5**). [308]

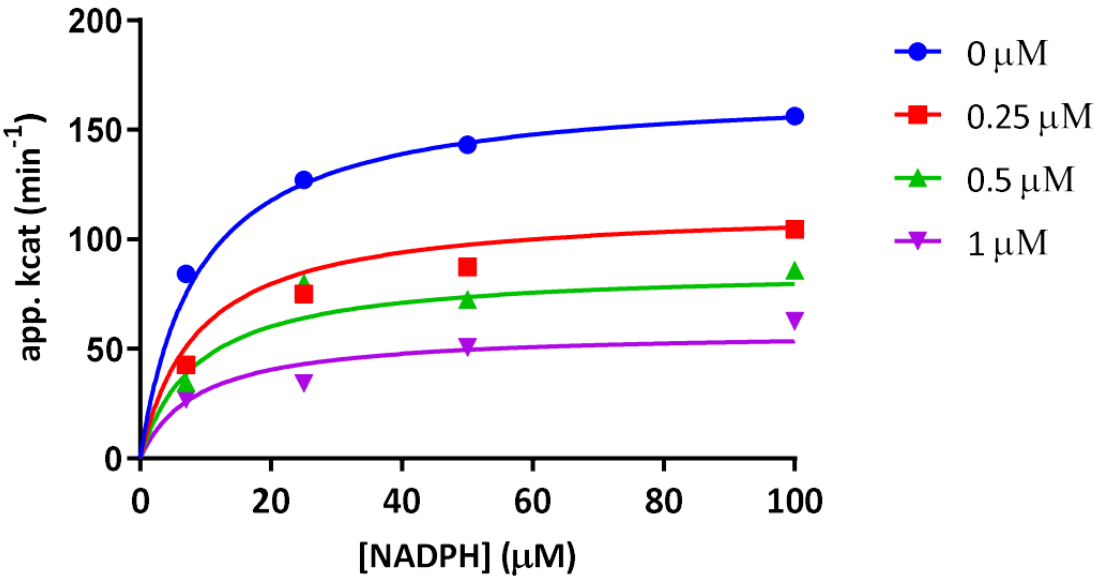

Figure 2.4. *Ki determination for compound M41 on the dehydrogenase of C. stagnale NOX5. The inhibitor was tested at three different concentrations (from 0.25 μM to 1 μM).* [308]

The resulting structural determination revealed the coexistence of both ligands. Specifically, the AMPP moiety of $NADP^+$ binds to the protein in a position that conforms to that expected for a prototypical ferredoxin-reductase structure, with the 2′-phosphate in contact with two conserved Arg residues. [329] The nicotinamide moiety was found to stay parallel to M41, forming a three-layered stack of molecules in the active site alongside the flavin and inhibitor. This finding demonstrates that NADP(H) can adopt multiple conformations within the active site: the out conformation in the presence of an inhibitor and a catalytic 'in' conformation. Additionally, the structure of the ternary complex revealed that compound M41 undergoes a 120° rotation about an axis perpendicular to the inhibitor's four-ring moiety when $NADP^+$ binds, moving from the dark blue to the

cyan conformation. This new orientation appears necessary to provide sufficient space for the bound $NADP^+$ and prevent steric clashes (**Figure 2.5**). [308]

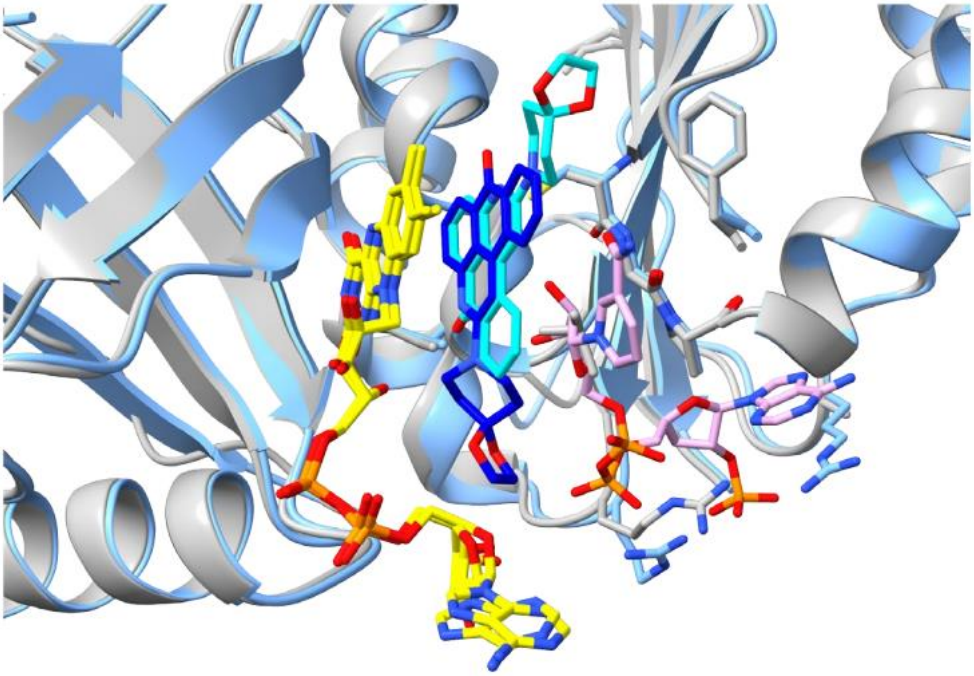

Figure 2.5. *Crystal structures of M41 bound to the csNOX5 DH in the absence (dark blue inhibitor carbons, gray ribbon) and presence (cyan inhibitor carbons, blue ribbon) of $NADP^+$ (pink carbons) – team of Professor Andrea Mattevi, Pavia Univeristy.* [308]

Given the adaptable binding mode of compound M41, we investigated the contributions of the various chemical groups present in the lead compound, obtaining a first series of simplified derivatives (**Figure 2.6**).

For this aim:

(i) We first opened the central ring of the original scaffold, resulting in a 4-phenylquinoline molecule **10a**, to reduce the planarity of the molecule.

(ii) Subsequently, we decided to modify the amino substituent on the C2 of the quinoline ring in the open derivative 10a, to evaluate the Structure-Activity Relationship (SAR). We initially replaced the spiroamine (1,4-dioxa-8-azaspiro[4.5]decane) of compound M41 with its isomer (**10b**). Then, we substituted it with two lower homologs (**10c** and **10d**) as well as with its upper homolog **10e** and its bioisostere **10f**. To conclude with the series of 1,4-dioxa-8-azaspiro[4.5]decane- analogues, compound **10g** was obtained by

moving the spiroamine nitrogen outside the spiro ring system, introducing a more flexible linker to enable rotational freedom of the spiro group.

(iii) Fluorine, being highly electronegative, can strengthen hydrogen bonding interactions in the enzyme active site, so it was introduced as a substituent, yielding derivatives **10h-k**.

(iv) Further, we decided to reduce the complexity of spiroamine, by placing in the C2 of the quinolinic nucleus an N-methylpiperazine (**10l**), a morpholine (**10m**), as well as a piperidine ring with substituents at the C4 position: a methyl ester (**10n**), which was hydrolyzed to a carboxylic acid (**10o**), followed by a series of amide derivatives: primary (**10p**), secondary (**10q**), and tertiary (**10r**).

(v) Based on preliminary biochemical results, compound 10g, with the spiroamine nitrogen exocyclically positioned, showed promising activity. Therefore, we simplified the spiroamine by attaching a 4-piperidine group to the exocyclic nitrogen, resulting in compounds **10s** (with a Boc-protected amino group) and **10t** (with a deprotected amino group).

(vi) Finally, we aimed to covalently trap Cys668 in the catalytic dehydrogenase domain of NOXs. Based on the co-crystal structure of lead compound M41 (**Figure 2.4**), we introduced an acrylamide moiety at the C6 position of compound 10g (**compound 13**). [309] We also tested nitro (**11**) and amino (**12**) derivatives to explore possible reversible non-covalent binding.

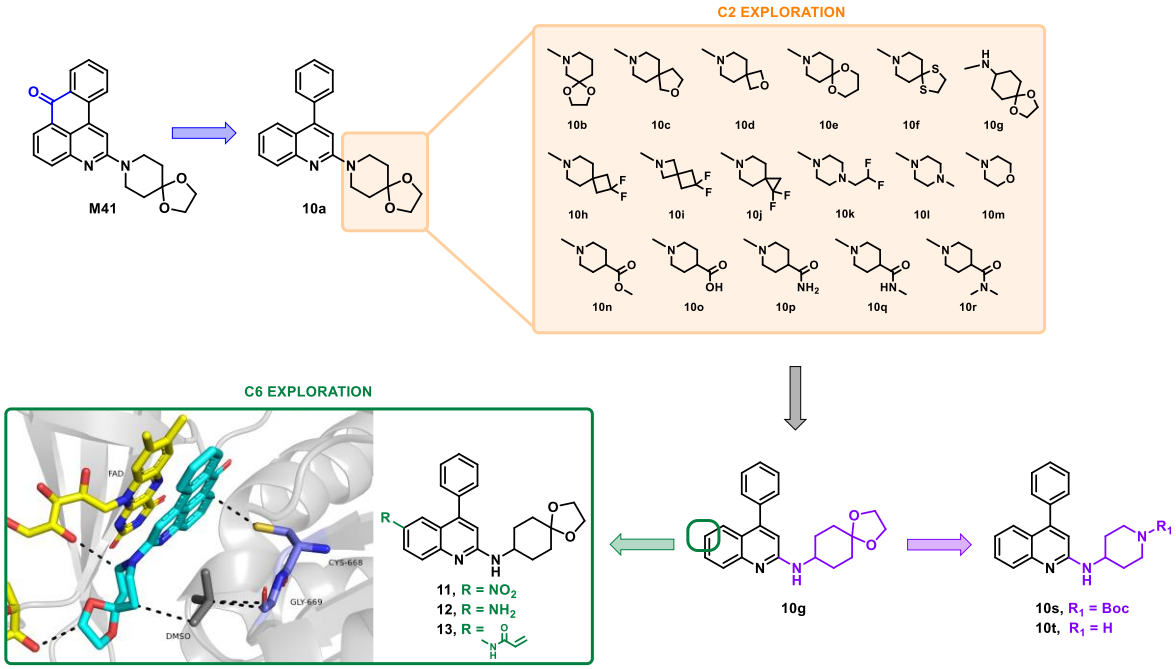

Figure 2.6. *First series of simplified derivatives.*

2.2. Results and discussion

2.2.1. Chemistry

For the synthesis of compounds **10a-n** and **10s** the commercially available 2-chloro-4-phenylquinoline was subjected to Buchwald-Hartwig cross coupling reaction with palladium(II)Acetate ($Pd(OAc)_2$), 2,2'-Bis(diphenylphosphino)-1,1'-binaphthyl (BINAP), in a basic environment by Cesium Carbonate (Cs_2CO_3) in dry toluene, with the opportune commercially available amines, obtaining derivatives 10a-n and 10s. Furthermore, the obtained ester 10n was hydrolysed in basic medium by potassium hydroxide solution (2N) to the corresponding carboxylic acid **10o** which, activated with O-(1H-benzotriazol-1-yl)-N,N,N',N'-tetramethyluronium tetrafluoroborate (TBTU), in presence of triethylamine (TEA) in dry N,N-dimethylformamide, was subjected to three different amidation reactions, using ammonia solution for compound **10p**, methylamine for compound **10q**, and N,N-dimethylamine for compound **10r**. Additionally, the obtained compound tert-butyl 4-((4-phenylquinolin-2-yl)amino)piperidine-1-carboxylate 10s was treated with 4 N HCl in 1,4-dioxane in dry THF at 0°C and, after 6 h, the desired hydrochloride derivative 4-phenyl-N-(piperidin-4-yl)quinolin-2-amine **10t** was isolated as a white powder (**Scheme 2.1**).

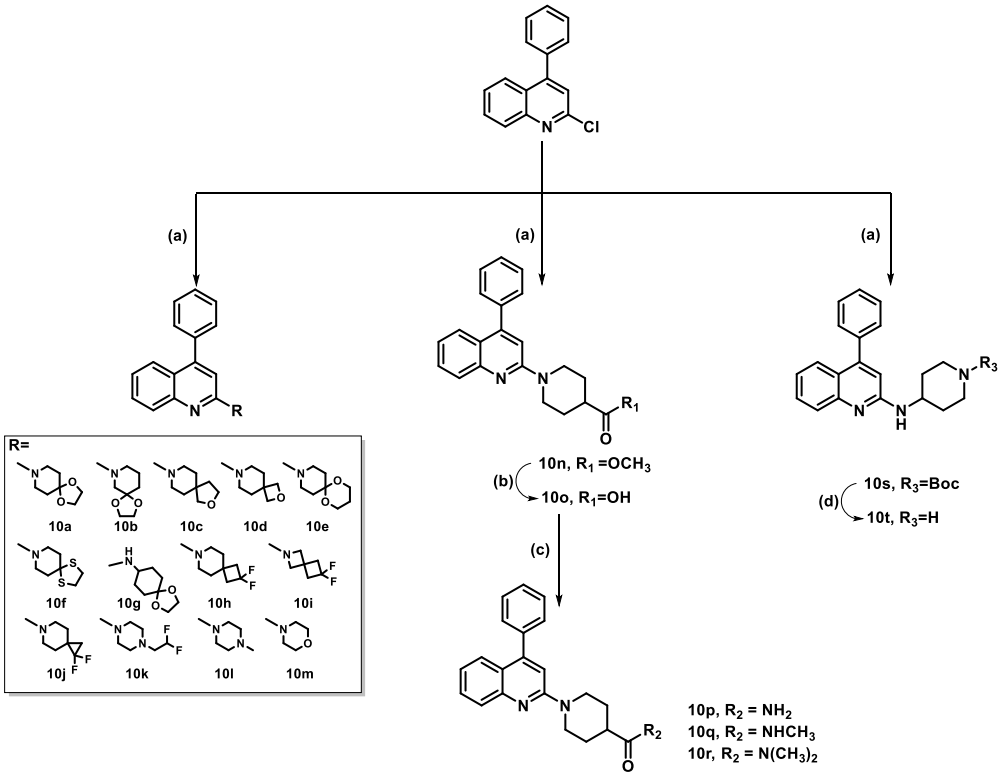

Scheme 2.1. Synthesis of compounds 10a-t. Reagents and conditions. a) Opportune amine, $Pd(OAc)_2$, BINAP, Cs_2CO_3, dry toluene, N_2, 125 °C, 12-24 h. **b)**

2N KOH, EtOH, 0 °C to RT, 4h. **c)** ammonia solution or methylamine or N,N-dimethylamine, TBTU, TEA, dry DMF, RT, 2h. **d)** 4N HCl in 1,4-dioxane, dry THF, 0°C to RT, 6h.

For the synthesis of compounds **11**, **12**, and **13**, the commercially available 2,4-dibromo-6-nitroquinoline was subjected to a nucleophilic displacement with the 1,4-dioxaspiro[4.5]decan-8-amine in dry DMF for 5 hours, obtaining the bromoquinoline **38**, that underwent a Suzuki-Miyaura cross-coupling reaction with phenylboronic acid, using tetrakistriphenylphosphine palladium as catalyst, in a basic medium by potassium carbonate in 1,4-dioxane and water in 1:1 ratio as a mixture of solvents at 90 °C for 24 hours to obtain compound **11**. The nitro derivative 11 was reduced to the amino one (**12**) by palladium-catalyzed hydrogenation, using palladium on carbon 10%w/w in dry methanol (MeOH) for 1 hour. Finally, the acylation of compound 12 with acryloyl chloride and triethylamine in dry DCM afforded, after 10 minutes, to the final compound **13 (Scheme 2.2)**.

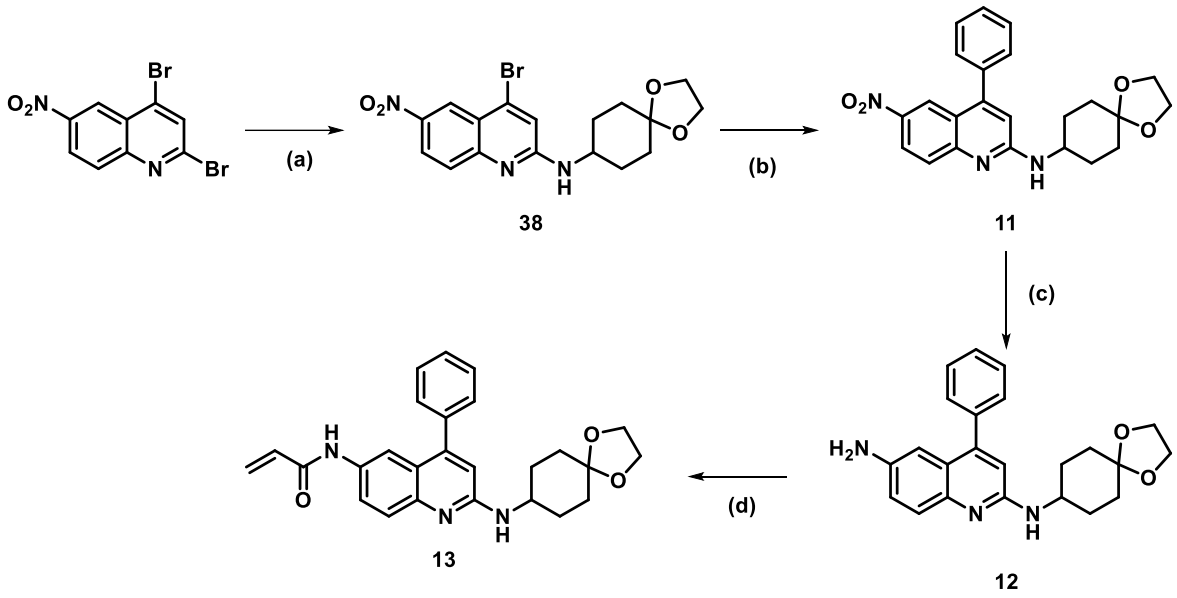

Scheme 2.2. Synthesis of compounds 11, 12, and 13. Reagents and conditions. a) 1,4-dioxaspiro[4.5]decan-8-amine, dry DMF, RT, 5h. **b)** phenylboronic acid, tetrakis triphenylphosphine palladium, K_2CO_3, 1,4-dioxane:H_2O=1:1, N_2, 90 °C, 24h. **c)** Pd/C 10 % w/w, H_2 (50 psi), dry MeOH, 40°C, 1h. **d)** acryloyl chloride, dry TEA, dry DCM, 0°C to RT, 10 minutes.

2.2.2. Biochemical activities towards *human* NOXs

The first series of derivatives was tested at 100 μM against the *human* NOX1, -2, -4, and -5 by Professor Andrea Mattevi's team of Pavia University (**Table 2.1**).

Table 2.1. *Percentage of inhibition of compound 10a-r against human hNOX1, -2, -4, and -5.*

CPD	STRUCTURE	% inhibition [100 μM]			
		*h*NOX1 (Amplex Red)	*h*NOX2 (NADPH consumption)	*h*NOX4 (Amplex Red)	*h*NOX5 (Amplex Red)
M41	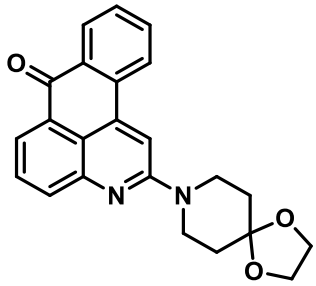	**52.0 ± 5.9**	**nd**	**92.5 ± 4.6**	**30.7 ± 3.8**
10a	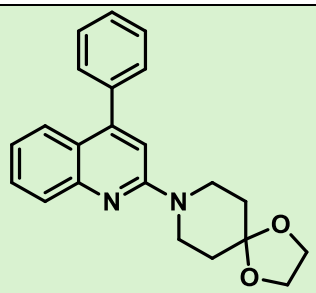	**0**	**52.0 ± 1.0**	**62.2 ± 5.1**	**13.5 ± 3.6**
10b	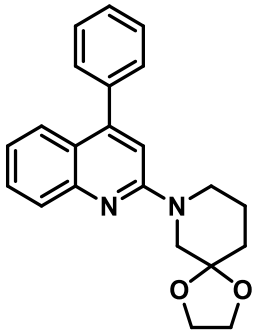	**52.0 ± 20.5**	**0**	**nd**	**36.3 ± 2.4**
10c	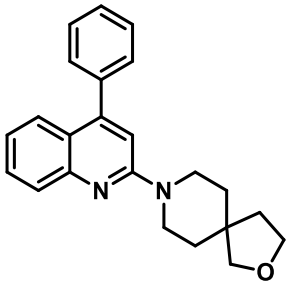	**59.8 ± 27.2**	**nd**	**nd**	**0**

10d	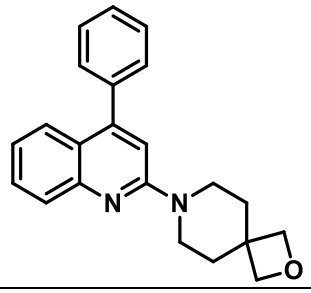	**35.0 ± 1.0**	**47.3 ± 1.0**	**nd**	**33.8 ± 1.8**
10e	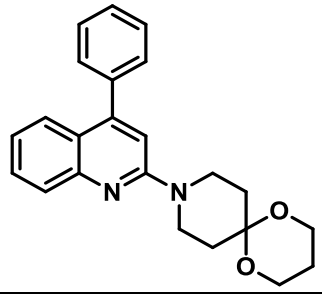	**16.7 ± 0.7**	**nd**	**10.6 ± 5.1**	**12.7 ± 8.9**
10f	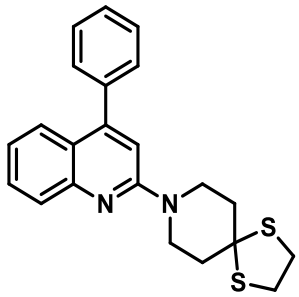	**5.2 ± 1.9**	**nd**	**0**	**0**
10g	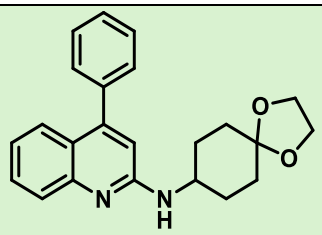	**70.9 ± 4.6**	**76.7 ± 0.1**	**68.9 ± 5.1**	**70.5 ± 2.3**
10h	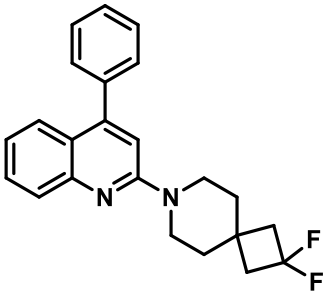	**20.3 ± 10.0**	**nd**	**nd**	**18.4 ± 1.5**
10i	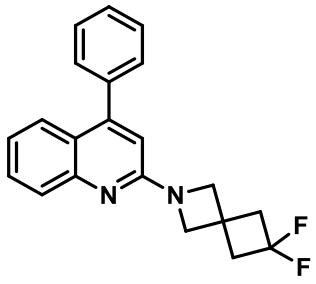	**59.3 ± 2.6**	**nd**	**28.9 ± 2.6**	**30.0 ± 3.5**

10j	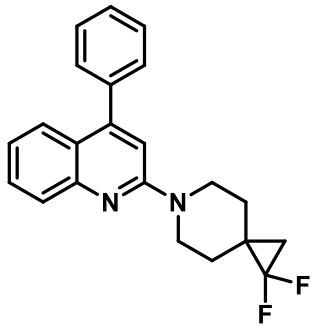	**29.5 ± 6.6**	**nd**	**0**	**18.9 ± 2.9**
10k	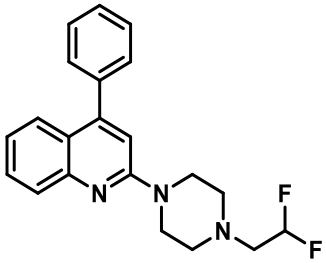	**8.5 ± 10.6**	**nd**	**0**	**16.1 ± 7.7**
10l	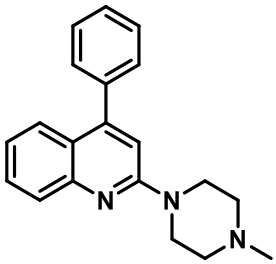	**40.8 ± 2.2**	**50.9 ± 1.3**	**nd**	**37.8 ± 1.1**
10m	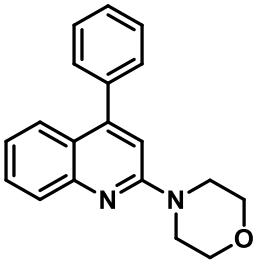	**43.4 ± 10.5**	**nd**	**nd**	**32.0 ± 7.1**
10n	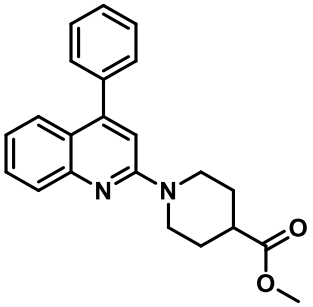	**0**	**nd**	**25.0 ± 8.5**	**24.7 ± 11.2**
10o	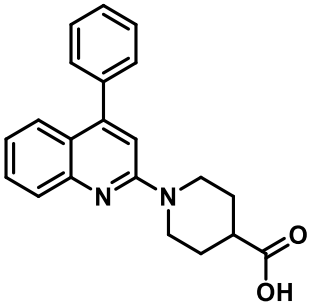	**27.8 ± 10.0**	**nd**	**41.9 ± 8.6**	**12.4 ± 5.4**

10p	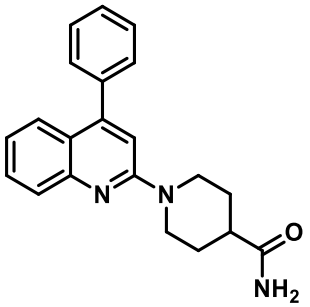	**36.7 ± 1.6**	**nd**	**37.3 ± 1.4**	**50.5 ± 1.4**
10q	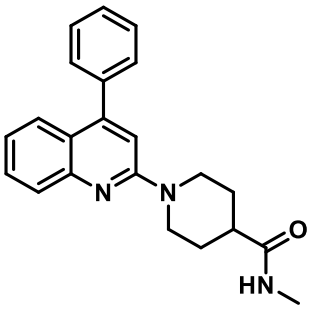	**44.9 ± 1.9**	**70.3 ± 1.7**	**27.5 ± 6.2**	**18.3 ± 1.5**
10r	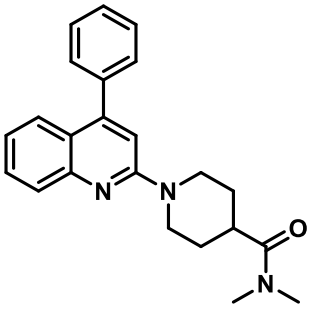	**30.3 ± 3.7**	**nd**	**17.4 ± 1.7**	**38.1 ± 2.3**

nd: not determined

The results obtained from the quinoline-based simplified derivatives towards *h*NOX1, -2, -4, and -5 (**Table 2.1**) highlighted that **compound 10a**, which features the opening of the central ring of the original scaffold, retained a certain degree of inhibitory potency against NOX2, -4, and -5. For this reason, considering that the goal of our project is to improve the drug-like properties of the lead compound M41, we decided to continue the SAR study of the open derivative 10a. The exploration of C2 of compound 10a showed that various substituents had different effects on NOX isoforms. For the **NOX1** isoform, the most promising candidate was compound **10g**. The lower homologue **10c** and the fluorinated derivative **10i** also exhibited around 60% inhibition and could be considered in the evaluation of NOX1 inhibition. Regarding NOX2 inhibition, compound **10g** demonstrated the highest percentage of inhibition, as well as it displayed strong inhibition also against **isoform 4** of NOXs. For **NOX5**, none of the compounds achieved significant inhibition, with values generally not exceeding 50%, except for compound **10g**, which stood out once more. The promising inhibition values observed for

compound **10g** led us to hypothesize that introducing a more flexible linker might enhance the rotation of the spiro group, thereby improving its adaptability to the active site of the target enzyme.

Table 2.2. *Percentage of inhibition of compound 11-13 against human hNOX1, -2, -4, and -5.*

CPD	STRUCTURE	% inhibition [100 μM]				% inhibition [10 μM]
		*h*NOX1 (Amplex Red)	*h*NOX2 (NADPH cons.)	*h*NOX4 (Amplex Red)	*h*NOX5 (Amplex Red)	DH NOX5
11	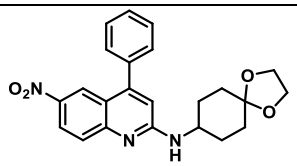	**58.2 ± 2.2**	**73.9 ± 2.0**	**56.4 ± 3.6**	**54.3 ± 2.7**	**37.7±7.7**
12	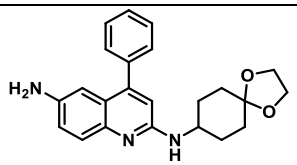	**98.4 ± 0.4**	**31.4 ± 1.5**	**nd**	**94.0 ± 0.3**	**0**
13	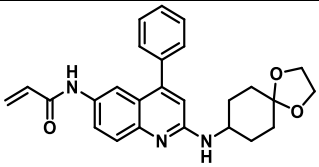	**96.5 ± 2.4**	**0**	**68.9 ± 2.0**	**47.7 ± 1.2**	**13.3±11.5**

Compound **13**, designed as a trapping compound, displayed percentage of inhibition against NOX1 comparable to that of the amino derivative **12.** However, compound 13 was less potent than 12 against NOX2 and NOX5. Interestingly, nitro derivative **11** showed good activity against all tested NOX isoenzymes, suggesting that other amino acid residues might be involved in the interaction with these compounds. We also evaluated these compounds against the dehydrogenase (DH) domain of NOX5, which includes Cys668. While compounds 11-13 displayed good inhibition rates on full-length protein, their inhibition of the DH domain was significantly lower, suggesting that Cys668 covalent binding did not occur. This conclusion is further supported by the fact that compounds 11 and 12, which lack the acrylamide group, displayed a very similar potency to compound 13 (**Table 2.2**).

Thus, we decided to revisit the most promising open derivative against all NOX isoenzymes, compound 10g. By reducing the complexity of its spiro amine, we obtained derivatives 10s and 10t, in which the 1,4-dioxaspiro was replaced with a piperidine group, with the amino group protected with a Boc group in 10s or left unprotected in 10t.

For these two compounds, we have the IC_{50} values against membrane full-length *human* NOXs, which we compared with the ones of lead compound M41 (**Table 2.3**).

Table 2.3. *Biochemical inhibition data against membrane full-length human NOXs.*

CPD	MOLECULAR STRUCTURE	IC_{50}, μM			
		***h*NOX1 (Amplex Red)**	***h*NOX2 (MCLA)**	***h*NOX4 (Amplex Red)**	***h*NOX5 (Amplex Red)**
M41	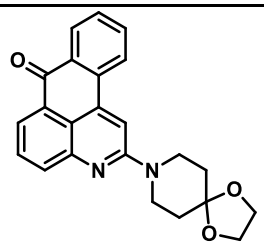	24.9 ± 2.6	5.1 ± 1.2	5.7 ± 0.7	>100
10s	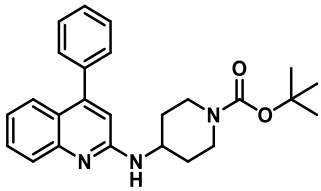	>100	>100	>100	**1.6 ± 0.4**
10t	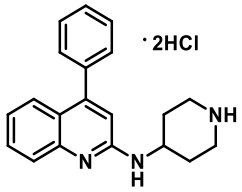	71.2 ± 1.0	**7.7 ± 0.1**	81.2 ± 11.4	63.5 ± 1.9

This modification conferred selectivity toward NOX5 and NOX2, with single-digit micromolar IC_{50} values. Specifically, compound **10s** completely lost inhibitor activity against NOX1, -2, and -4 but showed a strong IC_{50} value of 1.6 ± 0.4 μM against NOX5.

In contrast, compound **10t** emerged as a selective and potent NOX2 inhibitor. These initial results demonstrate the feasibility of obtaining isoform-specific NOX inhibitors through appropriate modifications of a pan-NOX scaffold, such as lead compound **M41**. The *Ki* value of 7.3 ± 0.6 μM of compound **10t** on purified *h*NOX2, determined through NADPH consumption assay, confirms its inhibition of NOX2, consistent with the IC_{50} results (**Figure 2.7**). The inhibitory activity of compound 10t was further validated in cellular assays, as detailed in the next section.

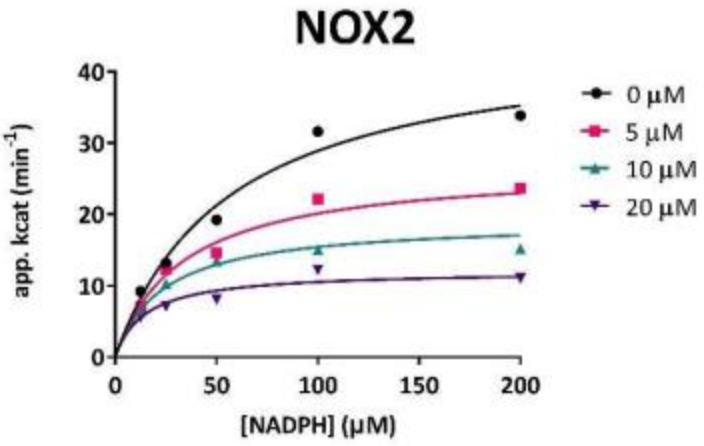

Figure 2.7. ***Ki determination for compound 10t on the purified NOX2.*** *The Ki values were determined by applying a nonlinear regression with GraphPad Prism software 9.0. The progress curves were determined in the presence and in the absence of inhibitor by plotting the apparent kcat as a function of the substrate (ranging from 0 to 200 μM). The inhibitor was tested at three different concentrations, ranging from 5 to 20 μM.*

2.2.3. *In cellulo* assays of compound 10t

The results achieved through biochemical experiments were complemented by *in cellulo* enzymatic activities and target-engagement experiments, performing these experiments on HEK293 cells overexpressing NOX4 or NOX5 (Amplex Red or peroxidase protocol) and PLB-985 cells producing high levels of endogenous NOX2 (cytochrome c reduction) in collaboration with Pavia University. The NOX1 activities were too low to be measured probably because of insufficient levels of the cytosolic activators. Compound 10t exhibited selectivity toward NOX2 ($EC_{50} = 5.7 \pm 1.2$) and moderate activity against NOX4 ($EC_{50} = 18.0 \pm 3.8$) and NOX5 ($EC_{50} = 11.6 \pm 2.9$) expressing cells. Additionally, CETSA experiment confirmed the NOX engagement by the compound (**Figure 2.8, 10t is reported under the name MC4876**). Collectively, these results demonstrated that the tested compound is an effective NOX inhibitor.

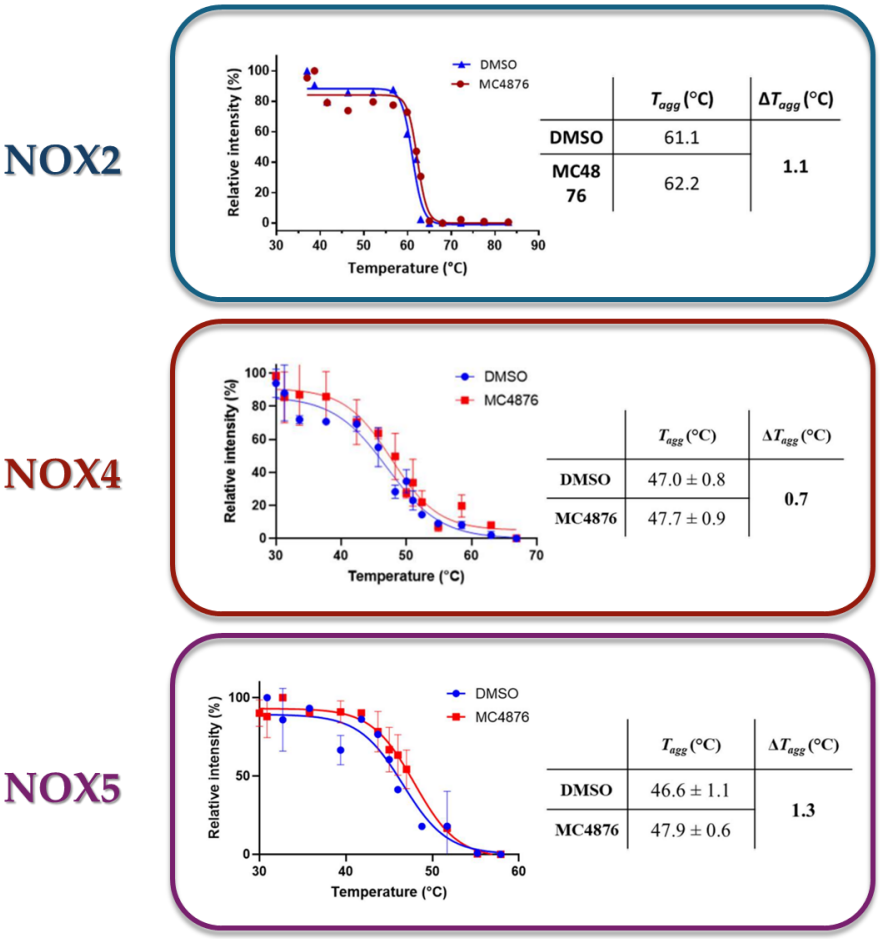

Figure 2.8. ***CETSA experiments****. Protein quantification based on the western blots and apparent and delta aggregation temperatures for* ***MC4876*** *(**10t**) on NOX2, NOX4, and NOX5.*

2.2.4. Investigating the effect of NOX inhibition by 10t in cancer

As was seen for lead compound M41, the same was evaluated for its simplified derivative 10t. Also in this case, U937 cells proved to be sensitive to this inhibitor with IC_{50} values in the single-digit micromolar range, in agreement with the PRISM analysis. Viability was assessed by ATP quantification and, in a second experiment, phorbol 12-myristate13-acetate was used to differentiate the monocytic U937 cells into macrophages where NOX2 acts as the primary source of ROS in the immune reaction against microbial infections. We observed that differentiation does not greatly alter the sensitivity to compound 10t (**Figure 2.9**). [308]

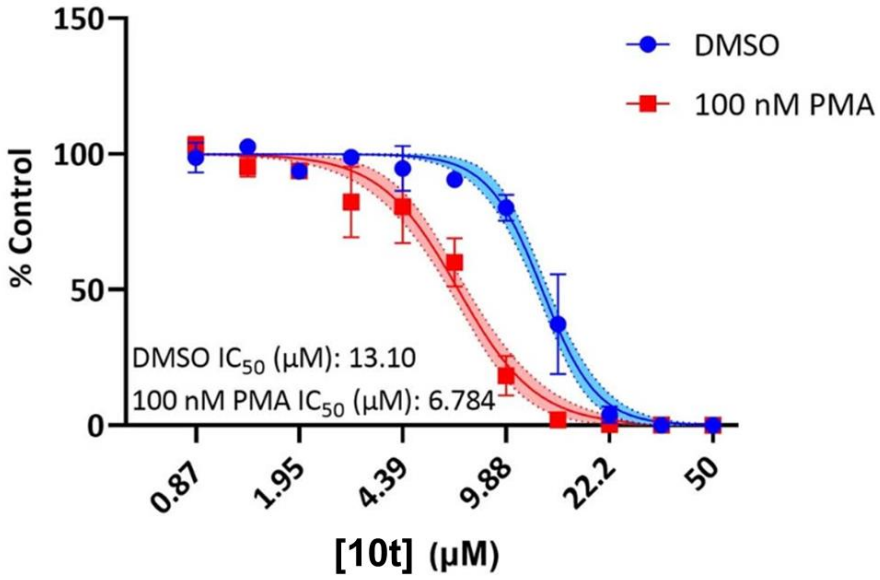

Figure 2.9. *Cell viability study (ATP quantification) on the U937 cells incubated for 72 hours with compound 10t with and without phorbol 12-myristate13-acetate (PMA) – team of Professor Andrea Mattevi, Pavia University.* [308]

2.3. Conclusions

Our research has identified a panel of NOX inhibitors that offer important tools for studying the chemical biology and pharmacology of these ROS-producing enzymes. Along the way, we had to eliminate many molecules that appeared active but showed unwanted, interfering activities. We also found that even small changes in a compound's structure could lead to these undesirable effects. The binding of inhibitors to NOX enzymes is likely influenced by the flexible nature of the protein's C-terminus, which is located within the dehydrogenase active site. These highly conserved and adaptable C-terminal residues seem to control both substrate binding and product release. This flexibility also allows NADPH's nicotinamide to shift out of the catalytic center, adopting a non-catalytic position that makes space for inhibitor binding. For example, compound M41 can bind to the active site without displacing NADP(H), which is supported by kinetic data showing that compound M41 inhibits through a non-competitive mechanism. We speculate that the equilibrium between the 'in' (NADPH close to flavin) and 'out' conformations could be a key regulatory mechanism for NOX activity. Considering the adaptable binding mode of compound M41, an intensive SAR study helped generate important insights. Results from the first series demonstrated that targeting the NADPH-binding site can lead to selective inhibition of specific NOX isoenzymes. Notably, the introduction of a more flexible ring and the reduction of the complexity of the spiro amine led to the development of the first *bona-fine* selective NOXs inhibitors, with effects in cellular models. Further investigation of the two newly identified lead compounds (**10s** and **10t**) could bring out what is the specific chemical structure responsible for selective inhibition. This research also enables a shift beyond general correlations between ROS and cancer, toward exploring specific NOX-produced ROS sources. Since NOX-generated ROS promote cell growth and oncogenes drive cancer by altering ROS pathways, NOX inhibitors could potentially synergize with drugs targeting oncoproteins or the disrupted pathways.

2.4. Experimental section

2.4.1. Chemistry

Melting points were determined on a Buchi 530 melting point apparatus and are uncorrected. ^{1}H-NMR and ^{13}C-NMR spectra were recorded at 400 MHz on a Bruker AC 400 spectrometer; chemical shifts are reported in δ (ppm) units relative to the internal reference tetramethyl silane (Me4Si). EIMS spectra were recorded with a ThermoFisher MSQplus mass spectrometer; only molecular ions (M+) and base peaks are given. All compounds were routinely checked by TLC, 1H-NMR, and 13C-NMR spectra. TLC was performed on aluminum-backed silica gel plates (Merck DC, Alufolien Kieselgel 60 F254) with spots visualized by UV light. All solvents were reagent grade and, when necessary, were purified and dried by standard methods. The concentration of solutions after reactions and extractions involved using a rotary evaporator operating at a reduced pressure of ca. 20 Torr. Organic solutions were dried over anhydrous sodium sulfate. Elemental analysis has been used to determine the purity of the described compounds, which is >95 %. Analytical results are within±0.40 % of the theoretical values (Table S1 in Supporting Information). All chemicals were purchased from Sigma Aldrich, Milan (Italy), Alfa Aesar, Karlsruhe (Germany), Fluorochem, Manchester (UK), or BLD-Pharma, Kaiserslautern (Germany) and were of the highest purity.

General procedure for the synthesis of compounds 10a-n and 10s

Example: Synthesis of 4-phenyl-N-(1,4-dioxaspiro[4.5]decan-8-yl)quinolin-2-amine (10g): To a solution of 2-chloro-4-phenylquinoline (0.070 g, 0.292 mmol) in dry toluene, 1,4-dioxaspiro[4.5]decan-8-amine (0.08 mL, 0.584 mmol), $Pd(OAc)_2$ (0.0034 g, 0.015 mmol), BINAP (0.000225 g, 0.0036 mmol), and Cs_2CO_3 (0.285 g, 0.876 mmol) were added under nitrogen flow. After stirring at 125 °C for 4 hours, water was added, and the resulting mixture was extracted with diethyl ether (3x20 mL). The organic extracts were collected, washed with brine, dried with sodium sulfate, and concentrated under reduced pressure. The remaining residue was purified by column chromatography (SiO_2, eluting with ethyl acetate/n-hexane 1:3) to provide the pure compound **10g**.

M.p. 185-188 °C; recrystallization solvent: acetonitrile; yield: 33.4%; ^{1}H NMR ($CDCl_3$, 400 MHz, δ; ppm): 1.53-1.59 (m, 4H, -C*H*$_2$-CR$_2$-C*H*$_2$-), 1.65 (s, 2H, -CH$_2$-), 1.91(s, 2H, -CH$_2$-), 4.02 (s, 4H, -O-C*H*$_2$-C*H*$_2$-O-), 6.13 (d, 1H, -N*H*-CHR-, J=8Hz), 6.51 (s, 1H, -NH-C*H*R-), 7.00 (s, 1H, aromatic protons), 7.10 (t, 1H, aromatic proton, J=

7.6 Hz), 7.39-7.50 (m, 6H, quinoline and phenyl aromatic protons), 7.53 (d, 1H, aromatic protons, J= 8 Hz), 7.67 (d, 1H, aromatic proton, J= 8 Hz).

10a, 8-(4-phenylquinolin-2-yl)-1,4-dioxa-8-azaspiro[4.5]decane: M.p. n.d (colourless liquid); yield: 21.6%; ^{1}H NMR ($CDCl_3$, 400 MHz, δ; ppm): 1.74 (t, 4h, -C*H*$_2$-NR-C*H*$_2$-, J= 5.6), 3.84 (t, 4H, -C*H*$_2$-CR$_2$-C*H*$_2$-, J= 5.6 Hz), 3.93 (s, 4H, -O-C*H*$_2$-C*H*$_2$-O-), 6.86 (s, 1H, aromatic proton), 7.07 (t, 1H, aromatic proton, J= 7.6 Hz), 7.38-7.54 (m, 6H, quinoline and phenyl aromatic proton), 7.53 (d, 1H, aromatic proton, J= 8 Hz), 7.68 (d, 1H, aromatic proton, J= 8 Hz).

10b, 7-(4-phenylquinolin-2-yl)-1,4-dioxa-7-azaspiro[4.5]decane: M.p. n.d. (colourless liquid); yield: 11.4%; ^{1}H NMR ($CDCl_3$, 400 MHz, δ; ppm): 1.81 (s, 2H, -NR-C*H*$_2$-CR$_2$-), 3.70 (s, 4H, -C*H*$_2$-), 3.90 (s, 2H, -C*H*$_2$--CR$_2$-), 4.04 (s, 4H, -O-C*H*$_2$-C*H*$_2$-O-), 6.83 (s, 1H, aromatic proton), 7.09 (t, 1H, aromatic proton, J= 8 Hz), 7.39-7.52 (m, 6H, quinoline and phenyl aromatic protons), 7.67 (d, 1H, aromatic proton, J= 8 Hz), 7.85 (d, 1H, aromatic proton, J= 8 Hz).

10c, 8-(4-phenylquinolin-2-yl)-2-oxa-8-azaspiro[4.5]decane: M.p. 84-84 °C; recrystallization solvent: cyclohexane/toluene; yield: 23.13%; ^{1}H NMR ($CDCl_3$, 400 MHz, δ; ppm): 1.67 (s, 4H, -C*H*$_2$-CR$_2$-C*H*$_2$-), 1.77 (t, 2H, -C*H*$_2$-CH$_2$-CO-, J= 8Hz), 3.43 (s, 2H, -CH$_2$-C*H*$_2$-CO-), 3.75 (d, 4H, -C*H*$_2$-NR-C*H*$_2$-, J= 8 Hz), 3.84 (t, 2H, -O-C*H*$_2$-, J= 6.8 Hz), 6.85 (s, 1H, aromatic protone), 7.11 (t, 1H, aromatic proton, J= 7.6 Hz), 7.39-7.48 (m, 6H, quinoline and phenyl aromatic protons), 7.54 (d, 1H, aromatic proton, J= 8 Hz), 7.85 (d, 1H, aromatic proton, J= 8 Hz).

10d, 7-(4-phenylquinolin-2-yl)-2-oxa-7-azaspiro[3.5]nonane: M.p. 101-103 °C; recrystallization solvent: cyclohexane/toluene; yield: 8.1%; ^{1}H NMR ($CDCl_3$, 400 MHz, δ; ppm): 2.01 (s, 4H, -C*H*$_2$-), 3.68 (s, 4H, -C*H*$_2$-NR-C*H*$_2$-), 4.45 (s, 4H, -C*H*$_2$-O-C*H*$_2$-), 6.85 (s, 1H, aromatic proton), 7.19 (t, 2H, aromatic protons, J= 8 Hz), 7.39-7.48 (m, 6H, quinoline and phenyl aromatic protons), 7.54 (d, 1H, aromatic protons, J= 8 Hz).

10e, 9-(4-phenylquinolin-2-yl)-1,5-dioxa-9-azaspiro[5.5]undecane: M.p. n.d. (colourless liquid); yield:10.1%; ^{1}H NMR ($CDCl_3$, 400 MHz, δ; ppm): 1.70 (t, 2H, -O-CH_2-C*H*$_2$-, J= 6 Hz), 1.94 (t, 4H, -NR-CH_2-*C*H$_2$-, J= 6 Hz), 3.74 (t, 4H, -C*H*$_2$-NR-C*H*$_2$-, J= 5.6), 3.90 (t, 4H, -OC*H*$_2$-, J= 5.6 Hz), 6.86 (s, 1H, aromatic proton), 7.19 (t, 1H, aromatic proton, J= 7.6 Hz), 7.47-7.39 (m, 6H, quinoline and phenyl aromatic protons), 7.54 (d, 1H, aromatic proton, J= 8 Hz), 7.69 (d, 1H, aromatic proton, J= 8 Hz).

10f, 8-(4-phenylquinolin-2-yl)-1,4-dithia-8-azaspiro[4.5]decane: M.p. 52-54 °C; recrystallization solvent: cyclohexane/toluene; yield: 43.42%; ^{1}H NMR ($CDCl_3$, 400 MHz, δ; ppm): 2.14 (t, 4H, -NR-CH_2-*C*H$_2$-, J= 5.6 Hz), 3.29 (s, 4H, -S-C*H*$_2$-), 3.84-3.82 (t, 4H, -C*H*$_2$-NR-C*H*$_2$-, J= 5.6), 6.85 (s, 1H, aromatic proton), 7.19 (t, 1H, aromatic proton, J= 8 Hz), 7.39-7.48 (m, 6H, quinoline and phenyl aromatic protons), 7.54 (d, 1H, aromatic proton, J= 8 Hz), 7.69 (d, 1H, aromatic proton, J= 8 Hz).

10h, 2-(2,2-difluoro-7-azaspiro[3.5]nonan-7-yl)-4-phenylquinoline: M.p. 139-140 °C; recrystallization solvent: toluene; yield: 14%; ^{1}H NMR ($CDCl_3$, 400 MHz, δ; ppm): 1.73 (s, 4H, -NR-CH_2-*C*H$_2$-), 2.35 (t, 4H, -C*H*$_2$-CR-F_2-, J= 12 Hz), 3.68 (s, 4H, -C*H*$_2$-NR-C*H*$_2$-), 6.85 (s, 1H, aromatic proton), 7.11 (t, 1H, aromatic proton, J= 8Hz), 7.39-7.48 (m, 6H, quinoline and phenyl aromatic protons), 7.54 (d, 1H, aromatic protons, J= 8 Hz), 7.69 (s, 1H, aromatic protons).

10i, 2-(6,6-difluoro-2-azaspiro[3.3]heptan-2-yl)-4-phenylquinoline: M.p. 124-125 °C; recrystallization solvent: toluene; yield: 28.5%; ^{1}H NMR ($CDCl_3$, 400 MHz, δ; ppm): 2.77 (t, 4H, -C*H*$_2$-CR-F_2-, J= 12 Hz), 4.21 (s, 4H, -C*H*$_2$-NR-C*H*$_2$-), 6.84 (s, 1H, aromatic proton), 7.11 (t, 1H, aromatic proton, J=8 Hz), 7.37-7.50 (m, 6H, quinoline and phenyl aromatic protons), 7.57 (d, 1H, aromatic proton, J= 8 Hz), 7.78 (d, 1H, aromatic proton, J= 8 Hz).

10j, 2-(1,1-difluoro-6-azaspiro[2.5]octan-6-yl)-4-phenylquinoline: M.p. 100-102 °C; recrystallization solvent: cyclohexane/toluene; yield: 25.1%; ^{1}H NMR ($CDCl_3$, 400 MHz, δ; ppm): 1.07-1.20 (m, 2H, -C*H*$_2$-CR-F_2-, J= 20 Hz), 1.70 (d, 4H, -NR-CH_2-*C*H$_2$-, J= 20 Hz), 3.70 (s, 2H, -NR-C*H*$_2$-), 3.88 (s, 2H, -C*H*$_2$-NR-), 6.84 (s, 1H, aromatic

proton), 7.27 (t, 1H, aromatic proton, J= 8 Hz), 7.41-7.56 (m, 6H, quinoline and phenyl aromatic protons), 7.70 (d, 1H, aromatic proton, J= 8 Hz), 7.80 (d, 1H, aromatic proton, J= 8 Hz).

10k, 2-(4-(2,2-difluoroethyl)piperazin-1-yl)-4-phenylquinoline: M.p. n.d. (colourless liquid); yield: 31%; ^{1}H NMR ($CDCl_3$, 400 MHz, δ; ppm): 2.65-2.78 (m, 2H, C*H*$_2$-NR-C*H*$_2$-), 3.15 (td, 2H, -C*H*$_2$-CHF_2), 3.75 (s, 4H, -C*H*$_2$-NR-C*H*$_2$-), 5.87 (tt, 1H, F-CR*H*-F), 6.82 (s, 1H, aromatic proton), 7.19 (t, 1H, aromatic proton, J= 8 Hz), 7.41-7.56 (m, 6H, quinoline and phenyl aromatic protons), 7.70 (d, 1H, aromatic proton, J= 8 Hz), 7.80 (d, 1H, aromatic proton, J= 8 Hz).

10l, 2-(4-methylpiperazin-1-yl)-4-phenylquinoline: M.p. 123-125 °C; recrystallization solvent: toluene; yield: 16%; ^{1}H NMR ($CDCl_3$, 400 MHz, δ; ppm): 2.37 (s, 3H, -NC*H*$_3$-), 2.61 (s, 4H, -C*H*$_2$-NCH_3-C*H*$_2$-), 3.81 (s, 4H, -C*H*$_2$-NR-C*H*$_2$-), 6.83 (s, 1H, aromatic proton), 7.19 (t, 1H, aromatic proton, J= 8 Hz), 7.39-7.57 (m, 6H, quinoline and phenyl aromatic protons), 7.56 (d, 1H, aromatic proton, J= 8 Hz), 7.71 (d, 1H, aromatic proton, J= 8 Hz).

10m, 4-(4-phenylquinolin-2-yl)morpholine: M.p. n.d. (colourless liquid); yield: 27.7%; ^{1}H NMR ($CDCl_3$, 400 MHz, δ; ppm): 3.69 (s, 4H, -C*H*$_2$-NR-C*H*$_2$-), 3.80 (s, 4H, -C*H*$_2$-O-C*H*$_2$-), 6.81 (s, 1H, aromatic proton), 7.19 (t, 1H, aromatic proton, J= 8 Hz), 7.39-7.57 (m, 6H, quinoline and phenyl aromatic proton), 7.56 (d, 1H, aromatic proton, J= 8 Hz), 7.71 (d, 1H, aromatic proton, J= 8 Hz).

10n, methyl 1-(4-phenylquinolin-2-yl)piperidine-4-carboxylate: M.p. 84-86 °C; recrystallization solvent: cyclohexane/toluene; yield: 22%; ^{1}H NMR ($CDCl_3$, 400 MHz, δ; ppm): 1.78-1.81 (m, 2H, , -NR-CH_2-*C*H$_2$-), 1.94-1.98 (m, 2H, -NR-CH_2-*C*H$_2$-), 4.42 (d, 2H, -C*H*$_2$-NR-, J= 10 Hz), 2.49-2.57 (m, 1H, -C*H*-$COOCH_3$), 3.05 (t, 2H, -NR-C*H*$_2$-, J= 13 Hz), 3.63 (s, 3H, -COOC*H*$_3$), 6.84 (s, 1H, aromatic proton), 7.18 (t, 1H, aromatic proton, J= 8 Hz), 7.38-7.47 (m, 6H, quinoline and phenyl aromatic protons), 7.53 (d, 1H, aromatic proton, J= 8 Hz), 7.69 (d, 1H, aromatic proton, J= 8 Hz).

10s, tert-butyl 4-((4-phenylquinolin-2-yl)amino)piperidine-1-carboxylate: M.p. 78-80 °C; recrystallization solvent: cyclohexane/toluene; yield: 20.7%; ^{1}H NMR ($CDCl_3$, 400 MHz, δ; ppm): 1.42 (s, 9H, -OC(CH_3)$_3$), 2.05-2.09 (m, 2H, piperidine protons), 2.36 (t, 1H, piperidine proton, J= 6 Hz), 2.93 (t, 2H, piperidine protons, J= 12 Hz), 3.63-3.66 (m, 1H, piperidine proton), 4.02-4.15 (m, 3H, piperidine protons), 4.69 (s, 1H, -N*H*-CH-), 6.47 (s, 1H, aromatic proton), 7.09 (t, 1H, aromatic proton, J= 7.2 Hz), 7.38-7.48 (m, 6H, aromatic protons), 7.54 (d, 1H, aromatic proton, J= 8 Hz), 7.66 (d, 1H, aromatic proton, J= 8 Hz).

Synthesis of 1-(4-phenylquinolin-2-yl)piperidine-4-carboxylic acid (10o): To a solution of 10n (0.073g, 0.2107 mmol) in ethanol, a solution of 2N potassium hydroxide (0.421 mL, 0.421 mmol) was added at 0 °C. The reaction was stirred at room temperature for 4 hours. Afterward, ethanol was removed under reduced pressure, and the residue was acidified by adding a saturated NH_4Cl solution until pH 6. The aqueous layer was extracted with ethyl acetate (3 x 30 mL). The organic extracts were collected, washed with brine, dried with sodium sulfate, and concentrated under reduced pressure to provide the pure compound **10o**.

M.p. 104-106 °C; recrystallization solvent: cyclohexane/toluene; yield: 90%; ^{1}H NMR ($CDCl_3$, 400 MHz, δ; ppm): 1.25 (s, 1H, -C*H*-COOH), 1.65 (q, 2H, -NR-CH_2-*CH_2*-, J= 10.4), 1.96 (d, 2H, -NR-CH_2-*CH_2*-, J= 10.4), 3.15 (t, 2H, -NR-C*H_2*-, J= 13 Hz), 4.53 (d, 2H, -NR-C*H_2*-, J= 13 Hz), 7.17 (s, 1H, aromatic proton), 7.25 (t, 1H, aromatic proton, J= 6Hz), 7.38-7.47 (m, 7H, quinoline and phenyl aromatic protons), 7.69 (d, 1H, aromatic proton, J= 8 Hz), 12.39 (s, 1H, -COO*H*).

General procedure for the synthesis of compounds 10p-r

Example: Synthesis of N-methyl-1-(4-phenylquinolin-2-yl)piperidine-4-carboxamide (10q): To a solution of 10o (0.0015 g, 0.045 mmol) in dry DMF, TEA (0.025 mL, 0.181 mmol) and TBTU (0.017 g, 0.054 mmol)were added under nitrogen atmosphere. The resulting solution was stirred at room temperature for 30 minutes, and then 2M methylamine in THF (0.113 mL, 0.225 mmol) was added under nitrogen atmosphere. After 2 hours, the reaction was quenched with a saturated sodium chloride solution and extracted with ethyl acetate (3 × 10 mL). The organic extracts were collected, washed with brine, dried with sodium sulfate, and concentrated under reduced pressure. The remaining residue was purified by column chromatography (SiO_2, eluting with ethyl acetate/n-hexane 2.5:1) to provide the pure compound **10q**.

M.p. 207-208 °C; recrystallization solvent: acetonitrile/methanol; yield: 72%; ^{1}H NMR ($CDCl_3$, 400 MHz, δ; ppm): 1.58-1.90 (m, 4H, -NR-CH_2-CH_2-), 2.70 (s, 2H, -NR-CH_2), 2.89 (s, 6H, -CO-N(CH_3)$_2$), 3.04 (s, 2H, -NR-CH_2), 4.55 (d, 1H, -CH-CO-, J=13 Hz), 6.85 (s, 1H, aromatic proton), 7.10 (t, 1H, aromatic proton, J= 8Hz), 7.38-7.47 (m, 6H, quinoline and phenyl aromatic protons), 7.53 (d, 1H, aromatic proton, J= 8 Hz), 7.68 (d, 1H, aromatic proton, J= 8 Hz).

10p, 1-(4-phenylquinolin-2-yl)piperidine-4-carboxamide: M.p. 206-207 °C; recrystallization solvent: acetonitrile/methanol; yield: 54.2%; ^{1}H NMR ($CDCl_3$, 400 MHz, δ; ppm): 1.57-1.78 (m, 2H, -NR-CH_2-CH_2-), 1.93-1.97 (d, 2H, -NR-CH_2-CH_2-, J= 6 Hz), 2.35-2.42 (m, 1H, -CH-CO-NH_2), 2.94-2.99 (d, 2H, -NR-CH_2, J= 13.6 Hz), 4.55 (d, 2H, -NR-CH_2, J= 13.6 Hz), 5.41 (s, 2H, -NH_2), 6.85 (s, 1H, aromatic proton), 7.10 (t, 1H, aromatic proton, J= 8Hz), 7.41-7.48 (m, 6H, quinoline and phenyl aromatic protons), 7.54 (d, 1H, aromatic proton, J= 8 Hz), 7.69 (d, 1H, aromatic proton, J= 8 Hz).

10r, N,N-dimethyl-1-(4-phenylquinolin-2-yl)piperidine-4-carboxamide: M.p. 64-66 °C; recrystallization solvent: cyclohexane/toluene; yield: 69.4%; ^{1}H NMR ($CDCl_3$, 400 MHz, δ; ppm): 1.57-1.78 (m, 2H, -NR-CH_2-CH_2-), 1.90 (d, 2H, -NR-CH_2-CH_2-, J= 6 Hz), 2.28-2.33 (m, 1H, -CH-CO-NH-CH_3), 2.75 (d, 3H, -CO-NH-CH_3, J= 4.4 Hz), 2.94 (t, 2H, -NR-CH_2, J= 13.6 Hz), 4.55 (d, 2H, -NR-CH_2, J= 13.6 Hz), 5.46 (s, 2H, -CO-NH-CH_3-), 6.85 (s, 1H, aromatic proton), 7.10 (t, 1H, aromatic proton, J= 8Hz), 7.4-7.48 (m, 6H, quinoline and phenyl aromatic protons), 7.54 (d, 1H, aromatic proton, J= 8 Hz), 7.68 (d, 1H, aromatic proton, J= 8 Hz).

Synthesis of 4-phenyl-N-(piperidin-4-yl)quinolin-2-amine dihydrochloride (10t): the tert-butyl 4-((4-phenylquinolin-2-yl)amino)piperidine-1-carboxylate (**10s**) (0.06 g, 0.000149 mol,) was solubilized in dry toluene (2 mL). Afterward, at 0 °C, dry 4N HCl in 1,4-dioxane (15 eq, 0.0022303 mol, 0.56 mL) was added. After stirring at room temperature for 3 hours, the reaction was quenched with diethyl ether (5 mL); the resulting precipitate was filtered off and dried, obtaining the white solid **10t**.
M. p.115–117 °C; recrystallization solvent: cyclohexane/toluene; yield: 77.2 %; ^{1}H NMR: (DMSO, 400 MHz, δ, ppm): 1.85-1.91 (m, 2H, -CH_2-NH-CH_2-), 2.20-2.23 (m, 2H, -CH_2-NH-CH_2-), 3.00-3.10 (m, 2H, -CH_2-CH-CH_2-), 3.17-3.22 (m, 2H, -CH_2-CH-CH_2-), 4.68-4.83 (m, 1H, -CH_2-CH-CH_2-), 7.14 (s, 1H, aromatic proton), 7.55-7.61 (m, 7H, aromatic proton), 7.80 (s, 1H, -NH-CH-), 8.57 (s, 1H, aromatic proton), 8.88-8.97

(m, 2H, -CH_2-NH_2^+-CH_2-), 10.05 (s, 1H, aromatic proton), 13.86 (s, 1H, -NH-CH-·*H*Cl).

Synthesis of 4-bromo-6-nitro-N-(1,4-dioxaspiro[4.5]decan-8-yl)quinolin-2-amine (38):

To a solution of the commercially available 2,4-dibromo-6-nitroquinoline (0.153 g, 0.461 mmol) in dry DMF, the 1,4-dioxaspiro[4.5]decan-8-amine (0.195 mL, 1.383 mmol) was added. The reaction was stirred at room temperature for 5 hours. Afterward, the reaction was quenched with a saturated solution of sodium chloride, and the precipitated product was filtered. The product was triturated with diethyl ether and was filtered to obtain **38** as a pure yellow solid.

M. p. 240-242 °C; yield: 70.7 %; ^{1}H NMR: (DMSO, 400 MHz, δ, ppm): 1.77-1.54 (m, 6H, cyclohexane protons), 1.94 (s, 2H, -CH_2-), 3.90 (s, 4H, -O-C*H*$_2$-C*H*$_2$-O-), 4.12 (s, 1H, -NH-C*H*-C_2H_4-), 7.33 (s, 1H, aromatic proton), 7.61 (d, 1H, -N*H*-, J=8 Hz), 7.90 (d, 1H, aromatic proton, J= 7.6), 8.28 (dd, 1H, aromatic proton, J= 4 Hz), 8.65 (d, 1H, aromatic proton, J=2.4 Hz).

Synthesis of 6-nitro-4-phenyl-N-(1,4-dioxaspiro[4.5]decan-8-yl)quinolin-2-amine (11):

To a solution of 4-bromo-6-nitro-N-(1,4-dioxaspiro[4.5]decan-8-yl)quinolin-2-amine (**38**) (0.145 g, 0.355 mmol) in 1,4-dioxane and water in a ratio 1:1 as mixture of solvents, phenylboronic acid (0.065 mg, 0.533 mmol), potassium carbonate (0.128 g, 0.923 mmol), tetrakis triphenylphosphine palladium (0.037 g, 0.032 mmol) were added under nitrogen atmosphere. The reaction was stirred at 90 °C for 24 hours. Afterward, the reaction was quenched with water and extracted with ethyl acetate (3 × 10 mL). The organic extracts were collected, washed with brine, dried with sodium sulfate, and concentrated under reduced pressure. The remaining residue was triturated with diethyl ether and was filtered to obtain **11** as a pure green solid.

M. p. >250 °C; recrystallization solvent: methanol; yield: 62.53 %; ^{1}H NMR: (DMSO, 400 MHz, δ, ppm): 1.57-1.79 (m, 6H, cyclohexane protons), 1.99 (s, 2H, -CH_2-), 3.89 (s, 4H, -O-C*H*$_2$-C*H*$_2$-O-), 4.19 (s, 1H, -NH-C*H*-C_2H_4-), 6.54 (s, 1H, aromatic proton), 6.85 (s, 1H, -N*H*-), 7.46-7.56 (m, 5H, aromatic protons), 7.79 (d, 1H, aromatic proton, J= 8), 8.23 (dd, 1H, aromatic proton, J= 4 Hz), 8.32 (d, 1H, aromatic proton, J=2.4 Hz).

Synthesis of 4-phenyl-N2-(1,4-dioxaspiro[4.5]decan-8-yl)quinoline-2,6-diamine (12): A suspension of 6-nitro-4-phenyl-N-(1,4-dioxaspiro[4.5]decan-8-yl)quinolin-2-amine (**11**) (0.088 g, 0.21 mmol) and 10% w/w palladium on carbon (0.0088 g) in dry methanol (30 mL) was placed in a Parr apparatus and hydrogenated at 50 psi and 40 °C for 1 hour. Afterwards, palladium was filtered and methanol was evaporated to afford the residue that was chromatographed over silica gel by eluting with chloroform:methanol:ammonia 80:1:0.1 to provide the derivative **12**.

Mp: 107-112 °C; recrystallization solvent: cyclohexane; yield: 60.37 %; ^{1}H-NMR (DMSO d6, 400 MHz, δ, ppm): 1.53 -1.59 (m, 4H, -C*H*$_2$-CR$_2$-C*H*$_2$-), 1.65 (s, 2H, -CH$_2$-), 1.91(s, 2H, -CH$_2$-), 3.88 (s, 4H, -O-C*H*$_2$-C*H*$_2$-O-), 4.00 (s, 1H, -NH-C*H*-C$_2$H$_4$-), 4.98 (s, 2H, -N*H*$_2$-), 6.57 (s, 1H, aromatic proton), 6.61 (s, 1H, -N*H*-), 6.93 (d, 1H, aromatic proton, J= 8Hz), 7.31-7.55 (m, 7H, quinoline and phenyl aromatic protons).

Synthesis of N-(2-((1,4-dioxaspiro[4.5]decan-8-yl)amino)-4-phenylquinolin-6-yl)acrylamide (13): to a solution of 4-phenyl-N2-(1,4-dioxaspiro[4.5]decan-8-yl)quinoline-2,6-diamine (12) (0.001 g, 0.027 mmol) in dry DCM, were added TEA (2.4x10^{-3} mL, 0.029 mmol) and, at 0 °C, acryloyl chloride (4.45x10^{-3} mL, 0.032 mmol). After 10 minutes, the reaction was quenched with water and extracted with DCM (3 × 10 mL). The organic extracts were collected, washed with brine, dried with sodium sulfate, and concentrated under reduced pressure. The remaining residue was chromatographed over silica gel by eluting with Chloroform:Methanol 10:1 to provide the derivative **13**.

Mp: 129-130 °C; recrystallization solvent: toluene; yield: 30.1 %; ^{1}H-NMR (DMSO d6, 400 MHz, δ, ppm): 1.53-1.66 (m, 4H, -C*H*$_2$-CR$_2$-C*H*$_2$-), 1.75(s, 2H, -C*H*$_2$-), 1.96 (s, 2H, -CH$_2$-), 3.88 (s, 4H, -O-C*H*$_2$-C*H*$_2$-O-), 4.06 (s, 1H, -NH-C*H*-C$_2$H$_4$-), 6.20 (dd, 1H, -CH=C*H*-, J=7 Hz), 6.37 (q, 1H,-C*H*=CH-, J= 6.8 Hz), 6.67 (s, 1H, -N*H*-), 6.89 (d, 1H, aromatic proton, J= 8 Hz), 7.50-7.57 (m, 6H, quinoline and phenyl aromatic protons), 7.81 (d, 1H, aromatic proton, J=4 Hz), 7.84 (s, 1H, aromatic proton), 10.11 (s, 1H, -N*H*-C=O-).

Table 2.4. Elemental analysis of compounds 10a-t and 11-13.

CPD	MW	Elemental Analysis									
		Calculated, %					Found, %				
		C	N	O	H	Other	C	N	O	H	Other
10a	346.43	76.28	8.09	9.24	6.40		76.36	8.05	9.22	6.39	
10b	346.43	76.28	8.09	9.24	6.40		76.38	8.04	9.22	6.38	
10c	344.46	80.20	8.13	4.64	7.02		80.29	80.16	4.63	7.00	
10d	330.43	79.97	8.48	4.84	6.71		80.28	8.42	4.82	6.70	
10e	360.46	76.64	7.77	8.88	6.71		76.72	7.70	8.86	6.69	
10f	378.55	69.80	7.40		5.86	16.94 (S)	69.89	7.36		5.85	16.92 (S)
10g	360.46	76.64	7.77	8.88	6.71		76.71	7.72	8.87	6.70	
10h	364.44	75.80	7.69		6.08	10.43 (F)	75.87	7.63		6.06	10.41 (F)
10i	336.39	74.98	8.33		5.39	11.30 (F)	75.10	8.29		5.37	11.28 (F)
10j	350.41	75.41	7.99		5.75	10.84 (F)	75.48	7.95		5.74	10.82 (F)
10k	353.42	71.37	11.89		5.99	10.75 (F)	71.45	11.83		5.98	10.74 (F)
10l	303.41	79.17	13.85		6.98		79.24	13.80		6.97	
10m	290.37	78.59	9.65	5.51	6.25		78.60	9.60	5.50	6.23	
10n	346.43	76.28	8.09	9.24	6.40		76.40	8.03	9.22	6.38	
10o	332.40	75.88	8.43	9.63	6.06		75.95	8.39	9.61	6.04	
10p	331.42	76.11	12.68	4.83	6.39		76.19	12.62	4.82	6.38	
10q	345.45	76.49	12.16	4.63	6.71		76.58	12.12	4.61	6.70	
10r	359.47	76.85	11.69	4.45	7.01		76.93	11.65	4.44	7.00	
10s	403.53	74.41	10.41	7.93	7.24		74.48	10.37	7.91	7.23	
10t	376.32	63.83	11.17		6.16	18.84 (Cl)	63.90	11.13		6.18	18.83 (Cl)
11	405.45	68.13	10.36	15.78	5.72		68.20	10.31	15.76	5.70	
12	375.47	73.57	11.19	8.52	6.71		73.84	11.12	8.50	6.70	
13	429.52	72.71	9.78	11.17	6.34		72.80	9.72	11.16	6.32	

2.4.2. Materials and methods

2.4.2.1. Reagents

FAD disodium salt hydrate (FAD-Na_2), β-nicotinamide adenine dinucleotide 2′-phosphate reduced tetrasodium salt (NADPH), Roswell Park Memorial Institute (RPMI) 1640 medium with l-glutamine and sodium bicarbonate, phosphate-buffered saline (PBS), lithium dodecyl sulfate (LiDS), $CaCl_2$, sodium chloride, HEPES buffer, sodium di-hydrogen phosphate ($NaH_2PO_4 \cdot H_2O$), phenylmethylsulfonyl fluoride, glycerol, pepstatin, leupeptin, SigmaFastTM Protease Inhibitor Cocktail Tablets EDTA-Free, cytochrome c from equine heart, hemin, superoxide dismutase, Ampliflu Red (Amplex Red) and horseradish peroxidase were purchased from Sigma Aldrich. MCLA was purchased from MedChemExpress. Cholesteryl hemisuccinate Tris salt (CHS) and dodecyl-beta-d-maltopyranoside (DDM) were purchased from Anatrace. Fetal bovine serum (FBS) and FreeStyle medium were purchased from Invitrogen. All tested compounds were purchased from MolPort, Vita-M-Labs, and ChemSpace or Enamine suppliers.

2.4.2.2. Virtual screening on the DH of csNOX5

(Group of Prof. Andrea Mattevi, Department of Biology and Biotechnology Lazzaro Spallanzani, University of Pavia)

Receptor preparation - The receptor structure was the DH of csNOX5 (Protein Data Bank (PDB) 5O0X). For screens 1 and 2, the C-terminal sequence (^{694}PWLEL^{698}) of the mutant used for the original structure determination was removed from the model. Screen 3 was performed with the C-terminal Phe693 in the open conformation observed in the complex with compound M41 conformation Maestro from Schrödinger was used to remove solvent molecules of the crystal structure, assign missing hydrogen atoms, correct protonation states at pH 7.4 and assign the correct bond orders. AutoDockTools (v.4.2.6) [330] was used to convert the structure from the PDB format to the PDBQT format.

Docking scenario setup - The site that was targeted comprises the FAD and NADPH-binding sites. In screen 1, FAD was present in the active site of the used receptor structure, while in screen 2 FAD was not present. The size of the docking box was set to 22.5 × 15 × 25.5 Å in screens 1 and 2, and 26.5 × 15 × 25.5 Å in screen 3. The protein was held rigid during the virtual screens. The docking programs used

are QuickVina 2 [331] and Smina [332] with the Vinardo scoring function. [333] The exhaustiveness values were set to 1. The VirtualFlow open-source drug-discovery platform was used to carry out the virtual screens. The number of replicas was set to 1. The virtual screens were run on the Harvard Odyssey supercomputer, a heterogeneous cluster with Intel and AMD CPUs with more than 70,000 CPUs in total. Postprocessing of the results was done with DataWarrior. [334] Basic filters have been applied, such as logP less than 5, and compounds with problematic functional groups and predicted toxicity (mutagenic compounds, compounds with reproductive effects, tumorigenic compounds) were removed.

2.4.2.3. Protein expression

(Group of Prof. Andrea Mattevi, Department of Biology and Biotechnology Lazzaro Spallanzani, University of Pavia)

DH of *C. stagnale* NOX5 - The N-terminally histidine-tagged wild-type DH (residues 413–693) was expressed as described in '**1.4.2. Materials and methods'** of the previous project. [54] For the production of U-[^{15}N]-*cs*DH NOX5 used in NMR, the bacteria were grown at 37 °C in M9 medium prepared with 4 g l^{-1} of D-glucose (Sigma) and 1 g l^{-1} $^{15}NH_4Cl$ (CIL). At an OD_{600} of 1 the protein production was induced with 0.3 mM isopropyl-β-D-thiogalactoside and the expression was performed at 17 °C overnight.

DH of *human* NOX4 - The gene encoding for the DH of human NOX4 (residues 299-578 of isoform 1) carrying a multiple N-terminal $(His)_6$, Twin-STREP, Maltose Binding Protein tag was cloned into a pET28a and expressed in the *E. coli* BL21 (DE3, RP-Plus) (Novagen). Cell pellets were resuspended in buffer A (50 mM HEPES pH 7.4, 10% (v/v) glycerol, 0.5 M NaCl) and supplemented with 1 mM PMSF (phenylmethylsulfonyl fluoride) and proteases inhibitor cocktail (SigmaFastTM Protease Inhibitor Cocktail Tablets, EDTA-Free, Sigma Aldrich) before cell disruption by sonication.

***Human* NOX2 -** The enzyme was expressed as described before. [281] Briefly, X-CGD PLB-985 cells, transduced with the RD114-pseudotyped MFGS-NOX2 vector (PLB-985 cells from now on) were a kind gift from H. Malech (National Institutes of Health). The cells were maintained in suspension in RPMI-1640 medium supplemented with 10% (v/v) heat-inactivated FBS at 37 °C and 5% CO_2. Cells were centrifuged at 1,200g for 10 min. Cells were resuspended in PBS and centrifuged again at 1,200g for 10 min and the pellet frozen at −80 °C.

***Human* NOX1 and NOX2 cytosolic partners -** The full-length human $p67^{phox}$, $p47^{phox}$ and the constitutively active mutant Rac1 Q61L were expressed as described before. [281 302]

***Human* NOX1 and NOX5 -** The complementary DNAs (cDNAs) encoding for the human NOX1 (isoform 1), human NOX5 (isoform v/2), and human $p22^{phox}$ were obtained from Genescript, cloned into a pEG BacMam vector (kindly gifted by E. Gouaux, Oregon Health and Science University, Portland). The NOX1 construct contains a Kozak sequence, followed by two FLAG tags, a Twin-STREP tag, and a tobacco etch virus (TEV) cleavage site at the N terminus. The NOX5 construct contained a Kozak sequence, followed by N-terminal FLAG tag and TEV cleavage site. The $p22^{phox}$ construct carried a Kozak sequence. HEK293-EBNA1-6E cells were given by Y. Durocher (NRC-BRI). [335] Cultured cells were maintained in suspension using FreeStyle medium (Invitrogen). Cells were seeded at a concentration of 5×10^5 cells per ml, the day before transfection. For transient NOX1-$p22^{phox}$ cotransfection or NOX5 transfection, polyethyleneimine (linear MW 25000, Polyscience Europe Gmbh) was used as transfection agent, in a ratio of 1/3 DNA/polyethyleneimine (0.75 µg of NOX1 vector, 0.25 µg $p22^{phox}$ vector per 1 µg of NOX5 vector, 3 µg polyethyleneimine per ml of culture). After 48 h, the transfected cells were gathered by centrifugation (1,200g, 5 min, 4 °C). Trypan Blue exclusion assay (Trypan Blue solution w/v, Sigma) was used to evaluate cell viability. The cell pellet was rapidly frozen using liquid nitrogen and then stored at a temperature of −80 °C.

Human NOX4 expression - The cDNAs encoding for the human NOX4 (isoform 1 from GeneWiz) and human $p22^{phox}$ were obtained from GeneWiz, cloned into pTT22 (puromycin resistance) and pYD7 vectors, respectively (vectors obtained from Y. Durocher, NRC-BRI, Montreal, Canada). [335] [336] The NOX4 construct contained a Kozak sequence, followed by two $(His)_6$ tags, a Twin-STREP tag, an eGFP moiety, and a TEV cleavage site at the N terminus. The $p22^{phox}$ construct contained a Kozak sequence. Both vectors contained an EBV origin of replication in their construct that allows them to be maintained episomally in HEK293 EBNA1-6E. Cultured cells were maintained in suspension using FreeStyle medium (Invitrogen). Cells were seeded at a concentration of 5×10^5 cells per ml, the day before transfection. For stable NOX4-$p22^{phox}$ cotransfection, polyethyleneimine (linear MW 25,000, Polyscience Europe) was used as transfection agent, in a ratio of 1/3 DNA/polyethyleneimine (0.90 μg of NOX4 vector, 0.10 μg of $p22^{phox}$ vector and 3 μg of polyethyleneimine per ml of culture). The next day, 5 μg ml−1 of puromycin was added to the cell culture. After 48 h, transfected cells were gathered by centrifugation (1,200g, 5 min, 4 °C). Trypan Blue exclusion assay (Trypan Blue solution w/v, Sigma) was used to evaluate cell viability. The cell pellet was rapidly frozen using liquid nitrogen and then stored at a temperature of −80 °C.

2.4.2.4. Protein purification

(Group of Prof. Andrea Mattevi, Department of Biology and Biotechnology Lazzaro Spallanzani, University of Pavia)

Membrane preparations - Membrane isolation from NOX-expressing human cells was performed as described before. [281] Briefly, frozen PLB-985 cells or transfected HEK293-EBNA1-6E cells pellets were resuspended at a concentration of 2×10^8 cells per ml in sonication buffer containing 10 mM HEPES (pH 7.4), 10 mM NaCl, 100 mM KCl, 1 mM PMSF and supplemented with 1 μM leupeptin, 1 μM pepstatin just before sonication. The lysate was centrifuged at 500g for 5 min at 4 °C, and the supernatant was collected. The cell pellet was resuspended in sonication buffer and sonicated again on ice twice. The cell lysate was centrifuged at 500g for 5 min at 4 °C and the supernatant was collected. Both supernatants were pooled and ultracentrifuged (200,000g for 30 min) at 4 °C (Optima MAX-XP Ultracentrifuge, Beckman Coulter). Protein concentration was assessed by the Biuret Assay. Protein quality was evaluated by detecting protein bands thorough western blots stained with monoclonal anti-STREP tag-HRP antibody (Bio-Rad, for NOX1 detection),

monoclonal anti-FLAG M2-Peroxidase antibody (Sigma, for NOX5 detection) and anti-NOX2 antibody (54.1, kind gift of A. Jesaitis, Montana State University). Antimouse IgG HRP-linked antibody (Cell-Signaling Technology) was used as a secondary antibody for 54.1 antibody detection. Detection of NOX4 involved quantifying the fluorescence emitted by the eGFP moiety through intensity-based fluorescence detection on an SDS–PAGE gel (Bio-Rad; ChemiDoc MP imager; Alexa Fluor 488 for eGFP detection).

***Human* cytosolic protein purification -** The full-length human $p67^{phox}$, $p47^{phox}$ and the constitutively active mutant Rac1 Q61L were purified as described before. [281]

DH of *C. stagnale* NOX5 purification - The N-terminally histidine-tagged wild-type protein was purified as described in ref. [54]

STREP affinity chromatography purification of the isolated DH of *human* NOX4 - Disrupted cells were centrifuged at 56,000g for 45 min at 4 °C. The supernatant was collected and filtered with a 0.45 μm cut-off and loaded on a gravity column containing STREP-tactin XT (Cytiva) resin. Washes in buffer A (50 mM HEPES (pH 7.4), 500 mM NaCl, 12 mM EGTA, 3.5 mM $MgCl_2$) were performed. The subsequent elution was performed with buffer A supplemented with 5 mM biotin. The eluted sample was injected in a high-pressure liquid chromatography ÄKTA system (Cytiva), using a Superdex200 10/300 column (Cytiva) to perform size-exclusion chromatography. Protein quality was evaluated by detecting protein bands on SDS–PAGE gel and thorough western blots stained with monoclonal anti-STREP tag-HRP antibody (Bio-Rad).

STREP affinity chromatography purification of human NOX1-$p22^{phox}$ complex - *Human* NOX1-$p22^{phox}$ cell membranes were gently thawed in ice and supplemented with 1% DDM and 0.2% CHS (v/v). Solubilization proceeded for 90 min at 4 °C. Following centrifugation at 100,000g for 40 min at 4 °C, the supernatant was collected and loaded on a STREP-tactin XT resin (Cytiva) previously equilibrated with buffer A (10 mM HEPES (pH 7.4), 10 mM NaCl, 100 mM KCl, 12 mM EGTA, 3.5 mM $MgCl_2$) supplemented with 0.1% DDM and 0.02% CHS. The binding was

allowed to proceed in batch mode for 90 min at 4 °C. The resin was washed with 20 column volumes of buffer A supplemented with 0.1% DDM and 0.02% CHS. Protein elution was performed with buffer A supplemented with 0.03% DDM, 0.006% CHS, and 2.5 mM biotin. The eluted complex NOX1-p22^{phox} was then applied to a Superdex200 5/150 (Cytiva) fast protein liquid chromatography column. Protein quality was evaluated by detecting protein bands on SDS gel and through western blots stained with monoclonal anti-STREP tag-HRP antibody (Bio-Rad, for NOX1 detection).

CS9 hybridoma culture and CS9 antibody purification - The hybridoma cell line was kindly provided by A. Jesaitis (Montana State University, USA). The cell line was cultured in Hybridoma-SFM medium (Thermo Fisher Scientific) supplemented with 5% (v/v) FBS ultra-low IgG (Thermo Fisher Scientific) in stationary T-75 Eppendorf Cell Culture Flask (Sigma), at 37 °C with 5% CO_2. The cells were kept going for 7 days for the expression of mAb CS9. They were then centrifuged at 1,000g for 10 min and the supernatant was collected and frozen at −20 °C. The hybridoma supernatant was thawed and precipitated with 50% saturation of ammonium sulfate, at 4 °C for 16 h while agitating it with a magnetic stirrer and then centrifuged at 7,450g for 45 min at 4 °C. The precipitated antibody was resuspended in PBS and dialyzed for 48 h with a 12–14 kDa cut-off SpectraPor Standard Grade RC (regenerated cellulose) membrane (REPLIGEN) against 2 l of PBS with six changes of buffer. The precipitated monoclonal antibody was then applied to a HiTrap Protein G HP column (Cytiva), and binding allowed to proceed at 1 ml min^{-1}. The column was then washed with ten column volumes of 20 mM sodium phosphate buffer, pH 7.4. The antibody was eluted with elution buffer (0.1 M Glycine, pH 2.7), and immediately buffered with 1 M Tris-HCl pH 9.0. The eluted antibody was then dialyzed with a 12–14 kDa cut-off membrane against 2 l of PBS for 20 h and kept at a concentration of 0.5 mg ml^{-1}.

Immunoaffinity purification of human NOX2-p22^{phox} complex - PLB-985 cell-membrane fractions were supplemented with 1% (v/v) DDM and 0.2% (v/v) CHS. Solubilization proceeded for 90 min at 4 °C. Following centrifugation 100,000g for 40 min at 4 °C, detergent extraction was applied on a Protein G Sepharose 4 Fast Flow Resin (Cytiva), prepacked with the mAb CS9 and equilibrated with sonication buffer (10 mM HEPES (pH 7.4), 10 mM NaCl, 100 mM KCl) supplemented with 0.5%

DDM and 0.1% CHS. The binding was allowed to proceed in batch mode for 60 min at 4 °C. The resin was washed three times with sonication buffer supplemented with decreasing concentrations of DDM and CHS. NOX2-p22^{phox} was eluted with 200 μM peptide Ac-AEARKKPSEEEAA-NH_2 (GenScript), mixed in five column volumes of sonication buffer containing 0.026% DDM (v/v) and 0.0052% CHS (v/v). The eluted complex NOX2-p22^{phox} was then applied to a Superdex200 5/150 (Cytiva) fast protein liquid chromatography column. Protein quality was evaluated by detecting protein bands on SDS gel.

2.4.2.5. Biochemical assays

(Group of Prof. Andrea Mattevi, Department of Biology and Biotechnology Lazzaro Spallanzani, University of Pavia)

Evaluation of *human* NOX1, NOX4 and NOX5 membranes - The assay was assessed as described before. [281]. In brief, NOX1- (100 μg), NOX4- (100 μg) or NOX5-containing (25 μg) membranes were added to a reaction mixture of PBS with 0.02 U ml^{-1} horseradish peroxidase, 12.5 μM Amplex Red, 40 μM FAD, 1.5 μM cytosolic proteins p67^{phox}, p47^{phox}, Rac1 Q61L (for NOX1) and 1 mM $CaCl_2$ (for NOX5) in a final volume of 100 μl. The compounds were added to the mixture and incubated for 10 min at 4 °C at varying concentrations from the micromolar to the low nanomolar range. The reaction was started with the addition of 40 μM NADPH, a concentration selected to minimize potential interference effects. [337] Measurements were performed using a ClarioStar plate reader (excitation 572 nm/emission 583 nm) (BMG Labtech). We pursued the expression and purification of the physiological NOX1 activators, NOXA1 and NOXO1. However, all NOXO1 constructs evaluated suffered from a heavy tendency to aggregate and the protein was never purified in an active form. Hence, p47^{phox} was used together with NOXA1 to measure NOX1 activity. This mixture NOX2-organizer and NOX1-activator was successful in the activation of purified NOX1-p22^{phox}. However, the use of p67^{phox} instead of NOXA1 did not significantly change the overall activity. Given the higher purification yields of p67^{phox} compared to NOXA1, p47^{phox}-p67^{phox} system was finally exploited for NOX1 activation.

***Ki* determination on *human* NOXs -** K_i were measured on human NOX1, human NOX2, DH of human NOX4 and DH of *cs*NOX5 following NADPH oxidation by monitoring the absorbance 340 nm with Cary 100 UV-vis spectrophotometer (Varian) or the fluorescence (excitation 340 nm/emission 460 nm) with Cary Eclipse fluorescence spectrometer (Varian). 200 nM of purified NOX2 was added in a final volume of 200 µl of 65 mM sodium phosphate buffer (pH 7.0), 50 µM FAD, 130 µM LiDS and 1 µM recombinant cytosolic proteins $p67^{phox}$, $p47^{phox}$, Rac1 Q61L. For NOX1, 1 µM of purified enzyme was assayed in a final volume of 200 µl of 65 mM sodium phosphate buffer (pH 7.0), 50 µM FAD, 130 µM LiDS and 5 µM recombinant cytosolic proteins $p67^{phox}$, $p47^{phox}$, Rac1 Q61L. Inhibitors were tested with concentrations varying from micromolar to low nanomolar.

Microscale thermophoresis binding assay and thermal shift analysis on bacterial NOX5 DH - The affinity between the *cs*NOX DH and compound 3 was assayed using microscale thermophoresis. The ligand was titrated to a maximum concentration of 6.4 mM using a fixed concentration of the fluorescently labelled protein (~200 nM). All binding reactions were carried out in a buffer containing Hepes 50 mM, NaCl 240 mM, 0.5% glycerol, 250 µM FAD and 0.1% pluronic acid at pH 7.5. Samples were loaded into NT.115 premium treated capillaries (Nanotemper Technologies) after the reaction was incubated at 25 °C for 10 min. Consequently, the samples were mounted in the Monolith NT.115 apparatus (Nanotemper Technologies) for binding measurements. The data for microscale thermophoresis analysis were recorded at 25 °C. All binding experiments were followed using a red fluorescence channel (red filter; excitation 605–645 nm, emission 680–685 nm). Data analysis was performed with the software NTAffinityAnalysis (Nanotemper Technologies) where the binding isotherms were derived from the raw fluorescence data. The experiments were performed in triplicate and the resulting standard deviation calculated with NTAffinityAnalysis. [281]

2.4.2.6. Statistical analysis

Data analyses were performed as described in before. All graphs were prepared using GraphPad Prism and all data are expressed as mean ± standard deviation. Sigmoidal curve-fitting of concentration–response curve, IC_{50} values and statistical tests were all performed with GraphPad Prism. Concentration–response curves are presented as a percentage of the control, with control being the untreated condition. For K_i determination, initial velocities obtained at multiple NADPH and inhibitor concentrations were fitted globally to competitive, uncompetitive, and noncompetitive models. The best-fit model was identified based on the R2 parameter given by GraphPad Prism software (GraphPad Software, Inc.).

2.4.2.7. X-ray crystallography

(Group of Prof. Andrea Mattevi, Department of Biology and Biotechnology Lazzaro Spallanzani, University of Pavia)

The DH of *cs*NOX5 in 50 mM HEPES, pH 7.5, 200 mM NaCl, and 5% (v/v) glycerol was cocrystallized with the tested inhibitors (1–5 mM) in the presence of the FAD cofactor (5 mM). Cocrystallization experiments were performed at 20 °C using Oryx8 robot (Douglas Instruments) and sitting-drop vapor-diffusion technique. The drops were composed of 0.2 µl of 8 mg ml^{-1} protein and 0.2 µl of reservoir from commercial screens (the PEGs Suite, MORPHEUS from Qiagen). Crystals grew between 1 and 3 days depending on the inhibitor. The precipitant solutions were as follows: 0.3 M diethylene glycol; 0.3 M tri ethylene glycol, 0.3 M tetra ethylene glycol, 0.3 M pentamethylene glycol, Tris-HCl 0.1 M pH 8.0, 20% (v/v) ethylene glycol, 10% (w/v) PEG8000, MES 0.1 mM pH 6.5, 0.1 M carboxylic acids. X-ray diffraction data were collected at the beamlines of the Swiss Light Source in Villigen (Switzerland) and European Synchrotron Radiation Facility in Grenoble (France). Before data collection, crystals were transferred into a mother liquor solution with 20% (v/v) glycerol and flash-cooled in a stream of gaseous nitrogen at 100 K (−173.15 °C). Data processing and scaling were performed using XDS (v.5 February 2021) [338] and the CCP4 package. [339] The coordinates of the *cs*DH-PWLELAAA-mutant [27] were used as the initial model. The program Coot (v.0.9.4) [340] was used for electron density inspection and model building, whereas crystallographic refinement was performed with the program REFMAC5 (v.5.5) [341]. Figures were generated by the program ChimeraX (v.1.5.0) [342] and Maestro (release 2020-1).

2.4.2.8. In cellulo analyses

(Group of Prof. Andrea Mattevi, Department of Biology and Biotechnology Lazzaro Spallanzani, University of Pavia)

In cellulo measurement of human NOX2 activity by cytochrome c reduction assay - $O_2^{\bullet-}$ production of intact PLB-985 cells (3×10^5 cells) in PBS containing 20 mM glucose and 200 μM cytochrome c was measured after PMA (phorbol 12-myristate 13-acetate) stimulation (5 μM). Incubation with PMA proceeded for 20 min at 37 °C. The tested compounds (single inhibitory activity measurement at 40 or 0.04–40 μM for EC_{50} determination) were added to the stimulated cells and incubated for 30 min at 37 °C and 5% CO_2, 120 rpm (New Brunswick S41i Incubator Shaker, Eppendorf). The absorbance at 550 nm was monitored at 37 °C, over a time course of 15 min in a Cary 100 UV-vis spectrophotometer and over a time course of 30 min in a ClarioStar plate reader (EC_{50} determination). The activity of NOX2 in intact PLB-985 cells not previously stimulated with PMA was also evaluated as negative control.

In cellulo measurement of human NOX4 and NOX5 activities by the Amplex Red assay - Intact NOX4- and NOX5-expressing HEK293-EBNA1-6E cells (5×10^4 cells per well) were resuspended in PBS. The tested compounds (single inhibitory activity measurement at 40 μM or 0.04–40 μM for EC_{50} determination) and PMA (100 nM for NOX5 activated cells, none for NOX4) were added to HEK293-EBNA1-6E cell cultures. The cells were incubated for 30 min at 37 °C and 5% CO_2, 120 rpm (New Brunswick S41i Incubator Shaker, Eppendorf), each condition in triplicate in a 96-well plate (NUNC 96-well, Thermo Scientific). Here, 100 μM Amplex Red and 0.6 U ml^{-1} horseradish peroxidase were added to the reaction mixture in a final volume of 100 μl per well. Also, 1 μM ionomycin and 1 mM $CaCl_2$ were specifically added only in the NOX5 PMA-stimulated condition. Measurements were performed using a ClarioStar plate reader (excitation 572 nm and emission 583 nm) (BMG Labtech). Nontransfected cells and NOX5 cells not stimulated with PMA were used as negative controls of NOX4 and NOX5, respectively.

Cellular thermal shift assay (on human NOX2, 4 and 5 expressing cells) - Thirty million intact NOX2-PLB-985 cells and NOX4- and NOX5-expressing HEK293-EBNA1-6E cells were incubated with dimethylsulfoxide (DMSO) or 40 μM of the tested inhibitor for 1 h at 37 °C with 5% CO_2, after the stimulation with 5 μM PMA for PLB-985 cells and 100 nM PMA for NOX5-expressing HEK293-EBNA1-6E cells. After centrifugation at 1,300*g* for 10 min at room temperature, cell pellets were washed twice in PBS and resuspended at 1.5×10^7 cells per ml and aliquoted to PCR-strips at 100 μl per tube. Samples were then heated (spanning from 30 °C to 66.9 °C for NOX4, from 37 °C to 88 °C for NOX2, from 30 °C to 57.9 °C for NOX5) for 3 min in a T100 Thermal Cycler (Bio-Rad). NOXs were extracted from intact cells by adding 1% DDM (v/v) to each tube, and solubilization proceeded for 60 min at 4 °C. After centrifugation at 20,000*g* for 30 min at 4 °C, each supernatant was analyzed by loading 20 μl of each sample onto a SDS gel (Bio-Rad, Mini-PROTEAN TGX). For NOX2 and NOX5 SDS gel bands were transferred to a Trans-Blot Turbo Mini 0.2 μm PVDF (polyvinylidene difluoride) membrane (Bio-Rad) using a Trans-Blot Turbo Transfer System (Bio-Rad). For NOX2, western blot analysis was performed by immunoblotting the PVDF membrane with NOX2 monoclonal antibody (54.1, kindly gifted by A. Jesaitis, Montana State University), following the addition of goat horseradish peroxidase-conjugated antimouse secondary antibody (Bio-Rad). For NOX5, western blot analyses were performed by immunoblotting the PVDF membrane with monoclonal anti-FLAG M2-Peroxidase antibody (Sigma). Chemiluminescent detection of NOX2 and NOX5 was performed by using the ECL detection kit (Bio-Rad, ChemiDoc MP image). NOX4 was detected by quantifying the fluorescence emitted by the eGFP moiety through intensity-based fluorescence detection on an SDS–PAGE gel (Bio-Rad; ChemiDoc MP imager; Alexa Fluor 488 for eGFP detection). Melting curves were generated by plotting the band intensities of each heated sample against the respective temperatures (°C). Data were first normalized by setting the highest and lowest intensity value in each set to 100 and 0%, respectively. Fitting of curves was performed by applying a Boltzmann sigmoidal dose-response model within GraphPad Prism. The T_{agg} values obtained were the results of two different experiments and the mean ± standard deviation was calculated.

PRISM assay - Detailed information on cell lines, barcoding of tumor cell lines as well as PRISM detection and analysis can be found in the work by Yu et al. [343] and Corsello et al. [344].

2.4.2.9. Cancer cell line analysis

(Group of Prof. Haribabu Arthanari, Department of Biological Chemistry and Molecular Pharmacology, Blavatnik Institute, Harvard Medical School (HMS); Department of Cancer Biology, Dana-Farber Cancer Institute (DFCI), Boston, MA, USA)

Cell culture and treatments - U937 cells were grown in RPMI-1640 (Euroclone) supplemented with 10% FBS (Sigma Aldrich), 50 U ml^{-1} penicillin and 50 mg ml^{-1} streptomycin at 37 °C and 5% CO_2. U937 cells were propagated in RPMI-1640 (Euroclone). Cells were cultured with 5% CO_2 at 37 °C. For differentiation experiments with U937, cells were treated with 100 nM phorbol 12-myristate13-acetate or 1% DMSO and incubated for 72 h. For cellular proliferation and toxicity assays, cells were seeded in 96-well plate at 1.0×10^4 cells per well, then treated with compounds 3 and 10t. Plates were incubated in treatment conditions at 37 °C and 5% CO_2 for 24, 48 or 72 h. [345] After incubation, results were evaluated with CellTox Green Cytotoxicity Assay (Promega) multiplexed with CellTiter-Glo 2.0 Cell Viability Assay (Promega) according to manufacturer protocol. U937 viability was further assessed by the propidium iodide (50 μg ml^{-1}) assay. For drug synergy assay, cells were plated at 5×10^3 cells per well in 384-well plates. Then 24 h postplating, cells were treated with compound 3 or MRTX1133 or a combination of M41 and MRTX1133 at increasing concentrations of 0–50 μM for compound M41 and 0-5 μM for MRTX1133 using D300e digital drug printer (Tecan Life Sciences). The cell viability was assessed 72 h posttreatment using CellTiter-Glo v.2.0 Cell Viability Assay (Promega) according to the manufacturer's instructions. The synergistic effect between M41 and MRTX1133 was analyzed using Synergyfiner. [346]

3. DEVELOPMENT OF QUINOLINE – CONTAINING NOXs INHIBITORS: SECOND SERIES

3.1. Research Project

Starting from 10t and 10s of the first series of quinoline-based simplified derivatives, which came out as selective and potent NOX2 and NOX5 inhibitors, we designed and synthesized a series of homologues of piperidine derivatives.

Specifically, we explored NOX2 inhibition by modifying various amine groups in **10t**. These modifications included cyclic homologues (both upper and lower rings) and open-chain derivatives of piperidine, leading to the synthesis of derivatives **14b, 14g, 14i, 14k, 14m, 14o**, and **14q**.

Additionally, seeing the biochemical results of **10s**, which shows potency and selectivity against NOX5, we planned the synthesis of the Boc-protected analogues of these derivatives. This led to the synthesis of compounds **14a, 14c-f, 14h, 14j, 14l**, and **14n**. These Boc-protected analogues allowed us to investigate the role of the Boc group in NOX5 selectivity, as well as the impact of deprotected amines on NOX2 selectivity.

Interestingly, during the synthesis of compound **14h**, we unexpectedly obtained the bisquinolinic derivative **15a**, which was subsequently tested for its biochemical activity. Given the good biochemical results obtained for compound 15a, which will be explained more deeply in the section "**3.2.2. Biochemical activity of the second series of simplified derivatives towards *human* NOXs**", we further explored its structure by modifying various chemical groups. Our first modification focused on replacing the Boc group. We completely removed substituents from the endocyclic nitrogen of the azetidine ring, producing the deprotected derivative **15b**, similar to the second series of simplified derivatives mentioned earlier. Additionally, we substituted it with acyl groups, specifically acetyl and benzoyl ones, yielding derivatives **15c** and **15d**, respectively, and with a benzyl carbamate, resulting in the derivative **15e**.

With the aim of exploring as much as possible the selectivity of NOX isoforms, we synthesized asymmetric bisadducts.

In these, one of the two 4-phenyl quinoline moieties was replaced with a naphthalene group. We synthesized both the Boc-protected derivative (**16a**) and its deprotected counterpart **16b**. Finally, we replaced the 4-phenyl quinoline moiety

with a pyridine group, yielding **17a** (with the Boc group) and **17b** (with a deprotected amino group) (**Figure 3.1**).

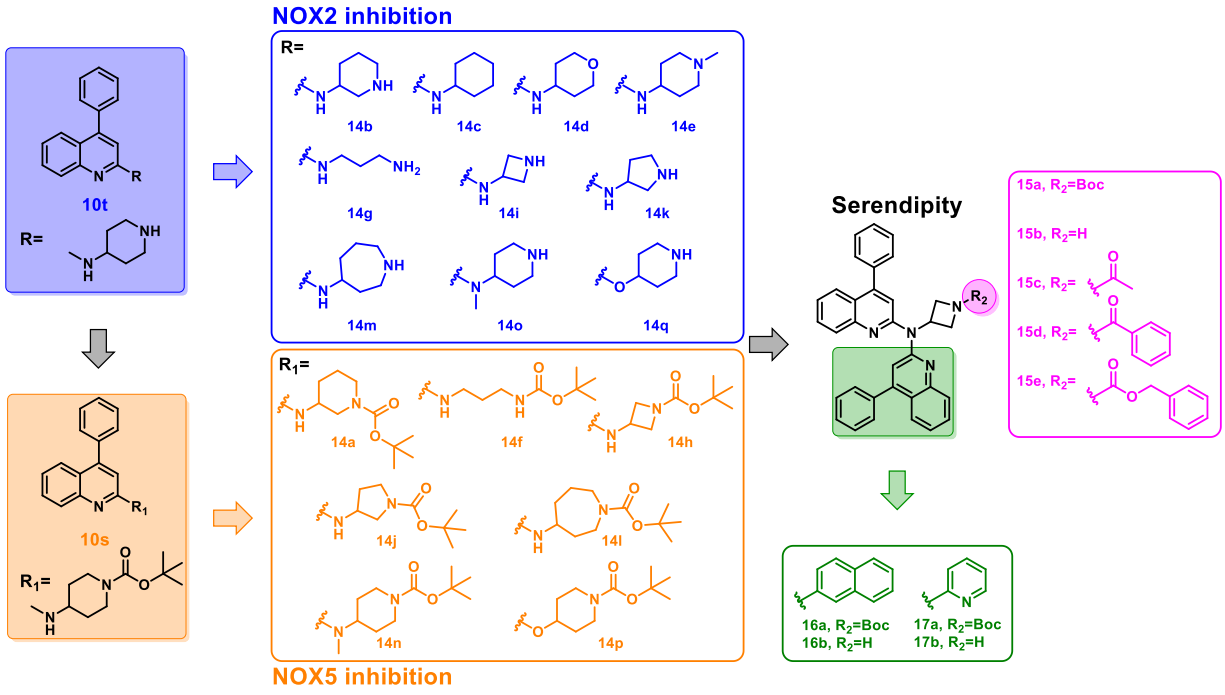

Figure 3.1. *Rational design of the second series of simplified derivatives.*

3.2. Results and discussion

3.2.1. Chemistry

The final compounds **14 a-s** have been synthesized following the synthetic scheme reported in **Scheme 3.1**. The final compounds **14a, 14c-f, 14h, 14j, 14l,** and **14n** were obtained via Buchwald-Hartwig reaction. Particularly, the commercially available 2-chloro-4-phenylquinoline was treated with the opportune commercial amine, $Pd(OAc)_2$, BINAP, and Cesium Carbonate solubilized in dry toluene, under nitrogen atmosphere at 125 °C for 12-24 hours. For the synthesis of the final compound **14p**, the chloro-derivative was treated with tert-butyl-4-hydroxyperidine-1-carboxylate, in a basic medium by t-BuOK, in dry tetrahydrofuran, under a nitrogen atmosphere at 70°C overnight. The final compounds **14b, 14g, 14i, 14k, 14m, 14o,** and **14q,** were obtained from a deprotection reaction of the final compounds **14a, 14f, 14h, 14j, 14l, 14n,** and **14q,**

respectively, with 4N HCl in 1,4-dioxane, in dry tetrahydrofuran, starting from 0°C to room temperature overnight.

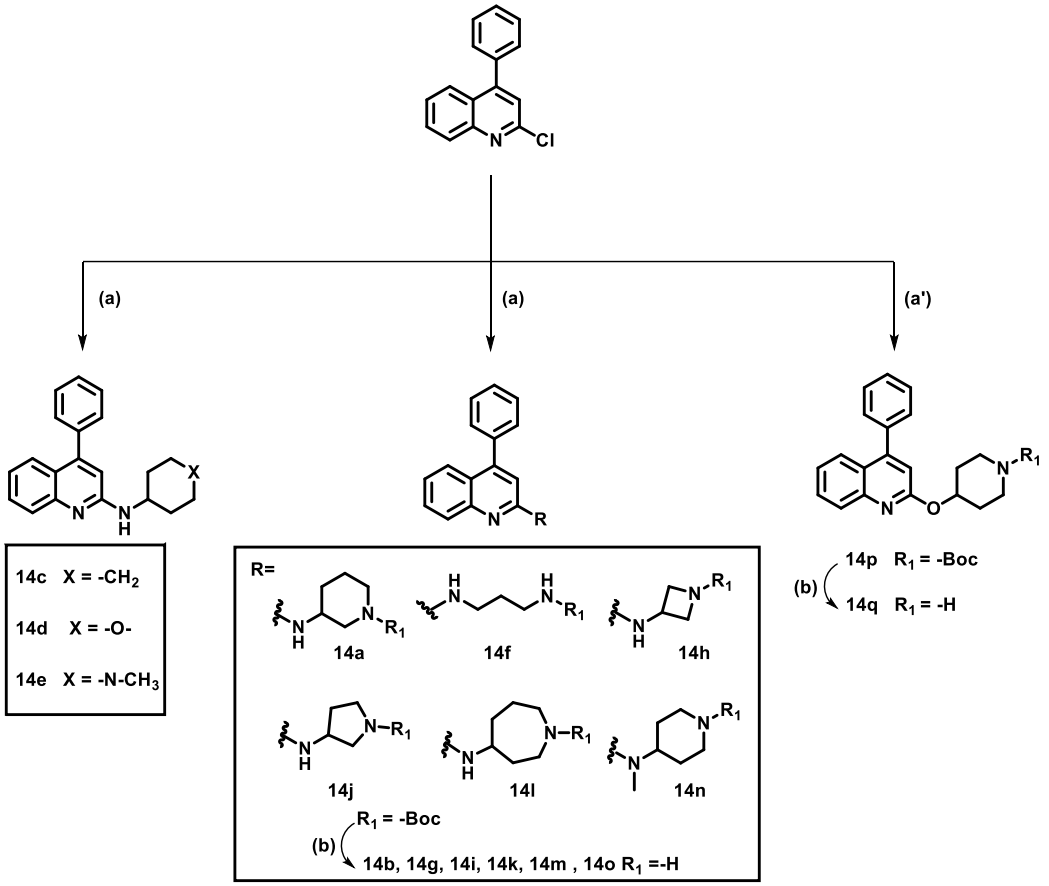

Scheme 3.1. Synthesis of compounds 14a-q. Reagents and conditions. a) Appropriate amine**,** $Pd(OAc)_2$, BINAP, Cs_2CO_3, dry toluene, N_2, 125°C, 12-24 h. **a')** *tert*-butyl-4-hydroxyperidine-1-carboxylate, t-BuOK, dry THF, N_2, 70°C, overnight. **b)** 4N HCl in 1,4-dioxane, dry THF, from 0°C to RT, overnight.

The final compounds **14r, 15a-e, 16a-b,** and **17a-b** have been synthesized following the synthetic scheme reported in **Scheme 3.2**. The Buchwald-Hartwig reaction of the commercially available 2-chloro-4-phenylquinoline with either benzyl 3-aminoazetidine-1-carboxylate or *tert*-butyl 3-aminoazetidine-1-carboxylate was carried out in presence of $Pd(OAc)_2$, BINAP, and Cesium Carbonate. These reagents were solubilized in dry toluene, and the reaction was performed under a nitrogen atmosphere at 125°C, overnight. This process resulted in the obtaining of derivatives **14r** and **14h**, respectively. However, unexpectedly, bisadduct derivatives **15e** and **15a** were also obtained along with the desired products. Compound 15a was then deprotected with 4N HCl in 1,4-dioxane in dry THF from 0 °C to room temperature

overnight, yielding compound **15b**. The subsequent reaction of 15b with either acetyl chloride or benzoyl chloride, in a basic medium by TEA, in dry DCM, from 0 °C to room temperature for 30 minutes, afforded compounds **15c** and **15d**, respectively. Derivative 14h underwent further Buchwald-Hartwig aminations, the first with 2-bromonaphthalene, and the second with 2-bromopyridine as aryl halide under the same conditions as the initial reaction. These reactions led to derivatives **16a** and **17a**, respectively. Both of these Boc-protected compounds were then deprotected with 4N HCl in 1,4-dioxane in dry THF, starting from 0 °C to room temperature for 3 hours, to yield compounds **16b** and **17b**, respectively.

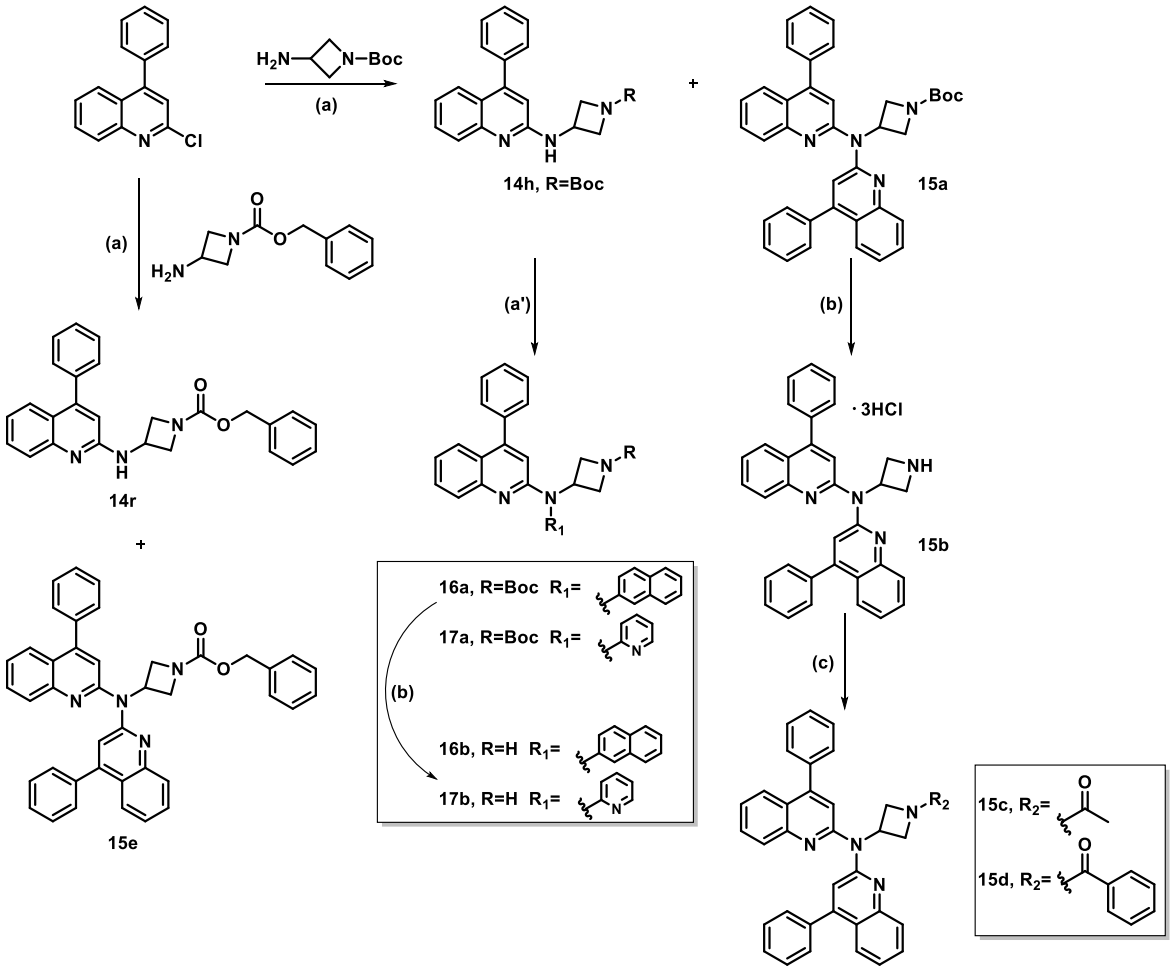

Scheme 3.2. Synthesis of compounds 14h, 14r, 15a-e, 16a-b, and 17a-b. Reagents and conditions. a) $Pd(OAc)_2$, BINAP, Cs_2CO_3, dry toluene, N_2, 125°C, overnight. **a')** 2-bromonaphthalene or 2-bromopyridine, $Pd(OAc)_2$, BINAP, Cs_2CO_3, dry toluene, N_2, 125°C, 24h. **b)** 4N HCl in 1,4-dioxane, dry THF, from 0 °C to RT, 3-12h. **c)** acetyl chloride or benzoyl chloride, TEA, dry DCM, from 0 °C to RT, 30 min.

3.2.2. Biochemical activities of the second series of simplified derivatives towards *human* NOXs

All the compounds were tested against the full length of the *human* NOX isoforms by the group of Professor Andrea Mattevi at Pavia University (**Table 3.1**).

Table 3.1. *Biochemical inhibition data against membrane full-length human NOXs.*

CPD	MOLECULAR STRUCTURE	IC_{50}, μM			
		***h*NOX1 (Amplex Red)**	***h*NOX2 (MCLA)**	***h*NOX4 (Amplex Red)**	***h*NOX5 (Amplex Red)**
10s	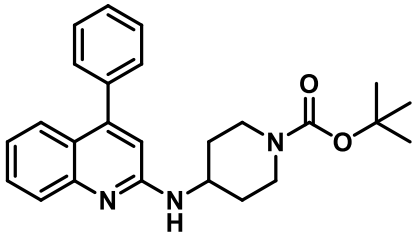	>100	>100	>100	1.6±0.4
10t	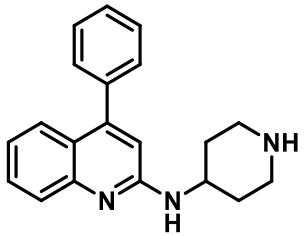	71.2±1.0	7.7±0.1	48.4±4.7	47.9±7.1
14a	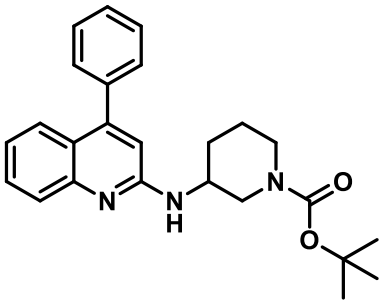	>100	>100	>100	>100
14b	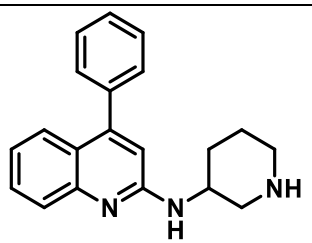	41.8 ± 8.4	85.6 ± 7.2	>100	33.6±1.5

14c	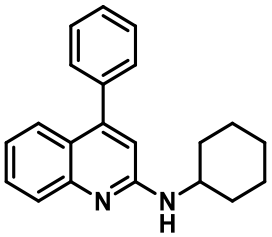	5.6±0.2	>100	>100	>100
14d	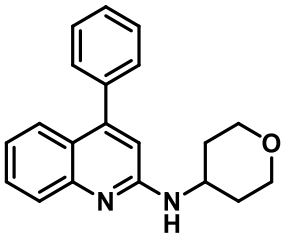	3.4±0.6	>100	>100	>100
14e	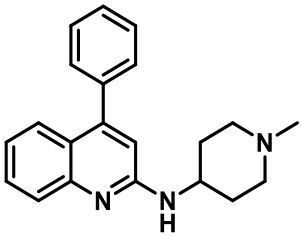	86.1±21.1	16.1±0.7	>100	26.5±1.8
14f	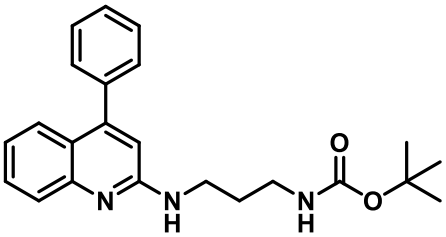	>100	>100	>100	>100
14g	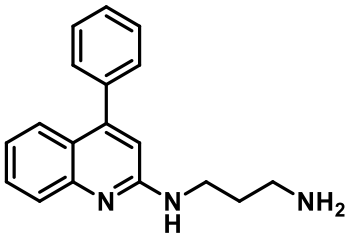	42.9±2.9	26.4±1.4	>100	>100
14h	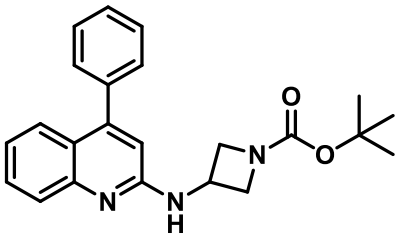	>100	>100	>100	>100
14i	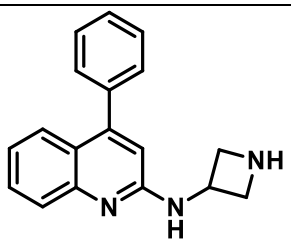	>100	12.7±3.8	>100	>100

14j	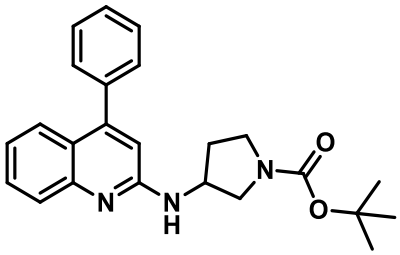	>100	>100	>100	>100
14k	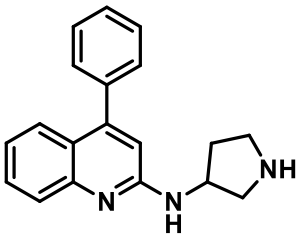	50.3±3.1	>100	>100	39.5±3.5
14l	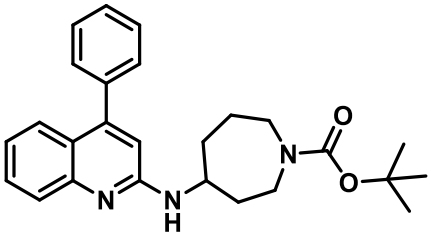	>100	>100	>100	6.1±1.5
14m	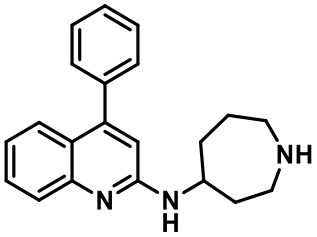	>100	19.3±5.9	>100	>100
14n	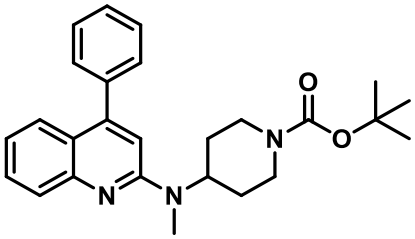	>100	>100	>100	5.0±1.0
14o	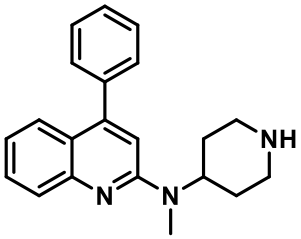	>100	18.3±4.4	>100	>100
14p	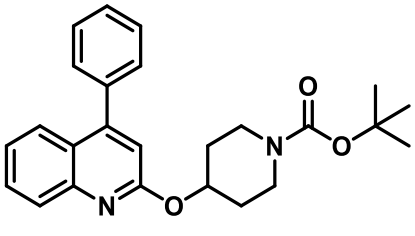	>100	>100	>100	>100

14q	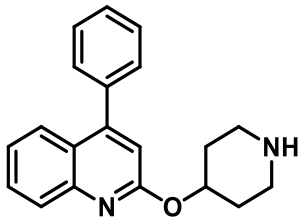	28.9±1.8	11.1±4.9	>100	45.4±9.2
15a	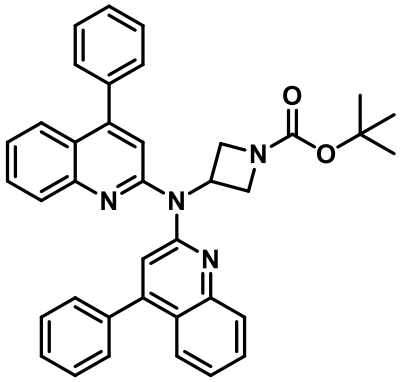	>100	1.4±0.1	>100	>100

The m*eta* isomers (**14a** and **14b**) of lead compounds showed a significant reduction in both potency and selectivity, with compound 14a being completely inactive on NOX isoforms. Substituting the piperidine with cyclohexyl (**14c**) or tetrahydropyran (**14d**) led to a total loss of potency on NOX2 but resulted in selectivity for NOX1, as confirmed by *Ki* values of 8.8 ± 1.8 μM for 14c and, 3.0 ± 0.4 μM for 14d. NOX1 inhibition by **14d** was also confirmed by CETSA on *h*NOX1 (ΔT_m = +1.04 °C). In contrast, adding a methyl group to the piperidine nitrogen (**14e**) caused a loss of potency, and, also selectivity, on NOX2. When studying the biochemical profile of the *seco*-derivatives (**14f** and **14g**) we observed the complete loss of potency in the protected derivative (14f) and recovery of a slight selectivity towards NOX2 with the deprotected one (14g). Similarly, the Boc-protected azetidine derivative **14h** showed no inhibition activity against all NOX isoenzymes, but its deprotected form (**14i**) displayed selectivity against NOX2, anyway with an IC_{50} value twice lower than the lead compound 10t. Introducing a 3-amino pyrrolidine group at position 2 of the 4-phenyl quinoline (**14j** and **14k**) yielded IC_{50} values comparable to those seen for *meta* isomers, suggesting that the position of the endocyclic amino group is critical. Conversely, the upper cyclic homologues (**14l** and **14m**) restored the selectivity profile of the two initial piperidine prototypes 10s and 10t, albeit with reduced potency. Exploring the exocyclic nitrogen of the piperidine ring, we tested Boc-protected derivative **14n** and its corresponding deprotected amine **14o**, which maintained the selectivity profile for NOX5 and NOX2, respectively, similar to the lead compounds. However, the hydroxy derivatives **14p** and **14q**, indeed, lost both selectivity and potency.

During the Buchwald-Hartwig cross-coupling reaction to synthesize the protected azetidine derivative 14h (inactive against all NOX isoforms), we unexpectedly obtained the bisquinolinic derivative **15a**, which we decided to test. This turned out to be our most promising NOX2 inhibitor among all the tested derivatives, with an IC_{50} value of 1.4 μM against NOX2 and a complete loss of inhibitory potency against all the other NOX isoforms. Its efficacy was confirmed by K_i (2.1 ± 0.2 μM) on *h*NOX2, IC_{50} in PLB-985 cells, that overexpress NOX2, (2.2 ± 1.5 μM) and CETSA on cell membrane (ΔT_m = +6.0 °C).

After these promising results, we synthesized analogues of derivative 15a and tested them against NOX2, to explore the possibility of having an improvement in the potency and explore the contribution of the various chemical moiety of the molecule (**Table 3.2**).

Table 3.2. *Percentage of inhibition of derivatives **14r**, **15b-e**, **16a-b**, and **17a-b** against NOX2.*

CPD	MOLECULAR STRUCTURE	% INHIBITION NOX2 (MCLA assay) [10 μM]
15b	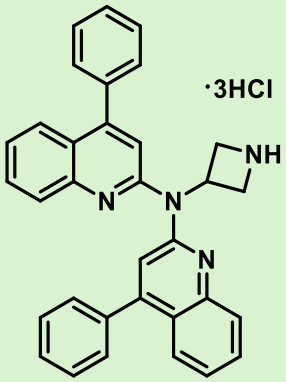	32.3
15c	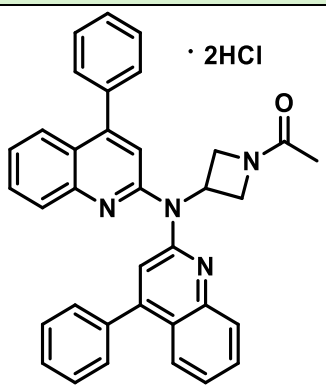	23.5

15d	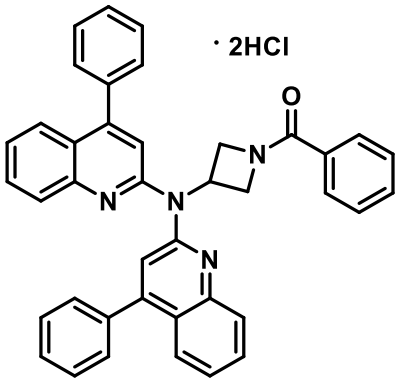	22.0
14r	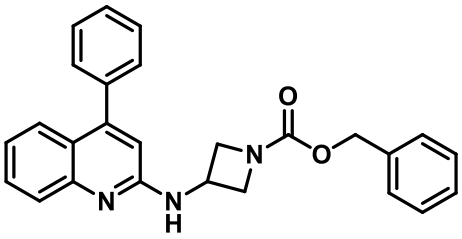	17.2
15e	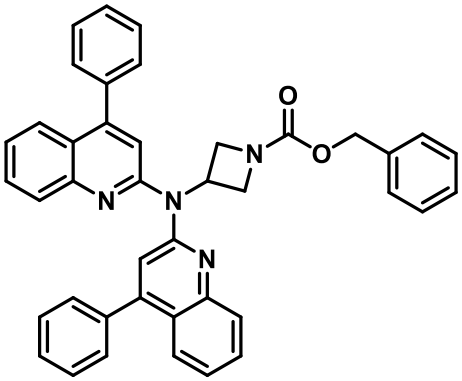	15.6
16a	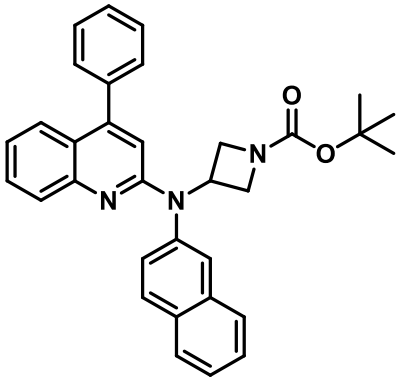	22.1
16b	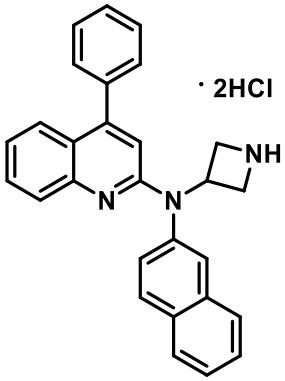	29.5

17a	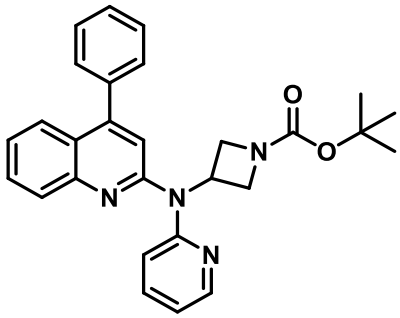	12.1
17b	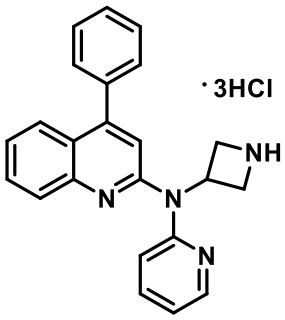	12.4

The synthesized compounds generally exhibited low levels of inhibition against NOX2, with inhibition values not exceeding 30%. The only exception was the deprotected derivative 15b, which showed a slightly higher inhibition of 32.3%. The introduction of acyl groups, such as acetyl (in compound **15c**) and benzoyl (in compound **15d**), led to a reduction in inhibitory potency. Furthermore, the replacement with benzyl carbamate was poorly tolerated, as seen in both the mono and bis adduct derivatives, **14r** and **15e,** respectively. When the 4-phenylquinoline moiety was substituted with a naphthalene ring, neither the Boc-protected derivative **16a** nor the deprotected variant **16b** demonstrated improved inhibition on NOX2. Despite this, the naphthalene substitution was better tolerated than replacing the same moiety with a pyridine ring, as the pyridine-based derivatives **17a** and **17b** showed the lowest inhibition values of all compounds tested. For a direct comparison with the bisquinolinic derivative **15a**, the IC_{50} value of **15b**, the compound with the highest percentage of inhibition, was calculated. However, it displayed an IC_{50} value of 8.4 ± 1.9 μM against NOX2, much less potent than **15a,** which had an IC_{50} of 1.4 ± 0.1 μM. This result suggests that structural modifications to the compound 15a led to decreased inhibitory effects and **15a** remained the most potent NOX2 inhibitor among those tested.

3.2.3. Effects of selective NOX1 and -2 inhibitors in Kras^{G12D} colorectal cancer cells

The relationship between **IKKα (IκB kinase α)** inactivation and tumor development is well established, particularly in cancers driven by **Kras mutations**. As explored by Song *et al.* in 2018, KRAS-activating mutations are often accompanied by the loss of IKKα function, which leads to an increase in NOX2 levels. [347] This imbalance plays a critical role in cancer progression. When IKKα is inactivated, the antitumorigenic effects of Kras-induced ROS are reversed, shifting to a protumorigenic effect. This transformation enhances cancer progression by promoting oxidative stress and survival pathways that support Kras-driven oncogenesis. The loss of IKKα disrupts the cellular redox balance, which typically helps to suppress tumor formation under normal conditions, thus exacerbating Kras's oncogenic potential. This finding builds on research, such as Shaw *et al.* in 2011 [348] and Lim *et al.* in 2019, [349] which also highlight the critical role of IKKα in maintaining redox homeostasis and preventing tumorigenesis. The cumulative evidence underscores how IKKα inactivation can convert the natural defense mechanisms against Kras-induced oxidative stress into drivers of cancer growth, particularly through the upregulation of NOX2, which amplifies the production of ROS in tumor cells. In summary, IKKα ablation, in combination with Kras mutations, leads to a fundamental shift in ROS signaling from tumor suppression to tumor promotion, further driving cancer progression through elevated NOX2 activity.

For this reason, we decided to verify whether NOX inhibition could enhance the effect of the ***KRAS^{G12D}*** inhibitor **MRTX1133** in colorectal cancer cells, particularly those harboring the *KRAS^{G12D}* mutation. The research was conducted in collaboration with Prof. Haribabu Arthanari's team at Harvard Medical School. For the study, four NOX inhibitors were selected. These included the lead **compound M41**, then the first simplified derivative **10t**, which came out as a NOX2 selective inhibitor, the NOX1 selective inhibitor **14d,** and, finally, the bisadduct derivative **15a,** which emerged as the most potent and selective NOX2 inhibitor. The experimental work involved using 293T cells as negative control, along with three colorectal cancer cell lines: LS513, LS180, and LS174T. Notably, the LS513 and LS180 cancer cell lines possess the *KRAS^{G12D}* mutation, which was a key focus of the study. The results demonstrated that combining NOX1 and NOX2 inhibitors with MRTX1133 significantly enhanced its efficacy, indicating a potential therapeutic approach for *KRAS* mutant cancers. Specifically, the NOX1 inhibitor **14d** and, even

more effectively, the NOX2 inhibitor **15a** synergized with MRTX1133, particularly in the LS513 cancer cell line, which carries the *KRAS*^{G12D} mutation (**Figure 3.2**). These outcomes indicate that inhibiting NOX1 and, to an even greater extent NOX2, could potentially increase the therapeutic response to *KRAS*^{G12D}-targeted treatments in colorectal cancer.

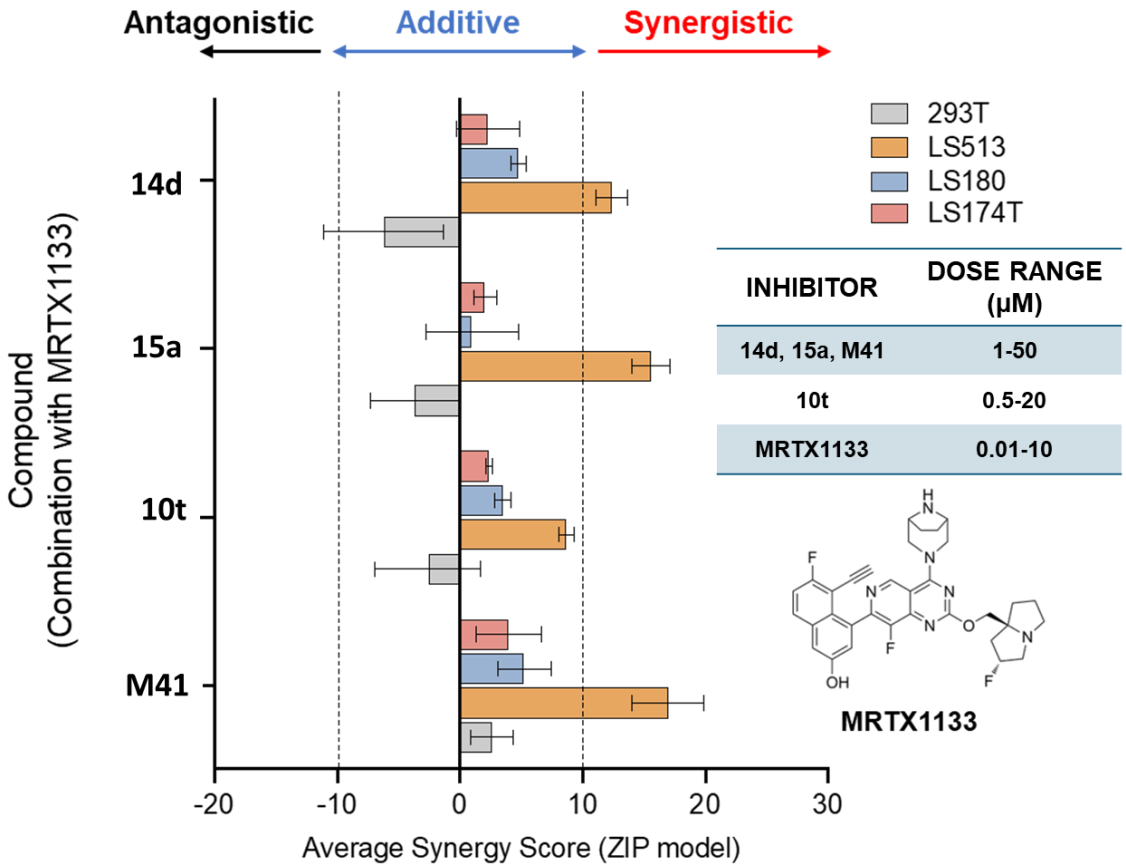

Figure 3.2. *Evaluation of synergism in drug combinations of NOX inhibitors and KRAS*^{G12D} *inhibitor MRTX1133.*

3.3. Conclusions

The research described focuses on the synthesis and biochemical evaluation of quinoline-based simplified derivatives aimed at inhibiting NOX isoforms, particularly NOX2 and NOX5. Starting with two lead compounds, 10t and 10s, which exhibited selectivity and potency for NOX2 and NOX5, respectively, the study explored modifications in the piperidine scaffold and other chemical structures to further enhance these properties. Derivatives were synthesized by altering the piperidine groups, and the nitrogens, both exocyclic and endocyclic, to study their effects on NOX inhibition. The results revealed that certain modifications led to a complete loss of potency or selectivity, while others maintained or slightly improved inhibitory profiles. Unexpectedly, during the synthesis of one derivative (**14h**), a bisquinolinic compound (**15a**) was obtained, which turned out to be the most promising NOX2 inhibitor, with high selectivity and potency. Following this discovery, a series of analogues of 15a were synthesized, but none surpassed its inhibitory effectiveness, indicating that 15a's structure plays a critical role in its activity. Moreover, the substitution of different chemical groups, including the replacement of the quinoline moiety with naphthalene or pyridine groups, generally resulted in diminished NOX2 inhibition. The study also explored the potential therapeutic relevance of our selective NOX inhibitors in *KRAS*-mutant colorectal cancer, where NOX2, particularly, is upregulated due to IKKα inactivation. It was found that selective inhibition of NOX1 and NOX2 could enhance the efficacy of the $KRAS^{G12D}$ inhibitor MRTX1133, particularly in cancer cells harboring the $KRAS^{G12D}$ mutation. Among the tested inhibitors, compound 15a emerged as the most effective in combination with MRTX1133, indicating a potential for NOX inhibition to improve treatment outcomes in KRAS-driven cancers. Overall, the study demonstrates the importance of specific structural features for NOX selectivity and potency and suggests a therapeutic application in enhancing the effects of KRAS inhibitors in colorectal cancer.

3.4. Experimental section

3.4.1. Chemistry

Melting points were determined on a Buchi 530 melting point apparatus. ^{1}H NMR and ^{13}C NMR spectra were recorded at 400 MHz on a Bruker AC 400 spectrometer; chemical shifts are reported in δ (ppm) units relative to the internal reference tetramethyl silane (Me_4Si). All compounds were routinely checked by TLC, ^{1}H NMR, and ^{13}C NMR spectra. TLC was performed on aluminum-backed silica gel plates (Merck DC, Alufolien Kieselgel 60 F254) with spots visualized by UV light. All solvents were reagent grade and, when necessary, were purified and dried by standard methods. The concentration of solutions after reactions and extractions involved using a rotary evaporator operating at a reduced pressure of ca. 20 Torr. Organic solutions were dried over anhydrous sodium sulfate. Elemental analysis has been used to determine the purity of the described compounds, which is >95 %. Analytical results are within ± 0.40 % of the theoretical values (Table S1 in Supporting Information). All chemicals were purchased from Sigma Aldrich, Milan (Italy), Alfa Aesar, Karlsruhe (Germany), Fluorochem, Manchester (UK), or BLD-Pharma, Kaiserslautern (Germany) and were of the highest purity.

General procedure for the synthesis of the final compounds 14a, 14c-f, 14h, 14j, 14l, 14n, 14r, 15a, and 15e.

Example: Synthesis of *Tert*-butyl 3-((4-phenylquinolin-2-yl)amino)azetidine-1-carboxylate (14h)

To a solution of 2-chloro-4-phenylquinoline (0.417 mmol, 100 mg), the *Tert*-butyl 3-aminoazetidine-1-carboxylate (0.834 mmol, 0.13 mL) in dry toluene was added. After, $Pd(OAc)_2$ (0.0217 mmol, 4.87 mg), BINAP (0.00517 mmol, 3.22 mg), and Cs_2CO_3 (1.252 mmol, 407.8 mg) were added. The mixture was stirred under a nitrogen atmosphere at 125°C for 4 hours. Then, the reaction was quenched with distilled water and extracted with AcOEt (3x15 mL). The organic extracts were collected, washed with brine, dried with sodium sulfate, and concentrated under reduced pressure. The obtained crude was purified by column chromatography (SiO_2, eluting with ethyl acetate/n-hexane 1:3) to obtain 52.7 mg of the pure compound **14h** as a white solid.

M.p. 169-171°C; recrystallization solvent: toluene/acetonitrile; yield: 45.9%; ^{1}H-NMR ($CDCl_3$, 400 MHz, δ, ppm): 1.39 (s, 9H, -Boc), 3.79 (dd, 2H, -C*H*$_2$ azetidine), 4.32 (dd, 2H, -C*H*$_2$ azetidine), 4.73-4.81 (m, 1H, -C*H* azetidine), 5.08 (bs, 1H, -N*H*), 6.48 (s, 1H, aromatic proton quinoline), 7.13 (td, 1H, aromatic proton quinoline), 7.37-7.45 (m, 5H, aromatic protons phenyl), 7.49 (td, 1H, aromatic proton quinoline), 7.57 (dd, 1H, aromatic proton quinoline), 7.68 (dd, 1H, aromatic proton quinoline).

14a, tert-butyl 3-((4-phenylquinolin-2-yl)amino)piperidine-1-carboxylate: M.p. 95-100 °C; recrystallization solvent: cyclohexane/toluene; yield: 49.7 %; ^{1}H-NMR ($CDCl_3$, 400 MHz, δ, ppm): 1.41 (s, 9H, -Boc), 1.64-1.70 (m, 1H, -CHC*H*HCH$_2$- piperidine), 1.78-1.81 (m, 2H, -CHCH$_2$C*H*H- and -CHC*H*HCH$_2$- piperidine), 1.98-2.13 (m, 1H, -CHCH$_2$CH*H*- piperidine), 3.26-3.29 (m, 2H, -CHC*H*HN- and -CH$_2$CH$_2$C*H*HN- piperidine), 3.61-3.65 (m, 1H, -CH$_2$CH$_2$CH*H*N- piperidine), 3.95-3.99 (m, 1H, -CHCH*H*N- piperidine), 4.04-4.14 (m, 1H, -C*H*- piperidine), 4.80 (bs, 1H, -N*H*), 6.60 (s, 1H, aromatic proton quinoline), 7.19 (td, 1H, aromatic proton quinoline), 7.47-7.58 (m, 6H, 1 aromatic proton quinoline and 5 aromatic protons phenyl), 7.64 (dd, 1H, aromatic proton quinoline), 7.75 (dd, 1H, aromatic proton quinoline).

14c, N-cyclohexyl-4-phenylquinolin-2-amine: M.p. 140-142 °C; recrystallization solvent: toluene; yield: 36.5 %; ^{1}H-NMR ($CDCl_3$, 400 MHz, δ, ppm): 1.32-1.34 (m, 2H, -CH$_2$CH$_2$C*H*$_2$CH$_2$- cyclohexane), 1.36-4.43 (m, 2H, -CH$_2$C*H*$_2$CH$_2$- cyclohexane), 1.57-1.62 (m, 2H, -CHC*H*$_2$CH$_2$- cyclohexane), 1.69-1.78 (m, 2H, -CH$_2$C*H*$_2$CH$_2$- cyclohexane), 2.03-2.07 (m, 2H, -CHC*H*$_2$CH$_2$- cyclohexane), 3.74-3.81 (m, 1H, -C*H*- cyclohexane), 4.69 (bs, 1H, -N*H*), 6.5 (s, 1H, aromatic proton quinoline), 7.04 (dt, 1H, aromatic proton quinoline), 7.39-7.47 (m, 6H, 1 aromatic proton quinoline and 2 aromatic protons phenyl), 7.53 (dd, 1H, aromatic proton quinoline), 7.62 (dd, 1H, aromatic proton quinoline).

***14d, 4-phenyl-N-(tetrahydro-2H-pyran-4-yl)quinolin-2-amine*:** M.p. 205-207 °C; recrystallization solvent: acetonitrile/methanol; yield: 60.9 %; ^{1}H-NMR ($CDCl_3$, 400 MHz, δ, ppm): 1.47-1.57 (m, 2H, -C*H*HCH$_2$O- and -C*H*HCH$_2$O- tetrahydropyran), 2.06-2.09 (m, 2H, -C*H*HCH$_2$O- and -C*H*HCH$_2$O- tetrahydropyran), 3.50-3.57 (m, 2H, -CH$_2$CH*H*O- and -CH$_2$CH*H*O- tetrahydropyran), 3.94-3.98 (m, 2H, -CH$_2$CH*H*O- and -CH$_2$CH*H*O- tetrahydropyran), 4.10-4.19 (m, 1H, -C*H* tetrahydropyran), 4.62 (bs, 1H, -N*H*), 6.48 (s, 1H, aromatic proton quinoline), 7.09 (td, 1H, aromatic proton quinoline), 7.38-7.49 (m, 6H, 1 aromatic proton quinoline and 5 aromatic protons phenyl), 7.54 (dd, 1H, aromatic proton quinoline), 7.65 (dd, 1H, aromatic proton quinoline).

***14e, N-(1-methylpiperidin-4-yl)-4-phenylquinolin-2-amine*:** M.p. 117-122 °C; recrystallization solvent: cyclohexane/toluene; yield: 32.8 %; ^{1}H-NMR ($CDCl_3$, 400 MHz, δ, ppm): 1.59-1.68 (m, 2H, -CHC*H*$_2$- piperidine), 2.16-2.26 (m, 4H, -CHC*H*$_2$- and -C*H*$_2$N- piperidine), 2.34 (s, 3H, -C*H*$_3$), 2.86 (d, 2H, -C*H*$_2$N- piperidine, J = 11.6Hz), 3.98-4.02 (m, 1H, -C*H* piperidine), 4.70 (d, 2H, -*CH*$_2$N- piperidine, J=7.6 Hz), 6.58 (s, 1H, aromatic proton quinoline), 7.16 (td, 1H, aromatic proton quinoline), 7.48-7.57 (m, 6H, 1 aromatic proton quinoline and 5 aromatic protons phenyl), 7.63 (dd, 1H, aromatic proton quinoline), 7.74 (dd, 1H, aromatic proton quinoline).

***14f, tert-butyl (3-((4-phenylquinolin-2-yl)amino)propyl)carbamate*:** M.p. 118-120 °C; recrystallization solvent: cyclohexane/toluene; yield: 25.8 %; ^{1}H-NMR ($CDCl_3$, 400 MHz, δ, ppm): 1.43 (s, 9H, -Boc), 1.70-1.76 (m, 2H, -NHCH$_2$C*H*$_2$CH$_2$NHCO-), 3.18 (q, 2H, -NHCH$_2$CH$_2$C*H*$_2$NHCO-), 3.62 (q, 2H, -NHC*H*$_2$CH$_2$CH$_2$NHCO-), 4.99 (s, 1H,-N*H*CO-), 6.16 (s, 1H, -N*H*-), 6.47 (s, 1H, aromatic proton quinoline), 7.09 (td, 1H, aromatic proton quinoline), 7.37-7.48 (m, 6H, 1 aromatic proton quinoline and 5 aromatic protons phenyl), 7.54 (dd, 1H, aromatic proton quinoline), 7.76 (dd, 1H, aromatic proton quinoline).

14j, tert-butyl 3-((4-phenylquinolin-2-yl)amino)pyrrolidine-1-carboxylate: M.p. 88-91 °C; recrystallization solvent: cyclohexane/toluene; yield: 74.2 %; ^{1}H-NMR ($CDCl_3$, 400 MHz, δ, ppm): 1.50 (s, 9H, -Boc), 2.01-2.07 (m, 1H, -CHC*H*HCH$_2$- pyrrolidine), 2.33-2.34 (m, 1H, -CHCH*H*CH$_2$- pyrrolidine), 3.28-3.39 (m, 1H, -CH$_2$C*H*HN- pyrrolidine), 3.52-3.55 (m, 2H, -CH$_2$C*H*HN- and -CHCH*H*N- pyrrolidine), 3.83-3.84 (m, 1H, -CHC*H*HN- pyrrolidine), 4.70-4.78 (m, 2H, -C*H* pyrrolidine and -N*H*), 6.59 (s, 1H, aromatic proton quinoline), 7.21 (td, 1H, aromatic proton quinoline), 7.47-7.59 (m, 6H, 1 aromatic proton quinoline and 5 aromatic protons phenyl), 7.65 (dd, 1H, aromatic proton quinoline), 7.77 (dd, 1H, aromatic proton quinoline).

14l, tert-butyl 4-((4-phenylquinolin-2-yl)amino)azepane-1-carboxylate: M.p. 105-107 °C; recrystallization solvent: cyclohexane/toluene; yield: 43.2 %; ^{1}H-NMR ($CDCl_3$, 400 MHz, δ, ppm): 1.41 (s, 9H, -Boc), 1.53-1.72 (m, 3H, -CHC*H*HCH$_2$N-, -CHC*H*HCH$_2$CH$_2$- and -CHCH$_2$C*H*HCH$_2$- cycloheptane), 1.80-1.85 (m, 1H, -CHCH*H*CH$_2$N- cycloheptane), 1.98-2.06 (m, 1H, -CHCH$_2$CH*H*CH$_2$- cycloheptane), 2.13-2.20 (m, 1H, -CHCH*H*CH$_2$CH$_2$- cycloheptane), 2.56-2.59 (m, 1H, -CHCH$_2$CH$_2$C*H*H- cycloheptane), 3.19-3.26 (m, 1H, -CHCH$_2$C*H*HN- cycloheptane), 3.45-3.53 (m, 2H, -CHCH$_2$CH$_2$CH*H*- and -CHCH$_2$C*H*HN- cycloheptane), 4.07-4.09 (m, 1H, -C*H* cycloheptane), 4.68 (bs, 1H, -N*H*), 6.46 (s, 1H, aromatic proton quinoline), 7.09 (td, 1H, aromatic proton quinoline), 7.38-7.48 (m, 6H, 1 aromatic proton quinoline and 5 aromatic protons phenyl), 7.53 (dd, 1H, aromatic proton quinoline), 7.65 (dd, 1H, aromatic proton quinoline).

***14n, tert-butyl 4-(methyl(4-phenylquinolin-2-yl)amino)piperidine-1-carboxylate*:** M.p. 105-110 °C; recrystallization solvent: cyclohexane/toluene; yield: 5.8 %; ^{1}H-NMR ($CDCl_3$, 400 MHz, δ, ppm): 1.42 (s, 9H, -Boc), 1.58-1.69 (m, 4H, -CHC*H*$_2$- piperidine), 2.79-2.89 (m, 2H, -CH*H*N- and -CH*H*N- piperidine), 2.94 (s, 3H, -C*H*$_3$), 4.13-4.25 (m, 2H, -CH*H*N- and -CH*H*N- piperidine), 4.84-4.94 (m, 1H, -C*H* piperidine), 6.72 (s, 1H, aromatic proton quinoline), 7.04-7.07 (m, 1H, aromatic proton quinoline), 7.38-7.49 (m, 6H, 1 aromatic proton quinoline and 5 aromatic protons phenyl), 7.52 (dd, 1H, aromatic proton quinoline), 7.67 (dd, 1H, aromatic proton quinoline).

14r, benzyl 3-((4-phenylquinolin-2-yl)amino)azetidine-1-carboxylate: M.p. 159-160 °C; recrystallization solvent: toluene/acetonitrile; yield: 33.1 %; ^{1}H-NMR ($CDCl_3$, 400 MHz, δ, ppm): 3.89-3.92 (m, 2H, -C*H*$_2$ azetidine), 4.38-4.43 (m, 2H, -C*H*$_2$ azetidine), 4.79-4.80 (m, 1H, -C*H* azetidine), 5.05 (s, 2H, -CH_2 benzyl), 6.48 (s, 1H, -NH-), 7.13-7-17 (m, 1H, aromatic protons), 7.23-7.25 (m, 2H, aromatic protons), 7.27-7.30 (m, 4H, aromatic protons), 7.37-7.39 (m, 2H, aromatic protons), 7.41-7.44 (m, 3H, aromatic protons), 7.48-7.52 (m, 1H, aromatic proton), 7.58 (dd, 1H, aromatic proton), 7.68 (dd, 1H, aromatic proton).

15a, tert-butyl 3-(bis(4-phenylquinolin-2-yl)amino)azetidine-1-carboxylate: M.p. 98-100 °C; recrystallization solvent: cyclohexane/toluene; yield: 21.29 %; ^{1}H-NMR ($CDCl_3$, 400 MHz, δ, ppm): 1.47 (s, 9H, -Boc), 4.28-4.32 (m, 2H, -C*H*$_2$ azetidine), 4.45-4.49 (m, 2H, -C*H*$_2$ azetidine), 5.47-5.54 (m, 1H, -C*H* azetidine), 7.22 (s, 2H, aromatic protons quinoline), 7.38-7.42 (m, 2H, aromatic protons quinoline), 7.45-7.53 (m, 10H, aromatic protons phenyl), 7.67-7.71 (m, 2H, aromatic protons quinoline), 7.82 (dd, 2H, aromatic protons quinoline), 8.00 (dd, 2H, aromatic protons quinoline).

15e, benzyl 3-(bis(4-phenylquinolin-2-yl)amino)azetidine-1-carboxylate: M.p. 88-90 °C; recrystallization solvent: cyclohexane/toluene; yield: 15.3 %; ^{1}H-NMR ($CDCl_3$, 400 MHz, δ, ppm): 4.02-4.08 (m, 2H, -C*H*$_2$ azetidine), 4.31-4.35 (m, 2H, -C*H*$_2$ azetidine), 4.44-4.53 (m, 1H, -C*H* azetidine), 5.04 (s, 2H, -CH_2 benzyl), 7.10 (s, 2H, aromatic protons), 7.21-7.24 (m, 2H, aromatic protons), 7.26-7.30 (m, 4H, aromatic protons), 7.30-7.32 (m, 2H, aromatic protons), 7.34-7.39 (m, 4H, aromatic protons), 7.41-7.43 (m, 7H, aromatic protons), 7.61 (t, 2H, aromatic protons, J=8 Hz), 7.71 (d, 2H, aromatic protons, J=8 Hz).

General procedure for the synthesis of the final compound *Tert*-butyl 4-((4-phenylquinolin-2-yl)oxy)piperidine-1-carboxylate (14p)

To a solution of 2-chloro-4-phenylquinoline (0.0834 mmol, 20 mg) in dry tetrahydrofuran, *tert*-butyl-4-hydroxyperidine-1-carboxylate (0.0834 mmol, 16.8 mg) and t-BuOK (0.0834 mmol, 9.34 mg) were added at 0°C under nitrogen atmosphere. The mixture was stirred at 70°C overnight. Then, the reaction was quenched with distilled water and extracted with AcOEt (3x15 mL). The organic extracts were collected, washed with brine, dried with sodium sulfate, and concentrated under reduced pressure. The obtained crude was purified by column chromatography (SiO_2, eluting with ethyl acetate/n-hexane 1:10) to obtain 40 mg of the pure compound **14p** as a white solid.

M.p. 110-115°C; recrystallization solvent: cyclohexane/toluene; yield: 98%; ^{1}H-NMR ($CDCl_3$, 400 MHz, δ, ppm): 1.42 (s, 9H, -Boc), 1.71-1.79 (m, 2H, -CHC*H*$_2$- piperidine), 1.99-2.04 (m, 2H, -CHC*H*$_2$- piperidine), 3.27-3.33 (m, 2H, -C*H*$_2$N- piperidine), 3.72-3.75 (m, 2H, -*CH*$_2$N- piperidine), 5.45-5.53 (m, 1H, -C*H* piperidine), 6.75 (s, 1H, aromatic proton quinoline), 7.25 (td, 1H, aromatic proton quinoline), 7.38-7.46 (m, 5H, aromatic protons phenyl), 7.54 (td, 1H, aromatic proton quinoline), 7.68 (dd, 1H, aromatic proton quinoline), 7.79 (dd, 1H, aromatic proton quinoline).

General procedure for the synthesis of the final compounds 14b, 14g, 14i, 14k, 14m, 14o, and 14q.

Example: Synthesis of 4-phenyl-2-(piperidin-4-yl)oxy)quinoline (14q)

To a solution of *tert*-butyl 4-((4-phenylquinolin-2-yl)oxy)piperidine-1-carboxylate (**14p**) (0.0729 mmol, 29.5 mg) in dry tetrahydrofuran, 4N HCl in 1,4-dioxane (0.367 mmol, 0.09 mL) was added at 0°C. The mixture was stirred at room temperature overnight. Then, the reaction was quenched with a saturated solution of Na_2CO_3 and extracted with AcOEt. The organic extracts were collected, washed with brine, dried with sodium sulfate, and concentrated under reduced pressure. The obtained crude was purified by column chromatography (SiO_2, eluting with chloroform/methanol/NH_3 60:1:0.1) to obtain 12.7 mg of the pure compound **14q** as an oil.

M.p. n.d.; yield: 57.2 %; ^{1}H-NMR ($CDCl_3$, 400 MHz, δ, ppm): 1.75-1.83 (m, 2H, -CHC*H*$_2$- piperidine), 2.12-2.17 (m, 2H, -CHC*H*$_2$- piperidine), 2.85-2.91 (m, 2H, -

C*H*$_2$N- piperidine), 3.13-3.19 (m, 2H, -C*H*$_2$N- piperidine), 3.43-3.81 (m, 1H, -N*H* piperidine), 5.41-5.47 (m, 1H, -C*H* piperidine), 7.19 (s, 1H, aromatic proton quinoline), 7.25 (td, 1H, aromatic proton quinoline), 7.43 (m, 5H, aromatic protons phenyl), 7.53 (td, 1H, aromatic proton quinoline), 7.68 (dd, 1H, aromatic proton quinoline), 7.79 (dd, 1H, aromatic proton quinoline).

14b, 4-phenyl-N-(piperidin-3-yl)quinolin-2-amine: M.p. 115-117 °C; recrystallization solvent: cyclohexane/toluene; yield: 28.4 %; ^{1}H-NMR ($CDCl_3$, 400 MHz, δ, ppm): 1.63-1.77 (m, 4H, -CHC*H*$_2$C*H*$_2$CH$_2$- piperidine), 1.90-2.00 (m, 1H, -CHC*H*HNH- piperidine), 2.61-2.73 (m, 2H, -CH$_2$C*H*$_2$NH- piperidine), 2.82-2.86 (m, 1H, -CHCH*H*NH- piperidine), 3.23 (dd, 1H, -N*H* piperidine), 4.04-4.06 (m, 1H, -C*H* piperidine), 5.06 (bs, 1H, -N*H*), 6.53 (s, 1H, aromatic proton quinoline), 7.07-7.09 (m, 1H, aromatic proton quinoline), 7.36-7.47 (m, 6H, 1 aromatic proton quinoline and 5 aromatic protons phenyl), 7.55 (dd, 1H, aromatic proton quinoline), 7.65 (dd, 1H, aromatic proton quinoline).

***14g, N1-(4-phenylquinolin-2-yl)propane-1,3-diamine*:** M.p. n.d.; yield: 47.6 %; ^{1}H-NMR ($CDCl_3$, 400 MHz, δ, ppm): 1.72-1.79 (m, 4H, -NHC*H*$_2$C*H*$_2$CH$_2$NHCO-), 1.91 (m, 1H, -N*H*), 2.81 (bs, 2H, -N*H*$_2$); 3.57 (t, 2H, -NHCH$_2$CH$_2$C*H*$_2$NHCO-), 6.49 (s, 1H, aromatic proton quinoline), 7.06 (td, 1H, aromatic proton quinoline), 7.37-7.47 (m, 6H, 1 aromatic proton quinoline and 5 aromatic protons phenyl), 7.53 (dd, 1H, aromatic proton quinoline), 7.65 (dd, 1H, aromatic proton quinoline).

***14i, N-(azetidin-3-yl)-4-phenylquinolin-2-amine*:** M.p. n.d.; yield: 12.7 %; ^{1}H-NMR ($CDCl_3$, 400 MHz, δ, ppm): 1.84 (s, 1H , -N*H* azetidine), 2.79-2.84 (m, 1H, -CHC*H*HNH- azetidine), 2.98-3.02 (m, 1H, -CHC*H*HNH- azetidine), 3.70-3.85 (m, 1H, -CHC*H*HNH- azetidine), 4.06-4.11 (m, 1H, -CHC*H*HNH- azetidine), 4.30-4.33 (m, 1H, -C*H* azetidine), 6.53 (s, 1H, aromatic proton quinoline), 6.80 (d, 1H, -N*H*, J = 8.4 Hz), 6.88 (td, 1H, aromatic proton quinoline), 7.25 (dd, 1H, aromatic proton quinoline), 7.31-7.43 (m, 7H, 2 aromatic protons quinoline and 5 aromatic protons phenyl).

14k, 4-phenyl-N-(pyrrolidin-3-yl)quinolin-2-amine: M.p. 80-85 °C; recrystallization solvent: cyclohexane/toluene; yield: 31.2 %; ^{1}H-NMR ($CDCl_3$, 400 MHz, δ, ppm): 1.76-1.84 (m, 1H, -CHC*H*HCH$_2$- pyrrolidine), 1.98-2.03 (m, 1H, -N*H* pyrrolidine), 2.27-2.36 (m, 1H, -CHCH*H*CH$_2$- pyrrolidine), 2.96-3.09 (m, 2H, -CHCH*H*NH- and -CH$_2$C*H*HNH- pyrrolidine), 3.17-3.23 (m, 1H, -CHC*H*HNH- pyrrolidine), 3.31-3.38 (m, 1H, -CH$_2$CH*H*NH- pyrrolidine), 4.54-4.62 (m, 1H, -C*H* pyrrolidine), 4.99 (bs, 1H, -N*H*), 6.60 (s, 1H, aromatic proton quinoline), 7.15-7.20 (m, 1H, aromatic proton quinoline), 7.46-7.58 (m, 6H, 1 aromatic proton quinoline and 5 aromatic protons phenyl), 7.64 (dd, 1H, aromatic proton quinoline), 7.75 (dd, 1H, aromatic proton quinoline).

14m, N-(azepan-4-yl)-4-phenylquinolin-2-amine: M.p. n.d.; yield: 18.5 %; ^{1}H-NMR ($CDCl_3$, 400 MHz, δ, ppm): 3.20-3.26 (m, 1H, -CHC*H*HCH$_2$N- cycloheptane), 3.42-3.48 (m, 2H, -CHC*H*HCH$_2$CH$_2$- and -CHCH$_2$C*H*HCH$_2$- cycloheptane), 3.47-3.50 (m, 2H, -CHCH*H*CH$_2$N- and -CHCH$_2$CH*H*CH$_2$- cycloheptane), 3.57-3.61 (m, 2H, -CHCH*H*CH$_2$CH$_2$- and -CHCH$_2$CH$_2$C*H*H- cycloheptane), 3.70-3.73 (m, 2H, -CHCH$_2$C*H*HN- and -CHCH$_2$CH$_2$CH*H*- cycloheptane), 3.77-3.80 (m, 2H, -CHCH$_2$C*H*HN- and -C*H* cycloheptane), 4.42 (bs, 1H, -N*H* cycloheptane), 5.98 (bs, 1H, -N*H*), 6.57 (s, 1H, aromatic proton quinoline), 7.09 (td, 1H, aromatic proton quinoline), 7.36-7.48 (m, 6H, 1 aromatic proton quinoline and 5 aromatic protons phenyl), 7.53 (dd, 1H, aromatic proton quinoline), 7.65 (dd, 1H, aromatic proton quinoline).

14o, N-methyl-4-phenyl-N-(piperidin-4-yl)quinolin-2-amine: M.p. n.d.; yield: 22.3 %; ^{1}H-NMR ($CDCl_3$, 400 MHz, δ, ppm): 1.68-1.72 (m, 2H, -CHCH$_2$- piperidine), 1.95-2.02 (m, 2H, -CHCH$_2$- piperidine), 2.57-2.63 (m, 1H, -NH-), 2.79-2.83 (m, 2H, -CH$_2$-NH-C*H*$_2$-), 2.98-3.02 (m, 2H, -CH$_2$-NH-C*H*$_2$-), 3.13 (d, 3H, -N-CH$_3$, J=8 Hz), 4.08-4.14 (m, 1H, -N-CH- piperidine), 7.14 (s, 1H, quinoline proton), 7.36-7.40 (m, 1H, aromatic proton), 7.48-7.57 (m, 6H, aromatic proton), 7.93 (dd, 1H, quinoline proton), 8.17 (dd, 1H, quinoline proton).

General procedure for the synthesis of the final compounds 16a and 17a

Example: Synthesis of *tert*-butyl 3-(naphthalen-2-yl(4-phenylquinolin-2-yl)amino)azetidine-1-carboxylate (16a)

To a solution of 2-bromonaphthalene (0.066 mmol, 13.79 mg) in dry toluene, *tert*-butyl 3-((4-phenylquinolin-2-yl)amino)azetidine-1-carboxylate (**14h**) (0.133 mmol, 50 mg) was added. After, $Pd(OAc)_2$ (0.0035 mmol, 0.78 mg), BINAP (0.0008 mmol, 0.51 mg), and Cs_2CO_3 (0.20 mmol, 65.08 mg) were added. The mixture was stirred under a nitrogen atmosphere at 125°C over night. Then, the reaction was quenched with distilled water and extracted with AcOEt (3x15 mL). The organic extracts were collected, washed with brine, dried with sodium sulfate, and concentrated under reduced pressure. The obtained crude was purified by column chromatography (SiO_2, eluting with ethyl acetate/n-hexane 1:10) to obtain 48 mg of the pure compound **16a** as a yellow solid.

M.p. > 250 °C; recrystallization solvent: methanol; yield: 71.9 %; ^{1}H-NMR ($CDCl_3$, 400 MHz, δ, ppm): 1.34 (s, 9H, -Boc), 3.88-3.92 (m, 2H, -CH_2- azetidine), 4.21-4.28 (m, 2H, -CH_2- azetidine), 5.23-5.29 (m, 1H, -CH- azetidine), 6.36 (s, 1H, aromatic proton), 7.21-7.23 (m, 3H, aromatic protons), 7.26-7.29 (m, 4H, aromatic protons), 7.47 (s, 2H, aromatic protons), 7.51-7.56 (m, 2H, aromatic protons), 7.69 (s, 1H, aromatic proton), 7.78-7.88 (m, 4H, aromatic protons).

17a, tert-butyl 3-((4-phenylquinolin-2-yl)(pyridin-2-yl)amino)azetidine-1-carboxylate: M.p. > 250 °C; recrystallization solvent: methanol; yield: 53.4 %; ^{1}H-NMR ($CDCl_3$, 400 MHz, δ, ppm): 1.36 (s, 9H, -Boc), 3.97-4.02 (m, 2H, -CH_2- azetidine), 4.25-4.32 (m, 2H, -CH_2- azetidine), 5.21-5.25 (m, 1H, -CH- azetidine), 6.81 (s, 1H, aromatic proton), 7.01-7.04 (m, 1H, aromatic proton), 7.12 (d, 1H, aromatic proton, J=8 Hz), 7.22-7.26 (m, 1H, aromatic proton), 7.32-7.40 (m, 5H, aromatic protons), 7.55-7.63 (m, 4H, aromatic protons), 8.40-8.42 (m, 1H, aromatic proton).

General procedure for the synthesis of the final compounds 15b, 16b, and 17b.

Example: Synthesis of N-(azetidin-3-yl)-4-phenyl-N-(4-phenylquinolin-2-yl)quinolin-2-amine trihydrochloride (15b).

To a solution of *tert*-butyl 3-(bis(4-phenylquinolin-2-yl)amino)azetidine-1-carboxylate (**15a**) (0.173 mmol, 100 mg) in dry tetrahydrofuran, 4N HCl in 1,4-dioxane (2.592 mmol, 0.864 mL) was added at 0°C. The mixture was stirred at room temperature overnight. Then, the reaction was quenched with diethyl ether and the precipitated was triturated for 1 hours with diethyl ether. After, the solid was dried to give 88 mg of the pure compound **15b** as a yellow solid.

M.p. 200-202°C; recrystallization solvent: acetonitrile/methanol; yield: 86.6 %; ^{1}H-NMR (DMSO, 400 MHz, δ, ppm): 3.45-3.48 (m, 1H, -C*H*HNH azetidine), 3.57 (s, 1H, -N*H* azetidine), 3.59-3.69 (m, 1H, -CH*H*NH azetidine), 5.23 (t, 1H, -C*H*HNH azetidine), 5.68 (dd, 1H, -CH*H*NH azetidine), 5.81-5.85 (m, 1H, -C*H* azetidine), 7.63-7.73 (m, 12H, 2 aromatic protons quinoline and 10 aromatic protons phenyl), 7.79-7.83 (m, 2H, aromatic protons quinoline), 7.88-7.91 (m, 2H, aromatic protons quinoline), 7.96-7.99 (m, 2H, aromatic protons quinoline), 8.04-8.06 (m, 1H, aromatic proton quinoline), 8.18-8.22 (m, 1H, aromatic proton quinoline), 8.69 (bs, 2H, *H*Cl), 8.78 (bs, 1H, *H*Cl).

16b, N-(azetidin-3-yl)-N-(naphthalen-2-yl)-4-phenylquinolin-2-amine dihydrochloride: M.p.> 250 °C; recrystallization solvent: methanol; yield: 61.6 %; ^{1}H-NMR (DMSO, 400 MHz, δ, ppm): 3.29-3.34 (m, 2H, -CH_2- azetidine), 3.35-3.40 (m, 2H, -CH_2- azetidine), 5.14-5.17 (m, 1H, -CH- azetidine), 7.02 (s, 1H, aromatic proton), 7.52-7.54 (m, 2H, aromatic protons), 7.58-7.60 (m, 3H, aromatic protons), 7.64-7.73 (m, 3H, aromatic protons), 7.80-7.86 (m, 3H, aromatic protons), 8.03-8,08 (m, 2H, aromatic protons), 8.12 (t, 1H, aromatic proton, J=7.6 Hz), 8.20 (d, 1H, aromatic proton, J=8.8 Hz), 8.33 (s, 1H, aromatic proton), 8.59 (s, 2H, N*H* x*H*Cl).

17b, N-(azetidin-3-yl)-4-phenyl-N-(pyridin-2-yl)quinolin-2-amine trihydrochloride:

M.p. 207-209 °C; recrystallization solvent: acetonitrile/methanol; yield: 56.1 %; ^{1}H-NMR (DMSO, 400 MHz, δ, ppm): 3.27-3.31 (m, 2H, -CH_2- azetidine), 3.41-3.46 (m, 2H, -CH_2- azetidine), 4.97-5.01 (m, 1H, -CH- azetidine), 7.37-7.40 (m, 1H, aromatic proton), 7.42-7.44 (m, 1H, aromatic proton), 7.45-7.47 (m, 2H, aromatic protons), 7.49-7.52 (m, 1H, aromatic proton), 7.54-7.57 (m, 2H, aromatic protons), 7.68-7.71 (m, 1H, aromatic proton), 7.80-7.84 (m, 2H, aromatic proton), 8.13 (td, 1H, aromatic proton), 8.33 (s, 1H, aromatic proton), 8.18 (dd, 1H, aromatic proton), 8.22-8.25 (m, 2H, N*H* x*H*Cl), 8.34 (dd, 1H, aromatic proton), 8.38 (td, 1H, aromatic proton).

General procedure for the synthesis of the final compounds 15c and 15d.

Example: Synthesis of (3-(bis(4-phenylquinolin-2-yl)amino)azetidin-1-yl)(phenyl)methanone dihydrochloride (15d).

To a solution of N-(azetidin-3-yl)-4-phenyl-N-(4-phenylquinolin-2-yl)quinolin-2-amine trihydrochloride (**15b**) (0.052 mmol, 25mg) in dry DCM, TEA (0.125 mmol, 0.017), and benzoyl chloride (0.068 mmol, 0.008 mL) were added at 0 °C. After 30 minutes, the reaction was quenched with saturated solution of sodium chloride and extracted with AcOEt (3x15 mL). The organic extracts were collected, washed with brine, dried with sodium sulfate, and concentrated under reduced pressure to provide the pure compound **15d.**

M.p. > 250 °C; recrystallization solvent: methanol; yield: 72.3%; ^{1}H-NMR ($CDCl_3$, 400 MHz, δ, ppm): 3.96 (s, 1H, -C*H*HN- azetidine), 4.33 (d, 1H, -CH*H*N- azetidine, J=10.8 Hz), 4.90 (s, 1H, -C*H*HN- azetidine), 5.76 (m, 1H, -CHN- azetidine), 6.96 (d, 1H, -CH*H*N- azetidine, J=10.8 Hz), 7.47-7.51 (m, 3H, aromatic protons), 7.57-7.62 (m, 1H, aromatic protons), 7.62-7.68 (m, 9H, aromatic protons), 7.79 (t, 3H, aromatic protons, J=8 Hz), 7.97 (d, 1H, aromatic proton, J=8 Hz), 8.02-8.09 (m, 3H, aromatic protons), 8.18-8.33 (m, 4H, aromatic protons), 9.09 (s, 1H, aromatic proton), 10.09 (s, 1H, -NH^+Cl^-), 12.16 (s, 1H, -NH^+Cl^-).

15c, 1-(3-(bis(4-phenylquinolin-2-yl)amino)azetidin-1-yl)ethan-1-one dihydrochloride: M.p. > 250 °C; recrystallization solvent: methanol; yield: 73.2%; ^{1}H-NMR ($CDCl_3$, 400 MHz, δ, ppm): 2.17 (s, 3H, -CH_3), 3.53-3.60 (m, 1H, -C*H*HN- azetidine), 4.13 (d, 1H, -CH*H*N- azetidine, J=12.4 Hz), 4.94 (s, 1H, -C*H*HN- azetidine), 5.61 (s, 1H, -CHN- azetidine), 6.69 (d, 1H, -CH*H*N- azetidine, J=12.4 Hz), 7.54-7.59 (m, 3H, aromatic protons), 7.61-7.69 (m, 9H, aromatic protons), 7.79 (t, 1H, aromatic protons, J=7.2 Hz), 7.98-8.04 (m, 4H, aromatic protons), 8.09 (t, 1H, aromatic protons, J=7.2 Hz), 8.31 (d, 1H, aromatic protons, J=8 Hz), 9.04 (s, 1H, aromatic proton), 9.60 (s, 1H, -NH^+Cl^-).

Table 3.3. Elemental analysis of final compounds 14a-r, 15a-e, 16a-b, and 17a-b.

CPD	MW	Elemental Analysis									
		Calculated, %					Found, %				
		C	N	O	H	Cl	C	N	O	H	Cl
14a	403.53	74.41	10.41	7.93	7.24		74.48	10.37	7.95	7.25	
14b	303.41	79.17	13.85		6.98		79.28	13.80		6.99	
14c	302.42	83.40	9.26		7.33		83.48	9.21		7.35	
14d	304.39	78.92	9.20	5.26	6.62		78.99	9.16	5.27	6.64	
14e	317.44	79.46	13.24		7.30		79.53	13.20		7.31	
14f	377.49	73.18	11.13	8.48	7.21		73.26	11.07	8.49	7.23	
14g	277.37	77.95	15.15		6.90		78.03	15.08		6.91	
14h	375.47	73.57	11.19	8.52	6.71		73.67	11.15	8.54	6.72	
14i	275.36	78.52	15.26		6.22		78.62	15.20		6.23	
14j	389.50	74.01	10.79	8.22	6.99		74.10	10.72	8.23	7.01	
14k	289.38	78.86	14.52		6.62		78.97	14.48		6.63	
14l	417.55	74.79	10.06	7.66	7.48		74.88	10.02	7.67	7.50	
14m	317.44	79.46	13.24		7.30		79.54	13.20		7.31	
14n	417.55	74.79	10.06	7.66	7.48		74.88	10.00	7.68	7.49	
14o	317.44	79.46	13.24		7.30		79.53	13.19		7.31	
14p	404.51	74.23	6.93	11.87	6.98		74.30	6.89	11.89	6.99	
14q	304.39	78.92	9.20	5.26	6.62		79.01	9.14	5.28	6.64	
14r	409.49	76.26	10.26	7.81	5.66		76.33	10.19	7.82	5.67	
15a	578.72	78.87	9.68	5.53	5.92		78.94	9.61	5.54	5.93	
15b	587.97	67.41	9.53		4.97	18.09	67.49	9.49		4.99	18.08
15c	593.55	70.83	9.44	2.70	5.09	11.95	70.93	9.40	2.71	5.10	11.93
15d	655.62	73.28	8.55	2.44	4.92	10.81	73.39	8.51	2.46	4.93	10.80
15e	612.73	80.37	9.14	5.22	5.26		80.44	9.08	5.23	5.27	
16a	501.63	79.02	8.38	6.38	6.23		79.09	8.31	6.40	6.24	
16b	474.43	70.89	8.86		5.31	14.94	71.02	8.82		5.33	14.91
17a	452.56	74.31	12.38	7.07	6.24		74.38	12.32		6.26	
17b	461.81	59.82	12.13		5.02	23.03	59.89	12.08		5.03	23.00

3.4.2. Materials and methods

3.4.2.1. Reagents

FAD disodium salt hydrate (FAD-Na_2), β-nicotinamide adenine dinucleotide 2′-phosphate reduced tetrasodium salt (NADPH), Roswell Park Memorial Institute (RPMI) 1640 medium with l-glutamine and sodium bicarbonate, phosphate-buffered saline (PBS), lithium dodecyl sulfate (LiDS), $CaCl_2$, sodium chloride, HEPES buffer, sodium di-hydrogen phosphate ($NaH_2PO_4 \cdot H_2O$), phenylmethylsulfonyl fluoride, glycerol, pepstatin, leupeptin, SigmaFastTM Protease Inhibitor Cocktail Tablets EDTA-Free, cytochrome c from equine heart, hemin, superoxide dismutase, Ampliflu Red (Amplex Red) and horseradish peroxidase were purchased from Sigma Aldrich. MCLA was purchased from MedChemExpress. Cholesteryl hemisuccinate Tris salt (CHS) and dodecyl-beta-d-maltopyranoside (DDM) were purchased from Anatrace. Fetal bovine serum (FBS) and FreeStyle medium were purchased from Invitrogen. All tested compounds were purchased from MolPort, Vita-M-Labs, and ChemSpace or Enamine suppliers.

3.4.2.2. Protein expression

(Group of Prof. Andrea Mattevi, Department of Biology and Biotechnology Lazzaro Spallanzani, University of Pavia)

DH of *C. stagnale* NOX5 - The N-terminally histidine-tagged wild-type DH (residues 413–693) was expressed as described in the corresponding section of the previous project. [54] For the production of U-[^{15}N]-*cs*DH NOX5 used in NMR, the bacteria were grown at 37 °C in M9 medium prepared with 4 g l^{-1} of D-glucose (Sigma) and 1 g l^{-1} $^{15}NH_4Cl$ (CIL). At an OD_{600} of 1 the protein production was induced with 0.3 mM isopropyl-β-D-thiogalactoside and the expression was performed at 17 °C overnight.

DH of *human* NOX4 - The gene encoding for the DH of human NOX4 (residues 299-578 of isoform 1) carrying a multiple N-terminal $(His)_6$, Twin-STREP, Maltose Binding Protein tag was cloned into a pET28a and expressed in the *E. coli* BL21 (DE3, RP-Plus) (Novagen). Cell pellets were resuspended in buffer A (50 mM HEPES pH 7.4, 10% (v/v) glycerol, 0.5 M NaCl) and supplemented with 1 mM PMSF (phenylmethylsulfonyl fluoride) and proteases inhibitor cocktail (SigmaFastTM

Protease Inhibitor Cocktail Tablets, EDTA-Free, Sigma Aldrich) before cell disruption by sonication.

***Human* NOX2 -** The enzyme was expressed as described before. [281] Briefly, X-CGD PLB-985 cells, transduced with the RD114-pseudotyped MFGS-NOX2 vector (PLB-985 cells from now on) were a kind gift from H. Malech (National Institutes of Health). The cells were maintained in suspension in RPMI-1640 medium supplemented with 10% (v/v) heat-inactivated FBS at 37 °C and 5% CO_2. Cells were centrifuged at 1,200g for 10 min. Cells were resuspended in PBS and centrifuged again at 1,200g for 10 min and the pellet frozen at −80 °C.

***Human* NOX1 and NOX2 cytosolic partners -** The full-length human $p67^{phox}$, $p47^{phox}$ and the constitutively active mutant Rac1 Q61L were expressed as described before. [281 302]

***Human* NOX1 and NOX5 -** The complementary DNAs (cDNAs) encoding for the human NOX1 (isoform 1), human NOX5 (isoform v/2), and human $p22^{phox}$ were obtained from Genescript, cloned into a pEG BacMam vector (kindly gifted by E. Gouaux, Oregon Health and Science University, Portland). The NOX1 construct contains a Kozak sequence, followed by two FLAG tags, a Twin-STREP tag, and a tobacco etch virus (TEV) cleavage site at the N terminus. The NOX5 construct contained a Kozak sequence, followed by N-terminal FLAG tag and TEV cleavage site. The $p22^{phox}$ construct carried a Kozak sequence. HEK293-EBNA1-6E cells were given by Y. Durocher (NRC-BRI). [335] Cultured cells were maintained in suspension using FreeStyle medium (Invitrogen). Cells were seeded at a concentration of 5×10^5 cells per ml, the day before transfection. For transient NOX1-$p22^{phox}$ cotransfection or NOX5 transfection, polyethyleneimine (linear MW 25000, Polyscience Europe Gmbh) was used as transfection agent, in a ratio of 1/3 DNA/polyethyleneimine (0.75 μg of NOX1 vector, 0.25 μg $p22^{phox}$ vector per 1 μg of NOX5 vector, 3 μg polyethyleneimine per ml of culture). After 48 h, the transfected cells were gathered by centrifugation (1,200g, 5 min, 4 °C). Trypan Blue exclusion assay (Trypan Blue solution w/v, Sigma) was used to evaluate cell viability. The cell pellet was rapidly frozen using liquid nitrogen and then stored at a temperature of −80 °C.

Human NOX4 expression - The cDNAs encoding for the human NOX4 (isoform 1 from GeneWiz) and human $p22^{phox}$ were obtained from GeneWiz, cloned into pTT22 (puromycin resistance) and pYD7 vectors, respectively (vectors obtained from Y. Durocher, NRC-BRI, Montreal, Canada). [335] [336] The NOX4 construct contained a Kozak sequence, followed by two $(His)_6$ tags, a Twin-STREP tag, an eGFP moiety, and a TEV cleavage site at the N terminus. The $p22^{phox}$ construct contained a Kozak sequence. Both vectors contained an EBV origin of replication in their construct that allows them to be maintained episomally in HEK293 EBNA1-6E. Cultured cells were maintained in suspension using FreeStyle medium (Invitrogen). Cells were seeded at a concentration of 5×10^5 cells per ml, the day before transfection. For stable NOX4-$p22^{phox}$ cotransfection, polyethyleneimine (linear MW 25,000, Polyscience Europe) was used as transfection agent, in a ratio of 1/3 DNA/polyethyleneimine (0.90 μg of NOX4 vector, 0.10 μg of $p22^{phox}$ vector and 3 μg of polyethyleneimine per ml of culture). The next day, 5 μg ml−1 of puromycin was added to the cell culture. After 48 h, transfected cells were gathered by centrifugation (1,200g, 5 min, 4 °C). Trypan Blue exclusion assay (Trypan Blue solution w/v, Sigma) was used to evaluate cell viability. The cell pellet was rapidly frozen using liquid nitrogen and then stored at a temperature of −80 °C.

3.4.2.3. Protein purification

(Group of Prof. Andrea Mattevi, Department of Biology and Biotechnology Lazzaro Spallanzani, University of Pavia)

Membrane preparations - Membrane isolation from NOX-expressing human cells was performed as described before. [281] Briefly, frozen PLB-985 cells or transfected HEK293-EBNA1-6E cells pellets were resuspended at a concentration of 2×10^8 cells per ml in sonication buffer containing 10 mM HEPES (pH 7.4), 10 mM NaCl, 100 mM KCl, 1 mM PMSF and supplemented with 1 μM leupeptin, 1 μM pepstatin just before sonication. The lysate was centrifuged at 500g for 5 min at 4 °C, and the supernatant was collected. The cell pellet was resuspended in sonication buffer and sonicated again on ice twice. The cell lysate was centrifuged at 500g for 5 min at 4 °C and the supernatant was collected. Both supernatants were pooled and ultracentrifuged (200,000g for 30 min) at 4 °C (Optima MAX-XP Ultracentrifuge, Beckman Coulter). Protein concentration was assessed by the Biuret Assay. Protein quality was evaluated by detecting protein bands thorough western blots stained with monoclonal anti-STREP tag-HRP antibody (Bio-Rad, for NOX1 detection),

monoclonal anti-FLAG M2-Peroxidase antibody (Sigma, for NOX5 detection) and anti-NOX2 antibody (54.1, kind gift of A. Jesaitis, Montana State University). Antimouse IgG HRP-linked antibody (Cell-Signaling Technology) was used as a secondary antibody for 54.1 antibody detection. Detection of NOX4 involved quantifying the fluorescence emitted by the eGFP moiety through intensity-based fluorescence detection on an SDS–PAGE gel (Bio-Rad; ChemiDoc MP imager; Alexa Fluor 488 for eGFP detection).

***Human* cytosolic protein purification -** The full-length human $p67^{phox}$, $p47^{phox}$ and the constitutively active mutant Rac1 Q61L were purified as described before. [281]

DH of *C. stagnale* NOX5 purification - The N-terminally histidine-tagged wild-type protein was purified as described in ref. [54]

3.4.2.4. Biochemical assays

(Group of Prof. Andrea Mattevi, Department of Biology and Biotechnology Lazzaro Spallanzani, University of Pavia)

MCLA assay on NOX2 membranes - MCLA assay was performed as described before. [281] Briefly, 20 μg of NOX2-$p22^{phox}$ containing membranes were added to a reaction mixture containing 65 mM sodium phosphate buffer (pH 7.0), 0.5 μM FAD, 130 μM LiDS, 160 nM recombinant cytosolic proteins $p67^{phox}$ $p47^{phox}$, Rac1 Q61L and 1 μM MCLA. The tested compounds were added to the mixture and incubated for 10 min at 4 °C. Inhibitors were tested with concentrations varying from the micromolar to the low nanomolar range. The reaction was initiated by the addition of 240 μM NADPH. Measurements were performed using a GloMax plate reader.

Evaluation of *human* NOX1, NOX4 and NOX5 membranes - The assay was assessed as described before. [281]. In brief, NOX1- (100 μg), NOX4- (100 μg) or NOX5-containing (25 μg) membranes were added to a reaction mixture of PBS with 0.02 U ml^{-1} horseradish peroxidase, 12.5 μM Amplex Red, 40 μM FAD, 1.5 μM cytosolic proteins $p67^{phox}$, $p47^{phox}$, Rac1 Q61L (for NOX1) and 1 mM $CaCl_2$ (for NOX5) in a final volume of 100 μl. The compounds were added to the mixture and

incubated for 10 min at 4 °C at varying concentrations from the micromolar to the low nanomolar range. The reaction was started with the addition of 40 μM NADPH, a concentration selected to minimize potential interference effects. [337] Measurements were performed using a ClarioStar plate reader (excitation 572 nm/emission 583 nm) (BMG Labtech). We pursued the expression and purification of the physiological NOX1 activators, NOXA1 and NOXO1. However, all NOXO1 constructs evaluated suffered from a heavy tendency to aggregate and the protein was never purified in an active form. Hence, $p47^{phox}$ was used together with NOXA1 to measure NOX1 activity. This mixture NOX2-organizer and NOX1-activator was successful in the activation of purified NOX1-$p22^{phox}$. However, the use of $p67^{phox}$ instead of NOXA1 did not significantly change the overall activity. Given the higher purification yields of $p67^{phox}$ compared to NOXA1, $p47^{phox}$-$p67^{phox}$ system was finally exploited for NOX1 activation.

***K*i determination on *human* NOXs -** K_i were measured on human NOX1, human NOX2, DH of human NOX4 and DH of *cs*NOX5 following NADPH oxidation by monitoring the absorbance 340 nm with Cary 100 UV-vis spectrophotometer (Varian) or the fluorescence (excitation 340 nm/emission 460 nm) with Cary Eclipse fluorescence spectrometer (Varian). 200 nM of purified NOX2 was added in a final volume of 200 μl of 65 mM sodium phosphate buffer (pH 7.0), 50 μM FAD, 130 μM LiDS and 1 μM recombinant cytosolic proteins $p67^{phox}$, $p47^{phox}$, Rac1 Q61L. For NOX1, 1 μM of purified enzyme was assayed in a final volume of 200 μl of 65 mM sodium phosphate buffer (pH 7.0), 50 μM FAD, 130 μM LiDS and 5 μM recombinant cytosolic proteins $p67^{phox}$, $p47^{phox}$, Rac1 Q61L. Inhibitors were tested with concentrations varying from micromolar to low nanomolar.

3.4.2.5. Statistical analysis

Data analyses were performed as described in before. All graphs were prepared using GraphPad Prism and all data are expressed as mean ± standard deviation. Sigmoidal curve-fitting of concentration–response curve, IC_{50} values and statistical tests were all performed with GraphPad Prism. Concentration–response curves are presented as a percentage of the control, with control being the untreated condition. For K_i determination, initial velocities obtained at multiple NADPH and inhibitor concentrations were fitted globally to competitive, uncompetitive, and

noncompetitive models. The best-fit model was identified based on the R2 parameter given by GraphPad Prism software (GraphPad Software, Inc.).

3.4.2.6. In cellulo analyses

(Group of Prof. Andrea Mattevi, Department of Biology and Biotechnology Lazzaro Spallanzani, University of Pavia)

In cellulo measurement of human NOX2 activity by cytochrome c reduction assay - $O_2^{\bullet-}$ production of intact PLB-985 cells (3×10^5 cells) in PBS containing 20 mM glucose and 200 μM cytochrome c was measured after PMA (phorbol 12-myristate 13-acetate) stimulation (5 μM). Incubation with PMA proceeded for 20 min at 37 °C. The tested compounds (single inhibitory activity measurement at 40 or 0.04–40 μM for EC_{50} determination) were added to the stimulated cells and incubated for 30 min at 37 °C and 5% CO_2, 120 rpm (New Brunswick S41i Incubator Shaker, Eppendorf). The absorbance at 550 nm was monitored at 37 °C, over a time course of 15 min in a Cary 100 UV-vis spectrophotometer and over a time course of 30 min in a ClarioStar plate reader (EC_{50} determination). The activity of NOX2 in intact PLB-985 cells not previously stimulated with PMA was also evaluated as negative control.

Cellular thermal shift assay (on human NOX2, 4, and 5 expressing cells) - Thirty million intact NOX2-PLB-985 cells and NOX4- and NOX5-expressing HEK293-EBNA1-6E cells were incubated with dimethylsulfoxide (DMSO) or 40 μM of the tested inhibitor for 1 h at 37 °C with 5% CO_2, after the stimulation with 5 μM PMA for PLB-985 cells and 100 nM PMA for NOX5-expressing HEK293-EBNA1-6E cells. After centrifugation at 1,300*g* for 10 min at room temperature, cell pellets were washed twice in PBS and resuspended at 1.5×10^7 cells per ml and aliquoted to PCR-strips at 100 μl per tube. Samples were then heated (spanning from 30 °C to 66.9 °C for NOX4, from 37 °C to 88 °C for NOX2, from 30 °C to 57.9 °C for NOX5) for 3 min in a T100 Thermal Cycler (Bio-Rad). NOXs were extracted from intact cells by adding 1% DDM (v/v) to each tube, and solubilization proceeded for 60 min at 4 °C. After centrifugation at 20,000*g* for 30 min at 4 °C, each supernatant was analyzed by loading 20 μl of each sample onto a SDS gel (Bio-Rad, Mini-PROTEAN TGX). For NOX2 and NOX5 SDS gel bands were transferred to a Trans-Blot Turbo Mini 0.2 μm PVDF (polyvinylidene difluoride) membrane (Bio-Rad) using a Trans-Blot Turbo Transfer System (Bio-Rad). For NOX2, western blot analysis was performed by

immunoblotting the PVDF membrane with NOX2 monoclonal antibody (54.1, kindly gifted by A. Jesaitis, Montana State University), following the addition of goat horseradish peroxidase-conjugated antimouse secondary antibody (Bio-Rad). For NOX5, western blot analyses were performed by immunoblotting the PVDF membrane with monoclonal anti-FLAG M2-Peroxidase antibody (Sigma). Chemiluminescent detection of NOX2 and NOX5 was performed by using the ECL detection kit (Bio-Rad, ChemiDoc MP image). NOX4 was detected by quantifying the fluorescence emitted by the eGFP moiety through intensity-based fluorescence detection on a SDS–PAGE gel (Bio-Rad; ChemiDoc MP imager; Alexa Fluor 488 for eGFP detection). Melting curves were generated by plotting the band intensities of each heated sample against the respective temperatures (°C). Data were first normalized by setting the highest and lowest intensity value in each set to 100 and 0%, respectively. Fitting of curves was performed by applying a Boltzmann sigmoidal dose-response model within GraphPad Prism. The T_{agg} values obtained were the results of two different experiments and the mean ± standard deviation was calculated.

3.4.2.7. Cancer cell line analysis

(Group of Prof. Haribabu Arthanari, Department of Biological Chemistry and Molecular Pharmacology, Blavatnik Institute, Harvard Medical School (HMS); Department of Cancer Biology, Dana-Farber Cancer Institute (DFCI), Boston, MA, USA)

Cell culture and treatments – Colorectal cancer cell lines were grown in RPMI-1640 (Euroclone) supplemented with 10% FBS (Sigma Aldrich), 50 U ml^{-1} penicillin and 50 mg ml^{-1} streptomycin at 37 °C and 5% CO_2. For drug synergy assay, cells were plated at 5×10^3 cells per well in 384-well plates. Then 24 h postplating, cells were treated with the combination of compounds and MRTX1133 at concentrations of 1–50 μM for compound M41, 14d, and 15a, 0.5-20 μM for 10t, and 0.01-10 μM for MRTX1133 using D300e digital drug printer (Tecan Life Sciences). The cell viability was assessed 72 h post-treatment using CellTiter-Glo v.2.0 Cell Viability Assay (Promega) according to the manufacturer's instructions. The synergistic effects between compounds and MRTX1133 were analyzed using Synergyfiner. [346]

PART II.

DESIGN, SYNTHESIS, AND BIOLOGICAL EVALUATION OF NOVEL DUAL EZH2/HDACs INHIBITORS AS AN EPI-POLYPHARMACOLOGICAL APPROACH FOR LYMPHOMA TREATMENT

1. Epigenetics

The first scientific definition of the word "epigenetics" can be attributed to Conrad Waddington (1905-1975), a British biologist who, in 1942, defined this term as "the branch of biology which studies the causal interactions between genes and their products, which bring the phenotype into being".[350] We can better define epigenetics as the study of meiotically/mitotically heritable and potentially stable changes in gene expression that are not caused by alteration of the DNA sequence (**Figure 1.1**).[351] Thus, we can look at epigenetics as the bridge between the genotype and the phenotype, the factor that, according to Waddington's epigenetic landscape, drives what potentially can take several different ways, into a defined path. In these regards, epigenetics can explain how in a complex multicellular organism, even though all the cells have the same genome, they can stably differentiate and generate populations of cells with different identities. To date, at least five different events are known to contribute to the epigenetic regulation of gene expression. These events include DNA methylation, histone tails post-translational modifications (PTMs), an interchange between histone variants, non-coding RNAs, and nucleosome/chromatin remodeling.[352]

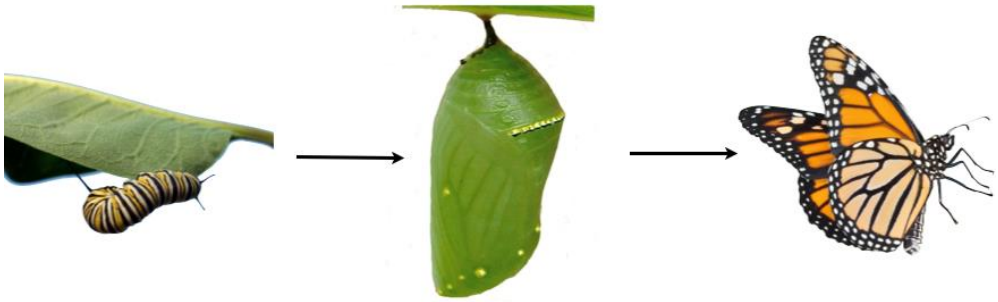

Figure 1.1. *A fantastic example of epigenetics in action is the metamorphosis of a caterpillar into a butterfly. A butterfly contains the same genome as the caterpillar from which it develops. Epigenetics ensures the expression of the right genes at the right time during metamorphosis, by activating some genes and silencing others in a controlled manner.*[353]

The nucleosome is defined as the fundamental repeating unit of chromatin in eukaryotes. The nucleosome comprises an octamer containing two copies of each of the four core histones (H2A, H2B, H3, and H4), around which are wrapped 147 DNA base pairs in 1.75 superhelical turns (**Figure 1.2**).[354] Given the intimate

association between DNA and histone proteins in the 8 nucleosomes, it is easy to understand the importance of nucleosomes in influencing DNA functions and gene expression.

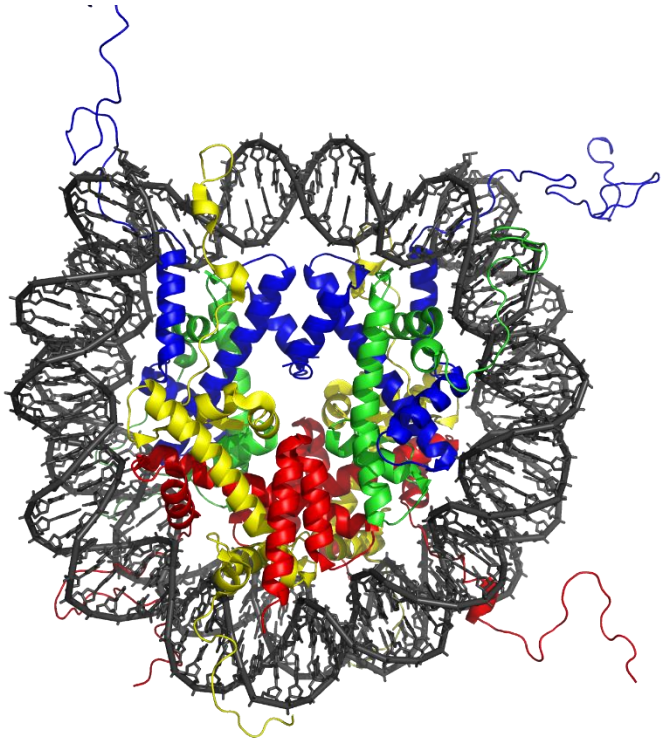

Figure 1.2. *The X-ray crystal structure of the nucleosome core particle is shown (PDB: 1AOI). It consists of H2A, H2B, H3, and H4 core histones, and DNA. The view in this picture is from the top through the superhelical axis.* [354]

Nucleosomes are dynamic structures. They can change their position sliding on the DNA, [355] they can partially disassemble, [356] and histone variants can replace their components. [357] One could think that the nucleosome, and histones, have a mere physical role, hiding certain DNA regions from transcription factors or influencing polymerase progression. However, this is not the sole effect related to the nucleosome-DNA interaction. In fact, the histone tails, protruding from the octamer, are objects of numerous PTMs. [358] The histone PTMs, together with the methylation of specific cytosine residues on the DNA, constitute the epigenetic code, the unique combination of enzyme-catalyzed covalent modifications of DNA and histones that allow a specific gene to be expressed or not expressed in a specific moment in a certain cell. Aberrant epigenetic mechanisms can drive genetic mutations, and mutations in the epigenetic regulators cause alterations in the epigenome, leading to inappropriate genes, or signalling pathways activation or

inhibition, resulting in a disease state. [359] Additionally, epigenetic alterations are potentially reversible and can be reverted to their normal state. Therefore, these evidences have encouraged the idea that epigenetic regulators are druggable targets in diverse diseases such as cancer, neurological, autoimmune, and cardiovascular diseases, developmental disorders, and aging. [360] [361] Numerous cellular activities are regulated by epigenetic modifications throughout the genome; however, aberration may result in expression abnormalities or even gene silencing due to such activities. Epigenome alterations can play a role in the etiology of various diseases at prenatal and postnatal life levels. [362]

1.1. The complex interplay of epigenetic players: writers, readers, and erasers

As already mentioned above, the epigenome of a single cell is defined by the combination of distinct epigenetic processes such as DNA methylation, histone tails PTMs, exchanges of histone variants, non-coding RNAs, and nucleosome/chromatin remodeling. Interestingly, all these epigenetic events are reversible and are closely related to each other. Each of them can communicate certain information and influence the establishment of other marks, generating what is commonly known as epigenetic crosstalk. [363] It is evident that epigenetics drug discovery covers a broad spectrum of complex and transient modifications to the nucleosome, which are carried out and interpreted by numerous diverse proteins. As such, the field, although tempting to classify as a distinct specialism, comprises many target classes and a multitude of potential opportunities for intervention, making generalization across approaches and learning from previous outcomes difficult. Nevertheless, we can attempt to classify the action of these epigenetics-related proteins into distinct categories based on their role. Writers catalyze the addition of moieties to DNA and histones and result in changes as subtle as a single methyl addition, to the formation of larger protein adducts. Readers recognize such features and influence the interactions between the modified protein and DNA, histone proteins, and other macromolecular binding partners. Erasers ensure a dynamic epigenetic response, because they catalyze the removal of the modification, allowing the reversal of the modified interactions and any altered downstream events. **Figure 1.3** describes the role of methyl and acetyl-writers, readers, and erasers and identifies proteins currently known to have a role in carrying out these activities. [364] Dysregulation of the processes controlled by these

writers, readers, and erasers occurs in a variety of ways in the disease state, including changes in the activity or expression levels or mutations conferring a change of function. Our appreciation of the differences in the epigenetic states between normal physiology and many disease processes is increasing and proteins from all three categories represent opportunities for small-molecule drug discovery. [365]

a)

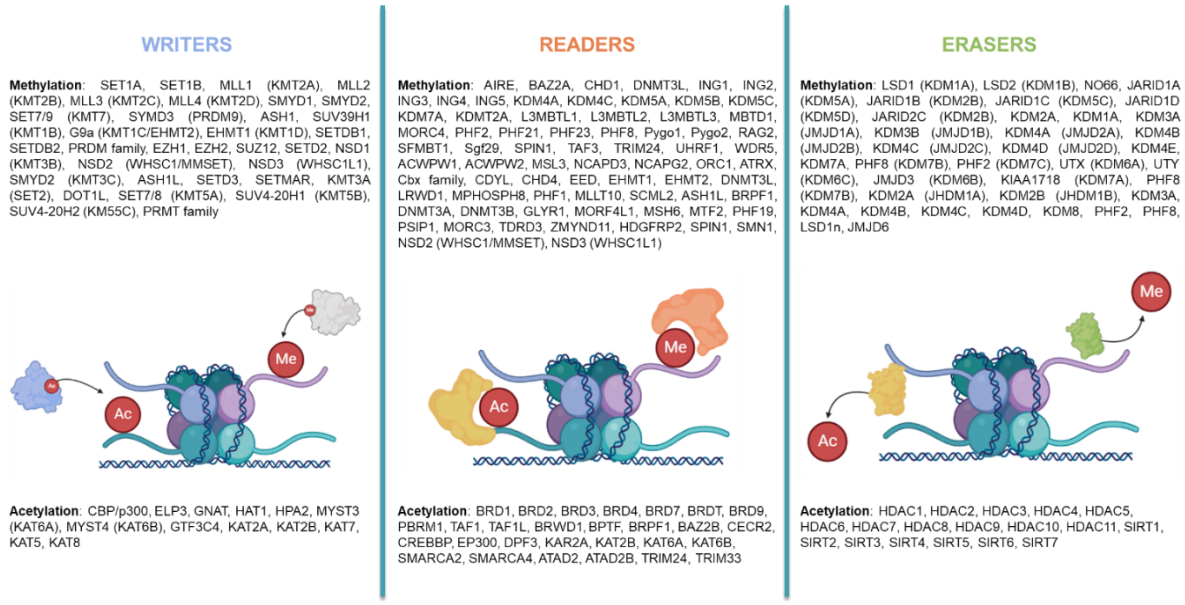

b)

Figure 1.3. *Proteins involved in epigenetic modification of proteins and nucleic acids.* ***a)*** *Overview of the histone modification and recognition processes carried out by methyl and acetyl writers, readers, and erasers. The proteins known to be associated with these roles are listed above the schematic for methyl modifications and below for acetyl modifications.* ***b)*** *Overview of nucleic acid modification. The proteins known to be associated with these roles are listed, along with the roles they have been associated with.* Adapted from [364]

1.2. The role of covalent histone modifications and chromatin remodeling

Recently, it has become clear that epigenetic changes, which are modifications of the genetic information that do not alter the DNA sequence, can have a role in disease's biology. [364] To date, eight covalent modifications of histone tails have been identified and studied: acetylation, [366] methylation, [367] phosphorylation, [368] ubiquitination, [369] sumoylation, [370] ADP-ribosylation, [371] deamination, [372] and proline isomerization. [373] Histone tails PTMs contribute to defining a closed (heterochromatin) or opened state of the chromatin (euchromatin), [374] [375] and they generate a code able to recruit specific binding proteins which would, in turn, influence chromatin structure and functions (**Figure 1.4**). [376] [351]

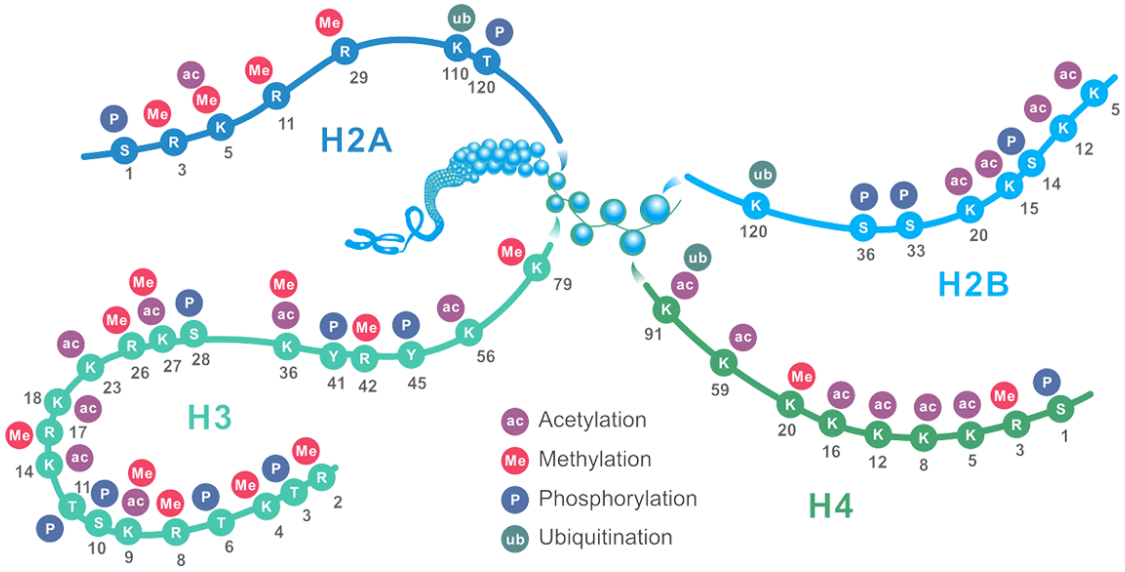

Figure 1.4. *Schematic representation of common Histone modification sites.*

Additionally, histone modifications are essential to modulate nucleosome mobility and turnover. [377] In 2017, Lai *et al.* reviewed nucleosome dynamics and their effects on gene expression and DNA replication. [378] In this review, they underline how the study of nucleosome dynamics should be regarded as the study of genome regulation. The DNA accessibility of various proteins and their complexes is regulated by the interplay between nucleosome occupancy and positioning, affecting thus gene expression programs. Several different regulatory factors operate in an independent or concerted manner to ensure that a certain organization

and composition of the nucleosome is maintained at specific genomic loci. The authors suggest that such dynamic and complex organization may be useful to enable the genome to adapt and respond to external stimuli, as well as to recover from chromatin-disruptive activities (such as replication and transcription). [378]

2. Histone Deacetylases (HDACs): Erasers of Acetyl group

Until now, eighteen mammalian deacetylase enzymes have been identified. These enzymes are subdivided into four classes according to their sequence homology to yeast HDACs, size, subcellular localization, tissue specificity, and enzymatic activity. [379] [380] Discovered for their specific enzymatic activity on histone lysines, HDACs can also deacetylate a myriad of non-histone proteins such as transcription factors, cytoskeletal proteins, molecular chaperones, and nuclear import factors. [381]

The class I HDACs (HDAC1, -2, -3, and -8) share sequence similarity to the yeast transcriptional regulator Rpd3. These enzymes are generally located in the nucleus where histones and additional nuclear proteins are their major substrates. Generally, class I HDACs are ubiquitously expressed in diverse human tissues, and function as transcriptional co-repressors.

The class II HDACs have sequence similarity to yeast Hda1 and are further divided into classes IIa (HDAC4, -5, -7, -9) and IIb (HDAC6 and -10). Compared to class I, the class IIa isoforms are tissue-specific, larger in size, and are able to shuttle between the nucleus and the cytoplasm. These enzymes have a minimal deacetylase activity, and it is possible that their primary cellular activity is to function as scaffold to recruit catalytically active HDACs within multiprotein complexes. [382] Alternatively, there is the possibility of an underscored substrate [383] or allosteric stimulation of activity. [384] HDAC6 and HDAC10, the only two components of class IIb HDACs, are preferentially cytoplasmic and contain a second catalytic domain not found in other HDACs isoforms.

The class III HDACs (SIRT1-7) are homologues of the yeast protein Sir2 and are structurally and biochemically unrelated to the other classes. [385] [386] [387]

The class IV is composed by the only HDAC11 isoform that shares similar sequence with the catalytic domain of both class I and II HDACs but the overall sequence similarity is too low to be placed in either class. Two distinct catalytic mechanism have been described for these deacetylase enzymes. Class I, II and IV HDACs are

Zinc-dependent hydrolases also named classical HDACs while class III HDACs, referred also to as Sirtuins, transfer the acetyl group through the ribose sugar of their NAD^+ cofactor (**Figure 2.1**). [388]

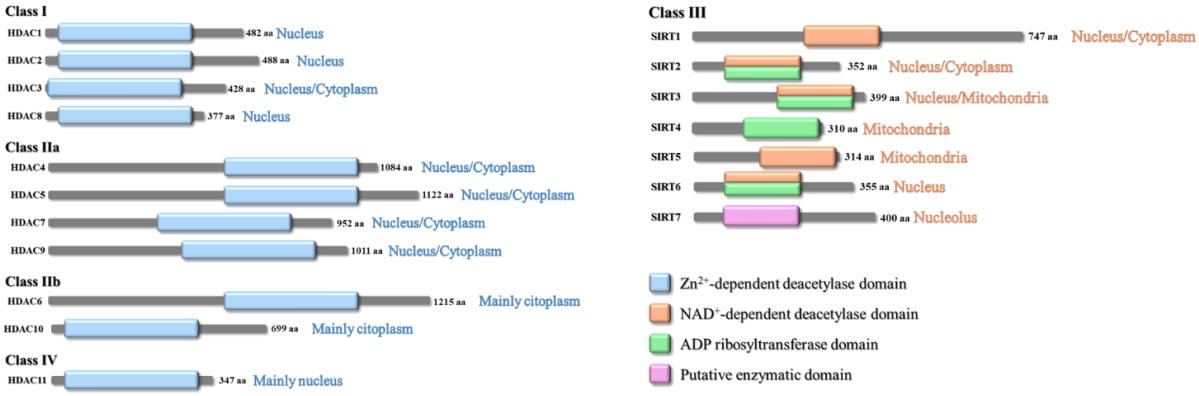

Figure 2.1. *Summary of domain organization, size, and localization of eighteen mammalian deacetylase enzymes.*

2.1. Classical HDACs: Crystal Structure and Mechanism of Enzymatic Activity

Over the years, structural, biochemical, and mutational analysis have provided the current overall knowledge of classical HDACs (class I, II and IV HDACs) catalytic mechanism that require a Zn^{2+} ion for the hydrolytic catalysis.

The first X-ray crystal structure of a classical HDAC isoform was determined for the histone deacetylase-like protein (HDLP), an archeobacterial homolog of eukaryotic deacetylase. [389] According to this study, HDLP has the same topology as arginase containing an open α/β fold made by eight-stranded parallel β-sheet and sixteen α-helices in which four helices pack on either face of the β-sheet, forming the classical core α/β structure. Arginase is a metalloproteinase catalyzing the hydrolysis of arginine to ornithine and the HDLP similarity to arginase suggests that HDLP evolved from a common metalloproteinase ancestor. X-ray crystal structures of mammalian HDACs are essentially similar to HDLP catalytic domain structure suggesting that the residues composing the active site are conserved across the HDAC family. The active site of HDLP is composed by an about 11 Å long hydrophobic, deep and narrow tunnel that becomes wider at the bottom, where the Zn^{2+} ion is located. Hydrophobic and aromatic residues (Pro22, Gly140, Phe141,

Phe141, and Phe198) compose the wall of the tunnel. The two aromatic components, Phe141 and Phe198, are parallel to each other and form the slenderest portion of the pocket. Inside the deepest part of the tunnel, the Zn^{2+} ion is penta-coordinated with three sites occupied by Asp168, His170, Asp258, and the other two sites by the oxygen of the acetyl moiety and a water molecule under the natural substrate conditions. Additionally, two histidine (His131 and His132), two aspartic acids (Asp166 and Asp173) and a tyrosine (Tyr297) complete the structure. Since each of the $N_{\delta 1}$ histidine forms a hydrogen bond with the aspartic acid carboxylate oxygen, two His-Asp charge-relay systems polarizing the imidazole Nε and increasing its basicity activate the water molecule for peptide substrate hydrolysis. The tyrosine is positioned next to the Zn^{2+} ion and stabilizes the tetrahedral intermediate during the catalysis, besides polarizing the substrate carbonyl (C=O) for the nucleophilic attack (**Figure 2.2**). [389]

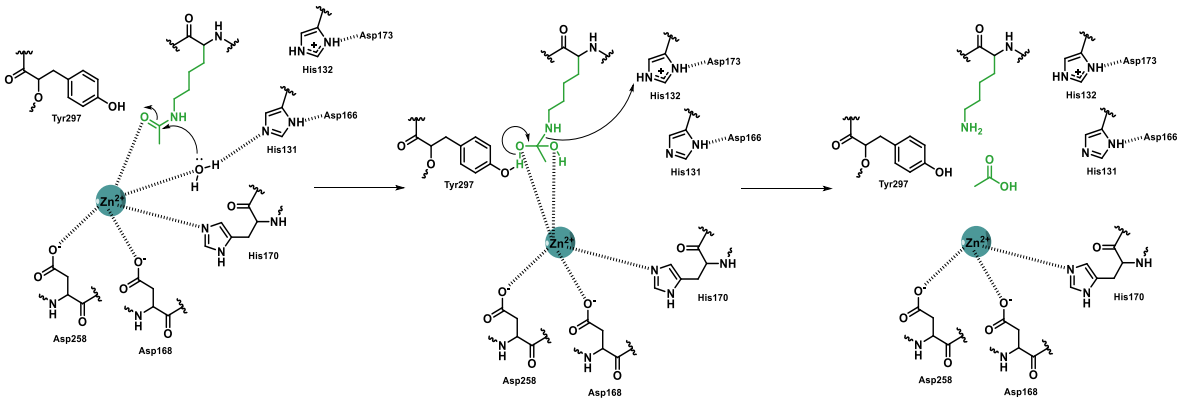

Figure 2.2. *Mechanism of action of classical HDACs.*

All the HDACs share the same catalytic mechanism, and all the catalytic residues are conserved in other HDACs except for class IIa HDACs in which the tyrosine residue is replaced by a histidine. Given the important role of tyrosine in HDAC catalytic mechanism, Lahm *et al*. reported that the lack of the tyrosine residue in HDAC4 and other class IIa HDACs could be responsible for their low catalytic activity. [383] Adjacent to the catalytic pocket, these enzymes have also an internal cavity that may provide a space for the diffusion of the acetate product away from the catalytic center. Interestingly, this cavity could be useful for the design of isoform selective HDAC inhibitors (see below) since Tyr96 in HDAC3 replaces the Ser113 in the internal cavity of HDAC1. [390]

2.1.1. Class I HDACs

The first class includes HDAC1, 2, 3, and 8. These isoforms, similar to yeast *Saccharomyces cerevisiae* transcriptional regulator Rpd3, are mainly located in the nucleus from which it derives their primary function is the regulation of gene expression (except for HDAC3 that could be localized also in cytoplasm). [391] HDAC1 and HDAC2 are highly similar enzymes with an overall sequence identity of 82% and are generally found together in at least three repressive complexes called Sin3, NuRD (Nucleosome Remodeling and Deacetylating), and Co-REST (Co-REpressor for element-1-Silencing Transcription factor). [392] HDAC3 is evolutionary most related to HDAC8, with 34% overall sequence identity. While HDAC3 operates in distinct complexes such as SMRT/N-CoR, no complex has been described for HDAC8. [380]

HDAC1 and HDAC2 are characterized by a large N-terminus that forms the major part of the protein and contains the catalytic domain. HDAC1 and HDAC2 only display activity within a multiprotein complex. Early studies demonstrated that the isolation of these proteins from their associated co-factors generally yielded very low enzymatic activity. Sin3 and the NuRD complexes share the same core containing four proteins: HDAC1, HDAC2, Rb-associated protein 48 (RbAp48) and RbAp46. To guarantee the maximal HDAC activity both Sin3 and NuRD need additional cofactor (Sin3, SAP18, and SAP30 in the Sin3 complex; Mi2, MTA2, and MBD3 in the NuRD complex). [393] [352] Similarly, in the CoREST complex, the association of HDAC1/HDAC2 with CoREST is essential for HDAC enzymatic activity. [394] In addition to the regulation of HDAC1 and HDAC2activity by the interaction with fundamental co-factor, post-translational modifications of HDAC1 and HDAC2 constitute another important contribute in regulating their catalytic activity. Phosphorylation has been the most extensively studied modification widely affecting deacetylase functionality. HDAC1 is phosphorylated by cAMP-dependent kinase PKA and protein kinase CK2 on the C-terminal residues S421 and S423. Serine phosphorylation of both the residues is such essential for the enzymatic activity of HDAC1 that mutation to alanine not only induces a significant reduction in enzymatic activity but also disrupts protein interaction of HDAC1 with RbAp48, MTA2, Sin3, and CoREST. [395] Similarly, S394, S422, and S424 residues of HDAC2 can be phosphorylated and like for HDAC1, HDA2 phosphorylation increases enzymatic activity and influences protein complex formation with Sin3 and Mi2. [396] According to other evidence, HDAC1 and HDAC2 phosphorylation can be reversibly regulated by the protein phosphatase PP1. [397] In addition to histones, the

best-characterized non-histone substrate for HDAC1 has been the tumor suppressor p53. Acetylation of p53 is a reversible enzymatic process that occurs in response to DNA damage and genotoxic stress and is indispensable for p53-dependent induction of cell growth arrest or apoptosis. [398] HDAC1-containing complexes interact with and deacetylate p53 thus downregulating its transcriptional activity. [399] HDAC1 and 2 have a central role in mice development confirmed by the evidence that deletion of both the enzymes leads to lethality in all cases. HDAC1-null mice die before embryonic day 10.5 and display severe proliferation defects and general growth retardation. [400] HDAC1-null embryonic stem cells (ESCs) showed proliferation defects associated with increased expression of the cyclin-dependent kinase inhibitors p21 and p27. [401] Additionally, these cells show a modest hyperacetylation oh histones H3 and H4, suggesting that HDAC1 is a major deacetylase in ESCs. Deletion of all HDAC1 and HDAC2 alleles in cardiac lineage results in neonatal lethality, accompanied by cardiac arrhythmias, dilated cardiomyopathy, and upregulation of genes encoding skeletal muscle-specific contractile proteins and calcium channel in the heart. [402] Therefore, HDAC1 and HDAC2 have central role in cardiac growth and development.

HDAC3 has the same domain structure as all class I HDACs. Although HDAC3 shares structural and functional properties with other class I HDACs, it exists in multiprotein complexes different from those of HDAC1 and 2, suggesting that HDAC3 has distinct functions due to its complex specificity. Similarly to HDAC1 and 2, HDAC3 enzymatic activity depends on the presence of two co-repressor: SMRT (silencing mediator for retinoic acid and thyroid hormone receptor) and N-CoR (nuclear receptor-repressor). Guenther and Lazar reported that SMRT and N-CoR not function merely as platforms for HDAC3 recruitment but also constitute an integral corepressor directly activating cellular HDAC3 enzymatic activity. [403] Interestingly, overexpression coupled to immunoprecipitation has allowed to discover that HDAC3 can co-precipitate with HDAC4, 5, and 7 suggesting that these class IIa HDACs can contribute to the formation of SMRT and N-CoR complexes. [404] In addition to protein-protein interactions with SMRT/N-CoR, the activity of HDAC3 is also regulated by phosphorylation. CK2 and DNA-PKcs can phosphorylate HDAC3 on S424 and this post-translational modification significantly enhances HDAC3 activity. [405] Moreover, GSK-3β can also phosphorylate HDAC3 and inhibition of GSK-3β protects against HDAC3-induced neurotoxicity. [406] In-mice deletion studies have showed that HDAC3 has an important role in liver and heart homeostasis. Deletion of HDAC3 in the postnatal

mouse liver lead mice developing hepatomegaly related to a hepatocyte hypertrophy and an imbalance between carbohydrate and lipid metabolism. These changes are associated to derepression of a gene program that is usually under the regulation of nuclear hormone receptors such as the thyroid hormone receptor and the peroxisome proliferator-activated receptor gamma (PPARγ), which control key steps in lipid and cholesterol biosynthesis. [407] In cardiomyocytes, deletion of HDAC3 produces mice that survive until 3-4 month of age and shows at this time massive cardiac hypertrophy and upregulation of genes associated with fatty acid uptake, fatty acid oxidation, and electron transport/oxidative phosphorylation accompanied by fatty acid-induced myocardial lipid accumulation and elevated triglyceride. All these abnormalities that mimic the metabolic derangements observed in diabetic cardiomyopathies can be attributed to an excessive activity of the nuclear PPARα. [408]

Unlike the other class I HDACs, HDAC8 does not interact with co-factor proteins but its activity is regulated by post-translational phosphorylation on S39. However, in this case, phosphorylation of HDAC8 inhibits rather than to enhance its activity. Indeed, S39A mutation improve HDAC8 activity, whereas an activator of HDAC8 phosphorylation causes a reduction in HDAC8 activity. [409] According to another evidence, phosphorylation of S39 predictably provoke a major structural disruption of this region of the surface, which ultimately would negatively influence HDAC8 activity. [410]

2.1.2. Class IIa HDACs

Class IIa comprises HDAC4, HDAC5, HDAC7, and HDAC9. These isoforms are homologs of Hda1 of *Saccharomyces cerevisiae*. The HDAC domain, which is located at the C terminus and is a region of 400-450 amino acids, shows the highest homology to yeast Hda1. In addition to this common region, class IIa isoforms present a 450-600 amino acid extension at their N terminus, and, in this part, the sequence homology is much lower (around 30-45%). The N terminus extremity presents a series of domains with regulatory functions, such as binding sites for MEF2 (myocyte enhancer factor 2) and domains for proteins 14-3-3. [411] Class IIa HDACs can shuttle between the cytoplasm and the nucleus in response to certain cellular signals and this ability has been extensively studied in differentiating muscle cells. [412] MEF2, in fact, is a DNA-binding transcription factor that plays an essential role in muscle differentiation. [413] When MEF2 is associated with HDAC4, -

5, or -7, its DNA binding activity is inhibited thus blocking muscle cell differentiation. However, following HDACs phosphorylation by kinases calcium/calmodulin-dependent protein kinase (CaMK) or protein kinase (PKD), the MEF2-HDAC complex dissociates. In this way, HDACs bind 14-3-3 and shuttle from the nucleus to the cytoplasm while MEF2 associates to HAT p300, thus providing muscle cell differentiation. [414] [415] Class IIa HDACs possess only minimal catalytic activity and often the deacetylation function of these enzymes is dependent on the interaction with class I HDACs. Fischle *et al.* showed that HDAC4, -5, and -7 are recruited by the SMRT/N-CoR complex and associated with HDAC3 in vivo. The authors reported also that the loss of HDAC3 from the complex leads to enzymatic inactivity. [416] [417] These evidences suggest that class IIa HDACs function as a link between DNA-binding recruiters and the HDAC3-containing HDAC complex subunit.

Class IIa HDACs are specifically expressed in tissues where they have well-defined functions. HDAC5 and HDAC9 are highly expressed in muscles, heart, and brain; [418] [419] HDAC4 is highly enriched in the brain and growth plates of the skeleton; [420] HDAC7 is more expressed in endothelial cells and thymocytes. [421] Diverse evidences have revealed that HDAC5 and HDAC9 control cardiovascular growth and function. [419] MEF2, in fact, has a central role in the control of cardiomyocyte differentiation and compound mutant mice lacking both HDAC5 and -9 have shown a propensity for lethal ventricular septal defects and thin-walled myocardium derived from abnormalities in growth and maturation of cardiomyocytes. Therefore, these defects in the cardiac development of mutant mice could be due to a super activation of MEF2 with consequent precocious differentiation and cell-cycle withdrawal of cardiomyocytes. Additionally, class IIa HDACs modulate also the activity of numerous other transcription factors involved in myocardial growth, such as calmodulin binding transcription activator 2 (CAMTA2). [422] Thus, the absence of HDAC5 and -9 interferes with the precisely coordinated gene expression program responsible for the myocyte differentiation, proliferation, and morphogenesis required for heart formation. On the other end, HDAC4 has a central role in the formation of the skeleton by controlling chondrocyte hypertrophy. [420] The ossification process provides that the cartilaginous elements named chondrocytes undergo hypertrophy followed by apoptosis and consequent invasion of osteoblasts that produce mature bone matrix. [423] HDAC4 is expressed in pre-hypertrophic chondrocytes where interacts with two transcription factors having vital roles in the control of chondrocytes hypertrophy

and bone formation: RUNX2 and MEF2C. [424] Therefore, the evidence that mice-lacking HDAC4 die for ectopic ossification of endochondral cartilage suggests that the absence of HDAC4 produces a hyperactivation of RUNX2 and MEF2C with consequent excessive bone formation. The evidence that RUNX2 or MEF2C gain-of-function phenotype in developing chondrocytes mimics the HDAC4 loss-of-function phenotype strengthens the proposed mechanism. [425] Thus, by repressing the activity of MEF2C and RUNX2, HDAC4 delays chondrocyte hypertrophy and control timing and extent of endochondral bones ossification. During embryogenesis, HDAC7 is specifically expressed in endothelial cells forming the inner lining of the cardiovascular system. [421] HDAC7-null mice die for the loss of integrity of endothelial-cell interactions with consequent rupture of blood vessels and hemorrhaging. In these mice, the absence of HDAC7 is accompanied by the upregulation of MMP10, an endoprotease that degrades the extracellular matrix, thereby perturbing the integrity of blood vessels. MEF2 also regulates the activity of MMP10 suggesting that in the absence of HDAC7, MEF2 activity is elevated, leading to pathological levels of MMP10.

2.1.3. Class IIb HDACs

Class IIb of the HDAC family comprises HDAC6 and HDAC10, which are closely related both phylogenetically and structurally. Both enzymes contain two deacetylase domains, though the functions and activity of these domains differ between the two. [426]

HDAC6 is the largest enzyme of the human HDAC family, with 1215 amino acids. It features two catalytic domains, arranged in tandem, and a C-terminal zinc finger domain that plays a role in the ubiquitination process. [427] The two deacetylase domains, CD1 and CD2, might function independently, but when separated, enzymatic activity is lost. [428] CD1 has both deacetylase and ubiquitin E3 ligase activity, suggesting that HDAC6 is prone to degradation, while CD2 exhibits broader substrate specificity. [429] Structurally, HDAC6 is primarily localized in the cytoplasm, due to a nuclear export signal (NES), and is involved in non-histone protein deacetylation. Its primary function is deacetylating α-tubulin, which forms part of the cytoskeleton, thus regulating microtubule stability. [430] Overexpression of HDAC6 results in potent deacetylation of α-tubulin, promoting cellular motility, particularly during chemotaxis. [431] Additionally, HDAC6 deacetylates a variety of other proteins, including HSP90, cortactin, β-catenin, and Tat, influencing

numerous cellular processes. [432] Interestingly, HDAC6 also has functions independent of its deacetylase activity, such as mediating the degradation of polyubiquitinated misfolded proteins through aggresome formation and regulating autophagy, heat shock factor-1 (HSF-1), and platelet-derived growth factor (PDGF) signaling. [433]

In contrast, HDAC10 has a more limited catalytic profile. While it also contains two deacetylase domains, the second is catalytically inactive and is referred to as a pseudo deacetylase domain. [434] HDAC10 has been shown to function primarily as a polyamine deacetylase (PDAC), with specificity for N^8-acetylspermidine over other polyamines like N^1-acetylspermidine. [435] This specificity is attributed to structural preferences, particularly the arrangement of four methylene units between the secondary amine and the amide function. [436] Although HDAC10 is a poor lysine deacetylase, some studies suggest that it might interact with other HDAC isoforms, potentially functioning more as a recruiter than a direct deacetylase. HDAC10's functions are less well understood compared to HDAC6, but evidence points to its involvement in regulating polyamine metabolism rather than broader cellular processes like transcription or protein degradation. [437]

2.1.4. Class IV HDACs

HDAC11 is the sole member of class IV HDAC phylogenetically related to HDAC3 and HDAC8 isoforms suggesting that it might be more related to class I HDACs than to the class II HDACs. HDAC11 contains a catalytic domain located at the N-terminus with proven deacetylase. [438] Still today, its function remains unknown. Very recently three independent studies have revealed that HDAC11 works as a defattyacylase instead of deacetylase enzyme. [439] HDAC11-dependent deacetylation of serine hydroxymethyl transferase 2 (SHMT2) affects the ability of SHMT2 to deubiquitinate the type I interferon receptor. Other studies are needed to better understand the biological roles of HDAC11 in cells. [440] HDACs involvement in many key regulator processes through their histone deacetylase activities as well as non-histone deacetylation and deacetylase-independent functions supports the scientific belief that HDACs play central roles in nearly every aspect of health and disease. Indeed, over the years, many reports documenting the involvement of HDACs in cancer, neurodegenerative diseases, metabolic disorders, inflammatory processes, immunological disorders, and cardiac and pulmonary diseases have been published.

2.2. HDACs Implication in Cancer

Cancer is the most dreadful disease in which classical HDACs are involved. Altered expression of different HDAC isoforms reported in the literature has confirmed the active role of HDACs in modulating all the hallmarks of cancer (**Figure 2.3**). [441] [442] Thus, the development of HDAC inhibitors (HDACi) has been strongly sustained with the aim to elucidate the roles of HDACs in cancer deeply and precisely and, therefore, to prove their anti-cancer efficacy.

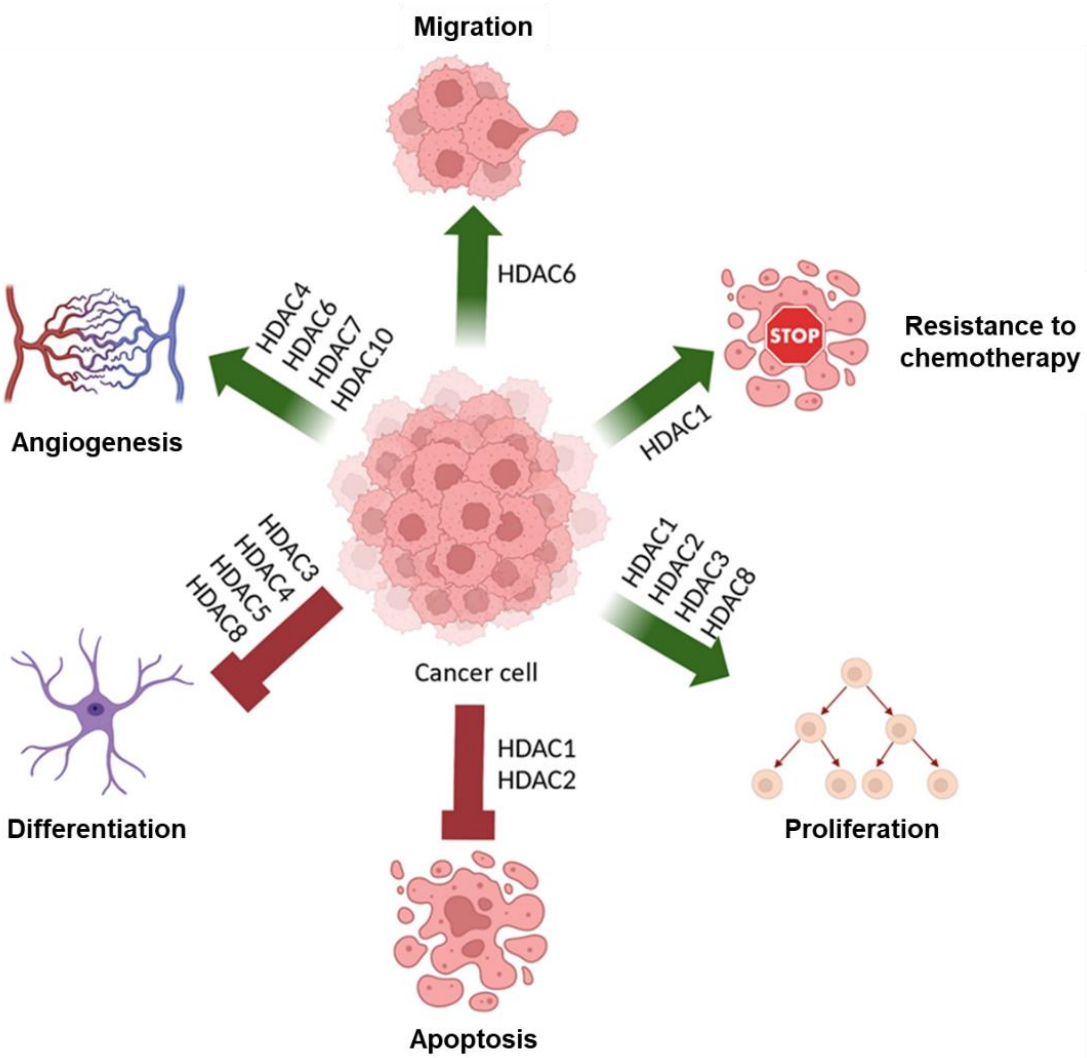

Figure 2.3. *HDAC family controls the hallmarks of cancer by preventing differentiation and apoptosis and promoting angiogenesis, migration, resistance to chemotherapy, and proliferation.* [442]

HDACs are involved in uncontrolled cell cycle and inhibition of differentiation by modulating the activity of tumor suppressor p21/WAF1 through distinct mechanisms. Firstly, HDAC2 is recruited by B-cell lymphoma 6 (B-CL6), an oncogenic transcription factor overexpressed in diffuse large B-cell lymphomas, to repress CDKN1A, which encodes p21/WAF1. However, HDAC-dependent deacetylation of B-CL6 also regulates its activity by disrupting its ability to recruit HDACs. [443] Secondly, as already mentioned above, HDAC1 directly deacetylates the tumor suppressor p53 that, once deacetylated, loses the ability to promote p21 transcription with consequent uncontrolled proliferation of cells. Therefore, HDAC1/2 inhibitors might up-regulate p21 expression and therefore provoke cell cycle arrest through both hyperacetylation of p53 and indirect transcriptional activation of CDKN1A. In concordance with these results, other papers have demonstrated, for example, that the knockdown of HDAC1 results in the arrest of the cell cycle, cell growth inhibition, and increase of apoptotic cells in osteosarcoma and breast cancer cells. [444] Moreover, HDAC1 overexpression has been found to increase proliferation and undifferentiated phenotype in cultured prostate cancer cells. [445] Similarly, in breast cancer cells, the knockdown of HDAC2 increases the functional DNA binding activity of p53 with consequent inhibition of proliferation and induction of cellular senescence. [446] HDAC1 has also been found overexpressed in chemotherapy-resistant neuroblastoma cells in vivo, while HDAC1 siRNA knockdown sensitized cells for etoposide treatment. These results suggest that HDAC1 might also have important roles in multidrug resistance. [447] HDACs are also involved in the regulation of hypoxia-induced angiogenesis, which is highly related to tumorigenesis. Among the angiogenesis factors, hypoxia-inducible factor 1 (HIF1) stimulates the expression of vascular endothelial growth factor (VEGF), which directly induces the angiogenesis process. For example, under hypoxic conditions, HDAC7 associates with HIF1 leading to an increased HIF1 transcriptional activity with a consequently improved expression of VEGF. [448] These results are confirmed by another study demonstrating that HDAC7 silencing in endothelial cells alters their morphology and migration forms a capillary tube-like structure. [449] In addition to HDAC7, also HDAC4, -6, and -10 control angiogenesis. Qian *et al.* demonstrated that HDAC4 and HDAC6 bind and regulate HIF-1α transcriptional activity in renal carcinoma cells, [450] while knockdown of HDAC10 and HDAC6 has been found to reduce VEGF receptor 1 and 2 expression in cancer cells. [451] The involvement of HDACs in angiogenesis has also been confirmed by the effects of HDACi, which reduce the expression of HIF1 and VEGF under hypoxic

conditions. [452] The roles of HDACs in cancer migration, invasion, and metastasis can be elucidated in many aspects. Firstly, changes in the extracellular matrix (ECM) regulate the ability of cancer cells to invade through the ECM itself. Whetstine et al. demonstrated that class I HDACs regulate the expression of ECM-related proteins such as ECM components, proteinases, proteinase inhibitors, and ECM-associated proteins with consequent modulation of ECM composition, deposition, and removal and induction of cancer cell invasion. [453] Secondly, the expression of many metastasis suppressors, such as KAI1 [454] and RECK, [455] has been found repressed by HDACs. HAI1 is a member of the tetraspanin family, capable of inhibiting the progression of cancer metastasis. [456] KAI1 downregulation in cancer cells depends on the interaction between β-catenin and a reptin chromatin-remodeling complex, which, in turn, require HDAC1 for their inhibitory functions. Thirdly, many other proteins, such as MMP2 and the metastasis-associated protein 1 (MTA1) promote cancer migration, invasion, and metastasis. Different studies have revealed the ability of HDACs to up-regulate also these proteins. [457] Finally, other studies have highlighted the involvement of HDAC6 overexpression in the increased migration of embryonic fibroblasts. Haggarty *et al.* reported that specific inhibition of HDAC6 reduces the migration of fibroblasts but does not alter cell cycle progression. [458]

2.2.1. HDACs and Lymphoma

Diffuse large B-cell lymphoma (DLBCL) stands as the most prevalent form of lymphoma, comprising 23-25% of non-Hodgkin's lymphoma cases. [459] While R-CHOP immunochemotherapy, a regimen combining rituximab, cyclophosphamide, doxorubicin, vincristine, and prednisone, offers a cure for approximately 60-65% of patients, a significant 35-40% experience disheartening outcomes, including disease relapse or refractory conditions. [460] This stark reality underscores an urgent necessity to delve deeper into the molecular underpinnings of DLBCL and to identify reliable prognostic biomarkers that could refine treatment strategies. Recent findings reveal that the expression levels of several HDACs, particularly HDAC1, HDAC2, HDAC3, HDAC6, HDAC7, HDAC8, and HDAC9, are markedly elevated in tumor tissues compared to normal controls. Wu *et al.* demonstrated that treating WSU-DLCL-2 and DB cells with Chidamide, the CFDA-approved HDAC inhibitor, for 24 to 48 hours resulted in dose- and time-dependent reductions in cell viability, likely through the induction of apoptosis. [461] This treatment impacted multiple biological processes, including PI3K/AKT signaling, mTOR signaling, cell

cycle regulation, and apoptosis pathways. The PI3K/AKT/mTOR pathway is crucial for B-cell proliferation and is often hyperactive in lymphomas. [462] [463] [464] Among the HDAC family, HDAC1 has garnered attention for its association with poor prognosis in DLBCL, with its overexpression linked to adverse outcomes. [465] Meanwhile, HDAC3 serves as a pivotal regulator of PD-L1 transcription in B-cell lymphomas, where its inhibition has been shown to enhance responsiveness to anti-PD-1 therapies. [466] Thus, targeting HDAC3 emerges as a potential avenue for immunotherapy in B-cell lymphomas. Additionally, in follicular lymphoma (FL) and diffuse large B cell lymphoma (DLBCL), Bcl6 recruits HDAC3 to repress transcription and trigger B cell lymphoma. [467] Furthermore, other HDACs, such as HDAC5 and HDAC8, have demonstrated efficacy in treating T-cell lymphomas, highlighting the therapeutic promise of HDAC inhibition. [468] All these data strongly suggest that HDACs are promising therapeutic targets for GC lymphomas, including DLBCL. In parallel, the pathogenesis of peripheral T-cell lymphoma (PTCL) is a complex interplay of genetic and epigenetic alterations that influence both the inherent characteristics of post-thymic T cells and the surrounding tumor microenvironment. [469] [470] Gene expression profiling has delineated distinct molecular subtypes of PTCL, revealing their relationship to normal T-cell origins. For instance, angioimmunoblastic T-cell lymphoma shares genetic signatures with normal T follicular helper cells. In PTCL, HDACs critically modulate downstream gene expression and signaling networks by deacetylating transcription factors and mediators. Integrating gene expression profiling with mutational analysis has solidified the rationale for employing HDAC inhibitors (HDACis) as therapeutic agents for mature T-cell lymphomas. These inhibitors can induce apoptosis in PTCL cells by rectifying aberrant signaling pathways mediated by HDACs, often stemming from dysregulated gene expression or the premature degradation of pro-apoptotic proteins. Notably, mutations in TET2 and DNMT3A frequently emerge early in PTCL development, where HDAC1 and HDAC2 facilitate the deacetylation and subsequent degradation of TET2 via the ubiquitin-proteasome pathway. [471] Furthermore, HDAC1, HDAC2, and HDAC3 are implicated in repressing the transcription of STAT3 target genes within the JAK/STAT pathway, contributing to the epigenetic silencing of tumor suppressor genes. [472] Inhibiting these HDACs could therefore halt cell growth or trigger apoptosis. [296] Additionally, alterations in the TP53 gene and disruptions in the p53 pathway play critical roles in the dysregulation of cell cycle control and apoptosis in PTCL. [473] TP53 mutations are typically associated with late-stage T-cell lymphomas and correlate with poor

prognosis. The deacetylation of TP53 by HDAC1 compromises its functionality, leading to reduced expression of p21 and impaired apoptotic signaling. [474] Conversely, HDAC inhibitors can enhance TP53 acetylation, restoring its activity and apoptotic capacity in TP53-deficient tumors. Moreover, HDACs facilitate the activation of NF-κB within the TCR/CD3 pathway, representing another potential target for small molecule inhibitors. Beyond promoting apoptosis, HDAC inhibitors may also encourage autophagy, adding another layer of therapeutic potential in T-cell lymphomas. [475] For example, SAHA (Vorinostat) has been shown to enhance autophagy by inhibiting mTOR, which subsequently boosts autophagic factors' efficacy. [476] Finally, HDAC inhibitors can also influence the tumor microenvironment by disrupting angiogenesis. [474] Evidence suggests that these agents can modulate pro-angiogenic signaling pathways, leading to reduced expression of vital pro-angiogenic factors such as basic fibroblast growth factor (bFGF), vascular endothelial growth factor (VEGF), angiopoietin, and endothelial nitric oxide synthase. In summary, targeting HDACs presents a multifaceted approach to diagnosing and treating DLBCL and PTCL, offering promising avenues for future therapeutic strategies. [112]

2.3. HDACs Relevance in Neurodegenerative, Cardiovascular, Immune and Inflammatory Diseases

Considerable evidence has highlighted that dysregulation of the balance between HDACs and HATs (especially CBP and p300) availability is responsible for synaptic plasticity and cognition disorders. Loss of CBP and therefore increase in HDACs availability and functionality, seems to be pivotal in facilitating a neurodegenerative cascade of events. [477] Indeed, oxidative stress, reported to be correlated to several neurodegenerative diseases, such as Alzheimer's disease (AD), Parkinson's disease, Huntington's disease (HD), stroke, multiple sclerosis, and Friedreich's ataxia, fail to induce neuronal apoptosis when cells are treated with HDAC inhibitors. [478] Therefore, HDAC inhibitors currently represent potential therapeutics for neurodegenerative disorders. Diverse evidence has demonstrated that HDAC inhibitors reactivate multiple genes encoding for proteins that contribute to neurotrophicity, anti-inflammation, and subsequently neuroprotection such as brain-derived neurotrophic factor (BDNF), glial-derived neurotrophic factor (GDNF), heat shock protein 70 (HSP70), p21, Blc2, Bcl-XL, and gelosolin. [479] For example, two HDAC inhibitors protect against α-synuclein-dependent neurotoxicity in a Parkinson's disease transgenic fly model. [480] Moreover, HDAC2

overexpression results in decreased synaptic plasticity, synapse number, and memory formation in Alzheimer's disease and HDAC inhibition rescues the synaptic number and learning impairments. [481] In addition, HDAC6 protein levels are increased in Alzheimer's disease brains where it has been demonstrated that HDAC6 can interact with tau, a microtubule-associated protein that forms neurofibrillary tangles. [482] Numerous small molecule HDAC inhibitors reducing cardiac injury and pathological remodeling in preclinical models of myocardial infarction, [483] [484] pressure overload, [485] [486] pulmonary hypertension, [487] diabetic cardiomyopathy [488] [489] and ischemia/reperfusion injury have confirmed the involvement of HDACs in cardiovascular pathologies. [490] [491] For example, HDAC inhibition has been reported to prevent cardiomyocyte hypertrophy and apoptosis, interstitial collagen deposition, capillarity rarefaction, and the development of cardiac dysfunction in a streptozotocin mouse model of diabetic cardiomyopathy. [106] HDACs also play central roles in inflammation and innate immune response. For example, inhibition of HDAC activity promotes the downregulation of IL-6, TNF-α, IL-1-β, NO, and IFN-γ by macrophages in response to lipopolysaccharide (LPS) stimulation in both mice and humans. [492] [493]

2.4. HDAC inhibitors approved for therapy and in clinical trials

A Zn^{2+} ion can be found at the bottom of the active site in most of the known HDAC isoforms. Such catalytic tunnel is highly conserved across many species. Therefore, the developed HDACi possess a precise pharmacophore model formed by a zinc-binding group (ZBG), crucial for the coordination of the catalytic zinc ion, a linker chain like hydrophobic spacer (HS), mimicking the lysine chain, a connecting unit (CU), that typically is represented by a carbonyl group involved in various chemical functions (ketone, amide, reverse amide, sulphonamide, carbamate, etc.) or by a heterocyclic ring, and a "cap" group responsible for the interaction with the rim at the active site's entrance (**Figure 2.4**). [494]

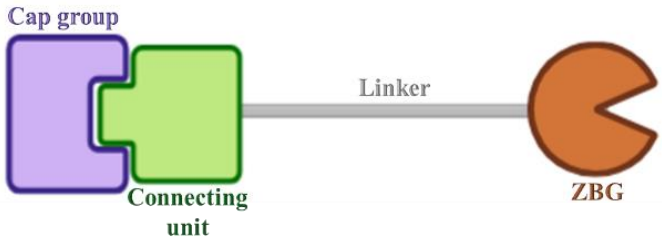

Figure 2.4. *Schematic representation of pharmacophore model for HDAC inhibitors.* [495]

The major classes of HDAC inhibitors comprise short-chain fatty acid-derived inhibitors, hydroxamic acids, benzamides (2'-aminoanilides), and cyclic peptides. [496]

Hydrazide-based HDAC inhibitors were also described. [497] In most of HDACi, the ZBG are hydroxamates, anilides, or thiols, with strong chelating properties for the catalytic Zn^{2+} ion.

Hydroxamic acid-based HDAC inhibitors were the first to be developed. In fact, the history of HDACi started from the natural metabolite Trichostatin A (TSA), the first potent HDAC inhibitor described by Yoshida *et al.* in 1990. [498]

TSA can be used as a perfect example of the HDAC pharmacophore: the hydroxamic acid functions as a bidentate zinc chelator, the diene as a rigid linker, and the substituted phenyl ring as the cap group. TSA was the most known HDACi and one of the most used as a chemical probe to dissect physio- and pathological roles of HDACs in many contexts.

In 2006, suberoylanilide hydroxamic, SAHA (Vorinostat), was the first synthetic FDA-approved non-selective HDAC inhibitor used in the treatment of cutaneous T-cell lymphoma. [499] SAHA acts as a zinc chelator in the HDAC active site in a bidentate fashion. [500] As shown in preclinical studies, SAHA reduces metastatic potential and proliferation of tumor cells via the induction of apoptosis and cell-cycle arrest. SAHA also sensitized tumor cells to chemotherapy and/or radiotherapy. [501] [502] Even if it was the first approved, the metabolic and kinetic profiles *in vivo* are far from ideal. [503] [504]

TSA and SAHA are substrate-competitive inhibitors of HDACs. Both the compounds, in fact, insert their aliphatic chains into the tube-like hydrophobic portion of the pocket and mimic the lysine side chain of the natural substrate. The hydroxamic groups, instead, reach the polar bottom at the end of the tunnel, where the zinc ion is coordinated through the carbonyl and the hydroxyl groups.

Additionally, hydroxamates can form hydrogen bonds with the charge-relay systems histidines/aspartates, and with the Tyr297 hydroxy group with the consequent removal of the water molecule from the catalytic site. The two aromatic portions (4-dimethylaminophenyl and phenyl groups of TSA and SAHA, respectively) interact at the pocket entrance and in an adjacent surface groove, resulting in a capping of the pocket (**Figure 2.5**). [495]

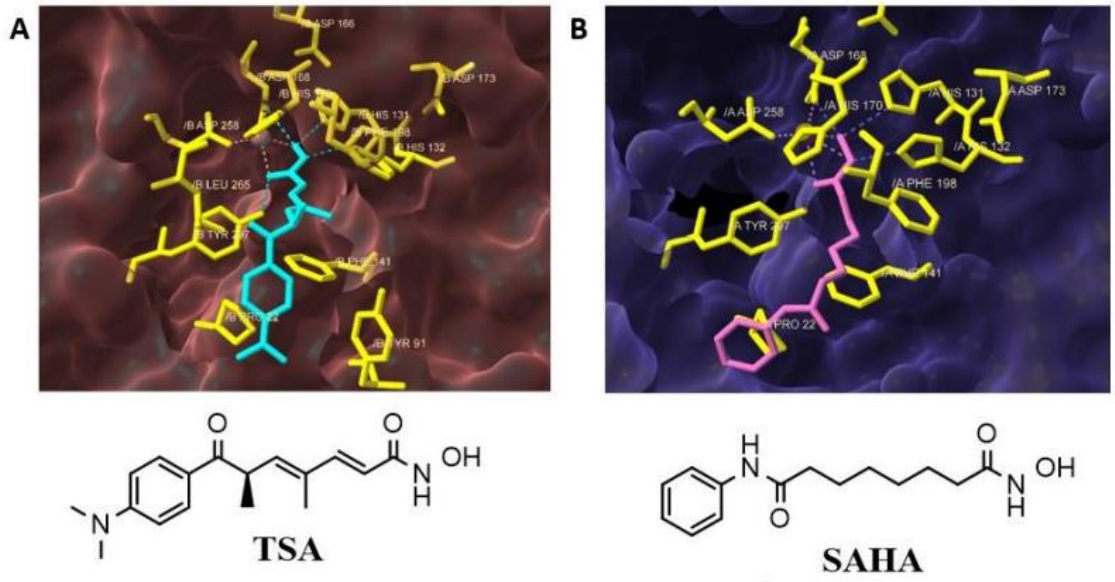

Figure 2.5. ***A****) Crystal structure of Trichostatin A (TSA) with HDLP (PMID: 1C3R);* ***B****) Crystal structure of Suberoylanilide hydroxamic acid (SAHA) with HDLP (PMID: 1C3S).* [495]

So far, six HDACi have been approved for cancer treatment by the US Food and Drug Administration (FDA) and Chinese FDA (CFDA) and Vorinostat (Zolinza®) was the first approved HDAC inhibitor as a pan-HDAC inhibitor.

The second one was the depsipeptide Romidepsin (FK228, Istodax®), a class I-selective inhibitor able to treat relapsed or refractory cutaneous T-cell lymphoma (CTCL) and peripheral T-cell lymphoma (PTCL). [505] [506] Romidepsin, isolated from the bacterium *Chromobacterium violaceum*, is a bicyclic depsipeptide antibiotic with antineoplastic activity. Since thiols are not very stable and possess poor bioavailability, the disulfide in Romidepsin resulted in higher stability and cell permeability. [507] It is a prodrug, as in the target cells the disulfide is reduced to an active metabolite containing a thiol group able to chelate the zinc ions in the active site of the class I HDACs. [508] After intracellular activation, Romidepsin inhibits histone deacetylase (HDAC) at low nanomolar levels; in particular, it shows more selectivity for HDAC1 e HDAC2. This led to alterations in gene expression and the induction of cell cycle arrest, cell differentiation, and apoptosis.

Panobinostat (LBH589, Farydak®) and Belinostat (PXD101, Beleodaq®) are on the market upon FDA approval for patients with multiple myeloma (MM), cutaneous

T-cell lymphoma, PTCL (peripheral T-cell lymphoma). [509] [510] Panobinostat is a pan-deacetylase hydroxamic acid-based inhibitor approved for the treatment of adult patients with relapsed and/or refractory multiple myeloma (RRMM). These patients did not respond (anymore) to at least two previous therapies, such as by bortezomib or immunomodulatory agents. It is administered orally and has been formulated in capsules containing the active principle as a lactate salt. [511] Panobinostat has been noted to play important apoptotic roles in cancer cells. Since Panobinostat monotherapy in people with RRMM has not shown sufficient activity, an attempt was made to switch to a combination therapy of HDACis with bortezomib and dexamethasone. The most prominent side effects of Panobinostat are diarrhea, fatigue, thrombocytopenia, asthenia, lymphopenia, and peripheral neuropathy. [512] Belinostat is a pan-deacetylase hydroxamate-based inhibitor approved for the treatment of patients with relapsed or refractory peripheral T-cell lymphoma (PTCL), a heterogenous non-Hodgkin Lymphoma, with poor outcomes. [510] Malignant T cells are particularly susceptible to the effects of this inhibitor as an accumulation of acetyl groups on histone tails causes cell cycle arrest and apoptotic cell death. [309] It is present in lyophilized form for intravenous administration. Belinostat's most common adverse reactions are nausea, vomiting, fatigue, pyrexia, and anemia in patients with PTCL. Beyond these, hepatotoxicity is undoubtedly the most serious side effect of Belinostat, not to be underestimated.

Tucidinostat (Chidamide, Epidaza®) is the only HDAC inhibitor approved by the Chinese FDA (CFDA) for the treatment of relapsed or refractory peripheral T-cell lymphoma (PTCL). [495] [513] It inhibits HDAC1, HDAC2, HDAC3, and HDAC10 with IC_{50} of 95, 160, 67, and 78 nM, respectively. [514] According to the crystal structure, this compound coordinates the zinc ion in a bidentate way, mainly via the amine group and much weakly via the carbonyl oxygen. Compared to the hydroxamic acid HDAC inhibitors, benzamide derivatives are usually characterized by class I selectivity or individual HDAC isoform selectivity.

On the 21st of March 2024, the FDA approved Givinostat (Duvyzat®) for the treatment of Duchenne Muscular Dystrophy (DMD) in patients six years of age and older. [515] It is a potent inhibitor of class I and II HDACs, developed by the Italian company Italfarmaco. It represents the first nonsteroidal drug approved to treat patients with all genetic variants of DMD. It is a histone deacetylase (HDAC) inhibitor that works by targeting pathogenic processes to reduce inflammation and loss of muscle. [516] This HDAC inhibitor represents the first approved non-cancerous HDAC inhibitor. [517]

To summarize, until today there is a total of six approved HDAC inhibitors (**Figure 2.6**).

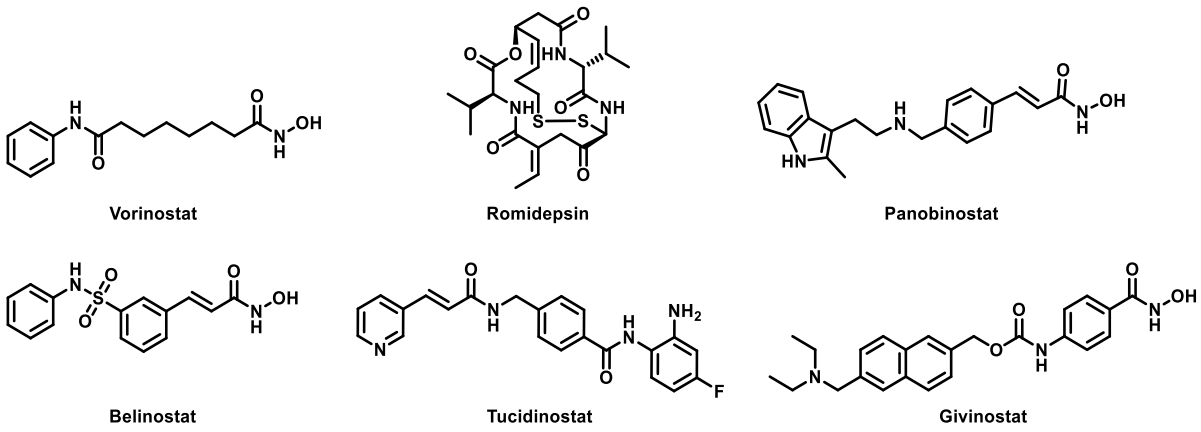

Figure 2.6. *Chemical structure of FDA-approved HDACi: Vorinostat, Romidepsin, Panobinostat, Belinostat, and Givinostat; chemical structure of CFDA-approved HDACi: Tucidinostat.*

In addition to these just-mentioned approved HDAC inhibitors, there are other important HDAC inhibitors, both hydroxamates and 2'-aminoanilides. Some representative examples are reported in **Figure 2.7**. Between the HDAC inhibitors containing cinnamyl- and benzoyl-hydroxamate ZBG, we find Resminostat and Pracinostat. Resminostat is an orally available class I, IIB, and IV HDAC selective HDACi with a potent inhibition for HDAC1, HDAC3, and HDAC6, with IC_{50} values in the nanomolar range (42.5, 50.1, 71.8 nM, respectively). [518] It has been used in clinical trials, for example, to treat hepatocellular carcinoma and Hodgkin's lymphoma. Structurally, Belinostat and Panobinostat are similar to Resminostat and to another clinical candidate, Pracinostat, [519] since all these molecules contain a cinnamoyl linker replacing the polymethylene moiety of vorinostat. Generally, these cinnamates are characterized by a longer metabolic half-life, while the addition of a polar function in Pracinostat and Resminostat improves their oral bioavailability. Moreover, there is a series of compounds containing a rigid benzoylhydroxamic acid includes Givinostat (ITF2357) 140 and AR-42 (OSU-HDAC42). [520] Structurally, these molecules are characterized by a more rigid benzoyl linker. AR-42 is a nanomolar HDAC inhibitor (IC_{50}=16 nM) related to hydroxamate-tethered phenylbutyrate. [520] [521] AR-42 has been evaluated in clinical trials to treat various diseases such as acoustic neuroma, intraocular lymphoma,

meningioma, testicular lymphoma, and vestibular schwannoma, among others. [522] [523] Entinostat is a synthetic benzamide HDAC inhibitor showing selectivity against isoforms 1 and 3 of the HDAC's family, with an IC_{50} of 0.3 and 8 μM for HDAC1 and HDAC3, respectively. Entinostat is an orally bioavailable drug; its most common adverse events include fatigue, gastrointestinal effects, hematologic and metabolic abnormalities. Entinostat has been studied in numerous phase I and II trials for solid and liquid tumors, including breast cancer. [524] Mocetinostat is a 2'-aminoanilide HDAC inhibitor with potential antineoplastic activity, inhibiting isoforms 1, 2, and 3 of HDAC. It possesses antitumor properties mainly in hematological tumors and much less in solid tumors, and it induces cell death, in part via the mitochondrial pathway and the destabilization of microtubules. [525] The most common side effects are manageable such as fatigue, nausea, and vomiting. [526]

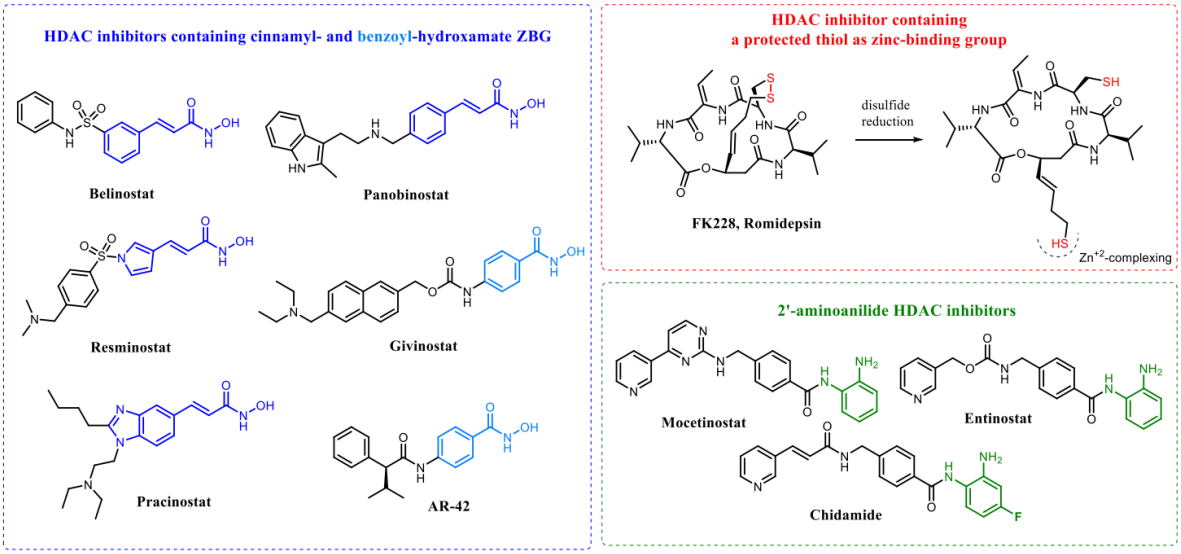

Figure 2.7. *Examples of approved or in clinical trials HDAC inhibitors containing cinnamyl- (in blue) and benzoyl- (in light blue) hydroxamate ZBG; protected thiol as ZBG; 2'-aminoanilide HDAC inhibitors.*

Currently, there are more than 20 HDACi in various stages of clinical evaluation, either as single agents or in combination with other chemotherapeutic agents or radiation therapy for the treatment of solid or liquid tumors (Search for HDAC inhibitors - List Results - ClinicalTrials.gov).

3. Histone Methylation

Although the first evidence of histone methylation dates to 1964, it was only in 2000 that the first histone methyltransferase was reported in literature and starting from that moment the potential of the histone methylation marks to control epigenetic events has greatly fascinated scientific researchers. [527] [528] Initially, protein methylation was believed to be irreversible. However, in 2004 after the discovery of the first demethylase (LSD1), [529] this process was regarded as reversible and dynamic, involved in the regulation of a variety of events. [530] Considering that methylation does not change the charge of lysine or arginine residue, it seems that its effect on chromatin structure is indirect. However, each methyl mark should be regarded as a signal that can be recognized by specific reader domains and lead to downstream effects. Histone methyltransferases, able to catalyse the methylation of specific aminoacids transferring activated methyl groups from the SAM co-substrate to the target residue, can be divided into two major types: lysine-specific (KMTs) and arginine-specific methyltransferases (PRMTs). The 4 lysine specific methyltransferases are the largest class, including 51 members. [352] With the sole exception of DOT1L, all the KMTs are SET domain containing proteins. The SET domain itself contains the catalytic core. DOT1L contains a different catalytic domain, and for structure and sequence similarity is closer to PRMTs than KMTs. [352] Nevertheless, all the KMTs have a similar catalytic mechanism, promoting the transfer of a methyl group from S-adenosyl-L-methionine (SAM) to the ε-amino group of lysine. [531] Much of what we know about lysine methylation derives from the study of chromatin and histone methylation so the enzymes catalyzing these reactions were first named histone lysine methyltransferases (HKMTs) and histone lysine demethylases (HKDMs), respectively. [532] [533] Subsequently, together with the growing body of evidence reporting that these enzymes have non-histone substrates, they were renamed as lysine methyltransferases (KMTs) and demethylases (KDMs). Lysine methylation can occur at three different levels (mono-, di-, and tri-methylation), having different outcomes depending on the differently recruited binding proteins (readers) able to recognize this mark. In contrast to acetylation, regarded exclusively as a gene-activating PTM, histone lysine methylation can be associated both with gene activation or silencing, depending on the degree and location of the methylated residue. For example, di- and tri-methylation of H3K9, H3K27, and H4K20 are generally associated with gene silencing, whereas H3K4, H3K36, or H3K79 methylation is a mark of gene expression. [534] [535] Protein arginine methyltransferases can be divided into three

classes: type I PRMTs (PRMT1, PRMT2, PRMT3, PRMT4, PRMT6, and PRMT8), able to produce monomethyl arginine (MMA) and asymmetric dimethylarginine (ADMA) (dimethylation of one of the terminal guanidino nitrogens); type II PRMTs (PRMT5 and PRMT9), able to produce MMA and symmetric dimethylarginine (SDMA) (monomethylation of both terminal guanidino nitrogens); type III PRMT or PRMT7, the only known PRMT able to produce only MMA. [536] As lysine methylation, also arginine histone methylation can favor or prevent the interaction of nuclear factors with other nearby histone marks. [537] [538] Arginine methylation can influence histone function by either impairing the ability of arginine to form hydrogen bonds, [539] or recruiting specific reader-domain-containing proteins. [540] Generally, histone SDMA is associated with transcriptional repression, while histone ADMA is related to gene expression. [541] Commonly methylated arginine residues include: H2AR3, H4R3, H3R8, and H3R2. 51 In our research, we focused our attention on the lysine methyltransferase EZH2 and the PRC2 complex.

3.1. The PRC2 complex

First identified in the fruit fly *Drosophila melanogaster* as key repressive regulators of developmental genes (e.g. homeobox HOX genes), [542] the polycomb group (PcG) proteins were later proved to be highly evolutionary conserved, from unicellular organisms to humans. [543] PcG proteins, assembled in multiprotein Polycomb Repressive Complexes (PRCs), control gene silencing mainly, but not only, through histone Post-Translational Modifications (PTMs). Two main polycomb group complexes are described in mammals: Polycomb Repressive Complex 1 (PRC1) and 2 (PRC2). Additionally, the PhoRepressive Complex (PhoRC) and the Polycomb Repressive Deubiquitinase (PR-DUB) have been identified. [544] [545] [546] The PRCs possess histone-modifying activities. PRC1 monoubiquitinates lysine 119 of histone 2A (H2A), and can compact chromatin by binding to nucleosomes, while PRC2 catalyzes up to tri-methylation of lysine 27 of the histone 3 (H3K27), a repressive chromatin mark. [546] [547] [548] Interestingly, PRC1 has been shown to recognize and bind H3K27me3, and PRC2 is able to recognize H3K27me3 as well as H2AK119ub1. [549] [550] [551] [552] In this way PRC1 and PRC2, being recruited at specific genomic loci, can cooperate in silencing gene expression. [553] The minimal PRC2 core complex, endowed with catalytic activity, includes the following subunits: Enhancer of Zeste Homologue 1 (EZH1) or Enhancer of Zeste Homologue 2 (EZH2), Suppressor of Zeste 12 (SUZ12), and Embryonic Ectoderm Development (EED). Additional

protein subunits such as Retinoblastoma Associated protein 47 or 48 (RbAp46/48, also named RBBP4/7), Adipocyte Enhancer-Binding Protein 2 (AEBP2), Polycomb-like proteins (PCLs), and Jumonji and AT-Rich Interaction Domain 2 (JARID2) have been reported to play a role in the PRC2, modulating its activity in different contexts. [554] Many of these non-core subunits contain DNA or histone binding domains and can favor the recruitment of PRC2 to certain regions, promoting H3K27 methylation. [555] [556] [557] Since its discovery, there has been intense research activity in trying to elucidate the PRC2 structure, in order to explain its functions better.

Even though structural and biochemical data on individual subunits started to be available around 2007, the first structural study on the PRC2 complex was published only in 2012, when Ciferri *et al.* reported the first low-resolution electron microscopy (EM) structure of the PRC2 complex bound to AEBP2. [558] Here, we will give an overview of the structure and functions of the diverse subunits, as well as of the PRC2.

An updated review of PRC2 structure and functions has been published by *Moritz et al*. [557] Not much is known about SUZ12. SUZ12 may be involved in chromatin silencing in association with the ncRNA HOTAIR, as suggested by the studies of Rinn *et al.* [559] The C-terminus of SUZ12 contains a Zinc-finger motif, that seems to be involved in ncRNA binding. Much more is known about EED structure and functions. EED folds into a WD-repeat structure, containing seven copies of the WD-repeat motif forming the seven-bladed propeller structure. WD-domains act as scaffolding elements; thus, they can bind many proteins and have different functions. The primary sequence of EED shares only 18% identity with other WD-repeat proteins, nevertheless, structural comparisons show a good level of conservation of the WD-repeat domain. [560]

In 2007, Han *et al.* first identified a minimal 30-residue (aa 39-68) motif of EZH2 essential for EED binding, named EED-binding-domain (EDB). In the same work, they also reported the crystal structure of mouse EED bound with an EDB peptide. The crystal structure showed that the EDB binds to the bottom of the WD-repeat domain. Interestingly, in this work, they demonstrated that the key residues for EZH-EED binding are conserved not only in EZH2 and EZH1 but also in the *Drosophila* homolog. Additionally, they have demonstrated how mutations in critical interaction residues, both in EED or EZH2, totally abolish the interaction. [560] Following studies by Margueron *et al.* further proved and defined the essential role

of EED. [561] They found that EED binds preferentially histone methylated residues associated with gene silencing, and after crystal structure resolution, they were also able to explain the molecular basis of this selective recognition. Through kinetic studies, they also showed that EED binding to H3K27me3, but not to H3K27me1 or H3K27me2, stimulated PRC2 catalytic activity, thus proving the function of EED as a promoter of the propagation of repressive histone marks. [561]

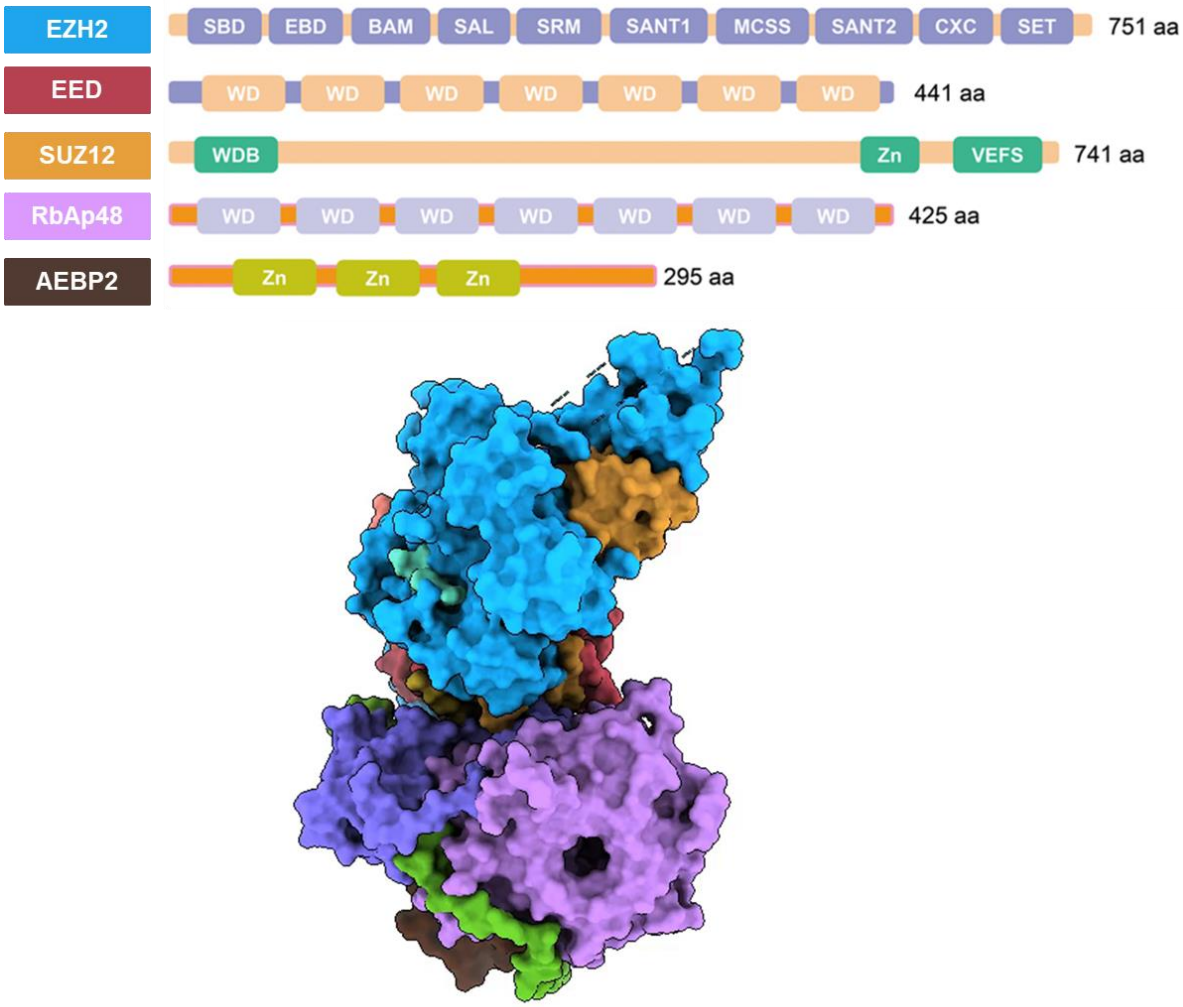

Figure 3.1. *Domain organization of each subunit in the human PRC2 complex (aa, amino acid) and surface image of PRC2 complex. (PDB ID: 6C23).*

3.1.1. PRC2 crystal structure

In 2015, Jiao and Liu reported the first crystal structure of an active PRC2 complex (170 kDa) from the yeast *Chaetomium thermophilum* (*Ct*PRC2). [562] In this work, they show the structure of the PRC2 complex both in a basal and stimulated state. Interestingly, comparing the two structures, they noticed the presence of a mobile EZH2 motif being allosterically modulated and regulating active site accessibility. [562]

Justin *et al.*, in 2016, solved the crystal structure of the stimulated state of a human PRC2 complex (*Hs*PRC2), containing EZH2 and EED polypeptides with the Vefs fragment of the SUZ12 subunit, together with a SAH cofactor, and the two peptides JARID2-K116me3 peptide (a high affinity activator), and H3K27M peptide (based on the oncogenic histone H3 mutation, binding and inhibiting the SET domain) (**Figure 3.2.A**). [563] [564] The reported complex is arranged to form a trilobated tri-dimensional structure, where the first two lobes have regulatory functions, and the third is involved in catalysis. The so-called N-lobe is composed of EED and the N-terminal region of EZH2. The middle lobe includes SUZ12 Vefs and the MCSS and SANT2 domains of EZH2. Finally, the catalytic lobe comprises the pre-SET and SET domains of EZH2 and the N-terminus of the Vefs domain. A superimposition of the *Ct*PRC2 and *Hs*PRC2 revealed a surprising evolutionary conservation of the core complex, even though there are evident differences between the two crystal structures (**Figure 3.2.B**). Additionally, the key interactions for the allosteric activation of the SET domain have been highlighted by comparing the structures of the isolated SET domain and the *Hs*PRC2 (**Figure 3.2.C**). The most important difference resides in the cSET motif organization. In fact, in the isolated SET domain, this motif is mostly disordered. Partially occupying the substrate binding pocket, it contributes to the auto-inhibited state. Conversely, in *Hs*PRC2 the cSET motif is flipped out of the substrate cleft, thus being available for catalysis.

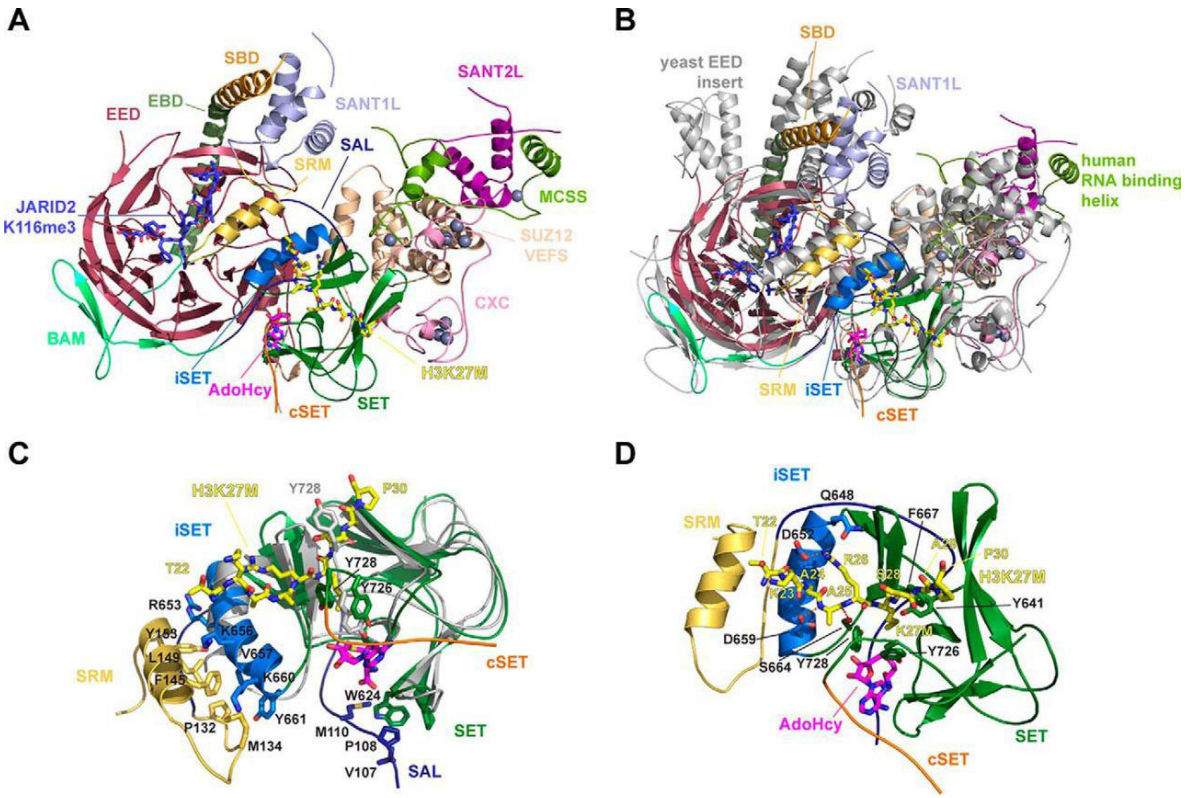

Figure 3.2. ***Structure and regulation of the HsPRC2 core complex.*** ***A****. HsPRC2 in complex with JARID2K116me3, H3K27M peptides, and AdoHcy (PDB: 5HYN).* ***B****. Superimposition of the stimulated CtPRC2 complex (gray) and the stimulated human PRC2 complex (PDB: 5KJH and 5HYN).* ***C****. Structural alignment of the isolated SET domain of EZH2 (gray) and the SAL, SRM, iSET, cSET, and SET domains of EZH2 in the HsPRC2 stimulated complex (PDB: 4MI0 and 5HYN).* ***D****. Close-up view of the H3K27M peptide and AdoHcy bound to HsPRC2 (PDB: 5HYN).* [557]

3.1.2. PRC2 catalytic core (EZH1 and EZH2), and the importance of the complex

The lysine methyltransferases EZH1 or EZH2 constitute the catalytic subunit of the PRC2 complex. They contain the conserved catalytic SET domain found in many other KMTs, and they both use S-adenosyl-L-methionine (SAM) as a co-substrate. Even though EZH1 and EZH2 possess a high sequence similarity, with 76% overall identity and 96% sequence identity in their catalytic SET domains, they exhibit different catalytic efficiencies, distinct chromatin binding properties, and expression patterns. EZH1 is expressed both in dividing and non-proliferative differentiated/adult cells, while EZH2 is only active in dividing cells. [554] Besides that, EZH1- containing PRC2 (PRC2-EZH1) displays lower methyltransferase activity than PRC2-EZH2. [565] Several pieces of evidence suggest that PRC2-EZH2 should establish cellular H3K27me1/2/3 levels, while PRC2-EZH1 is involved in restoring H3K27me1/2/3 that could have been lost upon histone exchange or through demethylase activity. [565] By themselves, EZH1 and EZH2 are not able to catalyze H3K27 methylation, but they require the co-presence of at least two other protein subunits in the complex: EED and SUZ12. [566] [567] [568] EZH2 has been proved to have also PRC2-independent functions, being involved in the methylation of several non-histone substrates, such as the transcription factors GATA4 and PLZF. [569] [570] The non-PRC2 activity of EZH2 could drive transcriptional activation, rather than repression. [571] As with all the other epigenetic marks, H3K27 methylation is reversible due to the activity of the histone demethylases UTX and JMJD3. [572] [573] [574] [575] [576]

3.1.3. EZH2 SET domain structure

The crystal structure of the EZH2 SET-containing catalytic domain was resolved independently by two different groups in 2013. [577] [578] The crystal structure shows that the catalytic domain is typically folded as a SET domain methyltransferase in the absence of binding partners. It contains two zinc-binding domains at the N-terminal, each of them binding three zinc ions (CXC domain). The C-terminal region is composed of the SET domain, with an inserted SET (iSET) motif and a C-terminal SET (cSET or postSET) motif following the SET domain. The SET domain of EZH2 is a typical SET methyltransferase domain characterized by a highly hydrophobic channel (Y641, F667, F724, Y726, and Y728) which accommodates the long aliphatic chain of the lysine substrate. At the end of this channel, a second pocket contains the SAM co-substrate, which is orientated so it brings the methyl group in close proximity to the lysine ε-amino group. [579] Some residues that lie at the interface

between the two pockets (e.g. Y641, A677, and A687) are crucial for catalysis (**Figure 3.3**). Their mutations, in fact, provoke changes in affinity for the substrate that are associated with gain-of-function phenotypes (see below). Noteworthy, this active conformation, differently from the other SET-containing methyltransferases, is possible only when EZH2 interacts with the other components of the PRC2 catalytic core. Remarkably, the isolated EZH2 SET-domain adopts a conformation that does not allow the binding of the co-substrate SAM and of the substrate (auto-inhibited), being thus unable to methylate its H3K27 substrate in the absence of protein interaction partners, EED and SUZ12. The authors proposed that the isolated SET domain acquires an auto-inhibited conformation, and the interactions with N-terminal regions of full-length EZH2 and/or other PRC2 subunits induce conformational changes defining an active cofactor binding site. [580]

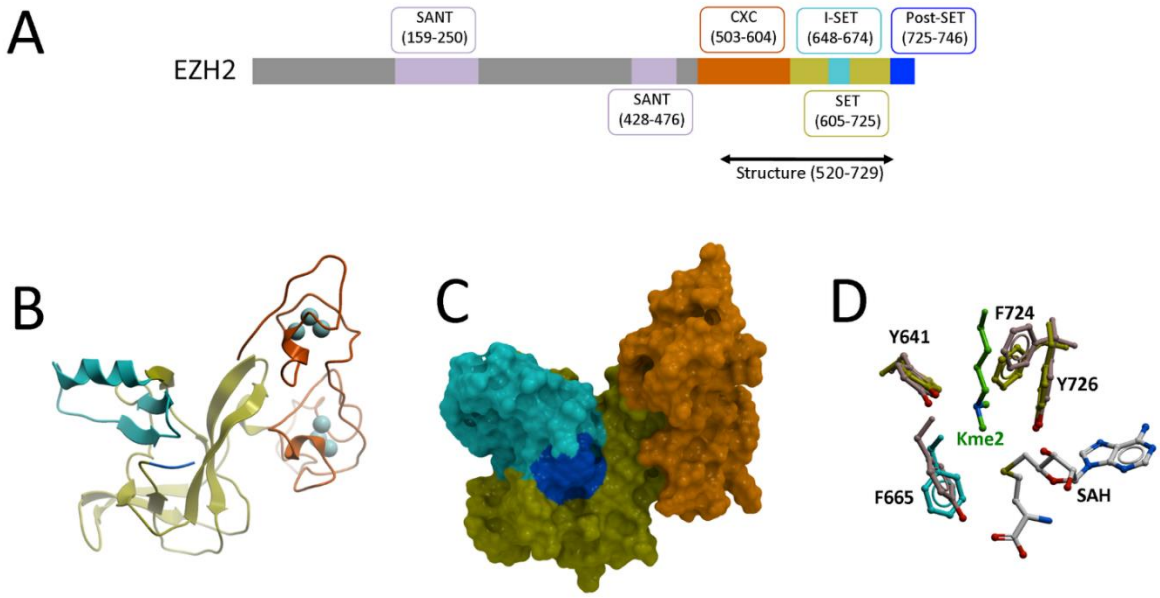

Figure 3.3. A) *Representation of the linear domain architecture of EZH2: it shows the crystallized construct (520-729), which indicates the parts of EZH2 successfully crystallized for structural analysis;* **B)** *Catalytic SET-domain and associated structures: the SET domain is depicted in yellow; the post-SET domain structure is not clearly defined in the crystallized construct and its first five residues (in blue) are oriented away from its expected position, suggesting potential flexibility or structural rearrangements in this region; the CXC domain (in orange), unique to EZH2, adopts a structure characterized by clusters of zinc ions (represented in light blue spheres). It plays a role in stabilizing the overall structure or in protein-protein interactions.* **C)** *Mesh representation of EZH2 in the same orientation;* **D)** *Residues forming the substrate lysine-binding channel in EHMT1/GLP (in beige, PDB: 2RFI) are conserved in EZH2 (color as in A-C).*

3.2. Relevance of EZH2 in cancer, stem cell maintenance, and other biological processes

The wide biological role of EZH2 and, especially, its deep involvement in the regulation of cell cycle progression and its pivotal role in several cellular pathways explains why its dysfunction is associated with several solid or hematological cancers. Several literature examples show its dysregulation in cancers, as well as its involvement in stem cell maintenance and tumor development. [524] [581] [582] EZH2 overexpression has been related to an increase in H3K27me3, involved in the repression of tumor suppressor genes, [583] [584] as well as to the establishment of specific methylation patterns driving a global epigenetic reprogramming. [585] EZH2 overexpression in cancer was reported for the first time in prostate [586] and breast [587] cancers. Its overexpression in prostate cancer was associated with aggressiveness and metastasis, [586] similarly in endometrial, melanoma, and bladder cancer it correlated with invasiveness and poor outcome. [588] [586] [589] [590] [591] Moreover, EZH2 ectopic expression in primary cells war correlated to proliferative advantage. [588] However, it was found that the sole EZH2 overexpression is not sufficient to cause leukemia but can prevent hematopoietic stem cell exhaustion. [592] Additionally, EZH2 knock-in leads to the development of myeloproliferative disorders in mice. [593] Tanaka *et al.* found that EZH2 knock-out in the MLL-AF9 AML mouse model slowed leukemia progression *in vivo*, and compromised leukemia cell proliferation *in vitro*. [594] Conversely, the work by Vo *et al.* showed that, in a mouse model of Myc-driven group 3 medulloblastoma, EZH2 inactivation accelerated tumor initiation and progression. In particular, they found that EZH2 normally represses Gfi1 proto-oncogene expression, but in the case of EZH2 inactivation, Gfi 1 is overexpressed and collaborates with Myc, inducing tumor development. [595] Even though EZH2 is involved in regulating the epithelial-mesenchymal transition (EMT), its role in this process is still debated. On the one hand, in laryngeal squamous cells carcinoma (LSCC), EZH2 is described to promote EMT through down-regulation of E-cadherin (Ca^{2+}-dependent cell adhesion molecule E), and up-regulation of H3K27me3 *in vitro* and *in vivo*, [596] on the other hand it was recently reported to maintain an epithelial phenotype in ovarian cancer cells. [597] This evidence could also suggest a different role of EZH2 depending on the cell/cancer type. Recently, EZH2 was described as a key regulator of multiple myeloma development through the regulation of different factors, including the oncogenes IRF-4, XBP-1, PRDM1/BLIMP-1 (also known as immune response regulators), [598] [599] and c-Myc, and the tumor suppressor microRNAs miR-125a-3p and miR-320c. [600] EZH2 has PRC2 independent functions,

but also non-canonical functions, whose mechanism is not yet fully understood. However, also these unconventional activities seem to play a role in cancers. For example, in natural killer/T-cell lymphoma, EZH2 acts as a transcriptional activator. Its activity is methylation-independent, based on binding and activation of the CCND1 promoter. [601] Some examples of non-histone targets methylation in cancers are given by androgen receptor in prostate cancer and STAT3 in glioblastoma. [602] [580] The role of EZH2 in maintaining the self-renewal potential in adult and embryonic stem cells (ESC) has been pointed out by numerous studies. Already in 2006, it has been reported that PRC2 was able to maintain pluripotency in ESCs by targeting and repressing a special set of developmental genes (including OCT4, SOX2, and NANOG), whose expression would promote differentiation. [603] Both the PRCs are involved in a temporal and spatial control of epigenetic modifications in stem cells, repressing undesirable differentiation programs, while stepwise and selectively establishing a specific terminal differentiation program. [183] A study by Shan *et al.* provided new insights into the role played by EZH2/PRC2 in cell fate decisions in ESC. [604] Interestingly, they have shown that PRC2 is differently required for maintaining pluripotency in ESC, being essential for the primed state ESC, but dispensable in naïve state cells. A direct correlation between ESC and poorly differentiated cancer cells has been established by a shared gene expression signature of PRC2 target genes. [605] Accordingly, EZH2 was found to be essential for cancer stem cell formation and also for the expansion of an aggressive cancer stem cell population that promotes cancer progression. [606] In light of the aforementioned findings, it is evident that EZH2 is primarily regarded as a target in cancer. However, EZH2 activity is also affecting hematopoietic stem cell proliferation and differentiation, thymopoiesis, and lymphopoiesis. [607] Several studies also assessed EZH2 as a regulator of T-cell differentiation and plasticity, as well as of the development of autoimmune diseases, and graft-versus-host disease (GVHD). These shreds of evidence suggest that modulation of histone methylation may have significant implications in the development of novel therapeutic strategies against GVHD or other T cell-mediated inflammatory disorders. These aspects have been well reviewed by Karantanos *et al.* [607] The capability of EZH2 to maintain the multipotent identity has been proved also in non-cancer adult stem cells, including muscle cell precursors (myoblasts) and neural stem cells (NSCs). [608] [609] EZH2 overexpression in NSCs results in increasing oligodendrocytes and decreasing astrocyte differentiation. [609] More recently, EZH2 has been reported to be essential for astroglial differentiation in adult mice by inhibition of Ink4a (p16)/Arf (p19) and

Olig2. [610] [611] In contrast, EZH2 knock-out during mice's cerebral development resulted in a reduction of H3K27me3 level in cortical progenitor cells, and led to differentiation directly (into neurons), as well as indirectly (in the cerebral cortex). [611] Aberrant EZH2 expression has been found also in muscular disorders. For instance, in Duchenne muscular dystrophy increased amount of TNF-α from myotubes inhibited the regenerative potential of satellite cells via epigenetic silencing of the Notch-1 signaling, by NF-κB-stimulated recruitment of EZH2 and DNMT3b on Notch1 gene promoter. [612] It has been shown that Pax7 activation and satellite cells proliferation is promoted by pharmacological inhibition or genetic knockdown of either p38a kinase or EZH2, with subsequent muscle regeneration in dystrophic or normal mice. [613] Proliferation of β-cells in pancreatic islets plays a pivotal role in self-renewal and adaptive islet expansion. In this context, EZH2 has been described to repress Ink4a/Arf in β-cells. [614] EZH2 induced Ink4a repression in young adult mice was sufficient to increase replication and regeneration of β- cells. [615] Additionally, EZH2 was found involved in osteogenesis and adipogenesis. Human mesenchymal stem cells (hMSCs) can be activated for osteogenesis, after EZH2 inactivation by cyclin-dependent kinase 1-mediated phosphorylation. [616] Dissociation of EZH2 from the promoter region of myocyte enhancer factor-2-interacting transcriptional repressor (MITR) gene resulted in its upregulation and association with PPARγ 2, impairing its activity and preventing adipogenesis while enhancing osteogenic differentiation from hMSCs. [617] In contrast, EZH2 was able to induce adipogenesis by disrupting the Wnt/β-catenin signaling through direct binding to the promoters of Wnt genes to repress their expression. [618]

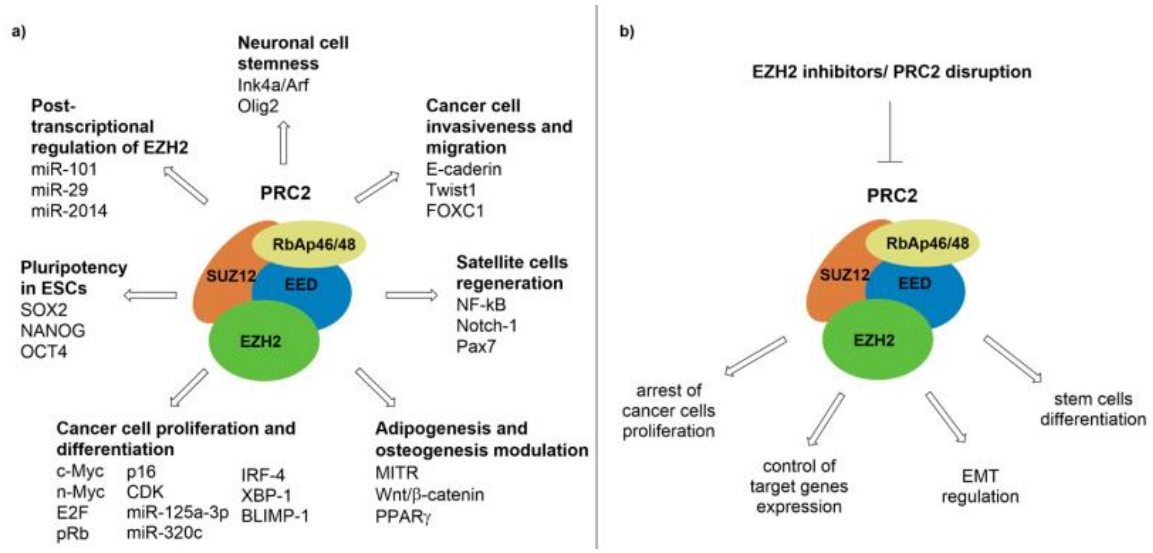

Figure 3.4. a) *Overview of the different factors (proteins, miRs) interacting with PRC2;* **b)** *Effects of PRC2 activity modulation by EZH2 inhibitors or PRC2 disruption.* [619]

3.2.1. EZH2 and lymphoma

Follicular lymphoma (FL) is a non-Hodgkin lymphoma that originates from germinal center (GC) B cells. The primary factor driving the development of follicular lymphoma is epigenetic dysregulation. [620] Extensive genomic studies have revealed that almost every FL biopsy sample contains mutations in at least one gene associated with epigenetic control. [531] [621] These mutations impact genes responsible for encoding histone acetyltransferases (CREBBP and EP300), histone methyltransferases (EZH2 and KMT2D), proteins involved in nucleosome remodeling (ARID1A, ARID1B, and BCL7A), as well as histones H1 and H2, and transcription factors (MEF2B).[621] [622] Notably, the histone methyltransferase EZH2 is mutated in approximately 22–28% of FL cases.[623] [624] These EZH2 mutations are primarily clonal and can occur at various stages of FL progression. [625] Interestingly, such mutations are also observed in diffuse large B-cell lymphomas (DLBCL) that arise from GC B cells, but not in DLBCL of the activated B-cell type. [626] Furthermore, EZH2 mutations remain stable during the transition from FL to DLBCL and are thought to originate from a shared progenitor clone. Patients with FL harboring EZH2 mutations often have a significantly improved prognosis when treated initially with immunochemotherapy compared to others, though the exact mechanism remains unclear. [625] This mutation serves as a favorable prognostic indicator within the m7-FLIPI scoring system. Additionally, the EZH2 gene is amplified in a small subset (15%) of FL patients, which may coexist with an activating mutation of the gene. [621] Tumors with EZH2 amplification display similar transcriptional profiles to those with EZH2 mutations, and patient outcomes appear comparable. In GC B cells, EZH2 is significantly upregulated and it is crucial for the GC reaction by hypermethylating H3K27 at several target genes linked to cell cycle inhibition (CDKN1A and CDKN2A), plasma cell differentiation (PRMD1, IRF4, and CD138), and GC exit (CD40, IL10, and NFKB). [601] [627] EZH2 is also vital for shielding GC B cells from apoptosis triggered by AID-related DNA damage. [628] The mutations in EZH2 that occur in lymphomas most commonly affect the protein's SET domain, which is responsible for the methylation process. [629] Several mutations result in an amino acid alteration at tyrosine 646 (Y646N, Y646S, and Y646F), although mutations at A687 and A697 have also been documented. [630] [631] These *gain-of-function* mutations produce a hypermorphic protein that exhibits increased affinity for H3K27me2 and enhances the conversion of dimethylated to trimethylated H3K27. [632] In fact, studies demonstrated that wild-type (WT) EZH2 preferentially mono-methylates H3K27, whereas the Y641 mutants display increased efficiency for

H3K27 di and tri-methylation, demonstrating that all the reported Y641 mutations are heterozygous, thus the mutant allele is always associated with a WT allele. [632] The rise in H3K27me3 further suppresses the transcription of EZH2 target genes, particularly those involved in cell cycle regulation and GC exit, thereby encouraging proliferation and hindering the differentiation of GC B cells into memory or plasma cells. More recent research indicates that mutant EZH2 can also enhance gene expression by redistributing H3K27 methylation across the genome, indicating a neomorphic function of the mutant protein rather than mere hyperactivity. EZH2 mutations work in tandem with BCL2 rearrangements and BCL6 protein to promote lymphomagenesis. [633] [634]

In T-cell acute lymphoblastic leukemia, myeloproliferative disorders, and myeloid malignancies, have been recorded a number of missense, nonsense, and frameshift EZH2 heterozygous or homozygous mutations. [635] [636] [637] These mutations have been associated with loss of methyltransferase activity, leading in particular cases, to an enhancement of NOTCH1 or RUNX1 oncogenic signaling. This evidence suggest that also loss of EZH2 can contribute to tumor development. Even though there is a number of data about EZH2 mutations in hematological cancers, not much has been investigated about such mutations in solid cancers. In conclusion, considering that both gain and loss of function EZH2 mutations have been reported in cancers, we could conclude that EZH2 behaves in turn as an oncogene or as an onco-suppressor, based on the context. However, in each situation, a balanced EZH2 activity is required to keep homeostasis. [591]

3.3. EZH2 inhibitors

Given all these findings, EZH2 has been considered a very attractive target for cancer therapy. Over the last years, multiple biotech and pharmaceutical companies have pursued the development of EZH2-specific inhibitors by managing to identify catalytic SAM-competitive EZH2 inhibitors with some of them currently in clinical trials and one, Tazemetostat, approved by the FDA in January 2020. Interestingly, crystal structure resolution has allowed us to identify the structural elements required for the EZH2 inhibition. The carbocyclic adenosine analog 3-deazaneplanocin (DZNep), a derivative of the natural antibiotic neplanocin-A, has been one of the first small molecules to be tested as EZH2 inhibitor. [638] By mechanism, DZNep is an S-adenosyl-L-homocysteine hydrolase inhibitor, blocking the methionine cycle and SAM regeneration, thus affecting all SAM-dependent

processes. DZNep is thus an indirect and unselective inhibitor. [639] The poor PK and toxicological profile of DZNep encouraged the development of novel, potent and selective inhibitors of EZH2. [640] High-throughput biochemical screenings led to the development of SAM-competitive catalytic EZH2 inhibitors, many of them containing a dimethylpyridone moiety. In 2012 Epizyme, Inc., USA reported EPZ005687 as a potent, selective, and SAM-competitive small-molecule inhibitor of EZH2 with a Ki of 24 nM. [641] Treatment with it in EZH2– WT, and Y641- or A677-mutant lymphoma cells, as well as in other cancer cell lines, including breast and prostate cancers, resulted in dose-dependent ablation of H3K27 methylation. Simultaneously, Glaxo Smith Kline (GSK), USA, via a high-throughput biochemical screening, followed by an extensive medicinal chemistry optimization, disclosed GSK2816126 that was able to potently (Ki app of 0.5–3 nM) and selectively inhibit WT and mutant EZH2. [642] GSK126 markedly inhibits the growth of EZH2 mutant diffuse large B-cell lymphoma in xenograft mice and is currently being under evaluation in phase I clinical trials against various types of lymphoma. [643] [644] GSK343 is another potent EZH2 inhibitor which, differently from GSK126, contains an indazole nucleus instead of an indole. [645] EI1, a SAM-competitive inhibitor, is effective against WT and mutant EZH2, and displays more than 10000-fold selectivity for EZH2 over other methyltransferases, and 90-fold selectivity over EZH1. [646] In cell-based studies, EI1 was reported to reduce H3K27 methylation levels and activate PRC2 target genes. Moreover, it was able to decrease proliferation and to induce cell cycle arrest and apoptosis in Y641 mutant large B-cell lymphoma. [646] Reported as the first orally bioavailable inhibitor in mice, UNC1999 was a dual and highly selective inhibitor of WT and Y641 mutant EZH2, as well as of EZH1. UNC1999 is a SAM-competitive inhibitor, able to reduce H3K27 methylation levels in cells and to induce apoptosis in Y641N mutant large B-cell lymphoma. [647] The indole-based compound CPI-360, first reported in 2015, showed a good activity profile in the biochemical assays as well as in a KARPAS-422 mouse xenograft model. [648] In 2016, an optimization study on this compound led to the identification of CPI-1205, a highly potent (biochemical IC_{50} = 0.002 μM, cellular EC_{50} = 0.032 μM) and selective EZH2 inhibitor. [649] Vaswani *et al.* also disclosed the co-crystal structure of CPI-1205 bound to the *human* PRC2 complex. This compound showed once again a potent antitumor activity in a KARPAS-422 mouse xenograft model. [649] It is currently in Phase I clinical trials for B-cell lymphoma treatment and in Phase II in patients with Metastatic Castration-Resistant Prostate Cancer. In 2018, also the crystal structure of PRC2 with GSK126 was disclosed. [650] It showed as the pyridone

moiety of GSK126 compete with S-adenosylmethionine for EZH2 binding and effectively inhibit PRC2 activity (**Figure 3.5**).

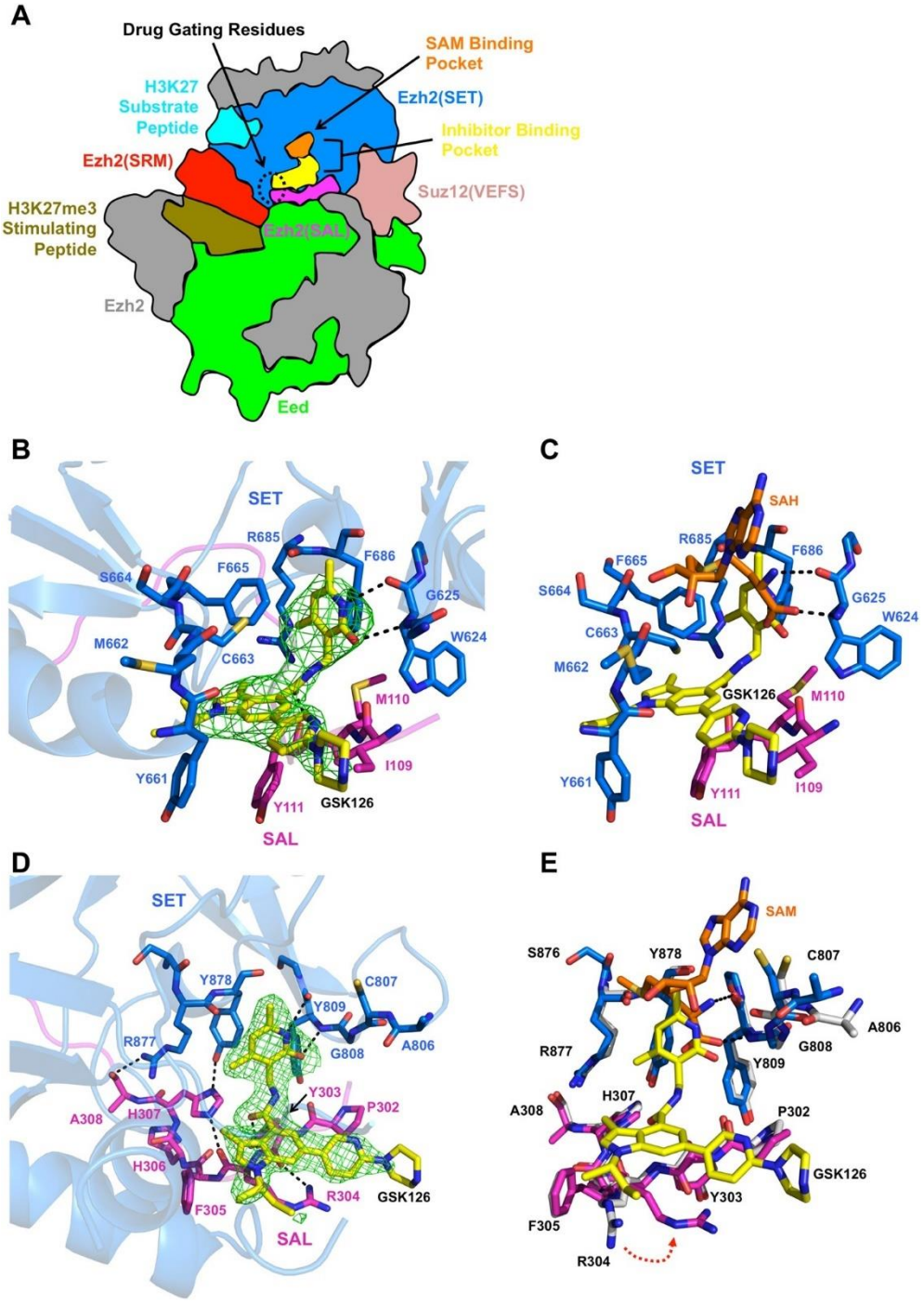

Figure 3.5. *(**A**) Schematic representation of PRC2 with important regions color-coded. (**B**) Structure of human PRC2 in complex with GSK126 (yellow sticks). The SET and SAL domains are colored in blue and magenta sticks, respectively while the Fo − Fc difference electron density is shown as green mesh. Black, dashed lines indicate hydrogen bonds. (**C**)*

*Alignment of the GSK126-bound human PRC2 structure with the human PRC2/SAH/K27M/K27me3 structure (PDB 5HYN). (**D**) Structure of ctPRC2 bound to GSK126. (**E**) GSK126 partially overlaps with the SAM binding site. Alignment of GSK126 bound ctPRC2 (with SET and SAL domains color-code as above) with the stimulated state ctPRC2 structure (gray sticks, PDB 5KKL). SAM and GSK126 are in orange and yellow sticks, respectively. Residue R304 undergoes a rotameric conformational change from the SAM-bound to GSK126-bound structures (red, dotted arrow).* [650]

In 2017, the ligand-based and property-based design strategies led to the identification of an oxetane-containing compound, PF-06821497, also known as Mevrometostat, that displayed an adequate overlap of EZH2 inhibitory potency, in vitro ADME properties, and physical-chemical properties (e.g., thermodynamic solubility). The molecule also displayed robust tumor growth inhibition activity in mouse xenograft models along with strong associated pharmacodynamic effects (such as reduction of H3K27me3 in tumors). [651] It is in Phase I for the treatment of Relapsed/Refractory SCLC, Castration-Resistant Prostate Cancer, and Follicular Lymphoma. Later, Tazemetostat (EPZ6438, Tazverik®) was developed through a follow-up optimization of the EPZ005687 scaffold. [652] Tazemetostat was approved in January 2020 by FDA for the treatment of adults and adolescents aged ≥ 16 years with locally advanced or metastatic epithelioid sarcoma not eligible for complete resection and for relapsed/refractory (R/R) EZH2-mutated follicular lymphoma. [653] [654] These indications were approved by the FDA through accelerated approval based on objective response rate and duration of response that resulted from phase 2 clinical trials. Tazemetostat competes with SAM cofactor to inhibit EZH2, reducing the levels of trimethylated lysine 27 of histone 3 (H3K27me3). Tazemetostat is orally bioavailable, characterized by rapid absorption and dose-proportional exposure, which is not influenced by coadministration with food or gastric acid-reducing agents. It is highly distributed in tissues but with limited access to the central nervous system. Overall, Tazemetostat is the *first-in-class* EZH2 inhibitor approved by the FDA for cancer treatment. Current clinical studies are evaluating combination therapies in patients with several malignancies. [654] In 2021, Wang *et al.* presented a novel highly selective EZH2 inhibitor, SHR2554 (known also as EZH2-IN-15), which specifically inhibits both wild-type and mutant EZH2 methyltransferase activity with similar potencies. It is currently undergoing clinical trials for the treatment of lymphoma patients. [126] Valemetostat, also known simply as DS-3201, is a selective dual inhibitor of EZH1 and EZH2 developed by Daiichi

Sankyo Company, Ltd for the treatment of various haematological malignancies and solid tumors, including types of non-Hodgkin lymphomas (NHL). In September 2022 Japan FDA approved Valemetostat (Ezharmia®) for the treatment of patients with relapsed or refractory adult T-cell leukaemia/lymphoma (R/R ATL), a subtype of NHL. [655]

An overview of the most widely reported EZH2 inhibitors is given in **Figure 3.6**.

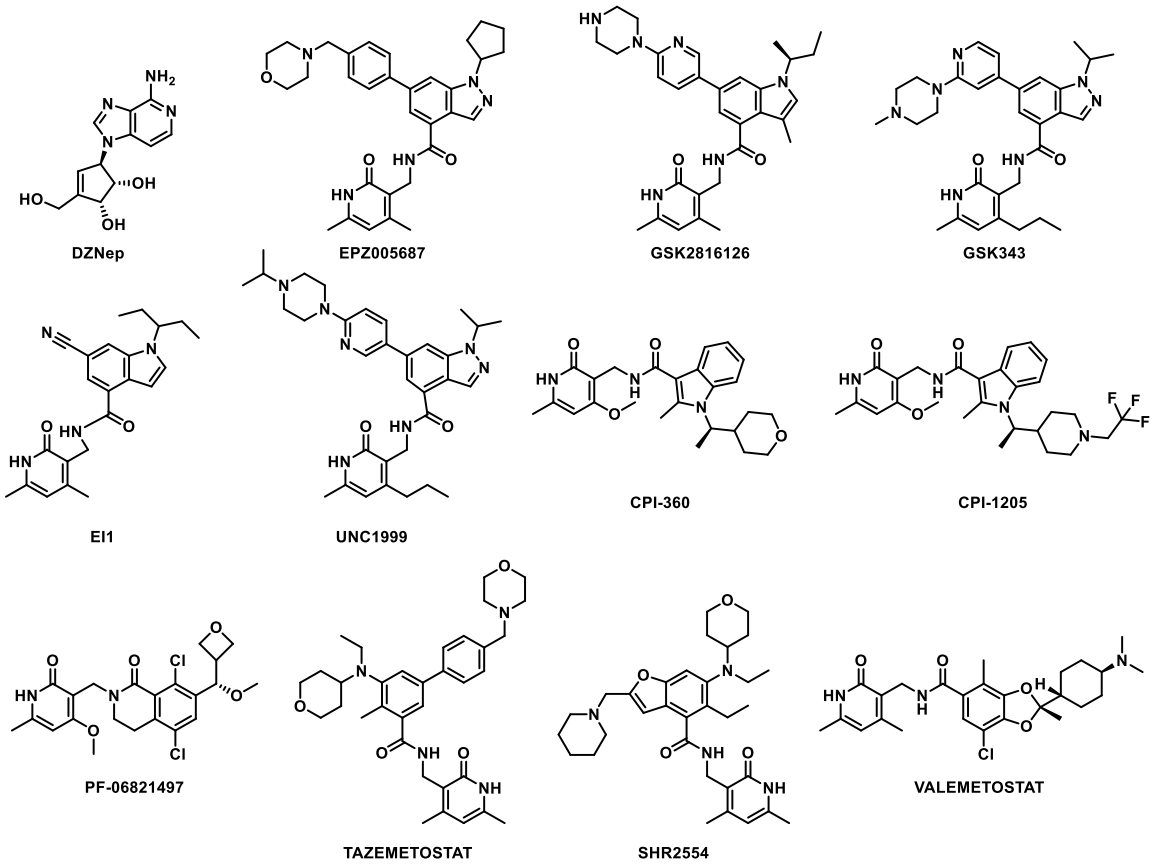

Figure 3.6. *Overview of the most widely reported EZH2 inhibitors.*

What immediately catches the eye, having a look at the EZH2 inhibitors reported so far, is that the dimethylpyridone moiety is almost a constant, with a few exceptions. The observation of PRC2 crystal structure alone and with small molecule inhibitors allowed us to understand the role of this moiety in the EZH2 inhibition, confirming the SAM competitive mechanism of this class of compounds. The binding mode also explains the lack of selectivity of many of these inhibitors for wild-type versus mutant EZH2, in fact, EZH2 mutations occur far from the inhibitor binding site. The

importance of this pharmacophore moiety was also confirmed during the years by SAR studies, where was demonstrated that the structural manipulation of this moiety could give selective EZH2 versus EZH1 inhibitors or keep the simultaneous EZH1/2 inhibition. [656]

4. Role of HDACs and EZH2 in combination therapy

It is now known that numerous carcinogenic pathways involve the overexpression of multiple epigenetic targets and/or are mechanistically dependent on their functions. [657] [658] For this reason, during the last few years, researchers in medicinal chemistry have significantly shifted the drug discovery paradigm from the "one target, one drug" to the "network active compound" approach, which is the cornerstone of modern polypharmacology. [659] Molecular microenvironments are complex, and their homeostasis depends on the correct interaction of genetic, epigenetic, and metabolic components at each time and in a given context. [660] Therefore, it is intuitive that the traditional "single-target" approach is often reductive, inadequate, and fraught with adverse side effects. Conversely, focusing on a holistic view of the disease and simultaneously targeting all the disease-relevant targets is currently considered an efficient strategy to achieve the desired therapeutic effects. [661] In this scenario, two distinct approaches are applied: *i)* Combination of two or more drugs acting on different targets; *ii)* Hybrid compounds containing in a single molecule both pharmacophore entities able to simultaneously modulate the activity of multiple targets. So far, the combination of HDAC and EZH2 inhibitors seems to be a promising approach, which is largely investigated in preclinical and clinical settings. [662] [663] Evidence suggests that using these inhibitors synergistically can enhance treatment outcomes across various tumors affected by dysregulated expression of these targets.

For instance, in B-cell non-Hodgkin lymphoma (B-NHL), various epigenetic deregulations contribute to B lymphomagenesis. Hence, B-NHL occurrence as a result of disruption in epigenetic mechanisms has generated a strong rationale to target contemporary epigenetic and chromatin regulators for drug discovery attempts. [664] In 2019, Lue *et al.* demonstrated that combining GSK126, an EZH2 inhibitor, with Romidepsin, a pan-HDAC inhibitor, yielded potent synergistic effects in lymphoma models with EZH2 dysregulation, both *in vitro* and *in vivo mouse xenograft model*. [665] This combination led to the disassembly of the PRC2

complex due to acetylation of RbAP 46/48. This in turn caused attenuation of H3K27 methylation, increased acetylation, and upregulation of p21, which together triggered apoptosis. [665]

This kind of study was done not only in the lymphoma field. In fact, in 2020, De La Rosa *et al.* reported the synergistic effect of DZ-Nep, the EZH2 inhibitor, with Panobinostat, an HDAC inhibitor, in the treatment of glioblastoma, a highly aggressive brain tumor. [666] The cell lines they used were LN405 and A172, both with resistance to Temozolomide. DZ-Nep + Panobinostat combined treatment showed an additive/synergistic effect at the highest concentrations. Additionally, the combined treatment reduced cell clonogenicity of glioblastoma cells and enhanced apoptosis. [666]

Overall, cancer is a multifactorial disease resulting from genetic and epigenetic alterations that lead to the malfunction of numerous pathways. By choosing a polypharmacological approach, where there is simultaneous inhibition of two or more targets involved in pathogenesis, may enhance therapeutic efficacy compared to traditional single-target strategies.

4.1. Why dual-target inhibitors?

As previously mentioned, most approved drugs using the "single target single drug" approach are often ineffective in treating incurable, multi-target, and polygenic cancer disease. [667] [668] [669] The combination of two or more drugs acting at different targets is used in preclinical and clinical settings. However, drug combination therapy is often denied because of poor drug-drug interactions, unpredictable pharmacokinetics (PKs) and safety characteristics, and poor patient compliance. [659] [670] Recently, dual-target drugs have attracted significant attention. [671] [672] Dual-target drugs may assist in solving the problems of single-target drugs with limited efficiency and frequent resistance. Additionally, compared with combination therapy, dual-target drugs take advantage of predictable bioavailability, pharmacokinetics, and metabolism, with no risk of drug interaction. [673] [674] However, while embracing lots of opportunities, dual-target drugs also come with several challenges. Designing a single molecule that effectively targets both sites while maintaining the required efficacy and pharmacokinetic properties for each target is complex. [675] Achieving a balance in activity across both targets is particularly challenging, as an ideal dual-target drug should exert similar effects on

each target. Furthermore, ensuring that the combination of targets is rational and biologically meaningful can be difficult. [675] However, with the rise of new and innovative technologies, the development of dual-target drugs may become more feasible. Interestingly, the simple pharmacophore model of HDACi has brought out HDACi as a privileged tool for the development of hybrid drugs. [676] As already mentioned above, the cap group moiety just interacts with the entrance of the catalytic tunnel therefore it has been used to incorporate the pharmacophore of the second orthogonal target. The hydroxamic acid or *ortho*-aminoanilide must be kept fixed as an HDAC-inhibiting zinc-binding group, as well as the linker connecting the two components. Recent literature highlights various HDACi-based hybrids, including kinase inhibitors, cytotoxic agents, other epigenetic modulators, HMG-CoA reductase inhibitors, hormone and vitamin D receptor modulators, natural products, and other anticancer drugs. [494] Additionally, dual inhibitors based on EZH2 have been developed for cancer treatment, particularly in combination with PARP, BRD4, and HDACs. [677]

5. The *first-in-class* dual EZH2/HDACs inhibitor and another reported EZH2/HDACs hybrid compound

In 2018, our research team reported a series of 2-pyridone pyrazole-containing EZH2 inhibitors, among which **compound 60** demonstrated significant anti-cancer effects. [678] When tested in several cancer cell lines, such as breast MDA-MB231, leukemia K562, and neuroblastoma SK-N-BE, it induced growth arrest and led to a reduction in H3K27me3 levels, as well as modulating markers of apoptosis and autophagy. [678] In human medulloblastoma stem-like cells (SHH MB-SLCs), compound 60 impaired cell proliferation and self-renewal, also inducing apoptosis both in vitro and in orthotopic xenografted MB-SLCs nude mice models. [679]

Encouraged by these findings, in 2019, our group designed a new series of compounds by replacing the pyrazole moiety with a pyrrole nucleus. Among these, **compound 61** was identified as the prototype, with two analogues, **61a** and **61b**, which featured a piperidine or morpholine moiety at C3 of the N-phenyl ring, respectively. These compounds effectively reduced H3K27me3 levels and increased the expression of cell cycle regulators p21 and p27, impairing the viability of primary glioblastoma (GBM) and U-87 GBM cells in a dose- and time-dependent manner. [680] Moreover, compounds 61a and 61b attenuated the malignant phenotype

of GBM by reducing VEGFR1/VEGF expression, reversing epithelial-mesenchymal transition (EMT), inhibiting cell invasion, and lowering levels of inflammatory cytokines. Building on these successes and recognizing recent reports of the synergistic effects of combining EZH2 inhibitors with HDAC inhibitors, particularly in various cancers such as lymphoma, multiple myeloma, and triple-negative breast cancer, in 2020 our group designed two hybrid compounds (**62** and **63**) as dual EZH2/HDAC inhibitors. These hybrids merged the structural features of compounds 60 and 61, respectively, with the HDAC inhibitor **Vorinostat** to exploit potential therapeutic advantages against aggressive cancer types. [680] **Hybrid compound 63** displayed submicromolar inhibition against EZH2 and HDACs and, when tested across several cancer cell lines, demonstrated potent anti-cancer activity, impairing cell viability at low micromolar concentrations. In leukemia U937 and rhabdomyosarcoma RH4 cells, it induced G1 phase cell cycle arrest, promoted apoptosis, and increased cell differentiation. These effects were accompanied by elevated levels of acetyl-H3 and acetyl-α-tubulin, along with a reduction in H3K27me3 levels. In glioblastoma U87 cells, compound 63 inhibited the epithelial-to-mesenchymal transition (EMT) by upregulating E-cadherin expression, highlighting its potential as an important *first-in-class* EZH2/HDAC hybrid inhibitor (**Figure 5.1**). [680]

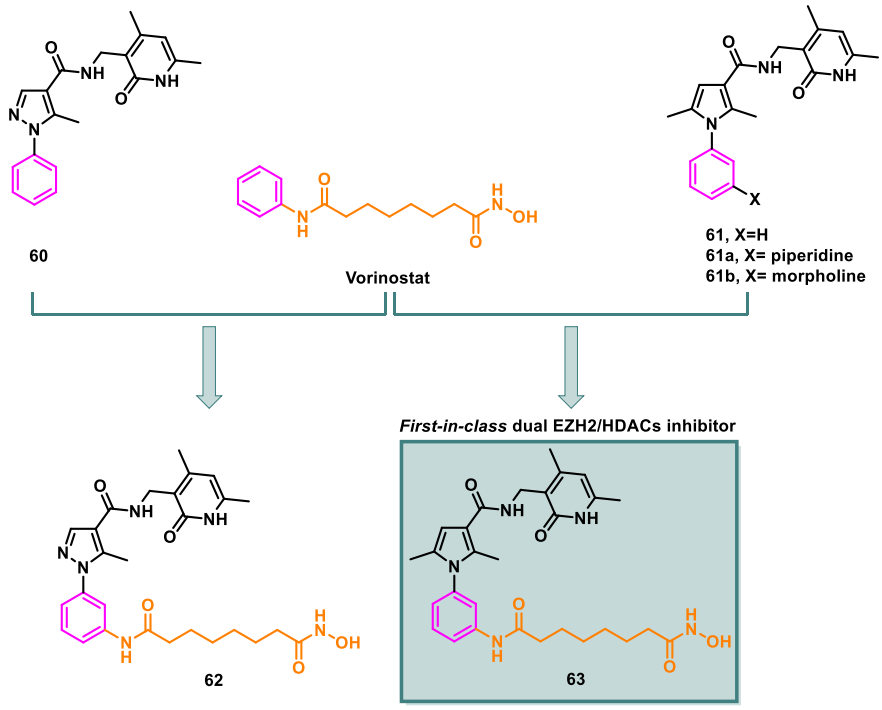

Figure 5.1. *Rational design of dual EZH2/HDAC inhibitors 62 and 63. Compound 63 was distinctive because it potently inhibited the proliferation of hematological and solid cancers,*

induced apoptosis, and increased cell differentiation, becoming the first-in-class dual EZH2/HDAC inhibitor. Adapted from Romanelli, 2020. [680]

In 2022, Lu *et al.* introduced **compound 64** as a significant dual inhibitor of EZH2/HDACs, based on the synergistic effect of Vorinostat, a pan-HDAC inhibitor, and GSK126, an EZH2 inhibitor. [681] Earlier, Yang *et al.* (2016) had reported C24, an EZH2 inhibitor with IC_{50} of 12 nM and notable selectivity (SI EZH2/EZH1 >200), which was derived from structural modification of GSK126. [256] This groundwork facilitated the design of compound 64 (**Figure 5.2**) When tested, dual inhibitor 64 did not only show antiproliferation activity of MV4-11 cells *in vitro* but also exhibited good antitumor activity *in vivo*. Particularly, compound 64 showed an IC_{50} value of 0.17 μM in MV4-11 cells, outperforming the combination therapy of SAHA and GSK126 (IC_{50} = 0.40 μM). It induced cell apoptosis and, through Western blot analysis, confirmed its ability to inhibit simultaneously both HDAC and EZH2 activities in MV4-11 cells. *In vivo*, compound 64 exhibited comparable antitumor efficacy to the combination therapy. However, compound 64 did not exhibit satisfactory pharmacokinetic (PK) properties, indicating a need for further optimization. [681]

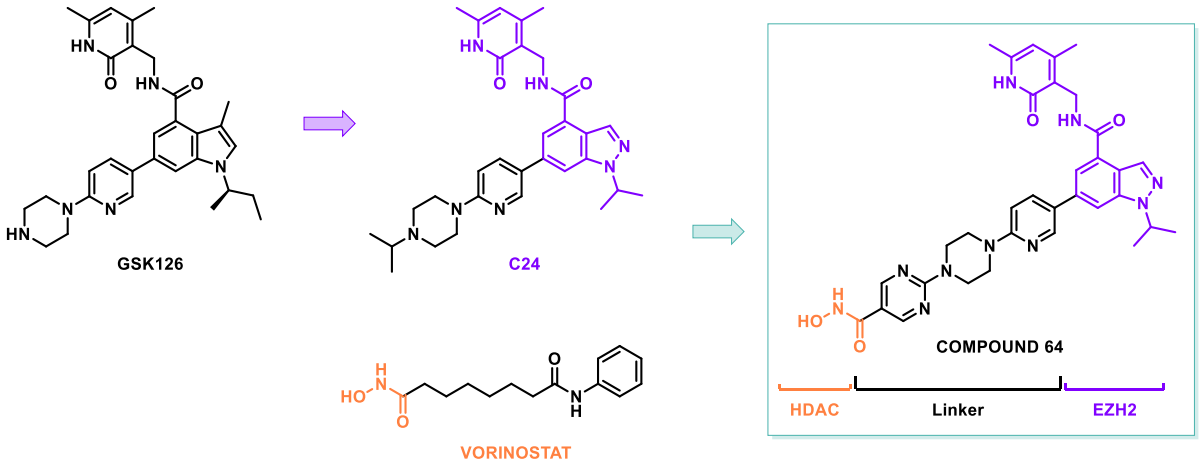

Figure 5.2. *Rational design of dual EZH2/HDACs inhibitor, compound 64.* [681]

6. DEVELOPMENT OF NOVEL DUAL EZH2/HDACs INHIBITORS

6.1. Research Project

Building upon the promising results obtained with derivatives 63 and 64, we developed novel Tazemetostat-based dual EZH2/HDACs inhibitors. These inhibitors were based on the structural scaffold of Tazemetostat, currently the only FDA-approved EZH2 inhibitor, and used in the treatment of metastatic or locally advanced epithelioid sarcoma and follicular lymphoma. [653] [682] To incorporate HDAC inhibition, the methyl-morpholine group of Tazemetostat was replaced with zinc-binding groups (ZBGs), known to be effective in HDAC inhibitors. Two ZBGs were selected: 2-aminoanilide (similar to Entinostat) and hydroxamic acid (similar to Vorinostat), resulting in compounds **18a** and **19a**, respectively.

In an isosteric design study, the proximal benzylic portion of Tazemetostat was removed, while the 4,6-dimethyl-pyridin-2-one moiety was preserved, as it is a crucial component in EZH2 inhibitors that competitively target SAM binding. The N-ethyl-N-tetrahydro-2H-pyranyl group and the central aromatic ring were also retained. Various aromatic monocyclic groups and linear chains were substituted for the benzyl portion, such as a a 3-phenyl regioisomer (**18b** and **19b**), a 5-thienyl group (**18c** and **19c**), and a N-methyl-5-pyrrolyl (**18d** and **19d**). Additionally, vinyl groups were introduced in some analogs (**18e** and **19e**) to mimic the hydrophobic portion of Panobinostat. Saturated linear chains, resembling the hydrophobic spacer from Vorinostat, were also incorporated, resulting in octanammidic (**19g**) and heptanammidic (**19f**) derivatives. These hydrophobic linkers functioned as spacers akin to those found in various HDAC inhibitors. For the pharmacophoric portions targeting HDAC, in **18h** a 1,1'-biphenyl scaffold was functionalized with 2-amino-4-fluorophenyl carboxamide moiety. The introduction of an electronegative atom like fluorine in *meta* position to the amino group in *ortho* position in the *ortho*-aminoanilide aimed to enhance the selectivity of the compound towards HDAC3, potentially by influencing binding interactions within the enzyme's active site. Fluorine's electronegativity can alter electronic distribution, which may improve affinity or specificity for HDAC3 compared to other isoforms. On the other hand, compound **18i** features a (2-amino-5-(thiofen-2-yl)phenyl) carboxamide moiety, which was employed for selectivity towards HDAC isoforms 1 and 2. In fact, the introduction in *para* position to the amino group in *ortho* position in the *ortho*-aminoanilide is reported in literature to confer selectivity of isoforms 1 and 2 of HDACs.[683] Compounds featuring 3-phenyl, 5-phenyl, 5-pyrrole N-methylate, and

vinyl groups were functionalized with *ortho*-aminoanilide and hydroxamic acid, the first being a pharmacophore found in Entinostat while the latter in Vorinostat. For the compounds with linear hydrophobic spacers, only the terminal hydroxamic group was retained (**Figure 6.1**).

The synthesized compounds underwent enzyme assays to evaluate their EZH2 inhibition potential and selectivity across HDAC isoforms 1, 2, 3, 4, 6, and 8. These assessments aimed to identify compounds with dual EZH2 and HDAC inhibitory activity while providing isoform-specific selectivity for HDAC inhibition.

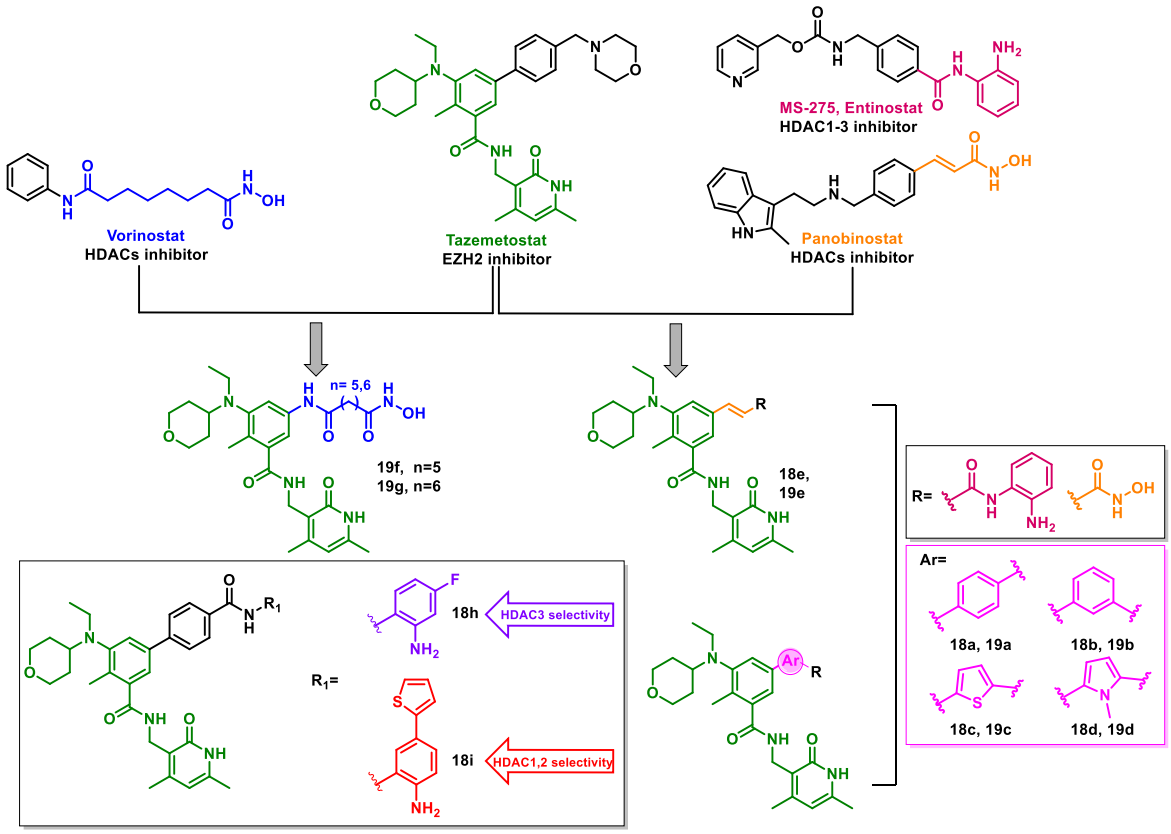

Figure 6.1. *Rational design of novel Tazemetostat-based dual EZH2/HDACs inhibitors.*

6.2. Results and Discussion

6.2.1. Chemistry

To obtain all the planned derivatives, **18a-e** and **18h-i,** as well as **19a-g,** we first synthesized the starting material, compound **40**, as reported in **Scheme 6.1**. The commercially available *tert*-butyl 3-amino-5-bromo-2-methylbenzoate was subjected to two successive reductive aminations, the first in the presence of tetrahydro-4H-pyran-4-one in dry DCE, at room temperature for 6 hours, obtaining derivative **39**, the second in the presence of acetaldehyde in dry DCE at room temperature for 2 hours, obtaining the starting material **40**, in both cases using sodium triacetoxy borohydride as a reducing agent. Therefore, this Bromo-derivative **40** was subjected to different chemical reactions in order to obtain the different dual EZH2/HDACs inhibitors.

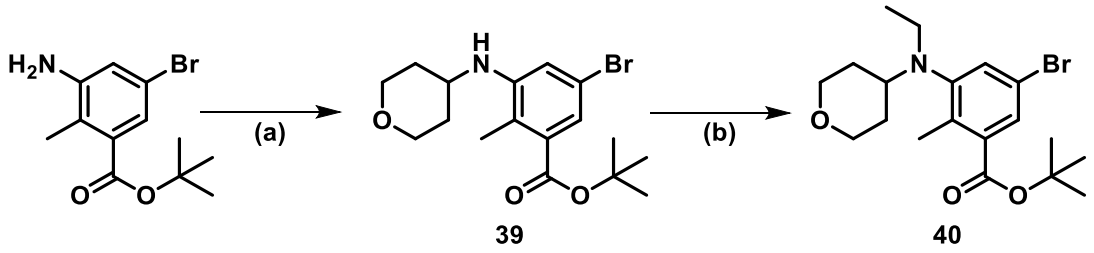

Scheme 6.1. Synthesis of starting material (39). Reagents and conditions. a) Tetrahydro-4H-pyran-4-one, $Na(CH_3COO)_3BH$, dry DCE, RT, 6h; **d)** CH_3CHO, $Na(CH_3COO)_3BH$, dry DCE, RT, 2h.

The final compounds **18a-d** and **19a-d** have been synthesized following the synthetic scheme reported in **Scheme 6.2**. The synthesized bromo-derivative **40** was subjected to different **Suzuki-Miyaura Coupling** reactions, using the opportune boronic ester, in the presence of tetrakis(triphenylphosphine)-palladium(0) as catalyst, in a basic environment by 2N Na_2CO_3 in toluene and ethanol in a 1:1 ratio as a mixture of solvents, under an inert atmosphere of nitrogen, at 105 °C, overnight. The obtained derivatives **41a-d** underwent a deprotection reaction with trifluoroacetic acid, in dry DCM, from 0 °C to room temperature for 6 hours, yielding derivatives **42a-d.** These were subjected to HATU-mediated amidations with 3-(aminomethyl)-4,6-dimethylpyridin-2(1H)-one in a basic environment by TEA, in dry DMF, under an inert atmosphere of nitrogen at room temperature for 2 hours. Derivatives **43a-d** underwent basic hydrolysis in the presence of LiOH in H_2O/THF in a 1:1 ratio to obtain the corresponding acids (**44a-b**). Subsequently, the

latter were reacted with *ortho*-phenylenediamine or *O*-(tetrahydro-2H-pyran-2-yl)hydroxylamine in the presence of HATU, TEA, in dry DMF under nitrogen flow, to give rise to final compounds **18a-d** and derivatives **45a-d**, respectively. Finally, these intermediates **45a-d** were subjected to cleavage with 4M HCl in 1,4-dioxane in dry THF to yield hydroxamates **19a-d.**

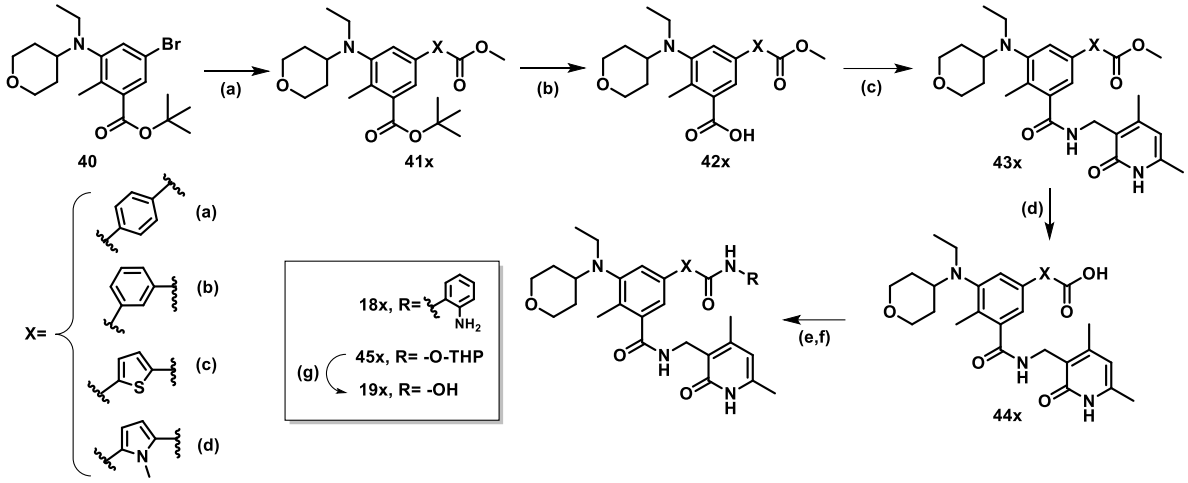

Scheme 6.2. Synthesis of compounds 18a-d and 19a-d. Reagents and conditions. a) Respective boronic ester, tetrakis(triphenylphosphine)-palladium(0), 2N Na_2CO_3, Toluene/EtOH 1:1, N_2, 105°C (reflux), overnight; **b)** TFA, dry DCM, 0°C to RT, 6h; **c)** 3-(aminomethyl)-4,6-dimethylpyridin-2(1H)-one, TEA, HATU, dry DMF, N_2, RT, 2h; **d)** LiOH, H_2O/THF 1:1, 0 °C to RT, 4h; **e,f)** *o*-phenylenediamine or *O*-(tetrahydro-2H-pyran-2-yl)hydroxylamine, HATU, TEA, dry DMF, N_2, RT, 2h; **g)** 4M HCl in 1,4-dioxane, dry THF, 0°C > RT, 2h.

The final compounds **18e** and **19e** have been synthesized following the synthetic scheme reported in **Scheme 6.3**. The bromo derivative **40** was subjected to a **Mizoroki–Heck reaction** with butyl acrylate, $Pd(OAc)_2$ as catalyst, triphenylphosphine as bulky phosphine ligand, in a basic environment by $NaHCO_3$, TEA, in dry DMF, under an inert atmosphere of nitrogen, at 110°C, overnight. The obtained derivative **46** underwent the same reaction of the previous Synthetic Scheme 4.2. Specifically, derivative 46 was subjected to a deprotection reaction with trifluoroacetic acid, in dry DCM, from 0 °C to room temperature for 6 hours, to yield the corresponding acid **42e**. This latter was treated with 3-(aminomethyl)-4,6-dimethylpyridin-2(1H)-one, in a basic medium by TEA, using HATU to generate the corresponding activated carboxylic acid, in dry DMF, under nitrogen atmosphere, at room temperature for 3 hours. These led to the obtaining of

derivative **43e**, which was hydrolyzed with LiOH, in H_2O and THF (1:1) as a solvents mixture, from 0 °C to room temperature for 4h. The corresponding acid **44e** was reacted with *ortho*-phenylenediamine or *O*-(tetrahydro-2H-pyran-2-yl)hydroxylamine in the presence of HATU, TEA, in dry DMF under nitrogen flow, to give rise to final compounds **18e** and derivative **45e**, respectively. Finally, this intermediate **45e** was subjected to deprotection reaction with 4M HCl in 1,4-dioxane in dry THF to yield hydroxamate **19e.**

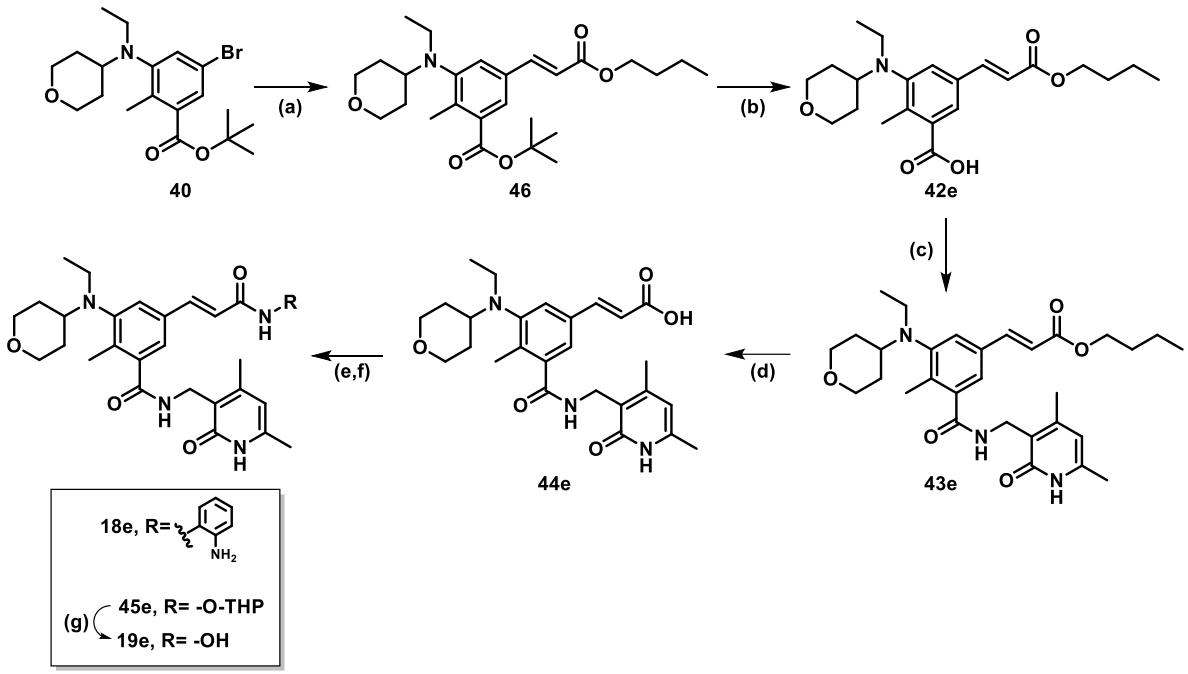

Scheme 6.3. Synthesis of compounds 18e and 19e. Reagents and conditions. a) Butyl Acrylate, Pd(II)OAc, Triphenylphosphine, $NaHCO_3$, TEA, dry DMF, N_2, 110°C (reflux), over night; **b)** TFA, dry DCM, 0°C to RT, 6h; **c)** 3-(aminomethyl)-4,6-dimethylpyridin-2(1H)-one, TEA, HATU, dry DMF, N_2, RT, 3h; **d)** LiOH, H_2O/THF 1:1, 0 °C to RT, 4h; **e,f)** *o*-phenylenediamine or *O*-(tetrahydro-2H-pyran-2-yl)hydroxylamine, HATU, TEA, dry DMF, N_2, RT, 2h; **g)** 4M HCl in 1,4-dioxane, dry THF, 0°C to RT, 2h.

The final compounds **19f** and **19g** have been synthesized following the synthetic scheme reported in **Scheme 6.4**. The bromo derivative **40** underwent Ullmann amination with ammonia solution 17M, in the presence of copper iodide, 2,4-pentandione, Cs_2CO_3, in dry DMF, under nitrogen flow, at 90°C, overnight, obtaining derivative **47.** This one was subjected to HATU-mediated amidation with ethyl hydrogen pimelate or ethyl hydrogen suberate, yielding **48f** and **48g,** respectively. Derivatives **48f,g** were subjected to deprotection reaction with trifluoracetic acid in dry DCM to obtain the corresponding acids **42f,g**, which were subsequently reacted with 3-(aminomethyl)-4,6-dimethylpyridin-2(1H)-one in the presence of TEA in dry DMF under nitrogen flow to obtain the latter intermediates **43f,g**. These were hydrolyzed with LiOH, in H_2O and THF (1:1) as solvents mixture, from 0 °C to room temperature for 4h. The corresponding acids **44f,g** were reacted with *O*-(tetrahydro-2H-pyran-2-yl)hydroxylamine in the presence of HATU, TEA, in dry DMF, under nitrogen flow, to give rise to derivatives **45f,g**. Finally, these intermediates were subjected to deprotection reaction with 4M HCl in 1,4-dioxane in dry THF to yield hydroxamates **19f,g.**

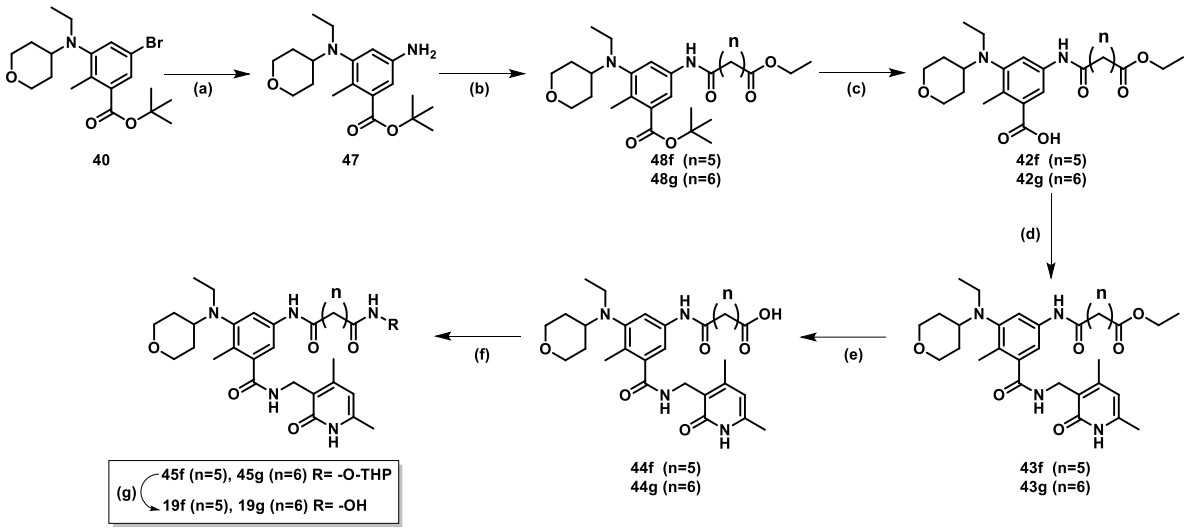

Scheme 6.4. Synthesis of compounds 19f and 19g. Reagents and conditions. a) 17M NH_4OH, CuI, 2,4-pentandione, Cs_2CO_3, dry DMF, N_2, 90°C, over night; **b)** Ethyl hydrogen pimelate or ethyl hydrogen suberate, HATU, TEA, dry DMF, N_2, RT, 3h; **c)** TFA, dry DCM, 0°C to RT, 7h; **d)** 3-(aminomethyl)-4,6-dimethylpyridin-2(1H)-one, TEA, HATU, dry DMF, N_2, RT, 3h; **e)** LiOH, H_2O/THF 1:1, 0 °C to room temperature, 7h; **f)** *O*-(tetrahydro-2H-pyran-2-yl)hydroxylamine, HATU, TEA, dry DMF, N_2, RT, 12h; **g)** 4M HCl in 1,4-dioxane, dry THF, 0°C to RT, 3h.

The final compounds which attempted the selectivity of HDAC isoforms (**18i** and **18h**) have been synthesized following the synthetic scheme reported in **Scheme 6.5**. The bromo derivative **40** was subjected to a **Suzuki-Miyaura Coupling** reaction with 4-methoxycarbonylphenylboronic acid, in presence of tetrakis(triphenylphosphine)-palladium(0) as catalyst, in a basic environment by 2N Na_2CO_3 in toluene and ethanol in a 1:1 ratio as a mixture of solvents, under an inert atmosphere of nitrogen, at 105 °C, overnight. The obtained derivative **41a** underwent a deprotection reaction with trifluoroacetic acid, in dry DCM, yielding acid **42a.** This was subjected to HATU-mediated amidations with 3-(aminomethyl)-4,6-dimethylpyridin-2(1H)-one in a basic environment by TEA, in dry DMF, under an inert atmosphere of nitrogen at room temperature to obtain derivative **43a.** The latter underwent basic hydrolysis in the presence of LiOH in H_2O/THF in a 1:1 ratio to obtain the corresponding acid **44a**. Subsequently, it was reacted with *tert*-butyl (2-amino-5-fluorophenyl)carbamate or *tert*-Butyl (2-amino-4-(thiophen-2-yl)phenyl)carbamate in the presence of HATU, TEA, in dry DMF, under nitrogen flow, to give derivatives **49h-i**, respectively. Finally, these intermediates were subjected to deprotection with 4M HCl in 1,4-dioxane in dry THF to yield final compounds **18h-i.**

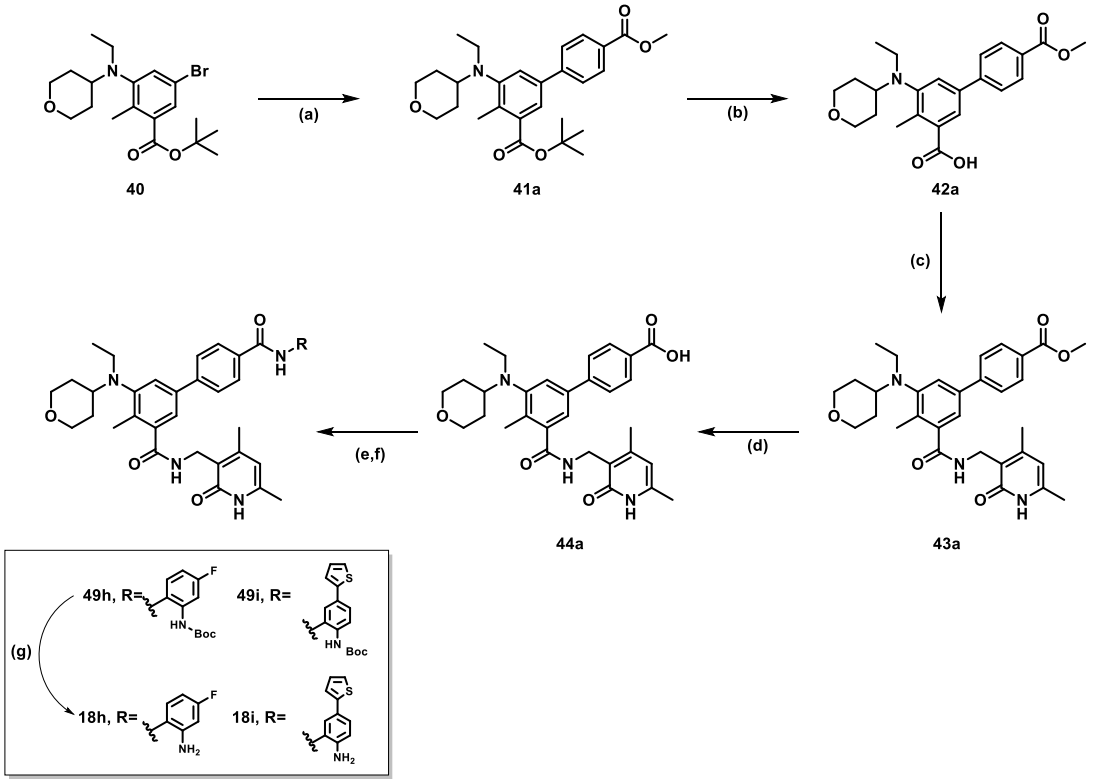

Scheme 6.5. Synthesis of compounds 18h and 18i. Reagents and conditions. a) (4-(methoxycarbonyl)phenyl)boronic acid, tetrakis(triphenylphosphine)-

palladium(0), 2N Na_2CO_3, Toluene/EtOH 1:1, N_2, 105°C (reflux), overnight; **b)** TFA, dry DCM, 0°C to RT, 6h; **c)** 3-(aminomethyl)-4,6-dimethylpyridin-2(1H)-one, TEA, HATU, dry DMF, N_2, RT, 2h; **d)** LiOH, H_2O/THF 1:1, 4h; **e,f)** *tert*-butyl (2-amino-5-fluorophenyl)carbamate or *tert*-Butyl (2-amino-4-(thiophen-2-yl)phenyl)carbamate, HATU, TEA, dry DMF, N_2, RT, overnight; **g)** 4M HCl in 1,4-dioxane, dry THF, 0°C to RT, 24h.

6.2.2. Biochemical activity of novel dual EZH2/HDACs inhibitors

All the synthesized hybrid compounds were tested *in vitro* with an enzymatic assay against a *human* five-component PRC2 complex containing EZH2 (with AEBP2, EED, RbAp48, and SUZ12) to evaluate their inhibition potency against EZH2, and against HDAC isoforms 1, 2, 3, 4, 6, and 8, to assess their capability to inhibit some representative members of the histone deacetylases. Dual inhibitors were tested in 10-dose IC_{50} with 3-fold serial dilution, starting at 100 μM (**Table 6.1**). The assays were done by Reaction Biology Corporation following the protocols described below.

Table 6.1. *Biochemical inhibition data of novel dual EZH2/HDACs inhibitors* ***18a-e, 18h-i,*** *and* ***19a-g*** *against EZH2 and HDACs (1, 2, 3, 4, 6, and 8 isoforms). EZH2* IC_{50} *values are reported in nanomolar (nM) while those of HDAC isoforms are reported in μM.*

CPD	Molecular Structure	EZH2 (IC_{50}, nM)	*h*HDAC isoforms (IC_{50}, μM)					
			1	2	3	4	6	8
18a	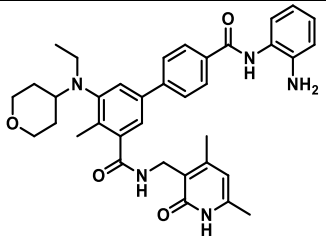	**0.032**	**0.48**	**4.097**	**2.85**	**>100**	**>100**	**13.9**
19a	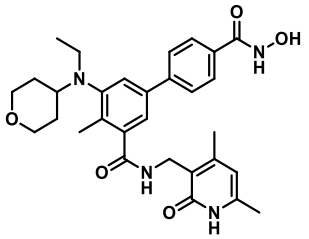	**0.032**	**0.358**	**0.854**	**0.38**	**14.4**	**0.016**	**0.174**

18b	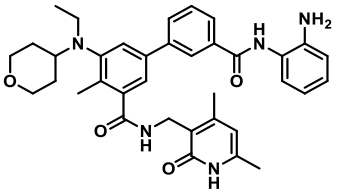	**0.013**	**2.682**	**5.28**	**2.171**	**>100**	**0.052**	**20.81**
19b	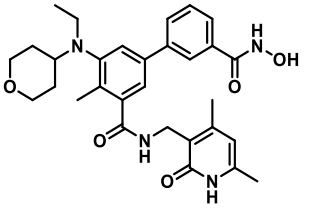	**0.015**	**16.1**	**46.86**	**>100**	**>100**	**9.311**	**0.064**
18c	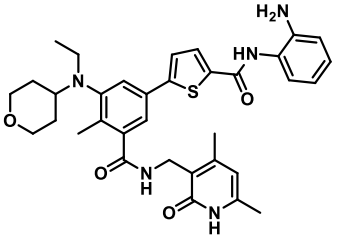	**0.009**	**0.885**	**0.695**	**1.201**	**>100**	**>100**	**25.78**
19c	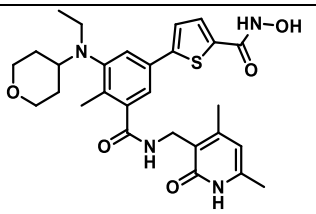	**0.012**	**1.776**	**4.644**	**1.156**	**39.65**	**0.002**	**0.082**
18d	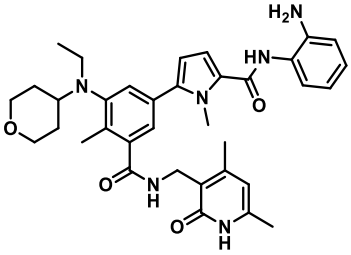	**0.356**	**95.28**	**79.97**	**18.38**	**>100**	**>100**	**39.9**
19d	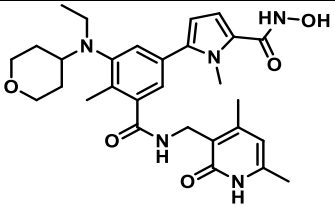	**0.027**	**56.63**	**>100**	**>100**	**>100**	**4.319**	**9.276**
18e	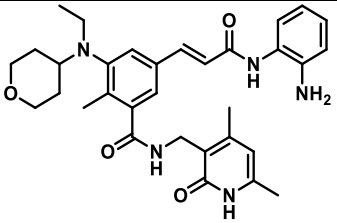	**0.011**	**>100**	**>100**	**38.59**	**>100**	**>100**	**>100**
19e	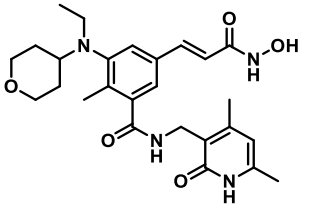	**0.037**	**>100**	**>100**	**96.6**	**>100**	**9.314**	**1.87**

19f	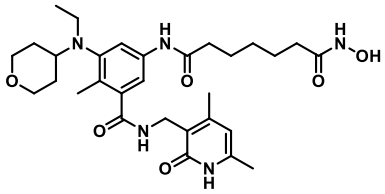	**6.975**	**8.018**	**26.12**	**7.978**	**>100**	**0.585**	**12.81**
19g	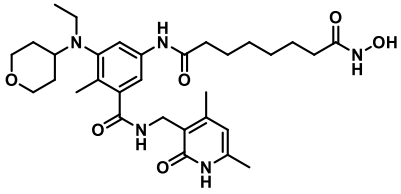	**0.26**	**0.481**	**1.325**	**1.275**	**>100**	**0.111**	**0.873**
18h	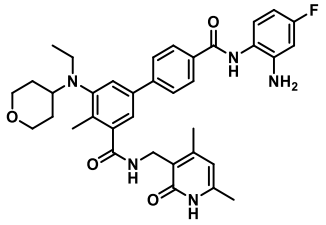	**0.01**	**1.582**	**1.55**	**1.738**	**>100**	**>100**	**>100**
18i	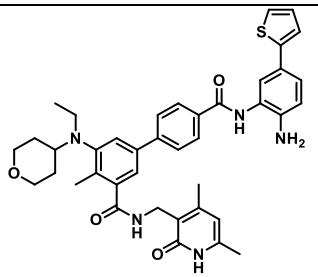	**0.011**	**0.194**	**1.68**	**>100**	**>100**	**>100**	**>100**

All the tested compounds demonstrated nanomolar inhibition activity on EZH2 and, in some cases, even picomolar one. Several of these compounds were more potent than the reference inhibitor, Tazemetostat, which is able to inhibit EZH2 with an IC_{50} value of 11 nM. Furthermore, these compounds inhibited HDAC isoforms within the submicromolar to nanomolar range. Among them, the hybrid compound **18c** exhibited the strongest inhibitory potency toward EZH2, with an IC_{50} of 9 pM. Regarding HDAC inhibition, the dual compounds showed inhibitory activity across all or some of the tested isoforms. For the most promising compounds, a Selectivity Index (SI) was calculated to assess their selectivity toward different HDAC isoforms, in addition to their potency.

Specifically, analyzing every compound's inhibitory activity against HDACs, the *para*-biphenyl anilide derivative **18a** displayed its highest inhibitory activity against **HDAC1,** with an IC_{50} of 0.48 μM. It was approximately 6-fold more potent against HDAC1 than HDAC3 (SI = 5.9) and over 8-fold more potent compared to HDAC2 (SI = 8.5). Its hydroxamic acid analogue, **19a,** exhibited an IC_{50} of 16 nM against HDAC6, with around 11-fold higher potency on HDAC6 than HDAC8 (SI = 10.9).

Meta isomers of 18a and 19a stood out due to their IC_{50} values against HDACs. These compounds demonstrated not only potent inhibitory effects but also high selectivity for specific HDAC isoforms, achieving the best Selectivity Index values. Notably, the *meta* anilide derivative **18b**, had an IC_{50} of 52 nM for HDAC6, with a Selectivity Index of 41.7 compared to HDAC3. The *meta* hydroxamic derivative **19b** was the most potent against HDAC8, with an IC_{50} of 64nM, and was highly selective, with an SI of 145.5 for HDAC6. This dual compound could be considered an important example of a dual EZH2/HDAC8 inhibitor, balanced across both targets, with an IC_{50} of 15nM for EZH2. It shows potential for further exploration in glioblastoma, where both EZH2 and HDAC8 play critical roles in tumor progression. [684] [685] The anilide thiophene derivative **18c** showed low micromolar IC_{50} values against class I HDACs, while the corresponding hydroxamic **19c** had an IC_{50} of 2nM for HDAC6 and 82 nM for HDAC8. In contrast, both N-methyl pyrrolyl derivatives (**18d** and **19d**) and cinnamic ones (**18e** and **19e**) showed very low HDAC inhibitory activity. The pimelic derivative **19f** displayed IC_{50} values in the high micromolar range, whereas its longer-chain analogue, compound **19g**, which incorporates the Vorinostat portion, functioned as a pan-HDAC inhibitor, resembling the Vorinostat profile. Finally, the introduction of a fluorine atom in the *meta* position relative to the amino group in the *ortho* position of the *o*-phenylenediamine moiety did not confer selectivity for HDAC3. However, dual compound **18h** represents a class I HDACs selective compound, with IC_{50} in the single-digit micromolar range. On the other hand, the insertion of a 2-thienyl group in the *para* position with compound **18i** aligned with the pharmacophoric model of HDAC1,2 selectivity, resulting in a complete loss of inhibitory activity against the other HDAC isoforms.

6.2.3. Effects of novel dual EZH2/HDACs inhibitors on lymphoma cells

Considering the biochemical results just analyzed, we proceeded to assess the biological effects of the most promising derivatives in lymphoma cell lines. As we already said, both EZH2 and HDACs are strongly implicated in the progression of hematological malignancies, especially lymphoma. For this reason, we decided to evaluate hybrid compounds in both wild-type lymphoma cell lines and those harboring EZH2 mutation. This approach allowed us to examine the cellular effects of these compounds in a relevant disease context. The biological assays were conducted during my six-month visiting period at the Lymphoma Genomics Laboratory at the Institute of Oncology Research in Bellinzona, Switzerland, under the guidance of Professor Francesco Bertoni and Dr. Afua Adjeiwaa Mensah.

To investigate the anticancer potential of these hybrid inhibitors, we performed MTT assays on several lymphoma cell lines, both wild-type and with EZH2 mutation. This assay enabled us to determine the compounds' cytotoxic effects and their overall potential as cancer therapies. Moreover, to ascertain the cellular target engagement, Western Blot analysis was performed to evaluate the hybrids' ability to decrease the levels of the EZH2-related mark H3K27me3 and to increase H3 acetylation (H3Ac), which is indicative of HDAC inhibition. Furthermore, cell cycle analysis was conducted to provide insights into the effects of the hybrids on cell cycle progression. Lastly, we explored the modulation of HDAC- and EZH2-related gene expression through RNA-sequencing. This allowed us to gain a deeper understanding of how these compounds affect the transcriptional landscape of lymphoma cells and provided valuable insights into their mechanisms of action at the molecular level.

6.2.4. Investigating the anti-proliferative activity of dual EZH2/HDACs inhibitors

Performing MTT assays, we tested all the selected Entinostat-based compounds (they are characterized by 2'-aminoanilide moiety as ZBG) in six different lymphoma cell lines, with wild-type or mutated EZH2. Compounds were added to cells at a maximum concentration of **20 μM,** with a serial dilution of 1:3, for **72 hours**.

The lymphoma cell lines selected were all derived from diffuse large B cell lymphomas (DLBCL), a histological subtype that comprises a defined genetic subset of EZH2 mutated tumors. In our panel, wild-type EZH2 cell lines were **DOHH2** and **Toledo**, and mutated EZH2 cell lines were **SU-DHL-4, WSU-DLCL2, Pfeiffer,** and **KARPAS422**. Three of the four mutated EZH2 cell lines carry a hotspot mutation at tyrosine 641 (Y641); specifically, SU-DHL-4 has the EZH2 Y641S mutation, WSU-DLCL2 the EZH2 Y641F mutation, and KARPAS-422 the Y641N mutation. [630] [629] [686] The remaining cell line, Pfeiffer, harbors a heterozygous A677G mutation in EZH2. [631]

The anilide compounds selected as the most promising, based on the results of the biochemical assay, and further analyzed *in cellulo* were **18a, 18b, 18c, 18h,** and **18i.**

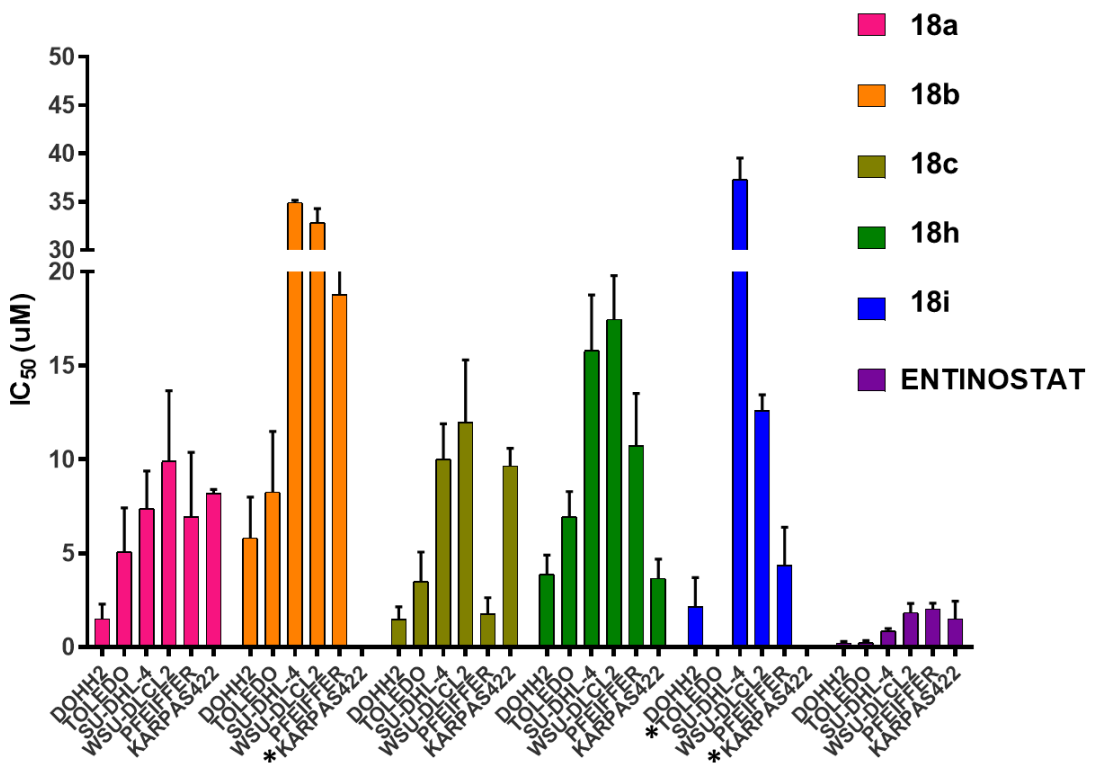

Cell lines	18a	18b	18c	18h	18i	Ent	Taz
	IC_{50} (μM)						
DOHH2	1.49	5.81	1.49	3.87	2.16	0.21	NA
Toledo	5.08	8.25	3.49	6.95	NA	0.24	NA
SU-DHL-4	7.38	34.94	10.0	15.80	37.29	0.85	NA
WSU-DLCL2	9.89	32.84	11.98	17.46	12.59	1.82	NA
Pfeiffer	6.93	18.77	1.76	10.72	4.33	2.03	NA
KARPAS422	8.18	NA	9.65	3.66	NA	1.49	NA

Figure 6.2. *Antiproliferative activity (IC_{50}, μM) of the selected anilide compounds in a panel of human DLBCL cell lines. Top, bar chart depicting IC_{50} values of each compound in the 6 cell lines. *Toledo and KARPAS422 were insensitive to 18i at the concentrations tested; KARPAS422 were also insensitive to18b. Bottom, table showing exact IC_{50} values obtained for each compound. (NA: not active). Error bars correspond to the standard deviation of ≥3 biological replicates.*

Dual compounds displayed inhibitory activity already at 72 hours after treatment, in contrast to Tazemetostat which is inactive at the same concentration. Specifically, **Toledo** appeared responsive to all the newly synthesized compounds, except for **18i**, which appeared also inactive against **KARPAS422. 18b** demonstrated no inhibitory potency against mutated lymphoma cell line KARPAS422. While **Entinostat,** the HDAC reference inhibitor, displayed IC_{50} values in the single-digit micromolar range against all the tested lymphoma cell lines, **Tazemetostat**, the EZH2 reference inhibitor, was unable to inhibit the proliferation of lymphoma cell lines after 72 hours of treatment (**Figure 6.2**). In fact, it is reported in the literature that Tazemetostat requires a longer time of administration to exert an anti-proliferative effect. [687]

The compounds selected as more promising in the anilide series were the *para*-biphenyle compound **18a**, the anilide thiophene derivative **18c,** and the anilide derivative with the insertion of a fluorine atom in *meta* position to the amino group in the *ortho* position in the *o*-phenylenediamine moiety **18h** (**Figure 6.3**)**.** We selected these three compounds because they exhibited at 72 hours good IC_{50} values against the tested lymphoma cell lines. **18a**, the most potent compound, displayed IC_{50} values in the single-digit micromolar range for all the six cell lines, while **18c** and **18h** exhibited variable IC_{50} values, ranging from single to double-digit micromolar IC_{50}, depending on the specific lymphoma cell lines tested (**Figure 6.2**).

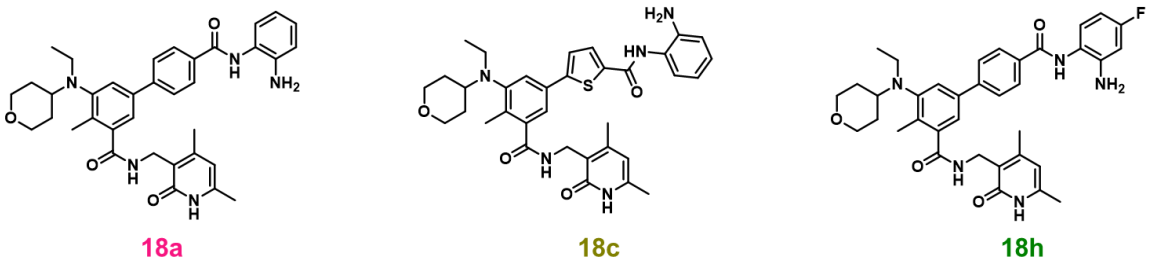

Figure 6.3. *Best Entinostat-based compounds from the MTT assay with a time-point of 72 hours.*

In addition to the Entinostat-based compounds, Vorinostat-based derivatives (**19a, 19b, 19c**, and **19g**), which feature a hydroxamic acid moiety as the ZBG, were also tested under the same conditions. As before, compounds were tested in six different

DLBCL cell lines, with wild-type or mutated EZH2, at a maximum concentration of **20 μM,** serially diluted 1:3, for **72 hours** (**Figure 6.4**).

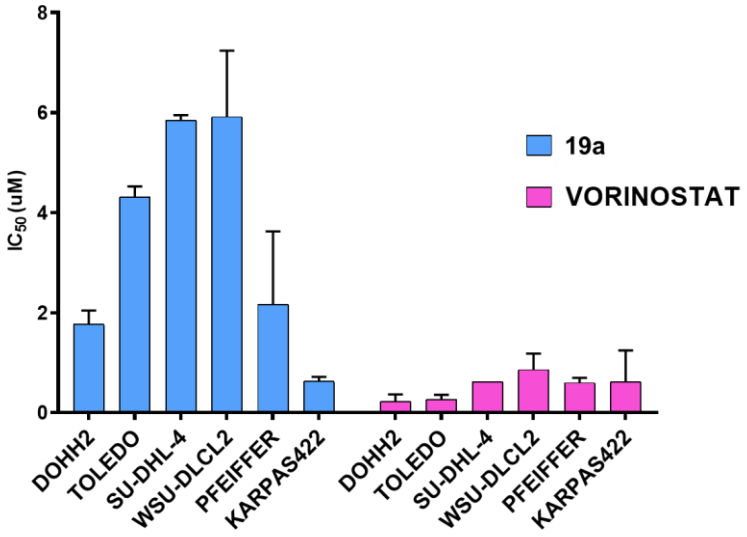

Cell lines	19a	19b	19c	19g	Vor	Taz
	IC_{50} (μM)					
DOHH2	1.77	NA	31.14	NA	0.23	NA
Toledo	4.32	24.96	NA	NA	0.26	NA
SU-DHL-4	5.84	NA	NA	NA	0.66	NA
WSU-DLCL2	5.92	NA	NA	NA	0.86	NA
Pfeiffer	2.16	27.13	10.37	NA	0.60	NA
KARPAS422	0.63	NA	NA	NA	0.62	NA

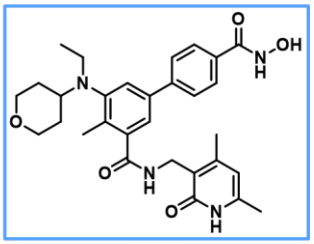

19a

Figure 6.4. *Antiproliferative activity (IC_{50}, μM) of the selected hydroxamic compounds in a panel of human DLBCL cell lines. Top, bar chart showing IC_{50} values for 19a and Vorinostat. Bottom, IC_{50} values for all Vorinostat-based compounds tested. Also represented, the molecular structure of **19a**, the best hydroxamic compound based on the results of the MTT assay at 72 hours (NA: not active). Error bars correspond to the standard deviation of ≥3 biological replicates.*

Among the hydroxamic compounds, only compound **19a** showed inhibitory activity against all the tested lymphoma cell lines, with IC_{50} values in the single-digit micromolar range. It demonstrated inhibitory activity against both wild-type and mutated cell lines. Contrarily, 19b, 19c, and 19g appeared inactive against the lymphoma cell lines at the same concentration (**Figure 6.4**).

At this point, the four best-performing compounds from the initial 72-hour MTT assay (dual compounds **18a**, **18c**, **18h**, and **19a**) were further evaluated against two selected lymphoma cell lines (wild-type DOHH2 and mutated SU-DHL-4) for a longer time-point of 7 days. SU-DHL-4 was chosen as the EZH2 mutant cell line because differently from most mutated lymphoma cell lines, it is insensitive to EZH2 inhibition, [631] and we wanted to determine if dual compounds were more active than Tazemetostat in this model. The longer treatment for 7 days allowed for a direct comparison with Tazemetostat, which had previously shown no activity at 72 hours. (**Figure 6.5**)

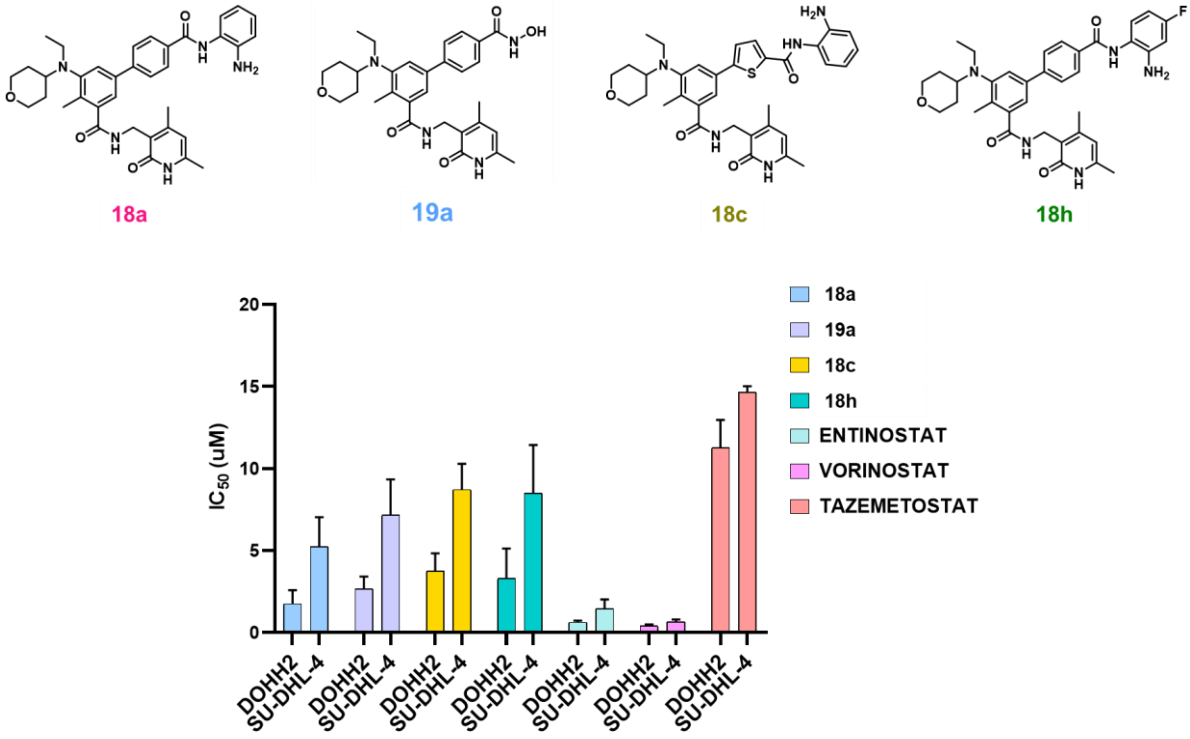

Cell lines	18a	19a	18c	18h	Ent	Vor	Taz
	IC_{50} (μM)						
DOHH2	1.74	2.67	3.74	3.28	0.63	0.40	11.26
SU-DHL-4	5.24	7.14	8.71	8.49	1.46	0.64	14.4

Figure 6.5. *Comparison of the antiproliferative activities of dual EZH2/HDACs inhibitors with single agents (Entinostat, Vorinostat, as HDACs inhibitors and Tazemetostat as EZH2 inhibitor). At the top of the figure are represented the molecular structures of the four best compounds, both hydroxamic and 2-aminoanilide derivatives. At the center of the figure is represented the bar chart, while at the bottom the corresponding exact values of* IC_{50}*. Error bars correspond to the standard deviation of ≥3 biological replicates.*

Dual inhibitors displayed IC_{50} values in the range of single-digit micromolar against the two lymphoma cell lines. The anilide derivative **18a** and the hydroxamic **19a** exhibited the best IC_{50} values in both cell lines. However, all dual compounds were more potent than Tazemetostat and less than HDAC inhibitors at the same concentration (**Figure 6.5**). In particular, the higher sensitivity of SU-DHL-4 to dual compounds compared to Tazemetostat indicated that dual compounds might increase sensitivity to EZH2 inhibition in this cell line.

In conclusion, the MTT assays identified compounds **18a**, **18c**, **18h**, and **19a** as the most promising candidates for further biological investigation due to their strong antiproliferative activity against non-Hodgkin's B-cell lymphoma cell lines, with efficacy superior to Tazemetostat but lower than standard HDAC inhibitors at comparable concentrations.

6.2.5. Dual EZH2/HDACs inhibitors effectively modulate histone marks (H3Ac and H3K27me3)

To assess the target engagement of 2-aminoanilides **18a**, **18c**, and **18h** and the hydroxamate **19a**, Western blot analyses were performed for histone H3 proteins in DOHH2 and WSU-DLCL2 cells after treatment for 24 and 72 hours. Cells were treated with the median IC_{50} values of each compound from the initial screening: **18a** was tested at 7 μM, **19a** at 3 μM, **18c** at 7 μM, and **18h** at 9 μM. Immunoblotting for acetylated histone H3 at lysine 27 (H3K27ac) was carried out to assess the acetylation capacity of the dual inhibitors. At the same time, the levels of trimethylated histone H3 at lysine 27 (H3K27me3) were analyzed to confirm the capability of dual inhibitors to reduce the levels of this histone mark. Detection of GAPDH, a housekeeping protein, served as an internal control to verify that equal amounts of protein were loaded into each well. Immunoblotting of total histone H3, a nuclear protein, served as an additional loading control for the histone marks H3K27ac and H3K27me3. The levels of EZH2 were also examined to determine if dual inhibitors specifically modulated the levels of H3K27ac and H3K27me3 and not EZH2 levels.

As shown in **Figure 6.6**, both in DOHH2 and in WSU-DLCL2 cell lines, all four hybrid compounds (**18a**, **19a**, **18c**, and **18h**) increased H3K27ac levels and decreased H3K27me3 levels in a time-dependent manner. Particularly, the effect on H3K27ac was observable as early as 24 hours after treatment, while the reduction in

H3K27me3 became more pronounced after 72 hours. We analyzed also the single-target inhibitors, confirming that in these cases the modulation concerned only the histone mark of interest. Specifically, Tazemetostat (EZH2 inhibitor) reduced H3K27me3 without affecting H3K27ac and this modulation is already clear at 24 hours. In contrast, Entinostat and Vorinostat, both HDACs inhibitors, increased H3K27ac without affecting H3K27me3. These results confirm the dual activity of the hybrid inhibitors, as they are capable of modulating both acetylation and methylation of histone H3, unlike single-target inhibitors, which affect only one histone modification.

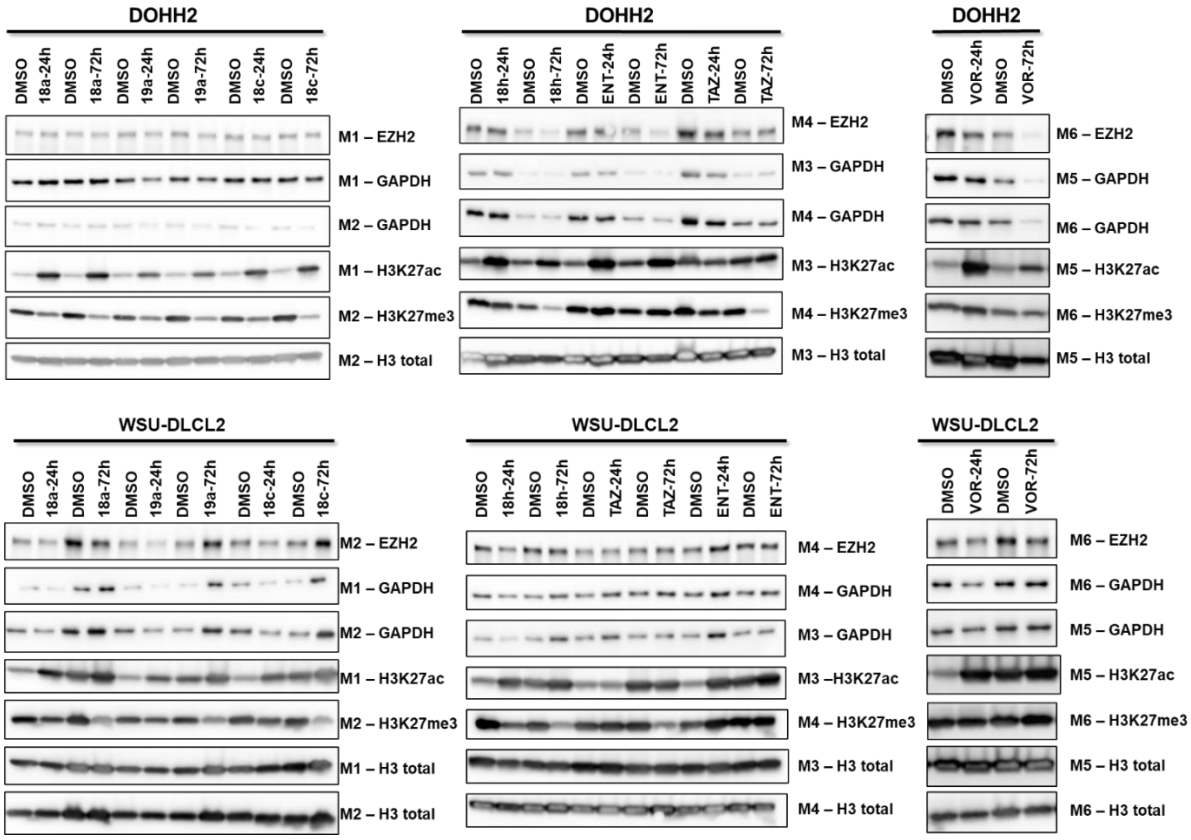

Figure 6.6. *Representative Western blot analyses of 2 biological replicates. DOHH2 (top) and WSU-DLCL2 (bottom) were exposed to 18a, 19a, 18c, and 18h, as well as to their corresponding DMSO treatment, for 24 and 72 hours. Levels of GAPDH and H3 served as loading controls.*

6.2.6. Cell cycle analysis

Next, we studied the effects of dual compounds **18a**, **19a**, **18c**, and **18h** on cell cycle progression in two *human* lymphoma cell lines, **DOHH2** and **WSU-DLCL2**, which are wild-type and mutated for EZH2, respectively. Cell cycle analyses were performed by flow cytometry (FACS analysis). Vorinostat and Entinostat were used as reference controls for HDAC inhibition, while Tazemetostat was employed as the control for EZH2 inhibition. The new dual inhibitors were tested for 24 and 72 hours at a concentration derived from their median IC_{50} values obtained from the initial screening: **18a** was tested at 7 μM, **19a** at 3 μM, **18c** at 7 μM, and **18h** at 9 μM.

In the **DOHH2** cell line (**Figure 6.7.a**), the tested compounds exhibited modest effects at 24 hours, with a slight increase in the G1 peak, suggesting an early cytostatic response. When tested at 72 hours, derivatives induced a significant accumulation of cells in sub-G1, demonstrating a cytotoxic effect, alongside a further increase in the G1 peak. Specifically, compound **18a** caused a strong accumulation in sub-G1, and also an increase in the G1 peak. Compound **19a** showed only an increase of the G1 peak. Compound **18c** exhibited both an evident accumulation of cells in sub-G1 and G1-peak increase, similar to the profile seen for compound **18h**.

In the **WSU-DLCL2** cell line (**Figure 6.7.b**), the dual compounds showed clear cytostatic effects as early as 24 hours, with a significant block in the G1 phase of the cell cycle. By 72 hours, this effect became more evident, with a large percentage of cells being arrested in the G1 phase. This suggests that the compounds efficiently halted cell cycle progression at this stage, further emphasizing their cytostatic activity.

Overall, the dual compounds were shown to induce both cytotoxic and cytostatic effects in the lymphoma cell lines, with stronger impacts observed after 72 hours of treatment.

a) DOHH2

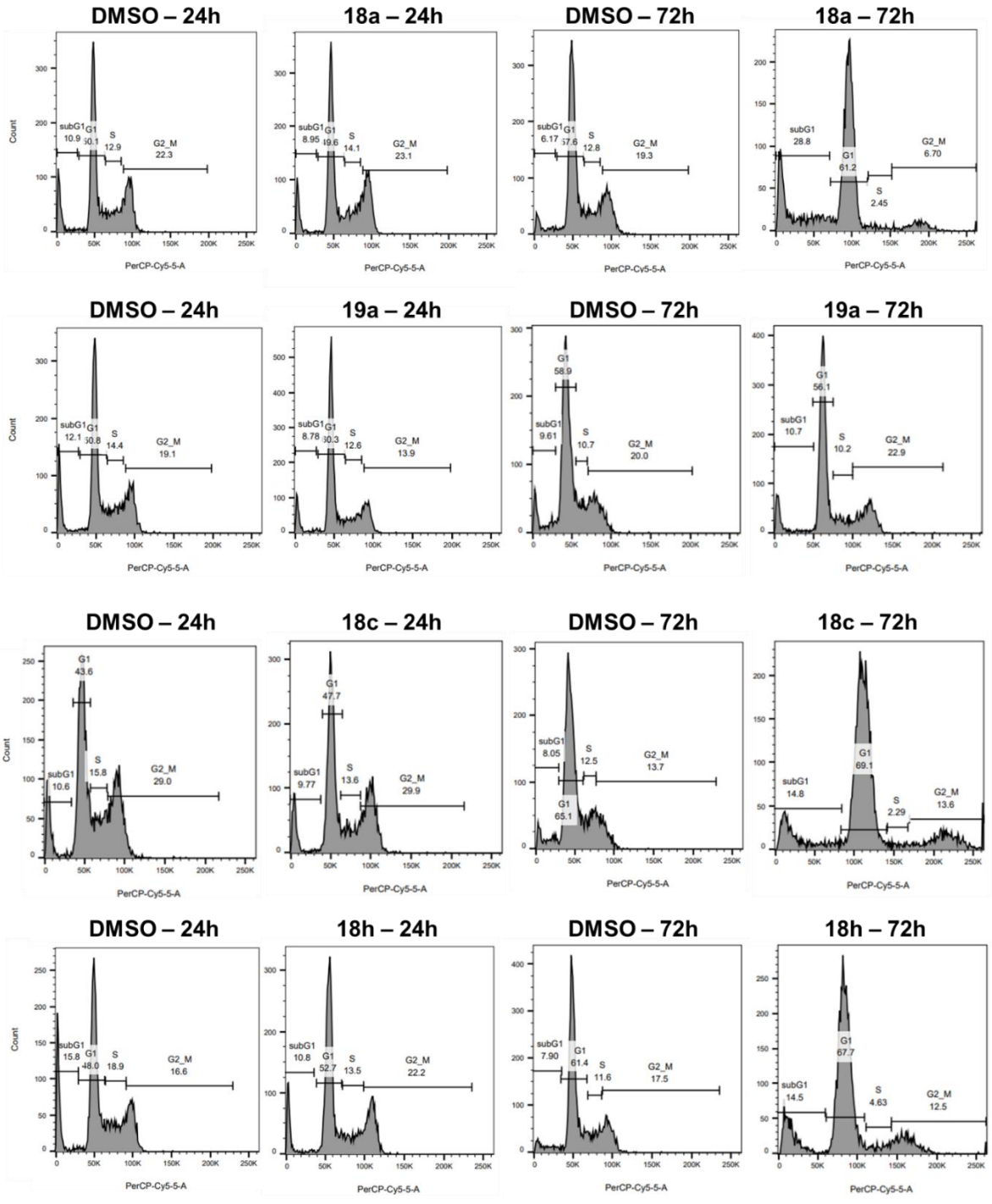
DMSO – 24h
18a – 24h
DMSO – 72h
18a – 72h
DMSO – 24h
19a – 24h
DMSO – 72h
19a – 72h
DMSO – 24h
18c – 24h
DMSO – 72h
18c – 72h
DMSO – 24h
18h – 24h
DMSO – 72h
18h – 72h
Count
PerCP-Cy5-5-A
subG1
G1
S
G2_M

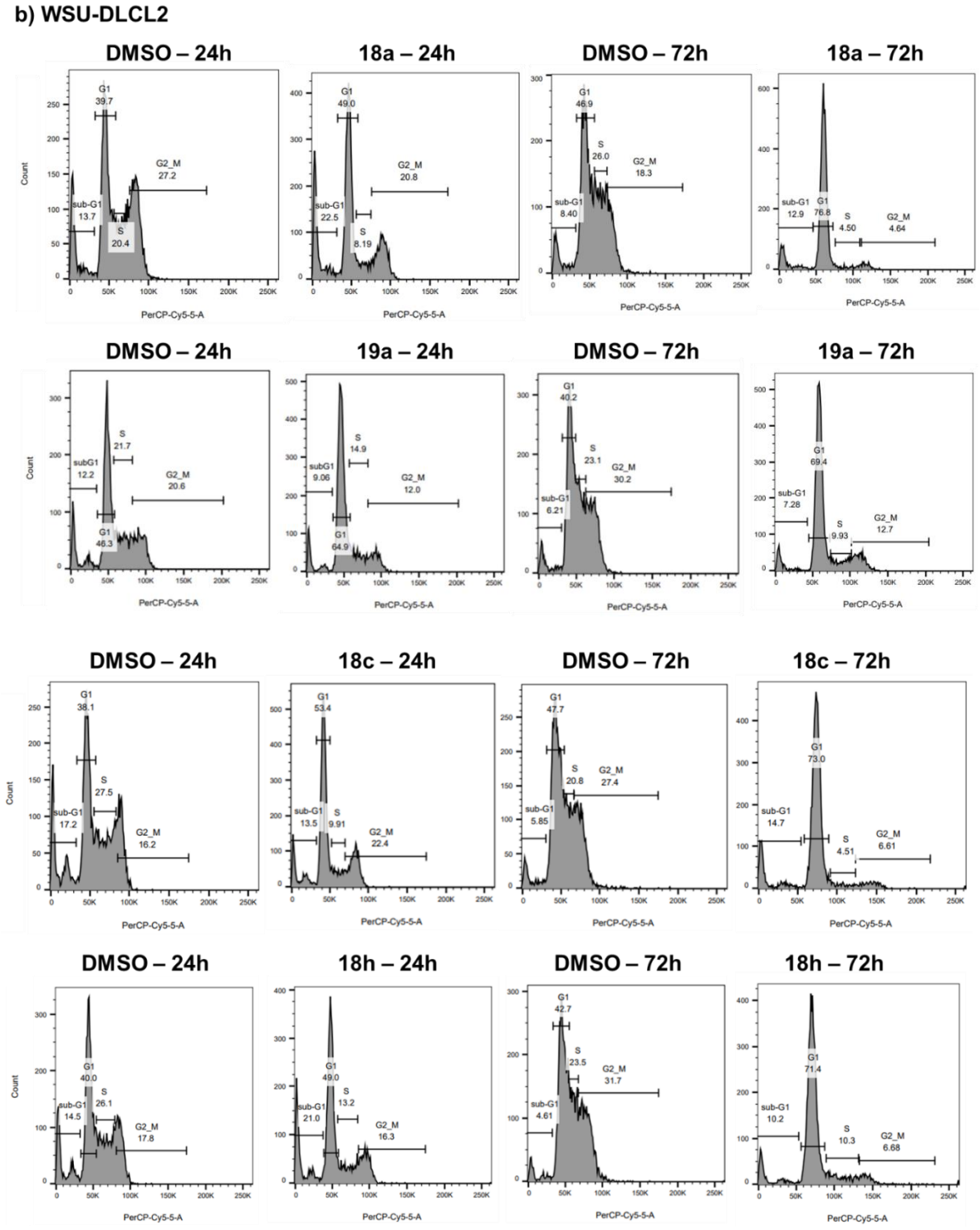

Figure 6.7. *Effects of dual inhibitors **18a, 19a, 18c,** and **18h** on cell cycle phases at 24 hours and 72 hours **a)** in DOHH2 cell line, **b)** in WSU-DLCL2 cell line. These are representative cell cycle profiles of 2 biological replicates.*

6.2.7. RNA-sequencing

To uncover the effects of dual compounds on the transcriptomes of DLBCL cells, we treated two DLBCL cell lines, **DOHH2** (wildtype EZH2) and **WSU-DLCL2** (mutated EZH2) with **18a**, **19a**, **Vorinostat**, **Entinostat**, **Tazemetostat** or DMSO for 24 hours and performed RNA sequencing on total RNA extracted from these cells. Gene set enrichment analysis (GSEA) of the transcriptome data revealed the modulation of common gene sets in DLBCL cells treated with dual inhibitors or single agents. In particular, transcriptional targets of the oncogene MYC were significantly downregulated in both cell lines following treatment with dual compounds, HDAC inhibitors, or Tazemetostat. The mammalian target of rapamycin complex 1 (mTORC1) signaling, which regulates cell growth and metabolism, was downregulated in DOHH2 treated with 19a and in WSU-DLCL2 treated with 18a. Treatment with single agents downregulated mTORC1 signaling only in DOHH2 treated with Vorinostat; single agents did not significantly modulate mTORC1 signaling in WSUDLCL2. Transcripts involved in DNA repair, G2/M cell cycle checkpoint genes, and oxidative phosphorylation were all downregulated in WSU-DLCL2 treated with dual inhibitors; of these gene sets, only DNA repair was downregulated in DOHH2 by 18a. Single-agent Vorinostat downregulated DNA repair, G2-M checkpoint and cell cycle targets of E2F transcription factors in both cell lines. Entinostat and Tazemetostat downregulated DNA repair genes in WSU-DLCL2 but not in DOHH2. GSEA performed with a custom gene sets database comprised of transcripts modulating lymphoma-specific processes (https://lymphochip.nih.gov/signaturedb/) further supported the downregulation of genes involved in proliferation and cell cycle as well as MYC target genes. Tazemetostat significantly downregulated proliferation transcripts in WSU-DLCL2 but not in DOHH2, supporting the higher anti-tumor activity of Tazemetostat in EZH2 mutant lymphoma compared to EZH2 wildtype disease. Overall, the transcriptome analyses indicated that dual inhibitors were more effective at modulating the expression of transcripts involved in lymphomagenesis than Tazemetostat and Entinostat while Vorinostat often downregulated similar gene sets to both dual compounds (**Figure 6.8**). The common downregulation of MYC target genes by dual compounds, HDAC inhibitors, and Tazemetostat suggested that MYC transcriptional regulation is an important component of epigenetic dysregulation in DLBCL. Indeed, MYC is recognized as a regulator of the cancer epigenome and recruits chromatin remodeling complexes to alter chromatin architecture. [688] The common processes modulated by dual inhibitors and single

agents further underlined that dual agents effectively retain the biological activity of their individual components within a single compound.

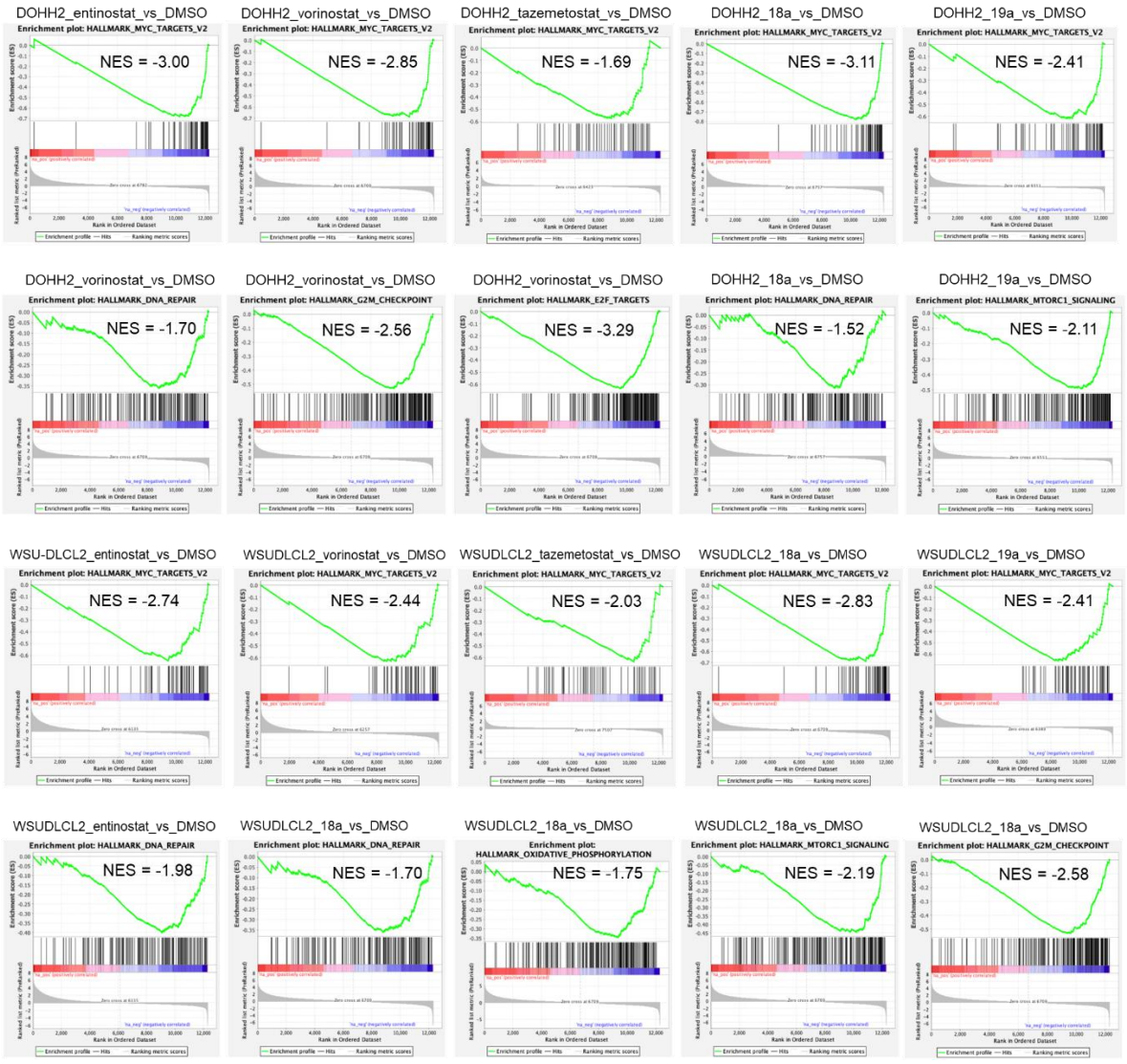

Figure 6.8. *Effects of dual inhibitors, Entinostat, Vorinostat, and Tazemetostat on the transcriptomes of DOHH2 and WSU-DLCL2 after 24 hours treatment. Gene set enrichment analysis (GSEA) was performed on RNA-Seq data to determine biological processes and signaling pathways downregulated by dual inhibitors and single agents. Top, GSEA enrichment plots for DOHH2; bottom, GSEA enrichment plots for WSU-DLCL2. Representative enrichment plots for Hallmark gene sets are shown. NES, normalized enrichment score; p <0.05 and false discovery rate (FDR) < 0.05.*

6.3. Conclusions

Our research focused on the development of novel dual inhibitors targeting two key epigenetic regulators, EZH2 (Enhancer of Zeste Homolog 2) and HDACs (Histone Deacetylases), both of which play crucial roles in cancer biology. These epigenetic enzymes are often dysregulated in various types of cancer, contributing to aberrant gene expression, uncontrolled cell proliferation, and tumor progression. Specifically, EZH2 is involved in the trimethylation of histone H3 on lysine 27 (H3K27me3), leading to transcriptional repression of tumor suppressor genes. HDACs, which remove acetyl groups from lysine groups on histone tails, promote chromatin condensation and gene silencing, further promoting oncogenic processes. Given the critical role of these enzymes in cancer, they have emerged as important therapeutic targets. Our study aims to leverage a polypharmacological approach by designing dual inhibitors that simultaneously target EZH2 and HDACs, based on the rationale that co-inhibition of these enzymes could lead to synergistic effects, enhancing the therapeutic outcome compared to single-agent inhibition. This strategy contrasts with classical combination therapy, where two or more drugs are administered simultaneously but act independently. Instead, our approach integrates the activity of both inhibitors into a single molecule, enhancing specificity, reducing off-target effects, and simplifying dosing regimens.

To achieve this dual inhibition, we synthesized hybrid molecules by combining structural elements of Tazemetostat, a selective and the only FDA-approved EZH2 inhibitor, with pharmacophore moieties from various well-known HDAC inhibitors. Tazemetostat acts by inhibiting the methyltransferase activity of EZH2, preventing trimethylation of H3K27, and restoring the expression of tumor suppressor genes. The HDAC inhibitor pharmacophores were selected based on their ability to effectively inhibit histone deacetylation, a critical step in reversing epigenetic silencing in cancer cells. The structural design of these hybrid compounds was meticulously crafted to ensure they would effectively interact with both the catalytic domain of EZH2 and the active sites of HDACs, achieving dual activity. By optimizing linker regions and modifying functional groups, we created compounds that maintained potent inhibitory activity against both targets. The results from biochemical assays performed on these hybrid compounds demonstrated their dual activity against both EZH2 and HDACs.

Notably, the hybrids exhibited enhanced inhibitory potency on EZH2 compared to Tazemetostat alone, with lower IC_{50} values indicating stronger binding affinity and

greater effectiveness. This enhanced potency suggests that the hybrid molecules not only successfully inhibit EZH2 but do so more efficiently than the single-agent inhibitor, potentially offering a therapeutic advantage in cancers driven by EZH2 dysregulation. To further evaluate the efficacy of these dual inhibitors, they were tested in several lymphoma cell lines, including those that harbor EZH2 mutations. These mutations are commonly associated with a gain-of-function effect, leading to increased H3K27me3 and more aggressive cancer phenotypes. The hybrid inhibitors displayed potent antiproliferative effects, with low micromolar concentrations sufficient to inhibit cell proliferation. This promising result underscores the potential of these dual inhibitors as a treatment option for lymphomas with EZH2 mutations.

In DOHH2 and WSU-DLCL2 cell lines, the dual inhibitors were shown to modulate specific histone marks, confirming their engagement with both HDAC and EZH2 targets. In particular, the inhibition of EZH2 resulted in the reduction of H3K27me3 levels, while HDAC inhibition led to increased histone acetylation, both of which are associated with transcriptional activation of tumor suppressor genes. The simultaneous modulation of these epigenetic markers suggests that these hybrid molecules can effectively reverse cancer-associated epigenetic alterations.

Further analysis of the effects of the dual inhibitors on cell cycle progression revealed significant alterations in lymphoma cells. The compounds induced a G1 phase cell cycle arrest, preventing cells from progressing to the S phase, which is essential for DNA replication. This cytostatic effect limits the ability of cancer cells to proliferate. Additionally, an accumulation of cells in sub-G1 was observed, indicating a cytotoxic effect of the dual inhibitors. This dual mechanism of action on cell cycle progression highlights the anti-proliferative effects of the inhibitors and their potential to not only halt tumor growth but also promote cancer cell death. While the in vitro results provide strong evidence for the efficacy of these dual EZH2/HDAC inhibitors, the next critical step in our research involves moving to *in vivo* studies. The use of patient-derived xenograft (PDX) mouse models of lymphoma will allow for a more comprehensive evaluation of the therapeutic potential of these compounds in a biological context that more closely mimics human disease. These PDX models will enable the exploration of critical pathways involved in lymphoma progression, providing insights into the broader molecular mechanisms affected by the dual inhibition of EZH2 and HDACs. Additionally, *in vivo* studies will allow for the assessment of pharmacokinetics, pharmacodynamics,

and toxicity, which are essential for advancing these compounds toward clinical development.

In summary, our study on dual EZH2/HDACs inhibitors represents a significant advancement in the field of cancer epigenetics by demonstrating the potential of dual EZH2/HDAC inhibitors as a novel therapeutic strategy. The ability to simultaneously target two epigenetic regulators that play complementary roles in cancer progression offers several advantages. By inhibiting both EZH2-mediated methylation and HDAC-mediated deacetylation, these dual inhibitors more effectively restored normal gene expression patterns, suppressed tumor growth, and overcame resistance mechanisms that limit the efficacy of single-agent therapies.

6.4. Experimental section

6.4.1. Chemistry

Melting points were determined on a Buchi 530 melting point apparatus. ^{1}H NMR and ^{13}C NMR spectra were recorded at 400 MHz on a Bruker AC 400 spectrometer; chemical shifts are reported in δ (ppm) units relative to the internal reference tetramethyl silane (Me_4Si). All compounds were routinely checked by TLC, ^{1}H NMR, and ^{13}C NMR spectra. TLC was performed on aluminum-backed silica gel plates (Merck DC, Alufolien Kieselgel 60 F254) with spots visualized by UV light. All solvents were reagent grade and, when necessary, were purified and dried by standard methods. The concentration of solutions after reactions and extractions involved using a rotary evaporator operating at a reduced pressure of ca. 20 Torr. Organic solutions were dried over anhydrous sodium sulfate. Elemental analysis has been used to determine the purity of the described compounds, which is >95 %. Analytical results are within ± 0.40 % of the theoretical values (Table S1 in Supporting Information). All chemicals were purchased from Sigma Aldrich, Milan (Italy), Alfa Aesar, Karlsruhe (Germany), Fluorochem, Manchester (UK), or BLD-Pharma, Kaiserslautern (Germany) and were of the highest purity.

Synthesis of *tert*-butyl 5-bromo-2-methyl-3-((tetrahydro-2H-pyran-4-yl)amino)benzoate (39): To a solution of the commercially available *tert*-butyl 3-amino-5-bromo-2-methylbenzoate (0.0104 mol, 2.97 g) in dry DCE, were added tetrahydro-4H-pyran-4-one (0.0207 mol, 2.07 g), sodium triacetoxyborohydride ($Na(CH_3COO)_3BH$) (0.0207 mol, 4.40 g), and acetic acid (2.97 mL). The reaction was stirred at room temperature for 6 hours. After this time, the reaction was quenched with 100 mL di 2N NaOH and extracted with AcOEt (3x15 mL). The organic extracts were collected, washed with brine, dried with sodium sulfate, and concentrated under reduced pressure. The obtained crude was purified by trituration with Et_2O and, subsequently, filtered off to obtain 3.84 g of the pure compound **39** as a yellow solid.

M.p. 118-121 °C; yield: 99.9%; ^{1}H-NMR ($CDCl_3$, 400 MHz, δ, ppm): 1.62 (9H, s, -Boc), 2.19 (3H, s, $-CH_3$), 3.59 (1H, s, -NH), 2.07 (4H, m, $-CH_2$ THP), 2.22 (1H, m, -CH THP), 4.03 (4H, m, $-CH_2$ THP), 6.82 (1H, s, aromatic proton), 6.82 (1H, s, aromatic proton).

Synthesis of *tert*-butyl 5-bromo-3-(ethyl(tetrahydro-2H-pyran-4-yl)amino)-2-methylbenzoate (40): To a solution of *tert*-butyl 5-bromo-2-methyl-3-((tetrahydro-2H-pyran-4-yl)amino)benzoate (39) (0.0104 mol, 3.84 g) in dry DCE, acetic acid (0.0622 mol, 3.56 mL) was added. After 15 minutes, acetaldehyde (0.0207 mol, 1.16 mL) and $Na(CH_3COO)_3BH$ (0.0311 mol, 6.60 g), were added at 0 °C. The reaction was stirred at room temperature for 2 hours. After this time, the reaction was quenched with $NaHCO_3$ solution and extracted with DCM (5x15 mL). The organic extracts were collected, washed with brine, dried with sodium sulfate, and concentrated under reduced pressure. 4.16 g of the pure compound **40** was obtained as orange oil.

M.p. -; yield: 98.8%; ^{1}H-NMR ($CDCl_3$, 400 MHz, δ, ppm): 0.82 (3H, m, aliphatic protons), 1.55 (9H, s, -Boc), 2.33 (3H, s, C*H*$_3$-CH$_2$-NRR'), 3.33 (2H, m, CH$_3$-C*H*$_2$-NRR'), 2.07 (4H, m, THP protons), 2.13 (1H, m, THP protons), 3.84 (4H, m, THP protons), 7.48 (1H, s, aromatic proton), 7.490 (1H, s, aromatic proton).

General procedure for the synthesis of compounds 41a-d

Example: Synthesis of 3-(*tert*-butyl) 4'-methyl 5-(ethyl(tetrahydro-2H-pyran-4-yl)amino)-4-methyl-[1,1'-biphenyl]-3,4'-dicarboxylate (41a)

The *tert*-butyl 5-bromo-3-(ethyl(tetrahydro-2H-pyran-4-yl)amino)-2-methylbenzoate (**40**) (0.0020 mol, 0.800 g) was solubilized into a solvent mixture of Toluene and Ethanol in 1:1 ratio. Subsequently, (4-(methoxycarbonyl)phenyl)boronic acid (0.00301 mol, 0.542 g), 2N Na_2CO_3 solution (0.0042 mol, 2.11 mL), and tetrakis(triphenylphosphine)palladium(0) (0.000140 mol, 0.163 g) were added under nitrogen flow. The reaction was stirred at 105 °C overnight. After this time, the reaction was quenched with distilled water and extracted with AcOEt (3x10 mL). The organic extracts were collected, washed with brine, dried with sodium sulfate, and concentrated under reduced pressure. The obtained crude was purified by column chromatography (SiO_2, eluting with ethyl acetate/n-hexane 1:7) to obtain 688 mg of the pure compound **41a** as a colourless oil.

M.p. -; yield: 76.1%; ^{1}H-NMR ($CDCl_3$, 400 MHz, δ, ppm): 0.83 (3H, m, aliphatic protons), 1.56 (9H, s, -Boc), 1.71 (4H, m, THP protons), 2.45 (3H, s, aliphatic protons), 2.94 (1H, m, THP protons), 2.96 (2H, m, aliphatic protons), 2.98 (4H, m, aliphatic protons), 3.09 (3H, s, -O-CH$_3$), 7.54 (1H, s, aromatic protons), 7.56 (2H, d, aromatic

protons, J= 4 Hz), 7.64 (1H, s, aromatic protons), 8.05 (2H, d, aromatic protons, J= 8 Hz).

Synthesis of *tert*-butyl (E)-5-(3-butoxy-3-oxoprop-1-en-1-yl)-3-(ethyl(tetrahydro-2H-pyran-4-yl)amino)-2-methylbenzoate (46): To a solution of *tert*-butyl 5-bromo-3-(ethyl(tetrahydro-2H-pyran-4-yl)amino)-2-methylbenzoate (**40**) (0.00126 mol, 0.500 g) in dry DMF, butyl acrylate (0.00377 mol, 0.54 mL), $NaHCO_3$ (0.00753 mol, 0.422 g), TEA (0.008475 mol, 1.19 mL), triphenylphosphine (PPh_3) (0.000113 mol, 0.02963 g), and, finally, $Pd(OAc)_2$ (0.000189 mol, 0.04227 g) were added, under nitrogen flow. The reaction was stirred at 110 °C for 15 hours. After this time, the reaction was quenched with distilled water and extracted with AcOEt (3x10 mL). The organic extracts were collected, washed with brine, dried with sodium sulfate, and concentrated under reduced pressure. The obtained crude was purified by column chromatography (SiO_2, eluting with ethyl acetate/n-hexane 1:9) to obtain 385 mg of the pure compound **46** as a yellow oil.

M.p. -; yield: 68.7%; ^{1}H-NMR ($CDCl_3$, 400 MHz, δ, ppm): 0.94 (3H, t, aliphatic protons, J= 7 Hz), 1.21 (3H, t, C*H*$_3$-CH$_2$-NRR', J= 7 Hz), 1.41 (2H, m, aliphatic protons), 1.56 (9H, s, -Boc), 1.58 (2H, m, aliphatic protons), 1.84 (2H, m, THP protons), 2.09 (2H, m, THP protons), 2.43 (3H, s, -CH_3 phenyl), 3.46 (2H, q, CH_3-C*H*$_2$-N-R,R'), 3.52 (3H, m, THP protons), 3.69 (2H, m, THP protons), 4.13 (2H, t, aliphatic protons, J= 6.7 Hz), 6.40 (1H, d, Ar-C*H*=CH-CO, J= 16 Hz), 7.03 (1H, s, aromatic proton), 7.58 (1H, d, Ar-CH=C*H*-CO, J= 16 Hz), 7.80 (1H, s, aromatic proton).

Synthesis of *tert*-butyl 5-amino-3-(ethyl(tetrahydro-2H-pyran-4-yl)amino)-2-methylbenzoate (47): To a solution of CuI (0.001552 mol, 0.395 g) in dry DMF were added Cs_2CO_3 (0.03111 mol, 13.52 g), *tert*-butyl 5-bromo-3-(ethyl(tetrahydro-2H-pyran-4-yl)amino)-2-methylbenzoate (**40**) (0.01037 mol, 4.13 g), 2,4-pentandione (0.00933 mol, 1.278 mL), and, finally, 17M NH_4OH (0.0777 mol, 6.09 mL). The reaction was stirred at room temperature for 19 hours under an inert atmosphere by nitrogen. Afterward, the reaction was quenched with NaCl-saturated solution and extracted with AcOEt (3x10 mL). The organic extracts were collected, washed with brine, dried with sodium sulfate, and concentrated under reduced pressure. The obtained crude was purified by column chromatography (SiO_2, eluting with ethyl acetate/n-hexane 1:2) to obtain 1.47 g of the pure compound **47** as a green oil.

M.p. -; yield: 42.4%; ^{1}H-NMR ($CDCl_3$, 400 MHz, δ, ppm): 1.21 (3H, t, C*H*$_3$-CH_2-NRR', J= 7 Hz), 1.56 (9H, s, -Boc), 1.58 (2H, m, aliphatic protons), 1.84 (2H, m, THP protons), 2.09 (2H, m, THP protons), 2.43 (3H, s, -CH_3 phenyl), 3.46 (2H, q, CH_3-C*H*$_2$- N-R,R'), 3.52 (3H, m, THP protons), 3.69 (2H, m, THP protons), 4.95 (2H, s, Ar-NH_2), 6.19 (1H, s, aromatic proton), 6.96 (1H, s, aromatic proton).

General procedure for the synthesis of compounds 48a-g

Example: Synthesis of *tert*-butyl 5-(8-ethoxy-8-oxooctanamido)-3-(ethyl(tetrahydro-2H-pyran-4-yl)amino)-2-methylbenzoate (48g)

To a solution of *tert*-butyl 5-amino-3-(ethyl(tetrahydro-2H-pyran-4-yl)amino)-2-methylbenzoate (**47**) (0.0003674 mol, 0.0743 g) in dry DMF were added TEA (0.001469 mol, 0.20 mL), HATU (0.0004410 mol, 0.16761g), and, finally, 8-ethoxy-8-oxooctanoic acid (0.0003674 mol, 0.12 mL). The reaction was stirred at room temperature for 2 hours. After this time, the reaction was quenched with NaCl-saturated solution and extracted with AcOEt (3x10 mL). The organic extracts were collected, washed with brine, dried with sodium sulfate, and concentrated under reduced pressure. The obtained crude was purified by column chromatography (SiO_2, eluting with ethyl acetate/n-hexane 1:2) to obtain 187.6 g of the pure compound **48g** as a yellow oil.

M.p. -; yield: 98.45%; ^{1}H-NMR ($CDCl_3$, 400 MHz, δ, ppm): 1.21 (3H, t, C*H*$_3$-CH_2-NRR', J= 7 Hz), 1.24 (3H, t, aliphatic protons, J= 7 Hz), 1.35 (4H, m, aliphatic protons), 1.56 (9H, s, -Boc), 1.58 (2H, m, aliphatic protons), 1.65 (2H, m, aliphatic protons), 1.84 (2H, m, THP protons), 2.09 (2H, m, THP protons), 2.29 (2H, t, aliphatic protons, J= 13 Hz), 2.34 (2H, t, aliphatic protons, J= 13 Hz), 2.43 (3H, s, -CH_3 phenyl), 3.46 (2H, q, CH_3-C*H*$_2$- N-R,R'), 3.52 (3H, m, THP protons), 3.69 (2H, m, THP protons), 4.13 (2H, m, aliphatic protons), 7.32 (1H, s, aromatic proton), 7.78 (1H, s, aromatic proton), 9.87 (1H, s, Ar-N*H*-CO).

General procedure for the synthesis of compounds 42a-g

Example: Synthesis of 5-(ethyl(tetrahydro-2H-pyran-4-yl)amino)-4'-(methoxycarbonyl)-4-methyl-[1,1'-biphenyl]-3-carboxylic acid (42a)

To a solution of 3-(*tert*-butyl) 4'-methyl 5-(ethyl(tetrahydro-2H-pyran-4-yl)amino)-4-methyl-[1,1'-biphenyl]-3,4'-dicarboxylate (**41a**) (0.000843 mol, 0.382 g) in dry DCM, trifluoroacetic acid (0.0126 mol, 1.94 mL) was added at 0 °C. The reaction was stirred at room temperature for 7 hours. After this time, the crude of the reaction was concentrated under reduced pressure. Subsequently, washes with Et_2O and MeOH were done, in order to remove all the TFA residues. The solid was purified by trituration with Et_2O overnight. Afterward, the precipitate was filtered off and dried to give 330 mg of white pure compound **42a**.

M.p. 196-198 °C; yield: 98.5%; ^{1}H-NMR ($CDCl_3$, 400 MHz, δ, ppm): 1.21 (3H, t, C*H*$_3$-CH_2-NRR', J= 7 Hz), 1.84 (2H, m, THP protons), 2.09 (2H, m, THP protons), 2.43 (3H, s, -CH_3), 3.46 (2H, q, CH_3-C*H*$_2$-N-R,R'), 3.52 (3H, m, THP protons), 3.69 (2H, m, THP protons), 3.87 (1H, s, aliphatic proton), 7.06 (1H, s, aromatic proton), 7.61 (2H, m, aromatic proton), 8.00 (2H, m, aromatic protons), 8.05 (1H, s, aromatic proton), 12.52 (1H, s, -COOH).

General procedure for the synthesis of compounds 43a-g

Example: Synthesis of methyl 5-(3-(((4,6-dimethyl-2-oxo-1,2-dihydropyridin-3-yl)methyl)carbamoyl)-5-(ethyl(tetrahydro-2H-pyran-4-yl)amino)-4-methylphenyl)thiophene-2-carboxylate (43c)

To a solution of 3-(ethyl(tetrahydro-2H-pyran-4-yl)amino)-5-(5-(methoxycarbonyl)thiophen-2-yl)-2-methylbenzoic acid (**42c**) (0.000413 mol, 0.167 g) in dry DMF, TEA (0.002071 mol, 0.29 mL), HATU (0.0006212 mol, 0.236 g), and 3-(aminomethyl)-4,6-dimethylpyridin-2(1H)-one (0.0006212 mol, 0.095 g) were added under inert atmosphere by nitrogen. The reaction was stirred at room temperature for 3 hours. Afterward, the reaction was quenched with NaCl-saturated solution, forming a precipitate, which was filtered off and dried. 240.3 mg of **43c** were obtained as a pure orange solid.

M.p. 183-184 °C; yield: 99.9%; ^{1}H-NMR (DMSO, 400 MHz, δ, ppm): 1.21 (3H, t, C*H*$_3$-CH_2-N-R,R', J= 4 Hz), 1.84 (2H, m, THP protons), 2.09 (2H, m, THP protons), 2.10 (3H, d, -CH_3 pyridinone, J= 8 Hz), 2.33 (3H, d, -CH_3 pyridinone, J= 8 Hz), 2.46 (3H,

s, -CH_3 phenyl), 3.46 (2H, q, CH_3-C*H*$_2$-N-R,R'), 3.52 (3H, m, THP protons), 3.69 (2H, m, THP protons), 3.88 (3H, s, aliphatic protons), 4.28 (2H, d, NH-C*H*$_2$-pyridinone, J= 6 Hz), 6.03 (1H, s, C=CH pyridinone), 6.96 (1H, d, aromatic proton, J= 2 Hz), 7.44 (1H, s, aromatic proton), 7.66 (1H, s, aromatic proton), 7.78 (1H, d, aromatic proton, J= 6.8 Hz), 8.30 (1H, t, CO-N*H*-CH_2, J= 4 Hz), 11.48 (1H, s, N*H* pyridinone).

General procedure for the synthesis of compounds 44a-g

Example: Synthesis of (*E*)-3-(3-(((4,6-dimethyl-2-oxo-1,2-dihydropyridin-3-yl)methyl)carbamoyl)-5-(ethyl(tetrahydro-2H-pyran-4-yl)amino)-4-methylphenyl)acrylic acid (44e)

To a solution of butyl (*E*)-3-(3-(((4,6-dimethyl-2-oxo-1,2-dihydropyridin-3-yl)methyl)carbamoyl)-5-(ethyl(tetrahydro-2H-pyran-4-yl)amino)-4-methylphenyl)acrylate (**43e**) (0.000468 mol, 0.245 g) in THF was added, at 0 °C, a solution of LiOH (0.004667 mol, 0.196 gr). The reaction was stirred at room temperature for 6 hours. After the concentration of the reaction under reduced pressure, 2 N HCl was added at 0 °C until pH 5 was reached. The mixture was extracted with AcOEt (3 × 15 mL), washed with brine, dried with sodium sulfate, filtered, and concentrated under reduced pressure, obtaining 173 mg of compound **44e** as a yellow solid.

M.p. 226-229 °C; yield: 80.3%; ^{1}H-NMR (DMSO, 400 MHz, δ, ppm): 1.21 (3H, t, C*H*$_3$-CH_2-N-R,R', J= 8 Hz), 1.84 (2H, m, THP protons), 2.09 (2H, m, THP protons), 2.10 (3H, d, -CH_3 pyridinone, J= 4 Hz), 2.33 (3H, d, -CH_3 pyridinone, J= 4 Hz), 2.46 (3H, s, -CH_3 phenyl), 3.46 (2H, q, CH_3-C*H*$_2$-N-R,R', J= 8 Hz), 3.52 (3H, m, THP protons), 3.69 (2H, m, THP protons), 4.28 (2H, d, NH-C*H*$_2$-pyridinone, J= 8 Hz), 6.03 (1H, s, -C=CH pyridinone), 6.48 (1H, d, CO-C*H*=CH-Ar, J= 12.8 Hz), 7.09 (1H, d, aromatic proton, J= 1.8 Hz), 7.54 (1H, d, CO-CH=C*H*-Ar, J= 8 Hz), 7.73 (1H, d, aromatic proton, J= 1.8 Hz), 8.17 (1H, t, CO-N*H*-CH_2, J= 4 Hz), 11.48 (1H, s, NH pyridinone), 12.27 (1H, s, -COOH).

General procedure for the synthesis of compounds 45a-g

Example: Synthesis of *N*1-(3-(((4,6-dimethyl-2-oxo-1,2-dihydropyridin-3-yl)methyl)carbamoyl)-5-(ethyl(tetrahydro-2H-pyran-4-yl)amino)-4-methylphenyl)-N7-((tetrahydro-2H-pyran-2-yl)oxy)heptanediamide (45f)

To a solution of 7-((3-(((4,6-dimethyl-2-oxo-1,2-dihydropyridin-3-yl)methyl)carbamoyl)-5-(ethyl(tetrahydro-2H-pyran-4-yl)amino)-4-methylphenyl)amino)-7-oxoheptanoic acid (**44f**) (0.000085 mol, 0.0471 g) in dry DMF were added TEA (0.000338 mol, 0.047 mL), HATU (0.000101 mol, 0.0386 g), and, finally, *O*-(tetrahydro-2H-pyran-2-yl)hydroxylamine (0.000254 mol, 0.0297 g), under nitrogen flow. The reaction was stirred at room temperature for 12 hours. Afterward, the reaction was quenched with NaCl-saturated solution, forming a precipitate, which was filtered off and dried. 55.6 mg of **45f** were obtained as a pure white solid.

M.p. 193-195 °C; yield: 99.9%; ^{1}H-NMR (DMSO, 400 MHz, δ, ppm): 1.21 (3H, t, CH_3-CH_2-N-R,R', J= 4 Hz), 1.51 (2H, m, -CH_2-C*H*$_2$-CH_2-), 1.60 (2H, m, -C*H*$_2$-CH_2-CH_2-), 1.62 (2H, m, OTHP protons), 1.65 (2H, m, -CH_2-CH_2-C*H*$_2$-), 1.74 (2H, m, OTHP protons), 1.84 (2H, m, THP protons), 1.89 (2H, m, OTHP protons), 1.96 (2H, t, CO-C*H*$_2$-CH_2, J= 8 Hz), 2.09 (2H, m, THP protons), 2.10 (3H, d, -CH_3 pyridinone, J= 8 Hz), 2.33 (3H, d, -CH_3 pyridinone, J= 8 Hz), 2.34 (2H, t, NH-CO-CH_2-C*H*$_2$, J= 8 Hz), 2.49 (3H, s, -CH_3 phenyl), 3.46 (2H, q, CH_3-C*H*$_2$-N-R,R'), 3.52 (3H, m, THP protons), 3.63 (2H, m, OTHP protons), 3.69 (2H, m, THP protons), 4.29 (2H, d, NH-C*H*$_2$-pyridinone, J= 6 Hz), 4.91 (1H, t, OTHP protons, J= 3.3 Hz), 6.03 (1H, s ,-CH pyridinone), 7.36 (1H, d, aromatic proton, J= 1.5 Hz), 7.65 (1H, d, aromatic proton, J= 1.5 Hz), 8.01 (1H, t, CO-N*H*-CH_2, J= 4 Hz), 8.78 (1H, s, Ar-N*H*-CO), 9.34 (1H, s, CO-N*H*-OTHP), 9.76 (1H, s, NH pyridinone).

General procedure for the synthesis of final compounds 19a-g

Example: Synthesis of (*E*)-N-((4,6-dimethyl-2-oxo-1,2-dihydropyridin-3-yl)methyl)-3-(ethyl(tetrahydro-2H-pyran-4-yl)amino)-5-(3-(hydroxyamino)-3-oxoprop-1-en-1-yl)-2-methylbenzamide (19e)

To a solution of (*E*)-N-((4,6-dimethyl-2-oxo-1,2-dihydropyridin-3-yl)methyl)-3-(ethyl(tetrahydro-2H-pyran-4-yl)amino)-2-methyl-5-(3-oxo-3-(((tetrahydro-2H-pyran-2-yl)oxy)amino)prop-1-en-1-yl)benzamide (**45e**) (0.0001235 mol, 0.070 g) in dry THF were added, at 0 °C, 4N HCl in 1,4-dioxane (0.0006176 mol, 0.15 mL) and dry MeOH. After 2 hours at room temperature, the reaction was quenched with Et_2O. It was observed the formation of a white precipitate, that was filtered off and dried, obtaining 53 mg of **19e**.

M.p. 192-193 °C; recrystallization solvent: acetonitrile; yield: 88.1%; ^{1}H-NMR (DMSO, 400 MHz, δ, ppm): 1.21 (3H, t, CH_3-CH_2-N-R,R', J= 8 Hz), 1.84 (2H, m, THP protons), 2.09 (2H, m, THP protons), 2.10 (3H, d, -CH_3 pyridinone, J= 4 Hz), 2.33 (3H, d, -CH_3 pyridinone, J= 4 Hz), 2.46 (3H, s, -CH_3 phenyl), 3.46 (2H, q, CH_3-C*H*$_2$-N-R,R'), 3.52 (3H, m, THP protons), 3.69 (2H, m, THP protons), 4.28 (2H, d, -NH-C*H*$_2$-pyridinone, J= 8 Hz), 6.03 (1H, s, -C=CH pyridinone), 6.76 (1H, d, CO-C*H*=CH-Ar, J= 12.8 Hz), 7.12 (1H, d, aromatic proton, J= 1.8 Hz), 7.60 (1H, d, CO-CH=C*H*-Ar, J= 8 Hz), 7.79 (1H, d, aromatic proton, J= 1.8 Hz), 8.17 (1H, t, CO-NH-CH_2, J= 4 Hz), 8.94 (1H, d, CO-N*H*-OH, J= 4 Hz), 9.59 (1H, d, CO-NH-O*H*, J= 4 Hz), 9.76 (1H, s, NH pyridinone).

19a, N^3-((4,6-dimethyl-2-oxo-1,2-dihydropyridin-3-yl)methyl)-5-(ethyl(tetrahydro-2H-pyran-4-yl)amino)-N4'-hydroxy-4-methyl-[1,1'-biphenyl]-3,4'-dicarboxamide:

M.p. 198-200 °C; recrystallization solvent: acetonitrile/methanol; yield: 83.5%; ^{1}H-NMR (DMSO, 400 MHz, δ, ppm): 1.14 (3H, t, C*H*$_3$-CH_2-), 1.70 (1H, m, THP protons), 1.72 (1H, m, THP protons), 1.95 (1H, m, THP protons), 1.97 (1H, m, THP protons), 2.28 (3H, s, -CH_3), 2.32 (3H, s, -CH_3), 2,37 (3H, s, -CH_3), 3.28 (2H, dq, -C*H*$_2$-CH_3), 3.44 (1H, m, THP protons), 3.46 (1H, m, THP protons), 3.47 (1H, m, THP protons), 3,84 (1H, m, THP protons), 3.85 (1H, m, THP protons), 3.87 (2H, s, -CO-NH-C*H*$_2$-), 5.43 (1H, s, -NH-O*H*), 5.55 (1H, s, -CH- pyridinone), 6.74 (1H, s, -N*H*-OH), 7.05 (1H, s, aromatic proton), 7.50 (1H, s, CO-N*H*-CH_2), 7.52 (1H, s, aromatic proton), 7.74 (2H, m, aliphatic protons), 8.07 (2H, m, aromatic proton), 9.68 (1H, s, NH pyridinone).

19b, N3-((4,6-dimethyl-2-oxo-1,2-dihydropyridin-3-yl)methyl)-5-(ethyl(tetrahydro-2H-pyran-4-yl)amino)-N3′-hydroxy-4-methyl-[1,1′-biphenyl]-3,3′-dicarboxamide:

M.p. 198-200 °C; recrystallization solvent: acetonitrile/methanol; yield: 46.1%; ^{1}H-NMR (DMSO, 400 MHz, δ, ppm): 1.21 (3H, t, C*H*$_3$-CH$_2$-N-R,R′, J= 4 Hz), 1.84 (2H, m, THP protons), 2.09 (2H, m, THP protons), 2.10 (3H, d, -CH$_3$ pyridinone, J= 8 Hz), 2.33 (3H, d, -CH$_3$ pyridinone, J= 8 Hz), 2.46 (3H, s, -CH$_3$ phenyl), 3.46 (2H, q, CH$_3$-C*H*$_2$-N-R,R′), 3.52 (3H, m, THP protons), 3.69 (2H, m, THP protons), 4.03 (2H, s, Ar-NH$_2$), 4.28 (2H, d, NH-C*H*$_2$-pyridinone, J= 6 Hz), 6.03 (1H, s ,-CH pyridinone), 7.06 (1H, d, aromatic proton, J= 2 Hz), 7.68 (1H, d, aromatic proton, J= 4 Hz), 7.79 (1H, m, aromatic proton), 7.87 (1H, m, aromatic proton), 7.95 (1H, d, aromatic proton, J= 4 Hz), 8.17 (1H, t, aromatic proton, J= 6 Hz), 8.21 (1H, t, CO-N*H*-CH$_2$, J= 4 Hz), 9.76 (1H, s, NH pyridinone), 10.74 (1H, d, CO-N*H*-OH, J= 8 Hz), 11.28 (1H, d, CO-NH-O*H*, J= 8 Hz).

19c, 5-(3-(((4,6-dimethyl-2-oxo-1,2-dihydropyridin-3-yl)methyl)carbamoyl)-5-(ethyl(tetrahydro-2H-pyran-4-yl)amino)-4-methylphenyl)-N-hydroxythiophene-2-carboxamide:

M.p. 192-194 °C; recrystallization solvent: acetonitrile; yield: 30.6%; ^{1}H-NMR (DMSO, 400 MHz, δ, ppm): 1.21 (3H, t, C*H*$_3$-CH$_2$-N-R,R′, J= 4 Hz), 1.84 (2H, m, THP protons), 2.09 (2H, m, THP protons), 2.10 (3H, d, -CH$_3$ pyridinone, J= 8 Hz), 2.33 (3H, d, -CH$_3$ pyridinone, J= 8 Hz), 2.46 (3H, s, -CH$_3$ phenyl), 3.46 (2H, q, CH$_3$-C*H*$_2$-N-R,R′), 3.52 (3H, m, THP protons), 3.69 (2H, m, THP protons), 4.28 (2H, d, NH-C*H*$_2$-pyridinone, J= 6 Hz), 6.03 (1H, s, -C=CH pyridinone), 6.96 (1H, d, aromatic proton, J= 2 Hz), 7.29 (1H, d, aromatic proton, J= 2 Hz), 7.67 (1H, d, aromatic proton, J= 2 Hz), 7.81 (1H, d, aromatic proton, J= 4 Hz), 8.30 (1H, t, CO-N*H*-CH$_2$, J= 4 Hz), 9.76 (1H, s, NH pyridinone), 10.74 (1H, d, CO-NH-O*H*, J= 6 Hz), 11.42 (1H, d, CO-N*H*-OH, J= 6 Hz).

19d, 5-(3-(((4,6-dimethyl-2-oxo-1,2-dihydropyridin-3-yl)methyl)carbamoyl)-5-(ethyl(tetrahydro-2H-pyran-4-yl)amino)-4-methylphenyl)-N-hydroxy-1-methyl-1H-pyrrole-2-carboxamide:

M.p. 189-191 °C; recrystallization solvent: acetonitrile; yield: 97.3%; ^{1}H-NMR (DMSO, 400 MHz, δ, ppm): 1.21 (3H, t, C*H*$_3$-CH$_2$-N-R,R', J= 4 Hz), 1.84 (2H, m, THP protons), 2.09 (2H, m, THP protons), 2.10 (3H, d, -CH$_3$ pyridinone, J= 8 Hz), 2.33 (3H, d, -CH$_3$ pyridinone, J= 8 Hz), 2.46 (3H, s, -CH$_3$ phenyl), 3.46 (2H, q, CH$_3$-C*H*$_2$-N-R,R'), 3.52 (3H, m, THP protons), 3.69 (2H, m, THP protons), 3.76 (3H, s, -CH$_3$ pyrrole), 4.28 (2H, d, NH-C*H*$_2$-pyridinone, J= 6 Hz), 6.03 (1H, s, -C=CH pyridinone), 6.85 (1H, d, aromatic proton, J= 2 Hz), 7.02 (1H, d, aromatic proton, J= 2 Hz), 7.24 (1H, m, aromatic proton), 7.58 (1H, d, aromatic proton, J= 2 Hz), 8.19 (1H, t, CO-N*H*-CH$_2$, J= 4 Hz), 9.76 (1H, s, NH pyridinone), 10.59 (1H, d, CO-N*H*-OH, J= 4 Hz), 11.94 (1H, d, CO-NH-O*H*, J= 4 Hz).

19f, N1-(3-(((4,6-dimethyl-2-oxo-1,2-dihydropyridin-3-yl)methyl)carbamoyl)-5-(ethyl(tetrahydro-2H-pyran-4-yl)amino)-4-methylphenyl)-N7-hydroxyheptanediamide:

M.p. >250 °C; recrystallization solvent: methanol; yield: 37.4%; ^{1}H-NMR (DMSO, 400 MHz, δ, ppm): 1.21 (3H, t, C*H*$_3$-CH$_2$-N-R,R', J= 4 Hz), 1.50 (2H, m, -CH$_2$-CH$_2$-CH$_2$-), 1.60 (2H, m, -CH$_2$-CH$_2$-CH$_2$-), 1.65 (2H, m, -CH$_2$-CH$_2$-CH$_2$-), 1.84 (2H, m, THP protons), 1.96 (2H, t, CO-CH$_2$-CH$_2$-, J= 8 Hz), 2.09 (2H, m, THP protons), 2.10 (3H, d, -CH$_3$ pyridinone, J= 8 Hz), 2.33 (3H, d, -CH$_3$ pyridinone, J= 8 Hz), 2.34 (2H, t, NH-CO-CH$_2$-CH$_2$, J= 8 Hz), 2.49 (3H, s, -CH$_3$ phenyl), 3.46 (2H, q, CH$_3$-C*H*$_2$-N-R,R'), 3.52 (3H, m, THP protons), 3.69 (2H, m, THP protons), 4.29 (2H, d, NH-C*H*$_2$-pyridinone, J= 6 Hz), 6.029 (1H, s, -CH pyridinone), 7.36 (1H, d, aromatic proton, J= 1.5 Hz), 7.65 (1H, d, aromatic proton, J= 1.5 Hz), 8.01 (1H, t, CO-N*H*-CH$_2$, J= 4 Hz), 8.78 (1H, s, Ar-N*H*-CO), 8.80 (1H, d, CO-N*H*-OH, J= 8 Hz), 9.74 (1H, d, CO-NH-O*H*, J= 4 Hz), 9.76 (1H, s, NH pyridinone).

19g, N1-(3-(((4,6-dimethyl-2-oxo-1,2-dihydropyridin-3-yl)methyl)carbamoyl)-5-(ethyl(tetrahydro-2H-pyran-4-yl)amino)-4-methylphenyl)-N8-hydroxyoctanediamide:

M.p. >250 °C; recrystallization solvent: methanol; yield: 53.0%; ^{1}H-NMR (DMSO, 400 MHz, δ, ppm): 1.21 (3H, t, C*H*$_3$-CH$_2$-N-R,R', J= 7.2 Hz), 1.34 (2H, m, -CH$_2$-CH$_2$-CH$_2$-), 1.35 (2H, m, -CH$_2$-CH$_2$-CH$_2$-), 1.56 (2H, m, -CH$_2$-CH$_2$-CH$_2$-), 1.65 (2H, m, -CH$_2$-CH$_2$-CH$_2$-), 1.84 (2H, m, THP protons), 1.96 (2H, t, CO-CH$_2$-CH$_2$, J= 8 Hz), 2.08 (2H, m, THP protons), 2.10 (3H, s, -CH$_3$ pyridinone), 2.33 (3H, s, -CH$_3$ pyridinone), 2.34 (2H, t, NH-CO-C*H*$_2$-CH$_2$, J= 8 Hz), 2.49 (3H, s, -CH$_3$ phenyl), 3.46 (2H, q, CH$_3$-CH$_2$-N-R,R'), 3.52 (3H, m, THP protons), 3.69 (2H, m, THP protons), 4.29 (2H, d, NH-C*H*$_2$-pyridinone, J= 6 Hz), 6.03 (1H, s ,-CH pyridinone), 7.36 (1H, d, aromatic proton, J= 1.5 Hz), 7.65 (1H, d, aromatic proton, J= 1.5 Hz), 8.01 (1H, t, CO-NH-CH$_2$, J= 8 Hz), 8.78 (1H, s, Ar-NH-CO), 8.80 (1H, d, CO-N*H*-OH, J= 8 Hz), 9.74 (1H, d, CO-NH-O*H*, J= 8 Hz), 9.76 (1H, s, NH pyridinone).

General procedure for the synthesis of final compounds 18a-e

Example: Synthesis of (*E*)-5-(3-((2-aminophenyl)amino)-3-oxoprop-1-en-1-yl)-N-((4,6-dimethyl-2-oxo-1,2-dihydropyridin-3-yl)methyl)-3-(ethyl(tetrahydro-2H-pyran-4-yl)amino)-2-methylbenzamide (18e)

To a solution of (*E*)-3-(3-(((4,6-dimethyl-2-oxo-1,2-dihydropyridin-3-yl)methyl)carbamoyl)-5-(ethyl(tetrahydro-2H-pyran-4-yl)amino)-4-methylphenyl)acrylic acid (**44e**) (0.000107 mol, 0.050 g) in dry DMF, were added TEA (0.000428 mol, 0.06 mL), HATU (0.000128 mol, 0.0488 g), and *o*-phenylenediamine (0.000128 mol, 0.0138 g) under nitrogen flow. The reaction was stirred at room temperature for 2 hours. After this time, the reaction was quenched with NaCl-saturated solution, which led to the formation of a precipitate. It was filtered off and dried, obtaining 43 mg of **18e** as a yellow solid.

M.p. 153-156 °C; recrystallization solvent: toluene/acetonitrile; yield: 72.2%; ^{1}H-NMR (DMSO, 400 MHz, δ, ppm): 1.21 (3H, t, C*H*$_3$-CH$_2$-N-R,R', J= 8 Hz), 1.84 (2H, m, THP protons), 2.09 (2H, m, THP protons), 2.10 (3H, s, -CH$_3$ pyridinone), 2.33 (3H, s, -CH$_3$ pyridinone), 2.46 (3H, s, -CH$_3$ phenyl), 3.46 (2H, q, CH$_3$-CH$_2$- N-R,R'), 3.52 (3H, m, THP protons), 3.69 (2H, m, THP protons), 4.21 (2H, s, Ar-NH$_2$), 4.28 (2H, d, NH-C*H*$_2$-pyridinone, J= 8 Hz), 6.03 (1H, s ,-CH pyridinone), 6.72 (1H, d, CO-C*H*=CH, J= 12.8 Hz), 6.83 (1H, m, aromatic proton), 7.00 (1H, m, aromatic proton), 7.12 (1H, d,

aromatic proton, J= 1.8 Hz), 7.24 (1H, m, aromatic proton), 7.52 (1H, m, aromatic proton), 7.59 (1H, d, CO-CH=C*H*, J= 8 Hz), 7.79 (1H, d, aromatic proton, J= 1.8 Hz), 8.17 (1H, t, CO-N*H*-CH_2, J= 4 Hz), 9.09 (1H, s, Ar-NH-CO), 11.48 (1H, s, NH pyridinone).

18a, $N^{4'}$-(2-aminophenyl)-N^3-((4,6-dimethyl-2-oxo-1,2-dihydropyridin-3-yl)methyl)-5-(ethyl(tetrahydro-2H-pyran-4-yl)amino)-4-methyl-[1,1'-biphenyl]-3,4'-dicarboxamide:

M.p. 167-170 °C; recrystallization solvent: toluene/acetonitrile; yield: 56.8%; ^{1}H-NMR (DMSO, 400 MHz, δ, ppm): 0.84 (3H, t, -CH_2-C*H*$_3$), 1.56 (2H, m, THP protons), 1.68 (2H, m, THP protons), 2.12 (3H, s, -CH_3), 2.23 (3H, s, -CH_3), 2.27 (3H, s, -CH_3), 3.08 (1H, m, THP protons), 3.13 (2H, m, THP protons), 3.27 (2H, m, -C*H*$_2$-CH_3), 3.86 (2H, m, THP protons), 4.31 (1H, s, -C*H*$_2$-NH-), 4.32 (1H, s, -C*H*$_2$-NH-), 4,92 (2H, s, -NH_2 *o*-phenylendiamine), 5.88 (1H, s, aromatic proton), 7.01 (1H, s, aromatic proton), 7.15 (1H, s, aromatic proton), 7.18 (1H, s, aromatic proton), 7.20 (1H, s, aromatic proton), 7.33 (1H, s, aromatic proton), 7.35 (1H, s, aromatic proton), 7.36 (1H, m, aromatic proton), 7.50 (1H, s, aromatic proton), 7.78 (1H, m, aromatic proton), 7.80 (1H, m, aromatic proton), 8,06 (1H, t, R-CH_2-N*H*-CO), 9.71 (1H, m, CO-NH-Ar), 11.47 (1H, s, -NH- pyridinone).

18b, N3'-(2-aminophenyl)-N3-((4,6-dimethyl-2-oxo-1,2-dihydropyridin-3-yl)methyl)-5-(ethyl(tetrahydro-2H-pyran-4-yl)amino)-4-methyl-[1,1'-biphenyl]-3,3'-dicarboxamide:

M.p. 158-162 °C; recrystallization solvent: toluene/acetonitrile; yield: 35.4%; ^{1}H-NMR (DMSO, 400 MHz, δ, ppm): 1.21 (3H, t, C*H*$_3$-CH_2-N-R,R', J= 8 Hz), 1.84 (2H, m, THP protons), 2.09 (2H, m, THP protons), 2.10 (3H, s, -CH_3 pyridinone), 2.23 (3H, d, -CH_3 pyridinone, J= 8 Hz), 2.36 (3H, s, -CH_3 phenyl), 3.46 (2H, q, CH_3-CH_2- N-R,R'), 3.52 (3H, m, THP protons), 3.69 (2H, m, THP protons), 4.03 (2H, s, Ar-NH_2), 4.28 (2H, d, NH-C*H*$_2$-pyridinone, J= 6 Hz), 6.03 (1H, s, -CH pyridinone), 6.84 (1H, m, aromatic proton), 6.98 (1H, m, aromatic proton), 7.05 (1H, d, aromatic proton, J= 2 Hz), 7.24 (1H, m, aromatic proton), 7.57 (1H, m, aromatic proton), 7.65 (1H, t, aromatic proton, J= 8 Hz), 7.79 (1H, m, aromatic proton), 7.87 (1H, m, aromatic proton), 7.95 (1H, d, aromatic proton, J= 2 Hz), 8.10 (1H, t, aromatico proton, J= 4

Hz), 8.21 (1H, t, CO-N*H*-CH_2, J= 4 Hz), 9.70 (1H, d, Ar-NH-CO, J= 4 Hz), 11.47 (1H, s, NH pyridinone).

18c, N-(2-aminophenyl)-5-(3-(((4,6-dimethyl-2-oxo-1,2-dihydropyridin-3-yl)methyl)carbamoyl)-5-(ethyl(tetrahydro-2H-pyran-4-yl)amino)-4-methylphenyl)thiophene-2-carboxamide:

M.p. 155-158 °C; recrystallization solvent: toluene/acetonitrile; yield: 37%; ^{1}H-NMR (DMSO, 400 MHz, δ, ppm): 1.21 (3H, t, C*H*$_3$-CH_2-N-R,R', J= 4 Hz), 1.84 (2H, m, THP protons), 2.09 (2H, m, THP protons), 2.10 (3H, d, -CH_3 pyridinone, J= 8 Hz), 2.33 (3H, d, -CH_3 pyridinone, J= 8 Hz), 2.46 (3H, s, -CH_3 phenyl), 3.46 (2H, q, CH_3-CH_2-N-R,R'), 3.52 (3H, m, THP protons), 3.69 (2H, m, THP protons), 4.03 (2H, s, Ar-NH_2), 4.28 (2H, d, NH-C*H*$_2$-pyridinone, J= 6 Hz), 6.03 (1H, s, -CH pyridinone), 6.84 (1H, m, aromatic proton), 6.96 (1H, d, aromatic proton, J= 1.6 Hz), 6.98 (1H, m, aromatic proton), 7.24 (1H, m, aromatic proton), 7.30 (1H, d, aromatic proton, J= 5.2 Hz), 7.57 (1H, m, aromatic proton), 7.67 (1H, d, aromatic proton, J= 4 Hz), 7.83 (1H, d, aromatic proton, J= 4Hz), 8.30 (1H, t, CO-N*H*-CH_2, J= 4 Hz), 9.72 (1H, s, Ar-NH-CO), 11.49 (1H, s, NH pyridinone).

18d, N-(2-aminophenyl)-5-(3-(((4,6-dimethyl-2-oxo-1,2-dihydropyridin-3-yl)methyl)carbamoyl)-5-(ethyl(tetrahydro-2H-pyran-4-yl)amino)-4-methylphenyl)-1-methyl-1H-pyrrole-2-carboxamide:

M.p. 136-139 °C; recrystallization solvent: toluene; yield: 30.0%; ^{1}H-NMR (DMSO, 400 MHz, δ, ppm): 1.21 (3H, t, C*H*$_3$-CH_2-N-R,R', J= 4 Hz), 1.84 (2H, m, THP protons), 2.09 (2H, m, THP protons), 2.10 (3H, d, -CH_3 pyridinone, J= 8 Hz), 2.33 (3H, d, -CH_3 pyridinone, J= 8 Hz), 2.46 (3H, s, -CH_3 phenyl), 3.46 (2H, q, CH_3-CH_2-N-R,R'), 3.52 (3H, m, THP protons), 3.69 (2H, m, THP protons), 3.76 (3H, s, -CH_3 pyrrole), 4.03 (2H, s, Ar-NH_2), 4.28 (2H, d, NH-C*H*$_2$-pyridinone, J= 6 Hz), 6.03 (1H, s, -CH pyridinone), 6.10 (1H, d, aromatic proton, J= 4 Hz), 6.83 (1H, m, aromatic proton), 6.84 (1H, m, aromatic proton), 6.98 (1H, m, aromatic proton), 7.13 (1H, d, aromatic proton, J= 2 Hz), 7.24 (1H, m, aromatic proton), 7.55 (1H, m, aromatic proton), 7.57 (1H, d, aromatic proton, J= 4 Hz), 8.19 (1H, t, CO-N*H*-CH_2, J= 4 Hz), 9.29 (1H, s, Ar-NH-CO, J= 4 Hz), 11.47 (1H, s, NH pyridinone).

General procedure for the synthesis of compounds 49i and 49h

Example: Synthesis of *tert*-butyl (2-(3'-(((4,6-dimethyl-2-oxo-1,2-dihydropyridin-3-yl)methyl)carbamoyl)-5'-(ethyl(tetrahydro-2H-pyran-4-yl)amino)-4'-methyl-[1,1'-biphenyl]-4-carboxamido)-4-(thiophen-2-yl)phenyl)carbamate (49h)

To a solution of 3'-(((4,6-dimethyl-2-oxo-1,2-dihydropyridin-3-yl)methyl)carbamoyl)-5'-(ethyl(tetrahydro-2H-pyran-4-yl)amino)-4'-methyl-[1,1'-biphenyl]-4-carboxylic acid (**44a**) (0.0001352 mol, 0.070 g) in dry DMF were added TEA (0.0005409 mol, 0.0754 mL), HATU (0.000162 mol, 0.0617 g), 4-dimethylaminopyridine (DMAP) (0.00000676 mol, 0.000083 g), and, finally, *tert*-butyl (2-amino-4-(thiophen-2-yl)phenyl)carbamate (0.000162 mol, 0.0471g). The reaction was stirred at 60 °C for 4 hours and at room temperature for other 8 hours, under an inert atmosphere by nitrogen. Afterward, the reaction was quenched with NaCl saturated solution and $NaHCO_3$ saturated solution at 0°C to promote the precipitation. The solid was filtered off, dried, and purified by column chromatography (SiO_2, eluting with Chloroform/Methanol 80:1). 45 mg of the pure compound **49h** was obtained as a white solid.

M.p. 196-200 °C; yield: 42.0%; ^{1}H-NMR (DMSO, 400 MHz, δ, ppm): 0.86 (3H, t, C*H*$_3$-CH$_2$-N-R,R', J= 7.2 Hz), 1.24 (1H, s, THP proton), 1.43 (9H, s, -Boc), 1.55 (2H, m, THP protons), 1.69 (2H, d, THP protons, J= 11 Hz), 2.12 (3H, s, -CH$_3$ phenyl), 2.23 (3H, s, -CH$_3$ pyridinone), 2.28 (3H, s, -CH$_3$ pyridinone), 3.06 (1H, t, THP protons, J= 10.6 Hz), 3.13 (2H, q, CH$_3$-C*H*$_2$-N-R,R'), 3.26 (1H, m, THP protons), 3.85 (2H, d, THP protons, J= 10.4 Hz), 4.31 (2H, d, -CO-NH-CH$_2$-pyridinone, J= 4.8 Hz), 5.88 (1H, s, -CH pyridinone), 6.84 (1H, d, aromatic proton, J= 8 Hz), 7.06 (1H, q, aromatic proton), 7.3 (1H, d, aromatic proton, J= 3.2 Hz), 7.33 (3H, m, aromatic proton), 7.51 (2H, d, aromatic proton), 7.81 (2H, d, aromatic protons, J= 8 Hz), 8.09 (2H, d, aromatic proton, J= 8 Hz), 8.75 (1H, t, Ar-CO-NH-CH$_2$- pyridinone, J= 4.8 Hz), 9.99 (1H, s, -NH pyridinone), 11.48 (1H, s, -CO-NH-Ar).

General procedure for the synthesis of final compounds 18h and 18i

Example: Synthesis of $N^{4'}$-(2-amino-4-fluorophenyl)-N^{3}-((4,6-dimethyl-2-oxo-1,2-dihydropyridin-3-yl)methyl)-5-(ethyl(tetrahydro-2H-pyran-4-yl)amino)-4-methyl-[1,1'-biphenyl]-3,4'-dicarboxamide (18h)

To a solution of *tert*-butyl (2-(3'-(((4,6-dimethyl-2-oxo-1,2-dihydropyridin-3-yl)methyl)carbamoyl)-5'-(ethyl(tetrahydro-2H-pyran-4-yl)amino)-4'-methyl-[1,1'-biphenyl]-4-carboxamido)-5-fluorophenyl)carbamate (**49h**) (0.00004133 mol, 0.030 g) in dry THF was added, at 0 °C, 4N HCl in 1,4-dioxane (0.0020665 mol, 0.5166 mL). The reaction was stirred at room temperature for 24 hours. Afterward, the reaction was quenched with $NaHCO_3$ saturated solution, reaching pH = 9, and extracted with AcOEt (4x15 mL). The organic extracts were collected, washed with brine, dried with sodium sulfate, and concentrated under reduced pressure. The obtained crude was purified by column chromatography (SiO_2, eluting with Chloroform/Methanol 22:1) to obtain 13.3 mg of the pure compound **18h** as a white solid.

M.p. 192-196 °C; recrystallization solvent: acetonitrile; yield: 51.4%; ^{1}H-NMR (DMSO, 400 MHz, δ, ppm): 0.86 (3H, t, C*H*$_3$-CH$_2$-N-R,R', J= 7.2 Hz), 1.24 (1H, s, THP protons), 1.55 (2H, m, THP protons), 1.69 (2H, d, THP protons, J= 11 Hz), 2.12 (3H, s, -CH$_3$ phenyl), 2.23 (3H, d, -CH$_3$ pyridinone, J= 8 Hz), 2.28 (3H, d, -CH$_3$ pyridinone, J= 8 Hz), 3.06 (1H, t, THP protons, J= 10.6 Hz), 3.13 (2H, q, CH$_3$-C*H*$_2$-N-R,R'), 3.26 (1H, m, THP protons), 3.85 (2H, d, THP protons, J= 10.4 Hz), 4.31 (2H, d, -CO-NH-C*H*$_2$-pyridinone, J= 4.8 Hz), 5.18 (1H, s, -NH$_2$), 5.88 (1H, s, -CH pyridinone), 6.38 (1H, m, aromatic proton), 6.56 (1H, m, aromatic proton), 7.13 (1H, m, aromatic proton), 7.14 (1H, m, aromatic proton), 7.33 (1H, d, aromatic proton, J= 1.2 Hz), 7.50 (1H, s, aromatic proton), 7.787 (2H, d, aromatic protons, J= 8 Hz), 8.06 (2H, d, aromatic protons, J= 8 178 Hz), 8.25 (1H, t, Ar-CO-N*H*-CH$_2$, J= 4.8 Hz) 9.65 (1H, s, -NH pyridinone), 11.47 (1H, s, CO-NH-Ar).

18i, $N^{4'}$-(2-amino-5-(thiophen-2-yl)phenyl)-N^{3}-((4,6-dimethyl-2-oxo-1,2-dihydropyridin-3-yl)methyl)-5-(ethyl(tetrahydro-2H-pyran-4-yl)amino)-4-methyl-[1,1′-biphenyl]-3,4′-dicarboxamide:

M.p. 190-193 °C; recrystallization solvent: acetonitrile; yield: 40.0%; ^{1}H-NMR (DMSO, 400 MHz, δ, ppm): 0.86 (3H, t, C*H*$_3$-CH$_2$-N-R,R′, J= 7.2 Hz), 1.24 (1H, s, THP protons), 1.55 (2H, m, THP protons), 1.69 (2H, d, THP protons, J= 11 Hz), 2.12 (3H, s, -CH$_3$ phenyl), 2.23 (3H, d, -CH$_3$ pyridinone, J= 8 Hz), 2.28 (3H, d, -CH$_3$ pyridinone, J= 8 Hz), 3.06 (1H, t, THP protons, J= 10.6 Hz), 3.13 (2H, q, CH$_3$-C*H*$_2$-N-R,R′), 3.26 (1H, m, THP protons), 3.85 (2H, d, THP protons, J= 10.4 Hz), 4.31 (2H, d, -CO-NH-C*H*$_2$-pyridinone, J= 4.8 Hz), 5.18 (1H, s, -NH$_2$), 5.88 (1H, s, -CH pyridinone), 6.84 (1H, d, aromatic proton, J= 8 Hz), 7.06 (1H, q, aromatic proton), 7.27 (1H, d, aromatic proton, J= 3.2 Hz), 7.335 (3H, m, aromatic protons), 7.51 (2H, d, aromatic protons), 7.81 (2H, d, aromatic protons, J= 8 Hz), 8.09 (2H, d, aromatic protons, J= 8 Hz), 8.25 (1H, t, Ar-CO-N*H*-CH$_2$- pyridinone, J= 4.8 Hz), 9.80 (1H, s, -NH pyridinone), 11.48 (1H, s, -CO-NH-Ar).

Table 6.2. Elemental analysis of final compounds 18a-e, 18h-i, and 19a-g.

CPD	MW	Elemental Analysis									
		Calculated, %					Found, %				
		C	N	O	H	Other	C	N	O	H	Other
18a	607.75	71.15	11.52	10.53	6.80		71.25	11.48	10.52	6.81	
19a	532.64	67.65	10.52	15.02	6.81		67.73	10.48	15.01	6.83	
18b	607.75	71.15	11.52	10.53	6.80		71.24	11.45	10.51	6.81	
19b	532.64	67.65	10.52	15.02	6.81		67.73	10.47	15.01	6.82	
18c	613.78	66.53	11.41	10.43	6.40	5.22 (S)	66.60	11.35	10.42	6.41	5.23 (S)
19c	538.66	62.43	10.40	14.85	6.36	5.95 (S)	62.51	10.36	14.84	6.37	5.96 (S)
18d	610.76	68.83	13.76	10.48	6.93		68.92	13.71	10.46	6.95	
19d	535.64	65.03	13.07	14.93	6.96		65.10	13.03	14.92	6.97	
18e	557.69	68.92	12.56	11.48	7.05		69.01	12.50	11.46	7.06	
19e	482.58	64.71	11.61	16.58	7.10		64.78	11.57	16.57	7.12	
19f	569.70	63.25	12.29	16.85	7.61		63.33	12.25	16.84	7.63	
19g	583.73	63.79	12.00	16.44	7.77		63.88	11.96	16.42	7.79	
18h	625.74	69.10	11.19	10.23	6.44	3.04 (F)	69.17	11.15	10.21	6.46	3.05 (F)
18i	689.87	69.64	10.15	9.28	6.28	4.65 (S)	69.71	10.10	9.27	6.29	4.67S)

6.4.2. Materials and Methods

6.4.2.1. EZH2 and HDAC isoforms biochemical inhibition assay

(Reaction Biology Corporation, USA)

The EZH2 substrate (0.05 mg/mL core histone, or 5 μM H3/H4 octamer, or 5 μM H3/H4 tetramer, or 5 μM histone H3) was added to the freshly prepared reaction buffer (50 mM Tris-HCl (pH 8.0), 50 mM NaCl, 1 mM EDTA, 1mM DTT, 1 mM PMSF, 1 % DMSO). The PRC2 complex [complex of *human* EZH2, *human* EED, *human* SUZ12, *human* AEBP2, and *human* RbAp48] was delivered into the substrate solution and the mixture was mixed gently. Afterward, the tested compounds dissolved in DMSO were delivered into the enzyme/substrate reaction mixture by using Acoustic Technology (Echo 550, LabCyte Inc. Sunnyvale, CA) in the nanoliter range, and 3H-SAM was added into the reaction mixture to initiate the reaction. Compounds were tested in ten-dose IC_{50} mode with threefold serial dilution starting from 100 μM solution. The reaction mixture was incubated for 1 h at 30°C and then it was delivered to filter-paper for detection. Individual IC_{50} values for each HDAC isozyme were measured with the homogeneous fluorescence release HDAC assay. Purified recombinant enzymes were incubated with serially diluted inhibitors at the indicated concentration. The deacetylase activities of HDACs 1, -2, -3, -6, and -8 were determined by assaying enzyme activity using AMC-K(Ac)GL (classes I, IIb HDACs) or AMC-K(TFA)GL (class IIa HDACs) substrate as previously described.[689] [383] Deacetylated AMC-KGL was sensitive toward lysine peptidase, and free fluorogenic 4-methylcoumarin-7-amide was generated, which can be excited at 355 nm and observed at 460 nm (Reaction Biology Corporation, MD, USA). The data were analyzed using Excel and GraphPad Prism software for IC_{50} curve fits.

6.4.2.2. Cell culture

(Group of Prof. Francesco Bertoni, Institute of Oncology Research, Bellinzona, Switzerland)

Lymphoma cell lines (DOHH2, Toledo, SU-DHL-4, WSU-DLCL2, Pfeiffer, and KARPAS422) were cultured in RPMI 1640 medium (Gibco Thermo Fisher Scientific) supplemented with 10% or 20% fetal bovine serum (Capricorn Scientific), and penicillin–streptomycin (5000 units/mL penicillin, 5000 g/mL streptomycin, Gibco Thermo Fisher Scientific). Cells were maintained at 37 °C in a humidified incubator with 5% CO_2. Human cell line identities were confirmed by short tandem repeat

DNA fingerprinting. Cells were periodically tested for mycoplasma negativity using the MycoAlert Mycoplasma Detection Kit (Lonza, Visp, Switzerland).

6.4.2.3. MTT proliferation assay

(Group of Prof. Francesco Bertoni, Institute of Oncology Research, Bellinzona, Switzerland)

Cells were manually seeded in 96-well plates at the concentration of 50.000 cells/mL (10.000 cells, 100 μL per well) in RPMI-1640 without phenol red (Gibco Thermo Fisher Scientific) supplemented with 10% or 20% fetal bovine serum (Capricorn Scientific) and 1% penicillin-streptomycin (Gibco Thermo Fisher Scientific). Compounds, at 2x the final concentration, were added at increasing concentrations to cells (100 μL per well) Each compound was serially diluted 1:3, in RPMI-1640 without phenol red, starting from a maximum concentration of 20 μM down to the lowest concentration of 27.43 nM. For untreated cells, 100 μL of medium containing DMSO, at a concentration equivalent to 20 μM compound, was added. After 72 hours or 7 days of treatment, viable cells were determined by adding 20 μL of MTT reagent [3-(4,5-dimethylthiazolyl-2)-2, 5-diphenyltetrazoliumbromide] per well, and the reaction stopped after 4 hours with 50 μL SDS lysis buffer. The following day absorbance readings were obtained at 560 nm using a Cytation 3 microplate reader (BioTek). Sensitivity to inhibitor treatments was evaluated by the IC_{50} (4-parameter calculation upon log-scaled doses, R package calculation). [690]

6.4.2.4. Antibodies and Western Blot

(Group of Prof. Francesco Bertoni, Institute of Oncology Research, Bellinzona, Switzerland)

The following antibodies were used in this study: Acetyl-Histone H3 (Lys27) (Cell Signaling Technology, 4353), Tri-Methyl-Histone H3 (Lys27) (C36B11) (Cell Signaling Technology, 9733), EZH2 (Cell Signaling Technology, 4905), Histone H3 (Cell Signaling Technology, 9715), GAPDH (14C10) (Cell Signaling Technology, 2118). The secondary antibodies used were: ECL α-mouse IgG horseradish peroxidase-linked species-specific whole antibody and ECL α-Rabbit IgG horseradish peroxidase-linked species-specific whole antibody (GE Healthcare).

6.4.2.5. Proteins Extraction and Immunoblotting

(Group of Prof. Francesco Bertoni, Institute of Oncology Research, Bellinzona, Switzerland)

Cells were harvested and lysed by boiling samples in 2x Laemmli sample buffer (BioRad) supplemented with β-mercaptoethanol (Merck) for 10′. Protein lysates were resolved according to molecular weight by electrophoresis using Mini-PROTEAN TGX Precast gels 4–20% gradient (BioRad). After electrophoresis proteins were blotted onto 0.45 μm nitrocellulose membrane (Bio-Rad; 162-0115) by electric transfer and the membranes were blocked in TBST (20 mM Tris-HCl [pH 7.5], 150 mM NaCl, 0.1% Tween 20) with 5% nonfat dry milk (BioRad) for 1 h at room temperature (RT). After blocking with 5% milk, membranes were incubated with the appropriate primary antibody overnight. The next day, after three washes with 0.1% Tween 20 (Merck; P9416) in PBS (PBST) for 30 min at RT, membranes were incubated with the appropriate secondary antibody for 1 h at RT. After three more washes in PBST, the detection of the relevant protein was assessed by enhanced chemiluminescence (Lite Ablot TURBO, Euro-Clone; EMP012001). Densitometric analysis of the bands was performed using digital imaging with Fusion Solo (Vilber Lourmat).

6.4.2.6. Cell cycle analysis

(Group of Prof. Francesco Bertoni, Institute of Oncology Research, Bellinzona, Switzerland)

Cells treated with dual compounds or DMSO alone were harvested at 24 and 72 hours, washed once in cold 1x PBS, fixed in cold 70% ethanol and stored at -20 °C for at least one day. Fixed cells were stained with 7-Aminoactinomycin D (7-AAD) in PBS and analyzed for DNA content using the FACS Fortessa flow cytometer (BD Biosciences). The analysis of cell cycle profiles was performed using FlowJo software (TreeStar).

6.4.2.7. RNA extraction and RNA-sequencing

(Group of Prof. Francesco Bertoni, Institute of Oncology Research, Bellinzona, Switzerland)

Total RNA was extracted using TRI Reagent (Sigma-Aldrich) and contaminating traces of DNA removed with DNase (Qiagen). RNA concentration and purity were determined spectrophotometrically at 260 nm and 280 nm (A260/A280 ratio) using a DeNovix spectrophotometer (DeNovix Inc.). PolyA RNA sequencing was performed using a a NextSeq 500 System (Illumina, San Diego, CA), at the Genomic facility of IOR. Functional annotation was performed using gene set enrichment analysis on fold change preranked lists. We used the Hallmark gene set database from the MSigDB collection (Proc Natl Acad Sci USA. 2005;102(43):15545-15550) and a custom gene set database comprising transcripts relevant for lymphomagenesis (https://lymphochip.nih.gov/signaturedb/), applying as threshold $P < 0.05$ and false discovery rate (FDR) < 0.05.

Acknowledgments

This work was supported by funds from PRIN2020 (2020CW39SJ) (S. Valente), Ateneo Sapienza Project 2020 (RG120172B8E53D03) (S. Valente), FISR2019_00374 MeDyCa (A. Mai), and AIRC2021 (IG26172) (S.Valente).

REFERENCES

1. Bedard, K.; Krause, K. H., The NOX family of ROS-generating NADPH oxidases: physiology and pathophysiology. *Physiol Rev* **2007,** *87* (1), 245-313.
2. Lambeth, J. D.; Neish, A. S., Nox enzymes and new thinking on reactive oxygen: a double-edged sword revisited. *Annu Rev Pathol* **2014,** *9*, 119-45.
3. O'Neill, S.; Brault, J.; Stasia, M. J.; Knaus, U. G., Genetic disorders coupled to ROS deficiency. *Redox Biol* **2015,** *6*, 135-156.
4. Schieber, M.; Chandel, N. S., ROS function in redox signaling and oxidative stress. *Curr Biol* **2014,** *24* (10), R453-62.
5. Balaban, R. S.; Nemoto, S.; Finkel, T., Mitochondria, oxidants, and aging. *Cell* **2005,** *120* (4), 483-95.
6. Schrader, M.; Fahimi, H. D., Mammalian peroxisomes and reactive oxygen species. *Histochem Cell Biol* **2004,** *122* (4), 383-93.
7. Thannickal, V. J.; Fanburg, B. L., Reactive oxygen species in cell signaling. *Am J Physiol Lung Cell Mol Physiol* **2000,** *279* (6), L1005-28.
8. Bedard, K.; Lardy, B.; Krause, K. H., NOX family NADPH oxidases: not just in mammals. *Biochimie* **2007,** *89* (9), 1107-12.
9. Berendes, H.; Bridges, R. A.; Good, R. A., A fatal granulomatosus of childhood: the clinical study of a new syndrome. *Minn Med* **1957,** *40* (5), 309-12.
10. Quie, P. G.; White, J. G.; Holmes, B.; Good, R. A., In vitro bactericidal capacity of human polymorphonuclear leukocytes: diminished activity in chronic granulomatous disease of childhood. *J Clin Invest* **1967,** *46* (4), 668-79.
11. Baehner, R. L.; Nathan, D. G., Leukocyte oxidase: defective activity in chronic granulomatous disease. *Science* **1967,** *155* (3764), 835-6.
12. Klebanoff, S. J., Antimicrobial mechanisms in neutrophilic polymorphonuclear leukocytes. *Semin Hematol* **1975,** *12* (2), 117-42.
13. Segal, A. W.; Jones, O. T., Novel cytochrome b system in phagocytic vacuoles of human granulocytes. *Nature* **1978,** *276* (5687), 515-7.
14. Cross, A. R.; Parkinson, J. F.; Jones, O. T., The superoxide-generating oxidase of leucocytes. NADPH-dependent reduction of flavin and cytochrome b in solubilized preparations. *Biochem J* **1984,** *223* (2), 337-44.
15. Suh, Y. A.; Arnold, R. S.; Lassegue, B.; Shi, J.; Xu, X.; Sorescu, D.; Chung, A. B.; Griendling, K. K.; Lambeth, J. D., Cell transformation by the superoxide-generating oxidase Mox1. *Nature* **1999,** *401* (6748), 79-82.
16. Banfi, B.; Maturana, A.; Jaconi, S.; Arnaudeau, S.; Laforge, T.; Sinha, B.; Ligeti, E.; Demaurex, N.; Krause, K. H., A mammalian H+ channel generated through alternative splicing of the NADPH oxidase homolog NOH-1. *Science* **2000,** *287* (5450), 138-42.
17. Cheng, G.; Cao, Z.; Xu, X.; van Meir, E. G.; Lambeth, J. D., Homologs of gp91phox: cloning and tissue expression of Nox3, Nox4, and Nox5. *Gene* **2001,** *269* (1-2), 131-40.

18. Kikuchi, H.; Hikage, M.; Miyashita, H.; Fukumoto, M., NADPH oxidase subunit, gp91(phox) homologue, preferentially expressed in human colon epithelial cells. *Gene* **2000,** *254* (1-2), 237-43.
19. Geiszt, M.; Kopp, J. B.; Varnai, P.; Leto, T. L., Identification of renox, an NAD(P)H oxidase in kidney. *Proc Natl Acad Sci U S A* **2000,** *97* (14), 8010-4.
20. Banfi, B.; Molnar, G.; Maturana, A.; Steger, K.; Hegedus, B.; Demaurex, N.; Krause, K. H., A Ca(2+)-activated NADPH oxidase in testis, spleen, and lymph nodes. *J Biol Chem* **2001,** *276* (40), 37594-601.
21. De Deken, X.; Wang, D.; Many, M. C.; Costagliola, S.; Libert, F.; Vassart, G.; Dumont, J. E.; Miot, F., Cloning of two human thyroid cDNAs encoding new members of the NADPH oxidase family. *J Biol Chem* **2000,** *275* (30), 23227-33.
22. Dupuy, C.; Ohayon, R.; Valent, A.; Noel-Hudson, M. S.; Deme, D.; Virion, A., Purification of a novel flavoprotein involved in the thyroid NADPH oxidase. Cloning of the porcine and human cdnas. *J Biol Chem* **1999,** *274* (52), 37265-9.
23. Moloney, J. N.; Cotter, T. G., ROS signalling in the biology of cancer. *Semin Cell Dev Biol* **2018,** *80*, 50-64.
24. Magnani, F.; Mattevi, A., Structure and mechanisms of ROS generation by NADPH oxidases. *Curr Opin Struct Biol* **2019,** *59*, 91-97.
25. Cipriano, A.; Viviano, M.; Feoli, A.; Milite, C.; Sarno, G.; Castellano, S.; Sbardella, G., NADPH Oxidases: From Molecular Mechanisms to Current Inhibitors. *J Med Chem* **2023,** *66* (17), 11632-11655.
26. Sumimoto, H., Structure, regulation and evolution of Nox-family NADPH oxidases that produce reactive oxygen species. *FEBS J* **2008,** *275* (13), 3249-77.
27. Magnani, F.; Nenci, S.; Millana Fananas, E.; Ceccon, M.; Romero, E.; Fraaije, M. W.; Mattevi, A., Crystal structures and atomic model of NADPH oxidase. *Proc Natl Acad Sci U S A* **2017,** *114* (26), 6764-6769.
28. Ogboo, B. C.; Grabovyy, U. V.; Maini, A.; Scouten, S.; van der Vliet, A.; Mattevi, A.; Heppner, D. E., Architecture of the NADPH oxidase family of enzymes. *Redox Biol* **2022,** *52*, 102298.
29. Vermot, A.; Petit-Hartlein, I.; Smith, S. M. E.; Fieschi, F., NADPH Oxidases (NOX): An Overview from Discovery, Molecular Mechanisms to Physiology and Pathology. *Antioxidants (Basel)* **2021,** *10* (6).
30. Lapouge, K.; Smith, S. J.; Groemping, Y.; Rittinger, K., Architecture of the p40-p47-p67phox complex in the resting state of the NADPH oxidase. A central role for p67phox. *J Biol Chem* **2002,** *277* (12), 10121-8.
31. Noreng, S.; Ota, N.; Sun, Y.; Ho, H.; Johnson, M.; Arthur, C. P.; Schneider, K.; Lehoux, I.; Davies, C. W.; Mortara, K.; Wong, K.; Seshasayee, D.; Masureel, M.; Payandeh, J.; Yi, T.; Koerber, J. T., Structure of the core human NADPH oxidase NOX2. *Nat Commun* **2022,** *13* (1), 6079.
32. Sun, J., Structures of mouse DUOX1-DUOXA1 provide mechanistic insights into enzyme activation and regulation. *Nat Struct Mol Biol* **2020,** *27* (11), 1086-1093.

33. Wu, J. X.; Liu, R.; Song, K.; Chen, L., Structures of human dual oxidase 1 complex in low-calcium and high-calcium states. *Nat Commun* **2021,** *12* (1), 155.
34. Al Ghouleh, I.; Khoo, N. K.; Knaus, U. G.; Griendling, K. K.; Touyz, R. M.; Thannickal, V. J.; Barchowsky, A.; Nauseef, W. M.; Kelley, E. E.; Bauer, P. M.; Darley-Usmar, V.; Shiva, S.; Cifuentes-Pagano, E.; Freeman, B. A.; Gladwin, M. T.; Pagano, P. J., Oxidases and peroxidases in cardiovascular and lung disease: new concepts in reactive oxygen species signaling. *Free Radic Biol Med* **2011,** *51* (7), 1271-88.
35. Wingler, K.; Wunsch, S.; Kreutz, R.; Rothermund, L.; Paul, M.; Schmidt, H. H., Upregulation of the vascular NAD(P)H-oxidase isoforms Nox1 and Nox4 by the renin-angiotensin system in vitro and in vivo. *Free Radic Biol Med* **2001,** *31* (11), 1456-64.
36. Laurent, E.; McCoy, J. W., 3rd; Macina, R. A.; Liu, W.; Cheng, G.; Robine, S.; Papkoff, J.; Lambeth, J. D., Nox1 is over-expressed in human colon cancers and correlates with activating mutations in K-Ras. *Int J Cancer* **2008,** *123* (1), 100-7.
37. Szanto, I.; Rubbia-Brandt, L.; Kiss, P.; Steger, K.; Banfi, B.; Kovari, E.; Herrmann, F.; Hadengue, A.; Krause, K. H., Expression of NOX1, a superoxide-generating NADPH oxidase, in colon cancer and inflammatory bowel disease. *J Pathol* **2005,** *207* (2), 164-76.
38. Woods, C.; Wang, G.; Milner, T. A.; Glass, M. J., Tumor necrosis factor alpha induces NOX2-dependent reactive oxygen species production in hypothalamic paraventricular nucleus neurons following angiotensin II infusion. *Neurochem Int* **2024**, 105825.
39. Cross, A. R.; Segal, A. W., The NADPH oxidase of professional phagocytes--prototype of the NOX electron transport chain systems. *Biochim Biophys Acta* **2004,** *1657* (1), 1-22.
40. Meneses-Valdes, R.; Gallero, S.; Henriquez-Olguin, C.; Jensen, T. E., Exploring NADPH oxidases 2 and 4 in cardiac and skeletal muscle adaptations - A cross-tissue comparison. *Free Radic Biol Med* **2024,** *223*, 296-305.
41. Cooney, S. J.; Bermudez-Sabogal, S. L.; Byrnes, K. R., Cellular and temporal expression of NADPH oxidase (NOX) isotypes after brain injury. *J Neuroinflammation* **2013,** *10*, 155.
42. Guo, S.; Chen, X., The human Nox4: gene, structure, physiological function and pathological significance. *J Drug Target* **2015,** *23* (10), 888-96.
43. Fulton, D. J., Nox5 and the regulation of cellular function. *Antioxid Redox Signal* **2009,** *11* (10), 2443-52.
44. Chen, F.; Wang, Y.; Barman, S.; Fulton, D. J., Enzymatic regulation and functional relevance of NOX5. *Curr Pharm Des* **2015,** *21* (41), 5999-6008.
45. Caillou, B.; Dupuy, C.; Lacroix, L.; Nocera, M.; Talbot, M.; Ohayon, R.; Deme, D.; Bidart, J. M.; Schlumberger, M.; Virion, A., Expression of reduced nicotinamide adenine dinucleotide phosphate oxidase (ThoX, LNOX, Duox) genes and proteins in human thyroid tissues. *J Clin Endocrinol Metab* **2001,** *86* (7), 3351-8.

46. Gabig, T. G.; Babior, B. M., The O2(-) -forming oxidase responsible for the respiratory burst in human neutrophils. Properties of the solubilized enzyme. *J Biol Chem* **1979,** *254* (18), 9070-4.
47. Parkos, C. A.; Allen, R. A.; Cochrane, C. G.; Jesaitis, A. J., Purified cytochrome b from human granulocyte plasma membrane is comprised of two polypeptides with relative molecular weights of 91,000 and 22,000. *J Clin Invest* **1987,** *80* (3), 732-42.
48. Ray, P. D.; Huang, B. W.; Tsuji, Y., Reactive oxygen species (ROS) homeostasis and redox regulation in cellular signaling. *Cell Signal* **2012,** *24* (5), 981-90.
49. Diebold, B. A.; Smith, S. M.; Li, Y.; Lambeth, J. D., NOX2 As a Target for Drug Development: Indications, Possible Complications, and Progress. *Antioxid Redox Signal* **2015,** *23* (5), 375-405.
50. Nathan, C.; Cunningham-Bussel, A., Beyond oxidative stress: an immunologist's guide to reactive oxygen species. *Nat Rev Immunol* **2013,** *13* (5), 349-61.
51. Dang, P. M.; Cross, A. R.; Babior, B. M., Assembly of the neutrophil respiratory burst oxidase: a direct interaction between p67PHOX and cytochrome b558. *Proc Natl Acad Sci U S A* **2001,** *98* (6), 3001-5.
52. Bode, K.; Hauri-Hohl, M.; Jaquet, V.; Weyd, H., Unlocking the power of NOX2: A comprehensive review on its role in immune regulation. *Redox Biol* **2023,** *64*, 102795.
53. Wallach, T. M.; Segal, A. W., Analysis of glycosylation sites on gp91phox, the flavocytochrome of the NADPH oxidase, by site-directed mutagenesis and translation in vitro. *Biochem J* **1997,** *321 (Pt 3)* (Pt 3), 583-5.
54. Ceccon, M.; Millana Fananas, E.; Massari, M.; Mattevi, A.; Magnani, F., Engineering stability in NADPH oxidases: A common strategy for enzyme production. *Mol Membr Biol* **2017,** *34* (3-8), 67-76.
55. Leto, T. L.; Adams, A. G.; de Mendez, I., Assembly of the phagocyte NADPH oxidase: binding of Src homology 3 domains to proline-rich targets. *Proc Natl Acad Sci U S A* **1994,** *91* (22), 10650-4.
56. Nobuhisa, I.; Takeya, R.; Ogura, K.; Ueno, N.; Kohda, D.; Inagaki, F.; Sumimoto, H., Activation of the superoxide-producing phagocyte NADPH oxidase requires co-operation between the tandem SH3 domains of p47phox in recognition of a polyproline type II helix and an adjacent alpha-helix of p22phox. *Biochem J* **2006,** *396* (1), 183-92.
57. Zhu, Y.; Marchal, C. C.; Casbon, A. J.; Stull, N.; von Lohneysen, K.; Knaus, U. G.; Jesaitis, A. J.; McCormick, S.; Nauseef, W. M.; Dinauer, M. C., Deletion mutagenesis of p22phox subunit of flavocytochrome b558: identification of regions critical for gp91phox maturation and NADPH oxidase activity. *J Biol Chem* **2006,** *281* (41), 30336-46.

58. Liu, R.; Song, K.; Wu, J. X.; Geng, X. P.; Zheng, L.; Gao, X.; Peng, H.; Chen, L., Structure of human phagocyte NADPH oxidase in the resting state. *Elife* **2022,** *11*.
59. Lapouge, K.; Smith, S. J.; Walker, P. A.; Gamblin, S. J.; Smerdon, S. J.; Rittinger, K., Structure of the TPR domain of p67phox in complex with Rac.GTP. *Mol Cell* **2000,** *6* (4), 899-907.
60. Kami, K.; Takeya, R.; Sumimoto, H.; Kohda, D., Diverse recognition of non-PxxP peptide ligands by the SH3 domains from p67(phox), Grb2 and Pex13p. *EMBO J* **2002,** *21* (16), 4268-76.
61. Durand, D.; Vives, C.; Cannella, D.; Perez, J.; Pebay-Peyroula, E.; Vachette, P.; Fieschi, F., NADPH oxidase activator p67(phox) behaves in solution as a multidomain protein with semi-flexible linkers. *J Struct Biol* **2010,** *169* (1), 45-53.
62. Honbou, K.; Minakami, R.; Yuzawa, S.; Takeya, R.; Suzuki, N. N.; Kamakura, S.; Sumimoto, H.; Inagaki, F., Full-length p40phox structure suggests a basis for regulation mechanism of its membrane binding. *EMBO J* **2007,** *26* (4), 1176-86.
63. Miyano, K.; Ueno, N.; Takeya, R.; Sumimoto, H., Direct involvement of the small GTPase Rac in activation of the superoxide-producing NADPH oxidase Nox1. *J Biol Chem* **2006,** *281* (31), 21857-21868.
64. Ligeti, E.; Welti, S.; Scheffzek, K., Inhibition and termination of physiological responses by GTPase activating proteins. *Physiol Rev* **2012,** *92* (1), 237-72.
65. Majolee, J.; Podieh, F.; Hordijk, P. L.; Kovacevic, I., The interplay of Rac1 activity, ubiquitination and GDI binding and its consequences for endothelial cell spreading. *PLoS One* **2021,** *16* (7), e0254386.
66. Liu, X.; Shi, Y.; Liu, R.; Song, K.; Chen, L., Structure of human phagocyte NADPH oxidase in the activated state. *Nature* **2024,** *627* (8002), 189-195.
67. Geiszt, M.; Lekstrom, K.; Leto, T. L., Analysis of mRNA transcripts from the NAD(P)H oxidase 1 (Nox1) gene. Evidence against production of the NADPH oxidase homolog-1 short (NOH-1S) transcript variant. *J Biol Chem* **2004,** *279* (49), 51661-8.
68. Harper, R. W.; Xu, C.; Soucek, K.; Setiadi, H.; Eiserich, J. P., A reappraisal of the genomic organization of human Nox1 and its splice variants. *Arch Biochem Biophys* **2005,** *435* (2), 323-30.
69. Salles, N.; Szanto, I.; Herrmann, F.; Armenian, B.; Stumm, M.; Stauffer, E.; Michel, J. P.; Krause, K. H., Expression of mRNA for ROS-generating NADPH oxidases in the aging stomach. *Exp Gerontol* **2005,** *40* (4), 353-7.
70. Cui, X. L.; Brockman, D.; Campos, B.; Myatt, L., Expression of NADPH oxidase isoform 1 (Nox1) in human placenta: involvement in preeclampsia. *Placenta* **2006,** *27* (4-5), 422-31.
71. Perner, A.; Andresen, L.; Pedersen, G.; Rask-Madsen, J., Superoxide production and expression of NAD(P)H oxidases by transformed and primary human colonic epithelial cells. *Gut* **2003,** *52* (2), 231-6.

72. Banfi, B.; Clark, R. A.; Steger, K.; Krause, K. H., Two novel proteins activate superoxide generation by the NADPH oxidase NOX1. *J Biol Chem* **2003,** *278* (6), 3510-3.
73. Takeya, R.; Ueno, N.; Kami, K.; Taura, M.; Kohjima, M.; Izaki, T.; Nunoi, H.; Sumimoto, H., Novel human homologues of p47phox and p67phox participate in activation of superoxide-producing NADPH oxidases. *J Biol Chem* **2003,** *278* (27), 25234-46.
74. Sumimoto, H.; Miyano, K.; Takeya, R., Molecular composition and regulation of the Nox family NAD(P)H oxidases. *Biochem Biophys Res Commun* **2005,** *338* (1), 677-86.
75. Ago, T.; Nunoi, H.; Ito, T.; Sumimoto, H., Mechanism for phosphorylation-induced activation of the phagocyte NADPH oxidase protein p47(phox). Triple replacement of serines 303, 304, and 328 with aspartates disrupts the SH3 domain-mediated intramolecular interaction in p47(phox), thereby activating the oxidase. *J Biol Chem* **1999,** *274* (47), 33644-53.
76. Paffenholz, R.; Bergstrom, R. A.; Pasutto, F.; Wabnitz, P.; Munroe, R. J.; Jagla, W.; Heinzmann, U.; Marquardt, A.; Bareiss, A.; Laufs, J.; Russ, A.; Stumm, G.; Schimenti, J. C.; Bergstrom, D. E., Vestibular defects in head-tilt mice result from mutations in Nox3, encoding an NADPH oxidase. *Genes Dev* **2004,** *18* (5), 486-91.
77. Rybak, L. P.; Mukherjea, D.; Jajoo, S.; Kaur, T.; Ramkumar, V., siRNA-mediated knock-down of NOX3: therapy for hearing loss? *Cell Mol Life Sci* **2012,** *69* (14), 2429-34.
78. Krause, K. H., Tissue distribution and putative physiological function of NOX family NADPH oxidases. *Jpn J Infect Dis* **2004,** *57* (5), S28-9.
79. Ueno, N.; Takeya, R.; Miyano, K.; Kikuchi, H.; Sumimoto, H., The NADPH oxidase Nox3 constitutively produces superoxide in a p22phox-dependent manner: its regulation by oxidase organizers and activators. *J Biol Chem* **2005,** *280* (24), 23328-39.
80. Banfi, B.; Malgrange, B.; Knisz, J.; Steger, K.; Dubois-Dauphin, M.; Krause, K. H., NOX3, a superoxide-generating NADPH oxidase of the inner ear. *J Biol Chem* **2004,** *279* (44), 46065-72.
81. Cheng, G.; Ritsick, D.; Lambeth, J. D., Nox3 regulation by NOXO1, p47phox, and p67phox. *J Biol Chem* **2004,** *279* (33), 34250-5.
82. Yang, S.; Madyastha, P.; Bingel, S.; Ries, W.; Key, L., A new superoxide-generating oxidase in murine osteoclasts. *J Biol Chem* **2001,** *276* (8), 5452-8.
83. Yang, S.; Zhang, Y.; Ries, W.; Key, L., Expression of Nox4 in osteoclasts. *J Cell Biochem* **2004,** *92* (2), 238-48.
84. Ago, T.; Kitazono, T.; Kuroda, J.; Kumai, Y.; Kamouchi, M.; Ooboshi, H.; Wakisaka, M.; Kawahara, T.; Rokutan, K.; Ibayashi, S.; Iida, M., NAD(P)H oxidases in rat basilar arterial endothelial cells. *Stroke* **2005,** *36* (5), 1040-6.

85. Van Buul, J. D.; Fernandez-Borja, M.; Anthony, E. C.; Hordijk, P. L., Expression and localization of NOX2 and NOX4 in primary human endothelial cells. *Antioxid Redox Signal* **2005,** *7* (3-4), 308-17.
86. Ellmark, S. H.; Dusting, G. J.; Fui, M. N.; Guzzo-Pernell, N.; Drummond, G. R., The contribution of Nox4 to NADPH oxidase activity in mouse vascular smooth muscle. *Cardiovasc Res* **2005,** *65* (2), 495-504.
87. Hoidal, J. R.; Brar, S. S.; Sturrock, A. B.; Sanders, K. A.; Dinger, B.; Fidone, S.; Kennedy, T. P., The role of endogenous NADPH oxidases in airway and pulmonary vascular smooth muscle function. *Antioxid Redox Signal* **2003,** *5* (6), 751-8.
88. Piccoli, C.; Ria, R.; Scrima, R.; Cela, O.; D'Aprile, A.; Boffoli, D.; Falzetti, F.; Tabilio, A.; Capitanio, N., Characterization of mitochondrial and extra-mitochondrial oxygen consuming reactions in human hematopoietic stem cells. Novel evidence of the occurrence of NAD(P)H oxidase activity. *J Biol Chem* **2005,** *280* (28), 26467-76.
89. Cucoranu, I.; Clempus, R.; Dikalova, A.; Phelan, P. J.; Ariyan, S.; Dikalov, S.; Sorescu, D., NAD(P)H oxidase 4 mediates transforming growth factor-beta1-induced differentiation of cardiac fibroblasts into myofibroblasts. *Circ Res* **2005,** *97* (9), 900-7.
90. Colston, J. T.; de la Rosa, S. D.; Strader, J. R.; Anderson, M. A.; Freeman, G. L., H2O2 activates Nox4 through PLA2-dependent arachidonic acid production in adult cardiac fibroblasts. *FEBS Lett* **2005,** *579* (11), 2533-40.
91. Chamulitrat, W.; Stremmel, W.; Kawahara, T.; Rokutan, K.; Fujii, H.; Wingler, K.; Schmidt, H. H.; Schmidt, R., A constitutive NADPH oxidase-like system containing gp91phox homologs in human keratinocytes. *J Invest Dermatol* **2004,** *122* (4), 1000-9.
92. Brar, S. S.; Kennedy, T. P.; Sturrock, A. B.; Huecksteadt, T. P.; Quinn, M. T.; Whorton, A. R.; Hoidal, J. R., An NAD(P)H oxidase regulates growth and transcription in melanoma cells. *Am J Physiol Cell Physiol* **2002,** *282* (6), C1212-24.
93. Vallet, P.; Charnay, Y.; Steger, K.; Ogier-Denis, E.; Kovari, E.; Herrmann, F.; Michel, J. P.; Szanto, I., Neuronal expression of the NADPH oxidase NOX4, and its regulation in mouse experimental brain ischemia. *Neuroscience* **2005,** *132* (2), 233-8.
94. Martyn, K. D.; Frederick, L. M.; von Loehneysen, K.; Dinauer, M. C.; Knaus, U. G., Functional analysis of Nox4 reveals unique characteristics compared to other NADPH oxidases. *Cell Signal* **2006,** *18* (1), 69-82.
95. Serrander, L.; Cartier, L.; Bedard, K.; Banfi, B.; Lardy, B.; Plastre, O.; Sienkiewicz, A.; Forro, L.; Schlegel, W.; Krause, K. H., NOX4 activity is determined by mRNA levels and reveals a unique pattern of ROS generation. *Biochem J* **2007,** *406* (1), 105-14.
96. Lee, C. F.; Qiao, M.; Schroder, K.; Zhao, Q.; Asmis, R., Nox4 is a novel inducible source of reactive oxygen species in monocytes and macrophages and

mediates oxidized low density lipoprotein-induced macrophage death. *Circ Res* **2010,** *106* (9), 1489-97.
97. Moe, K. T.; Aulia, S.; Jiang, F.; Chua, Y. L.; Koh, T. H.; Wong, M. C.; Dusting, G. J., Differential upregulation of Nox homologues of NADPH oxidase by tumor necrosis factor-alpha in human aortic smooth muscle and embryonic kidney cells. *J Cell Mol Med* **2006,** *10* (1), 231-9.
98. Banks, T. E.; Rajapaksha, M.; Zhang, L. H.; Bai, F.; Wang, N. P.; Zhao, Z. Q., Suppression of angiotensin II-activated NOX4/NADPH oxidase and mitochondrial dysfunction by preserving glucagon-like peptide-1 attenuates myocardial fibrosis and hypertension. *Eur J Pharmacol* **2022,** *927*, 175048.
99. Nisimoto, Y.; Diebold, B. A.; Cosentino-Gomes, D.; Lambeth, J. D., Nox4: a hydrogen peroxide-generating oxygen sensor. *Biochemistry* **2014,** *53* (31), 5111-20.
100. Brar, S. S.; Corbin, Z.; Kennedy, T. P.; Hemendinger, R.; Thornton, L.; Bommarius, B.; Arnold, R. S.; Whorton, A. R.; Sturrock, A. B.; Huecksteadt, T. P.; Quinn, M. T.; Krenitsky, K.; Ardie, K. G.; Lambeth, J. D.; Hoidal, J. R., NOX5 NAD(P)H oxidase regulates growth and apoptosis in DU 145 prostate cancer cells. *Am J Physiol Cell Physiol* **2003,** *285* (2), C353-69.
101. Banfi, B.; Tirone, F.; Durussel, I.; Knisz, J.; Moskwa, P.; Molnar, G. Z.; Krause, K. H.; Cox, J. A., Mechanism of Ca2+ activation of the NADPH oxidase 5 (NOX5). *J Biol Chem* **2004,** *279* (18), 18583-91.
102. Jagnandan, D.; Church, J. E.; Banfi, B.; Stuehr, D. J.; Marrero, M. B.; Fulton, D. J., Novel mechanism of activation of NADPH oxidase 5. calcium sensitization via phosphorylation. *J Biol Chem* **2007,** *282* (9), 6494-507.
103. Cui, C.; Jiang, M.; Jain, N.; Das, S.; Lo, Y. H.; Kermani, A. A.; Pipatpolkai, T.; Sun, J., Structural basis of human NOX5 activation. *Nat Commun* **2024,** *15* (1), 3994.
104. Millana Fananas, E.; Todesca, S.; Sicorello, A.; Masino, L.; Pompach, P.; Magnani, F.; Pastore, A.; Mattevi, A., On the mechanism of calcium-dependent activation of NADPH oxidase 5 (NOX5). *FEBS J* **2020,** *287* (12), 2486-2503.
105. Chen, F.; Barman, S.; Yu, Y.; Haigh, S.; Wang, Y.; Black, S. M.; Rafikov, R.; Dou, H.; Bagi, Z.; Han, W.; Su, Y.; Fulton, D. J., Caveolin-1 is a negative regulator of NADPH oxidase-derived reactive oxygen species. *Free Radic Biol Med* **2014,** *73*, 201-13.
106. Chen, F.; Haigh, S.; Yu, Y.; Benson, T.; Wang, Y.; Li, X.; Dou, H.; Bagi, Z.; Verin, A. D.; Stepp, D. W.; Csanyi, G.; Chadli, A.; Weintraub, N. L.; Smith, S. M.; Fulton, D. J., Nox5 stability and superoxide production is regulated by C-terminal binding of Hsp90 and CO-chaperones. *Free Radic Biol Med* **2015,** *89*, 793-805.
107. Touyz, R. M.; Anagnostopoulou, A.; Rios, F.; Montezano, A. C.; Camargo, L. L., NOX5: Molecular biology and pathophysiology. *Exp Physiol* **2019,** *104* (5), 605-616.

108. Zhang, X.; Krause, K. H.; Xenarios, I.; Soldati, T.; Boeckmann, B., Evolution of the ferric reductase domain (FRD) superfamily: modularity, functional diversification, and signature motifs. *PLoS One* **2013,** *8* (3), e58126.
109. Tirone, F.; Radu, L.; Craescu, C. T.; Cox, J. A., Identification of the binding site for the regulatory calcium-binding domain in the catalytic domain of NOX5. *Biochemistry* **2010,** *49* (4), 761-71.
110. Wei, C. C.; Motl, N.; Levek, K.; Chen, L. Q.; Yang, Y. P.; Johnson, T.; Hamilton, L.; Stuehr, D. J., Conformational States and kinetics of the calcium binding domain of NADPH oxidase 5. *Open Biochem J* **2010,** *4*, 59-67.
111. Tirone, F.; Cox, J. A., NADPH oxidase 5 (NOX5) interacts with and is regulated by calmodulin. *FEBS Lett* **2007,** *581* (6), 1202-8.
112. Ameziane-El-Hassani, R.; Schlumberger, M.; Dupuy, C., NADPH oxidases: new actors in thyroid cancer? *Nat Rev Endocrinol* **2016,** *12* (8), 485-94.
113. Deme, D.; Virion, A.; Hammou, N. A.; Pommier, J., NADPH-dependent generation of H2O2 in a thyroid particulate fraction requires Ca2+. *FEBS Lett* **1985,** *186* (1), 107-10.
114. De Deken, X.; Wang, D.; Dumont, J. E.; Miot, F., Characterization of ThOX proteins as components of the thyroid H(2)O(2)-generating system. *Exp Cell Res* **2002,** *273* (2), 187-96.
115. Pachucki, J.; Wang, D.; Christophe, D.; Miot, F., Structural and functional characterization of the two human ThOX/Duox genes and their 5'-flanking regions. *Mol Cell Endocrinol* **2004,** *214* (1-2), 53-62.
116. Leseney, A. M.; Deme, D.; Legue, O.; Ohayon, R.; Chanson, P.; Sales, J. P.; Carvalho, D. P.; Dupuy, C.; Virion, A., Biochemical characterization of a Ca2+/NAD(P)H-dependent H2O2 generator in human thyroid tissue. *Biochimie* **1999,** *81* (4), 373-80.
117. De Deken, X.; Corvilain, B.; Dumont, J. E.; Miot, F., Roles of DUOX-mediated hydrogen peroxide in metabolism, host defense, and signaling. *Antioxid Redox Signal* **2014,** *20* (17), 2776-93.
118. Ameziane-El-Hassani, R.; Morand, S.; Boucher, J. L.; Frapart, Y. M.; Apostolou, D.; Agnandji, D.; Gnidehou, S.; Ohayon, R.; Noel-Hudson, M. S.; Francon, J.; Lalaoui, K.; Virion, A.; Dupuy, C., Dual oxidase-2 has an intrinsic Ca2+-dependent H2O2-generating activity. *J Biol Chem* **2005,** *280* (34), 30046-54.
119. Ma, Z. F.; Skeaff, S. A., Thyroglobulin as a biomarker of iodine deficiency: a review. *Thyroid* **2014,** *24* (8), 1195-209.
120. Damante, G.; Tell, G.; Di Lauro, R., A unique combination of transcription factors controls differentiation of thyroid cells. *Prog Nucleic Acid Res Mol Biol* **2001,** *66*, 307-56.
121. Lambeth, J. D.; Kawahara, T.; Diebold, B., Regulation of Nox and Duox enzymatic activity and expression. *Free Radic Biol Med* **2007,** *43* (3), 319-31.
122. Edens, W. A.; Sharling, L.; Cheng, G.; Shapira, R.; Kinkade, J. M.; Lee, T.; Edens, H. A.; Tang, X.; Sullards, C.; Flaherty, D. B.; Benian, G. M.; Lambeth, J. D.,

Tyrosine cross-linking of extracellular matrix is catalyzed by Duox, a multidomain oxidase/peroxidase with homology to the phagocyte oxidase subunit gp91phox. *J Cell Biol* **2001,** *154* (4), 879-91.
123. Geiszt, M.; Witta, J.; Baffi, J.; Lekstrom, K.; Leto, T. L., Dual oxidases represent novel hydrogen peroxide sources supporting mucosal surface host defense. *FASEB J* **2003,** *17* (11), 1502-4.
124. El Hassani, R. A.; Benfares, N.; Caillou, B.; Talbot, M.; Sabourin, J. C.; Belotte, V.; Morand, S.; Gnidehou, S.; Agnandji, D.; Ohayon, R.; Kaniewski, J.; Noel-Hudson, M. S.; Bidart, J. M.; Schlumberger, M.; Virion, A.; Dupuy, C., Dual oxidase2 is expressed all along the digestive tract. *Am J Physiol Gastrointest Liver Physiol* **2005,** *288* (5), G933-42.
125. Wang, D.; De Deken, X.; Milenkovic, M.; Song, Y.; Pirson, I.; Dumont, J. E.; Miot, F., Identification of a novel partner of duox: EFP1, a thioredoxin-related protein. *J Biol Chem* **2005,** *280* (4), 3096-103.
126. Wang, X.; Wang, D.; Ding, N.; Mi, L.; Yu, H.; Wu, M.; Feng, F.; Hu, L.; Zhang, Y.; Zhong, C.; Ye, Y.; Li, J.; Fang, W.; Shi, Y.; Deng, L.; Ying, Z.; Song, Y.; Zhu, J., The Synergistic Anti-Tumor Activity of EZH2 Inhibitor SHR2554 and HDAC Inhibitor Chidamide through ORC1 Reduction of DNA Replication Process in Diffuse Large B Cell Lymphoma. *Cancers (Basel)* **2021,** *13* (17).
127. Liu, X.; Gao, R. W.; Li, M.; Si, C. F.; He, Y. P.; Wang, M.; Yang, Y.; Zheng, Q. Y.; Wang, C. Y., The ROS derived mitochondrial respirstion not from NADPH oxidase plays key role in Celastrol against angiotensin II-mediated HepG2 cell proliferation. *Apoptosis* **2016,** *21* (11), 1315-1326.
128. Griendling, K. K.; Minieri, C. A.; Ollerenshaw, J. D.; Alexander, R. W., Angiotensin II stimulates NADH and NADPH oxidase activity in cultured vascular smooth muscle cells. *Circ Res* **1994,** *74* (6), 1141-8.
129. Higashi, M.; Shimokawa, H.; Hattori, T.; Hiroki, J.; Mukai, Y.; Morikawa, K.; Ichiki, T.; Takahashi, S.; Takeshita, A., Long-term inhibition of Rho-kinase suppresses angiotensin II-induced cardiovascular hypertrophy in rats in vivo: effect on endothelial NAD(P)H oxidase system. *Circ Res* **2003,** *93* (8), 767-75.
130. Santillo, M.; Colantuoni, A.; Mondola, P.; Guida, B.; Damiano, S., NOX signaling in molecular cardiovascular mechanisms involved in the blood pressure homeostasis. *Front Physiol* **2015,** *6*, 194.
131. Siu, K. L.; Li, Q.; Zhang, Y.; Guo, J.; Youn, J. Y.; Du, J.; Cai, H., NOX isoforms in the development of abdominal aortic aneurysm. *Redox Biol* **2017,** *11*, 118-125.
132. Braunersreuther, V.; Montecucco, F.; Asrih, M.; Pelli, G.; Galan, K.; Frias, M.; Burger, F.; Quindere, A. L.; Montessuit, C.; Krause, K. H.; Mach, F.; Jaquet, V., Role of NADPH oxidase isoforms NOX1, NOX2 and NOX4 in myocardial ischemia/reperfusion injury. *J Mol Cell Cardiol* **2013,** *64*, 99-107.
133. Jiang, Z.; Wu, L.; van der Leeden, B.; van Rossum, A. C.; Niessen, H. W. M.; Krijnen, P. A. J., NOX2 and NOX5 are increased in cardiac microvascular endothelium of deceased COVID-19 patients. *Int J Cardiol* **2023,** *370*, 454-462.

134. Violi, F.; Oliva, A.; Cangemi, R.; Ceccarelli, G.; Pignatelli, P.; Carnevale, R.; Cammisotto, V.; Lichtner, M.; Alessandri, F.; De Angelis, M.; Miele, M. C.; D'Ettorre, G.; Ruberto, F.; Venditti, M.; Pugliese, F.; Mastroianni, C. M., Nox2 activation in Covid-19. *Redox Biol* **2020,** *36*, 101655.
135. Liou, G. Y.; Storz, P., Reactive oxygen species in cancer. *Free Radic Res* **2010,** *44* (5), 479-96.
136. Kino, K.; Hirao-Suzuki, M.; Morikawa, M.; Sakaga, A.; Miyazawa, H., Generation, repair and replication of guanine oxidation products. *Genes Environ* **2017,** *39*, 21.
137. van Loon, B.; Markkanen, E.; Hubscher, U., Oxygen as a friend and enemy: How to combat the mutational potential of 8-oxo-guanine. *DNA Repair (Amst)* **2010,** *9* (6), 604-16.
138. Salmeen, A.; Andersen, J. N.; Myers, M. P.; Meng, T. C.; Hinks, J. A.; Tonks, N. K.; Barford, D., Redox regulation of protein tyrosine phosphatase 1B involves a sulphenyl-amide intermediate. *Nature* **2003,** *423* (6941), 769-73.
139. Vaquero, E. C.; Edderkaoui, M.; Pandol, S. J.; Gukovsky, I.; Gukovskaya, A. S., Reactive oxygen species produced by NAD(P)H oxidase inhibit apoptosis in pancreatic cancer cells. *J Biol Chem* **2004,** *279* (33), 34643-54.
140. Levine, A. P.; Segal, A. W., The NADPH Oxidase and Microbial Killing by Neutrophils, With a Particular Emphasis on the Proposed Antimicrobial Role of Myeloperoxidase within the Phagocytic Vacuole. *Microbiol Spectr* **2016,** *4* (4).
141. Leto, T. L.; Geiszt, M., Role of Nox family NADPH oxidases in host defense. *Antioxid Redox Signal* **2006,** *8* (9-10), 1549-61.
142. Schappi, M. G.; Jaquet, V.; Belli, D. C.; Krause, K. H., Hyperinflammation in chronic granulomatous disease and anti-inflammatory role of the phagocyte NADPH oxidase. *Semin Immunopathol* **2008,** *30* (3), 255-71.
143. Deffert, C.; Cachat, J.; Krause, K. H., Phagocyte NADPH oxidase, chronic granulomatous disease and mycobacterial infections. *Cell Microbiol* **2014,** *16* (8), 1168-78.
144. Rothfork, J. M.; Timmins, G. S.; Harris, M. N.; Chen, X.; Lusis, A. J.; Otto, M.; Cheung, A. L.; Gresham, H. D., Inactivation of a bacterial virulence pheromone by phagocyte-derived oxidants: new role for the NADPH oxidase in host defense. *Proc Natl Acad Sci U S A* **2004,** *101* (38), 13867-72.
145. Grandvaux, N.; Soucy-Faulkner, A.; Fink, K., Innate host defense: Nox and Duox on phox's tail. *Biochimie* **2007,** *89* (9), 1113-22.
146. Akira, S.; Uematsu, S.; Takeuchi, O., Pathogen recognition and innate immunity. *Cell* **2006,** *124* (4), 783-801.
147. Olufunmilayo, E. O.; Gerke-Duncan, M. B.; Holsinger, R. M. D., Oxidative Stress and Antioxidants in Neurodegenerative Disorders. *Antioxidants (Basel)* **2023,** *12* (2).
148. Barnham, K. J.; Masters, C. L.; Bush, A. I., Neurodegenerative diseases and oxidative stress. *Nat Rev Drug Discov* **2004,** *3* (3), 205-14.

149. Choi, D. H.; Cristovao, A. C.; Guhathakurta, S.; Lee, J.; Joh, T. H.; Beal, M. F.; Kim, Y. S., NADPH oxidase 1-mediated oxidative stress leads to dopamine neuron death in Parkinson's disease. *Antioxid Redox Signal* **2012,** *16* (10), 1033-45.
150. Belarbi, K.; Cuvelier, E.; Destee, A.; Gressier, B.; Chartier-Harlin, M. C., NADPH oxidases in Parkinson's disease: a systematic review. *Mol Neurodegener* **2017,** *12* (1), 84.
151. Keeney, M. T.; Hoffman, E. K.; Farmer, K.; Bodle, C. R.; Fazzari, M.; Zharikov, A.; Castro, S. L.; Hu, X.; Mortimer, A.; Kofler, J. K.; Cifuentes-Pagano, E.; Pagano, P. J.; Burton, E. A.; Hastings, T. G.; Greenamyre, J. T.; Di Maio, R., NADPH oxidase 2 activity in Parkinson's disease. *Neurobiol Dis* **2022,** *170*, 105754.
152. Abramov, A. Y.; Duchen, M. R., The role of an astrocytic NADPH oxidase in the neurotoxicity of amyloid beta peptides. *Philos Trans R Soc Lond B Biol Sci* **2005,** *360* (1464), 2309-14.
153. Wyssenbach, A.; Quintela, T.; Llavero, F.; Zugaza, J. L.; Matute, C.; Alberdi, E., Amyloid beta-induced astrogliosis is mediated by beta1-integrin via NADPH oxidase 2 in Alzheimer's disease. *Aging Cell* **2016,** *15* (6), 1140-1152.
154. Park, M. W.; Cha, H. W.; Kim, J.; Kim, J. H.; Yang, H.; Yoon, S.; Boonpraman, N.; Yi, S. S.; Yoo, I. D.; Moon, J. S., NOX4 promotes ferroptosis of astrocytes by oxidative stress-induced lipid peroxidation via the impairment of mitochondrial metabolism in Alzheimer's diseases. *Redox Biol* **2021,** *41*, 101947.
155. Marden, J. J.; Harraz, M. M.; Williams, A. J.; Nelson, K.; Luo, M.; Paulson, H.; Engelhardt, J. F., Redox modifier genes in amyotrophic lateral sclerosis in mice. *J Clin Invest* **2007,** *117* (10), 2913-9.
156. Wu, D. C.; Re, D. B.; Nagai, M.; Ischiropoulos, H.; Przedborski, S., The inflammatory NADPH oxidase enzyme modulates motor neuron degeneration in amyotrophic lateral sclerosis mice. *Proc Natl Acad Sci U S A* **2006,** *103* (32), 12132-7.
157. Lassegue, B.; Griendling, K. K., NADPH oxidases: functions and pathologies in the vasculature. *Arterioscler Thromb Vasc Biol* **2010,** *30* (4), 653-61.
158. Gimenez, M.; Schickling, B. M.; Lopes, L. R.; Miller, F. J., Jr., Nox1 in cardiovascular diseases: regulation and pathophysiology. *Clin Sci (Lond)* **2016,** *130* (3), 151-65.
159. Dikalova, A. E.; Gongora, M. C.; Harrison, D. G.; Lambeth, J. D.; Dikalov, S.; Griendling, K. K., Upregulation of Nox1 in vascular smooth muscle leads to impaired endothelium-dependent relaxation via eNOS uncoupling. *Am J Physiol Heart Circ Physiol* **2010,** *299* (3), H673-9.
160. Gavazzi, G.; Deffert, C.; Trocme, C.; Schappi, M.; Herrmann, F. R.; Krause, K. H., NOX1 deficiency protects from aortic dissection in response to angiotensin II. *Hypertension* **2007,** *50* (1), 189-96.
161. Niu, X. L.; Madamanchi, N. R.; Vendrov, A. E.; Tchivilev, I.; Rojas, M.; Madamanchi, C.; Brandes, R. P.; Krause, K. H.; Humphries, J.; Smith, A.; Burnand, K. G.; Runge, M. S., Nox activator 1: a potential target for modulation of vascular reactive oxygen species in atherosclerotic arteries. *Circulation* **2010,** *121* (4), 549-59.

162. Paolocci, N.; Biondi, R.; Bettini, M.; Lee, C. I.; Berlowitz, C. O.; Rossi, R.; Xia, Y.; Ambrosio, G.; L'Abbate, A.; Kass, D. A.; Zweier, J. L., Oxygen radical-mediated reduction in basal and agonist-evoked NO release in isolated rat heart. *J Mol Cell Cardiol* **2001,** *33* (4), 671-9.
163. Tarafdar, A.; Pula, G., The Role of NADPH Oxidases and Oxidative Stress in Neurodegenerative Disorders. *Int J Mol Sci* **2018,** *19* (12).
164. Nortley, R.; Korte, N.; Izquierdo, P.; Hirunpattarasilp, C.; Mishra, A.; Jaunmuktane, Z.; Kyrargyri, V.; Pfeiffer, T.; Khennouf, L.; Madry, C.; Gong, H.; Richard-Loendt, A.; Huang, W.; Saito, T.; Saido, T. C.; Brandner, S.; Sethi, H.; Attwell, D., Amyloid beta oligomers constrict human capillaries in Alzheimer's disease via signaling to pericytes. *Science* **2019,** *365* (6450).
165. Barton, M.; Meyer, M. R.; Prossnitz, E. R., Nox1 downregulators: A new class of therapeutics. *Steroids* **2019,** *152*, 108494.
166. Calabresi, P.; Mechelli, A.; Natale, G.; Volpicelli-Daley, L.; Di Lazzaro, G.; Ghiglieri, V., Alpha-synuclein in Parkinson's disease and other synucleinopathies: from overt neurodegeneration back to early synaptic dysfunction. *Cell Death Dis* **2023,** *14* (3), 176.
167. Choi, B. Y.; Jang, B. G.; Kim, J. H.; Lee, B. E.; Sohn, M.; Song, H. K.; Suh, S. W., Prevention of traumatic brain injury-induced neuronal death by inhibition of NADPH oxidase activation. *Brain Res* **2012,** *1481*, 49-58.
168. Cristovao, A. C.; Choi, D. H.; Baltazar, G.; Beal, M. F.; Kim, Y. S., The role of NADPH oxidase 1-derived reactive oxygen species in paraquat-mediated dopaminergic cell death. *Antioxid Redox Signal* **2009,** *11* (9), 2105-18.
169. Aguirre, J.; Lambeth, J. D., Nox enzymes from fungus to fly to fish and what they tell us about Nox function in mammals. *Free Radic Biol Med* **2010,** *49* (9), 1342-53.
170. Ravelli, K. G.; Santos, G. D.; Dos Santos, N. B.; Munhoz, C. D.; Azzi-Nogueira, D.; Campos, A. C.; Pagano, R. L.; Britto, L. R.; Hernandes, M. S., Nox2-dependent Neuroinflammation in An EAE Model of Multiple Sclerosis. *Transl Neurosci* **2019,** *10*, 1-9.
171. Choi, J. Y.; Byeon, H. W.; Park, S. O.; Uyangaa, E.; Kim, K.; Eo, S. K., Inhibition of NADPH oxidase 2 enhances resistance to viral neuroinflammation by facilitating M1-polarization of macrophages at the extraneural tissues. *J Neuroinflammation* **2024,** *21* (1), 115.
172. Park, L.; Zhou, P.; Pitstick, R.; Capone, C.; Anrather, J.; Norris, E. H.; Younkin, L.; Younkin, S.; Carlson, G.; McEwen, B. S.; Iadecola, C., Nox2-derived radicals contribute to neurovascular and behavioral dysfunction in mice overexpressing the amyloid precursor protein. *Proc Natl Acad Sci U S A* **2008,** *105* (4), 1347-52.
173. Dohi, K.; Ohtaki, H.; Nakamachi, T.; Yofu, S.; Satoh, K.; Miyamoto, K.; Song, D.; Tsunawaki, S.; Shioda, S.; Aruga, T., Gp91phox (NOX2) in classically

activated microglia exacerbates traumatic brain injury. *J Neuroinflammation* **2010,** *7*, 41.
174. Kim, S. Y.; Moon, K. A.; Jo, H. Y.; Jeong, S.; Seon, S. H.; Jung, E.; Cho, Y. S.; Chun, E.; Lee, K. Y., Anti-inflammatory effects of apocynin, an inhibitor of NADPH oxidase, in airway inflammation. *Immunol Cell Biol* **2012,** *90* (4), 441-8.
175. Song, S. X.; Gao, J. L.; Wang, K. J.; Li, R.; Tian, Y. X.; Wei, J. Q.; Cui, J. Z., Attenuation of brain edema and spatial learning de fi cits by the inhibition of NADPH oxidase activity using apocynin following diffuse traumatic brain injury in rats. *Mol Med Rep* **2013,** *7* (1), 327-31.
176. Zhang, Q. G.; Laird, M. D.; Han, D.; Nguyen, K.; Scott, E.; Dong, Y.; Dhandapani, K. M.; Brann, D. W., Critical role of NADPH oxidase in neuronal oxidative damage and microglia activation following traumatic brain injury. *PLoS One* **2012,** *7* (4), e34504.
177. Priller, C.; Bauer, T.; Mitteregger, G.; Krebs, B.; Kretzschmar, H. A.; Herms, J., Synapse formation and function is modulated by the amyloid precursor protein. *J Neurosci* **2006,** *26* (27), 7212-21.
178. Selkoe, D. J., Alzheimer's disease. *Cold Spring Harb Perspect Biol* **2011,** *3* (7).
179. Bianca, V. D.; Dusi, S.; Bianchini, E.; Dal Pra, I.; Rossi, F., beta-amyloid activates the O-2 forming NADPH oxidase in microglia, monocytes, and neutrophils. A possible inflammatory mechanism of neuronal damage in Alzheimer's disease. *J Biol Chem* **1999,** *274* (22), 15493-9.
180. Ansari, M. A.; Scheff, S. W., NADPH-oxidase activation and cognition in Alzheimer disease progression. *Free Radic Biol Med* **2011,** *51* (1), 171-8.
181. Shimohama, S.; Tanino, H.; Kawakami, N.; Okamura, N.; Kodama, H.; Yamaguchi, T.; Hayakawa, T.; Nunomura, A.; Chiba, S.; Perry, G.; Smith, M. A.; Fujimoto, S., Activation of NADPH oxidase in Alzheimer's disease brains. *Biochem Biophys Res Commun* **2000,** *273* (1), 5-9.
182. Park, L.; Anrather, J.; Zhou, P.; Frys, K.; Pitstick, R.; Younkin, S.; Carlson, G. A.; Iadecola, C., NADPH-oxidase-derived reactive oxygen species mediate the cerebrovascular dysfunction induced by the amyloid beta peptide. *J Neurosci* **2005,** *25* (7), 1769-77.
183. Ezhkova, E.; Pasolli, H. A.; Parker, J. S.; Stokes, N.; Su, I. H.; Hannon, G.; Tarakhovsky, A.; Fuchs, E., Ezh2 orchestrates gene expression for the stepwise differentiation of tissue-specific stem cells. *Cell* **2009,** *136* (6), 1122-35.
184. Smith, Y.; Wichmann, T.; Factor, S. A.; DeLong, M. R., Parkinson's disease therapeutics: new developments and challenges since the introduction of levodopa. *Neuropsychopharmacology* **2012,** *37* (1), 213-46.
185. Surace, M. J.; Block, M. L., Targeting microglia-mediated neurotoxicity: the potential of NOX2 inhibitors. *Cell Mol Life Sci* **2012,** *69* (14), 2409-27.
186. Wilkinson, B. L.; Landreth, G. E., The microglial NADPH oxidase complex as a source of oxidative stress in Alzheimer's disease. *J Neuroinflammation* **2006,** *3*, 30.

187. Wu, D. C.; Teismann, P.; Tieu, K.; Vila, M.; Jackson-Lewis, V.; Ischiropoulos, H.; Przedborski, S., NADPH oxidase mediates oxidative stress in the 1-methyl-4-phenyl-1,2,3,6-tetrahydropyridine model of Parkinson's disease. *Proc Natl Acad Sci U S A* **2003,** *100* (10), 6145-50.
188. Pratt, A. J.; Getzoff, E. D.; Perry, J. J., Amyotrophic lateral sclerosis: update and new developments. *Degener Neurol Neuromuscul Dis* **2012,** *2012* (2), 1-14.
189. Harraz, M. M.; Marden, J. J.; Zhou, W.; Zhang, Y.; Williams, A.; Sharov, V. S.; Nelson, K.; Luo, M.; Paulson, H.; Schoneich, C.; Engelhardt, J. F., SOD1 mutations disrupt redox-sensitive Rac regulation of NADPH oxidase in a familial ALS model. *J Clin Invest* **2008,** *118* (2), 659-70.
190. Simpson, D. S. A.; Oliver, P. L., ROS Generation in Microglia: Understanding Oxidative Stress and Inflammation in Neurodegenerative Disease. *Antioxidants (Basel)* **2020,** *9* (8).
191. Forte, M.; Nocella, C.; De Falco, E.; Palmerio, S.; Schirone, L.; Valenti, V.; Frati, G.; Carnevale, R.; Sciarretta, S., The Pathophysiological Role of NOX2 in Hypertension and Organ Damage. *High Blood Press Cardiovasc Prev* **2016,** *23* (4), 355-364.
192. Rajagopalan, S.; Kurz, S.; Munzel, T.; Tarpey, M.; Freeman, B. A.; Griendling, K. K.; Harrison, D. G., Angiotensin II-mediated hypertension in the rat increases vascular superoxide production via membrane NADH/NADPH oxidase activation. Contribution to alterations of vasomotor tone. *J Clin Invest* **1996,** *97* (8), 1916-23.
193. Carlstrom, M.; Lai, E. Y.; Ma, Z.; Patzak, A.; Brown, R. D.; Persson, A. E., Role of NOX2 in the regulation of afferent arteriole responsiveness. *Am J Physiol Regul Integr Comp Physiol* **2009,** *296* (1), R72-9.
194. Bendall, J. K.; Rinze, R.; Adlam, D.; Tatham, A. L.; de Bono, J.; Wilson, N.; Volpi, E.; Channon, K. M., Endothelial Nox2 overexpression potentiates vascular oxidative stress and hemodynamic response to angiotensin II: studies in endothelial-targeted Nox2 transgenic mice. *Circ Res* **2007,** *100* (7), 1016-25.
195. Rey, F. E.; Cifuentes, M. E.; Kiarash, A.; Quinn, M. T.; Pagano, P. J., Novel competitive inhibitor of NAD(P)H oxidase assembly attenuates vascular O(2)(-) and systolic blood pressure in mice. *Circ Res* **2001,** *89* (5), 408-14.
196. Sellers, K. W.; Sun, C.; Diez-Freire, C.; Waki, H.; Morisseau, C.; Falck, J. R.; Hammock, B. D.; Paton, J. F.; Raizada, M. K., Novel mechanism of brain soluble epoxide hydrolase-mediated blood pressure regulation in the spontaneously hypertensive rat. *FASEB J* **2005,** *19* (6), 626-8.
197. Zhou, X.; Bohlen, H. G.; Miller, S. J.; Unthank, J. L., NAD(P)H oxidase-derived peroxide mediates elevated basal and impaired flow-induced NO production in SHR mesenteric arteries in vivo. *Am J Physiol Heart Circ Physiol* **2008,** *295* (3), H1008-H1016.

198. Zhou, M. S.; Hernandez Schulman, I.; Pagano, P. J.; Jaimes, E. A.; Raij, L., Reduced NAD(P)H oxidase in low renin hypertension: link among angiotensin II, atherogenesis, and blood pressure. *Hypertension* **2006,** *47* (1), 81-6.
199. Khan, B. V.; Harrison, D. G.; Olbrych, M. T.; Alexander, R. W.; Medford, R. M., Nitric oxide regulates vascular cell adhesion molecule 1 gene expression and redox-sensitive transcriptional events in human vascular endothelial cells. *Proc Natl Acad Sci U S A* **1996,** *93* (17), 9114-9.
200. Sorescu, D.; Weiss, D.; Lassegue, B.; Clempus, R. E.; Szocs, K.; Sorescu, G. P.; Valppu, L.; Quinn, M. T.; Lambeth, J. D.; Vega, J. D.; Taylor, W. R.; Griendling, K. K., Superoxide production and expression of nox family proteins in human atherosclerosis. *Circulation* **2002,** *105* (12), 1429-35.
201. Judkins, C. P.; Diep, H.; Broughton, B. R.; Mast, A. E.; Hooker, E. U.; Miller, A. A.; Selemidis, S.; Dusting, G. J.; Sobey, C. G.; Drummond, G. R., Direct evidence of a role for Nox2 in superoxide production, reduced nitric oxide bioavailability, and early atherosclerotic plaque formation in ApoE-/- mice. *Am J Physiol Heart Circ Physiol* **2010,** *298* (1), H24-32.
202. Dourron, H. M.; Jacobson, G. M.; Park, J. L.; Liu, J.; Reddy, D. J.; Scheel, M. L.; Pagano, P. J., Perivascular gene transfer of NADPH oxidase inhibitor suppresses angioplasty-induced neointimal proliferation of rat carotid artery. *Am J Physiol Heart Circ Physiol* **2005,** *288* (2), H946-53.
203. Zhang, M.; Kho, A. L.; Anilkumar, N.; Chibber, R.; Pagano, P. J.; Shah, A. M.; Cave, A. C., Glycated proteins stimulate reactive oxygen species production in cardiac myocytes: involvement of Nox2 (gp91phox)-containing NADPH oxidase. *Circulation* **2006,** *113* (9), 1235-43.
204. Brownlee, M., Biochemistry and molecular cell biology of diabetic complications. *Nature* **2001,** *414* (6865), 813-20.
205. Hink, U.; Li, H.; Mollnau, H.; Oelze, M.; Matheis, E.; Hartmann, M.; Skatchkov, M.; Thaiss, F.; Stahl, R. A.; Warnholtz, A.; Meinertz, T.; Griendling, K.; Harrison, D. G.; Forstermann, U.; Munzel, T., Mechanisms underlying endothelial dysfunction in diabetes mellitus. *Circ Res* **2001,** *88* (2), E14-22.
206. Xiang, F. L.; Lu, X.; Strutt, B.; Hill, D. J.; Feng, Q., NOX2 deficiency protects against streptozotocin-induced beta-cell destruction and development of diabetes in mice. *Diabetes* **2010,** *59* (10), 2603-11.
207. Sukumar, P.; Viswambharan, H.; Imrie, H.; Cubbon, R. M.; Yuldasheva, N.; Gage, M.; Galloway, S.; Skromna, A.; Kandavelu, P.; Santos, C. X.; Gatenby, V. K.; Smith, J.; Beech, D. J.; Wheatcroft, S. B.; Channon, K. M.; Shah, A. M.; Kearney, M. T., Nox2 NADPH oxidase has a critical role in insulin resistance-related endothelial cell dysfunction. *Diabetes* **2013,** *62* (6), 2130-4.
208. Lynch, C. M.; Kinzenbaw, D. A.; Chen, X.; Zhan, S.; Mezzetti, E.; Filosa, J.; Ergul, A.; Faulkner, J. L.; Faraci, F. M.; Didion, S. P., Nox2-derived superoxide contributes to cerebral vascular dysfunction in diet-induced obesity. *Stroke* **2013,** *44* (11), 3195-201.

209. Pignatelli, P.; Sanguigni, V.; Lenti, L.; Ferro, D.; Finocchi, A.; Rossi, P.; Violi, F., gp91phox-dependent expression of platelet CD40 ligand. *Circulation* **2004,** *110* (10), 1326-9.
210. Carnevale, R.; Loffredo, L.; Sanguigni, V.; Plebani, A.; Rossi, P.; Pignata, C.; Martire, B.; Finocchi, A.; Pietrogrande, M. C.; Azzari, C.; Soresina, A. R.; Martino, S.; Cirillo, E.; Martino, F.; Pignatelli, P.; Violi, F., Different degrees of NADPH oxidase 2 regulation and in vivo platelet activation: lesson from chronic granulomatous disease. *J Am Heart Assoc* **2014,** *3* (3), e000920.
211. Walsh, T. G.; Berndt, M. C.; Carrim, N.; Cowman, J.; Kenny, D.; Metharom, P., The role of Nox1 and Nox2 in GPVI-dependent platelet activation and thrombus formation. *Redox Biol* **2014,** *2*, 178-86.
212. Delaney, M. K.; Kim, K.; Estevez, B.; Xu, Z.; Stojanovic-Terpo, A.; Shen, B.; Ushio-Fukai, M.; Cho, J.; Du, X., Differential Roles of the NADPH-Oxidase 1 and 2 in Platelet Activation and Thrombosis. *Arterioscler Thromb Vasc Biol* **2016,** *36* (5), 846-54.
213. Krotz, F.; Sohn, H. Y.; Gloe, T.; Zahler, S.; Riexinger, T.; Schiele, T. M.; Becker, B. F.; Theisen, K.; Klauss, V.; Pohl, U., NAD(P)H oxidase-dependent platelet superoxide anion release increases platelet recruitment. *Blood* **2002,** *100* (3), 917-24.
214. Gavriatopoulou, M.; Korompoki, E.; Fotiou, D.; Ntanasis-Stathopoulos, I.; Psaltopoulou, T.; Kastritis, E.; Terpos, E.; Dimopoulos, M. A., Organ-specific manifestations of COVID-19 infection. *Clin Exp Med* **2020,** *20* (4), 493-506.
215. Sindona, C.; Schepici, G.; Contestabile, V.; Bramanti, P.; Mazzon, E., NOX2 Activation in COVID-19: Possible Implications for Neurodegenerative Diseases. *Medicina (Kaunas)* **2021,** *57* (6).
216. Liu, T.; Zhang, L.; Joo, D.; Sun, S. C., NF-kappaB signaling in inflammation. *Signal Transduct Target Ther* **2017,** *2*, 17023-.
217. Geng, L.; Fan, L. M.; Liu, F.; Smith, C.; Li, J., Nox2 dependent redox-regulation of microglial response to amyloid-beta stimulation and microgliosis in aging. *Sci Rep* **2020,** *10* (1), 1582.
218. Gheblawi, M.; Wang, K.; Viveiros, A.; Nguyen, Q.; Zhong, J. C.; Turner, A. J.; Raizada, M. K.; Grant, M. B.; Oudit, G. Y., Angiotensin-Converting Enzyme 2: SARS-CoV-2 Receptor and Regulator of the Renin-Angiotensin System: Celebrating the 20th Anniversary of the Discovery of ACE2. *Circ Res* **2020,** *126* (10), 1456-1474.
219. To, E. E.; Vlahos, R.; Luong, R.; Halls, M. L.; Reading, P. C.; King, P. T.; Chan, C.; Drummond, G. R.; Sobey, C. G.; Broughton, B. R. S.; Starkey, M. R.; van der Sluis, R.; Lewin, S. R.; Bozinovski, S.; O'Neill, L. A. J.; Quach, T.; Porter, C. J. H.; Brooks, D. A.; O'Leary, J. J.; Selemidis, S., Endosomal NOX2 oxidase exacerbates virus pathogenicity and is a target for antiviral therapy. *Nat Commun* **2017,** *8* (1), 69.
220. Violi, F.; Pastori, D.; Pignatelli, P.; Cangemi, R., SARS-CoV-2 and myocardial injury: a role for Nox2? *Intern Emerg Med* **2020,** *15* (5), 755-758.

221. Thakur, A.; Sharma, V.; Averbek, S.; Liang, L.; Pandya, N.; Kumar, G.; Cili, A.; Zhang, K., Immune landscape and redox imbalance during neurological disorders in COVID-19. *Cell Death Dis* **2023,** *14* (9), 593.
222. Kelkka, T.; Pizzolla, A.; Laurila, J. P.; Friman, T.; Gustafsson, R.; Kallberg, E.; Olsson, O.; Leanderson, T.; Rubin, K.; Salmi, M.; Jalkanen, S.; Holmdahl, R., Mice lacking NCF1 exhibit reduced growth of implanted melanoma and carcinoma tumors. *PLoS One* **2013,** *8* (12), e84148.
223. Ligtenberg, M. A.; Cinar, O.; Holmdahl, R.; Mougiakakos, D.; Kiessling, R., Methylcholanthrene-Induced Sarcomas Develop Independently from NOX2-Derived ROS. *PLoS One* **2015,** *10* (6), e0129786.
224. Aydin, E.; Johansson, J.; Nazir, F. H.; Hellstrand, K.; Martner, A., Role of NOX2-Derived Reactive Oxygen Species in NK Cell-Mediated Control of Murine Melanoma Metastasis. *Cancer Immunol Res* **2017,** *5* (9), 804-811.
225. Okada, F.; Kobayashi, M.; Tanaka, H.; Kobayashi, T.; Tazawa, H.; Iuchi, Y.; Onuma, K.; Hosokawa, M.; Dinauer, M. C.; Hunt, N. H., The role of nicotinamide adenine dinucleotide phosphate oxidase-derived reactive oxygen species in the acquisition of metastatic ability of tumor cells. *Am J Pathol* **2006,** *169* (1), 294-302.
226. van der Weyden, L.; Speak, A. O.; Swiatkowska, A.; Clare, S.; Schejtman, A.; Santilli, G.; Arends, M. J.; Adams, D. J., Pulmonary metastatic colonisation and granulomas in NOX2-deficient mice. *J Pathol* **2018,** *246* (3), 300-310.
227. Betten, A.; Dahlgren, C.; Mellqvist, U. H.; Hermodsson, S.; Hellstrand, K., Oxygen radical-induced natural killer cell dysfunction: role of myeloperoxidase and regulation by serotonin. *J Leukoc Biol* **2004,** *75* (6), 1111-5.
228. Grauers Wiktorin, H.; Nilsson, M. S.; Kiffin, R.; Sander, F. E.; Lenox, B.; Rydstrom, A.; Hellstrand, K.; Martner, A., Histamine targets myeloid-derived suppressor cells and improves the anti-tumor efficacy of PD-1/PD-L1 checkpoint blockade. *Cancer Immunol Immunother* **2019,** *68* (2), 163-174.
229. Marlein, C. R.; Zaitseva, L.; Piddock, R. E.; Robinson, S. D.; Edwards, D. R.; Shafat, M. S.; Zhou, Z.; Lawes, M.; Bowles, K. M.; Rushworth, S. A., NADPH oxidase-2 derived superoxide drives mitochondrial transfer from bone marrow stromal cells to leukemic blasts. *Blood* **2017,** *130* (14), 1649-1660.
230. Adane, B.; Ye, H.; Khan, N.; Pei, S.; Minhajuddin, M.; Stevens, B. M.; Jones, C. L.; D'Alessandro, A.; Reisz, J. A.; Zaberezhnyy, V.; Gasparetto, M.; Ho, T. C.; Kelly, K. K.; Myers, J. R.; Ashton, J. M.; Siegenthaler, J.; Kume, T.; Campbell, E. L.; Pollyea, D. A.; Becker, M. W.; Jordan, C. T., The Hematopoietic Oxidase NOX2 Regulates Self-Renewal of Leukemic Stem Cells. *Cell Rep* **2019,** *27* (1), 238-254 e6.
231. Grauers Wiktorin, H.; Aydin, E.; Hellstrand, K.; Martner, A., NOX2-Derived Reactive Oxygen Species in Cancer. *Oxid Med Cell Longev* **2020,** *2020*, 7095902.
232. McFadden, S. L.; Ding, D.; Reaume, A. G.; Flood, D. G.; Salvi, R. J., Age-related cochlear hair cell loss is enhanced in mice lacking copper/zinc superoxide dismutase. *Neurobiol Aging* **1999,** *20* (1), 1-8.

233. Takyar, S.; Zhang, Y.; Haslip, M.; Jin, L.; Shan, P.; Zhang, X.; Lee, P. J., An endothelial TLR4-VEGFR2 pathway mediates lung protection against oxidant-induced injury. *FASEB J* **2016,** *30* (3), 1317-27.
234. Zhang, Y.; Shan, P.; Srivastava, A.; Jiang, G.; Zhang, X.; Lee, P. J., An Endothelial Hsp70-TLR4 Axis Limits Nox3 Expression and Protects Against Oxidant Injury in Lungs. *Antioxid Redox Signal* **2016,** *24* (17), 991-1012.
235. Shaw, J. E.; Sicree, R. A.; Zimmet, P. Z., Global estimates of the prevalence of diabetes for 2010 and 2030. *Diabetes Res Clin Pract* **2010,** *87* (1), 4-14.
236. Thallas-Bonke, V.; Jandeleit-Dahm, K. A.; Cooper, M. E., Nox-4 and progressive kidney disease. *Curr Opin Nephrol Hypertens* **2015,** *24* (1), 74-80.
237. Zhang, M.; Brewer, A. C.; Schroder, K.; Santos, C. X.; Grieve, D. J.; Wang, M.; Anilkumar, N.; Yu, B.; Dong, X.; Walker, S. J.; Brandes, R. P.; Shah, A. M., NADPH oxidase-4 mediates protection against chronic load-induced stress in mouse hearts by enhancing angiogenesis. *Proc Natl Acad Sci U S A* **2010,** *107* (42), 18121-6.
238. Kuroda, J.; Ago, T.; Matsushima, S.; Zhai, P.; Schneider, M. D.; Sadoshima, J., NADPH oxidase 4 (Nox4) is a major source of oxidative stress in the failing heart. *Proc Natl Acad Sci U S A* **2010,** *107* (35), 15565-70.
239. Schroder, K.; Zhang, M.; Benkhoff, S.; Mieth, A.; Pliquett, R.; Kosowski, J.; Kruse, C.; Luedike, P.; Michaelis, U. R.; Weissmann, N.; Dimmeler, S.; Shah, A. M.; Brandes, R. P., Nox4 is a protective reactive oxygen species generating vascular NADPH oxidase. *Circ Res* **2012,** *110* (9), 1217-25.
240. Ma, M. W.; Wang, J.; Zhang, Q.; Wang, R.; Dhandapani, K. M.; Vadlamudi, R. K.; Brann, D. W., NADPH oxidase in brain injury and neurodegenerative disorders. *Mol Neurodegener* **2017,** *12* (1), 7.
241. Hwang, S. Y.; Putney, J. W., Jr., Calcium signaling in osteoclasts. *Biochim Biophys Acta* **2011,** *1813* (5), 979-83.
242. Goettsch, C.; Babelova, A.; Trummer, O.; Erben, R. G.; Rauner, M.; Rammelt, S.; Weissmann, N.; Weinberger, V.; Benkhoff, S.; Kampschulte, M.; Obermayer-Pietsch, B.; Hofbauer, L. C.; Brandes, R. P.; Schroder, K., NADPH oxidase 4 limits bone mass by promoting osteoclastogenesis. *J Clin Invest* **2013,** *123* (11), 4731-8.
243. Hiraga, R.; Kato, M.; Miyagawa, S.; Kamata, T., Nox4-derived ROS signaling contributes to TGF-beta-induced epithelial-mesenchymal transition in pancreatic cancer cells. *Anticancer Res* **2013,** *33* (10), 4431-8.
244. Stathis, A.; Moore, M. J., Advanced pancreatic carcinoma: current treatment and future challenges. *Nat Rev Clin Oncol* **2010,** *7* (3), 163-72.
245. Touyz, R. M.; Anagnostopoulou, A.; Camargo, L. L.; Rios, F. J.; Montezano, A. C., Vascular Biology of Superoxide-Generating NADPH Oxidase 5-Implications in Hypertension and Cardiovascular Disease. *Antioxid Redox Signal* **2019,** *30* (7), 1027-1040.

246. Montezano, A. C.; De Lucca Camargo, L.; Persson, P.; Rios, F. J.; Harvey, A. P.; Anagnostopoulou, A.; Palacios, R.; Gandara, A. C. P.; Alves-Lopes, R.; Neves, K. B.; Dulak-Lis, M.; Holterman, C. E.; de Oliveira, P. L.; Graham, D.; Kennedy, C.; Touyz, R. M., NADPH Oxidase 5 Is a Pro-Contractile Nox Isoform and a Point of Cross-Talk for Calcium and Redox Signaling-Implications in Vascular Function. *J Am Heart Assoc* **2018,** *7* (12).
247. Gole, H. K.; Tharp, D. L.; Bowles, D. K., Upregulation of intermediate-conductance Ca2+-activated K+ channels (KCNN4) in porcine coronary smooth muscle requires NADPH oxidase 5 (NOX5). *PLoS One* **2014,** *9* (8), e105337.
248. Jha, J. C.; Watson, A. M. D.; Mathew, G.; de Vos, L. C.; Jandeleit-Dahm, K., The emerging role of NADPH oxidase NOX5 in vascular disease. *Clin Sci (Lond)* **2017,** *131* (10), 981-990.
249. Holterman, C. E.; Thibodeau, J. F.; Towaij, C.; Gutsol, A.; Montezano, A. C.; Parks, R. J.; Cooper, M. E.; Touyz, R. M.; Kennedy, C. R., Nephropathy and elevated BP in mice with podocyte-specific NADPH oxidase 5 expression. *J Am Soc Nephrol* **2014,** *25* (4), 784-97.
250. Antony, S.; Jiang, G.; Wu, Y.; Meitzler, J. L.; Makhlouf, H. R.; Haines, D. C.; Butcher, D.; Hoon, D. S.; Ji, J.; Zhang, Y.; Juhasz, A.; Lu, J.; Liu, H.; Dahan, I.; Konate, M.; Roy, K. K.; Doroshow, J. H., NADPH oxidase 5 (NOX5)-induced reactive oxygen signaling modulates normoxic HIF-1alpha and p27(Kip1) expression in malignant melanoma and other human tumors. *Mol Carcinog* **2017,** *56* (12), 2643-2662.
251. Gao, X.; Schottker, B., Reduction-oxidation pathways involved in cancer development: a systematic review of literature reviews. *Oncotarget* **2017,** *8* (31), 51888-51906.
252. Kalatskaya, I., Overview of major molecular alterations during progression from Barrett's esophagus to esophageal adenocarcinoma. *Ann N Y Acad Sci* **2016,** *1381* (1), 74-91.
253. Bedard, K.; Jaquet, V.; Krause, K. H., NOX5: from basic biology to signaling and disease. *Free Radic Biol Med* **2012,** *52* (4), 725-34.
254. Roy, K.; Wu, Y.; Meitzler, J. L.; Juhasz, A.; Liu, H.; Jiang, G.; Lu, J.; Antony, S.; Doroshow, J. H., NADPH oxidases and cancer. *Clin Sci (Lond)* **2015,** *128* (12), 863-75.
255. Fu, X.; Beer, D. G.; Behar, J.; Wands, J.; Lambeth, D.; Cao, W., cAMP-response element-binding protein mediates acid-induced NADPH oxidase NOX5-S expression in Barrett esophageal adenocarcinoma cells. *J Biol Chem* **2006,** *281* (29), 20368-82.
256. Dho, S. H.; Kim, J. Y.; Lee, K. P.; Kwon, E. S.; Lim, J. C.; Kim, C. J.; Jeong, D.; Kwon, K. S., STAT5A-mediated NOX5-L expression promotes the proliferation and metastasis of breast cancer cells. *Exp Cell Res* **2017,** *351* (1), 51-58.
257. Nishida, N.; Yano, H.; Nishida, T.; Kamura, T.; Kojiro, M., Angiogenesis in cancer. *Vasc Health Risk Manag* **2006,** *2* (3), 213-9.

258. Karar, J.; Maity, A., PI3K/AKT/mTOR Pathway in Angiogenesis. *Front Mol Neurosci* **2011,** *4*, 51.
259. Xia, C.; Meng, Q.; Liu, L. Z.; Rojanasakul, Y.; Wang, X. R.; Jiang, B. H., Reactive oxygen species regulate angiogenesis and tumor growth through vascular endothelial growth factor. *Cancer Res* **2007,** *67* (22), 10823-30.
260. Ashizawa, N.; Shimizu, H.; Sudo, M.; Furuya, S.; Akaike, H.; Hosomura, N.; Kawaguchi, Y.; Amemiya, H.; Kawaida, H.; Inoue, S.; Kono, H.; Ichikawa, D., Clinical Significance of NADPH Oxidase 5 in Human Colon Cancer. *Anticancer Res* **2019,** *39* (8), 4405-4410.
261. Demeester-Mirkine, N.; Van Sande, J.; Corvilain, J.; Dumont, J. E., Benign thyroid nodule with normal iodide trap and defective organification. *J Clin Endocrinol Metab* **1975,** *41* (06), 1169-71.
262. Szanto, I.; Pusztaszeri, M.; Mavromati, M., H(2)O(2) Metabolism in Normal Thyroid Cells and in Thyroid Tumorigenesis: Focus on NADPH Oxidases. *Antioxidants (Basel)* **2019,** *8* (5).
263. Bjorkman, U.; Ekholm, R., Generation of H2O2 in isolated porcine thyroid follicles. *Endocrinology* **1984,** *115* (1), 392-8.
264. Virion, A.; Michot, J. L.; Deme, D.; Kaniewski, J.; Pommier, J., NADPH-dependent H2O2 generation and peroxidase activity in thyroid particular fraction. *Mol Cell Endocrinol* **1984,** *36* (1-2), 95-105.
265. Alexandrova, A. Y.; Kopnin, P. B.; Vasiliev, J. M.; Kopnin, B. P., ROS up-regulation mediates Ras-induced changes of cell morphology and motility. *Exp Cell Res* **2006,** *312* (11), 2066-73.
266. Finkel, T., Redox-dependent signal transduction. *FEBS Lett* **2000,** *476* (1-2), 52-4.
267. Vafa, O.; Wade, M.; Kern, S.; Beeche, M.; Pandita, T. K.; Hampton, G. M.; Wahl, G. M., c-Myc can induce DNA damage, increase reactive oxygen species, and mitigate p53 function: a mechanism for oncogene-induced genetic instability. *Mol Cell* **2002,** *9* (5), 1031-44.
268. Ameziane-El-Hassani, R.; Talbot, M.; de Souza Dos Santos, M. C.; Al Ghuzlan, A.; Hartl, D.; Bidart, J. M.; De Deken, X.; Miot, F.; Diallo, I.; de Vathaire, F.; Schlumberger, M.; Dupuy, C., NADPH oxidase DUOX1 promotes long-term persistence of oxidative stress after an exposure to irradiation. *Proc Natl Acad Sci U S A* **2015,** *112* (16), 5051-6.
269. Lacroix, L.; Nocera, M.; Mian, C.; Caillou, B.; Virion, A.; Dupuy, C.; Filetti, S.; Bidart, J. M.; Schlumberger, M., Expression of nicotinamide adenine dinucleotide phosphate oxidase flavoprotein DUOX genes and proteins in human papillary and follicular thyroid carcinomas. *Thyroid* **2001,** *11* (11), 1017-23.
270. Ameziane El Hassani, R.; Buffet, C.; Leboulleux, S.; Dupuy, C., Oxidative stress in thyroid carcinomas: biological and clinical significance. *Endocr Relat Cancer* **2019,** *26* (3), R131-R143.

271. Weyemi, U.; Redon, C. E.; Parekh, P. R.; Dupuy, C.; Bonner, W. M., NADPH Oxidases NOXs and DUOXs as putative targets for cancer therapy. *Anticancer Agents Med Chem* **2013,** *13* (3), 502-14.
272. Moreno, J. C.; Bikker, H.; Kempers, M. J.; van Trotsenburg, A. S.; Baas, F.; de Vijlder, J. J.; Vulsma, T.; Ris-Stalpers, C., Inactivating mutations in the gene for thyroid oxidase 2 (THOX2) and congenital hypothyroidism. *N Engl J Med* **2002,** *347* (2), 95-102.
273. Chopra, K.; Ishibashi, S.; Amaya, E., Zebrafish duox mutations provide a model for human congenital hypothyroidism. *Biol Open* **2019,** *8* (2).
274. Figueiredo, M. D.; Cardoso, L. C.; Ferreira, A. C.; Campos, D. V.; da Cruz Domingos, M.; Corbo, R.; Nasciutti, L. E.; Vaisman, M.; Carvalho, D. P., Goiter and hypothyroidism in two siblings due to impaired Ca(+2)/NAD(P)H-dependent H(2)O(2)-generating activity. *J Clin Endocrinol Metab* **2001,** *86* (10), 4843-8.
275. Pfarr, N.; Korsch, E.; Kaspers, S.; Herbst, A.; Stach, A.; Zimmer, C.; Pohlenz, J., Congenital hypothyroidism caused by new mutations in the thyroid oxidase 2 (THOX2) gene. *Clin Endocrinol (Oxf)* **2006,** *65* (6), 810-5.
276. Moreno, J. C.; Visser, T. J., New phenotypes in thyroid dyshormonogenesis: hypothyroidism due to DUOX2 mutations. *Endocr Dev* **2007,** *10*, 99-117.
277. Dabravolski, S. A.; Nikiforov, N. G.; Zhuravlev, A. D.; Orekhov, N. A.; Mikhaleva, L. M.; Orekhov, A. N., The Role of Altered Mitochondrial Metabolism in Thyroid Cancer Development and Mitochondria-Targeted Thyroid Cancer Treatment. *Int J Mol Sci* **2021,** *23* (1).
278. Elbatreek, M. H.; Mucke, H.; Schmidt, H., NOX Inhibitors: From Bench to Naxibs to Bedside. *Handb Exp Pharmacol* **2021,** *264*, 145-168.
279. Invernizzi, P.; Carbone, M.; Jones, D.; Levy, C.; Little, N.; Wiesel, P.; Nevens, F.; study, i., Setanaxib, a first-in-class selective NADPH oxidase 1/4 inhibitor for primary biliary cholangitis: A randomized, placebo-controlled, phase 2 trial. *Liver Int* **2023,** *43* (7), 1507-1522.
280. Stuehr, D. J.; Fasehun, O. A.; Kwon, N. S.; Gross, S. S.; Gonzalez, J. A.; Levi, R.; Nathan, C. F., Inhibition of macrophage and endothelial cell nitric oxide synthase by diphenyleneiodonium and its analogs. *FASEB J* **1991,** *5* (1), 98-103.
281. Reis, J.; Massari, M.; Marchese, S.; Ceccon, M.; Aalbers, F. S.; Corana, F.; Valente, S.; Mai, A.; Magnani, F.; Mattevi, A., A closer look into NADPH oxidase inhibitors: Validation and insight into their mechanism of action. *Redox Biol* **2020,** *32*, 101466.
282. Szilagyi, J. T.; Mishin, V.; Heck, D. E.; Jan, Y. H.; Aleksunes, L. M.; Richardson, J. R.; Heindel, N. D.; Laskin, D. L.; Laskin, J. D., Selective Targeting of Heme Protein in Cytochrome P450 and Nitric Oxide Synthase by Diphenyleneiodonium. *Toxicol Sci* **2016,** *151* (1), 150-9.
283. Stolk, J.; Hiltermann, T. J.; Dijkman, J. H.; Verhoeven, A. J., Characteristics of the inhibition of NADPH oxidase activation in neutrophils by apocynin, a methoxy-substituted catechol. *Am J Respir Cell Mol Biol* **1994,** *11* (1), 95-102.

284. Petronio, M. S.; Zeraik, M. L.; Fonseca, L. M.; Ximenes, V. F., Apocynin: chemical and biophysical properties of a NADPH oxidase inhibitor. *Molecules* **2013,** *18* (3), 2821-39.
285. Cayatte, A. J.; Rupin, A.; Oliver-Krasinski, J.; Maitland, K.; Sansilvestri-Morel, P.; Boussard, M. F.; Wierzbicki, M.; Verbeuren, T. J.; Cohen, R. A., S17834, a new inhibitor of cell adhesion and atherosclerosis that targets nadph oxidase. *Arterioscler Thromb Vasc Biol* **2001,** *21* (10), 1577-84.
286. Jaquet, V.; Marcoux, J.; Forest, E.; Leidal, K. G.; McCormick, S.; Westermaier, Y.; Perozzo, R.; Plastre, O.; Fioraso-Cartier, L.; Diebold, B.; Scapozza, L.; Nauseef, W. M.; Fieschi, F.; Krause, K. H.; Bedard, K., NADPH oxidase (NOX) isoforms are inhibited by celastrol with a dual mode of action. *Br J Pharmacol* **2011,** *164* (2b), 507-20.
287. Kim, J. H.; Lee, J. O.; Lee, S. K.; Kim, N.; You, G. Y.; Moon, J. W.; Sha, J.; Kim, S. J.; Park, S. H.; Kim, H. S., Celastrol suppresses breast cancer MCF-7 cell viability via the AMP-activated protein kinase (AMPK)-induced p53-polo like kinase 2 (PLK-2) pathway. *Cell Signal* **2013,** *25* (4), 805-13.
288. Smith, S. M.; Min, J.; Ganesh, T.; Diebold, B.; Kawahara, T.; Zhu, Y.; McCoy, J.; Sun, A.; Snyder, J. P.; Fu, H.; Du, Y.; Lewis, I.; Lambeth, J. D., Ebselen and congeners inhibit NADPH oxidase 2-dependent superoxide generation by interrupting the binding of regulatory subunits. *Chem Biol* **2012,** *19* (6), 752-63.
289. Altenhofer, S.; Radermacher, K. A.; Kleikers, P. W.; Wingler, K.; Schmidt, H. H., Evolution of NADPH Oxidase Inhibitors: Selectivity and Mechanisms for Target Engagement. *Antioxid Redox Signal* **2015,** *23* (5), 406-27.
290. Laleu, B.; Gaggini, F.; Orchard, M.; Fioraso-Cartier, L.; Cagnon, L.; Houngninou-Molango, S.; Gradia, A.; Duboux, G.; Merlot, C.; Heitz, F.; Szyndralewiez, C.; Page, P., First in class, potent, and orally bioavailable NADPH oxidase isoform 4 (Nox4) inhibitors for the treatment of idiopathic pulmonary fibrosis. *J Med Chem* **2010,** *53* (21), 7715-30.
291. Zeng, S. Y.; Yang, L.; Yan, Q. J.; Gao, L.; Lu, H. Q.; Yan, P. K., Nox1/4 dual inhibitor GKT137831 attenuates hypertensive cardiac remodelling associating with the inhibition of ADAM17-dependent proinflammatory cytokines-induced signalling pathways in the rats with abdominal artery constriction. *Biomed Pharmacother* **2019,** *109*, 1907-1914.
292. Yamamoto, T.; Nakano, H.; Shiomi, K.; Wanibuchi, K.; Masui, H.; Takahashi, T.; Urano, Y.; Kamata, T., Identification and Characterization of a Novel NADPH Oxidase 1 (Nox1) Inhibitor That Suppresses Proliferation of Colon and Stomach Cancer Cells. *Biol Pharm Bull* **2018,** *41* (3), 419-426.
293. Wang, Q.; Zhou, H.; Gao, H.; Chen, S. H.; Chu, C. H.; Wilson, B.; Hong, J. S., Naloxone inhibits immune cell function by suppressing superoxide production through a direct interaction with gp91phox subunit of NADPH oxidase. *J Neuroinflammation* **2012,** *9*, 32.

294. Anvari, E.; Wikstrom, P.; Walum, E.; Welsh, N., The novel NADPH oxidase 4 inhibitor GLX351322 counteracts glucose intolerance in high-fat diet-treated C57BL/6 mice. *Free Radic Res* **2015,** *49* (11), 1308-18.
295. Szekeres, F. L. M.; Walum, E.; Wikstrom, P.; Arner, A., A small molecule inhibitor of Nox2 and Nox4 improves contractile function after ischemia-reperfusion in the mouse heart. *Sci Rep* **2021,** *11* (1), 11970.
296. Ji, M. M.; Huang, Y. H.; Huang, J. Y.; Wang, Z. F.; Fu, D.; Liu, H.; Liu, F.; Leboeuf, C.; Wang, L.; Ye, J.; Lu, Y. M.; Janin, A.; Cheng, S.; Zhao, W. L., Histone modifier gene mutations in peripheral T-cell lymphoma not otherwise specified. *Haematologica* **2018,** *103* (4), 679-687.
297. Wang, X.; Elksnis, A.; Wikstrom, P.; Walum, E.; Welsh, N.; Carlsson, P. O., The novel NADPH oxidase 4 selective inhibitor GLX7013114 counteracts human islet cell death in vitro. *PLoS One* **2018,** *13* (9), e0204271.
298. Elksnis, A.; Welsh, N.; Wikstrom, P.; Lau, J.; Carlsson, P. O., The selective NOX4 inhibitor GLX7013159 decreases blood glucose concentrations and human beta-cell apoptotic rates in diabetic NMRI nu/nu mice transplanted with human islets. *Free Radic Res* **2023,** *57* (6-12), 460-469.
299. Hirano, K.; Chen, W. S.; Chueng, A. L.; Dunne, A. A.; Seredenina, T.; Filippova, A.; Ramachandran, S.; Bridges, A.; Chaudry, L.; Pettman, G.; Allan, C.; Duncan, S.; Lee, K. C.; Lim, J.; Ma, M. T.; Ong, A. B.; Ye, N. Y.; Nasir, S.; Mulyanidewi, S.; Aw, C. C.; Oon, P. P.; Liao, S.; Li, D.; Johns, D. G.; Miller, N. D.; Davies, C. H.; Browne, E. R.; Matsuoka, Y.; Chen, D. W.; Jaquet, V.; Rutter, A. R., Discovery of GSK2795039, a Novel Small Molecule NADPH Oxidase 2 Inhibitor. *Antioxid Redox Signal* **2015,** *23* (5), 358-74.
300. Padilha, E. C.; Shah, P.; Rai, G.; Xu, X., NOX2 inhibitor GSK2795039 metabolite identification towards drug optimization. *J Pharm Biomed Anal* **2021,** *201*, 114102.
301. Mason, H.; Rai, G.; Kozyr, A.; De Jonge, N.; Gliniewicz, E.; Berg, L. J.; Wald, G.; Dorrier, C.; Henderson, M. J.; Zakharov, A.; Dyson, T.; Audley, J.; Pettinato, A. M.; Padilha, E. C.; Shah, P.; Xu, X.; Leto, T. L.; Simeonov, A.; Zarember, K. A.; McGavern, D. B.; Gallin, J. I., Development of an improved and specific inhibitor of NADPH oxidase 2 to treat traumatic brain injury. *Redox Biol* **2023,** *60*, 102611.
302. Solbak, S. M. O.; Zang, J.; Narayanan, D.; Hoj, L. J.; Bucciarelli, S.; Softley, C.; Meier, S.; Langkilde, A. E.; Gotfredsen, C. H.; Sattler, M.; Bach, A., Developing Inhibitors of the p47phox-p22phox Protein-Protein Interaction by Fragment-Based Drug Discovery. *J Med Chem* **2020,** *63* (3), 1156-1177.
303. Zang, J.; Peters, F.; Cambet, Y.; Cifuentes-Pagano, E.; Hissabu, M. M. S.; Dustin, C. M.; Svensson, L. H.; Olesen, M. M.; Poulsen, M. F. L.; Jacobsen, S.; Tuelung, P. S.; Narayanan, D.; Langkilde, A. E.; Gajhede, M.; Pagano, P. J.; Jaquet, V.; Vilhardt, F.; Bach, A., Targeting NOX2 with Bivalent Small-Molecule p47phox-p22phox Inhibitors. *J Med Chem* **2023,** *66* (21), 14963-15005.

304. Csanyi, G.; Cifuentes-Pagano, E.; Al Ghouleh, I.; Ranayhossaini, D. J.; Egana, L.; Lopes, L. R.; Jackson, H. M.; Kelley, E. E.; Pagano, P. J., Nox2 B-loop peptide, Nox2ds, specifically inhibits the NADPH oxidase Nox2. *Free Radic Biol Med* **2011,** *51* (6), 1116-25.
305. Quesada, I. M.; Lucero, A.; Amaya, C.; Meijles, D. N.; Cifuentes, M. E.; Pagano, P. J.; Castro, C., Selective inactivation of NADPH oxidase 2 causes regression of vascularization and the size and stability of atherosclerotic plaques. *Atherosclerosis* **2015,** *242* (2), 469-75.
306. Ranayhossaini, D. J.; Rodriguez, A. I.; Sahoo, S.; Chen, B. B.; Mallampalli, R. K.; Kelley, E. E.; Csanyi, G.; Gladwin, M. T.; Romero, G.; Pagano, P. J., Selective recapitulation of conserved and nonconserved regions of putative NOXA1 protein activation domain confers isoform-specific inhibition of Nox1 oxidase and attenuation of endothelial cell migration. *J Biol Chem* **2013,** *288* (51), 36437-50.
307. de Jesus, D. S.; DeVallance, E.; Li, Y.; Falabella, M.; Guimaraes, D.; Shiva, S.; Kaufman, B. A.; Gladwin, M. T.; Pagano, P. J., Nox1/Ref-1-mediated activation of CREB promotes Gremlin1-driven endothelial cell proliferation and migration. *Redox Biol* **2019,** *22*, 101138.
308. Reis, J.; Gorgulla, C.; Massari, M.; Marchese, S.; Valente, S.; Noce, B.; Basile, L.; Torner, R.; Cox, H., 3rd; Viennet, T.; Yang, M. H.; Ronan, M. M.; Rees, M. G.; Roth, J. A.; Capasso, L.; Nebbioso, A.; Altucci, L.; Mai, A.; Arthanari, H.; Mattevi, A., Targeting ROS production through inhibition of NADPH oxidases. *Nat Chem Biol* **2023,** *19* (12), 1540-1550.
309. Abdeldayem, A.; Raouf, Y. S.; Constantinescu, S. N.; Moriggl, R.; Gunning, P. T., Advances in covalent kinase inhibitors. *Chem Soc Rev* **2020,** *49* (9), 2617-2687.
310. Binda, C.; Hubalek, F.; Li, M.; Herzig, Y.; Sterling, J.; Edmondson, D. E.; Mattevi, A., Crystal structures of monoamine oxidase B in complex with four inhibitors of the N-propargylaminoindan class. *J Med Chem* **2004,** *47* (7), 1767-74.
311. Iacovino, L. G.; Magnani, F.; Binda, C., The structure of monoamine oxidases: past, present, and future. *J Neural Transm (Vienna)* **2018,** *125* (11), 1567-1579.
312. Singel, K. L.; Segal, B. H., NOX2-dependent regulation of inflammation. *Clin Sci (Lond)* **2016,** *130* (7), 479-90.
313. Cui, Y.; Liu, K. W.; Liang, Y.; Ip, M. S.; Mak, J. C., Inhibition of monoamine oxidase-B by selegiline reduces cigarette smoke-induced oxidative stress and inflammation in airway epithelial cells. *Toxicol Lett* **2017,** *268*, 44-50.
314. Won, W.; Choi, H. J.; Yoo, J. Y.; Kim, D.; Kim, T. Y.; Ju, Y.; Park, K. D.; Lee, H.; Jung, S. Y.; Lee, C. J., Inhibiting peripheral and central MAO-B ameliorates joint inflammation and cognitive impairment in rheumatoid arthritis. *Exp Mol Med* **2022,** *54* (8), 1188-1200.
315. An, H.; Heo, J. Y.; Lee, C. J.; Nam, M. H., The Pathological Role of Astrocytic MAOB in Parkinsonism Revealed by Genetic Ablation and Over-expression of MAOB. *Exp Neurobiol* **2021,** *30* (2), 113-119.

316. Shi, X.; Li, P.; Herb, M.; Liu, H.; Wang, M.; Wang, X.; Feng, Y.; van Beers, T.; Xia, N.; Li, H.; Prokosch, V., Pathological high intraocular pressure induces glial cell reactive proliferation contributing to neuroinflammation of the blood-retinal barrier via the NOX2/ET-1 axis-controlled ERK1/2 pathway. *J Neuroinflammation* **2024,** *21* (1), 105.
317. Putnins, E. E.; Goebeler, V.; Ostadkarampour, M., Monoamine Oxidase-B Inhibitor Reduction in Pro-Inflammatory Cytokines Mediated by Inhibition of cAMP-PKA/EPAC Signaling. *Front Pharmacol* **2021,** *12*, 741460.
318. Deczkowska, A.; Keren-Shaul, H.; Weiner, A.; Colonna, M.; Schwartz, M.; Amit, I., Disease-Associated Microglia: A Universal Immune Sensor of Neurodegeneration. *Cell* **2018,** *173* (5), 1073-1081.
319. Gao, C.; Jiang, J.; Tan, Y.; Chen, S., Microglia in neurodegenerative diseases: mechanism and potential therapeutic targets. *Signal Transduct Target Ther* **2023,** *8* (1), 359.
320. Gorgulla, C.; Boeszoermenyi, A.; Wang, Z. F.; Fischer, P. D.; Coote, P. W.; Padmanabha Das, K. M.; Malets, Y. S.; Radchenko, D. S.; Moroz, Y. S.; Scott, D. A.; Fackeldey, K.; Hoffmann, M.; Iavniuk, I.; Wagner, G.; Arthanari, H., An open-source drug discovery platform enables ultra-large virtual screens. *Nature* **2020,** *580* (7805), 663-668.
321. Sterling, T.; Irwin, J. J., ZINC 15--Ligand Discovery for Everyone. *J Chem Inf Model* **2015,** *55* (11), 2324-37.
322. Germon, Z. P.; Sillar, J. R.; Mannan, A.; Duchatel, R. J.; Staudt, D.; Murray, H. C.; Findlay, I. J.; Jackson, E. R.; McEwen, H. P.; Douglas, A. M.; McLachlan, T.; Schjenken, J. E.; Skerrett-Byrne, D. A.; Huang, H.; Melo-Braga, M. N.; Plank, M. W.; Alvaro, F.; Chamberlain, J.; De Iuliis, G.; Aitken, R. J.; Nixon, B.; Wei, A. H.; Enjeti, A. K.; Huang, Y.; Lock, R. B.; Larsen, M. R.; Lee, H.; Vaghjiani, V.; Cain, J. E.; de Bock, C. E.; Verrills, N. M.; Dun, M. D., Blockade of ROS production inhibits oncogenic signaling in acute myeloid leukemia and amplifies response to precision therapies. *Sci Signal* **2023,** *16* (778), eabp9586.
323. Cox, J. A.; Jeng, A. Y.; Sharkey, N. A.; Blumberg, P. M.; Tauber, A. I., Activation of the human neutrophil nicotinamide adenine dinucleotide phosphate (NADPH)-oxidase by protein kinase C. *J Clin Invest* **1985,** *76* (5), 1932-8.
324. Takashiba, S.; Van Dyke, T. E.; Amar, S.; Murayama, Y.; Soskolne, A. W.; Shapira, L., Differentiation of monocytes to macrophages primes cells for lipopolysaccharide stimulation via accumulation of cytoplasmic nuclear factor kappaB. *Infect Immun* **1999,** *67* (11), 5573-8.
325. Brune, B.; Dehne, N.; Grossmann, N.; Jung, M.; Namgaladze, D.; Schmid, T.; von Knethen, A.; Weigert, A., Redox control of inflammation in macrophages. *Antioxid Redox Signal* **2013,** *19* (6), 595-637.
326. Aydin, E.; Hallner, A.; Grauers Wiktorin, H.; Staffas, A.; Hellstrand, K.; Martner, A., NOX2 inhibition reduces oxidative stress and prolongs survival in murine KRAS-induced myeloproliferative disease. *Oncogene* **2019,** *38* (9), 1534-1543.

327. Jayavelu, A. K.; Moloney, J. N.; Bohmer, F. D.; Cotter, T. G., NOX-driven ROS formation in cell transformation of FLT3-ITD-positive AML. *Exp Hematol* **2016,** *44* (12), 1113-1122.
328. Paolillo, R.; Boulanger, M.; Gatel, P.; Gabellier, L.; De Toledo, M.; Tempe, D.; Hallal, R.; Akl, D.; Moreaux, J.; Baik, H.; Gueret, E.; Recher, C.; Sarry, J. E.; Cartron, G.; Piechaczyk, M.; Bossis, G., The NADPH oxidase NOX2 is a marker of adverse prognosis involved in chemoresistance of acute myeloid leukemias. *Haematologica* **2022,** *107* (11), 2562-2575.
329. Kean, K. M.; Carpenter, R. A.; Pandini, V.; Zanetti, G.; Hall, A. R.; Faber, R.; Aliverti, A.; Karplus, P. A., High-resolution studies of hydride transfer in the ferredoxin:NADP(+) reductase superfamily. *FEBS J* **2017,** *284* (19), 3302-3319.
330. Morris, G. M.; Huey, R.; Lindstrom, W.; Sanner, M. F.; Belew, R. K.; Goodsell, D. S.; Olson, A. J., AutoDock4 and AutoDockTools4: Automated docking with selective receptor flexibility. *J Comput Chem* **2009,** *30* (16), 2785-91.
331. Alhossary, A.; Handoko, S. D.; Mu, Y.; Kwoh, C. K., Fast, accurate, and reliable molecular docking with QuickVina 2. *Bioinformatics* **2015,** *31* (13), 2214-6.
332. Koes, D. R.; Baumgartner, M. P.; Camacho, C. J., Lessons learned in empirical scoring with smina from the CSAR 2011 benchmarking exercise. *J Chem Inf Model* **2013,** *53* (8), 1893-904.
333. Quiroga, R.; Villarreal, M. A., Vinardo: A Scoring Function Based on Autodock Vina Improves Scoring, Docking, and Virtual Screening. *PLoS One* **2016,** *11* (5), e0155183.
334. Sander, T.; Freyss, J.; von Korff, M.; Rufener, C., DataWarrior: an open-source program for chemistry aware data visualization and analysis. *J Chem Inf Model* **2015,** *55* (2), 460-73.
335. Durocher, Y.; Perret, S.; Kamen, A., High-level and high-throughput recombinant protein production by transient transfection of suspension-growing human 293-EBNA1 cells. *Nucleic Acids Res* **2002,** *30* (2), E9.
336. Zhang, J.; Liu, X.; Bell, A.; To, R.; Baral, T. N.; Azizi, A.; Li, J.; Cass, B.; Durocher, Y., Transient expression and purification of chimeric heavy chain antibodies. *Protein Expr Purif* **2009,** *65* (1), 77-82.
337. Zhao, B.; Summers, F. A.; Mason, R. P., Photooxidation of Amplex Red to resorufin: implications of exposing the Amplex Red assay to light. *Free Radic Biol Med* **2012,** *53* (5), 1080-7.
338. Kabsch, W., Xds. *Acta Crystallogr D Biol Crystallogr* **2010,** *66* (Pt 2), 125-32.
339. Winn, M. D.; Ballard, C. C.; Cowtan, K. D.; Dodson, E. J.; Emsley, P.; Evans, P. R.; Keegan, R. M.; Krissinel, E. B.; Leslie, A. G.; McCoy, A.; McNicholas, S. J.; Murshudov, G. N.; Pannu, N. S.; Potterton, E. A.; Powell, H. R.; Read, R. J.; Vagin, A.; Wilson, K. S., Overview of the CCP4 suite and current developments. *Acta Crystallogr D Biol Crystallogr* **2011,** *67* (Pt 4), 235-42.
340. Emsley, P.; Cowtan, K., Coot: model-building tools for molecular graphics. *Acta Crystallogr D Biol Crystallogr* **2004,** *60* (Pt 12 Pt 1), 2126-32.

341. Murshudov, G. N.; Skubak, P.; Lebedev, A. A.; Pannu, N. S.; Steiner, R. A.; Nicholls, R. A.; Winn, M. D.; Long, F.; Vagin, A. A., REFMAC5 for the refinement of macromolecular crystal structures. *Acta Crystallogr D Biol Crystallogr* **2011,** *67* (Pt 4), 355-67.
342. Pettersen, E. F.; Goddard, T. D.; Huang, C. C.; Couch, G. S.; Greenblatt, D. M.; Meng, E. C.; Ferrin, T. E., UCSF Chimera--a visualization system for exploratory research and analysis. *J Comput Chem* **2004,** *25* (13), 1605-12.
343. Yu, C.; Mannan, A. M.; Yvone, G. M.; Ross, K. N.; Zhang, Y. L.; Marton, M. A.; Taylor, B. R.; Crenshaw, A.; Gould, J. Z.; Tamayo, P.; Weir, B. A.; Tsherniak, A.; Wong, B.; Garraway, L. A.; Shamji, A. F.; Palmer, M. A.; Foley, M. A.; Winckler, W.; Schreiber, S. L.; Kung, A. L.; Golub, T. R., High-throughput identification of genotype-specific cancer vulnerabilities in mixtures of barcoded tumor cell lines. *Nat Biotechnol* **2016,** *34* (4), 419-23.
344. Corsello, S. M.; Nagari, R. T.; Spangler, R. D.; Rossen, J.; Kocak, M.; Bryan, J. G.; Humeidi, R.; Peck, D.; Wu, X.; Tang, A. A.; Wang, V. M.; Bender, S. A.; Lemire, E.; Narayan, R.; Montgomery, P.; Ben-David, U.; Garvie, C. W.; Chen, Y.; Rees, M. G.; Lyons, N. J.; McFarland, J. M.; Wong, B. T.; Wang, L.; Dumont, N.; O'Hearn, P. J.; Stefan, E.; Doench, J. G.; Harrington, C. N.; Greulich, H.; Meyerson, M.; Vazquez, F.; Subramanian, A.; Roth, J. A.; Bittker, J. A.; Boehm, J. S.; Mader, C. C.; Tsherniak, A.; Golub, T. R., Discovering the anti-cancer potential of non-oncology drugs by systematic viability profiling. *Nat Cancer* **2020,** *1* (2), 235-248.
345. Song, M. G.; Ryoo, I. G.; Choi, H. Y.; Choi, B. H.; Kim, S. T.; Heo, T. H.; Lee, J. Y.; Park, P. H.; Kwak, M. K., NRF2 Signaling Negatively Regulates Phorbol-12-Myristate-13-Acetate (PMA)-Induced Differentiation of Human Monocytic U937 Cells into Pro-Inflammatory Macrophages. *PLoS One* **2015,** *10* (7), e0134235.
346. Ianevski, A.; He, L.; Aittokallio, T.; Tang, J., SynergyFinder: a web application for analyzing drug combination dose-response matrix data. *Bioinformatics* **2017,** *33* (15), 2413-2415.
347. Song, N. Y.; Zhu, F.; Wang, Z.; Willette-Brown, J.; Xi, S.; Sun, Z.; Su, L.; Wu, X.; Ma, B.; Nussinov, R.; Xia, X.; Schrump, D. S.; Johnson, P. F.; Karin, M.; Hu, Y., IKKalpha inactivation promotes Kras-initiated lung adenocarcinoma development through disrupting major redox regulatory pathways. *Proc Natl Acad Sci U S A* **2018,** *115* (4), E812-E821.
348. Shaw, A. T.; Winslow, M. M.; Magendantz, M.; Ouyang, C.; Dowdle, J.; Subramanian, A.; Lewis, T. A.; Maglathin, R. L.; Tolliday, N.; Jacks, T., Selective killing of K-ras mutant cancer cells by small molecule inducers of oxidative stress. *Proc Natl Acad Sci U S A* **2011,** *108* (21), 8773-8.
349. Lim, J. K. M.; Leprivier, G., The impact of oncogenic RAS on redox balance and implications for cancer development. *Cell Death Dis* **2019,** *10* (12), 955.
350. Waddington, C. H., The epigenotype. 1942. *Int J Epidemiol* **2012,** *41* (1), 10-3.
351. Goldberg, A. D.; Allis, C. D.; Bernstein, E., Epigenetics: a landscape takes shape. *Cell* **2007,** *128* (4), 635-8.

352. Arrowsmith, C. H.; Bountra, C.; Fish, P. V.; Lee, K.; Schapira, M., Epigenetic protein families: a new frontier for drug discovery. *Nat Rev Drug Discov* **2012,** *11* (5), 384-400.
353. Merlin, C.; Liedvogel, M., The genetics and epigenetics of animal migration and orientation: birds, butterflies and beyond. *J Exp Biol* **2019,** *222* (Pt Suppl 1).
354. Luger, K.; Mader, A. W.; Richmond, R. K.; Sargent, D. F.; Richmond, T. J., Crystal structure of the nucleosome core particle at 2.8 A resolution. *Nature* **1997,** *389* (6648), 251-60.
355. Narlikar, G. J.; Sundaramoorthy, R.; Owen-Hughes, T., Mechanisms and functions of ATP-dependent chromatin-remodeling enzymes. *Cell* **2013,** *154* (3), 490-503.
356. Rhee, H. S.; Bataille, A. R.; Zhang, L.; Pugh, B. F., Subnucleosomal structures and nucleosome asymmetry across a genome. *Cell* **2014,** *159* (6), 1377-88.
357. Weber, C. M.; Henikoff, S., Histone variants: dynamic punctuation in transcription. *Genes Dev* **2014,** *28* (7), 672-82.
358. Strahl, B. D.; Allis, C. D., The language of covalent histone modifications. *Nature* **2000,** *403* (6765), 41-5.
359. Kouzarides, T., Chromatin modifications and their function. *Cell* **2007,** *128* (4), 693-705.
360. Portela, A.; Esteller, M., Epigenetic modifications and human disease. *Nat Biotechnol* **2010,** *28* (10), 1057-68.
361. Pfister, S. X.; Ashworth, A., Marked for death: targeting epigenetic changes in cancer. *Nat Rev Drug Discov* **2017,** *16* (4), 241-263.
362. Duan, Y. T.; Sangani, C. B.; Liu, W.; Soni, K. V.; Yao, Y., New Promises to Cure Cancer and Other Genetic Diseases/Disorders: Epi-drugs Through Epigenetics. *Curr Top Med Chem* **2019,** *19* (12), 972-994.
363. Turner, B. M., Cellular memory and the histone code. *Cell* **2002,** *111* (3), 285-91.
364. Holdgate, G. A.; Bardelle, C.; Lanne, A.; Read, J.; O'Donovan, D. H.; Smith, J. M.; Selmi, N.; Sheppard, R., Drug discovery for epigenetics targets. *Drug Discov Today* **2022,** *27* (4), 1088-1098.
365. Copeland, R. A.; Huryn, D. M., Special Issue on Epigenetics: Targeting Chromatin- and RNA- Modifications. *ACS Med Chem Lett* **2020,** *11* (11), 2051-2052.
366. Sterner, D. E.; Berger, S. L., Acetylation of histones and transcription-related factors. *Microbiol Mol Biol Rev* **2000,** *64* (2), 435-59.
367. Zhang, Y.; Reinberg, D., Transcription regulation by histone methylation: interplay between different covalent modifications of the core histone tails. *Genes Dev* **2001,** *15* (18), 2343-60.
368. Nowak, S. J.; Corces, V. G., Phosphorylation of histone H3: a balancing act between chromosome condensation and transcriptional activation. *Trends Genet* **2004,** *20* (4), 214-20.

369. Shilatifard, A., Chromatin modifications by methylation and ubiquitination: implications in the regulation of gene expression. *Annu Rev Biochem* **2006,** *75*, 243-69.
370. Nathan, D.; Ingvarsdottir, K.; Sterner, D. E.; Bylebyl, G. R.; Dokmanovic, M.; Dorsey, J. A.; Whelan, K. A.; Krsmanovic, M.; Lane, W. S.; Meluh, P. B.; Johnson, E. S.; Berger, S. L., Histone sumoylation is a negative regulator in Saccharomyces cerevisiae and shows dynamic interplay with positive-acting histone modifications. *Genes Dev* **2006,** *20* (8), 966-76.
371. Hassa, P. O.; Haenni, S. S.; Elser, M.; Hottiger, M. O., Nuclear ADP-ribosylation reactions in mammalian cells: where are we today and where are we going? *Microbiol Mol Biol Rev* **2006,** *70* (3), 789-829.
372. Cuthbert, G. L.; Daujat, S.; Snowden, A. W.; Erdjument-Bromage, H.; Hagiwara, T.; Yamada, M.; Schneider, R.; Gregory, P. D.; Tempst, P.; Bannister, A. J.; Kouzarides, T., Histone deimination antagonizes arginine methylation. *Cell* **2004,** *118* (5), 545-53.
373. Nelson, C. J.; Santos-Rosa, H.; Kouzarides, T., Proline isomerization of histone H3 regulates lysine methylation and gene expression. *Cell* **2006,** *126* (5), 905-16.
374. Jenuwein, T.; Allis, C. D., Translating the histone code. *Science* **2001,** *293* (5532), 1074-80.
375. Gaspar-Maia, A.; Alajem, A.; Meshorer, E.; Ramalho-Santos, M., Open chromatin in pluripotency and reprogramming. *Nat Rev Mol Cell Biol* **2011,** *12* (1), 36-47.
376. Margueron, R.; Trojer, P.; Reinberg, D., The key to development: interpreting the histone code? *Curr Opin Genet Dev* **2005,** *15* (2), 163-76.
377. Zentner, G. E.; Henikoff, S., Regulation of nucleosome dynamics by histone modifications. *Nat Struct Mol Biol* **2013,** *20* (3), 259-66.
378. Lai, W. K. M.; Pugh, B. F., Understanding nucleosome dynamics and their links to gene expression and DNA replication. *Nat Rev Mol Cell Biol* **2017,** *18* (9), 548-562.
379. Gregoretti, I. V.; Lee, Y. M.; Goodson, H. V., Molecular evolution of the histone deacetylase family: functional implications of phylogenetic analysis. *J Mol Biol* **2004,** *338* (1), 17-31.
380. de Ruijter, A. J.; van Gennip, A. H.; Caron, H. N.; Kemp, S.; van Kuilenburg, A. B., Histone deacetylases (HDACs): characterization of the classical HDAC family. *Biochem J* **2003,** *370* (Pt 3), 737-49.
381. Glozak, M. A.; Sengupta, N.; Zhang, X.; Seto, E., Acetylation and deacetylation of non-histone proteins. *Gene* **2005,** *363*, 15-23.
382. Di Giorgio, E.; Dalla, E.; Franforte, E.; Paluvai, H.; Minisini, M.; Trevisanut, M.; Picco, R.; Brancolini, C., Different class IIa HDACs repressive complexes regulate specific epigenetic responses related to cell survival in leiomyosarcoma cells. *Nucleic Acids Res* **2020,** *48* (2), 646-664.

383. Lahm, A.; Paolini, C.; Pallaoro, M.; Nardi, M. C.; Jones, P.; Neddermann, P.; Sambucini, S.; Bottomley, M. J.; Lo Surdo, P.; Carfi, A.; Koch, U.; De Francesco, R.; Steinkuhler, C.; Gallinari, P., Unraveling the hidden catalytic activity of vertebrate class IIa histone deacetylases. *Proc Natl Acad Sci U S A* **2007,** *104* (44), 17335-40.
384. Schuetz, A.; Min, J.; Allali-Hassani, A.; Schapira, M.; Shuen, M.; Loppnau, P.; Mazitschek, R.; Kwiatkowski, N. P.; Lewis, T. A.; Maglathin, R. L.; McLean, T. H.; Bochkarev, A.; Plotnikov, A. N.; Vedadi, M.; Arrowsmith, C. H., Human HDAC7 harbors a class IIa histone deacetylase-specific zinc binding motif and cryptic deacetylase activity. *J Biol Chem* **2008,** *283* (17), 11355-63.
385. Sauve, A. A.; Wolberger, C.; Schramm, V. L.; Boeke, J. D., The biochemistry of sirtuins. *Annu Rev Biochem* **2006,** *75*, 435-65.
386. Lambona, C.; Zwergel, C.; Valente, S.; Mai, A., SIRT3 Activation a Promise in Drug Development? New Insights into SIRT3 Biology and Its Implications on the Drug Discovery Process. *J Med Chem* **2024,** *67* (3), 1662-1689.
387. Zwergel, C.; Aventaggiato, M.; Garbo, S.; Di Bello, E.; Fassari, B.; Noce, B.; Castiello, C.; Lambona, C.; Barreca, F.; Rotili, D.; Fioravanti, R.; Schmalz, T.; Weyand, M.; Niedermeier, A.; Tripodi, M.; Colotti, G.; Steegborn, C.; Battistelli, C.; Tafani, M.; Valente, S.; Mai, A., Novel 1,4-Dihydropyridines as Specific Binders and Activators of SIRT3 Impair Cell Viability and Clonogenicity and Downregulate Hypoxia-Induced Targets in Cancer Cells. *J Med Chem* **2023,** *66* (14), 9622-9641.
388. Yoshida, M.; Kudo, N.; Kosono, S.; Ito, A., Chemical and structural biology of protein lysine deacetylases. *Proc Jpn Acad Ser B Phys Biol Sci* **2017,** *93* (5), 297-321.
389. Finnin, M. S.; Donigian, J. R.; Cohen, A.; Richon, V. M.; Rifkind, R. A.; Marks, P. A.; Breslow, R.; Pavletich, N. P., Structures of a histone deacetylase homologue bound to the TSA and SAHA inhibitors. *Nature* **1999,** *401* (6749), 188-93.
390. Seto, E.; Yoshida, M., Erasers of histone acetylation: the histone deacetylase enzymes. *Cold Spring Harb Perspect Biol* **2014,** *6* (4), a018713.
391. Kurdistani, S. K.; Grunstein, M., Histone acetylation and deacetylation in yeast. *Nat Rev Mol Cell Biol* **2003,** *4* (4), 276-84.
392. Yang, X. J.; Seto, E., Collaborative spirit of histone deacetylases in regulating chromatin structure and gene expression. *Curr Opin Genet Dev* **2003,** *13* (2), 143-53.
393. Heinzel, T.; Lavinsky, R. M.; Mullen, T. M.; Soderstrom, M.; Laherty, C. D.; Torchia, J.; Yang, W. M.; Brard, G.; Ngo, S. D.; Davie, J. R.; Seto, E.; Eisenman, R. N.; Rose, D. W.; Glass, C. K.; Rosenfeld, M. G., A complex containing N-CoR, mSin3 and histone deacetylase mediates transcriptional repression. *Nature* **1997,** *387* (6628), 43-8.
394. You, A.; Tong, J. K.; Grozinger, C. M.; Schreiber, S. L., CoREST is an integral component of the CoREST- human histone deacetylase complex. *Proc Natl Acad Sci U S A* **2001,** *98* (4), 1454-8.

395. Pflum, M. K.; Tong, J. K.; Lane, W. S.; Schreiber, S. L., Histone deacetylase 1 phosphorylation promotes enzymatic activity and complex formation. *J Biol Chem* **2001,** *276* (50), 47733-41.
396. Tsai, S. C.; Seto, E., Regulation of histone deacetylase 2 by protein kinase CK2. *J Biol Chem* **2002,** *277* (35), 31826-33.
397. Galasinski, S. C.; Resing, K. A.; Goodrich, J. A.; Ahn, N. G., Phosphatase inhibition leads to histone deacetylases 1 and 2 phosphorylation and disruption of corepressor interactions. *J Biol Chem* **2002,** *277* (22), 19618-26.
398. Brooks, C. L.; Gu, W., The impact of acetylation and deacetylation on the p53 pathway. *Protein Cell* **2011,** *2* (6), 456-62.
399. Luo, J.; Su, F.; Chen, D.; Shiloh, A.; Gu, W., Deacetylation of p53 modulates its effect on cell growth and apoptosis. *Nature* **2000,** *408* (6810), 377-81.
400. Lagger, G.; O'Carroll, D.; Rembold, M.; Khier, H.; Tischler, J.; Weitzer, G.; Schuettengruber, B.; Hauser, C.; Brunmeir, R.; Jenuwein, T.; Seiser, C., Essential function of histone deacetylase 1 in proliferation control and CDK inhibitor repression. *EMBO J* **2002,** *21* (11), 2672-81.
401. Zupkovitz, G.; Tischler, J.; Posch, M.; Sadzak, I.; Ramsauer, K.; Egger, G.; Grausenburger, R.; Schweifer, N.; Chiocca, S.; Decker, T.; Seiser, C., Negative and positive regulation of gene expression by mouse histone deacetylase 1. *Mol Cell Biol* **2006,** *26* (21), 7913-28.
402. Montgomery, R. L.; Davis, C. A.; Potthoff, M. J.; Haberland, M.; Fielitz, J.; Qi, X.; Hill, J. A.; Richardson, J. A.; Olson, E. N., Histone deacetylases 1 and 2 redundantly regulate cardiac morphogenesis, growth, and contractility. *Genes Dev* **2007,** *21* (14), 1790-802.
403. Guenther, M. G.; Barak, O.; Lazar, M. A., The SMRT and N-CoR corepressors are activating cofactors for histone deacetylase 3. *Mol Cell Biol* **2001,** *21* (18), 6091-101.
404. Yang, W. M.; Tsai, S. C.; Wen, Y. D.; Fejer, G.; Seto, E., Functional domains of histone deacetylase-3. *J Biol Chem* **2002,** *277* (11), 9447-54.
405. Zhang, X.; Ozawa, Y.; Lee, H.; Wen, Y. D.; Tan, T. H.; Wadzinski, B. E.; Seto, E., Histone deacetylase 3 (HDAC3) activity is regulated by interaction with protein serine/threonine phosphatase 4. *Genes Dev* **2005,** *19* (7), 827-39.
406. Bardai, F. H.; D'Mello, S. R., Selective toxicity by HDAC3 in neurons: regulation by Akt and GSK3beta. *J Neurosci* **2011,** *31* (5), 1746-51.
407. Knutson, S. K.; Chyla, B. J.; Amann, J. M.; Bhaskara, S.; Huppert, S. S.; Hiebert, S. W., Liver-specific deletion of histone deacetylase 3 disrupts metabolic transcriptional networks. *EMBO J* **2008,** *27* (7), 1017-28.
408. Montgomery, R. L.; Potthoff, M. J.; Haberland, M.; Qi, X.; Matsuzaki, S.; Humphries, K. M.; Richardson, J. A.; Bassel-Duby, R.; Olson, E. N., Maintenance of cardiac energy metabolism by histone deacetylase 3 in mice. *J Clin Invest* **2008,** *118* (11), 3588-97.

409. Lee, H.; Rezai-Zadeh, N.; Seto, E., Negative regulation of histone deacetylase 8 activity by cyclic AMP-dependent protein kinase A. *Mol Cell Biol* **2004,** *24* (2), 765-73.
410. Somoza, J. R.; Skene, R. J.; Katz, B. A.; Mol, C.; Ho, J. D.; Jennings, A. J.; Luong, C.; Arvai, A.; Buggy, J. J.; Chi, E.; Tang, J.; Sang, B. C.; Verner, E.; Wynands, R.; Leahy, E. M.; Dougan, D. R.; Snell, G.; Navre, M.; Knuth, M. W.; Swanson, R. V.; McRee, D. E.; Tari, L. W., Structural snapshots of human HDAC8 provide insights into the class I histone deacetylases. *Structure* **2004,** *12* (7), 1325-34.
411. Bertos, N. R.; Wang, A. H.; Yang, X. J., Class II histone deacetylases: structure, function, and regulation. *Biochem Cell Biol* **2001,** *79* (3), 243-52.
412. McKinsey, T. A.; Zhang, C. L.; Lu, J.; Olson, E. N., Signal-dependent nuclear export of a histone deacetylase regulates muscle differentiation. *Nature* **2000,** *408* (6808), 106-11.
413. McKinsey, T. A.; Zhang, C. L.; Olson, E. N., Control of muscle development by dueling HATs and HDACs. *Curr Opin Genet Dev* **2001,** *11* (5), 497-504.
414. Lu, J.; McKinsey, T. A.; Zhang, C. L.; Olson, E. N., Regulation of skeletal myogenesis by association of the MEF2 transcription factor with class II histone deacetylases. *Mol Cell* **2000,** *6* (2), 233-44.
415. Youn, H. D.; Grozinger, C. M.; Liu, J. O., Calcium regulates transcriptional repression of myocyte enhancer factor 2 by histone deacetylase 4. *J Biol Chem* **2000,** *275* (29), 22563-7.
416. Fischle, W.; Dequiedt, F.; Hendzel, M. J.; Guenther, M. G.; Lazar, M. A.; Voelter, W.; Verdin, E., Enzymatic activity associated with class II HDACs is dependent on a multiprotein complex containing HDAC3 and SMRT/N-CoR. *Mol Cell* **2002,** *9* (1), 45-57.
417. Fischle, W.; Dequiedt, F.; Fillion, M.; Hendzel, M. J.; Voelter, W.; Verdin, E., Human HDAC7 histone deacetylase activity is associated with HDAC3 in vivo. *J Biol Chem* **2001,** *276* (38), 35826-35.
418. Zhang, C. L.; McKinsey, T. A.; Chang, S.; Antos, C. L.; Hill, J. A.; Olson, E. N., Class II histone deacetylases act as signal-responsive repressors of cardiac hypertrophy. *Cell* **2002,** *110* (4), 479-88.
419. Chang, S.; McKinsey, T. A.; Zhang, C. L.; Richardson, J. A.; Hill, J. A.; Olson, E. N., Histone deacetylases 5 and 9 govern responsiveness of the heart to a subset of stress signals and play redundant roles in heart development. *Mol Cell Biol* **2004,** *24* (19), 8467-76.
420. Vega, R. B.; Matsuda, K.; Oh, J.; Barbosa, A. C.; Yang, X.; Meadows, E.; McAnally, J.; Pomajzl, C.; Shelton, J. M.; Richardson, J. A.; Karsenty, G.; Olson, E. N., Histone deacetylase 4 controls chondrocyte hypertrophy during skeletogenesis. *Cell* **2004,** *119* (4), 555-66.
421. Chang, S.; Young, B. D.; Li, S.; Qi, X.; Richardson, J. A.; Olson, E. N., Histone deacetylase 7 maintains vascular integrity by repressing matrix metalloproteinase 10. *Cell* **2006,** *126* (2), 321-34.

422. Song, K.; Backs, J.; McAnally, J.; Qi, X.; Gerard, R. D.; Richardson, J. A.; Hill, J. A.; Bassel-Duby, R.; Olson, E. N., The transcriptional coactivator CAMTA2 stimulates cardiac growth by opposing class II histone deacetylases. *Cell* **2006,** *125* (3), 453-66.
423. Karsenty, G., The complexities of skeletal biology. *Nature* **2003,** *423* (6937), 316-8.
424. Cohen, M. M., Jr., The new bone biology: pathologic, molecular, and clinical correlates. *Am J Med Genet A* **2006,** *140* (23), 2646-706.
425. Arnold, M. A.; Kim, Y.; Czubryt, M. P.; Phan, D.; McAnally, J.; Qi, X.; Shelton, J. M.; Richardson, J. A.; Bassel-Duby, R.; Olson, E. N., MEF2C transcription factor controls chondrocyte hypertrophy and bone development. *Dev Cell* **2007,** *12* (3), 377-89.
426. Verdin, E.; Dequiedt, F.; Kasler, H. G., Class II histone deacetylases: versatile regulators. *Trends Genet* **2003,** *19* (5), 286-93.
427. Liu, Y.; Li, L.; Min, J., Structural biology: HDAC6 finally crystal clear. *Nat Chem Biol* **2016,** *12* (9), 660-1.
428. Hai, Y.; Christianson, D. W., Histone deacetylase 6 structure and molecular basis of catalysis and inhibition. *Nat Chem Biol* **2016,** *12* (9), 741-7.
429. Qu, M.; Zhang, H.; Cheng, P.; Wubshet, A. K.; Yin, X.; Wang, X.; Sun, Y., Histone deacetylase 6's function in viral infection, innate immunity, and disease: latest advances. *Front Immunol* **2023,** *14*, 1216548.
430. Ustinova, K.; Novakova, Z.; Saito, M.; Meleshin, M.; Mikesova, J.; Kutil, Z.; Baranova, P.; Havlinova, B.; Schutkowski, M.; Matthias, P.; Barinka, C., The disordered N-terminus of HDAC6 is a microtubule-binding domain critical for efficient tubulin deacetylation. *J Biol Chem* **2020,** *295* (9), 2614-2628.
431. Hubbert, C.; Guardiola, A.; Shao, R.; Kawaguchi, Y.; Ito, A.; Nixon, A.; Yoshida, M.; Wang, X. F.; Yao, T. P., HDAC6 is a microtubule-associated deacetylase. *Nature* **2002,** *417* (6887), 455-8.
432. Li, Y.; Shin, D.; Kwon, S. H., Histone deacetylase 6 plays a role as a distinct regulator of diverse cellular processes. *FEBS J* **2013,** *280* (3), 775-93.
433. Kawaguchi, Y.; Kovacs, J. J.; McLaurin, A.; Vance, J. M.; Ito, A.; Yao, T. P., The deacetylase HDAC6 regulates aggresome formation and cell viability in response to misfolded protein stress. *Cell* **2003,** *115* (6), 727-38.
434. Kao, H. Y.; Lee, C. H.; Komarov, A.; Han, C. C.; Evans, R. M., Isolation and characterization of mammalian HDAC10, a novel histone deacetylase. *J Biol Chem* **2002,** *277* (1), 187-93.
435. Cheng, F.; Zheng, B.; Wang, J.; Zhao, G.; Yao, Z.; Niu, Z.; He, W., Histone deacetylase 10, a potential epigenetic target for therapy. *Biosci Rep* **2021,** *41* (6).
436. Lambona, C.; Zwergel, C.; Fioravanti, R.; Valente, S.; Mai, A., Histone deacetylase 10: A polyamine deacetylase from the crystal structure to the first inhibitors. *Curr Opin Struct Biol* **2023,** *82*, 102668.

437. Hai, Y.; Shinsky, S. A.; Porter, N. J.; Christianson, D. W., Histone deacetylase 10 structure and molecular function as a polyamine deacetylase. *Nat Commun* **2017,** *8*, 15368.
438. Moreno-Yruela, C.; Galleano, I.; Madsen, A. S.; Olsen, C. A., Histone Deacetylase 11 Is an epsilon-N-Myristoyllysine Hydrolase. *Cell Chem Biol* **2018,** *25* (7), 849-856 e8.
439. Kutil, Z.; Novakova, Z.; Meleshin, M.; Mikesova, J.; Schutkowski, M.; Barinka, C., Histone Deacetylase 11 Is a Fatty-Acid Deacylase. *ACS Chem Biol* **2018,** *13* (3), 685-693.
440. Cao, J.; Sun, L.; Aramsangtienchai, P.; Spiegelman, N. A.; Zhang, X.; Huang, W.; Seto, E.; Lin, H., HDAC11 regulates type I interferon signaling through defatty-acylation of SHMT2. *Proc Natl Acad Sci U S A* **2019,** *116* (12), 5487-5492.
441. Zhang, Y.; Fang, H.; Jiao, J.; Xu, W., The structure and function of histone deacetylases: the target for anti-cancer therapy. *Curr Med Chem* **2008,** *15* (27), 2840-9.
442. Witt, O.; Deubzer, H. E.; Milde, T.; Oehme, I., HDAC family: What are the cancer relevant targets? *Cancer Lett* **2009,** *277* (1), 8-21.
443. Pasqualucci, L.; Bereshchenko, O.; Niu, H.; Klein, U.; Basso, K.; Guglielmino, R.; Cattoretti, G.; Dalla-Favera, R., Molecular pathogenesis of non-Hodgkin's lymphoma: the role of Bcl-6. *Leuk Lymphoma* **2003,** *44 Suppl 3*, S5-12.
444. Senese, S.; Zaragoza, K.; Minardi, S.; Muradore, I.; Ronzoni, S.; Passafaro, A.; Bernard, L.; Draetta, G. F.; Alcalay, M.; Seiser, C.; Chiocca, S., Role for histone deacetylase 1 in human tumor cell proliferation. *Mol Cell Biol* **2007,** *27* (13), 4784-95.
445. Halkidou, K.; Gaughan, L.; Cook, S.; Leung, H. Y.; Neal, D. E.; Robson, C. N., Upregulation and nuclear recruitment of HDAC1 in hormone refractory prostate cancer. *Prostate* **2004,** *59* (2), 177-89.
446. Harms, K. L.; Chen, X., Histone deacetylase 2 modulates p53 transcriptional activities through regulation of p53-DNA binding activity. *Cancer Res* **2007,** *67* (7), 3145-52.
447. Keshelava, N.; Davicioni, E.; Wan, Z.; Ji, L.; Sposto, R.; Triche, T. J.; Reynolds, C. P., Histone deacetylase 1 gene expression and sensitization of multidrug-resistant neuroblastoma cell lines to cytotoxic agents by depsipeptide. *J Natl Cancer Inst* **2007,** *99* (14), 1107-19.
448. Kato, H.; Tamamizu-Kato, S.; Shibasaki, F., Histone deacetylase 7 associates with hypoxia-inducible factor 1alpha and increases transcriptional activity. *J Biol Chem* **2004,** *279* (40), 41966-74.
449. Mottet, D.; Bellahcene, A.; Pirotte, S.; Waltregny, D.; Deroanne, C.; Lamour, V.; Lidereau, R.; Castronovo, V., Histone deacetylase 7 silencing alters endothelial cell migration, a key step in angiogenesis. *Circ Res* **2007,** *101* (12), 1237-46.
450. Qian, D. Z.; Kachhap, S. K.; Collis, S. J.; Verheul, H. M.; Carducci, M. A.; Atadja, P.; Pili, R., Class II histone deacetylases are associated with VHL-

independent regulation of hypoxia-inducible factor 1 alpha. *Cancer Res* **2006,** *66* (17), 8814-21.
451. Park, J. H.; Kim, S. H.; Choi, M. C.; Lee, J.; Oh, D. Y.; Im, S. A.; Bang, Y. J.; Kim, T. Y., Class II histone deacetylases play pivotal roles in heat shock protein 90-mediated proteasomal degradation of vascular endothelial growth factor receptors. *Biochem Biophys Res Commun* **2008,** *368* (2), 318-22.
452. Kwon, H. J.; Kim, M. S.; Kim, M. J.; Nakajima, H.; Kim, K. W., Histone deacetylase inhibitor FK228 inhibits tumor angiogenesis. *Int J Cancer* **2002,** *97* (3), 290-6.
453. Whetstine, J. R.; Ceron, J.; Ladd, B.; Dufourcq, P.; Reinke, V.; Shi, Y., Regulation of tissue-specific and extracellular matrix-related genes by a class I histone deacetylase. *Mol Cell* **2005,** *18* (4), 483-90.
454. Kim, J. H.; Kim, B.; Cai, L.; Choi, H. J.; Ohgi, K. A.; Tran, C.; Chen, C.; Chung, C. H.; Huber, O.; Rose, D. W.; Sawyers, C. L.; Rosenfeld, M. G.; Baek, S. H., Transcriptional regulation of a metastasis suppressor gene by Tip60 and beta-catenin complexes. *Nature* **2005,** *434* (7035), 921-6.
455. Liu, L. T.; Chang, H. C.; Chiang, L. C.; Hung, W. C., Histone deacetylase inhibitor up-regulates RECK to inhibit MMP-2 activation and cancer cell invasion. *Cancer Res* **2003,** *63* (12), 3069-72.
456. Dong, J. T.; Lamb, P. W.; Rinker-Schaeffer, C. W.; Vukanovic, J.; Ichikawa, T.; Isaacs, J. T.; Barrett, J. C., KAI1, a metastasis suppressor gene for prostate cancer on human chromosome 11p11.2. *Science* **1995,** *268* (5212), 884-6.
457. Mazumdar, A.; Wang, R. A.; Mishra, S. K.; Adam, L.; Bagheri-Yarmand, R.; Mandal, M.; Vadlamudi, R. K.; Kumar, R., Transcriptional repression of oestrogen receptor by metastasis-associated protein 1 corepressor. *Nat Cell Biol* **2001,** *3* (1), 30-7.
458. Haggarty, S. J.; Koeller, K. M.; Wong, J. C.; Grozinger, C. M.; Schreiber, S. L., Domain-selective small-molecule inhibitor of histone deacetylase 6 (HDAC6)-mediated tubulin deacetylation. *Proc Natl Acad Sci U S A* **2003,** *100* (8), 4389-94.
459. Sehn, L. H.; Salles, G., Diffuse Large B-Cell Lymphoma. *N Engl J Med* **2021,** *384* (9), 842-858.
460. Fan, L.; Li, L.; Zhou, Y.; Li, J., Rituximab-Based Therapy in Newly Diagnosed Diffuse Large B-Cell Lymphoma Patients: Individualized Risk-Adapted Therapy Approach Using Molecular Subtypes. *J Hematol* **2017,** *6* (2-3), 33-43.
461. Wu, C.; Song, Q.; Gao, S.; Wu, S., Targeting HDACs for diffuse large B-cell lymphoma therapy. *Sci Rep* **2024,** *14* (1), 289.
462. Zhang, H.; Chi, F.; Qin, K.; Mu, X.; Wang, L.; Yang, B.; Wang, Y.; Bai, M.; Li, Z.; Su, L.; Yu, B., Chidamide induces apoptosis in DLBCL cells by suppressing the HDACs/STAT3/Bcl-2 pathway. *Mol Med Rep* **2021,** *23* (5).
463. Porta, C.; Paglino, C.; Mosca, A., Targeting PI3K/Akt/mTOR Signaling in Cancer. *Front Oncol* **2014,** *4*, 64.

464. Yang, Q.; Jiang, W.; Hou, P., Emerging role of PI3K/AKT in tumor-related epigenetic regulation. *Semin Cancer Biol* **2019,** *59*, 112-124.
465. Min, S. K.; Koh, Y. H.; Park, Y.; Kim, H. J.; Seo, J.; Park, H. R.; Cho, S. J.; Kim, I. S., Expression of HAT1 and HDAC1, 2, 3 in Diffuse Large B-Cell Lymphomas, Peripheral T-Cell Lymphomas, and NK/T-Cell Lymphomas. *Korean J Pathol* **2012,** *46* (2), 142-50.
466. Panjwani, P. K.; Charu, V.; DeLisser, M.; Molina-Kirsch, H.; Natkunam, Y.; Zhao, S., Programmed death-1 ligands PD-L1 and PD-L2 show distinctive and restricted patterns of expression in lymphoma subtypes. *Hum Pathol* **2018,** *71*, 91-99.
467. Hopken, U. E., Targeting HDAC3 in CREBBP-Mutant Lymphomas Counterstrikes Unopposed Enhancer Deacetylation of B-cell Signaling and Immune Response Genes. *Cancer Discov* **2017,** *7* (1), 14-16.
468. Rettig, I.; Koeneke, E.; Trippel, F.; Mueller, W. C.; Burhenne, J.; Kopp-Schneider, A.; Fabian, J.; Schober, A.; Fernekorn, U.; von Deimling, A.; Deubzer, H. E.; Milde, T.; Witt, O.; Oehme, I., Selective inhibition of HDAC8 decreases neuroblastoma growth in vitro and in vivo and enhances retinoic acid-mediated differentiation. *Cell Death Dis* **2015,** *6* (2), e1657.
469. Pizzi, M.; Margolskee, E.; Inghirami, G., Pathogenesis of Peripheral T Cell Lymphoma. *Annu Rev Pathol* **2018,** *13*, 293-320.
470. Piccaluga, P. P.; Tabanelli, V.; Pileri, S. A., Molecular genetics of peripheral T-cell lymphomas. *Int J Hematol* **2014,** *99* (3), 219-26.
471. Van Arnam, J. S.; Lim, M. S.; Elenitoba-Johnson, K. S. J., Novel insights into the pathogenesis of T-cell lymphomas. *Blood* **2018,** *131* (21), 2320-2330.
472. Wang, P.; Wang, Z.; Liu, J., Role of HDACs in normal and malignant hematopoiesis. *Mol Cancer* **2020,** *19* (1), 5.
473. Yu, X.; Li, H.; Zhu, M.; Hu, P.; Liu, X.; Qing, Y.; Wang, X.; Wang, H.; Wang, Z.; Xu, J.; Tan, R.; Guo, Q.; Hui, H., Involvement of p53 Acetylation in Growth Suppression of Cutaneous T-Cell Lymphomas Induced by HDAC Inhibition. *J Invest Dermatol* **2020,** *140* (10), 2009-2022 e4.
474. Irimia, R.; Piccaluga, P. P., Histone Deacetylase Inhibitors for Peripheral T-Cell Lymphomas. *Cancers (Basel)* **2024,** *16* (19).
475. Xie, C.; Li, X.; Zeng, H.; Qian, W., Molecular insights into pathogenesis and targeted therapy of peripheral T cell lymphoma. *Exp Hematol Oncol* **2020,** *9* (1), 30.
476. Li, Y.; Seto, E., HDACs and HDAC Inhibitors in Cancer Development and Therapy. *Cold Spring Harb Perspect Med* **2016,** *6* (10).
477. Saha, R. N.; Pahan, K., HATs and HDACs in neurodegeneration: a tale of disconcerted acetylation homeostasis. *Cell Death Differ* **2006,** *13* (4), 539-50.
478. Ryu, H.; Lee, J.; Olofsson, B. A.; Mwidau, A.; Dedeoglu, A.; Escudero, M.; Flemington, E.; Azizkhan-Clifford, J.; Ferrante, R. J.; Ratan, R. R., Histone deacetylase inhibitors prevent oxidative neuronal death independent of expanded polyglutamine repeats via an Sp1-dependent pathway. *Proc Natl Acad Sci U S A* **2003,** *100* (7), 4281-6.

479. Chuang, D. M.; Leng, Y.; Marinova, Z.; Kim, H. J.; Chiu, C. T., Multiple roles of HDAC inhibition in neurodegenerative conditions. *Trends Neurosci* **2009,** *32* (11), 591-601.
480. Harrison, I. F.; Dexter, D. T., Epigenetic targeting of histone deacetylase: therapeutic potential in Parkinson's disease? *Pharmacol Ther* **2013,** *140* (1), 34-52.
481. Graff, J.; Rei, D.; Guan, J. S.; Wang, W. Y.; Seo, J.; Hennig, K. M.; Nieland, T. J.; Fass, D. M.; Kao, P. F.; Kahn, M.; Su, S. C.; Samiei, A.; Joseph, N.; Haggarty, S. J.; Delalle, I.; Tsai, L. H., An epigenetic blockade of cognitive functions in the neurodegenerating brain. *Nature* **2012,** *483* (7388), 222-6.
482. Ding, H.; Dolan, P. J.; Johnson, G. V., Histone deacetylase 6 interacts with the microtubule-associated protein tau. *J Neurochem* **2008,** *106* (5), 2119-30.
483. Zhang, L.; Qin, X.; Zhao, Y.; Fast, L.; Zhuang, S.; Liu, P.; Cheng, G.; Zhao, T. C., Inhibition of histone deacetylases preserves myocardial performance and prevents cardiac remodeling through stimulation of endogenous angiomyogenesis. *J Pharmacol Exp Ther* **2012,** *341* (1), 285-93.
484. Mani, S. K.; Kern, C. B.; Kimbrough, D.; Addy, B.; Kasiganesan, H.; Rivers, W. T.; Patel, R. K.; Chou, J. C.; Spinale, F. G.; Mukherjee, R.; Menick, D. R., Inhibition of class I histone deacetylase activity represses matrix metalloproteinase-2 and -9 expression and preserves LV function postmyocardial infarction. *Am J Physiol Heart Circ Physiol* **2015,** *308* (11), H1391-401.
485. Kee, H. J.; Sohn, I. S.; Nam, K. I.; Park, J. E.; Qian, Y. R.; Yin, Z.; Ahn, Y.; Jeong, M. H.; Bang, Y. J.; Kim, N.; Kim, J. K.; Kim, K. K.; Epstein, J. A.; Kook, H., Inhibition of histone deacetylation blocks cardiac hypertrophy induced by angiotensin II infusion and aortic banding. *Circulation* **2006,** *113* (1), 51-9.
486. Gallo, P.; Latronico, M. V.; Gallo, P.; Grimaldi, S.; Borgia, F.; Todaro, M.; Jones, P.; Gallinari, P.; De Francesco, R.; Ciliberto, G.; Steinkuhler, C.; Esposito, G.; Condorelli, G., Inhibition of class I histone deacetylase with an apicidin derivative prevents cardiac hypertrophy and failure. *Cardiovasc Res* **2008,** *80* (3), 416-24.
487. Cho, Y. K.; Eom, G. H.; Kee, H. J.; Kim, H. S.; Choi, W. Y.; Nam, K. I.; Ma, J. S.; Kook, H., Sodium valproate, a histone deacetylase inhibitor, but not captopril, prevents right ventricular hypertrophy in rats. *Circ J* **2010,** *74* (4), 760-70.
488. Chen, Y.; Du, J.; Zhao, Y. T.; Zhang, L.; Lv, G.; Zhuang, S.; Qin, G.; Zhao, T. C., Histone deacetylase (HDAC) inhibition improves myocardial function and prevents cardiac remodeling in diabetic mice. *Cardiovasc Diabetol* **2015,** *14*, 99.
489. Fan, X. D.; Wan, L. L.; Duan, M.; Lu, S., HDAC11 deletion reduces fructose-induced cardiac dyslipidemia, apoptosis and inflammation by attenuating oxidative stress injury. *Biochem Biophys Res Commun* **2018,** *503* (2), 444-451.
490. Granger, A.; Abdullah, I.; Huebner, F.; Stout, A.; Wang, T.; Huebner, T.; Epstein, J. A.; Gruber, P. J., Histone deacetylase inhibition reduces myocardial ischemia-reperfusion injury in mice. *FASEB J* **2008,** *22* (10), 3549-60.

491. Xie, M.; Kong, Y.; Tan, W.; May, H.; Battiprolu, P. K.; Pedrozo, Z.; Wang, Z. V.; Morales, C.; Luo, X.; Cho, G.; Jiang, N.; Jessen, M. E.; Warner, J. J.; Lavandero, S.; Gillette, T. G.; Turer, A. T.; Hill, J. A., Histone deacetylase inhibition blunts ischemia/reperfusion injury by inducing cardiomyocyte autophagy. *Circulation* **2014,** *129* (10), 1139-51.
492. Leoni, F.; Zaliani, A.; Bertolini, G.; Porro, G.; Pagani, P.; Pozzi, P.; Dona, G.; Fossati, G.; Sozzani, S.; Azam, T.; Bufler, P.; Fantuzzi, G.; Goncharov, I.; Kim, S. H.; Pomerantz, B. J.; Reznikov, L. L.; Siegmund, B.; Dinarello, C. A.; Mascagni, P., The antitumor histone deacetylase inhibitor suberoylanilide hydroxamic acid exhibits antiinflammatory properties via suppression of cytokines. *Proc Natl Acad Sci U S A* **2002,** *99* (5), 2995-3000.
493. Hu, Y.; Suliman, B. A., Roles of HDACs in the Responses of Innate Immune Cells and as Targets in Inflammatory Diseases. *Adv Exp Med Biol* **2017,** *1024*, 91-110.
494. Stazi, G.; Fioravanti, R.; Mai, A.; Mattevi, A.; Valente, S., Histone deacetylases as an epigenetic pillar for the development of hybrid inhibitors in cancer. *Curr Opin Chem Biol* **2019,** *50*, 89-100.
495. Di Bello, E.; Noce, B.; Fioravanti, R.; Mai, A., Current HDAC Inhibitors in Clinical Trials. *Chimia (Aarau)* **2022,** *76* (5), 448-453.
496. Falkenberg, K. J.; Johnstone, R. W., Histone deacetylases and their inhibitors in cancer, neurological diseases and immune disorders. *Nat Rev Drug Discov* **2014,** *13* (9), 673-91.
497. McClure, J. J.; Zhang, C.; Inks, E. S.; Peterson, Y. K.; Li, J.; Chou, C. J., Development of Allosteric Hydrazide-Containing Class I Histone Deacetylase Inhibitors for Use in Acute Myeloid Leukemia. *J Med Chem* **2016,** *59* (21), 9942-9959.
498. Yoshida, M.; Kijima, M.; Akita, M.; Beppu, T., Potent and specific inhibition of mammalian histone deacetylase both in vivo and in vitro by trichostatin A. *J Biol Chem* **1990,** *265* (28), 17174-9.
499. Marks, P. A.; Breslow, R., Dimethyl sulfoxide to vorinostat: development of this histone deacetylase inhibitor as an anticancer drug. *Nat Biotechnol* **2007,** *25* (1), 84-90.
500. Vanommeslaeghe, K.; Van Alsenoy, C.; De Proft, F.; Martins, J. C.; Tourwe, D.; Geerlings, P., Ab initio study of the binding of Trichostatin A (TSA) in the active site of histone deacetylase like protein (HDLP). *Org Biomol Chem* **2003,** *1* (16), 2951-7.
501. Shi, W.; Lawrence, Y. R.; Choy, H.; Werner-Wasik, M.; Andrews, D. W.; Evans, J. J.; Judy, K. D.; Farrell, C. J.; Moshel, Y.; Berger, A. C.; Bar-Ad, V.; Dicker, A. P., Vorinostat as a radiosensitizer for brain metastasis: a phase I clinical trial. *J Neurooncol* **2014,** *118* (2), 313-319.
502. Xue, K.; Gu, J. J.; Zhang, Q.; Mavis, C.; Hernandez-Ilizaliturri, F. J.; Czuczman, M. S.; Guo, Y., Vorinostat, a histone deacetylase (HDAC) inhibitor, promotes cell cycle arrest and re-sensitizes rituximab- and chemo-resistant

lymphoma cells to chemotherapy agents. *J Cancer Res Clin Oncol* **2016,** *142* (2), 379-87.
503. Cai, Y. Y.; Yap, C. W.; Wang, Z.; Ho, P. C.; Chan, S. Y.; Ng, K. Y.; Ge, Z. G.; Lin, H. S., Solubilization of vorinostat by cyclodextrins. *J Clin Pharm Ther* **2010,** *35* (5), 521-6.
504. Konsoula, Z.; Cao, H.; Velena, A.; Jung, M., Adamantanyl-histone deacetylase inhibitor H6CAHA exhibits favorable pharmacokinetics and augments prostate cancer radiation sensitivity. *Int J Radiat Oncol Biol Phys* **2011,** *79* (5), 1541-8.
505. Mann, B. S.; Johnson, J. R.; Cohen, M. H.; Justice, R.; Pazdur, R., FDA approval summary: vorinostat for treatment of advanced primary cutaneous T-cell lymphoma. *Oncologist* **2007,** *12* (10), 1247-52.
506. VanderMolen, K. M.; McCulloch, W.; Pearce, C. J.; Oberlies, N. H., Romidepsin (Istodax, NSC 630176, FR901228, FK228, depsipeptide): a natural product recently approved for cutaneous T-cell lymphoma. *J Antibiot (Tokyo)* **2011,** *64* (8), 525-31.
507. Ho, T. C. S.; Chan, A. H. Y.; Ganesan, A., Thirty Years of HDAC Inhibitors: 2020 Insight and Hindsight. *J Med Chem* **2020,** *63* (21), 12460-12484.
508. Furumai, R.; Matsuyama, A.; Kobashi, N.; Lee, K. H.; Nishiyama, M.; Nakajima, H.; Tanaka, A.; Komatsu, Y.; Nishino, N.; Yoshida, M.; Horinouchi, S., FK228 (depsipeptide) as a natural prodrug that inhibits class I histone deacetylases. *Cancer Res* **2002,** *62* (17), 4916-21.
509. Laubach, J. P.; Moreau, P.; San-Miguel, J. F.; Richardson, P. G., Panobinostat for the Treatment of Multiple Myeloma. *Clin Cancer Res* **2015,** *21* (21), 4767-73.
510. Poole, R. M., Belinostat: first global approval. *Drugs* **2014,** *74* (13), 1543-54.
511. Redic, K. A.; Hough, S. M.; Price, E. M., Clinical developments in the treatment of relapsed or relapsed and refractory multiple myeloma: impact of panobinostat, the first-in-class histone deacetylase inhibitor. *Onco Targets Ther* **2016,** *9*, 2783-93.
512. Wahaib, K.; Beggs, A. E.; Campbell, H.; Kodali, L.; Ford, P. D., Panobinostat: A histone deacetylase inhibitor for the treatment of relapsed or refractory multiple myeloma. *Am J Health Syst Pharm* **2016,** *73* (7), 441-50.
513. Lu, X.; Ning, Z.; Li, Z.; Cao, H.; Wang, X., Development of chidamide for peripheral T-cell lymphoma, the first orphan drug approved in China. *Intractable Rare Dis Res* **2016,** *5* (3), 185-91.
514. Wang, H.; Guo, Y.; Fu, M.; Liang, X.; Zhang, X.; Wang, R.; Lin, C.; Qian, H., Antitumor activity of Chidamide in hepatocellular carcinoma cell lines. *Mol Med Rep* **2012,** *5* (6), 1503-8.
515. Lamb, Y. N., Givinostat: First Approval. *Drugs* **2024,** *84* (7), 849-856.
516. Comi, G. P.; Niks, E. H.; Vandenborne, K.; Cinnante, C. M.; Kan, H. E.; Willcocks, R. J.; Velardo, D.; Magri, F.; Ripolone, M.; van Benthem, J. J.; van de Velde, N. M.; Nava, S.; Ambrosoli, L.; Cazzaniga, S.; Bettica, P. U., Givinostat for

Becker muscular dystrophy: A randomized, placebo-controlled, double-blind study. *Front Neurol* **2023,** *14*, 1095121.
517. Oikonomou, A.; Watrin, T.; Valsecchi, L.; Scharov, K.; Savino, A. M.; Schliehe-Diecks, J.; Bardini, M.; Fazio, G.; Bresolin, S.; Biondi, A.; Borkhardt, A.; Bhatia, S.; Cazzaniga, G.; Palmi, C., Synergistic drug interactions of the histone deacetylase inhibitor givinostat (ITF2357) in CRLF2-rearranged pediatric B-cell precursor acute lymphoblastic leukemia identified by high-throughput drug screening. *Heliyon* **2024,** *10* (13), e34033.
518. Bitzer, M.; Horger, M.; Giannini, E. G.; Ganten, T. M.; Worns, M. A.; Siveke, J. T.; Dollinger, M. M.; Gerken, G.; Scheulen, M. E.; Wege, H.; Zagonel, V.; Cillo, U.; Trevisani, F.; Santoro, A.; Montesarchio, V.; Malek, N. P.; Holzapfel, J.; Herz, T.; Ammendola, A. S.; Pegoraro, S.; Hauns, B.; Mais, A.; Lauer, U. M.; Henning, S. W.; Hentsch, B., Resminostat plus sorafenib as second-line therapy of advanced hepatocellular carcinoma - The SHELTER study. *J Hepatol* **2016,** *65* (2), 280-8.
519. Novotny-Diermayr, V.; Sangthongpitag, K.; Hu, C. Y.; Wu, X.; Sausgruber, N.; Yeo, P.; Greicius, G.; Pettersson, S.; Liang, A. L.; Loh, Y. K.; Bonday, Z.; Goh, K. C.; Hentze, H.; Hart, S.; Wang, H.; Ethirajulu, K.; Wood, J. M., SB939, a novel potent and orally active histone deacetylase inhibitor with high tumor exposure and efficacy in mouse models of colorectal cancer. *Mol Cancer Ther* **2010,** *9* (3), 642-52.
520. Lu, Q.; Wang, D. S.; Chen, C. S.; Hu, Y. D.; Chen, C. S., Structure-based optimization of phenylbutyrate-derived histone deacetylase inhibitors. *J Med Chem* **2005,** *48* (17), 5530-5.
521. Meng, J.; Li, Y.; Camarillo, C.; Yao, Y.; Zhang, Y.; Xu, C.; Jiang, L., The anti-tumor histone deacetylase inhibitor SAHA and the natural flavonoid curcumin exhibit synergistic neuroprotection against amyloid-beta toxicity. *PLoS One* **2014,** *9* (1), e85570.
522. Welling, D. B.; Collier, K. A.; Burns, S. S.; Oblinger, J. L.; Shu, E.; Miles-Markley, B. A.; Hofmeister, C. C.; Makary, M. S.; Slone, H. W.; Blakeley, J. O.; Mansouri, S. A.; Neff, B. A.; Jackler, R. K.; Mortazavi, A.; Chang, L. S., Early phase clinical studies of AR-42, a histone deacetylase inhibitor, for neurofibromatosis type 2-associated vestibular schwannomas and meningiomas. *Laryngoscope Investig Otolaryngol* **2021,** *6* (5), 1008-1019.
523. Sborov, D. W.; Canella, A.; Hade, E. M.; Mo, X.; Khountham, S.; Wang, J.; Ni, W.; Poi, M.; Coss, C.; Liu, Z.; Phelps, M. A.; Mortazavi, A.; Andritsos, L.; Baiocchi, R. A.; Christian, B. A.; Benson, D. M.; Flynn, J.; Porcu, P.; Byrd, J. C.; Pichiorri, F.; Hofmeister, C. C., A phase 1 trial of the HDAC inhibitor AR-42 in patients with multiple myeloma and T- and B-cell lymphomas. *Leuk Lymphoma* **2017,** *58* (10), 2310-2318.
524. Connolly, R. M.; Rudek, M. A.; Piekarz, R., Entinostat: a promising treatment option for patients with advanced breast cancer. *Future Oncol* **2017,** *13* (13), 1137-1148.

525. Zhou, N.; Moradei, O.; Raeppel, S.; Leit, S.; Frechette, S.; Gaudette, F.; Paquin, I.; Bernstein, N.; Bouchain, G.; Vaisburg, A.; Jin, Z.; Gillespie, J.; Wang, J.; Fournel, M.; Yan, P. T.; Trachy-Bourget, M. C.; Kalita, A.; Lu, A.; Rahil, J.; MacLeod, A. R.; Li, Z.; Besterman, J. M.; Delorme, D., Discovery of N-(2-aminophenyl)-4-[(4-pyridin-3-ylpyrimidin-2-ylamino)methyl]benzamide (MGCD0103), an orally active histone deacetylase inhibitor. *J Med Chem* **2008,** *51* (14), 4072-5.
526. Boumber, Y.; Younes, A.; Garcia-Manero, G., Mocetinostat (MGCD0103): a review of an isotype-specific histone deacetylase inhibitor. *Expert Opin Investig Drugs* **2011,** *20* (6), 823-9.
527. Murray, K., The Occurrence of Epsilon-N-Methyl Lysine in Histones. *Biochemistry* **1964,** *3*, 10-5.
528. Rea, S.; Eisenhaber, F.; O'Carroll, D.; Strahl, B. D.; Sun, Z. W.; Schmid, M.; Opravil, S.; Mechtler, K.; Ponting, C. P.; Allis, C. D.; Jenuwein, T., Regulation of chromatin structure by site-specific histone H3 methyltransferases. *Nature* **2000,** *406* (6796), 593-9.
529. Shi, Y.; Lan, F.; Matson, C.; Mulligan, P.; Whetstine, J. R.; Cole, P. A.; Casero, R. A.; Shi, Y., Histone demethylation mediated by the nuclear amine oxidase homolog LSD1. *Cell* **2004,** *119* (7), 941-53.
530. Biggar, K. K.; Li, S. S., Non-histone protein methylation as a regulator of cellular signalling and function. *Nat Rev Mol Cell Biol* **2015,** *16* (1), 5-17.
531. Morin, R. D.; Mendez-Lago, M.; Mungall, A. J.; Goya, R.; Mungall, K. L.; Corbett, R. D.; Johnson, N. A.; Severson, T. M.; Chiu, R.; Field, M.; Jackman, S.; Krzywinski, M.; Scott, D. W.; Trinh, D. L.; Tamura-Wells, J.; Li, S.; Firme, M. R.; Rogic, S.; Griffith, M.; Chan, S.; Yakovenko, O.; Meyer, I. M.; Zhao, E. Y.; Smailus, D.; Moksa, M.; Chittaranjan, S.; Rimsza, L.; Brooks-Wilson, A.; Spinelli, J. J.; Ben-Neriah, S.; Meissner, B.; Woolcock, B.; Boyle, M.; McDonald, H.; Tam, A.; Zhao, Y.; Delaney, A.; Zeng, T.; Tse, K.; Butterfield, Y.; Birol, I.; Holt, R.; Schein, J.; Horsman, D. E.; Moore, R.; Jones, S. J.; Connors, J. M.; Hirst, M.; Gascoyne, R. D.; Marra, M. A., Frequent mutation of histone-modifying genes in non-Hodgkin lymphoma. *Nature* **2011,** *476* (7360), 298-303.
532. Martin, C.; Zhang, Y., The diverse functions of histone lysine methylation. *Nat Rev Mol Cell Biol* **2005,** *6* (11), 838-49.
533. Shi, Y.; Whetstine, J. R., Dynamic regulation of histone lysine methylation by demethylases. *Mol Cell* **2007,** *25* (1), 1-14.
534. Kouzarides, T., Histone methylation in transcriptional control. *Curr Opin Genet Dev* **2002,** *12* (2), 198-209.
535. Sims, R. J., 3rd; Nishioka, K.; Reinberg, D., Histone lysine methylation: a signature for chromatin function. *Trends Genet* **2003,** *19* (11), 629-39.
536. Blanc, R. S.; Richard, S., Arginine Methylation: The Coming of Age. *Mol Cell* **2017,** *65* (1), 8-24.

537. Kirmizis, A.; Santos-Rosa, H.; Penkett, C. J.; Singer, M. A.; Vermeulen, M.; Mann, M.; Bahler, J.; Green, R. D.; Kouzarides, T., Arginine methylation at histone H3R2 controls deposition of H3K4 trimethylation. *Nature* **2007,** *449* (7164), 928-32.
538. Guccione, E.; Bassi, C.; Casadio, F.; Martinato, F.; Cesaroni, M.; Schuchlautz, H.; Luscher, B.; Amati, B., Methylation of histone H3R2 by PRMT6 and H3K4 by an MLL complex are mutually exclusive. *Nature* **2007,** *449* (7164), 933-7.
539. Fuhrmann, J.; Clancy, K. W.; Thompson, P. R., Chemical biology of protein arginine modifications in epigenetic regulation. *Chem Rev* **2015,** *115* (11), 5413-61.
540. Gayatri, S.; Bedford, M. T., Readers of histone methylarginine marks. *Biochim Biophys Acta* **2014,** *1839* (8), 702-10.
541. McCabe, M. T.; Mohammad, H. P.; Barbash, O.; Kruger, R. G., Targeting Histone Methylation in Cancer. *Cancer J* **2017,** *23* (5), 292-301.
542. Lewis, E. B., A gene complex controlling segmentation in Drosophila. *Nature* **1978,** *276* (5688), 565-70.
543. Whitcomb, S. J.; Basu, A.; Allis, C. D.; Bernstein, E., Polycomb Group proteins: an evolutionary perspective. *Trends Genet* **2007,** *23* (10), 494-502.
544. Scheuermann, J. C.; de Ayala Alonso, A. G.; Oktaba, K.; Ly-Hartig, N.; McGinty, R. K.; Fraterman, S.; Wilm, M.; Muir, T. W.; Muller, J., Histone H2A deubiquitinase activity of the Polycomb repressive complex PR-DUB. *Nature* **2010,** *465* (7295), 243-7.
545. Klymenko, T.; Papp, B.; Fischle, W.; Kocher, T.; Schelder, M.; Fritsch, C.; Wild, B.; Wilm, M.; Muller, J., A Polycomb group protein complex with sequence-specific DNA-binding and selective methyl-lysine-binding activities. *Genes Dev* **2006,** *20* (9), 1110-22.
546. Simon, J. A.; Kingston, R. E., Mechanisms of polycomb gene silencing: knowns and unknowns. *Nat Rev Mol Cell Biol* **2009,** *10* (10), 697-708.
547. Schuettengruber, B.; Cavalli, G., Recruitment of polycomb group complexes and their role in the dynamic regulation of cell fate choice. *Development* **2009,** *136* (21), 3531-42.
548. Cao, R.; Wang, L.; Wang, H.; Xia, L.; Erdjument-Bromage, H.; Tempst, P.; Jones, R. S.; Zhang, Y., Role of histone H3 lysine 27 methylation in Polycomb-group silencing. *Science* **2002,** *298* (5595), 1039-43.
549. Fischle, W.; Wang, Y.; Jacobs, S. A.; Kim, Y.; Allis, C. D.; Khorasanizadeh, S., Molecular basis for the discrimination of repressive methyl-lysine marks in histone H3 by Polycomb and HP1 chromodomains. *Genes Dev* **2003,** *17* (15), 1870-81.
550. Min, J.; Zhang, Y.; Xu, R. M., Structural basis for specific binding of Polycomb chromodomain to histone H3 methylated at Lys 27. *Genes Dev* **2003,** *17* (15), 1823-8.
551. Blackledge, N. P.; Farcas, A. M.; Kondo, T.; King, H. W.; McGouran, J. F.; Hanssen, L. L. P.; Ito, S.; Cooper, S.; Kondo, K.; Koseki, Y.; Ishikura, T.; Long, H. K.; Sheahan, T. W.; Brockdorff, N.; Kessler, B. M.; Koseki, H.; Klose, R. J., Variant

PRC1 complex-dependent H2A ubiquitylation drives PRC2 recruitment and polycomb domain formation. *Cell* **2014,** *157* (6), 1445-1459.
552. Cooper, S.; Dienstbier, M.; Hassan, R.; Schermelleh, L.; Sharif, J.; Blackledge, N. P.; De Marco, V.; Elderkin, S.; Koseki, H.; Klose, R.; Heger, A.; Brockdorff, N., Targeting polycomb to pericentric heterochromatin in embryonic stem cells reveals a role for H2AK119u1 in PRC2 recruitment. *Cell Rep* **2014,** *7* (5), 1456-1470.
553. Holoch, D.; Margueron, R., Mechanisms Regulating PRC2 Recruitment and Enzymatic Activity. *Trends Biochem Sci* **2017,** *42* (7), 531-542.
554. Margueron, R.; Reinberg, D., The Polycomb complex PRC2 and its mark in life. *Nature* **2011,** *469* (7330), 343-9.
555. Cooper, S.; Grijzenhout, A.; Underwood, E.; Ancelin, K.; Zhang, T.; Nesterova, T. B.; Anil-Kirmizitas, B.; Bassett, A.; Kooistra, S. M.; Agger, K.; Helin, K.; Heard, E.; Brockdorff, N., Jarid2 binds mono-ubiquitylated H2A lysine 119 to mediate crosstalk between Polycomb complexes PRC1 and PRC2. *Nat Commun* **2016,** *7*, 13661.
556. Kim, H.; Kang, K.; Kim, J., AEBP2 as a potential targeting protein for Polycomb Repression Complex PRC2. *Nucleic Acids Res* **2009,** *37* (9), 2940-50.
557. Moritz, L. E.; Trievel, R. C., Structure, mechanism, and regulation of polycomb-repressive complex 2. *J Biol Chem* **2018,** *293* (36), 13805-13814.
558. Ciferri, C.; Lander, G. C.; Maiolica, A.; Herzog, F.; Aebersold, R.; Nogales, E., Molecular architecture of human polycomb repressive complex 2. *Elife* **2012,** *1*, e00005.
559. Rinn, J. L.; Kertesz, M.; Wang, J. K.; Squazzo, S. L.; Xu, X.; Brugmann, S. A.; Goodnough, L. H.; Helms, J. A.; Farnham, P. J.; Segal, E.; Chang, H. Y., Functional demarcation of active and silent chromatin domains in human HOX loci by noncoding RNAs. *Cell* **2007,** *129* (7), 1311-23.
560. Han, Z.; Xing, X.; Hu, M.; Zhang, Y.; Liu, P.; Chai, J., Structural basis of EZH2 recognition by EED. *Structure* **2007,** *15* (10), 1306-15.
561. Margueron, R.; Justin, N.; Ohno, K.; Sharpe, M. L.; Son, J.; Drury, W. J., 3rd; Voigt, P.; Martin, S. R.; Taylor, W. R.; De Marco, V.; Pirrotta, V.; Reinberg, D.; Gamblin, S. J., Role of the polycomb protein EED in the propagation of repressive histone marks. *Nature* **2009,** *461* (7265), 762-7.
562. Jiao, L.; Liu, X., Structural basis of histone H3K27 trimethylation by an active polycomb repressive complex 2. *Science* **2015,** *350* (6258), aac4383.
563. Justin, N.; Zhang, Y.; Tarricone, C.; Martin, S. R.; Chen, S.; Underwood, E.; De Marco, V.; Haire, L. F.; Walker, P. A.; Reinberg, D.; Wilson, J. R.; Gamblin, S. J., Structural basis of oncogenic histone H3K27M inhibition of human polycomb repressive complex 2. *Nat Commun* **2016,** *7*, 11316.
564. Zhang, Y.; Justin, N.; Wilson, J. R.; Gamblin, S. J., Comment on "Structural basis of histone H3K27 trimethylation by an active polycomb repressive complex 2". *Science* **2016,** *354* (6319), 1543.

565. Margueron, R.; Li, G.; Sarma, K.; Blais, A.; Zavadil, J.; Woodcock, C. L.; Dynlacht, B. D.; Reinberg, D., Ezh1 and Ezh2 maintain repressive chromatin through different mechanisms. *Mol Cell* **2008,** *32* (4), 503-18.
566. Cao, R.; Zhang, Y., SUZ12 is required for both the histone methyltransferase activity and the silencing function of the EED-EZH2 complex. *Mol Cell* **2004,** *15* (1), 57-67.
567. Ketel, C. S.; Andersen, E. F.; Vargas, M. L.; Suh, J.; Strome, S.; Simon, J. A., Subunit contributions to histone methyltransferase activities of fly and worm polycomb group complexes. *Mol Cell Biol* **2005,** *25* (16), 6857-68.
568. Pasini, D.; Bracken, A. P.; Jensen, M. R.; Lazzerini Denchi, E.; Helin, K., Suz12 is essential for mouse development and for EZH2 histone methyltransferase activity. *EMBO J* **2004,** *23* (20), 4061-71.
569. He, A.; Shen, X.; Ma, Q.; Cao, J.; von Gise, A.; Zhou, P.; Wang, G.; Marquez, V. E.; Orkin, S. H.; Pu, W. T., PRC2 directly methylates GATA4 and represses its transcriptional activity. *Genes Dev* **2012,** *26* (1), 37-42.
570. Vasanthakumar, A.; Xu, D.; Lun, A. T.; Kueh, A. J.; van Gisbergen, K. P.; Iannarella, N.; Li, X.; Yu, L.; Wang, D.; Williams, B. R.; Lee, S. C.; Majewski, I. J.; Godfrey, D. I.; Smyth, G. K.; Alexander, W. S.; Herold, M. J.; Kallies, A.; Nutt, S. L.; Allan, R. S., A non-canonical function of Ezh2 preserves immune homeostasis. *EMBO Rep* **2017,** *18* (4), 619-631.
571. Kim, K. H.; Roberts, C. W., Targeting EZH2 in cancer. *Nat Med* **2016,** *22* (2), 128-34.
572. Agger, K.; Cloos, P. A.; Christensen, J.; Pasini, D.; Rose, S.; Rappsilber, J.; Issaeva, I.; Canaani, E.; Salcini, A. E.; Helin, K., UTX and JMJD3 are histone H3K27 demethylases involved in HOX gene regulation and development. *Nature* **2007,** *449* (7163), 731-4.
573. Hong, S.; Cho, Y. W.; Yu, L. R.; Yu, H.; Veenstra, T. D.; Ge, K., Identification of JmjC domain-containing UTX and JMJD3 as histone H3 lysine 27 demethylases. *Proc Natl Acad Sci U S A* **2007,** *104* (47), 18439-44.
574. Lee, M. G.; Villa, R.; Trojer, P.; Norman, J.; Yan, K. P.; Reinberg, D.; Di Croce, L.; Shiekhattar, R., Demethylation of H3K27 regulates polycomb recruitment and H2A ubiquitination. *Science* **2007,** *318* (5849), 447-50.
575. Lan, F.; Bayliss, P. E.; Rinn, J. L.; Whetstine, J. R.; Wang, J. K.; Chen, S.; Iwase, S.; Alpatov, R.; Issaeva, I.; Canaani, E.; Roberts, T. M.; Chang, H. Y.; Shi, Y., A histone H3 lysine 27 demethylase regulates animal posterior development. *Nature* **2007,** *449* (7163), 689-94.
576. De Santa, F.; Totaro, M. G.; Prosperini, E.; Notarbartolo, S.; Testa, G.; Natoli, G., The histone H3 lysine-27 demethylase Jmjd3 links inflammation to inhibition of polycomb-mediated gene silencing. *Cell* **2007,** *130* (6), 1083-94.
577. Antonysamy, S.; Condon, B.; Druzina, Z.; Bonanno, J. B.; Gheyi, T.; Zhang, F.; MacEwan, I.; Zhang, A.; Ashok, S.; Rodgers, L.; Russell, M.; Gately Luz, J., Structural context of disease-associated mutations and putative mechanism of

autoinhibition revealed by X-ray crystallographic analysis of the EZH2-SET domain. *PLoS One* **2013,** *8* (12), e84147.
578. Wu, H.; Zeng, H.; Dong, A.; Li, F.; He, H.; Senisterra, G.; Seitova, A.; Duan, S.; Brown, P. J.; Vedadi, M.; Arrowsmith, C. H.; Schapira, M., Structure of the catalytic domain of EZH2 reveals conformational plasticity in cofactor and substrate binding sites and explains oncogenic mutations. *PLoS One* **2013,** *8* (12), e83737.
579. Chammas, P.; Mocavini, I.; Di Croce, L., Engaging chromatin: PRC2 structure meets function. *Br J Cancer* **2020,** *122* (3), 315-328.
580. Kim, E.; Kim, M.; Woo, D. H.; Shin, Y.; Shin, J.; Chang, N.; Oh, Y. T.; Kim, H.; Rheey, J.; Nakano, I.; Lee, C.; Joo, K. M.; Rich, J. N.; Nam, D. H.; Lee, J., Phosphorylation of EZH2 activates STAT3 signaling via STAT3 methylation and promotes tumorigenicity of glioblastoma stem-like cells. *Cancer Cell* **2013,** *23* (6), 839-52.
581. Chang, C. J.; Hung, M. C., The role of EZH2 in tumour progression. *Br J Cancer* **2012,** *106* (2), 243-7.
582. Chase, A.; Cross, N. C., Aberrations of EZH2 in cancer. *Clin Cancer Res* **2011,** *17* (9), 2613-8.
583. Wang, C.; Liu, Z.; Woo, C. W.; Li, Z.; Wang, L.; Wei, J. S.; Marquez, V. E.; Bates, S. E.; Jin, Q.; Khan, J.; Ge, K.; Thiele, C. J., EZH2 Mediates epigenetic silencing of neuroblastoma suppressor genes CASZ1, CLU, RUNX3, and NGFR. *Cancer Res* **2012,** *72* (1), 315-24.
584. Kim, J.; Yu, J., Interrogating genomic and epigenomic data to understand prostate cancer. *Biochim Biophys Acta* **2012,** *1825* (2), 186-96.
585. Fujikawa, D.; Nakagawa, S.; Hori, M.; Kurokawa, N.; Soejima, A.; Nakano, K.; Yamochi, T.; Nakashima, M.; Kobayashi, S.; Tanaka, Y.; Iwanaga, M.; Utsunomiya, A.; Uchimaru, K.; Yamagishi, M.; Watanabe, T., Polycomb-dependent epigenetic landscape in adult T-cell leukemia. *Blood* **2016,** *127* (14), 1790-802.
586. Varambally, S.; Dhanasekaran, S. M.; Zhou, M.; Barrette, T. R.; Kumar-Sinha, C.; Sanda, M. G.; Ghosh, D.; Pienta, K. J.; Sewalt, R. G.; Otte, A. P.; Rubin, M. A.; Chinnaiyan, A. M., The polycomb group protein EZH2 is involved in progression of prostate cancer. *Nature* **2002,** *419* (6907), 624-9.
587. Kleer, C. G.; Cao, Q.; Varambally, S.; Shen, R.; Ota, I.; Tomlins, S. A.; Ghosh, D.; Sewalt, R. G.; Otte, A. P.; Hayes, D. F.; Sabel, M. S.; Livant, D.; Weiss, S. J.; Rubin, M. A.; Chinnaiyan, A. M., EZH2 is a marker of aggressive breast cancer and promotes neoplastic transformation of breast epithelial cells. *Proc Natl Acad Sci U S A* **2003,** *100* (20), 11606-11.
588. Bracken, A. P.; Pasini, D.; Capra, M.; Prosperini, E.; Colli, E.; Helin, K., EZH2 is downstream of the pRB-E2F pathway, essential for proliferation and amplified in cancer. *EMBO J* **2003,** *22* (20), 5323-35.
589. Bachmann, I. M.; Halvorsen, O. J.; Collett, K.; Stefansson, I. M.; Straume, O.; Haukaas, S. A.; Salvesen, H. B.; Otte, A. P.; Akslen, L. A., EZH2 expression is associated with high proliferation rate and aggressive tumor subgroups in

cutaneous melanoma and cancers of the endometrium, prostate, and breast. *J Clin Oncol* **2006,** *24* (2), 268-73.
590. Sauvageau, M.; Sauvageau, G., Polycomb group proteins: multi-faceted regulators of somatic stem cells and cancer. *Cell Stem Cell* **2010,** *7* (3), 299-313.
591. Nichol, J. N.; Dupere-Richer, D.; Ezponda, T.; Licht, J. D.; Miller, W. H., Jr., H3K27 Methylation: A Focal Point of Epigenetic Deregulation in Cancer. *Adv Cancer Res* **2016,** *131*, 59-95.
592. Kamminga, L. M.; Bystrykh, L. V.; de Boer, A.; Houwer, S.; Douma, J.; Weersing, E.; Dontje, B.; de Haan, G., The Polycomb group gene Ezh2 prevents hematopoietic stem cell exhaustion. *Blood* **2006,** *107* (5), 2170-9.
593. Herrera-Merchan, A.; Arranz, L.; Ligos, J. M.; de Molina, A.; Dominguez, O.; Gonzalez, S., Ectopic expression of the histone methyltransferase Ezh2 in haematopoietic stem cells causes myeloproliferative disease. *Nat Commun* **2012,** *3*, 623.
594. Tanaka, S.; Miyagi, S.; Sashida, G.; Chiba, T.; Yuan, J.; Mochizuki-Kashio, M.; Suzuki, Y.; Sugano, S.; Nakaseko, C.; Yokote, K.; Koseki, H.; Iwama, A., Ezh2 augments leukemogenicity by reinforcing differentiation blockage in acute myeloid leukemia. *Blood* **2012,** *120* (5), 1107-17.
595. Vo, B. T.; Li, C.; Morgan, M. A.; Theurillat, I.; Finkelstein, D.; Wright, S.; Hyle, J.; Smith, S. M. C.; Fan, Y.; Wang, Y. D.; Wu, G.; Orr, B. A.; Northcott, P. A.; Shilatifard, A.; Sherr, C. J.; Roussel, M. F., Inactivation of Ezh2 Upregulates Gfi1 and Drives Aggressive Myc-Driven Group 3 Medulloblastoma. *Cell Rep* **2017,** *18* (12), 2907-2917.
596. Luo, H.; Jiang, Y.; Ma, S.; Chang, H.; Yi, C.; Cao, H.; Gao, Y.; Guo, H.; Hou, J.; Yan, J.; Sheng, Y.; Ren, X., EZH2 promotes invasion and metastasis of laryngeal squamous cells carcinoma via epithelial-mesenchymal transition through H3K27me3. *Biochem Biophys Res Commun* **2016,** *479* (2), 253-259.
597. Cardenas, H.; Zhao, J.; Vieth, E.; Nephew, K. P.; Matei, D., EZH2 inhibition promotes epithelial-to-mesenchymal transition in ovarian cancer cells. *Oncotarget* **2016,** *7* (51), 84453-84467.
598. Honma, K.; Udono, H.; Kohno, T.; Yamamoto, K.; Ogawa, A.; Takemori, T.; Kumatori, A.; Suzuki, S.; Matsuyama, T.; Yui, K., Interferon regulatory factor 4 negatively regulates the production of proinflammatory cytokines by macrophages in response to LPS. *Proc Natl Acad Sci U S A* **2005,** *102* (44), 16001-6.
599. Turner, C. A., Jr.; Mack, D. H.; Davis, M. M., Blimp-1, a novel zinc finger-containing protein that can drive the maturation of B lymphocytes into immunoglobulin-secreting cells. *Cell* **1994,** *77* (2), 297-306.
600. Alzrigat, M.; Parraga, A. A.; Agarwal, P.; Zureigat, H.; Osterborg, A.; Nahi, H.; Ma, A.; Jin, J.; Nilsson, K.; Oberg, F.; Kalushkova, A.; Jernberg-Wiklund, H., EZH2 inhibition in multiple myeloma downregulates myeloma associated oncogenes and upregulates microRNAs with potential tumor suppressor functions. *Oncotarget* **2017,** *8* (6), 10213-10224.

601. Beguelin, W.; Popovic, R.; Teater, M.; Jiang, Y.; Bunting, K. L.; Rosen, M.; Shen, H.; Yang, S. N.; Wang, L.; Ezponda, T.; Martinez-Garcia, E.; Zhang, H.; Zheng, Y.; Verma, S. K.; McCabe, M. T.; Ott, H. M.; Van Aller, G. S.; Kruger, R. G.; Liu, Y.; McHugh, C. F.; Scott, D. W.; Chung, Y. R.; Kelleher, N.; Shaknovich, R.; Creasy, C. L.; Gascoyne, R. D.; Wong, K. K.; Cerchietti, L.; Levine, R. L.; Abdel-Wahab, O.; Licht, J. D.; Elemento, O.; Melnick, A. M., EZH2 is required for germinal center formation and somatic EZH2 mutations promote lymphoid transformation. *Cancer Cell* **2013,** *23* (5), 677-92.
602. Xu, K.; Wu, Z. J.; Groner, A. C.; He, H. H.; Cai, C.; Lis, R. T.; Wu, X.; Stack, E. C.; Loda, M.; Liu, T.; Xu, H.; Cato, L.; Thornton, J. E.; Gregory, R. I.; Morrissey, C.; Vessella, R. L.; Montironi, R.; Magi-Galluzzi, C.; Kantoff, P. W.; Balk, S. P.; Liu, X. S.; Brown, M., EZH2 oncogenic activity in castration-resistant prostate cancer cells is Polycomb-independent. *Science* **2012,** *338* (6113), 1465-9.
603. Boyer, L. A.; Plath, K.; Zeitlinger, J.; Brambrink, T.; Medeiros, L. A.; Lee, T. I.; Levine, S. S.; Wernig, M.; Tajonar, A.; Ray, M. K.; Bell, G. W.; Otte, A. P.; Vidal, M.; Gifford, D. K.; Young, R. A.; Jaenisch, R., Polycomb complexes repress developmental regulators in murine embryonic stem cells. *Nature* **2006,** *441* (7091), 349-53.
604. Shan, Y.; Liang, Z.; Xing, Q.; Zhang, T.; Wang, B.; Tian, S.; Huang, W.; Zhang, Y.; Yao, J.; Zhu, Y.; Huang, K.; Liu, Y.; Wang, X.; Chen, Q.; Zhang, J.; Shang, B.; Li, S.; Shi, X.; Liao, B.; Zhang, C.; Lai, K.; Zhong, X.; Shu, X.; Wang, J.; Yao, H.; Chen, J.; Pei, D.; Pan, G., PRC2 specifies ectoderm lineages and maintains pluripotency in primed but not naive ESCs. *Nat Commun* **2017,** *8* (1), 672.
605. Piunti, A.; Pasini, D., Epigenetic factors in cancer development: polycomb group proteins. *Future Oncol* **2011,** *7* (1), 57-75.
606. Chang, C. J.; Yang, J. Y.; Xia, W.; Chen, C. T.; Xie, X.; Chao, C. H.; Woodward, W. A.; Hsu, J. M.; Hortobagyi, G. N.; Hung, M. C., EZH2 promotes expansion of breast tumor initiating cells through activation of RAF1-beta-catenin signaling. *Cancer Cell* **2011,** *19* (1), 86-100.
607. Karantanos, T.; Chistofides, A.; Barhdan, K.; Li, L.; Boussiotis, V. A., Regulation of T Cell Differentiation and Function by EZH2. *Front Immunol* **2016,** *7*, 172.
608. Caretti, G.; Di Padova, M.; Micales, B.; Lyons, G. E.; Sartorelli, V., The Polycomb Ezh2 methyltransferase regulates muscle gene expression and skeletal muscle differentiation. *Genes Dev* **2004,** *18* (21), 2627-38.
609. Sher, F.; Rossler, R.; Brouwer, N.; Balasubramaniyan, V.; Boddeke, E.; Copray, S., Differentiation of neural stem cells into oligodendrocytes: involvement of the polycomb group protein Ezh2. *Stem Cells* **2008,** *26* (11), 2875-83.
610. Hwang, W. W.; Salinas, R. D.; Siu, J. J.; Kelley, K. W.; Delgado, R. N.; Paredes, M. F.; Alvarez-Buylla, A.; Oldham, M. C.; Lim, D. A., Distinct and separable roles for EZH2 in neurogenic astroglia. *Elife* **2014,** *3*, e02439.

611. Pereira, J. D.; Sansom, S. N.; Smith, J.; Dobenecker, M. W.; Tarakhovsky, A.; Livesey, F. J., Ezh2, the histone methyltransferase of PRC2, regulates the balance between self-renewal and differentiation in the cerebral cortex. *Proc Natl Acad Sci U S A* **2010,** *107* (36), 15957-62.
612. Acharyya, S.; Sharma, S. M.; Cheng, A. S.; Ladner, K. J.; He, W.; Kline, W.; Wang, H.; Ostrowski, M. C.; Huang, T. H.; Guttridge, D. C., TNF inhibits Notch-1 in skeletal muscle cells by Ezh2 and DNA methylation mediated repression: implications in duchenne muscular dystrophy. *PLoS One* **2010,** *5* (8), e12479.
613. Palacios, D.; Mozzetta, C.; Consalvi, S.; Caretti, G.; Saccone, V.; Proserpio, V.; Marquez, V. E.; Valente, S.; Mai, A.; Forcales, S. V.; Sartorelli, V.; Puri, P. L., TNF/p38alpha/polycomb signaling to Pax7 locus in satellite cells links inflammation to the epigenetic control of muscle regeneration. *Cell Stem Cell* **2010,** *7* (4), 455-69.
614. Chen, H.; Gu, X.; Su, I. H.; Bottino, R.; Contreras, J. L.; Tarakhovsky, A.; Kim, S. K., Polycomb protein Ezh2 regulates pancreatic beta-cell Ink4a/Arf expression and regeneration in diabetes mellitus. *Genes Dev* **2009,** *23* (8), 975-85.
615. Zhou, J. X.; Dhawan, S.; Fu, H.; Snyder, E.; Bottino, R.; Kundu, S.; Kim, S. K.; Bhushan, A., Combined modulation of polycomb and trithorax genes rejuvenates beta cell replication. *J Clin Invest* **2013,** *123* (11), 4849-58.
616. Wei, Y.; Chen, Y. H.; Li, L. Y.; Lang, J.; Yeh, S. P.; Shi, B.; Yang, C. C.; Yang, J. Y.; Lin, C. Y.; Lai, C. C.; Hung, M. C., CDK1-dependent phosphorylation of EZH2 suppresses methylation of H3K27 and promotes osteogenic differentiation of human mesenchymal stem cells. *Nat Cell Biol* **2011,** *13* (1), 87-94.
617. Chen, Y. H.; Yeh, F. L.; Yeh, S. P.; Ma, H. T.; Hung, S. C.; Hung, M. C.; Li, L. Y., Myocyte enhancer factor-2 interacting transcriptional repressor (MITR) is a switch that promotes osteogenesis and inhibits adipogenesis of mesenchymal stem cells by inactivating peroxisome proliferator-activated receptor gamma-2. *J Biol Chem* **2011,** *286* (12), 10671-80.
618. Wang, L.; Jin, Q.; Lee, J. E.; Su, I. H.; Ge, K., Histone H3K27 methyltransferase Ezh2 represses Wnt genes to facilitate adipogenesis. *Proc Natl Acad Sci U S A* **2010,** *107* (16), 7317-22.
619. Stazi, G.; Zwergel, C.; Mai, A.; Valente, S., EZH2 inhibitors: a patent review (2014-2016). *Expert Opin Ther Pat* **2017,** *27* (7), 797-813.
620. Korfi, K.; Ali, S.; Heward, J. A.; Fitzgibbon, J., Follicular lymphoma, a B cell malignancy addicted to epigenetic mutations. *Epigenetics* **2017,** *12* (5), 370-377.
621. Pastore, A.; Jurinovic, V.; Kridel, R.; Hoster, E.; Staiger, A. M.; Szczepanowski, M.; Pott, C.; Kopp, N.; Murakami, M.; Horn, H.; Leich, E.; Moccia, A. A.; Mottok, A.; Sunkavalli, A.; Van Hummelen, P.; Ducar, M.; Ennishi, D.; Shulha, H. P.; Hother, C.; Connors, J. M.; Sehn, L. H.; Dreyling, M.; Neuberg, D.; Moller, P.; Feller, A. C.; Hansmann, M. L.; Stein, H.; Rosenwald, A.; Ott, G.; Klapper, W.; Unterhalt, M.; Hiddemann, W.; Gascoyne, R. D.; Weinstock, D. M.; Weigert, O., Integration of gene mutations in risk prognostication for patients receiving first-line immunochemotherapy for follicular lymphoma: a retrospective

analysis of a prospective clinical trial and validation in a population-based registry. *Lancet Oncol* **2015,** *16* (9), 1111-1122.
622. Julia, E.; Salles, G., EZH2 inhibition by tazemetostat: mechanisms of action, safety and efficacy in relapsed/refractory follicular lymphoma. *Future Oncol* **2021,** *17* (17), 2127-2140.
623. Bodor, C.; Grossmann, V.; Popov, N.; Okosun, J.; O'Riain, C.; Tan, K.; Marzec, J.; Araf, S.; Wang, J.; Lee, A. M.; Clear, A.; Montoto, S.; Matthews, J.; Iqbal, S.; Rajnai, H.; Rosenwald, A.; Ott, G.; Campo, E.; Rimsza, L. M.; Smeland, E. B.; Chan, W. C.; Braziel, R. M.; Staudt, L. M.; Wright, G.; Lister, T. A.; Elemento, O.; Hills, R.; Gribben, J. G.; Chelala, C.; Matolcsy, A.; Kohlmann, A.; Haferlach, T.; Gascoyne, R. D.; Fitzgibbon, J., EZH2 mutations are frequent and represent an early event in follicular lymphoma. *Blood* **2013,** *122* (18), 3165-8.
624. Huet, S.; Xerri, L.; Tesson, B.; Mareschal, S.; Taix, S.; Mescam-Mancini, L.; Sohier, E.; Carrere, M.; Lazarovici, J.; Casasnovas, O.; Tonon, L.; Boyault, S.; Hayette, S.; Haioun, C.; Fabiani, B.; Viari, A.; Jardin, F.; Salles, G., EZH2 alterations in follicular lymphoma: biological and clinical correlations. *Blood Cancer J* **2017,** *7* (4), e555.
625. Huet, S.; Sujobert, P.; Salles, G., From genetics to the clinic: a translational perspective on follicular lymphoma. *Nat Rev Cancer* **2018,** *18* (4), 224-239.
626. Pasqualucci, L.; Khiabanian, H.; Fangazio, M.; Vasishtha, M.; Messina, M.; Holmes, A. B.; Ouillette, P.; Trifonov, V.; Rossi, D.; Tabbo, F.; Ponzoni, M.; Chadburn, A.; Murty, V. V.; Bhagat, G.; Gaidano, G.; Inghirami, G.; Malek, S. N.; Rabadan, R.; Dalla-Favera, R., Genetics of follicular lymphoma transformation. *Cell Rep* **2014,** *6* (1), 130-40.
627. Su, I. H.; Basavaraj, A.; Krutchinsky, A. N.; Hobert, O.; Ullrich, A.; Chait, B. T.; Tarakhovsky, A., Ezh2 controls B cell development through histone H3 methylation and Igh rearrangement. *Nat Immunol* **2003,** *4* (2), 124-31.
628. Caganova, M.; Carrisi, C.; Varano, G.; Mainoldi, F.; Zanardi, F.; Germain, P. L.; George, L.; Alberghini, F.; Ferrarini, L.; Talukder, A. K.; Ponzoni, M.; Testa, G.; Nojima, T.; Doglioni, C.; Kitamura, D.; Toellner, K. M.; Su, I. H.; Casola, S., Germinal center dysregulation by histone methyltransferase EZH2 promotes lymphomagenesis. *J Clin Invest* **2013,** *123* (12), 5009-22.
629. Morin, R. D.; Johnson, N. A.; Severson, T. M.; Mungall, A. J.; An, J.; Goya, R.; Paul, J. E.; Boyle, M.; Woolcock, B. W.; Kuchenbauer, F.; Yap, D.; Humphries, R. K.; Griffith, O. L.; Shah, S.; Zhu, H.; Kimbara, M.; Shashkin, P.; Charlot, J. F.; Tcherpakov, M.; Corbett, R.; Tam, A.; Varhol, R.; Smailus, D.; Moksa, M.; Zhao, Y.; Delaney, A.; Qian, H.; Birol, I.; Schein, J.; Moore, R.; Holt, R.; Horsman, D. E.; Connors, J. M.; Jones, S.; Aparicio, S.; Hirst, M.; Gascoyne, R. D.; Marra, M. A., Somatic mutations altering EZH2 (Tyr641) in follicular and diffuse large B-cell lymphomas of germinal-center origin. *Nat Genet* **2010,** *42* (2), 181-5.
630. Bodor, C.; O'Riain, C.; Wrench, D.; Matthews, J.; Iyengar, S.; Tayyib, H.; Calaminici, M.; Clear, A.; Iqbal, S.; Quentmeier, H.; Drexler, H. G.; Montoto, S.;

Lister, A. T.; Gribben, J. G.; Matolcsy, A.; Fitzgibbon, J., EZH2 Y641 mutations in follicular lymphoma. *Leukemia* **2011,** *25* (4), 726-9.
631. McCabe, M. T.; Graves, A. P.; Ganji, G.; Diaz, E.; Halsey, W. S.; Jiang, Y.; Smitheman, K. N.; Ott, H. M.; Pappalardi, M. B.; Allen, K. E.; Chen, S. B.; Della Pietra, A., 3rd; Dul, E.; Hughes, A. M.; Gilbert, S. A.; Thrall, S. H.; Tummino, P. J.; Kruger, R. G.; Brandt, M.; Schwartz, B.; Creasy, C. L., Mutation of A677 in histone methyltransferase EZH2 in human B-cell lymphoma promotes hypertrimethylation of histone H3 on lysine 27 (H3K27). *Proc Natl Acad Sci U S A* **2012,** *109* (8), 2989-94.
632. Sneeringer, C. J.; Scott, M. P.; Kuntz, K. W.; Knutson, S. K.; Pollock, R. M.; Richon, V. M.; Copeland, R. A., Coordinated activities of wild-type plus mutant EZH2 drive tumor-associated hypertrimethylation of lysine 27 on histone H3 (H3K27) in human B-cell lymphomas. *Proc Natl Acad Sci U S A* **2010,** *107* (49), 20980-5.
633. Ryan, R. J.; Nitta, M.; Borger, D.; Zukerberg, L. R.; Ferry, J. A.; Harris, N. L.; Iafrate, A. J.; Bernstein, B. E.; Sohani, A. R.; Le, L. P., EZH2 codon 641 mutations are common in BCL2-rearranged germinal center B cell lymphomas. *PLoS One* **2011,** *6* (12), e28585.
634. Beguelin, W.; Teater, M.; Gearhart, M. D.; Calvo Fernandez, M. T.; Goldstein, R. L.; Cardenas, M. G.; Hatzi, K.; Rosen, M.; Shen, H.; Corcoran, C. M.; Hamline, M. Y.; Gascoyne, R. D.; Levine, R. L.; Abdel-Wahab, O.; Licht, J. D.; Shaknovich, R.; Elemento, O.; Bardwell, V. J.; Melnick, A. M., EZH2 and BCL6 Cooperate to Assemble CBX8-BCOR Complex to Repress Bivalent Promoters, Mediate Germinal Center Formation and Lymphomagenesis. *Cancer Cell* **2016,** *30* (2), 197-213.
635. Nikoloski, G.; Langemeijer, S. M.; Kuiper, R. P.; Knops, R.; Massop, M.; Tonnissen, E. R.; van der Heijden, A.; Scheele, T. N.; Vandenberghe, P.; de Witte, T.; van der Reijden, B. A.; Jansen, J. H., Somatic mutations of the histone methyltransferase gene EZH2 in myelodysplastic syndromes. *Nat Genet* **2010,** *42* (8), 665-7.
636. Ntziachristos, P.; Tsirigos, A.; Van Vlierberghe, P.; Nedjic, J.; Trimarchi, T.; Flaherty, M. S.; Ferres-Marco, D.; da Ros, V.; Tang, Z.; Siegle, J.; Asp, P.; Hadler, M.; Rigo, I.; De Keersmaecker, K.; Patel, J.; Huynh, T.; Utro, F.; Poglio, S.; Samon, J. B.; Paietta, E.; Racevskis, J.; Rowe, J. M.; Rabadan, R.; Levine, R. L.; Brown, S.; Pflumio, F.; Dominguez, M.; Ferrando, A.; Aifantis, I., Genetic inactivation of the polycomb repressive complex 2 in T cell acute lymphoblastic leukemia. *Nat Med* **2012,** *18* (2), 298-301.
637. Ernst, T.; Chase, A. J.; Score, J.; Hidalgo-Curtis, C. E.; Bryant, C.; Jones, A. V.; Waghorn, K.; Zoi, K.; Ross, F. M.; Reiter, A.; Hochhaus, A.; Drexler, H. G.; Duncombe, A.; Cervantes, F.; Oscier, D.; Boultwood, J.; Grand, F. H.; Cross, N. C., Inactivating mutations of the histone methyltransferase gene EZH2 in myeloid disorders. *Nat Genet* **2010,** *42* (8), 722-6.

638. Glazer, R. I.; Knode, M. C.; Tseng, C. K.; Haines, D. R.; Marquez, V. E., 3-Deazaneplanocin A: a new inhibitor of S-adenosylhomocysteine synthesis and its effects in human colon carcinoma cells. *Biochem Pharmacol* **1986,** *35* (24), 4523-7.
639. Miranda, T. B.; Cortez, C. C.; Yoo, C. B.; Liang, G.; Abe, M.; Kelly, T. K.; Marquez, V. E.; Jones, P. A., DZNep is a global histone methylation inhibitor that reactivates developmental genes not silenced by DNA methylation. *Mol Cancer Ther* **2009,** *8* (6), 1579-88.
640. Sun, F.; Lee, L.; Zhang, Z.; Wang, X.; Yu, Q.; Duan, X.; Chan, E., Preclinical pharmacokinetic studies of 3-deazaneplanocin A, a potent epigenetic anticancer agent, and its human pharmacokinetic prediction using GastroPlus. *Eur J Pharm Sci* **2015,** *77*, 290-302.
641. Knutson, S. K.; Wigle, T. J.; Warholic, N. M.; Sneeringer, C. J.; Allain, C. J.; Klaus, C. R.; Sacks, J. D.; Raimondi, A.; Majer, C. R.; Song, J.; Scott, M. P.; Jin, L.; Smith, J. J.; Olhava, E. J.; Chesworth, R.; Moyer, M. P.; Richon, V. M.; Copeland, R. A.; Keilhack, H.; Pollock, R. M.; Kuntz, K. W., A selective inhibitor of EZH2 blocks H3K27 methylation and kills mutant lymphoma cells. *Nat Chem Biol* **2012,** *8* (11), 890-6.
642. McCabe, M. T.; Ott, H. M.; Ganji, G.; Korenchuk, S.; Thompson, C.; Van Aller, G. S.; Liu, Y.; Graves, A. P.; Della Pietra, A., 3rd; Diaz, E.; LaFrance, L. V.; Mellinger, M.; Duquenne, C.; Tian, X.; Kruger, R. G.; McHugh, C. F.; Brandt, M.; Miller, W. H.; Dhanak, D.; Verma, S. K.; Tummino, P. J.; Creasy, C. L., EZH2 inhibition as a therapeutic strategy for lymphoma with EZH2-activating mutations. *Nature* **2012,** *492* (7427), 108-12.
643. Morera, L.; Lubbert, M.; Jung, M., Targeting histone methyltransferases and demethylases in clinical trials for cancer therapy. *Clin Epigenetics* **2016,** *8*, 57.
644. Yap, T. A.; Winter, J. N.; Giulino-Roth, L.; Longley, J.; Lopez, J.; Michot, J. M.; Leonard, J. P.; Ribrag, V.; McCabe, M. T.; Creasy, C. L.; Stern, M.; Pene Dumitrescu, T.; Wang, X.; Frey, S.; Carver, J.; Horner, T.; Oh, C.; Khaled, A.; Dhar, A.; Johnson, P. W. M., Phase I Study of the Novel Enhancer of Zeste Homolog 2 (EZH2) Inhibitor GSK2816126 in Patients with Advanced Hematologic and Solid Tumors. *Clin Cancer Res* **2019,** *25* (24), 7331-7339.
645. Verma, S. K.; Tian, X.; LaFrance, L. V.; Duquenne, C.; Suarez, D. P.; Newlander, K. A.; Romeril, S. P.; Burgess, J. L.; Grant, S. W.; Brackley, J. A.; Graves, A. P.; Scherzer, D. A.; Shu, A.; Thompson, C.; Ott, H. M.; Aller, G. S.; Machutta, C. A.; Diaz, E.; Jiang, Y.; Johnson, N. W.; Knight, S. D.; Kruger, R. G.; McCabe, M. T.; Dhanak, D.; Tummino, P. J.; Creasy, C. L.; Miller, W. H., Identification of Potent, Selective, Cell-Active Inhibitors of the Histone Lysine Methyltransferase EZH2. *ACS Med Chem Lett* **2012,** *3* (12), 1091-6.
646. Qi, W.; Chan, H.; Teng, L.; Li, L.; Chuai, S.; Zhang, R.; Zeng, J.; Li, M.; Fan, H.; Lin, Y.; Gu, J.; Ardayfio, O.; Zhang, J. H.; Yan, X.; Fang, J.; Mi, Y.; Zhang, M.; Zhou, T.; Feng, G.; Chen, Z.; Li, G.; Yang, T.; Zhao, K.; Liu, X.; Yu, Z.; Lu,

C. X.; Atadja, P.; Li, E., Selective inhibition of Ezh2 by a small molecule inhibitor blocks tumor cells proliferation. *Proc Natl Acad Sci U S A* **2012,** *109* (52), 21360-5.
647. Konze, K. D.; Ma, A.; Li, F.; Barsyte-Lovejoy, D.; Parton, T.; Macnevin, C. J.; Liu, F.; Gao, C.; Huang, X. P.; Kuznetsova, E.; Rougie, M.; Jiang, A.; Pattenden, S. G.; Norris, J. L.; James, L. I.; Roth, B. L.; Brown, P. J.; Frye, S. V.; Arrowsmith, C. H.; Hahn, K. M.; Wang, G. G.; Vedadi, M.; Jin, J., An orally bioavailable chemical probe of the Lysine Methyltransferases EZH2 and EZH1. *ACS Chem Biol* **2013,** *8* (6), 1324-34.
648. Gehling, V. S.; Vaswani, R. G.; Nasveschuk, C. G.; Duplessis, M.; Iyer, P.; Balasubramanian, S.; Zhao, F.; Good, A. C.; Campbell, R.; Lee, C.; Dakin, L. A.; Cook, A. S.; Gagnon, A.; Harmange, J. C.; Audia, J. E.; Cummings, R. T.; Normant, E.; Trojer, P.; Albrecht, B. K., Discovery, design, and synthesis of indole-based EZH2 inhibitors. *Bioorg Med Chem Lett* **2015,** *25* (17), 3644-9.
649. Vaswani, R. G.; Gehling, V. S.; Dakin, L. A.; Cook, A. S.; Nasveschuk, C. G.; Duplessis, M.; Iyer, P.; Balasubramanian, S.; Zhao, F.; Good, A. C.; Campbell, R.; Lee, C.; Cantone, N.; Cummings, R. T.; Normant, E.; Bellon, S. F.; Albrecht, B. K.; Harmange, J. C.; Trojer, P.; Audia, J. E.; Zhang, Y.; Justin, N.; Chen, S.; Wilson, J. R.; Gamblin, S. J., Identification of (R)-N-((4-Methoxy-6-methyl-2-oxo-1,2-dihydropyridin-3-yl)methyl)-2-methyl-1-(1-(1-(2,2,2-trifluoroethyl)piperidin-4-yl)ethyl)-1H-indole-3-carboxamide (CPI-1205), a Potent and Selective Inhibitor of Histone Methyltransferase EZH2, Suitable for Phase I Clinical Trials for B-Cell Lymphomas. *J Med Chem* **2016,** *59* (21), 9928-9941.
650. Bratkowski, M.; Yang, X.; Liu, X., An Evolutionarily Conserved Structural Platform for PRC2 Inhibition by a Class of Ezh2 Inhibitors. *Sci Rep* **2018,** *8* (1), 9092.
651. Kung, P. P.; Bingham, P.; Brooun, A.; Collins, M.; Deng, Y. L.; Dinh, D.; Fan, C.; Gajiwala, K. S.; Grantner, R.; Gukasyan, H. J.; Hu, W.; Huang, B.; Kania, R.; Kephart, S. E.; Krivacic, C.; Kumpf, R. A.; Khamphavong, P.; Kraus, M.; Liu, W.; Maegley, K. A.; Nguyen, L.; Ren, S.; Richter, D.; Rollins, R. A.; Sach, N.; Sharma, S.; Sherrill, J.; Spangler, J.; Stewart, A. E.; Sutton, S.; Uryu, S.; Verhelle, D.; Wang, H.; Wang, S.; Wythes, M.; Xin, S.; Yamazaki, S.; Zhu, H.; Zhu, J.; Zehnder, L.; Edwards, M., Optimization of Orally Bioavailable Enhancer of Zeste Homolog 2 (EZH2) Inhibitors Using Ligand and Property-Based Design Strategies: Identification of Development Candidate (R)-5,8-Dichloro-7-(methoxy(oxetan-3-yl)methyl)-2-((4-methoxy-6-methyl-2-oxo-1,2-dihydropyridin-3-yl)methyl)-3,4-dihydroisoquinolin-1(2H)-one (PF-06821497). *J Med Chem* **2018,** *61* (3), 650-665.
652. Knutson, S. K.; Warholic, N. M.; Wigle, T. J.; Klaus, C. R.; Allain, C. J.; Raimondi, A.; Porter Scott, M.; Chesworth, R.; Moyer, M. P.; Copeland, R. A.; Richon, V. M.; Pollock, R. M.; Kuntz, K. W.; Keilhack, H., Durable tumor regression in genetically altered malignant rhabdoid tumors by inhibition of methyltransferase EZH2. *Proc Natl Acad Sci U S A* **2013,** *110* (19), 7922-7.
653. Hoy, S. M., Tazemetostat: First Approval. *Drugs* **2020,** *80* (5), 513-521.

654. Orleni, M.; Beumer, J. H., Pharmacology and pharmacokinetics of tazemetostat. *Cancer Chemother Pharmacol* **2024,** *93* (5), 509-517.
655. Keam, S. J., Valemetostat Tosilate: First Approval. *Drugs* **2022,** *82* (16), 1621-1627.
656. Yang, X.; Li, F.; Konze, K. D.; Meslamani, J.; Ma, A.; Brown, P. J.; Zhou, M. M.; Arrowsmith, C. H.; Kaniskan, H. U.; Vedadi, M.; Jin, J., Structure-Activity Relationship Studies for Enhancer of Zeste Homologue 2 (EZH2) and Enhancer of Zeste Homologue 1 (EZH1) Inhibitors. *J Med Chem* **2016,** *59* (16), 7617-33.
657. Kaniskan, H. U.; Jin, J., Recent progress in developing selective inhibitors of protein methyltransferases. *Curr Opin Chem Biol* **2017,** *39*, 100-108.
658. Nader, N. E.; Frederico, S. C.; Miller, T.; Huq, S.; Zhang, X.; Kohanbash, G.; Hadjipanayis, C. G., Barriers to T Cell Functionality in the Glioblastoma Microenvironment. *Cancers (Basel)* **2024,** *16* (19).
659. Anighoro, A.; Bajorath, J.; Rastelli, G., Polypharmacology: challenges and opportunities in drug discovery. *J Med Chem* **2014,** *57* (19), 7874-87.
660. Benedetti, R.; Conte, M.; Iside, C.; Altucci, L., Epigenetic-based therapy: From single- to multi-target approaches. *Int J Biochem Cell Biol* **2015,** *69*, 121-31.
661. Bolognesi, M. L., Harnessing Polypharmacology with Medicinal Chemistry. *ACS Med Chem Lett* **2019,** *10* (3), 273-275.
662. Moertl, S.; Payer, S.; Kell, R.; Winkler, K.; Anastasov, N.; Atkinson, M. J., Comparison of Radiosensitization by HDAC Inhibitors CUDC-101 and SAHA in Pancreatic Cancer Cells. *Int J Mol Sci* **2019,** *20* (13).
663. Shirbhate, E.; Veerasamy, R.; Boddu, S. H. S.; Tiwari, A. K.; Rajak, H., Histone deacetylase inhibitor-based oncolytic virotherapy: A promising strategy for cancer treatment. *Drug Discov Today* **2022,** *27* (6), 1689-1697.
664. Ribeiro, M. L.; Reyes-Garau, D.; Armengol, M.; Fernandez-Serrano, M.; Roue, G., Recent Advances in the Targeting of Epigenetic Regulators in B-Cell Non-Hodgkin Lymphoma. *Front Genet* **2019,** *10*, 986.
665. Lue, J. K.; Prabhu, S. A.; Liu, Y.; Gonzalez, Y.; Verma, A.; Mundi, P. S.; Abshiru, N.; Camarillo, J. M.; Mehta, S.; Chen, E. I.; Qiao, C.; Nandakumar, R.; Cremers, S.; Kelleher, N. L.; Elemento, O.; Amengual, J. E., Precision Targeting with EZH2 and HDAC Inhibitors in Epigenetically Dysregulated Lymphomas. *Clin Cancer Res* **2019,** *25* (17), 5271-5283.
666. De La Rosa, J.; Urdiciain, A.; Zazpe, I.; Zelaya, M. V.; Melendez, B.; Rey, J. A.; Idoate, M. A.; Castresana, J. S., The synergistic effect of DZ-NEP, panobinostat and temozolomide reduces clonogenicity and induces apoptosis in glioblastoma cells. *Int J Oncol* **2020,** *56* (1), 283-300.
667. Thakur, A.; Tawa, G. J.; Henderson, M. J.; Danchik, C.; Liu, S.; Shah, P.; Wang, A. Q.; Dunn, G.; Kabir, M.; Padilha, E. C.; Xu, X.; Simeonov, A.; Kharbanda, S.; Stone, R.; Grewal, G., Design, Synthesis, and Biological Evaluation of Quinazolin-4-one-Based Hydroxamic Acids as Dual PI3K/HDAC Inhibitors. *J Med Chem* **2020,** *63* (8), 4256-4292.

668. Hanahan, D.; Weinberg, R. A., Hallmarks of cancer: the next generation. *Cell* **2011,** *144* (5), 646-74.
669. Kamb, A.; Wee, S.; Lengauer, C., Why is cancer drug discovery so difficult? *Nat Rev Drug Discov* **2007,** *6* (2), 115-20.
670. Peters, J. U., Polypharmacology - foe or friend? *J Med Chem* **2013,** *56* (22), 8955-71.
671. Singh, H.; Kinarivala, N.; Sharma, S., Multi-Targeting Anticancer Agents: Rational Approaches, Synthetic Routes and Structure Activity Relationship. *Anticancer Agents Med Chem* **2019,** *19* (7), 842-874.
672. Fu, R. G.; Sun, Y.; Sheng, W. B.; Liao, D. F., Designing multi-targeted agents: An emerging anticancer drug discovery paradigm. *Eur J Med Chem* **2017,** *136*, 195-211.
673. Morphy, R.; Rankovic, Z., Designed multiple ligands. An emerging drug discovery paradigm. *J Med Chem* **2005,** *48* (21), 6523-43.
674. Proschak, E.; Stark, H.; Merk, D., Polypharmacology by Design: A Medicinal Chemist's Perspective on Multitargeting Compounds. *J Med Chem* **2019,** *62* (2), 420-444.
675. Yang, Y.; Mou, Y.; Wan, L. X.; Zhu, S.; Wang, G.; Gao, H.; Liu, B., Rethinking therapeutic strategies of dual-target drugs: An update on pharmacological small-molecule compounds in cancer. *Med Res Rev* **2024,** *44* (6), 2600-2623.
676. Hesham, H. M.; Lasheen, D. S.; Abouzid, K. A. M., Chimeric HDAC inhibitors: Comprehensive review on the HDAC-based strategies developed to combat cancer. *Med Res Rev* **2018,** *38* (6), 2058-2109.
677. Yang, X.; Xu, L.; Yang, L., Recent advances in EZH2-based dual inhibitors in the treatment of cancers. *Eur J Med Chem* **2023,** *256*, 115461.
678. Mellini, P.; Marrocco, B.; Borovika, D.; Polletta, L.; Carnevale, I.; Saladini, S.; Stazi, G.; Zwergel, C.; Trapencieris, P.; Ferretti, E.; Tafani, M.; Valente, S.; Mai, A., Pyrazole-based inhibitors of enhancer of zeste homologue 2 induce apoptosis and autophagy in cancer cells. *Philos Trans R Soc Lond B Biol Sci* **2018,** *373* (1748).
679. Miele, E.; Valente, S.; Alfano, V.; Silvano, M.; Mellini, P.; Borovika, D.; Marrocco, B.; Po, A.; Besharat, Z. M.; Catanzaro, G.; Battaglia, G.; Abballe, L.; Zwergel, C.; Stazi, G.; Milite, C.; Castellano, S.; Tafani, M.; Trapencieris, P.; Mai, A.; Ferretti, E., The histone methyltransferase EZH2 as a druggable target in SHH medulloblastoma cancer stem cells. *Oncotarget* **2017,** *8* (40), 68557-68570.
680. Romanelli, A.; Stazi, G.; Fioravanti, R.; Zwergel, C.; Di Bello, E.; Pomella, S.; Perrone, C.; Battistelli, C.; Strippoli, R.; Tripodi, M.; Del Bufalo, D.; Rota, R.; Trisciuoglio, D.; Mai, A.; Valente, S., Design of First-in-Class Dual EZH2/HDAC Inhibitor: Biochemical Activity and Biological Evaluation in Cancer Cells. *ACS Med Chem Lett* **2020,** *11* (5), 977-983.
681. Lu, D.; Wang, C.; Qu, L.; Yin, F.; Li, S.; Luo, H.; Zhang, Y.; Liu, X.; Chen, X.; Luo, Z.; Cui, N.; Kong, L.; Wang, X., Histone Deacetylase and Enhancer of Zeste

Homologue 2 Dual Inhibitors Presenting a Synergistic Effect for the Treatment of Hematological Malignancies. *J Med Chem* **2022,** *65* (19), 12838-12859.
682. Straining, R.; Eighmy, W., Tazemetostat: EZH2 Inhibitor. *J Adv Pract Oncol* **2022,** *13* (2), 158-163.
683. Methot, J. L.; Chakravarty, P. K.; Chenard, M.; Close, J.; Cruz, J. C.; Dahlberg, W. K.; Fleming, J.; Hamblett, C. L.; Hamill, J. E.; Harrington, P.; Harsch, A.; Heidebrecht, R.; Hughes, B.; Jung, J.; Kenific, C. M.; Kral, A. M.; Meinke, P. T.; Middleton, R. E.; Ozerova, N.; Sloman, D. L.; Stanton, M. G.; Szewczak, A. A.; Tyagarajan, S.; Witter, D. J.; Secrist, J. P.; Miller, T. A., Exploration of the internal cavity of histone deacetylase (HDAC) with selective HDAC1/HDAC2 inhibitors (SHI-1:2). *Bioorg Med Chem Lett* **2008,** *18* (3), 973-8.
684. Mormino, A.; Cocozza, G.; Fontemaggi, G.; Valente, S.; Esposito, V.; Santoro, A.; Bernardini, G.; Santoni, A.; Fazi, F.; Mai, A.; Limatola, C.; Garofalo, S., Histone-deacetylase 8 drives the immune response and the growth of glioma. *Glia* **2021,** *69* (11), 2682-2698.
685. Suva, M. L.; Riggi, N.; Janiszewska, M.; Radovanovic, I.; Provero, P.; Stehle, J. C.; Baumer, K.; Le Bitoux, M. A.; Marino, D.; Cironi, L.; Marquez, V. E.; Clement, V.; Stamenkovic, I., EZH2 is essential for glioblastoma cancer stem cell maintenance. *Cancer Res* **2009,** *69* (24), 9211-8.
686. Yap, D. B.; Chu, J.; Berg, T.; Schapira, M.; Cheng, S. W.; Moradian, A.; Morin, R. D.; Mungall, A. J.; Meissner, B.; Boyle, M.; Marquez, V. E.; Marra, M. A.; Gascoyne, R. D.; Humphries, R. K.; Arrowsmith, C. H.; Morin, G. B.; Aparicio, S. A., Somatic mutations at EZH2 Y641 act dominantly through a mechanism of selectively altered PRC2 catalytic activity, to increase H3K27 trimethylation. *Blood* **2011,** *117* (8), 2451-9.
687. Morin, R. D.; Arthur, S. E.; Assouline, S., Treating lymphoma is now a bit EZ-er. *Blood Adv* **2021,** *5* (8), 2256-2263.
688. Poole, C. J.; van Riggelen, J., MYC-Master Regulator of the Cancer Epigenome and Transcriptome. *Genes (Basel)* **2017,** *8* (5).
689. Bradner, J. E.; West, N.; Grachan, M. L.; Greenberg, E. F.; Haggarty, S. J.; Warnow, T.; Mazitschek, R., Chemical phylogenetics of histone deacetylases. *Nat Chem Biol* **2010,** *6* (3), 238-243.
690. Smirnov, P.; Safikhani, Z.; El-Hachem, N.; Wang, D.; She, A.; Olsen, C.; Freeman, M.; Selby, H.; Gendoo, D. M.; Grossmann, P.; Beck, A. H.; Aerts, H. J.; Lupien, M.; Goldenberg, A.; Haibe-Kains, B., PharmacoGx: an R package for analysis of large pharmacogenomic datasets. *Bioinformatics* **2016,** *32* (8), 1244-6.